

---

---

MULTI-OBJECTIVE INVERSION-BASED  
CONTROL  
OF BUILDING INTEGRATED  
ENERGY SYSTEMS

---

---

John Allison, MEng

A thesis submitted for the  
Degree of Doctor of Philosophy

Energy Systems Research Unit  
Department of Mechanical & Aerospace Engineering  
University of Strathclyde

Spring 2018



# Declaration of authenticity and author's rights

This thesis is the result of the author's original research. It has been composed by the author and has not been previously submitted for examination which has led to the award of a degree.

The copyright of this thesis belongs to the author under the terms of the United Kingdom Copyright Acts as qualified by University of Strathclyde Regulation 3.50. Due acknowledgement must always be made of the use of any material contained in, or derived from, this thesis.

Signed: \_\_\_\_\_

Date: \_\_\_\_\_



*To the memory of my father*

*With special thanks to my  
colleagues & family,  
who believed.<sup>†</sup>*

---

<sup>†</sup>And also to my friends, without whom this thesis could have been completed several years earlier...love you all.



# Contents

LIST OF FIGURES	vi
LIST OF TABLES	xii
NOMENCLATURE	xiii
ACKNOWLEDGEMENTS	xxvii
ABSTRACT	xxviii
<b>1</b> INTRODUCTION	1
1.1 Building-integrated microgeneration ·	2
1.2 A rationale for improved control ·	7
1.3 Research objectives ·	13
1.4 Research scope, assumptions, and limitations ·	13
1.5 Contributions of the thesis ·	16
1.6 Thesis structure/overview ·	17
<b>2</b> LITERATURE REVIEW	23
2.1 Hierarchy of energy system controls ·	23
2.2 Coordination across control hierarchy ·	27
2.3 Conventional systems-level controls ·	30
2.4 Emergence of advanced systems-level controls ·	34
2.5 MIMO control systems ·	39
2.6 RIDE control methodology ·	43
2.7 Summary ·	47
<b>3</b> RESEARCH METHOD	54
3.1 Problem specification ·	54
3.2 Developing models of the system to be controlled ·	57
3.3 Inverse dynamics of systems ·	59
3.4 Robust inversion-based control ·	60
3.5 Assessment of control systems performance ·	65
3.6 Monte Carlo experiments ·	67
3.7 Summary ·	70





<b>4</b>	<b>DYNAMIC MODELLING OF ENERGY SYSTEMS</b>	<b>  72</b>
4.1	Combustion cogeneration	• 72
4.2	Thermal energy storage	• 84
4.3	Heat emitters	• 98
4.4	Electrical energy storage	• 101
4.5	Summary	• 106
<b>5</b>	<b>DYNAMIC MODELLING OF BUILDINGS</b>	<b>  109</b>
5.1	Model structure and assumptions	• 110
5.2	Building component heat transfer	• 111
5.3	Radiation heat transfer	• 122
5.4	Internal heat gains	• 128
5.5	Solar heat gains	• 135
5.6	State-space building zone model	• 139
5.7	Validation	• 141
5.8	Summary	• 141
<b>6</b>	<b>INVERSION-BASED CONTROL OF MIMO ENERGY SYSTEMS</b>	<b>  146</b>
6.1	External differential representation	• 147
6.2	Inverse dynamics controller design	• 153
6.3	Feedback linearisation	• 169
6.4	Limitations of inversion-based control laws	• 179
6.5	Summary	• 181
<b>7</b>	<b>ROBUST INVERSION-BASED CONTROL</b>	<b>  184</b>
7.1	Equivalent control via nonlinear inversion	• 185
7.2	Generalised outer-loop controller design	• 186
7.3	Input constrained control system	• 194
7.4	Variable-structure-system control	• 202
7.5	Controller design synthesis	• 203
7.6	Summary	• 209
<b>8</b>	<b>RESULTS &amp; DISCUSSION</b>	<b>  211</b>
8.1	Systems specifications	• 211
8.2	Controller test case	• 212
8.3	Case study without thermal storage	• 221
8.4	Case study with thermal storage	• 227
8.5	Discussion & reflection	• 233
<b>9</b>	<b>PERSPECTIVES, FUTURE WORK AND CONCLUSIONS</b>	<b>  240</b>
9.1	Summary	• 240
9.2	Contribution review	• 242
9.3	Future work	• 244
9.4	Perspective	• 250



<b>A</b>	MODELLING ADDENDUM   253
A.1	Thermal energy storage tank: Bulk flow rates . 253
A.2	Building component state-space models . 256
A.3	Radiation mesh network solution . 258
A.4	Modelling of solar heat gains . 263
<b>B</b>	MODEL VALIDATION   269
B.1	Combustion cogeneration . 269
B.2	Heat emitters . 309
B.3	Building model . 311
<b>C</b>	CONTROL THEORY ADDENDUM   319
C.1	LEDR of cogeneration device . 319
C.2	Performance metrics for underdamped PDF system . 321
C.3	H-infinity loop shaping controller . 323
<b>D</b>	MATHEMATICAL REVIEW   329
D.1	Blockwise matrix inversion . 329
D.2	Jacobian linearisation of nonlinear systems . 330
D.3	Derivatives of control-affine nonlinear systems . 332



# Figures

- 2.1 Two-position control algorithms . 31
- 2.2 Block diagram of MIMO control system . 39
- 2.3 Block diagram of original RIDE structure . 46
  
- 3.1 Schematic of case study system (without TES) . 56
- 3.2 Schematic of case study system (with TES) . 56
- 3.3 Inverse dynamics concept . 60
- 3.4 Block diagram of proposed controller structure . 62
  
- 4.1 Stateflow logic diagram for mode switching of an internal combustion based CHP unit . 80
- 4.2 Stateflow logic diagram for mode switching of an Stirling engine based CHP unit . 80
- 4.3 Input-output block diagram for the cogeneration model . 81
- 4.4 Schematic of cylindrical thermal energy storage tank . 85
- 4.5 Energy and mass flows in a node  $i$  of the thermal energy storage tank . 85
- 4.6 Comparison of max function approximations for continuous mass flow rates . 93
- 4.7 Input-output block diagram for the TES model . 98
- 4.8 Schematic of hydronic radiator model . 98
- 4.9 Validity of logarithmic temperature difference . 100
- 4.10 Input-output block diagram for the radiator model . 101
- 4.1.1 Integrator wind-up for constrained battery charge . 104
- 4.1.2 Constrained battery charge with anti-windup logic . 104
- 4.1.3 Input-output block diagram for the battery model . 106
  
- 5.1 Equivalent electrical network for an  $n$ -layer building component . 112
- 5.2 Equivalent electrical network for ROM building component . 113
- 5.3 Equivalent electrical network for the IDEAS component model . 114
- 5.4 Frequency response of component models . 116
- 5.5 Non-equilibrium zone-air temperature response of models . 117
- 5.6 Non-equilibrium heat flow & energy loss response of models . 117
- 5.7 Equilibrium zone-air temperature response of component models . 118
- 5.8 Non-equilibrium zone-facing surface temperature response of component models . 118



- 5.9 Equilibrium zone-facing surface temperature response of component models . 119
- 5.10 Schematic of the network method of radiation exchange from a surface  $i$  to the remaining surfaces of an  $m$ -surface enclosure. . 123
- 5.11 Wire-frame of building zone with orientation . 141
- 5.12 Yearly total energy needs compared with the reference results . 141
  
- 6.1 Signal-flow graphs for inverse dynamics control example. . 160
- 6.2 Input-output block diagrams for control structure design sets. . 161
- 6.3 Simulation results for inverse dynamics controller . 166
  
- 7.1 Second-order system response types . 188
- 7.2 Underdamped second-order system with desired response . 190
- 7.3 Plot of two main branches of Lambert-W function . 191
- 7.4 Plot of  $\mathcal{W}_{-1}(x)$  with settling time criteria . 191
- 7.5 Comparison of settling time criterion for critically damped RIDE control (1) . 193
- 7.7 Comparison of settling time criterion for critically damped RIDE control (2) . 195
- 7.6 Input constrained control system . 195
- 7.8 Comparison of control effort for different settling time criteria . 197
- 7.9 Design trade-off curves for excess-poles placement distance . 198
- 7.10 Design trade-off curve for  $\rho = 4$  . 199
- 7.11 Family of responses for output of system with  $\rho = 4$  . 199
- 7.12 Family of responses for control effort of system with  $\rho = 4$  . 199
- 7.13 Response of systems for a range of relative degree with optimal excess pole placement . 200
- 7.14 Linear regression fit for optimal pole distance . 200
- 7.15 Engine temperature control. . 203
- 7.16 Engine temperature control with anti-windup. . 207
- 7.17 Block diagram of new NI+PDF structure . 209
  
- 8.1 Wire frame drawing of building zone modelled . 212
- 8.2 Small power demand profile for case study . 212
- 8.3 Comparison of dynamic response of mCHP outlet temperature. . 218
- 8.4 Comparison of all electrical power interactions for case 1. . 218
- 8.5 Comparison of manipulated control inputs for case 1 . 218
- 8.6 Comparison of settling time due to first step-change in thermal reference setpoint for case 1 . 219
- 8.7 Comparison of overshoot due to first step-change in thermal reference setpoint for case 1 . 219
- 8.8 Comparison of control systems performance for case 1 . 219
- 8.9 Comparison of dynamic response of mCHP outlet temperature for case 2. . 220
- 8.10 Comparison of all electrical power interactions for case 2. . 220
- 8.11 Comparison of manipulated control inputs for case 2 . 220
- 8.12 Comparison of electrical power generation for case 2. . 221





- 8.13 Comparison of electrical power error for case 2. . 221
- 8.14 Comparison of settling time due to first step-change in thermal reference setpoint for case 2 . 222
- 8.15 Comparison of overshoot due to first step-change in thermal reference setpoint for case 2 . 222
- 8.16 Comparison of control systems performance for case 2 . 222
- 8.17 Schematic of case study system (No TES) . 223
- 8.18 On/off controller for case study 2 . 224
- 8.19 Comparison of dynamic response of air temperature for cs2 [1]. . 225
- 8.20 Comparison of dynamic response of air temperature for cs2 [2]. . 225
- 8.21 Comparison of dynamic response of air temperature for cs2 [3]. . 225
- 8.22 Comparison of manipulated fuel flow rate for case study 2 . 226
- 8.23 Comparison of manipulated battery power for case study 2 . 226
- 8.24 Comparison of dynamic response of hydronic system inlet and outlet temperatures . 226
- 8.25 Comparison of all electrical power interactions over 24 h period . 227
- 8.26 State-of-charge of battery over 24 h period . 227
- 8.27 Schematic of case study system (With TES) . 228
- 8.28 Comparison of dynamic response of air temperature for cs3 [1]. . 232
- 8.29 Comparison of dynamic response of air temperature for cs3 [2]. . 232
- 8.30 Comparison of dynamic response of air temperature for cs3 [3]. . 232
- 8.31 Comparison of manipulated fuel flow rate for case study 3 . 233
- 8.32 Comparison of manipulated battery power for case study 3 . 233
- 8.33 Comparison of dynamic response of hydronic system inlet and outlet temperatures . 233
- 8.34 Time evolution of thermal storage tank temperatures . 234
- 8.35 Comparison of all electrical power interactions over 24 h period . 234
- 8.36 State-of-charge of battery over 24 h period . 234
  
- B.1 100 series test case results: fuel lower heating value (1) . 269
- B.2 100 series test case results: fuel lower heating value (2) . 269
  
- B.3 Test case 201 results: electrical efficiency . 270
- B.4 Test case 201 results: thermal efficiency . 270
- B.5 Test case 201 results: gross heat input . 271
- B.6 Test case 201 results: heat generation . 271
- B.7 Test case 201 results: fuel flow rate . 271
- B.8 Test case 201 results: combustion air flow rate . 272
- B.9 Test case 202 results: electrical efficiency . 272
- B.10 Test case 202 results: thermal efficiency . 273
- B.11 Test case 203 results: electrical efficiency . 273
- B.12 Test case 203 results: thermal efficiency . 274
- B.13 Test case 204 results: cooling water flow rate . 274
- B.14 Test case 205 results: cooling water flow rate . 275
- B.15 Test case 301 results: dynamic model states . 275
- B.16 Test case 301 results: dynamic model heat transfer . 276
- B.17 Test case 302 results: dynamic model states . 276



B.18	Test case 302 results: dynamic model heat transfer	· 277
B.19	Test case 303 results: dynamic model states	· 277
B.20	Test case 303 results: dynamic model heat transfer	· 278
B.21	Test case 304 results: engine temperature	· 278
B.22	Test case 304 results: cooling water outlet temperature	· 279
B.23	Test case 304 results: heat transfer rate	· 279
B.24	Test case 304 results: heat loss rate	· 279
B.25	Test case 305 results: engine temperature	· 280
B.26	Test case 305 results: cooling water outlet temperature	· 280
B.27	Test case 305 results: heat transfer rate	· 281
B.28	Test case 305 results: heat loss rate	· 281
B.29	Test case 306 results: engine temperature	· 282
B.30	Test case 306 results: cooling water outlet temperature	· 282
B.31	Test case 306 results: heat transfer rate	· 282
B.32	Test case 306 results: heat loss rate	· 283
B.33	Test case 307 results: dynamic model states	· 283
B.34	Test case 307 results: dynamic model heat transfer	· 284
B.35	Test case 308 results: engine temperature	· 284
B.36	Test case 308 results: cooling water outlet temperature	· 285
B.37	Test case 308 results: heat transfer rate	· 285
B.38	Test case 308 results: heat loss rate	· 285
B.39	Test case 401 results (1)	· 286
B.40	Test case 401 results (2)	· 286
B.41	Test case 402 results (1)	· 287
B.42	Test case 402 results (2)	· 287
B.43	Test case 403 results (1)	· 288
B.44	Test case 403 results (2)	· 288
B.45	Test case 404 results (1)	· 289
B.46	Test case 404 results (2)	· 289
B.47	Test case 405 results (1)	· 290
B.48	Test case 405 results (2)	· 290
B.49	Test case 406 results (1)	· 291
B.50	Test case 406 results (2)	· 291
B.51	Test case 407 results (1)	· 292
B.52	Test case 407 results (2)	· 292
B.53	Test case 408 results (1)	· 293
B.54	Test case 408 results (2)	· 293
B.55	Test case 501: engine control volume temperature	· 294
B.56	Test case 501 results (2)	· 294
B.57	Test case 501 results (3)	· 294
B.58	Test case 502 results: engine temperature	· 295
B.59	Test case 502 results: fuel flow rate	· 295
B.60	Test case 502 results: net electric output	· 296
B.61	Test case 502 results (3)	· 296
B.62	Test case 503 results: engine temperature	· 297
B.63	Test case 503 results: fuel flow rate	· 297



B.64	Test case 503 results: net electric output	· 297
B.65	Test case 503 results (3)	· 298
B.66	Test case 504 results: engine temperature	· 298
B.67	Test case 504 results: fuel flow rate	· 299
B.68	Test case 504 results: net electric output	· 299
B.69	Test case 504 results (3)	· 299
B.70	Test case 505 results: engine temperature	· 300
B.71	Test case 505 results: fuel flow rate	· 300
B.72	Test case 505 results: net electric output	· 301
B.73	Test case 505 results (3)	· 301
B.74	Test case 506 results: engine temperature	· 302
B.75	Test case 506 results: fuel flow rate	· 302
B.76	Test case 506 results: net electric output	· 302
B.77	Test case 506 results (3)	· 303
B.78	Test case 601 results	· 303
B.79	Test case 602 results	· 304
B.80	Test case 603 results	· 304
B.81	Test case 604 results	· 305
B.82	Test case 701 results	· 305
B.83	Test case 701 results: cooling water outlet temperature	· 306
B.84	Test case 702 results	· 306
B.85	Test case 702 results: cooling water outlet temperature	· 306
B.86	Test case 801 results	· 307
B.87	Test case 802 results	· 307
B.88	Test case 901 results: carbon dioxide emissions	· 308
B.89	Test case 902 results: carbon dioxide emissions	· 308
B.90	Test case 903 results: carbon dioxide emissions	· 309
B.92	Radiator empirical validation T101 results (1)	· 310
B.93	Radiator empirical validation T101 results (2)	· 310
B.91	Radiator empirical validation T102 results (1)	· 311
B.94	Radiator empirical validation T102 results (2)	· 311
B.95	Wire-frame of building zone with orientation	· 312
B.98	Test 2: Monthly energy needs for heating and cooling	· 314
B.99	Test 3: Monthly energy needs for heating and cooling	· 314
B.100	Test 4: Monthly energy needs for heating and cooling	· 314
B.96	Test 1: Monthly energy needs for heating and cooling	· 314
B.104	Test 8: Monthly energy needs for heating and cooling	· 315
B.105	Test 9: Monthly energy needs for heating and cooling	· 315
B.106	Test 10: Monthly energy needs for heating and cooling	· 315
B.97	Test 5: Monthly energy needs for heating and cooling	· 315
B.101	Test 6: Monthly energy needs for heating and cooling	· 315
B.102	Test 7: Monthly energy needs for heating and cooling	· 315
B.103	Test 11: Monthly energy needs for heating and cooling	· 316
B.107	Test 12: Monthly energy needs for heating and cooling	· 316
B.108	Yearly energy needs for heating and cooling for each test case	· 316
B.109	Yearly heating energy needs compared with the reference results	· 317



B.110	Yearly cooling energy needs compared with the reference results	· 317
B.111	Yearly total energy needs compared with the reference results	· 317
C.1	Pole-zero plot of linearised dynamic system	· 324
C.2	Singular value plot for linearised dynamic system	· 324
C.3	Singular value plot for target- and actual-loop shape	· 326
C.4	Responses to step commands	· 326
C.5	Hankel singular values of $\mathbf{K}$	· 327
C.6	Singular values of $\mathbf{K}$ and approximation error $\mathbf{K} - \mathbf{K}_r$	· 328
C.7	Responses to step commands for controllers	· 328





# Tables

1.1	Types of microgeneration technology	2
2.1	Building domain controls	33
4.2	Model parameters for battery wind-up example	106
5.1	Thermal-electrical network analogy	110
5.2	Thermophysical properties of the example external wall	116
5.3	Calculated parameters of the example wall for reduced-order models	116
5.4	Precision of reduced-order methods for temperature calculations	119
5.5	Power conversion for 'white' light sources	131
5.6	Components of heat gain dissipated from office equipment	132
6.1	Model parameters for inverse dynamics controller example	165
8.1	mCHP model parameters for case study	213
8.2	Solar PV system specifications	213
8.3	Radiator parameters for case study	214
8.4	Battery parameters for case study	214
B.1	Radiator parameters for validation test 101	309
B.2	Radiator parameters for validation test 102	310
B.3	Thermophysical properties of constructions	312
B.6	Geometrical data & boundary conditions for Test 4 & 8	313
B.7	Geometrical data & boundary conditions for Test 9 & 11	313
B.8	Geometrical data & boundary conditions for Test 10	313
B.9	Geometrical data & boundary conditions for Test 12	313
B.4	Geometrical data & boundary conditions for Test 1, 3, 5, & 7	313
B.5	Geometrical data & boundary conditions for Test 2 & 6	313
B.10	Internal solar distribution for all test cases	314
B.11	Yearly energy needs and classification level for each test	317



# Nomenclature

## Greek Symbols

<i>Symbol</i>	<i>Description</i>	<i>Dimensions</i>	<i>Units</i>
$\alpha$	absorptivity	–	1
$\alpha_i$	Coefficients of characteristic equation, $\alpha_1 = 1, i = 1, \dots, n + 1$		
$\beta$	Angle between a surface normal and a ray between two differential areas	1	1
$\beta$	Dynamic decoupling matrix		
$\chi_a$	$(a_{\min} - a_{\max}) / (a_{\min} + a_{\max})$		
$\Delta$	Perturbation from nominal value		
$\delta(s)$	Characteristic equation of LTI state-space system		
$\varepsilon$	Surface emissivity	1	1
$\epsilon$	small positive number $\approx 1 \times 10^{-6}$	1	1
$\eta$	Efficiency	1	1
$\Gamma$	Distribution matrix	1	1
$\gamma$	Distribution vector	1	1
$\kappa$	Empirical coefficient		
$\lambda$	Thermal conductivity	$\text{MLT}^{-3}\Theta^{-1}$	$\text{W m}^{-1}\text{K}^{-1}$
$\mu$	System input		
$\mu$	System input vector, comprised of the system inputs		
$\mu$	System input vector		



$\mu_i$	System input $i$		
$\nu_i$	Coefficients of numerator polynomial		
$\Omega$	Region of state-space		
$\omega_n$	Undamped natural frequency		
$\Phi$	Heat flow rate	$ML^2T^{-3}$	W
$\varphi$	Arcic heat flow rate		$W m^{-2}$
$\varphi(\cdot)$	Higher-order external differential equation		
$\phi$	Heat flow rate vector	$ML^2T^{-3}$	W
$\psi$	Exogenous input vector		
$\rho$	Density		$kg m^{-3}$
$\rho$	Relative degree		
$\rho$	Vector relative degree		
$\Theta$	Thermodynamic temperature	$\Theta$	K
$\tau$	Time constant / variable of integration	T	s
$\Theta$	Thermodynamic temperature	$\Theta$	K
$\theta$	Temperature vector	$\Theta$	K
$\Xi$	Controlled system		
$\Xi$	State-space system		
$\zeta$	Damping ratio		

### Mathematical signs and symbols

<i>Symbol</i>	<i>Meaning / verbal equivalent</i>
$\Delta x$	Finite increment of $x$ i.e. $\Delta x = x_2 - x_1$
$\mathbb{1}(\cdot)$	Heaviside step function
$I_i$	$i \times i$ identity matrix
$\mathcal{J}$	Performance index
$\mathcal{L}$	Laplace transform
$\mathbb{R}$	The set of real numbers



$\mathbb{R}$	The set of real numbers
$\mathbb{R}^{i \times j}$	$i \times j$ matrix of real numbers
$\mathbb{R}^{i \times j}$	$i \times j$ matrix of real numbers
$V_n^k$	number of variations without repetition
${}^R V_n^k$	number of variations with repetition
$\mathcal{X}, \mathcal{U}$	Subset of a set of numbers

### Roman Symbols

<i>Symbol</i>	<i>Description</i>	<i>Dimensions</i>	<i>Units</i>
$A$	State-space system matrix		
$A$	Area	$L^2$	$m^2$
$A$	Surface area		$m^2$
$a$	Amplitude	–	1
$a$	General model parameter		
$\check{b}$	logical boolean variable $\check{b} \in \mathbb{Z} : \check{b} \in [0, 1]$	1	1
$B$	System/plant input matrix		
$C$	Heat capacity matrix	$ML^2T^{-2}\Theta^{-1}$	$JK^{-1}$
$C$	System output matrix		
$C$	Heat capacity	$ML^2T^{-2}\Theta^{-1}$	$JK^{-1}$
$c_p$	Specific heat at constant pressure	$L^2T^{-2}\Theta^{-1}$	$Jkg^{-1}K^{-1}$
$D$	Feedforward matrix		
$d$	Thickness		$m$
$E$	System perturbation matrix		
$E$	Energy	$ML^2T^{-2}$	$J$
$e$	Tracking/regulation error		
$E_b$	Blackbody emissive power	$MT^{-3}$	$W m^{-2}$
$F$	Output perturbation matrix		
$F$	View factor	1	1





$f$	fraction of heat	–	1
$G(s)$	Transfer function matrix		
$g(\cdot)$	System input function		
$g$	solar energy transmittance	–	1
$G(s)$	Transfer function		
$H$	Heat transfer matrix	$ML^2T^{-3}\Theta^{-1}$	$WK^{-1}$
$h$	Heat transfer vector	$ML^2T^{-3}\Theta^{-1}$	$WK^{-1}$
$H$	Heat transfer coefficient	$ML^2T^{-3}\Theta^{-1}$	$WK^{-1}$
$h$	Surface heat transfer coefficient		$Wm^{-2}K^{-1}$
$I$	Electric current	I	A
$i$	Index number	–	1
$J$	Radiosity	$MT^{-3}$	$Wm^{-2}$
$K$	Controller gain matrix		
$K$	Controller gain		
$k$	component/source/element index	–	1
$L$	Combination matrix	1	1
$l$	Length	L	m
$l$	Number of no-mass components within a building zone	–	1
$\overline{LHV}$	Lower heating value	$L^2T^{-2}$	$Jkg^{-1}$
$M$	Mass flow rate matrix	$MT^{-1}$	$kg s^{-1}$
$m$	Mass	M	kg
$m$	Number of enclosure components within a building zone	–	1
$m$	Number of system inputs		
$m$	mass	M	kg
$\dot{m}$	Mass flow rate	$MT^{-1}$	$kg s^{-1}$
$\dot{m}$	Mass flow rate vector	$MT^{-1}$	$kg s^{-1}$
$N(s)$	Numerator polynomial matrix		



$N$	General integer placeholder	–	1
$n$	Number of nodes / system order	–	1
$n$	Number of system states		
$\overline{OS}$	Overshoot		
$P$	Combination matrix	1	1
$P$	System inertia compensator		
$P$	Electrical power	$ML^2T^{-3}$	W
$p$	Number of internal heat gain sources within a zone	–	1
$p$	Number of system outputs		
$Q$	Input coupling matrix		
$Q$	Heat, amount of heat	$ML^2T^{-2}$	J
$q$	Electric charge	IT	C
$\dot{R}$	Radiative resistance	$L^{-2}$	$m^{-2}$
$R$	Conductive/convective thermal resistance		$KW^{-1}$
$r$	Distance between two surfaces	L	m
$r$	Poles (roots) of a characteristic equation		
$S$	Random number in open interval (0, 1)		
$s$	Complex Laplace variable		
$\overline{SOC}$	State-of-charge	1	%
$T$	Transformation matrix		
$T$	Amount of time		
$T$	Period of variations	T	s
$t$	Time	T	s
$U$	Weighting of control effort		
$u$	Control input vector		
$U$	Thermal transmittance under steady-state		$Wm^{-2}K^{-1}$



$U$	Voltage	$L^2MT^{-3}I^{-1}$	V
$u$	Control variable		
$V$	Synthetic control input vector		
$V$	Volume	$L^3$	$m^3$
$v$	Synthetic control input		
$\dot{W}$	Work rate	$ML^2T^{-3}$	W
$w$	Measured input vector		
$W$	Work, amount of work	$ML^2T^{-2}$	J
$w$	Measured input		
$x$	State vector		
$x$	State-variable		
$\dot{x}(t)$	State differential equation		
$x_i$	State variable $i$		
$Y$	Weighting of tracking errors		
$y$	Output vector		
$Z$	Percentage accuracy of parameter value		

### Subscripts

<i>Symbol</i>	<i>Description</i>
0	Nominal value
A	appliances
air	air
AM	arithmetic mean
aux	auxiliary
B	bottom
bat	battery
cap	capacity
c	convective



CHP	combined heat and power unit
cl	clothing
cond	conduction
cp	coupling
cw	cooling water
D	Pseudo-derivative
d	Desired/demanded
dem	demand
df	distribution factor
E	electrical
e	external
eff	effective
em	external mass
eng	engine
env	environment
eq	Equivalent
eq	equivalent
er	external-surface ↔ apparent sky
F	frame area
gen	generation
hg	Heat gain source
HX	heat exchanger
I	Integral
ICE	internal combustion engine
i	inlet
i	internal
im	internal mass
int	internal heat gain





I/O	input-output
L	lighting
lin	linear
LL	Lower limit
LL	lower limit
LM	logarithmic mean
lr	long-wave radiative
max	Maximum value
met	metabolic
min	Minimum value
nm	no mass
nom	nominal value of variable at the operating point of the system
o	Operation point
Oc	occupant
o	outlet
p	Peak
Q	thermal/heat
rad	radiator
r	radiative
s	Settling
SE	Stirling engine
se	surface external
sh	shading
si	surface internal
sol	solar
s	surface
ss	mean external-surface and effective sky temperature
T	top



TES	thermal energy storage tank
tot	total
tr	transmission
UL	Upper limit
UL	upper limit
vf	view factor
w	water

### **Acronyms**

AC	alternating current
BACS	building automation and control systems
BEMS	building energy management systems
BES	building energy simulation
BMS	battery management system
BPS	building performance simulation
CCGT	combined cycle gas turbine
CCHP	micro-combined cooling heat and power
CFD	computational fluid dynamics
CHP	combined heat and power
CHPV	combined heat and photovoltaics
COP	coefficient of performance
CSD	control structure design
DC	direct current
DLM	dominant layer method
DSM	demand-side management
DSR	demand side response
EDR	External Differential Representation
EES	electrical energy storage
EPBD <sub>2</sub>	Energy Performance of Buildings Directive



EPC	Energy Performance Certificate
EU	European Union
EV	electric vehicle
FIT	feed-in tariff
GHG	greenhouse gas
GSHP	ground source heat pump
HHV	higher heating value
HSV	Hankel singular values
HVAC	heating, ventilation, and air conditioning
ICE	internal combustion engine
ICT	information and communications technology
IDEAS	inverse dynamics based energy assessment and simulation
IEA	International Energy Agency
IMC	internal model control
IO	input-output
IPCC	Intergovernmental Panel on Climate Change
IR	infrared
LED	light-emitting diode
LEDR	linear external differential representation
LEN	local electrical network
LHS	Latin Hypercube Sampling
LHV	lower heating value
LPM	lumped parameter model
LQG	linear-quadratic-Gaussian
LQR	linear-quadratic regulator
LTI	linear time-invariant
MC	Monte Carlo
mCHP	micro combined heat and power



MGT	microgeneration technology
MIMO	multi-input multi-output
MPC	model predictive control
MPP	maximum power point
MPPT	maximum power point tracking
NCM	National Calculation Methodology
NI+PDF	nonlinear inversion plus pseudo-derivative-feedback
NZEB	nearly zero-energy building
ODE	ordinary differential equation
ORIGIN	Orchestration of Renewable Integrated Generation In Neighbourhoods
P	proportional
PCM	phase change material
PDF	pseudo-derivative-feedback
PI	proportional-integral
PID	proportional-integral-derivative
PV	photovoltaics
PVT	photovoltaic thermal
RES	renewable energy sources
RET	renewable energy technology
RIDE	robust inverse dynamics estimation
RMS	root-mean-square
RMSE	root-mean-square error
ROM	reduced order model
SAP	Standard Assessment Procedure
SBEM	Simplified Building Energy Model
SE	Stirling engine
SISO	single-input single-output
SL	systems level





SME	small and medium-sized enterprise
SOC	state-of-charge
TES	thermal energy storage
UK	United Kingdom
UV	ultraviolet



# Glossary

**building component** These are the structural building elements that form the enclosure of a building zone e.g. walls, floor/ground, and ceiling/roof. These can be pre-fabricated and consist of many constituent layers of different types of material that form the whole component. [104](#)

**building zone** An area of a building that can be distinguished from all others in contact with it by the activity within it, the HVAC system serving it, the lighting system within it, or its access to daylight. [105](#)

**built environment** the totality of places built or designed by humans, including buildings, grounds around buildings, layout of communities, transportation infrastructure, parks and trails, and features of locations where food is marketed, sold and served. [1](#)

**CO<sub>2</sub> emissions** carbon dioxide (CO<sub>2</sub>) emitted to the atmosphere through human activities, primarily produced by the burning of fossil fuels (coal, natural gas, and oil). [1](#)

**damping ratio** This ratio reflects the level of damping of a system's response, it is expressed as the ratio of a system's exponential decay frequency to natural frequency. A value of  $\zeta = 1$  indicates a critically damped response. [44](#)

**final energy consumption** energy that is supplied to the consumer for all final energy uses such as heating, cooling and lighting. [2, 5](#)

**greenhouse gas** any gaseous compound in the atmosphere that is capable of absorbing infrared radiation, thereby trapping and holding heat in the atmosphere. [1](#)

**higher heating value** the gross thermodynamic amount of heat produced by combustion of a fuel. [5](#)

**hydronic system** Hydronics is the use of water (or another liquid medium) as the heat-transfer mechanism in heating and cooling systems. The hydronic system is the network of components that facilitates the movement of the liquid/steam around the building. [12, 23](#)

**microgeneration** on-site small-scale renewable and low-carbon technologies. [2](#)



**multi-input multi-output (MIMO) control system** A control system with more than one manipulable input and more than one controlled output. 38

**nearly zero-energy building** a building that has a very high energy performance indicator, measured in  $\text{kW h m}^{-2} \text{ yr}^{-1}$ , whose value is determined at a national or regional level. The nearly zero or very low amount of energy required should be covered to a very significant extent by energy from renewable sources (including energy from on-site production or nearby). 2

**primary energy consumption** the direct use of energy at the source, or supply to users without transformation, of crude energy, that is, energy that has not been subjected to any conversion or transformation process. 2

**robust control** A robust control system provides stable, consistent performance – as specified by the designer – in spite of the wide variation of plant parameters and disturbances. 54

**state variables** The set of variables that describe a system of dynamic equations. 52

**state-space** A time-domain model comprised of the state differential equation(s) and output equation(s). 51

**undamped natural frequency** The frequency of oscillations of the system without damping. 44



*“It’s not worth doing something unless someone, somewhere, would much rather you weren’t doing it.”*

---

—TERRY PRATCHETT, *from the foreword to The Ultimate Encyclopaedia of Fantasy*, by David Pringle

## Acknowledgements

The role of supervisor has changed hands many times over the course of this work: My thanks to Professor John Counsell for first taking up the reins and showing me the fascinating world of controls. Thanks to Dr James Biggs, who then took me on and allowed me the freedom to chase many different threads in my research. And ultimately to Dr Nick Kelly, who not only pushed me to complete this work, but whose sharp eyes and diligence prevented confusing glitches from ever reaching these pages.

I would also like to thank my colleagues in ESRU for their advice and encouragement over the years; you have expedited my progress as a researcher a great deal.

To my friends and family; you have supported me through these years, listened to my many ramblings and picked me up on the days where I had nothing left. It might have saved you a lot of time if I just gave up and went mad, but you saw it through to the end with me. Thank you.

This research was funded in partnership with a BRE Trust grant as part of the University of Strathclyde’s BRE Centre of Excellence in Energy Utilisation and with an EPSRC research grant (EP/ P505747/1).





# Abstract

Buildings are a key target for energy efficiency measures and the integration of renewable technologies. However, a high penetration of intermittent renewable energy in the electrical grid and in the buildings themselves will result in a reduction of the grid's ability to absorb excess generation freely.

One method for improving the efficiency of buildings and addressing the intermittent availability of renewables is to make them more energy autonomous i.e. creating and consuming the majority of their own energy. The needs of a building cannot usually be met by a single energy resource alone, but requires the adoption and coordinated operation of a multitude of energy sources such as combined heat and power (CHP) units, thermal energy storage (TES), electrical energy storage (EES) and photovoltaics (PV). Making these systems work together presents a control challenge for their efficient use, especially since they can have a simultaneous effect on both the thermal and electrical energy networks.

This research addresses the design of a robust multi-input multi-output (MIMO) controller applicable to any configuration of the aforementioned systems, with the control goal of minimising the electrical grid utilisation of a building while fulfilling the thermal demands of the building. The controller employs the inverse dynamics of the building, mechanical/servicing systems, and energy storage with a robust control methodology. This inverse dynamics provides the controller with knowledge of the complex cause and effect relationships between the system, the controlled inputs, and the external disturbances, while an outer-loop control ensures robust, stable control in the presence of modelling deficiencies/uncertainty and unknown disturbances. The physical limitations of the systems are also accounted for via variable structure control whereby the control strategy employed switches depending on the current utilisation and availability of the energy supplies.

Results indicate that the control strategy is effective in minimising the electrical grid use and maximising the utilisation of the available energy when compared to conventional system operation.



*“The biggest gap today is between what science allows us to do, and what really happens in the political and economical world that we inhabit. We don’t need new inventions to improve the world, we just need proper applications of those we already have.”*

---

—MARTIN REES, *A Cosmic Perspective for the 21st Century*

1

## Introduction

THE need to address climate change has placed an increased emphasis on energy efficiency as a cost-effective means for the reduction of **greenhouse gas** (GHG) emissions. This commitment to expanded energy efficiency measures coupled with the increasing difficulty of extracting fossil fuels has also resulted in growth in the utilisation of renewable energy to ensure a sustainable, energy secure future.

There are numerous targets set at National and European levels with regards to combating climate change. The Climate Change (Scotland) Act 2009 has set an ‘interim target’ for a 42 % reduction in GHG emissions from the 1990 baseline levels by 2020, with the ‘2050 target’ of an 80 % reduction in emissions (1). These objectives align with the UK Climate Change Act 2008 that sets a target for an 80 % reduction by 2050 (2, c.27). Widening the perspective, the European Union (EU) has defined the so-called 20-20-20 targets: a 20 % reduction in GHG emissions; a 20 % improvement in energy efficiency; and deployment of 20 % of energy generation from renewable sources by 2020 (3). The specific target for the UK is that 15 % of energy consumed should come from renewable sources by 2020 (4). With further targets of 40-27-27 for 2030 adopted by EU leaders in October 2014 (5) and a key goal of 80 % to 95 % reduction in GHG emissions by 2050 (6) that is required to avoid severe climate change (7).<sup>1</sup>

The **built environment** is within the purview of these targets as it makes an extensive contribution to the global production of **CO<sub>2</sub> emissions** and energy use, with the building sector being the largest overall energy-consuming sector (8, p. 7). Within the sphere of the built environment, existing buildings account for 40 % of global **primary energy consumption** (9, p. 1) and also 40 % within the EU (8, p. 72). Similarly, buildings accounted for 32 % (118.6 EJ) of total **final energy consumption** in 2012 (10,

---

<sup>1</sup>It is probable that this amount of reduction is required to limit global warming (relative to pre-industrial levels) to 2 °C.

**Table 1.1 | Types of microgeneration technology.** The specific energy conversion process of each technology is provided.

Technology	Type(s)	Renewable	Primary energy source	Energy produced
Solar PV		✓	Sun	Electrical
Micro-hydro		✓	Sun	Electrical
Micro-wind		✓	Sun	Electrical
Micro-CHP	ICE		Natural gas <sup>a</sup>	Thermal+Electrical
	SE		Natural gas <sup>a</sup>	Thermal+Electrical
	Fuel cell		H <sub>2</sub> , CO, CH <sub>4</sub> , other <sup>b</sup>	Thermal+Electrical
Solar thermal		✓	Sun	Thermal
Biomass boilers		✓	Biomass	Thermal
Heat pumps	Air source	✓ <sup>c</sup>	Electricity	Thermal
	Ground source	✓ <sup>c</sup>	Electricity	Thermal

<sup>a</sup> There also exists prototype combustion-based CHP units that can run on biogas/biomass (16, 17) but the commercial availability is limited.

<sup>b</sup> The variable technology of fuel cells allows their fuel supply to be flexible as they can also be supplied with various light hydrocarbons, and may also be able to use biomass sources in the future (18).

<sup>c</sup> Renewable if grid is decarbonised.

p. 46). This figure is supported by the Intergovernmental Panel on Climate Change (IPCC) who state that the building sector accounted for 32 % of final energy use and 8.8 GtCO<sub>2</sub> emissions in 2010 (11, p. 22). In response, the EU has produced legislation to reduce the final energy consumption and CO<sub>2</sub> emissions of buildings.

The Energy Performance of Buildings Directive (EPBD<sub>2</sub>) 2010/31/EU on the energy performance of buildings has decreed that all new buildings be **nearly zero-energy buildings** (NZEBS) from 2020-12-31 (12, Article 9), with member states of the EU to also draw up national plans for increasing the number of NZEBs. There are two complementary approaches to meet these targets; with energy efficiency measures within buildings being cited as among “the most environmentally friendly and cost-effective instruments for emission reductions” (11, p. 23). Alongside energy efficiency efforts, greater implementation of renewable energy technologies (RETs) within buildings will be required to meet the major reduction targets in total building-related energy demands, with the UK and global uptake in the deployment of RETs steadily increasing (13, p. 344). As such, methods that improve the energy efficiency of building operations and aid in the integration of RETs to new and existing buildings is of utmost importance.

## **1.1 Building-integrated microgeneration**

**Microgeneration** technologies – on-site small-scale renewable and low-carbon technologies – are positioned to address both the building energy efficiency requirements and integration of renewables into buildings. Put simply; microgeneration technology facilitates energy production *in* the building *for* the building, which can provide a considerable improvement over the current model of centralised power stations servicing national-scale electrical grids. The UK definition of microgeneration was specified in the Climate Change and Sustainability Act 2006 as being systems that produce up to 50 kW for electricity and up to 300 kW for heat (14); however, most technologies integrated into residential-scale buildings are capped at 4 kWe and 30 kWth (15).

### **1.1.1 Available technologies**

The range of technologies that fall under the umbrella of microgeneration is wide, with the majority suitable for building integration. Table 1.1 summarises the primary microgeneration technologies that are available.

#### **Renewable microgeneration**

It is immediately apparent from table 1.1 that half of the microgeneration technologies available are renewable, which provides an immediate and obvious advantage in regards to the traditional view of energy efficiency since they do not require any import



of fuel for energy generation within the building. A defining property of the majority of renewable technologies (biomass excluded) is that their energy production is intermittent i.e. their power output is dependent on the prevailing weather conditions.

For solar photovoltaics (PV) and solar thermal systems, it is understood that their power output varies throughout the day based on the solar irradiance incident on the modules. The output of these systems will reach their maximum production in summer, where in the UK power output typically peaks for 4 h to 5 h, with potentially only 1 h of peak output in the winter. The amount of energy produced is also affected by shade and can exhibit minute-to-minute changes in power output based on cloud cover and rain.

Micro-hydro systems are usually run-of-river systems as opposed to the large-scale dams used in national-scale power plants. The output of these systems is dependent on the water cycle and seasonal rain – with more rain increasing the water level in the river which in turn enhances the strength of the water flow through the turbines placed in the stream.

Wind turbines are directly dependent on the local wind speed, with the highest power production typically during winter as it is the windiest season. It is worth pointing out that wind turbines also have a maximum and minimum operational speed. The maximum speed restriction can lead to the unfortunate situation where there is *too much* wind to produce a power output. So conversely, there are also occasions when the wind speed is too low to operate the turbines. Coupled with the fact that wind speed can change on very short time-scales leads to an intermittent resource with a power output that is highly irregular and discontinuous at the wind speed limits of the turbine.

A complete overview of the variability of renewables was compiled by the International Energy Agency (IEA) in 2005 (19) and goes into more detail than is required for the context herein. Essentially it is identified that all renewable microgeneration technologies have inherent intermittent availability which is a key issue for wide-scale uptake of microgeneration for ensuring a reliable, secure supply of energy to the building.

Related to its availability, the sizing of the electrical producing microgeneration for the needs of a building can be a complex task as it is dependent on both the location of installation and the anticipated power requirements. Further complications can arise from the deployment of multiple microgeneration technologies within a single building and/or the availability of electrical energy storage (EES).<sup>2</sup> In any case, fulfilling the electrical demands of a building with a single technology is unlikely, simply due to

---

<sup>2</sup>EES is almost exclusively implemented via batteries for micro-scale technologies.





the mismatch between when the power is available and when it is required. Another factor is that microgeneration can come at a significant capital cost, so installation of enough microgeneration technologies to cover the majority of the demand may not be possible from a purely fiscal point of view. This ‘under-sizing’ of the systems will then place more reliance on backup generators or the electrical grid if either are available. When there is simply not enough power available to cover the electrical demands of the whole building, implementation of load-shedding schemes to parts of the building may be necessary, or at worst there will be a loss of the power supply – an unacceptable situation.

### **Low-carbon heating**

In contrast to the electrical energy generating microgeneration technologies (MGTs) the majority of the heat energy generating MGTs can be controlled to produce heat-on-demand (excluding solar thermal, for which the discussion in the previous section applies). Heat pumps rely on the availability of electrical supply to operate, where the electricity is being used to ‘move’ heat from an external environment into the building via a type of refrigeration process. The ratio of thermal energy produced to electrical energy consumed is typically called the coefficient of performance (COP) of the heat pump. The COP is not a static attribute of a heat pump as it is dependent upon the external and internal temperatures, which obviously vary seasonally. Reported COP of units is its steady-state performance under fixed testing conditions. It also does not account for the self-consumption of the heat pump for its internal components.

Different operating conditions can lead to contrast in observed performance between field deployments and what is achieved in laboratory conditions. While an in-depth discussion of this disparity is out of the scope of this research, a considerable field trial (20) was conducted in the UK on the performance of 83 heat pumps in homes between 2008 and 2010 that provides a good indication of the variability in performance of heat pumps. The important outcome to note is that the real-time performance of a heat pump is hard to predict due to its dependence on the external temperature. Therefore, a heat pump can have a complex interaction with the electrical and thermal networks within a building due to its variance in energy consumption versus energy delivery.

Nevertheless, if the energy extracted from the environment is considered as a renewable source, and heat pumps are coupled in some way with the renewable electrical generating MGTs in a building, it would lead to a 100 % renewable and controllable thermal energy resource. Moreover, due to their controllable nature, heating MGTs can either be sized to supply the bulk of the heating demand of the



building or to supply a ‘base-load’ that can be topped up using auxiliary heating systems. Auxiliary heating is typically provided by a boiler or a type of electric heating, such as radiant, convection, fan or storage heaters. Using multiple systems in this manner adds complexity to the control of the overall system.

Micro combined heat and power (mCHP) units are unique among the microgeneration technologies in that they produce heat and electrical power simultaneously. Although commonly fuelled by fossil fuels, these units improve the primary fuel conversion efficiency compared to traditional power plants as the heat typically lost to the atmosphere in the burning of the fossil fuels is captured and utilised within the building. At the same time the electrical energy generation at the point-of-use also eliminates the need for long-range energy transmission from centralised power plants,<sup>3</sup> which can then contribute to a reduction in the need for new generation and transmission infrastructure.

The overall efficiency of the mCHP technologies is reported as 75 % to 85 % of the **higher heating value** (HHV) of the fuel supply (21, p. 154). This efficiency range is greater than that of the combined cycle gas turbine (CCGT) technologies used in large-scale power plants, attributed to the previously mentioned utilisation of the typically wasted heat. The electrical efficiency is most variable between the different technologies, with internal combustion engine (ICE)-based engines typically achieving 25 % to 30 % (21, p. 156). Stirling engine (SE)-based mCHP units’ electrical efficiency depends on the design of the engine, with kinematic designs managing only 4 % to 6 % (21, p. 156) and free piston based engines attaining up to 12 % (21, p. 157). Fuel cells achieve far greater electrical efficiencies than either combustion-based technologies, which can reach up to 50 % (21, p. 158).

As with heat pumps, operational efficiencies in real-world deployments can stray from those calculated in manufacturer’s tests, owing to their limited range of operating control patterns. It is also important to recognise that all mCHP units have internal/auxiliary components that require electricity to operate (low-level embedded controllers, pumps, fans). The power consumption of these elements is most important during start-up/cool-down/standby modes of operation, as the units will not be generating any electrical power to supply these items. During these modes of operation, these components will draw power from an external source.

While the fact that natural gas currently fuels mCHP units means that they are not a zero-carbon solution,<sup>4</sup> as noted in table 1.1, units are being developed that will be able to run on biogas/biomass that ensures the long-term suitability of these technologies (21,

---

<sup>3</sup>It is estimated that the losses from the transmission wires can be up to 9.5 % of **final energy consumption**.

<sup>4</sup>Although natural gas does find itself with the lowest carbon content of the fossil fuels.



p. 154). Even when fuelled by fossil fuels, research has shown a reduction in emissions with the current mCHP systems installed in various commercial buildings (22).

### 1.1.2 *The future of microgeneration*

The EU Parliament has recognised that microgeneration will become an integral part of the future of the EU energy system with the adoption of the Microgeneration Resolution (23). The outline of the main advantages to an increase in microgeneration deployment are:

- Will result in a reduction in the import of energy from other countries by increasing the proportion of renewables in the overall energy system (energy security);
- An abatement of CO<sub>2</sub> emissions;
- Enables efficient electricity consumption close to the point of generation while avoiding transmission losses;
- Promotes creation of new jobs and promotion of economic growth;
- A boost to ‘community cohesion’ as communities become energy producers leading to a more sustainable and participative society.

With the recognition of these apparent benefits, the analysis of microgeneration technology and its affect on many elements of society is vast. There are investigations into the implications of wide-scale uptake of microgeneration and how this can affect the internal energy market in the EU (24). The creation of ‘smart energy infrastructure’ for their integration into the national grid (25, 26). The environmental (27) and local sustainability (28) impact of microgeneration. The implications of wide-scale uptake of microgeneration on the distribution (gas pipes and electrical wires) network (29). The factors influencing adoption of microgeneration (30, 31), lifecycle analysis (32), and also government policy support schemes (33) are but a few examples. The technological development of new and improved microgeneration units is also an entire field of research in of itself.

This research is concerned with a small portion of the microgeneration discussion that being the *operation and control* of *building-integrated* microgeneration, from the single household to small and medium-sized enterprise (SME) scale.<sup>5</sup> One approach to meet the strict goals on emission reduction and energy efficiency is more intelligent

---

<sup>5</sup>It is acknowledged that changes to the control and operation of microgeneration may have an effect on several of the aforementioned topics but that is not within the scope of this research.



and efficient use of the technologies already at our disposal. The field of research into control of MGTs is still at an early stage of development, with domestic-scale technologies to “face steeper technological challenges, as the operating conditions they are subjected to cannot be controlled so tightly” (15, p. 28). The following section addresses many of the hindrances to the wide-spread use of MGTs that improvements to their control have the potential to overcome.

## **1.2** A rationale for improved control

### **1.2.1** *Intermittent sources and energy storage*

Microgeneration is frequently coupled with energy storage and collectively known as ‘distributed resources’. Instinctively, the pairing of these technologies facilitates control of otherwise intermittent resources by storing generated energy and then dispatching it from the storage when called upon from energy demands of the building.

The electrical-power-generating MGTs specifically benefit from being deployed in tandem with EES. The power output of micro-wind turbines can be erratic and are highly unlikely to match the electrical demands of the building at any given instant. However, the power output could first pass through a battery (assuming suitable charge controllers are available to accommodate) and then the batteries can be used to service the instantaneous electrical demands. Similarly, solar PV power output can be stored in banks of batteries during the day, and then the stored energy in the batteries can be used to satisfy electrical demands at night. Another benefit of EES is that – provided prior charging – it can be used to supply the power to the auxiliary components of the mCHP during the modes of operation where the mCHP is not generating its electrical energy (i.e. during start-up/cool-down/standby).

There are some barriers to the use of EES becoming commonplace with microgeneration deployments. The main reason being that they are considered to be “impractical and expensive” (21, p. 144). Aside from the upfront capital cost the life-expectancy of batteries is expected to be approximately 10 yr (34) (compared to estimated 25 yr for solar PV modules (35)), which adds further expense to the overall lifetime costs of the system due to battery replacement. Despite this, it is worth noting here that this research does not consider what is the most ‘economic’ use of the technologies, but rather considers their operation and use assuming they are available within the building.

Energy storage is not only advantageous for the intermittent resources, but also allows for flexible operation of the cogeneration devices. Thermal energy storage offers greater flexibility for a building with a mCHP unit in many ways:





- It can work in parallel with mCHP to fulfil heating demands of the building, which also often allows for a smaller unit to be deployed than without storage due to not needing to fulfil peak heating demands with the mCHP alone;
- It can reduce the on/off cycling of the mCHP unit by charging thermal store over time and then utilising the store instantaneously to fulfil the thermal demands as required;
- The mCHP can decouple from the heat network by passing its thermal output to the storage and operating based on the electrical requirements of the building.

The low-carbon heat microgeneration such as heat pumps may also benefit from thermal energy storage by allowing them to operate flexibly in time. Flexible operation in time is achieved by operating the heat-led technology at times of reduced electricity cost and passing the heat output to energy storage. The energy storage is then controlled to fulfil the thermal demands at times of increased electricity cost.

The sizing of the energy storage can become a complicated task. The factors that influence the sizing of the energy storage are how many, what types, and the relative sizes of the MGTs installed in the building. The thermal and electrical demands of the building have a considerable effect on the extent of the storage required. Finally, the level of interaction that is allowed with the external electrical network will impact the amount of storage installed in the building (discussed in the following section). Another problem is that all rechargeable storage technologies suffer from self-discharge, so the energy stored in the device will dissipate over time. This wasted energy has an effect on the overall efficiency of the system within the building.

### 1.2.2 *Electrical grid interaction*

The building's connection to the local electrical grid network is the prevalent 'solution' to the mismatch between the electrical power generation in the building and electrical demands of the building. When the combined utility of electrical energy storage, 'dispatchable' electrical-power generating microgeneration, and renewable resources cannot fulfil the electrical requirements of the building, then the building will import electrical power from the local network. Conversely, when there is an excess generation from all sources, then the building will export the surplus to the local network.

The future ability of buildings to freely import and export from/to the local electrical network at will may be coming to an end. As the local electrical network itself becomes more dependent on renewable resources, it will impact the stability of the grid as it becomes harder for utilities to regulate the supply. It can also affect the safety of the network as in the case of a power outage in the local network. In this case, the



building may still export to the grid causing unexpected power to be present on the transmission network.

Already countries such as Japan have placed restrictions on export to the grid, where mCHP systems are not allowed to export to the grid, but solar PV systems still are (36). There is a financial incentive for them (in the form of feed-in tariffs) to export the excess PV electricity to the grid. However, this has resulted in added reinforcement of the transmission and distribution networks to cope with this. A consequence of this is most Japanese mCHP plants only generate energy for consumption within the building (37). These regulations may eventually extend to other countries as they struggle to cope with more and more export from buildings at the same time as the network's intermittent resources are active on the network. An indicator of this is the reduction seen in the feed-in tariffs (FITs) being offered by governments for export of energy to the grid.

There may also become a time for which connection of mCHP to the local electrical network may incur a charge to cover the costs of network reinforcement required to accommodate the export from the unit (38). While a grid connection may be available in the short term, it is evident that eventually control strategies will need to be devised to cope with the (temporary or not) absence of a local electrical network.

As an added side-effect of the grid connection domestic-scale system often use an asynchronous alternating current (AC) generator connected to the mCHP unit which does not allow for load modulation (21, p. 163). The lack of potential for load modulation will inhibit the control of the mCHP unit if it can only run at a fixed speed.

### 1.2.3 *Technology combinations & hybrid systems*

As eluded to in the previous sections there is a synergy between some of the MGTs that can work together to fulfil the thermal and electrical demands of the building. The emerging technology combination is that of mCHP and solar PV or shorted to combined heat and photovoltaics (CHPV). CHPV is a combination that is receiving interest in Japan, likely due to the structure of the FIT mentioned earlier. The mCHP can be used to fulfil the majority of the electrical loads of the building with a small amount of solar PV meeting the deficit in generation, exporting the remainder of the solar PV generation to the grid at a profit.

Another harmony between the technologies in colder climates is that the mCHP units' maximum output is during winter when the thermal demands of the building are high while the solar PV generation is at its lowest. The opposite will be observed in the summer months when the heat demand from buildings is low (consequently, the electrical production from the unit is low) but the available electrical power from



the solar PV it at its highest. If this system were combined with EES to regulate the mismatch in generation (which could be small were the systems sized appropriately), then it could offer complete independence from the electrical network. However, matching the dynamic availability of PV systems with the power generation from an electrically-led mCHP engine can be challenging and will require intelligent control algorithms that are aware of the interaction the technologies have with both the thermal and electrical networks within the building.

As with mCHP units, heat pumps affect both the thermal and electrical demands of the building but in a fundamentally different way. Heat pumps *always* consume electricity while in operation but will then ‘generate’ thermal energy more than their consumption in electric power. This is a contrast to mCHP – when the unit is in normal operation it generates both thermal and electrical energy – where the electric power generation is more than its own consumption requirements. Having these two technologies run in complementary operation by utilising the excess electrical generation of the mCHP unit to supply (whole or part) of the electrical demands of the heat pump is an interesting and promising hybrid energy system (39, 40).

While there are technological combinations that are brought about by interconnecting existing systems, there are also technologies in development that are intrinsically hybrids of existing technologies. One such example is a hybrid photovoltaic-thermal system that uses only solar energy to create an NZEB (41).

No matter the technological combination, this will result in complex interconnected systems where the input-output control pathways are not always clear, and it is exceedingly difficult to determine what the ideal mix/utilisation of the various energy systems is *in real time*. The control of such systems will need to be ‘smart’ in that it is aware of how the technologies interact with the thermal and electrical loads of the building, but also how they interact with each other.

#### 1.2.4 Operational controls

Many of the current approaches to the control of local hybrid energy supply systems involve model predictive control (42, 43), and/or optimisation methods (44, 45). These are very useful tools for determining the feasibility of a proposed energy supply system or the optimal operational strategy over a future time horizon (>24 h) provided the assumptions on the performance of the systems be in line with the those predicted by the models. However, the issue with these approaches is that they not only rely on accurate models to predict the optimum operation regime but rarely is attention given to the control strategy used while *in operation*. It is assumed that a thermally-led mCHP is capable of providing the thermal load when it is required, and similarly for



electrically-led systems (46, p. 43).

Employment of optimal or model predictive control (MPC) strategies for micro-generation typically concerns minimising cost or maximising profit (15, § 3.1), with a secondary concern for operational constraints. These control strategies will be explored further in the next chapter.

### Multi-objective control

A significant control challenge posed by the deployment of microgeneration in buildings is consideration of both the thermal and electrical demands simultaneously i.e. a multi-objective control approach.

Controlling based on only one of these objectives could lead to poor control. Consider a case where an optimisation routine or model predictive control set to minimise the cost of electricity when deciding the operating pattern of a heat pump. If left to control without constraint or consideration of the thermal demands it could be very effective at shifting the electrical demand of a heat pump into the night period, but then the building occupants will have poor thermal comfort as heat is not being delivered when it is required. That is not necessarily the best utilisation of the technology. It is probable that a near opposite is true, there will be an optimal operation of the technologies that will minimise the cost of the electricity while fulfilling the thermal demands of the building. However, finding this optimum will essentially rely on accurately predicting the future, and any forecast of demand is subject to uncertainty and error. However, there may be a happy medium whereby a control strategy can compute (with limited or no knowledge of the future) what the ideal operation of the technologies is at *that time instant*.

Of the research into multi-objective control of microgeneration (see § 2.5) most still assume the presence and ‘infinite’ potential for utilisation of the electrical grid connection. As discussed in the previous section this may not always be the case, as future local electrical networks may impose a limit to when and how much energy can be imported and exported. Another consideration is that the dynamic demand for heat and power in buildings can be volatile. Coupled with the fact that the availability of the renewable energy is intermittent, the ‘dispatchable’ resources are not always dispatchable (e.g. mCHP could be in a mandatory cool-down mode), and the variable amount of available energy storage leads to a complex multi-input multi-output (MIMO) control problem.

Further to this point, concerning mCHP, it is conceivable that control strategies could be ‘led-agnostic’ whereby the operation of the unit is a function of not only both thermal and electrical demands of the building, but the availability and potential





interaction with the other technologies within the building.

### **Unit-specific controls**

Each microgeneration technology has low-level internal controls to ensure safe, efficient operation of the device. For example, they may pose a limit on the flow rate of fuel or water to a mCHP unit or determine the mode of operation of the device. The control strategy should be aware and respectful of these limitations to not only improve overall system performance but to ensure safe control by not asking something of the unit that it is not able to deliver.

Another factor to consider is the control of the unit with regards to the energy delivery network that it services. For example, the thermal efficiency of a mCHP unit is a function of the temperature and flow rate of the cooling water through its heat exchanger. Controllers that are aware of the relation between the unit's efficiency and the components to which it connects within the building energy delivery network are likely to result in more efficient utilisation of the technology.

### **Energy delivery network within the building**

The energy delivery network within the building is what transports the energy from the device to the thermal or electrical loads in the building. A building employing mCHP may deliver the heat energy generated via a [hydronic system](#). In this case the heat output from the emitters – be they underfloor heating, baseboard radiators – varies by manipulating the flow rate through them. The different radiating technologies and heat generators also require distinct ranges of supply temperature to work most effectively (15, p. 24). Control with knowledge of the design and interconnection of the energy delivery network will be able to control not only the technologies but the network in which they operate.

There is also a need for new methodologies for the optimisation of MGTs and the energy delivery network. This was recommended by Brett, Staffell (47, § 2.1) where they assert that methodologies of this nature will facilitate more efficient operation of the devices and allow the final energy delivery elements provide a more regulated thermal output.

### **Control input constraints**

Control input constraints are the physical limitations of microgeneration technologies and the components in the energy delivery network. There is an abundance of physical constraints within microgeneration systems. An obvious constraint is requesting more energy from a device than it can deliver. There are, however, many more constraints



that must be accounted for when designing advanced control algorithms: The actuating control value that supplies fuel to the mCHP engine has a maximum and minimum fuel supply, as well as a restricted rate of fuel delivery. Electrical energy storage has low-level electronics that restricts the maximum permissible current transfer to the device to avoid overheating and to protect their inner circuitry. Depending on the type of thermal energy store, these can have mechanical/hydraulic actuators that have physical limits on the magnitude or flow rate of water entering/exiting from the tank. Many of these discontinuous limits are designed to ensure safe performance of the energy system, and so the high-level controller should be respectful of these system limitations to ensure optimal and safe control.

### **1.3** Research objectives

The objective of this research was the design and application of MIMO control algorithms to the problem of controlling microgeneration devices and energy storage within a building. The controller should address the following issues identified in § 1.2:

1. The controller can prioritise the use of renewable and low-carbon resources.
2. To investigate a control structure that would allow for flexible/controllable integration with the local electrical network.
3. The controller can exploit the synergy of multiple energy systems to simultaneously fulfil the thermal and electrical demands of a building.
4. The controller can efficiently operate energy delivery networks with high inertia.
5. The controller is capable of handling multiple simultaneous input constraints.

### **1.4** Research scope, assumptions, and limitations

While there are inherent assumptions and limitations placed on the modelling resolution, the number of control theories trialled and the exhaustiveness of simulations that can be conducted in the body of research, the discussion here is related to the overarching scope of the research topic and the limitations of the aforementioned topics are discussed in their respective sections. Although there is significant overlap between the discussion of the limitations of the research and the potential avenues for future work, the reader should be informed of the following restrictions before reviewing the rest of the body of work.



#### 1.4.1 Absence of field trials

The general principals of Control System Design (48, ch. 10, 49, § 1.5) outlines that once the required goals of the final controller design have been established, and the models of the systems have been defined, the concluding stage is to assess the control system design via simulation and analysis. The real-world performance analysis of the controller should be tested by embedding the controller in hardware/software and testing the performance of a prototype of the system to be controlled. For systems that are difficult to test and rework as a prototype, or where the failure of the controller is dangerous, then design verification is completed via digital numerical simulation. In this work instead of a physical prototype, simulation has been used to gauge the performance of the design. While this may diminish the conclusions on the practical realisation of the control, significant effort has been made to ensure that the models of the systems that have been used cover the main dynamical modes of the systems, and that all fundamental limitations of the systems such as actuator limits, operational modes, low-level controls and nonlinear dynamics are accounted for in the simulation models.

#### 1.4.2 Subset of technologies considered

While the control algorithms developed in this work are designed so that they apply to many building-integrated energy systems, the list of technologies covered in this thesis is restricted to combustion-based cogeneration devices, solar PV, thermal energy storage (TES), and EES. Focus was given to these technologies as they comprise the most frequently deployed in practice, and attempting to make them work together to fulfil the electrical and thermal demands of a building is a challenge in and of itself. The remaining microgeneration technologies (see table 1.1) that are not considered, such as biomass, micro-wind turbines and micro-hydro systems are not as prevalent in building integration. Small or micro hydro systems, while not strictly *building integrable*, have been installed in Scotland by homeowners to fulfil the electrical loads for lighting and small appliances. However, development of hydropower schemes requires regulatory approval and planning permission to install (50), adding significant complication to implementing the technology. They are obviously also very site-specific and are not common renewable energy sources (RES). For these reasons hydro systems are not considered in this work.

However, notable exceptions from this research are heat pumps, which are readily applicable for building integration. However, the likelihood of having both mCHP and heat pump technologies available for manipulation in a single building is currently limited due to the high combined capital cost. Due to the difficulties in the modelling



of heat pumps (51, ch. 4) and the complex effect that control configuration and climate can have on the performance of the technology (52), the focus was given to the control of building-integrated mCHP units. Further discussion is provided in §§ 9.3.2.

Similarly, only combustion-based cogeneration devices have been considered in this work. Obtaining a model of fuel cells suitable for controller design is not a trivial task, and existing models in the literature are based on the (empirical) dynamic performance of a single unit, or general models that are only suitable for long-term dynamic performance (53, p. 18).

#### 1.4.3 *No employment of responsive demand*

Another approach to matching the availability of the intermittent resources to the electrical demands of the building is via responsive demand. Also known as demand-side management, this is a technique where the building's demand for electricity is manipulated to equal what is available from the energy being generated in the building.

There are two main approaches to demand-side management: price-based control and load automation. Research in this area has concluded that currently neither are 100% effective in matching demand to supply (54). Therefore, in this research intermittent power generation is treated as a disturbance to the controlled system.

This work assumes that there is no possibility of responsive demand of the electrical loads of the building. The term demand-side management is usually considered in reference to the electrical grid, whereby the lowering/adjustment of the electrical demand of the building from the point of view of the national grid is considered to be demand-side management. In this work, the term is used from the point of view of the control system i.e. the demand for electrical power generated within the building (lighting, small power equipment, etc.) cannot be manipulated to achieve minimal grid interaction. While not strictly a limitation but more of constraint/challenge on the controller design, this work takes the pragmatic approach – that just like the building thermal demands – the fulfilment of the electrical loads is non-negotiable.

If the control system cannot successfully operate the building-integrated energy systems to fulfil the loads then either load shedding will occur, or for grid-connected buildings the deficit will be supplied by the grid. The controller design places great emphasis on avoiding either outcome, but it may be unavoidable for the case of undersized systems or building operation far exceeding the design. For this reason, the work places an emphasis on robust control so that these limitations are handled by the controller. The general control theory used in this work would allow for the expanding the reach of the controller to manage the electrical loads of the building





simultaneously with the energy systems. This is an exciting area of future work that is also covered in § 9.3.

#### 1.4.4 *Non-manipulable solar PV system*

Finally, the availability of energy from solar PV is treated as a system disturbance i.e. the power generated by the PV panels contributes to the reduction of the electrical demands of the building, while the control system attempts to absorb the excess generation (if it exists) via operation of the other energy systems (see § 7.4 for details). If that is not possible, it is assumed that a grid connection is available to export the excess generation. Essentially the control system strives to operate the building as if it were controlled in ‘islanded’ operation (55) even if a grid connection exists. If a fully dynamic model of the PV were to be utilised (including modelling of a solar tracker), then it may be possible to control the PV array in such a way to reduce the amount of power generation to ensure safe, robust, operation in the absence of a grid connection. This is a limitation of the research that the author hopes to address in future work.

### **1.5 Contributions of the thesis**

The main contributions of the research presented in this thesis are outlined as follows:

- Development of state-space models of water-based TES and combustion-based mCHP that are suitable for control system design.
- Development of a state-space model of a building with validated energy consumption predictions that is suitable for controller design and integration with the preceding energy systems models.
- Creation of a system/control structure design methodology based on the inverse dynamics of the energy systems.
- Novel application of nonlinear inversion-based control to the control of building-integrated energy systems.
- Combining the inversion-based control methods with robust control techniques to ensure controller performance in the face of modelling inaccuracies and unpredicted system disturbances.
- An improved anti-windup strategy for control systems that employ integral action to systems with actuator limits.



- A variable structure control strategy for switching between inverse-dynamics based controllers when an energy system is not available for use or is in a fixed mode of operation.
- Application of all of the previous contributions to an energy system control problem of satisfying the thermal and electrical demands of a building in the presence of a constrained connection to the local electrical network.

The following is a list of relevant publications by the author that are related to this thesis. The list is sorted by original date of publication:

- Murphy, G. B., Counsell, J., Allison, J., Brindley, J. Calibrating a combined energy systems analysis and controller design method with empirical data. *Energy* 57: 484–94 (2013).
- Allison, J., Murphy, G. B. Control of micro-CHP and thermal energy storage for minimising electrical grid utilisation. *Microgen III: Proceedings of the 3rd International Conference on Microgeneration and Related Technologies*: 38–47 (2013). Naples, Italy, 15–17 April 2013
- Allison, J., Murphy, G. B., Counsell, J. M. Control of micro-CHP and thermal energy storage for minimising electrical grid utilisation. *International Journal of Low-Carbon Technologies* 11(1): 109–18 (2016). [First published online: 2014-08-21]
- Allison, J. Robust control of net-zero offices with integrated hybrid supply system and energy storage. *Microgen IV: Proceedings of the 4th International Conference on Microgeneration and Related Technologies*: 38–47 (2015). Tokyo, Japan, 28–30 October 2015
- Allison, J. Robust control of building-integrated energy systems with energy storage. *Applied Thermal Engineering* 114: 1498–1506 (2017).

## **1.6** Thesis structure/overview

The contents of the thesis have been subdivided into the following chapters:

CHAPTER 2 Reviews the current approaches to the control of building-integrated energy systems. Particular focus is placed upon contrasting the traditional control methods with the emerging ‘advanced’ control methods and how they relate to the objectives of this work. It is shown that the application of nonlinear inversion techniques coupled with robust controller design is novel to the control of building-integrated energy systems.



**CHAPTER 3** This chapter details the overall research method employed in the thesis. The system to be controlled is defined alongside a schematic describing the control actuation and measurement points. The case studies which demonstrate the application of the controller design methodology are described and the metrics upon which the performance is judged are also specified.

**CHAPTER 4** This chapter establishes energy systems models of appropriate resolution, to be used for the purposes of controller design. These models are drawn together from various sources and converted into state-space representations. Advancements are made to the models where necessary in order to ensure that the mathematical models of the physical systems adequately approximate reality so that all important dynamic characteristics are captured.

**CHAPTER 5** This chapter establishes a general state-space model of the thermodynamics of a building zone that is suitable for the application of controller design and integration with the models of the previous chapter.

**CHAPTER 6** The design of a MIMO controller based on the concept of nonlinear system inversion is detailed in this chapter. It is shown how this inverse dynamics provides the controller with knowledge of the complex cause and effect relationships between the system, the controlled inputs, and the external disturbances. A methodology for how this technique can be used for the design of interconnected energy systems is demonstrated.

**CHAPTER 7** This chapter augments the nonlinear inversion control of the previous chapter with an outer-loop control to ensure robust, stable control in the presence of modelling deficiencies/uncertainty and unknown disturbances. The physical limitations of the system are also addressed by smart switching logic.

**CHAPTER 8** First presents a ‘controller test case’ on a simplified system to demonstrate the application of the control strategy. Second, it presents case studies for the application of the controller design methodology of chapter 5–6 to a system consisting of an mCHP in combination with solar PV, electrical energy storage and with/ without a stratified TES tank.

**CHAPTER 9** Provides summary of the main results and contributions of the thesis, while detailing possible avenues of future research areas and the practical application of the controller design methodology established in this thesis.



## References

1. Scottish Parliament. *Climate Change (Scotland) Act 2009, c 12*. Tech. rep. asp 12. 2009: 68. URL: [http://www.legislation.gov.uk/asp/2009/12/pdfs/asp%7B%5C\\_%7D20090012%7B%5C\\_%7Den.pdf](http://www.legislation.gov.uk/asp/2009/12/pdfs/asp%7B%5C_%7D20090012%7B%5C_%7Den.pdf) (cited p. 1)
2. Parliament of the United Kingdom. *Climate Change Act 2008*. Tech. rep. 2008: 1–103. DOI: [10.1136/bmj.39469.569815.47](https://doi.org/10.1136/bmj.39469.569815.47) (cited p. 1)
3. European Union. L 140. *Official Journal of the European Union* **52**: 20 (2009) (cited p. 1)
4. European Parliament. Directive 2009/28/EC of the European Parliament and of the Council of 23 April 2009. *Official Journal of the European Union* **140**(16): 16–62 (2009). DOI: [10.3000/17252555.L\\_2009.140.eng](https://doi.org/10.3000/17252555.L_2009.140.eng). arXiv: [534](https://arxiv.org/abs/534) (cited p. 1)
5. European Council. 2030 Climate and energy policy framework - EUCO 169/14. (October): 1–15 (2014) (cited p. 1)
6. European Commission. COMMUNICATION FROM THE COMMISSION: A Roadmap for moving to a competitive low carbon economy in 2050. *COM(2011) 112 final* **34**(March): 1–34 (2011). DOI: [10.1002/jsc.572](https://doi.org/10.1002/jsc.572). arXiv: [arXiv:1011.1669v3](https://arxiv.org/abs/1011.1669v3) (cited p. 1)
7. Meinshausen, M., Meinshausen, N., Hare, W., Raper, S. C. B., Frieler, K., Knutti, R., Frame, D. J., Allen, M. R. Greenhouse-gas emission targets for limiting global warming to 2 degrees C. *Nature* **458**(7242): 1158–62 (2009). DOI: [10.1038/nature08017](https://doi.org/10.1038/nature08017) (cited p. 1)
8. OECD/IEA. *Transition to Sustainable Buildings*. 2013. ISBN: 9789264202412. DOI: [10.1787/9789264202955-en](https://doi.org/10.1787/9789264202955-en) (cited p. 1)
9. Energy Efficiency in Buildings, World Business Council for Sustainable Development. *Transforming the Market: Energy Efficiency in Buildings*. Tech. rep. 2009. URL: <http://www.wbcsd.org/transformingthemarketeeb.aspx> (cited p. 1)
10. International Energy Agency. Tracking Clean Energy Progress 2013. *Technology*: 1–82 (2012) (cited p. 1)
11. The Intergovernmental Panel on Climate Change (IPCC). *Climate Change 2014: Mitigation of Climate Change*. 2014: 1454. ISBN: 9781107654815. DOI: [10.1017/CBO9781107415416](https://doi.org/10.1017/CBO9781107415416) (cited p. 2)
12. EU. Directive 2010/31/EU of the European Parliament and of the Council of 19 May 2010 on the energy performance of buildings (recast). *Official Journal of the European Union*: 13–35 (2010). DOI: [doi:10.3000/17252555.L\\_2010.153.eng](https://doi.org/10.3000/17252555.L_2010.153.eng) (cited p. 2)
13. IEA. *World Energy Outlook*. 2014: 726. ISBN: 9789264208056. DOI: [10.1787/weo-2014-en](https://doi.org/10.1787/weo-2014-en) (cited p. 2)
14. HM Parliament. *Climate Change and Sustainable Energy Act 2006*. 2006. DOI: [10.1136/bmj.39469.569815.47](https://doi.org/10.1136/bmj.39469.569815.47) (cited p. 2)
15. Staffell, I., Brett, D. J. L., Brandon, N. P., Hawkes, A. D. *Domestic Microgeneration: Renewable and Distributed Energy Technologies, Policies and Economics*. Abingdon, Oxon, UK: Routledge, 2015. ISBN: 978-1-315-69710-9 (cited pp. 2, 7, 11, 12)
16. Thomas, B. Benchmark testing of Micro-CHP units. *Applied Thermal Engineering* **28**(16): 2049–54 (2008-11). DOI: [10.1016/j.applthermaleng.2008.03.010](https://doi.org/10.1016/j.applthermaleng.2008.03.010) (cited p. 2)





17. Arashnia, I., Najafi, G., Ghobadian, B., Yusaf, T., Mamat, R., Kettner, M. Development of Micro-scale Biomass-fuelled CHP System Using Stirling Engine. *Energy Procedia* **75**: 1108–13 (2015-08).  
DOI: [10.1016/j.egypro.2015.07.505](https://doi.org/10.1016/j.egypro.2015.07.505) (cited p. 2)
18. Liu, W., Mu, W., Liu, M., Zhang, X., Cai, H., Deng, Y. Solar-induced direct biomass-to-electricity hybrid fuel cell using polyoxometalates as photocatalyst and charge carrier. *Nature communications* **5**: 3208 (2014).  
DOI: [10.1038/ncomms4208](https://doi.org/10.1038/ncomms4208) (cited p. 2)
19. IEA. Variability of Wind Power and Other Renewables - Management options and strategies: 1–57 (2005) (cited p. 3)
20. Energy Saving Trust. Getting warmer: a field trial of heat pumps - Phase 1: 22 (2010) (cited p. 4)
21. Staffell, I. et al. UK microgeneration. Part II: technology overviews. *Proceedings of the Institution of Civil Engineers: Energy* **163**(4): 143–65 (2010).  
DOI: [10.1680/ener.2010.163.4.143](https://doi.org/10.1680/ener.2010.163.4.143) (cited pp. 5, 7, 9)
22. Mago, P. J., Hueffed, A., Chamra, L. M. Analysis and optimization of the use of CHP-ORC systems for small commercial buildings. *Energy and Buildings* **42**(9): 1491–8 (2010).  
DOI: [10.1016/j.enbuild.2010.03.019](https://doi.org/10.1016/j.enbuild.2010.03.019) (cited p. 6)
23. European Parliament. Motion for a resolution: 1–5 (2013) (cited p. 6)
24. Juntunen, J. K., Hyysalo, S. Renewable micro-generation of heat and electricity—Review on common and missing socio-technical configurations. *Renewable and Sustainable Energy Reviews* **49**: 857–70 (2015).  
DOI: [10.1016/j.rser.2015.04.040](https://doi.org/10.1016/j.rser.2015.04.040) (cited p. 6)
25. Network, E. S. Smart Grids, Microgeneration & Storage: Commercialising the benefits. (October) (2013) (cited p. 6)
26. Ruiz-Romero, S., Colmenar-Santos, A., Mur-Pérez, F., López-Rey, Á. Integration of distributed generation in the power distribution network: The need for smart grid control systems, communication and equipment for a smart city — Use cases. *Renewable and Sustainable Energy Reviews* **38**: 223–34 (2014).  
DOI: [10.1016/j.rser.2014.05.082](https://doi.org/10.1016/j.rser.2014.05.082) (cited p. 6)
27. Balcombe, P., Rigby, D., Azapagic, A. Environmental impacts of microgeneration: Integrating solar PV, Stirling engine {CHP} and battery storage. *Applied Energy* **139**: 245–59 (2015).  
DOI: [10.1016/j.apenergy.2014.11.034](https://doi.org/10.1016/j.apenergy.2014.11.034) (cited p. 6)
28. Brandoni, C., Arteconi, A., Ciriachi, G., Polonara, F. Assessing the impact of micro-generation technologies on local sustainability. *Energy Conversion and Management* **87**: 1281–90 (2014).  
DOI: [10.1016/j.enconman.2014.04.070](https://doi.org/10.1016/j.enconman.2014.04.070) (cited p. 6)
29. Bolton, R., Foxon, T. J. Infrastructure transformation as a socio-technical process — Implications for the governance of energy distribution networks in the {UK}. *Technological Forecasting and Social Change* **90, Part B**: 538–50 (2015).  
DOI: [10.1016/j.techfore.2014.02.017](https://doi.org/10.1016/j.techfore.2014.02.017) (cited p. 6)
30. Balcombe, P., Rigby, D., Azapagic, A. Motivations and barriers associated with adopting micro-generation energy technologies in the {UK}. *Renewable and Sustainable Energy Reviews* **22**: 655–66 (2013).  
DOI: [10.1016/j.rser.2013.02.012](https://doi.org/10.1016/j.rser.2013.02.012) (cited p. 6)



31. Balcombe, P., Rigby, D., Azapagic, A. Investigating the importance of motivations and barriers related to microgeneration uptake in the {UK}. *Applied Energy* **130**: 403–18 (2014).  
DOI: [10.1016/j.apenergy.2014.05.047](https://doi.org/10.1016/j.apenergy.2014.05.047) (cited p. 6)
32. Bush, R., Jacques, D. A., Scott, K., Barrett, J. The carbon payback of micro-generation: An integrated hybrid input–output approach. *Applied Energy* **119**: 85–98 (2014-04).  
DOI: [10.1016/j.apenergy.2013.12.063](https://doi.org/10.1016/j.apenergy.2013.12.063) (cited p. 6)
33. Walters, R., Walsh, P. R. Examining the financial performance of micro-generation wind projects and the subsidy effect of feed-in tariffs for urban locations in the United Kingdom. *Energy Policy* **39**(9): 5167–81 (2011).  
DOI: [10.1016/j.enpol.2011.05.047](https://doi.org/10.1016/j.enpol.2011.05.047) (cited p. 6)
34. BRE and RECC. *Batteries and Solar Power: Guidance for domestic and small commercial consumers*. Tech. rep. 2016. URL: [http://www.bre.co.uk/filelibrary/nsc/Documents%20Library/NSC%20Publications/88031-BRE%7B%5C\\_%7DSolar-Consumer-Guide-A4-12pp.pdf](http://www.bre.co.uk/filelibrary/nsc/Documents%20Library/NSC%20Publications/88031-BRE%7B%5C_%7DSolar-Consumer-Guide-A4-12pp.pdf) (cited p. 7)
35. Department of Trade and Industry. Domestic photovoltaic field trials: final technical report. *Department of trade and industry* (2006) (cited p. 7)
36. DELTA Energy & Environment. *Expertise in Decentralised Energy*. Tech. rep.: 1–5 (cited p. 9)
37. Pales, A. F. The IEA CHP and DHC Collaborative - CHP/DHC Country Scorecard: Japan (2013) (cited p. 9)
38. Harrison, J. Micro Combined Heat & Power. *Micro CHP IMech* (2002) (cited p. 9)
39. Hawkes, A. D., Brett, D. J. L., Brandon, N. P. Role of fuel cell based micro-cogeneration in low carbon heating. *Proceedings of the Institution of Mechanical Engineers, Part A: Journal of Power and Energy* **225**(2): 198–207 (2011).  
DOI: [10.1177/2041296710394268](https://doi.org/10.1177/2041296710394268) (cited p. 10)
40. Rogers, J. G., Cooper, S. J., McManus, M. C., Hammond, G. P. Use of micro-CHP plants to support the local operation of electric heat pumps. In *Microgen III: Proceedings of the 3rd International Conference on Microgeneration and Related Technologies*. Naples, Italy, 2013 (cited p. 10)
41. Good, C., Andresen, I., Hestnes, A. G. Solar energy for net zero energy buildings – A comparison between solar thermal, PV and photovoltaic–thermal (PV/T) systems. *Solar Energy* **122**: 986–96 (2015-12).  
DOI: [10.1016/j.solener.2015.10.013](https://doi.org/10.1016/j.solener.2015.10.013) (cited p. 10)
42. Sossan, F., Bindner, H., Madsen, H., Torregrossa, D., Chamorro, L. R., Paolone, M. A model predictive control strategy for the space heating of a smart building including cogeneration of a fuel cell-electrolyzer system. *International Journal of Electrical Power & Energy Systems* **62**: 879–89 (2014-11).  
DOI: [10.1016/j.ijepes.2014.05.040](https://doi.org/10.1016/j.ijepes.2014.05.040) (cited p. 10)
43. Kortela, J., Jämsä-Jounela, S.-L. Modeling and model predictive control of the BioPower combined heat and power (CHP) plant. *International Journal of Electrical Power & Energy Systems* **65**: 453–62 (2015-02).  
DOI: [10.1016/j.ijepes.2014.10.043](https://doi.org/10.1016/j.ijepes.2014.10.043) (cited p. 10)
44. Moradi, M. H., Hajinazari, M., Jamasb, S., Paripour, M. An energy management system (EMS) strategy for combined heat and power (CHP) systems based on a hybrid optimization method employing fuzzy programming. *Energy* **49**: 86–101 (2013-01).  
DOI: [10.1016/j.energy.2012.10.005](https://doi.org/10.1016/j.energy.2012.10.005) (cited p. 10)



45. Wolfrum, P., Kautz, M., Schäfer, J. Optimal control of combined heat and power units under varying thermal loads. *Control Engineering Practice* **30**: 105–11 (2014-09).  
DOI: [10.1016/j.conengprac.2013.08.014](https://doi.org/10.1016/j.conengprac.2013.08.014) (cited p. 10)
46. Entchev, E., Tzschentschler, P. *Integration of Microgeneration and Related Technologies in Building*. Tech. rep. October. Germany: International Energy Agency, 2014: 1–99 (cited p. 11)
47. Brett, D. J. L., Staffell, I. An introduction to microgeneration. In Staffell, I., Brett, D. J. L., Brandon, N. P., Hawkes, A. D. *Domestic Microgeneration: Renewable and Distributed Energy Technologies, Policies and Economics*. 2015. Chap. 1. ISBN: 978-1-315-69710-9. Google Books: [sZvwCQAAQBAJ](https://books.google.com/books?id=sZvwCQAAQBAJ) (cited p. 12)
48. Franklin, G. F., Powell, J. D., Emami-Naeini, A. *Feedback Control of Dynamic Systems*. 6th ed. Upper Saddle River, New Jersey: Pearson Education, Inc., 2010: 837. ISBN: 978-0-13-500150-9 (cited p. 14)
49. Dorf, R. C., Bishop, R. H. *Modern Control Systems*. 12th ed. Upper Saddle River, New Jersey: Prentice Hall, 2011: 1104. ISBN: 978-0-13-602458-3 (cited p. 14)
50. SEPA. Guide to hydropower construction best practice. (March) (2012) (cited p. 14)
51. Baster, E. Air source heat pump modelling for dynamic building simulation tools based on standard test data. PhD thesis. University of Strathclyde, 2017 (cited p. 15)
52. Cooper, S. J., Hammond, G. P., McManus, M. C., Ramallo-Gonzalez, A., Rogers, J. G. Effect of operating conditions on performance of domestic heating systems with heat pumps and fuel cell micro-cogeneration. *Energy and Buildings* **70**: 52–60 (2014-02).  
DOI: [10.1016/j.enbuild.2013.11.077](https://doi.org/10.1016/j.enbuild.2013.11.077) (cited p. 15)
53. Beausoleil-Morrison, I. *An experimental and simulation-based investigation of the performance of small-scale fuel cell and combustion-based cogeneration devices serving residential buildings*. Tech. rep. 2008: 70. URL: [http://www.ecbcs.org/docs/Annex%7B%5C\\_%7D42%7B%5C\\_%7DFinal%7B%5C\\_%7DReport.pdf](http://www.ecbcs.org/docs/Annex%7B%5C_%7D42%7B%5C_%7DFinal%7B%5C_%7DReport.pdf) (cited p. 15)
54. McKenna, E., Ghosh, K., Thomson, M. Demand response in low-carbon power systems: a review of residential electrical demand response projects. In *2nd International Conference on Microgeneration and Related Technologies*. Glasgow, UK, 2011.  
DOI: [10.2307/302397](https://doi.org/10.2307/302397) (cited p. 15)
55. Johnston, D. Islanding Operation of Electrical Systems in Buildings. *Energy and Power Engineering* **5**: 198–201 (2013).  
DOI: [10.4236/epe.2013.54B038](https://doi.org/10.4236/epe.2013.54B038) (cited p. 16)



*“The scientific man does not aim at an immediate result. He does not expect that his advanced ideas will be readily taken up. His work is like that of the planter – for the future. His duty is to lay the foundation for those who are to come, and point the way.”*

---

—NIKOLA TESLA, *Problem of Increasing Human Energy*

2

## Literature review

### 2.1 Hierarchy of energy system controls

§ 1.2 provided a rationale for improved control of microgeneration. However, the ‘level’ at which the control is applied to building-integrated energy systems varies and it is important to establish the separate areas to which research is focused. To that end, the control of building-integrated energy systems can be broadly separated into a hierarchy of three categories:

1. *Supervisory*: also known as *strategic* controllers. These consider what is the ‘optimal dispatch’ of the available energy systems to minimise operating cost or maximise utilisation of on-site generation over periods such as a day, month, year or greater. They are also used to assess lifetime economics or determining the potential for future penetration of specific technologies into a market (1, § 2.3).
2. *Systems-level*: also known as *regulation*, or *tracking* controllers. Systems level (SL) controllers are designed for balance-of-plant and manipulating the dynamic performance of the energy systems i.e. for the operation of the energy systems to meet the energy demands of the building based on the operating scheme imposed by the supervisory controller. These controls typically operate from secondly to sub-hourly time resolution.
3. *Low-level*: also known as *functional*, *embedded*, or *micro* controllers. These controllers are primarily designed to ensure safe, efficient operation of the device and typically operate at sub-secondly time resolution. They strive to operate the device according to the requests from the SL controllers.





Naturally there can be overlap between each of the hierarchies determined by the models used to assess the performance of the controllers.

Some also consider separate types of ‘control’ in the form of demand-side management (DSM) and demand side response (DSR), which attempt to shape or shift the demands of the building to match the generation capability of the energy systems. However, the typical ‘active’ DSM techniques such as active demand reduction, static time-of-use tariffs, and dynamic tariffs proposed by Darby (2) can all be considered forms of supervisory control as they *encourage* rather than *enforce* a change in demand.

DSR signals are requests that can arise from a local electrical network (LEN) or ‘smart grid’ to which the building is connected. A DSR signal would call for the building have an immediate or almost immediate change in demand (decrease or increase) in response to an unplanned variation on their end. That is, the LEN can ask the building to pick up excess generation from the network by reducing self-generation. Conversely, the LEN can ask the building to increase its generation above what is required to fulfil the internal loads to export electrical power to the network. In each case, the request to the building would be received via a SL controller, as it strives to change the balance-of-plant in response to requests.

### 2.1.1 Low-level controllers

Each of the energy systems considered in this work has low-level controls. Solar PV systems have maximum power point tracking (MPPT) control methodologies, where either the voltage or current of the solar cells is controlled to find the maximum power point (MPP) – a unique point on the P-V curve where the system exhibits maximum efficiency and power. A recent review of such techniques was conducted by Joshi, Arora (3). There are also emerging areas of application of MPPT to hybrid systems at domestic-sized building-integrated PV/wind (4) and fuel-cells/PV/wind-power (5). These have proved effective at increasing the instantaneous electrical power available from the hybrid system.

The efficient operation of mCHP units are subject to low-level controls for overheating protection, valve timings, fuel-air mixtures, mass flow controllers and operational modes. These low-level controls are vital to “ensuring safe, efficiency and reliable long term operation” of the device (6, § 2.1.8) and can also be complex and sophisticated when they need to respond to dynamic electrical or thermal load requests (6, p. 773).

Electrical energy storage in the form of batteries have many complex embedded controls for their safe and efficient operation. These embedded controls take the form of a battery management systems (BMSs). The BMS is responsible for estimation of the state-of-charge, state-of-health, thermal regulation, charging and discharging of the



battery. BMS controls have seen a resurgence in study due to the increase in electric vehicle production and the desire for reliable performance (7) and ‘fast charging’ controllers (8) in modern- and hybrid-electric vehicles.

Water-based TES tanks do not have embedded controllers as the other devices do, as their use is based on the systems to which they are connected. However, the auxiliary electrical heat elements within the tank will be subject to low-level controls, as will the water pumps connected to the tank that dictate the flow through the heat exchangers or through the main bulk water. In addition, they can still contain electronics in the form of sensors for inner-tank or inlet/output temperatures and water/mass flow rate.

The persistent research into the low-level controls will continue to make each of the technologies themselves work more efficiently and effectively.

### 2.1.2 Systems-level controllers

SL controllers for energy systems are primarily concerned with objectives such as reference tracking, disturbance rejection, and system stability. For example, in energy systems SL controllers are designed to follow desired temperature profiles for indoor conditions, water temperature/flow management in [hydronic systems](#), power flow control, and air quality control.

Depending on the problem at hand, there are many different controller architectures that can be used: on/off, proportional-integral-derivative (PID), lead-lag, linear-quadratic-Gaussian (LQG)/linear-quadratic regulator (LQR) & pole-placement techniques, and Kalman filters to name but a few. SL controllers are also responsible for practical aspects of controller implementation, such as compensating for measurement time delays, measurement noise, and actuator and plant capacity limits. These elements are necessary to ensure that the controller design developed would be feasible for real-world application.

Temperature control in buildings is handled by SL controllers and is subject to significant internal disturbances (such as people, lighting and equipment) and external disturbances (such as changes in temperature, wind speed, and solar insolation). The control system should be designed to be robust in the presence of these disturbances, which becomes more difficult as constraints are placed on their energy use. Furthermore, the disturbances can occur over vastly different time-scales and designing controllers to respond adequately across the entire spectrum of disturbances is an ever-present problem for control systems.

Transmission of power is called power flow and the improved control of power will increase its security and efficiency. The electrical network within buildings have inductive, capacitive, and resistive effects that result in dynamic impacts or disturbances.



The control system must anticipate and respond to system disturbances rapidly. In other words, the SL controller should be capable of managing significant disturbances in power flow occurring on very short time scales.

The development of controllers that consider both the thermal and electrical demands of the building will need to be able to respond to disturbances in each domain while not affecting the performance in the other. Therefore, hybrid energy supply systems will require unified, coordinated multi-objective control to be fundamental to the final control strategy.

### 2.1.3 Supervisory controllers

Supervisory controllers can take many forms, such as fuzzy logic (9), artificial neural networks (10), neuro-fuzzy control (11), or MPC (12), which have all been applied to different types of hybrid energy supply systems. There are two broad categories of supervisory controllers designed to determine the optimal deployment of technologies to fulfil the demand of the building but with different secondary objectives: (1) maximising the utilisation of on-site generation; (2) minimising total operating cost or maximising profit.

Supervisory controllers frequently use inputs of forecasts of climate, expected renewable generation, and predicted demand to determine what systems to use at what time to meet their control objectives. Padhy (13) describes it as the ‘unit commitment problem’ in the power industry, where the schedule of power generators is optimised to minimise total operating cost or maximising profit. Hawkes, Leach (14) extended the concept to microgeneration, which made use of mCHP, wind turbines, PV arrays, boilers, TES, and a grid connection to meet the energy requirements of a hotel, hospital and residences.

In the latter case, Hawkes et al. has stated that future research in micro-generation control needs to focus on “technically robust frameworks” that “consider a much wider range of technical options”, otherwise it could result in “a higher-cost and less efficient final energy system” (15, § 7). This is also supported by others working on the high-level controllers on hybrid microgeneration systems, such as Hellmers et al. (16) that “the schedule optimisation and the control problem should be coordinated so that input control actions (i.e. fuel consumption) and their discrepancy to their scheduled values [...] are used in the optimisation problem”. Moreover, Kneiske et al. (17) has stated that future supervisory control research will need to be concerned with the ‘transient’ behaviour of microgeneration systems and that “the influence of uncertainties in model components” is an open issue (17, § 4, ¶ 5). These factors highlight the need for improved coordination of control across the hierarchy of controllers.



## 2.2 Coordination across control hierarchy

As discussed in the previous section, effective control of energy systems will require coordination of control at many levels, and with hybrid energy systems this difficulty will be compounded. In the hierarchy of controllers, supervisory controllers are designed with the assumption that the low-level and systems-level controllers are working exactly as designed even in the presence of modelling uncertainty and disturbances. Similarly, SL controllers assume that the low-level controllers operate as they are designed/specified. Indeed, many of these control systems employ on-board special-purpose digital computers as integral components of the feedback loop. A useful comment was made by Bove et al. in this regard:

“When the primary purpose of the model is to provide performance, in order to analyze the whole system, the variation of the physical-chemical (such as gas concentration, temperature, pressure and current density, for example) are less relevant, compared to the performances, in terms of power, heat and input requirements.” (18, §1).

This statement was in reference to the modelling resolution required when assessing microgeneration technologies, which is directly related to the hierarchy of control. Therefore, the design of the SL controller should be able to integrate the performance capabilities and restrictions of the low-level controllers into the overall controller design without having to model them explicitly.

### 2.2.1 *Simulation-based works*

Moradi et al. (19) considers a hybrid system of mCHP and a boiler to serve the thermal and electrical demands of a hospital. The supervisory controller transmits control signals once per hour to the SL controllers that are assumed to be able to “optimize [the] energy flow of CHP system” without reference how this is achieved during each hourly period. The proposed scheme shows that the fuzzy controller is effective in optimising the deployment of the mCHP and boiler on an hourly time scale, and it also accounts for uncertainty in the unit size. However, it is assumed that the total thermal output of the boiler and mCHP satisfy the pre-determined thermal demands that are constant over one hour. Therefore, the work does not compensate for the transient dynamic behaviour of the systems as they modulate their output between each hourly update of the simulation.

Rouhani et al. (20) uses intelligent evolutionary algorithms for sizing of a hybrid system of wind/PV with fuel-cell and battery storage. Similar to (19), this work does not use any SL controllers and assumes that instantaneous switching between output levels of the systems is possible between each update of the evolutionary algorithm. While the results indicate suitable performance of the proposed method, by not accounting for the





dynamic transient behaviour of the systems they could be undersized. For example, the charging and discharging rates of the battery are a function of the remaining capacity, however, batteries have restrictions on the instantaneous charge and discharge rates. Likewise, it is assumed that the electrolyser can respond instantaneously to satisfy the power balance enforced in the optimisation routine. Note that in this work the hybrid system is only considered with the electrical power loads and not the thermal demands.

Brandoni et al. (21) addressed the design of a hybrid renewable system consisting of a micro-combined cooling heat and power (CCHP) unit and a solar PV device. The aim of the paper was to identify the optimal management strategy to minimise primary energy use, CO<sub>2</sub> emissions and operational costs (based on day-ahead electricity prices). The SL controller (denoted as the ‘control model’) developed for the work regulates the speed of the CCHP to provide the desired electrical power output when in ‘electrical priority’ mode. The calculated speed, however, was determined by a look-up optimisation table that was determined *a-priori* for the simulations and does not account for any disturbances on the load. In addition, the authors developed a ICE model but reduced the thermo-fluid-dynamic process of the engine to a quasi-stationary process – eliminating the restrictions on the transient thermal output of the system. Furthermore, it was assumed that there was no constraints on the amount of thermal power extracted from or sent to the TES. In ‘thermal priority’ mode, the thermal loads were controlled by linear programming techniques that enforced a load-balance between each simulation time-step. The work acknowledges that in “real working conditions” the modelled systems would have to account for a series of other losses such as balance-of-system and inverter losses. The absence of modelling or accounting for the dynamic performance and control of the TES could affect the optimal management strategy proposed in this work as it is difficult to supply and extract heat as specified in this work.

Canelli et al. (22) analyses two hybrid systems, one of a ground source heat pump (GSHP) and fuel cell and the second of GSHP and photovoltaic thermal (PVT) system.<sup>1</sup> In each case the energy, environmental and economic performance of each system is investigated. The heating and cooling systems are operated according to a time schedule, and on/off controllers are implemented with hysteresis on the heating, cooling and boiler outlet temperatures ( $(20.0 \pm 0.5)^\circ\text{C}$ ,  $(25.0 \pm 0.5)^\circ\text{C}$ ,  $(82 \pm 2)^\circ\text{C}$  respectively). The temperature of the fluid provided to the hydronic heating system is set at  $60^\circ\text{C}$  by a three-way (tempering) valve. The fuel cell is assumed to be running continuously

---

<sup>1</sup>An earlier paper (23) by several of the same authors investigated the performance of a hybrid GSHP/PVT system in comparison with a GSHP alone and a conventional boiler & chiller system. The SL controllers implemented in both works are almost identical and the same discussion applies.



at maximum capacity. The pump connected to the PVT system is also controlled by an on/off controller with hysteresis. (22, § 4.4). In this paper Canelli et al. acknowledges that the development of these SL controllers for the hybrid systems “brings about increased complexity in the control strategy and system configurations”.

### 2.2.2 Practical works

An example of practical implementation of control of a hybrid microgeneration system was conducted by Tuohy et al. (12) in the Orchestration of Renewable Integrated Generation In Neighbourhoods (ORIGIN) project. The objective of the control was to shape the demand of a group of 75 buildings in the north of Scotland to make the community approximately ‘net zero’ from the perspective of the LEN. The project made coordinated use of supervisory and SL controllers to achieve the design objectives. Supervisory control in the form of DSM techniques were used to encourage users to change their behaviour to maximise utilisation of on-site generation.

In addition to the DSM techniques, a supervisory controller, using an optimisation algorithm (updated every 30 min), made use of weather prediction, estimated renewable generation, demand prediction, and quantification of load shift opportunity to shape the future loads of the buildings. This was achieved via SL automated control that was able to remotely operate the space heating, hot water heating, electric vehicle (EV) charging and kitchen appliances. The operation of these devices was achieved via on/off controls that updated only when the optimisation algorithm updated.

Alongside the controllable plug loads, ORIGIN used a model of a solar hot water tank with a supervisory controller to optimise the charging and discharging of the TES tank for load shifting opportunities and thermal demand supply. The SL controllers were on/off for the use of the auxiliary electrical elements and thermal demands via manipulation of the pumps. In each case, the performance of the control is restricted by the capability of the SL controllers between each update of the supervisory controllers. It is hypothesised that by improving the control actions of the SL controllers between each update of the supervisory controllers not only could further energy savings be made, but better regulation of the thermal and electrical demands could be achieved.

### 2.2.3 Remarks

Many of the current approaches to the control of these hybrid energy supply systems involve similar MPC (24, 25), and/or optimisation methods (19, 26). In each case, these have shown to be useful tools for determining the feasibility of a proposed energy supply system or the optimal operational strategy over a future time horizon, provided the assumptions on the performance of the systems be in line with those predicted by



the models. However, the issue with these approaches is that they not only rely on accurate models to predict the optimum operation regime but rarely is attention given to the control strategy used while in operation. It assumes that a thermally-led mCHP unit is capable of providing the thermal load when it is required, and similarly for electrically-led systems (27, p. 43). Furthermore, the thermal and electrical demands that these studies use are pre-generated using computer simulations and fed to the optimisation routine – meaning the dynamic response of the systems to transient disturbances and operational constraints has not been considered (1, § 3.1).

The complication with using pre-generated building demands for determining the performance of supervisory controllers is that energy systems – and the external environment in which they operate – cannot be modelled precisely, may change in an unpredictable manner, and may be subject to significant disturbances. The design of these kind of ‘energy management systems’ in the presence of significant uncertainty requires the development of robust control algorithms.

Surveying a sample of the available literature of the control of hybrid microgeneration systems, it is evident that for the papers where ‘perfect’ control is not assumed between updates of the supervisory controller, on/off or PID variants are used. On/off operation is inefficient and many systems such as heat pumps and mCHP are less efficient when being cycled between standby and normal use. These conventional controls of energy systems are discussed further in § 2.3 and their suitability for MIMO control systems are discussed in § 2.5.

It would, therefore, be beneficial to look at improving the SL controls to the point where they are able to achieve what is expected from them by supervisory controllers. These SL controllers should take account of the transient and steady-state performance of technologies, and be able to provide predictable and effective control in the presence of modelling uncertainty and disturbances. Then, those looking at the long-term performance assessment of microgeneration deployment such as life-cycle assessment, techno-economic analysis (28) or to inform government policy on their impact on long-term emissions reductions can be more confident that the systems will operate as desired. Furthermore, it is theorised that improvements to the SL controllers could improve the energy efficiency, renewable energy utilisation and operational robustness of hybrid energy supply systems by making use of modern control techniques (§ 2.4 discusses emergent use of these modern controller architectures).

### **2.3 Conventional systems-level controls**

The basic idea of a feedback control system is that self-assessments are used to detect and analyse disturbances or changes in set-point so that corrective action can be applied

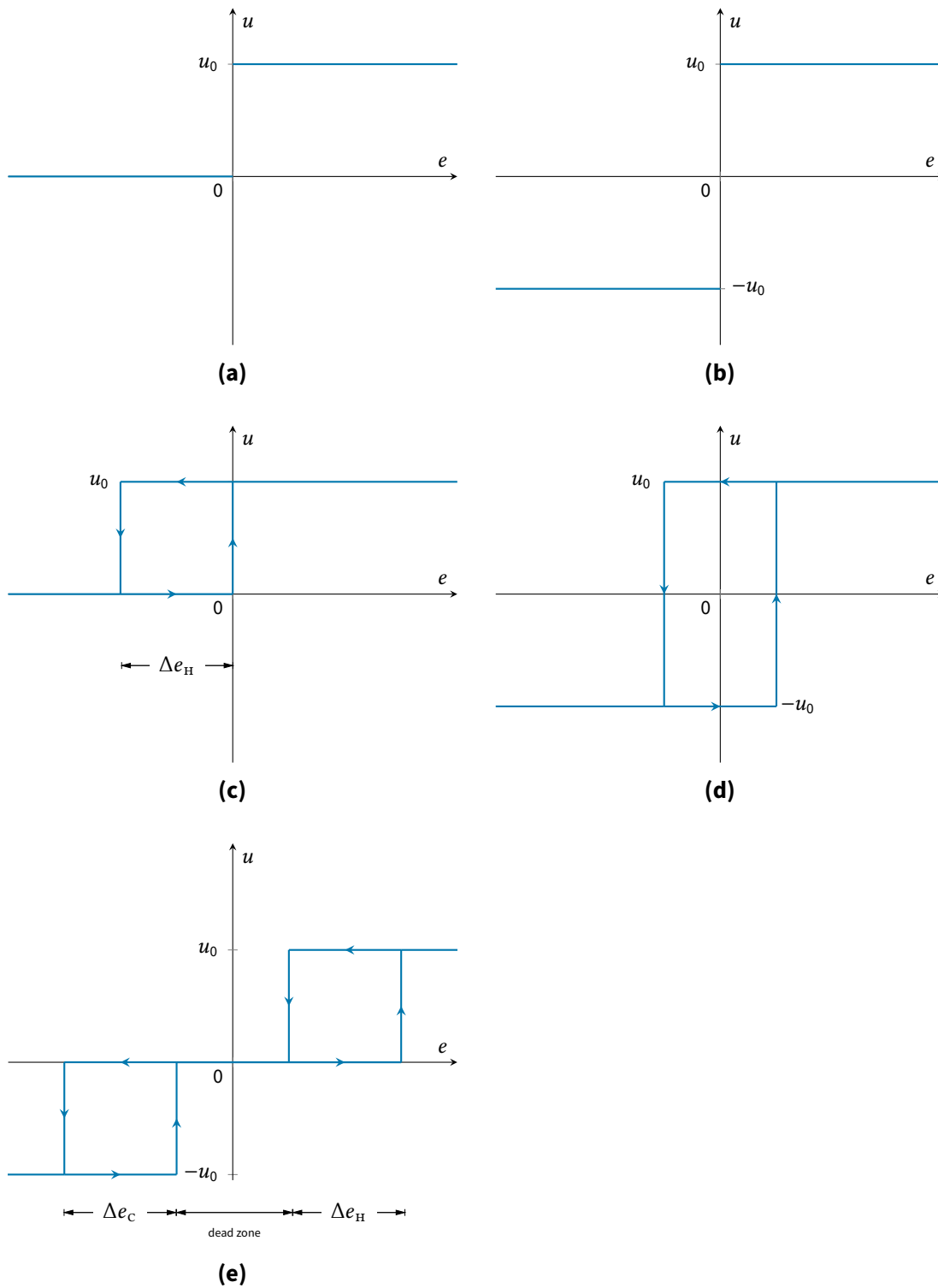


**Figure 2.1** | Visualisation of two-position control algorithms: **(a)** On-off control. **(b)** Bang-bang control. **(c)** On-off with hysteresis control. **(d)** Bang-bang with hysteresis control. **(e)** Bang-bang with hysteresis and dead-zone control.

to the system. This requires sensing and measurements to provide information to the control systems. This section reviews the conventional control system architectures that are used in the control of building-integrated energy systems.

### 2.3.1 Two-position control

One of the most widely used control algorithms in energy systems control remains the two-position control. And from the review of a sample of the literature in § 2.2, this is still the case for hybrid microgeneration systems. It is the simplest controller to implement and is also commonly used in thermostats in home central heating systems, water-supply systems, convective heaters, and many, many more. The low-level controllers are usually simple switches that are operated by differential thermal expansion, pressure, or position (29, p. 69).

There are many variants on two-position control, and the primary types encountered in practice have been represented pictorially as shown in fig. 2.1. The fundamental characteristic of all two-position controllers is that the output exists at only one of two discrete levels at any one time. The behaviour of each type of two-position controller can be inferred from fig. 2.1 and is not reiterated here. Potentially the most useful of the two-position controllers is that of the bang-bang with hysteresis and dead-zone shown in fig. 2.1e. For simple conditioning systems with heating and cooling, this controller can be effective when the performance requirements are not very demanding.

While being the simplest controllers to implement, the dynamics of all two-position controllers are nonlinear, therefore many of the common linear analysis techniques such as transfer functions do not apply. Therefore, controller designers will often have to resort to simulation to test out the operation of two-position controllers. Another obvious limitation of two-position controllers is that they are not the most efficient use of energy, as the fundamentals of their design will cause them to continuously oscillate around the required set-point for a finite sampling frequency.

### 2.3.2 PID control

The PID controller is “the most common solution to practical control problems” (30, p. v). The modern structure of the PID controller that is used today emerged in process control in the 1930s and 1940s (31). It is still widely used today because of their prevalence in many industries and there exists a mature body of literature on its design, application and tuning in a wide variety of fields. Furthermore, PID and its variants do not require models or knowledge of the controlled system, which can significantly simplify their application in practice. It is assumed that readers of this





work are very familiar with conventional PID controllers and further exploration of the history and future of PID controllers can be found in many books and review papers, such as (30, 32, 33).

The three components that comprise the structure of the PID controller are the proportional (P), integral (I), and derivative (D). These three components allow the controller to take action based on past (integral-term), present (proportional-term), and future (derivative-term) control errors. By tuning of the gains that multiply each of these terms, it has been found that PID controllers are capable of solving a wide variety of control problems (30, p. 5).

However, PID controllers are not suitable for highly nonlinear systems (32, § 6.6), or systems that have a large time delays (34, § 3.1). Furthermore, PID controllers are only applicable to single-input single-output (SISO) systems. In order to be used with MIMO systems methods, such as decoupling and cascade control need to be used alongside the traditional PID controller, but these also have their own shortcomings (these methods are considered briefly in §§ 2.5.2).

With these deficiencies in mind, it would be beneficial to look at alternative SL controls that are directly applicable to MIMO systems, and can be applied to complex nonlinear systems.

### 2.3.3 Buildings domain

There are several publications from industry and standards bodies that provide guidance and terminology for building automation and control systems (BACS). The International Standard BS EN ISO 16484-3:2005 (35) is intended for design of new buildings and retrofit of existing buildings for an acceptable indoor environment, practical energy conservation and efficiency. Part 3 of this Standard describes the software and the engineered functions used for building automation and control systems. CIBSE publish their Guide H on ‘Building Control Systems’ (36), which addresses the design and commissioning of control systems to control buildings and building services in an energy efficient way and to achieve the correct balance between human needs and how they interact with buildings and building services. ASHRAE publish their ‘Handbook—Fundamentals’ (37), where Chapter 7 addresses the fundamental concepts and types of control action found in BACS.

All institutions primarily cover the two-position control and PID variants<sup>2</sup> discussed in §§ 2.3.1 and 2.3.2 respectively. CIBSE and ASHRAE also provide details for tuning of

---

<sup>2</sup>That is, proportional (P), proportional-integral (PI) and proportional-integral-derivative (PID) control. While derivative action can reduce the overshoot in systems with high inertia, it can cause problems in practice as noisy measurement feedback can cause the controller to produce an erratic output. Due to this, CIBSE and ASHRAE state that the derivative term is seldom used in BACS (see: 36, p. 20, 37, p. 148).

**Table 2.1 | Building domain controls.** As terminology can change between each institution, control actions that are equivalent to each other have been categorised into the same row.

ISO	CIBSE	ASHRAE
Optimum start/stop	Optimum start	—
Energy tariff dependent switching	—	—
—	Weather compensation	Adaptive control (neural networks, self-learning performance-predictive)
—	Artificial intelligence (fuzzy logic, neural networks)	Fuzzy logic
—	Cascade control	—
—	—	Timed two-position control
—	—	Floating control (aka tri-state control)
—	—	Incremental control (pulse-width-modulation (PWM) control)

proportional-integral (PI) controllers: Both describe the **ultimate oscillation** and **first-order-plus-dead-time** methods using the well established Ziegler-Nichols calculation routine. CIBSE also provide information on ‘practical’ tuning of PID controllers with general principles and typical settings provided for a range of applications (e.g., heating coils, thermal wheels and supply fans).

Each institution uses slightly different terminology to describe the types of control action. The ISO refers to two-position control as a ‘fixed limit’ control while PID control is occasionally referred to as ‘three-term’ control by CIBSE. The hysteresis in two-position control is called the ‘differential gap/band’ by CIBSE and the ‘controller differential’ by ASHRAE.

In addition to two-position and PID control, the institutions also introduce a number of different types of control that are specific to the buildings domain. A list of these controls are provided in table 2.1.

Many of the controls listed in table 2.1 can be considered as a forms of supervisory control, such as optimum start and adaptive (weather compensating) control. The former can manipulate the time at which the systems-level controls are activated so that comfortable temperatures can be achieved at the start of the occupancy period with a minimum warm-up period prior to occupancy. Optimum start routines typically make use of the external climate, supply capacity of the energy systems and the thermal inertia of the building to determine the adaptive start time of the overall system.

Energy tariff dependent switching is another form of supervisory control, in which the configuration of the energy supply system can be changed, or the supply from different elements can be increased/reduced during variable cost energy periods. If tariffs are known ahead of time, this can also dictate the charging strategy of energy storage elements in the system.

Fuzzy logic is an alternative type of control to the traditional two-position and PID controllers. It uses a set of ‘if-then’ rules (that often emulate human language) written based on knowledge of the system being controlled. In contrast to ‘hard’ logic where the truth values may be either 0 or 1, the truth values in fuzzy logic may be any real number between 0 and 1. The common example of this is that we do not experience sudden change from ‘cold’ to ‘warm’ but a rather gradient from one ‘truth’ to the next. The advantage of this is that multiple rules can be combined in proportion to form the control action without the need of a model of the system; the knowledge gained from a model is already embedded into the rules. Studies involving the control of heating, ventilation, and air conditioning (HVAC) systems via fuzzy logic is considered in §§ 2.4.1.



Cascade controls are used when the system cannot be suitably controlled by one ‘master’ controller alone, but must be split into two or more subsystems, where the output from one controller becomes the input to another (inner) control loop. This type of control is considered further in §§ 2.5.2.

The final ASHRAE systems-level controls (timed two-position, floating and incremental) are all combinations of two-position components attached to a system that is capable of modulating its output. These are useful for cases where the actuators only have two states (e.g., on/off) but you wish to control the system over a continuous range. By manipulating the actuators ‘on-time’ and ‘cycle-time’ it is possible to make the system behave as if it was driven by a modulating controlled variable.

In addition to the control actions in table 2.1, there are several control actions described that are specific to the control of natural/mechanical ventilation: h,x-directed control, mixed-mode and night cooling. While these can improve the energy performance of a building, they are specific to air-based systems and are out with the scope of this work. In addition, room element control functions such as lighting control and shades/blinds control are not considered as part of this work. The focus of this work is on the systems-level control of the energy-supply/storage systems. The performance of the building could be improved by having one or more of these functions working alongside the closed-loop control of the energy supply systems.

## **2.4** Emergence of advanced systems-level controls

By extending the viewpoint of the literature to incorporate the application of control to different types and scales of energy systems it is possible to see an emergence of advanced systems-level controls that could be address the issues with the traditional methods.

### **2.4.1** HVAC controls

There is a wealth of research in SL HVAC controls (34, 38, 39), which are primarily designed to maintain a desirable indoor climate while minimising energy use (40, § 1.1), which align well with the objectives of the work of this thesis. However, the strength of many of the current approaches rely on accurate models to achieve improvements in control (41, § 7) and optimal control requires information on the internal and external disturbances acting on the building (40, § 5.2.1).

Wang, Ma (38) reviewed the types of supervisory controllers used in HVAC controls. Alongside the supervisory controllers, the most common type of SL control (commonly known as ‘local’ controls in HVAC literature) remain on/off and PID variants (38, p. 3). The local controllers are “designed to guarantee the robust operation and keep track of



the setpoint considering the dynamic characteristics of the local process environment”.

In contrast to the microgeneration control literature reviewed in § 2.2, in HVAC system controls “most research in [...] control focused on the local level controls, while relatively few studies focused on supervisory controls” (38, p. 16). With the wealth of experience in the SL controller development in HVAC systems, a key point to take away from this review is that the most effective local controls use a “robust control strategy” so that if the supervisory controllers are subject to errors in prediction or there is performance-degradation of the system components the “systems can still be controlled properly”.

Wright et al. (42) demonstrates that an intelligent supervisory control – that uses a multi-criterion genetic algorithm – can be combined with a local HVAC controller that assume perfect control with the set-points scheduled over a period of 24 h. The manipulation of the response of a system in this way are also used in H-infinity methods (43) that express the control problem as a mathematical optimisation problem and then finds the controller that solves the optimisation. These type of controllers can achieve impressive robustness and are readily applicable to multi-objective control problems. H-infinity controller synthesis is considered further in §§ 2.4.3.

Fundamentally though, in all the reviewed works they are primarily designed for the situation where their energy is supplied by a connection to a LEN. Although, a recent paper by Godina et al. (44) presents a comparison between on/off, PID and MPC of an HVAC system with solar PV microgeneration. The paper demonstrates that with the addition of the solar PV the control problem becomes more difficult and more advanced local control techniques are required to take full advantage of the local microgeneration.

The most recent review of HVAC control literature showed that vast majority of local HVAC controls are on/off, PID variants, fuzzy logic and MPC control methods (34, Fig. 2a). However, the recent work of Zaher (45) has looked at an alternative control structure to PID that “delivers significantly more energy efficient performance whilst achieving improved thermal comfort when compared to the industry standard HVAC design such as PID” (46, p. 1147, 47, p. 190). The controller method is based on the robust inverse dynamics estimation (RIDE) control methodology that was originally developed for the control of high-performance missiles (48) but has since been applied to assess the ideal controllability of buildings (49) and to the control and optimisation of HVAC systems (47). This promising controller architecture is considered further in §§ 2.4.4.





### 2.4.2 Microgrids

The focus of this work is building-integrated microgeneration. However, there are a number of useful control studies being conducted with microgeneration being used as part of a microgrid that are relevant to this work:

Liu et al. (50) proposes a hybrid AC/DC microgrid with coordinated control for low-level controls across a range of microgeneration technologies. The paper provides a comprehensive control strategy to tie together a diesel generator, wind power, tidal power, utility grid, fuel cells, flywheel, battery, EV, AC and DC loads. The controller provides coordinated control between all AC/DC and DC/AC converters to ensure stable system operation under many different load conditions. The work provides voltage and current control at the milli-second to deci-second resolution. As discussed throughout this chapter, the work of this thesis places emphasis on the SL control of the microgeneration energy systems. The utilising the work of Liu et al. in practice means would mean that any of the SL controllers developed in this work can be assured of coordinated control down to the low-level of the controller hierarchy.

Yang et al. (51) investigates a hybrid system of a GSHP and natural gas fuelled fuel cell serving multiple residences and small office buildings. The SL controllers use on/off operation for the GSHP and its auxiliary heaters and the fuel cell is set to run continuously at its maximum capacity (51, § 4.1.3). The combination of the GSHP and natural gas fuelled mCHP was able to reduce primary energy consumption and requires less electricity from the grid compared to the the GSHP alone. The work also concludes that as the system is capable of generating both thermal and electrical energy at the point of use, it is suitable for the inclusion in “smart” energy networks. Therefore, hybrid systems that work on both thermal and electrical networks is a promising area of study. Furthermore, the work suggests that improvements can be made to the system configuration and SL controls (51, § 5.1.2) to fully utilise the systems under consideration.

### 2.4.3 $H$ -infinity synthesis

$H_\infty$  control is a controller design methodology that is directly applicable to linear time-invariant (LTI) MIMO systems. It is a *robust* controller in that it is designed for systems with parametric uncertainty and external disturbances. The technique can be used to check if the design specifications of SL controllers are satisfied even in the presence of the worst case uncertainties (52, § 4). The concepts behind  $H_\infty$  control are mathematically intensive and readers are encouraged to review the work of Levine, Reichert (53) that provides a introduction targeted at engineers.

Conventional controls such as on/off and PID have a *fixed-structure* i.e. the elements



that make up the controller are known, such as the gains and mathematical operators of integration and differentiation. Traditional  $H_\infty$  controllers on the other hand *generate* the dynamics of the controller based on a model of the system to be controlled. This allows the controller to find a balance between parametric sensitivity, disturbance rejection, sensor noise rejection, tracking accuracy and controller effort, where the importance of each can be assigned a weighting function by the control designer.

The primary drawbacks of the development of  $H_\infty$  controllers is the mathematical understanding required to implement the theory as they do not easily reduce to formulaic algorithms for quick and routine implementation (54, p. 9). Another drawback is that the resulting controllers are often of high-order i.e. the order of the ordinary differential equations (ODEs) that the controller is comprised of can be high, which results in significant computational expense compared to the traditional approaches. Nevertheless, the  $H_\infty$  control approach has been successfully applied in several areas of energy systems control:

Sheela et al. (55) shows the application of  $H_\infty$  control for frequency and voltage regulation for microgrids operating in grid-connected and islanded operation. Similar to Liu et al. (50), the control is focussed on the low-level controls for power quality regulation between a wind turbine, solar PV, a fuel cell and battery storage. A key finding from this work is that the  $H_\infty$  control allows for smooth, robust, switching between grid-connected and islanded operation. A comparison with PID control is provided and the  $H_\infty$  controller displays superior performance under all load conditions. Likewise, Singh et al. (56) presents  $H_\infty$  control of a hybrid distribution generation system of wind turbines, diesel generators, aqua-electrolyzers, fuel cells and various energy storage units. The results demonstrate the robustness of the controller; the system is tested up to  $\pm 30\%$  changes in parameter values and shows only minimal variation in load frequency. Due to  $H_\infty$ 's direct application to MIMO systems and its performance robustness to parameter uncertainty, the application of  $H_\infty$  control of the hybrid microgeneration systems considered in this work is shown in § 8.2.

#### 2.4.4 Inversion-based control

All of the control techniques discussed thus far are primarily applied and designed for *linear* systems while the dynamic performance of nearly all real-world processes is nonlinear (29, p. 10). In many control problems, it is possible to design a linear controller based on the linearisation of the system around a certain equilibrium or operating point. When the requirements on system performance are moderate and the system operates in a small dynamic range, these controller designs are often acceptable. Nevertheless, there are several reasons why direct control of the nonlinear system



may be preferable:

- The nonlinearities in the system are so dominant that the linear controls can hardly meet the stringent requirements on systems performance in terms of satisfying the energy demands of the building.
- The dynamic interaction between the various components and systems could result in a complex nonlinear system where the linearised system is not controllable.
- Without extensive knowledge of the systems' behaviour against the full range of potential disturbances, the linear controllers may lead to aggressive response of manipulated inputs, fluctuation of the controlled outputs and also increased energy consumption.

These factors inevitably results in the endeavour to develop control approaches that will more or less incorporate the nonlinear dynamics into the design process.

Once such approach is (input-output) feedback linearisation. Unlike traditional system linearisation,<sup>3</sup> this approach utilises feedback of the controlled outputs through a reduced-order inverse of the system to render the given system linear in its input-output dynamics. Then, on the resulting linear sub-system the linear control techniques can be applied. This allows the controller to leverage the wealth of controller developments discussed throughout this chapter while still being directly applicable to the nonlinear system across its entire dynamic range.

The problem of feedback linearisation was first investigated in Brockett (57) for a restricted class of feedback transformations. The necessary and sufficient conditions for feedback linearisation were obtained in Jakubczyk, Respondek (58). And finally, feedback linearisation of the input-output map of the system was proposed in Isidori, Ruberti (59) and Isidori (60).

To date the application of the control theory has primarily been to problems in aircraft & missile control, process control, and robotics. Also in the last 5 years a lot of work has emerged on the application of the control technique to the MIMO boiler-turbine (thermal power plant) control problem. While a boiler-turbine is at a much larger scale than building-integrated microgeneration, the controller design faces many of the same challenges: complex dynamic interaction between components, control of multiple inputs and outputs across thermal and electrical networks,

---

<sup>3</sup>Typical linearisation of systems is obtained by taking the Taylor series expansion about an equilibrium point of the system for each multi-variable function and truncating the series above the first order terms. This procedure is detailed in appendix D.2.

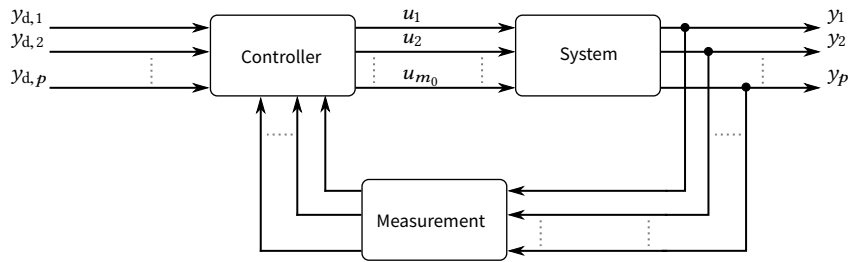


**Figure 2.2** | Block diagram of MIMO control system.

disturbance rejection, model parameter uncertainty, and it has multiple operation modes & configurations.

Moradi et al. (61) applied feedback linearisation control to regulate the performance of a boiler-turbine unit. The system is a  $3 \times 3$  MIMO system where the controller can manipulate the valve positions for fuel, steam and feed-water flow rates to control the drum pressure, electric output and water level of the drum. A PI controller is applied to the resulting linear sub-system. The controller is shown to guarantee the design performance specified for the system, even when the switching between different configurations across its entire dynamic range. It is able to tightly regulate the electrical power output with very small oscillations, even in the presence of modelling uncertainty in the geometrical parameters of the boiler-turbine.

The only drawback of the approach presented is that the ‘relative degree’ of all outputs are one, that is, a control output affects an input after only one time derivative of the output. Another way of thinking of the relative degree of an output in interconnected energy systems is that it is generally equivalent to the number of *inertial* or energy storage elements ‘downstream’ of the manipulated input in reference to a controlled output. Essentially, the relative degree represents the delay existing between a manipulated input and controlled output. The control building-integrated microgeneration, however, can result in systems with high relative degree. For example, consider a hybrid microgeneration system with an mCHP serving a hydronic heating system with the objective of regulating the air temperature of the building. The air temperature will only be indirectly related to the input fuel flow rate – which must first influence the engine, cooling water, and radiator temperatures before changes to the internal air temperature will be seen. Extension of the robust feedback linearisation controls to systems of any relative degree is then an important requirement of the controller design developed in this work.

## **2.5** MIMO control systems

As introduced in §§ 1.2.4, a significant control challenge posed by the deployment of microgeneration in buildings is consideration of both the thermal and electrical demands simultaneously. Of the works reviewed in § 2.2, it was always the job of the supervisory level controller to determine how the hybrid system should be controlled to fulfil the thermal and electrical demands over the evaluation period. This choice makes sense when considering their objectives of maximising the utilisation of on-site generation, minimising total operating cost or maximising profit: With *estimates* of climate, expected renewable generation, and predicted demand the studies have shown that it is possible to determine what systems to use at what time to meet their control





objectives.

Nevertheless, finding this optimum will essentially rely on accurately predicting the future, and any forecast of demand is subject to uncertainty and error. Furthermore, with the increase of renewables on the LEN, future LENs may impose a limit to when and how much energy can be imported and exported during a given period – that could also change dynamically during the day – something the supervisory control would have no knowledge of. Therefore, it is useful if the SL controllers were able to determine (with limited or no knowledge of the future) what the ideal operation of the technologies is at *that time instant* to account for modelling uncertainty and error in forecasts. In this way, it is thought that the hybrid microgeneration system can operate more efficiently without having to rely completely on the LEN as the fall back solution when there is mismatch between the predicted optimum dispatch and what actually occurs between updates.

When a SL controller has multiple controlled outputs and multiple manipulable inputs it is known as a **multi-input multi-output (MIMO) control system**. Figure 2.2 shows a diagram of the structure of a generic MIMO controller. Of all of the control architectures considered in § 2.3 and 2.4, one requirement is that the system is **square**, that is there are an equal number of control inputs (manipulated variables) to the system outputs (controlled variables). However, in hybrid microgeneration systems, there are often more sources of energy than controlled outputs. For example, designing a controller to satisfy the thermal and electrical demands of a building (2 controlled outputs) with a hybrid system consisting of an mCHP, TES, and EES (3 controllable energy sources). The following section considers the various approaches to the control of non-square systems.

### 2.5.1 Non-square systems

The discussion of the control of non-square systems is typically confined to the study of industrial and chemical processes (62). This is because in chemical processes there are good arguments to be made that ‘squaring’ a system results in inferior control as opposed to control methods that are applicable to non-square systems (63). That being said, the application of directly controlling non-square energy systems is left as future work (see §§ 9.3.1) and the discussion is restricted to methods to make the system square.

A system with an excess of control inputs is known as a **fat system** while a system with additional outputs is known as a **tall system** (64). The approach to each type is considered in the following.



### Excess measurements (Tall systems)

With the steady increase of pervasive environmental monitoring (65) and especially in the advent of low-cost sensing solutions (66) there is an increasing abundance of measurements available to the control engineer in commercial buildings e.g. building energy management systems (BEMS) can now have access ‘real-time’ temperature, humidity, lighting, energy consumption, occupancy/movement, air quality and noise level measurements for a low-cost (67). How these extra measurements can be used to improve the operation of energy systems in buildings is an emerging research topic (68) but is out with the scope of this work. In this research measurement signals will only be used for controlled variables or for estimation of controlled variables when they are not directly measurable. This is typically known as ‘squaring down’ the system were the control system never attempts to control more outputs than there are independent inputs.

There are methods of controlling more outputs than there are control inputs (64, p. 774) one such method is called **soft sharing control** where the importance of each output to be controlled is assigned a relative importance index, and the control system is designed to prioritise control to the outputs with a higher importance index. An example of this in energy systems control is given by (69, §B.4) where the control of tilt oscillations (output variables of generator speed & nacelle displacement) in a wind energy system were controlled by manipulating the blade pitch angle. While neither output could be controlled independently at all times the control system was still able to achieve adequate performance on minimising the deviation of the outputs from their set-points.

Another approach is to employ **switching strategies** where the control system will take care of a subset of the outputs at a time, switching between the different output subsets based upon time scheduling or decision logic.

### Excess inputs (Fat systems)

Fat systems are where the control engineer is ‘fortunate’ enough to have more manipulable inputs than there are controlled outputs. The simplest approach in this case is to control extra variables. However, since these extra variables are not being measured there are two alternative approaches: (1) Deploy extra monitoring equipment in the building so that the extra inputs can be utilised; (2) Construct an estimate of the additional variable(s) to be controlled from the existing measurements. The later case is an example of **observer** design, which is typically employed by control systems that require extra measurements or estimates of the internal states of the system being controlled.



**COORDINATED CONTROL** selects a subset of the inputs as the primary control variables, and the remaining inputs are used in some fixed or dynamic relationship to the primary controls (64, p. 773). Coordinated control has been successfully applied to microgrids with RES and electrical battery storage (70). The primary control action is the utilisation of the battery storage to satisfy the power output demand of the microgrid, while the use of the dispatchable distributed generation units is a function of the power output of the battery.

**SOFT LOAD SHARING** is where the load is shared between the available inputs. As discussed in § 2.3 this solution has been shown to be used in the control of hybrid energy systems. For example, the thermal demands of a home/office are fulfilled by the load sharing between a ground source heat pump, a fuel cell and a conventional boiler (22).

**HARD LOAD SHARING** is where the control is switched between different subsets of the inputs. Many of the optimisation techniques in § 2.2 are designed for the supervisory controller to operate in this fashion.

With all the different techniques available to ‘square’ the control problem, it would be beneficial to find an automated way to reduce hybrid energy systems that are not square to square systems.

### 2.5.2 *Decoupling & cascade control*

A common approach in energy systems control (after the system has been ‘squared’) is to reduce a MIMO system to individual SISO that can be tackled with traditional control methods. Then, the problem is to find a ‘decoupling’ control or to split the system in cascade control, in either case, the overall system is functionally broken up into independent controlled systems and then tasked with finding a way to control the supply of energy to each part individually. This requires selecting a reference or demand trajectory, manipulated input, and energy supply for each separate subsystem. The typical design procedure for cascade control is to first design the ‘fast acting’ inner loop and then the outer loop. For the control of building-integrated microgeneration systems e.g. systems with hydronic heating and a fixed-speed pump, it is not possible to break the system up into smaller fast-acting elements and the control of the overall system must be addressed. Therefore, this work places an emphasis on finding a controller that can tackle MIMO systems directly.



## 2.6 RIDE control methodology

A promising controller architecture introduced in §§ 2.4.1, that is also based on system inversion discussed in §§ 2.4.4, is the RIDE controller. The RIDE control methodology was originally developed for the control of high-performance missiles (48) but has since been applied to assess the ideal controllability of buildings (49) and to the control and optimisation of HVAC systems (47).

The objective of the work of this thesis was the the design and application of MIMO control algorithms to the problem of controlling microgeneration devices and energy storage within a building. The controller should address the following issues:

1. The controller can prioritise the use of renewable and low-carbon resources.
2. To investigate a control structure that would allow for flexible/controllable integration with the local electrical network.
3. The controller can exploit the synergy of multiple energy systems to simultaneously fulfil the thermal and electrical demands of a building.
4. The controller can efficiently operate energy delivery networks with high inertia.
5. The controller is capable of handling multiple simultaneous input constraints.

It is theorised that the RIDE controlled methodology can be developed to address the objectives of this work.

### 2.6.1 Original methodology review

This subsection contains a review of the original RIDE methodology so the reader is familiarised with the structure and design of RIDE controllers. The aim is to demonstrate the effectiveness of the theory, but also to illustrate where advancements/ modifications can be made to the theory to make it applicable to the energy systems considered in this work.

Assuming the linearised system to be controlled can be described by a LTI state-space model given by

$$\begin{aligned}\dot{\mathbf{x}}(t) &= \mathbf{A}\mathbf{x} + \mathbf{B}\boldsymbol{\mu}, \\ \mathbf{y}(t) &= \mathbf{C}\mathbf{x} + \mathbf{D}\boldsymbol{\mu},\end{aligned}\tag{2.1}$$

where  $\mathbf{x}(t) \in \mathbb{R}^n$  is the state vector,  $\boldsymbol{\mu}(t) \in \mathbb{R}^m$  is the input vector,  $\mathbf{y}(t) \in \mathbb{R}^p$  is the output vector,  $\mathbf{A} \in \mathbb{R}^{n \times n}$  is the system matrix,  $\mathbf{B} \in \mathbb{R}^{n \times m}$  is the input matrix,  $\mathbf{C} \in \mathbb{R}^{p \times n}$  is the output matrix and  $\mathbf{D} \in \mathbb{R}^{p \times m}$  is the feedforward matrix. Now, without loss of





generality, the system input vector can be split into sub-vectors as  $\boldsymbol{\mu} = (\mathbf{u}^T, \boldsymbol{\psi}^T)^T$ , where  $\mathbf{u} \in \mathbb{R}^p$  is the **control** input vector and  $\boldsymbol{\psi} \in \mathbb{R}^{m-p}$  is the **exogenous** input vector that contains all the inputs originating from outside the model and are unexplained by the model. Note that it is already assumed that the system is square – that is – there is the same number of control inputs as system outputs. The system (2.1) can now be expressed as

$$\dot{\mathbf{x}}(t) = \mathbf{A}\mathbf{x}(t) + \mathbf{B}_1\mathbf{u}(t) + \mathbf{B}_2\boldsymbol{\psi}(t), \quad (2.2a)$$

$$\mathbf{y}(t) = \mathbf{C}\mathbf{x}(t) + \mathbf{D}_1\mathbf{u}(t) + \mathbf{D}_2\boldsymbol{\psi}(t), \quad (2.2b)$$

Robust controllers are typically comprised of two parts (71, p. 276):

1. A nominal part – the inner model reduction component – commonly a feedback linearisation or inverse control law, and
2. An outer component used to account for model uncertainties and disturbances

The RIDE control methodology follows the same structure: with one part being comprised of an ‘equivalent control’ term that serves to reduce the model dynamics and decouple the control channels, and another part being a pseudo-derivative-feedback (PDF) controller, which can be thought of as being similar to a PID controller but with an alternative structure such that it achieves uniformly better performance (29, Appx. C).

### Equivalent control

The first component of the RIDE controller is the ‘equivalent control’,  $\mathbf{u}_{\text{eq}}$ , which is the control input required to maintain  $\dot{\mathbf{y}} = 0$  despite changes in system states or exogenous inputs. Taking first time derivative of (2.2b) gives

$$\dot{\mathbf{y}}(t) = \mathbf{C}\dot{\mathbf{x}}(t) + \mathbf{D}_1\dot{\mathbf{u}}(t) + \mathbf{D}_2\dot{\boldsymbol{\psi}}(t).$$

Substituting (2.2a) gives

$$\dot{\mathbf{y}}(t) = \mathbf{C}(\mathbf{A}\mathbf{x}(t) + \mathbf{B}_1\mathbf{u}(t) + \mathbf{B}_2\boldsymbol{\psi}(t)) + \mathbf{D}_1\dot{\mathbf{u}}(t) + \mathbf{D}_2\dot{\boldsymbol{\psi}}(t) \quad (2.3)$$

Taking the Laplace transform of (2.3) by utilising eq. (6.3), setting  $\dot{\mathbf{y}} = 0$ , and collecting terms results in the algebraic equation

$$\mathbf{0} = \mathbf{C}\mathbf{A}\mathbf{x}(s) + (\mathbf{C}\mathbf{B}_1 + s\mathbf{D}_1)\mathbf{u}(s) + (\mathbf{C}\mathbf{B}_2 + s\mathbf{D}_2)\boldsymbol{\psi}(s).$$



Defining  $\mathbf{u}_{\text{eq}}(s) := \mathbf{u}(s)$  and solving for  $\mathbf{u}_{\text{eq}}(s)$  gives

$$\boxed{\mathbf{u}_{\text{eq}}(s) = -(\mathbf{CB}_1 + s\mathbf{D}_1)^{-1}(\mathbf{CAx}(s) + (\mathbf{CB}_2 + s\mathbf{D}_2)\boldsymbol{\psi}(s))}, \quad (2.4)$$

where, provided  $\det(\mathbf{CB}_1 + s\mathbf{D}_1) \neq 0$ ,  $\mathbf{u}_{\text{eq}}$  is the control effort required to maintain  $\dot{\mathbf{y}} = 0$  i.e. regardless of changes to the system states, exogenous inputs or disturbances,  $\forall t : \mathbf{y}(t) \equiv \mathbf{y}_d$  provided  $\mathbf{y}(0) = \mathbf{y}_d$ . Said otherwise, this component ensures that when the output  $\mathbf{y}$  reaches  $\mathbf{y}_d$  it will be maintained.

Now consider the two terms of a robust controller combined as  $\mathbf{u}(s) = \mathbf{u}_{\text{eq}}(s) + \mathbf{u}_c(s)$ , then substituting this and (2.4) into (2.3) in the Laplace domain gives

$$s\mathbf{y}(s) = (\mathbf{CB}_1 + s\mathbf{D}_1)\mathbf{u}_c(s).$$

### Outer-loop control

The outer-loop controller is designed so that the output  $y_i$  asymptotically tracks the demand trajectory  $y_{d,i}$ . The outer-loop controller in the RIDE methodology is a combination of local asymptotic stabilisation (via pole placement) and integral action. This type of control, known as PDF control, was pioneered by Phelan (29) as an alternative to the traditional PI controller that is used in most of cases in the industry. Selecting the outer-loop controller as

$$\boxed{\mathbf{u}_c(s) = \mathbf{K}(s) (s^{-1}\mathbf{K}_I(\mathbf{y}_d(s) - \mathbf{y}(s)) - \mathbf{K}_D\mathbf{y}(s))}, \quad (2.5)$$

where the dynamic compensator is  $\mathbf{K}(s) = (\mathbf{CB}_1 + s\mathbf{D}_1)^{-1}$ , the integral gain matrix  $\mathbf{K}_I = \text{diag}(K_{I,1}, \dots, K_{I,p})$  and the pseudo-derivative<sup>4</sup> feedback gain matrix  $\mathbf{K}_D = \text{diag}(K_{D,1}, \dots, K_{D,p})$ .

This results in an ideal second-order non-interacting MIMO system given by

$$\begin{bmatrix} y_1(s) \\ y_2(s) \\ \vdots \\ y_p(s) \end{bmatrix} = \begin{bmatrix} \frac{K_{I,1}}{s^2 + K_{D,1}s + K_{I,1}} & 0 & \cdots & 0 \\ 0 & \frac{K_{I,2}}{s^2 + K_{D,2}s + K_{I,2}} & \cdots & 0 \\ \vdots & \vdots & \cdots & \vdots \\ 0 & 0 & \cdots & \frac{K_{I,p}}{s^2 + K_{D,p}s + K_{I,p}} \end{bmatrix} \begin{bmatrix} y_{d,1}(s) \\ y_{d,2}(s) \\ \vdots \\ y_{d,p}(s) \end{bmatrix}.$$

It is evident that the response of each output is given by a general second-order transfer

<sup>4</sup>The name pseudo-derivative comes from the fact that the control structure is identical to a system with integral action and  $(1 + K_D D)$  in the feedback loop. However, instead of taking the derivative of the output only to integrate it again in the forward loop, the structure can be changed so that the output feedback enters ahead of the integrator as shown in fig. 2.3.

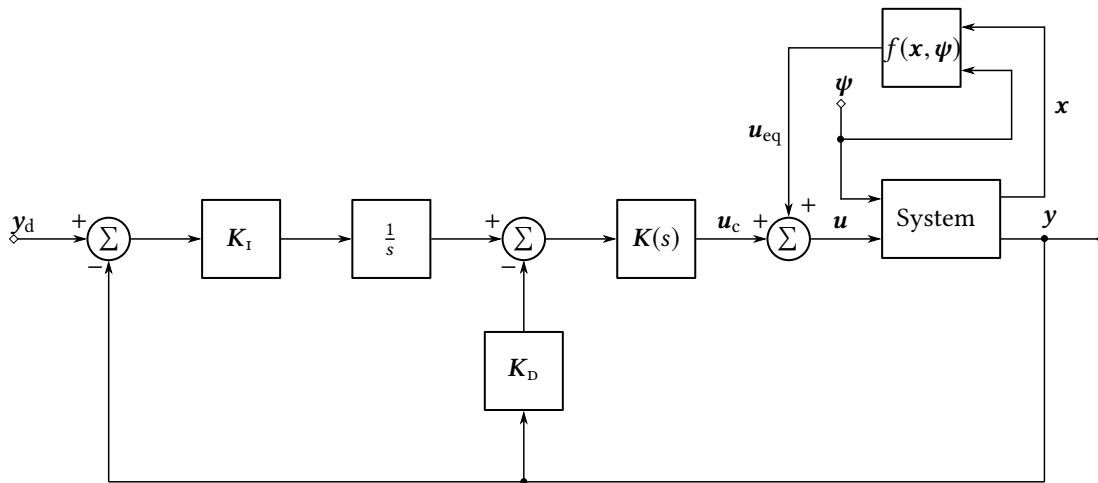


**Figure 2.3 |** Block diagram of original RIDE structure. Constraints on the magnitude of the inputs have been removed for clarity.

function as

$$G_{ii}(s) = \frac{K_{I,i}}{s^2 + K_{D,i}s + K_{I,i}} = \frac{\omega_n^2}{s^2 + 2\zeta\omega_n s + \omega_n^2}, \quad (2.6)$$

where the **damping ratio**,  $\zeta_i$ , and **undamped natural frequency**,  $\omega_{n,i}$  of the response of each output are used to characterise the response of a second-order system just as time constants describe first-order system response. These quantities can be selected independently from the appropriate choice of gains  $K_{I,i}$  and  $K_{D,i}$ . A schematic of the original RIDE structure is given in fig. 2.3. This design has satisfied both the asymptotic stabilisation and tracking problems for a system given by (2.2).

Note that the complete RIDE theory includes a method to estimate  $\mathbf{u}_{eq}$  based on measurement of the derivative of the output. The modifications made to the theory in this work result in this no longer being the case and will be addressed in § 7.1.

The theory also provides a method to handle constraints on the control inputs such that  $\mathbf{u} \in U$  with the set

$$U = \{\mathbf{u} = (u_1, \dots, u_p) \in \mathbb{R}^p : u_{LL,i} \leq u_i \leq u_{UL,i}, i = 1, \dots, p\}$$

and  $u_{LL,i}, u_{UL,i}$  are constants. These input constraints are addressed separately in § 7.3.

### 2.6.2 Drawbacks of standard method

The original RIDE methodology has shown to be effective in providing stable, robust control for dynamic systems defined as eq. (2.2). However, there are several deficiencies that need to be addressed so that it is suitable for application to the control of the energy systems considered in this work, such as an mCHP connected to a hydronic heating system.

First, consider the notion of a system having “fast” and “slow” modes (states). The term “fast” modes means that the manipulated input affects the controlled output either directly or after one time derivative of the output. This was demonstrated in eq. (2.4), where the equivalent control was computed using the first time derivative of the output, with the condition being that  $(CB_1 + sD_1)$  was invertible. The RIDE methodology as applied in current literature has only been used to control the “fast” modes of the system (72, p. 76, 73, p. 335, 74, p. 635, 45, p. 65).

Where “slow” modes have been encountered, such as the work by Counsell et al. (49), they applied the RIDE methodology to slow-acting heating systems where the original  $(CB_1 + sD_1)$  in eq. (2.4) was not invertible. This was achieved by introducing extra controlled variables on intermediate states between the manipulated inputs and controlled outputs to ensure  $(CB_1 + sD_1)$  became invertible. This is essentially using RIDE in cascade control, where the overall system is broken up into independent



first-order controlled systems and finding a way to control the supply of energy to each part individually. This requires selecting a reference or demand trajectory, manipulated input, and energy supply for each separate subsystem. For the control of building-integrated microgeneration systems e.g. systems with hydronic heating and a fixed-speed pump, it is not possible to break the system up into smaller fast-acting elements and the control of the overall system must be addressed.

## 2.7 Summary

This research explores the development of MIMO control algorithms and their application to the problem of controlling microgeneration devices and energy storage within a building with the primary goal of fulfilling the thermal and electrical demands of the building while minimising the interaction with the local electrical network.

The work will look at the design of MIMO SL controllers for hybrid microgeneration systems that are respectful of low-level controller performance, and can also be easily manipulated by supervisory controllers. The controller should be able to provide not only predictable performance but fast response to requests for change in balance-of-plant configuration and set-point changes.

The choice of controller is restricted to the following:

- It must be a MIMO controller that can strongly decouple the control channels so that the supply of heat and electrical energy can be controlled independently.
- The developed controller will be *robust* that is – will have adequate performance in the presence of unknown external disturbance inputs and modelling imprecision.
- Be of malleable design with a clear controller design procedure such that various configurations of energy systems can be utilised without requiring a complete re-design or re-tuning.

From the review of the literature, the most promising control technique is that of input-output feedback linearisation explored in §§ 2.4.4, combined with a robust controller methodology such as RIDE. The following chapter details the research method employed in the design and application of the controller to the control of building-integrated energy systems.

## References

1. Staffell, I., Brett, D. J. L., Brandon, N. P., Hawkes, A. D. *Domestic Microgeneration: Renewable and Distributed Energy Technologies, Policies and Economics*. Abingdon, Oxon, UK: Routledge, 2015. ISBN: 978-1-315-69710-9 (cited pp. 23, 30)





2. Darby, S. J. Load management at home: advantages and drawbacks of some 'active demand side' options. *Proceedings of the Institution of Mechanical Engineers, Part A: Journal of Power and Energy* **227**(1): 9–17 (2012).  
DOI: [10.1177/0957650912464623](https://doi.org/10.1177/0957650912464623) (cited p. 24)
3. Joshi, P., Arora, S. Maximum power point tracking methodologies for solar PV systems – A review. *Renewable and Sustainable Energy Reviews* **70**: 1154–77 (2017-04).  
DOI: [10.1016/j.rser.2016.12.019](https://doi.org/10.1016/j.rser.2016.12.019) (cited p. 24)
4. Indragandhi, V., Subramaniaswamy, V., Logesh, R. Resources, configurations, and soft computing techniques for power management and control of PV/wind hybrid system. *Renewable and Sustainable Energy Reviews* **69**: 129–43 (2017-03).  
DOI: [10.1016/j.rser.2016.11.209](https://doi.org/10.1016/j.rser.2016.11.209) (cited p. 24)
5. Fathabadi, H. Novel highly accurate universal maximum power point tracker for maximum power extraction from hybrid fuel cell/photovoltaic/wind power generation systems. *Energy* **116**: 402–16 (2016-12).  
DOI: [10.1016/j.energy.2016.09.095](https://doi.org/10.1016/j.energy.2016.09.095) (cited p. 24)
6. Hawkes, A., Staffell, I., Brett, D., Brandon, N. Fuel cells for micro-combined heat and power generation. *Energy & Environmental Science* **2**(7): 729–44 (2009).  
DOI: [10.1039/B902222H](https://doi.org/10.1039/B902222H) (cited p. 24)
7. Wang, Y., Chen, Z., Zhang, C. On-line remaining energy prediction: A case study in embedded battery management system. *Applied Energy* **194**: 688–95 (2017-05).  
DOI: [10.1016/j.apenergy.2016.05.081](https://doi.org/10.1016/j.apenergy.2016.05.081) (cited p. 25)
8. Zou, C., Hu, X., Wei, Z., Tang, X. Electrothermal dynamics-conscious lithium-ion battery cell-level charging management via state-monitored predictive control. *Energy* **141**: 250–9 (2017-12).  
DOI: [10.1016/j.energy.2017.09.048](https://doi.org/10.1016/j.energy.2017.09.048) (cited p. 25)
9. Roumila, Z., Rekioua, D., Rekioua, T. Energy management based fuzzy logic controller of hybrid system wind/photovoltaic/diesel with storage battery. *International Journal of Hydrogen Energy* **42**(30): 19525–35 (2017).  
DOI: [10.1016/j.ijhydene.2017.06.006](https://doi.org/10.1016/j.ijhydene.2017.06.006) (cited p. 26)
10. Entchev, E., Yang, L., Ghorab, M., Rosato, A., Sibilio, S. Energy, economic and environmental performance simulation of a hybrid renewable microgeneration system with neural network predictive control. *Alexandria Engineering Journal* (2016).  
DOI: [10.1016/j.aej.2016.09.001](https://doi.org/10.1016/j.aej.2016.09.001) (cited p. 26)
11. Yang, L., Entchev, E. Performance prediction of a hybrid microgeneration system using Adaptive Neuro-Fuzzy Inference System (ANFIS) technique. *Applied Energy* **134**(Supplement C): 197–203 (2014).  
DOI: [10.1016/j.apenergy.2014.08.022](https://doi.org/10.1016/j.apenergy.2014.08.022) (cited p. 26)
12. Tuohy, P. et al. Orchestration of Renewable Generation in Low Energy Buildings and Districts Using Energy Storage and Load Shaping. *Energy Procedia* **78**(Supplement C): 2172–7 (2015).  
DOI: [10.1016/j.egypro.2015.11.311](https://doi.org/10.1016/j.egypro.2015.11.311) (cited pp. 26, 29)
13. Padhy, N. P. Unit commitment problem under deregulated environment-a review. In *2003 IEEE Power Engineering Society General Meeting (IEEE Cat. No.03CH37491)*. Vol. 2. 2003-07: 1094 Vol. 2.  
DOI: [10.1109/PES.2003.1270467](https://doi.org/10.1109/PES.2003.1270467) (cited p. 26)



14. Hawkes, A., Leach, M. Modelling high level system design and unit commitment for a microgrid. *Applied Energy* **86**(7-8): 1253–65 (2009-07).  
DOI: [10.1016/j.apenergy.2008.09.006](https://doi.org/10.1016/j.apenergy.2008.09.006) (cited p. 26)
15. Hawkes, A. D., Brett, D. J. L., Brandon, N. P. Role of fuel cell based micro-cogeneration in low carbon heating. *Proceedings of the Institution of Mechanical Engineers, Part A: Journal of Power and Energy* **225**(2): 198–207 (2011).  
DOI: [10.1177/2041296710394268](https://doi.org/10.1177/2041296710394268) (cited p. 26)
16. Hellmers, A., Zugno, M., Skajaa, A., Morales, J. M. Operational strategies for a portfolio of wind farms and CHP plants in a two-price balancing market. *IEEE Transactions on Power Systems* **31**(3): 2182–91 (2016).  
DOI: [10.1109/TPWRS.2015.2439060](https://doi.org/10.1109/TPWRS.2015.2439060) (cited p. 26)
17. Kneiske, T. M., Braun, M., Hidalgo-Rodriguez, D. I. A new combined control algorithm for PV-CHP hybrid systems. *Applied Energy* (2017).  
DOI: [10.1016/j.apenergy.2017.06.047](https://doi.org/10.1016/j.apenergy.2017.06.047) (cited p. 26)
18. Bove, R., Lunghi, P., Sammes, N. M. SOFC mathematic model for systems simulations - Part 2: Definition of an analytical model. *International Journal of Hydrogen Energy* **30**(2): 189–200 (2005-02).  
DOI: [10.1016/j.ijhydene.2004.04.018](https://doi.org/10.1016/j.ijhydene.2004.04.018) (cited p. 27)
19. Moradi, M. H., Hajinazari, M., Jamasb, S., Paripour, M. An energy management system (EMS) strategy for combined heat and power (CHP) systems based on a hybrid optimization method employing fuzzy programming. *Energy* **49**: 86–101 (2013-01).  
DOI: [10.1016/j.energy.2012.10.005](https://doi.org/10.1016/j.energy.2012.10.005) (cited pp. 27, 29)
20. Rouhani, A., Kord, H., Mehrabi, M. A comprehensive method for optimum sizing of hybrid energy systems using intelligence evolutionary algorithms. *Indian Journal of Science and Technology* **6**(6): 4702–12 (2013).  
DOI: [10.1016/j.enconman.2010.09.028](https://doi.org/10.1016/j.enconman.2010.09.028) (cited p. 27)
21. Brandoni, C., Renzi, M., Caresana, F., Polonara, F. Simulation of hybrid renewable microgeneration systems for variable electricity prices. *Applied Thermal Engineering* **71**(2): 667–76 (2014-10).  
DOI: [10.1016/j.applthermaleng.2013.10.044](https://doi.org/10.1016/j.applthermaleng.2013.10.044) (cited p. 28)
22. Canelli, M., Entchev, E., Sasso, M., Yang, L., Ghorab, M. Dynamic simulations of hybrid energy systems in load sharing application. *Applied Thermal Engineering* **78**: 315–25 (2015-03).  
DOI: [10.1016/j.applthermaleng.2014.12.061](https://doi.org/10.1016/j.applthermaleng.2014.12.061) (cited pp. 28, 29, 42)
23. Entchev, E., Yang, L., Ghorab, M., Lee, E. Performance analysis of a hybrid renewable micro-generation system in load sharing applications. *Applied Thermal Engineering* **71**(2): 697–704 (2014-10).  
DOI: [10.1016/j.applthermaleng.2013.10.057](https://doi.org/10.1016/j.applthermaleng.2013.10.057) (cited p. 28)
24. Sossan, F., Bindner, H., Madsen, H., Torregrossa, D., Chamorro, L. R., Paolone, M. A model predictive control strategy for the space heating of a smart building including cogeneration of a fuel cell-electrolyzer system. *International Journal of Electrical Power & Energy Systems* **62**: 879–89 (2014-11).  
DOI: [10.1016/j.ijepes.2014.05.040](https://doi.org/10.1016/j.ijepes.2014.05.040) (cited p. 29)
25. Wolfrum, P., Kautz, M., Schäfer, J. Optimal control of combined heat and power units under varying thermal loads. *Control Engineering Practice* **30**: 105–11 (2014-09).  
DOI: [10.1016/j.conengprac.2013.08.014](https://doi.org/10.1016/j.conengprac.2013.08.014) (cited p. 29)



26. Kortela, J., Jämsä-Jounela, S.-L. Modeling and model predictive control of the BioPower combined heat and power (CHP) plant. *International Journal of Electrical Power & Energy Systems* **65**: 453–62 (2015-02).  
DOI: [10.1016/j.ijepes.2014.10.043](https://doi.org/10.1016/j.ijepes.2014.10.043) (cited p. 29)
27. Entchev, E., Tzscheutschler, P. *Integration of Microgeneration and Related Technologies in Building*. Tech. rep. October. Germany: International Energy Agency, 2014: 1–99 (cited p. 30)
28. Herrando, M., Markides, C. N. Hybrid PV and solar-thermal systems for domestic heat and power provision in the UK: Techno-economic considerations. *Applied Energy* **161**: 512–32 (2016-01).  
DOI: [10.1016/j.apenergy.2015.09.025](https://doi.org/10.1016/j.apenergy.2015.09.025) (cited p. 30)
29. Phelan, R. M. *Automatic control systems*. London, UK: Cornell University Press, 1977: 280. ISBN: 0-8014-1033-9 (cited pp. 31, 37, 44, 45)
30. Astrom, K. J., Haggglund, T. *Advanced PID Control*. Research Triangle Park, NC: ISA - The Instrumentation, Systems, and Automation Society, 2006. ISBN: 1556179421 (cited pp. 31, 32)
31. Bennett, S. *A History of Control Engineering, 1800-1930*. Stevenage, UK: Institution of Electrical Engineers, 1979. ISBN: 0906048079 (cited p. 31)
32. Åström, K., Häggglund, T. The future of PID control. *Control Engineering Practice* **9**(11): 1163–75 (2001-11).  
DOI: [10.1016/S0967-0661\(01\)00062-4](https://doi.org/10.1016/S0967-0661(01)00062-4) (cited p. 32)
33. Visioli, A. Research trends for PID controllers. *Acta Polytechnica* **52**(5) (2012) (cited p. 32)
34. Shaikh, P. H., Nor, N. B. M., Nallagownden, P., Elamvazuthi, I., Ibrahim, T. A review on optimized control systems for building energy and comfort management of smart sustainable buildings. *Renewable and Sustainable Energy Reviews* **34**: 409–29 (2014-06).  
DOI: [10.1016/j.rser.2014.03.027](https://doi.org/10.1016/j.rser.2014.03.027) (cited pp. 32, 34, 35)
35. BS EN ISO 16484-3:2005. *Building automation and control systems (BACS) — Part 3: Functions*. London, UK: British Standards Institution, 2005. ISBN: 0 580 45387 1 (cited p. 32)
36. CIBSE. *Guide H: Building control systems*. Ed. by Butcher, K. J. 2nd ed. London, UK: Chartered Institution of Building Services Engineers, 2009. ISBN: 978-1-906846-00-8 (cited p. 32)
37. ASHRAE. *2017 ASHRAE Handbook—Fundamentals (SI Edition)*. Ed. by Owen, M. S. Atlanta, GA: ASHRAE, 2017. ISBN: 978-1-939200-58-7 (cited p. 32)
38. Wang, S., Ma, Z. Supervisory and Optimal Control of Building HVAC Systems: A Review. *HVAC&R Research* **14**(1): 3–32 (2008-01).  
DOI: [10.1080/10789669.2008.10390991](https://doi.org/10.1080/10789669.2008.10390991) (cited pp. 34, 35)
39. Dounis, A. I., Caraiscos, C. Advanced control systems engineering for energy and comfort management in a building environment-A review. *Renewable and Sustainable Energy Reviews* **13**(6-7): 1246–61 (2009-08).  
DOI: [10.1016/j.rser.2008.09.015](https://doi.org/10.1016/j.rser.2008.09.015) (cited p. 34)
40. Gruber, M., Truschel, A., Dalenback, J. O. Alternative strategies for supply air temperature control in office buildings. *Energy and Buildings* **82**: 406–15 (2014-10).  
DOI: [10.1016/j.enbuild.2014.06.056](https://doi.org/10.1016/j.enbuild.2014.06.056) (cited p. 34)
41. Afroz, Z., Shafiullah, G., Urme, T., Higgins, G. Modeling techniques used in building HVAC control systems: A review. *Renewable and Sustainable Energy Reviews* (2017-12).  
DOI: [10.1016/j.rser.2017.10.044](https://doi.org/10.1016/j.rser.2017.10.044) (cited p. 34)



42. Wright, J. A., Loosemore, H. A., Farmani, R. Optimization of building thermal design and control by multi-criterion genetic algorithm. *Energy and Buildings* **34**(9): 959–72 (2002-10).  
DOI: [10.1016/S0378-7788\(02\)00071-3](https://doi.org/10.1016/S0378-7788(02)00071-3) (cited p. 35)
43. McFarlane, D., Glover, K. A loop-shaping design procedure using H-infinity synthesis. *IEEE Transactions on Automatic Control* **37**(6): 759–69 (1992).  
DOI: [10.1109/9.256330](https://doi.org/10.1109/9.256330) (cited p. 35)
44. Godina, R., Rodrigues, E. M., Pouresmaeil, E., Catalão, J. P. Optimal residential model predictive control energy management performance with PV microgeneration. *Computers & Operations Research* (2017-12).  
DOI: [10.1016/j.cor.2017.12.003](https://doi.org/10.1016/j.cor.2017.12.003) (cited p. 35)
45. Zaher, O. S. Advanced Control, Identification and Optimisation of Energy Systems. PhD thesis. University of Strathclyde, 2013: 205. URL: [http://oleg.lib.strath.ac.uk/R/?func=dbin-jump-full%7B%5C%7Dobject%7B%5C\\_%7Ddid=22632](http://oleg.lib.strath.ac.uk/R/?func=dbin-jump-full%7B%5C%7Dobject%7B%5C_%7Ddid=22632) (cited pp. 35, 46)
46. Counsell, J. M., Zaher, O. S., Brindley, J., Murphy, G. Robust nonlinear HVAC systems control with evolutionary optimisation. *Engineering Computations* **30**(8): 1147–69 (2013).  
DOI: [10.1108/EC-04-2012-0079](https://doi.org/10.1108/EC-04-2012-0079) (cited p. 35)
47. Zaher, O. S., Counsell, J. M., Brindley, J. Robust control of room temperature and relative humidity using advanced nonlinear inverse dynamics and evolutionary optimisation. In *Evolutionary and Deterministic Methods for Design, Optimization and Control*. Capua, Italy, 2011 (cited pp. 35, 43)
48. Counsell, J. M. Optimum and safe control algorithm (OSCA) for modern missile autopilot design. Ph.D. University of Lancaster, 1992 (cited pp. 35, 43)
49. Counsell, J. M., Khalid, Y. A., Brindley, J. Controllability of buildings: A multi-input multi-output stability assessment method for buildings with slow acting heating systems. *Simulation Modelling Practice and Theory* **19**(4): 1185–200 (2011-04).  
DOI: [10.1016/j.simpat.2010.08.006](https://doi.org/10.1016/j.simpat.2010.08.006) (cited pp. 35, 43, 46)
50. Liu, X., Wang, P., Loh, P. C. A hybrid AC/DC microgrid and its coordination control. *IEEE Transactions on Smart Grid* **2**(2): 278–86 (2011).  
DOI: [10.1109/TSG.2011.2116162](https://doi.org/10.1109/TSG.2011.2116162) (cited pp. 36, 37)
51. Yang, L., Entchev, E., Ghorab, M., Lee, E., Kang, E. Energy and cost analyses of a hybrid renewable microgeneration system serving multiple residential and small office buildings. *Applied Thermal Engineering* **65**(1-2): 477–86 (2014-04).  
DOI: [10.1016/j.applthermaleng.2014.01.049](https://doi.org/10.1016/j.applthermaleng.2014.01.049) (cited p. 36)
52. Moradi, H., Saffar-Avval, M., Bakhtiari-Nejad, F. Sliding mode control of drum water level in an industrial boiler unit with time varying parameters: A comparison with Hinf-robust control approach. *Journal of Process Control* **22**(10): 1844–55 (2012-12).  
DOI: [10.1016/j.jprocont.2012.10.003](https://doi.org/10.1016/j.jprocont.2012.10.003) (cited p. 36)
53. Levine, W., Reichert, R. An introduction to H-infinity control system design. In *29th IEEE Conference on Decision and Control*. Honolulu, Hawaii: IEEE, 1990: 2966–74.  
DOI: [10.1109/CDC.1990.203329](https://doi.org/10.1109/CDC.1990.203329) (cited p. 36)
54. Abu-Khalaf, M., Huang, J., Lewis, F. L. *Nonlinear H<sub>2</sub>/H-infinity Constrained Feedback Control*. Vol. 53. 9. 2006: 1689–99. ISBN: 1-84628-349-3.  
DOI: [10.1007/1-84628-350-7](https://doi.org/10.1007/1-84628-350-7). arXiv: [arXiv: 1011.1669v3](https://arxiv.org/abs/1011.1669v3) (cited p. 37)





55. Sheela, A., Vijayachitra, S., Revathi, S. H-infinity controller for frequency and voltage regulation in grid-connected and islanded microgrid. *IEEJ Transactions on Electrical and Electronic Engineering* **10**(5): 503–11 (2015).  
DOI: [10.1002/tee.22113](https://doi.org/10.1002/tee.22113) (cited p. 37)
56. Singh, V. P., Mohanty, S. R., Kishor, N., Ray, P. K. Robust H-infinity load frequency control in hybrid distributed generation system. *International Journal of Electrical Power & Energy Systems* **46**: 294–305 (2013-03).  
DOI: [10.1016/j.ijepes.2012.10.015](https://doi.org/10.1016/j.ijepes.2012.10.015) (cited p. 37)
57. Brockett, R. W. Feedback Invariants for Nonlinear Systems. *IFAC Proceedings Volumes* **11**(1): 1115–20 (1978-01).  
DOI: [10.1016/S1474-6670\(17\)66062-2](https://doi.org/10.1016/S1474-6670(17)66062-2) (cited p. 38)
58. Jakubczyk, B., Respondek, W. On linearization of control systems. *Bull. Acad. Polon. Sci. Ser. Ind. Appl. Math. Astron. Phys.* **28**(9-10): 517–22 (1980) (cited p. 38)
59. Isidori, A., Ruberti, A. On the synthesis of linear input-output responses for nonlinear systems. *Systems & Control Letters* **4**(1): 17–22 (1984-02).  
DOI: [10.1016/S0167-6911\(84\)80046-8](https://doi.org/10.1016/S0167-6911(84)80046-8) (cited p. 38)
60. Isidori, A. *Nonlinear Control Systems*. New York, NY, USA: Springer-Verlag, 1989 (cited p. 38)
61. Moradi, H., Alasty, A., Vossoughi, G. Nonlinear dynamics and control of bifurcation to regulate the performance of a boiler-turbine unit. *Energy Conversion and Management* **68**: 105–13 (2013-04).  
DOI: [10.1016/j.enconman.2012.12.027](https://doi.org/10.1016/j.enconman.2012.12.027) (cited p. 39)
62. Cao, Y., Rossiter, D. An input pre-screening technique for control structure selection. *Computers & Chemical Engineering* **21**(6): 563–9 (1997-02).  
DOI: [10.1016/S0098-1354\(96\)00296-7](https://doi.org/10.1016/S0098-1354(96)00296-7) (cited p. 40)
63. Loh, E. J., Chiu, M.-S. Robust decentralized control of non-square systems. *Chemical Engineering Communications* **158**(1): 157–80 (1997).  
DOI: [10.1080/00986449708936586](https://doi.org/10.1080/00986449708936586) (cited p. 40)
64. Goodwin, G. C., Graebe, S. F., Salgado, M. E. *Control System Design*. 1st ed. Prentice Hall, 2000: 908. ISBN: 0139586539 (cited pp. 40–42)
65. Reis, S. et al. Integrating modelling and smart sensors for environmental and human health. *Environmental Modelling & Software* **74**: 238–46 (2015).  
DOI: [10.1016/j.envsoft.2015.06.003](https://doi.org/10.1016/j.envsoft.2015.06.003) (cited p. 41)
66. Open Lab at Newcastle University. *BuildAX: Wireless Building Monitoring System*. 2016. URL: <https://github.com/digitalinteraction/openmovement/wiki/BuildAX> (visited on 2016-09-13) (cited p. 41)
67. Kumar, P., Martani, C., Morawska, L., Norford, L., Choudhary, R., Bell, M., Leach, M. Indoor air quality and energy management through real-time sensing in commercial buildings. *Energy and Buildings* **111**: 145–53 (2015-11).  
DOI: [10.1016/j.enbuild.2015.11.037](https://doi.org/10.1016/j.enbuild.2015.11.037) (cited p. 41)
68. Clarke, J. A., Hand, J., Kim, J.-m., Ladha, C., Olivier, P., Roskilly, T., Royapoor, M., Samuel, A., Wu, D. Pervasive sensing as a mechanism for the effective control of CHP plant in commercial buildings. In *Building Simulation and Optimisation (BSO14)*. Ed. by Malki-Epstein, L., Spataru, C., Halburd, L. M., Mumovic, D. London, UK: IBPSA-England, 2014 (cited p. 41)
69. Veen, G. V. D. *Identification of Wind Energy Systems*. 2013. ISBN: 9789461916655 (cited p. 41)



70. Zhao, H., Wu, Q., Wang, C., Cheng, L., Rasmussen, C. N. Fuzzy logic based coordinated control of battery energy storage system and dispatchable distributed generation for microgrid. *Journal of Modern Power Systems and Clean Energy* **3**(3): 422–8 (2015-09).  
DOI: [10.1007/s40565-015-0119-x](https://doi.org/10.1007/s40565-015-0119-x) (cited p. 42)
71. Slotine, J.-J. E., Li, W. *Applied Nonlinear Control*. New Jersey: Prentice Hall, 1991: 461. ISBN: 0-13-040890-5 (cited p. 44)
72. Bradshaw, A., Counsell, J. M. Design of autopilots for high performance missiles. *Proceedings of the Institution of Mechanical Engineers, Part I: Journal of Systems and Control Engineering* **206**(2): 75–84 (1992-05) (cited p. 46)
73. Muir, E., Bradshaw, A. Engineers , Part G : Journal of Aerospace Engineering. *Proceedings of the Institution of Mechanical Engineers, Part G: Journal of Aerospace Engineering* **210**(4): 333–43 (1996-10).  
DOI: [10.1243/PIME\\_PROC\\_1996\\_210\\_378\\_02](https://doi.org/10.1243/PIME_PROC_1996_210_378_02) (cited p. 46)
74. Brindley, J., Counsell, J. M., Zaher, O. S., Pearce, J. G. Design and simulation of a non-linear, discontinuous, flight control system using rate actuated inverse dynamics. *Proceedings of the Institution of Mechanical Engineers, Part G: Journal of Aerospace Engineering* **227**(4): 632–46 (2013-04).  
DOI: [10.1177/0954410012438829](https://doi.org/10.1177/0954410012438829) (cited p. 46)



*“A light you can feel it on your back  
Your jigsaw falling into place.”*

---

—RADIOHEAD, *In Rainbows*

3

## Research method

**T**HIS chapter describes the research method that will be employed for the remainder of the thesis for addressing the objectives of this work. The energy supply system to be controlled is specified in § 3.1, with descriptions of the case studies that will be used in this work. After which, discussion on the modelling-method and -resolution for the system is given in § 3.2. § 3.3 and 3.4 give an overview of the controller design techniques that will be used for the remainder of this work. § 3.4 also discusses how the work of this thesis characterises the uncertainties in the control of energy systems. How the control systems’ performance will be assessed and metrics for the performance are given in § 3.5. Finally, a description of the Monte Carlo experiments used to assess the controllers’ performance in the case studies is given in § 3.6.

### 3.1 Problem specification

The work of this thesis addresses the systems-level controls of the following **hybrid energy supply system**: The system utilises an mCHP in combination with an intermittent renewable energy source (in this case solar PV) and the potential for electrical and thermal energy storage. The thermal energy supply system attached to the mCHP is a hydronic system with radiators as the heat emitters to the building. There is an actuator that can operate the fuel valve on the mCHP based on a control signal. There is an external pump that can control the flow rate of water through the hydronic system. Finally, there is a digital actuator that can send a signal to charge or deplete the battery. A schematic block diagram for the overall system to be controlled is shown without TES in fig. 3.1 and with TES in fig. 3.2.

The controller is to combine the inverse dynamics of the building, servicing systems, and energy storage with a robust control methodology. These inverse dynamics



provides the controller with knowledge of the complex cause and effect relationships between the system, the controlled inputs, and the external disturbances, while an outer-loop control ensures robust, stable control in the presence of modelling deficiencies/uncertainty and unknown disturbances. The physical limitations of the systems are also accounted for depending on the current utilisation and availability of the energy supplies/ storage.

The research was broken down into a set of constituent stages:

1. Frame the control problem so that it can be approached from a controller design methodology.
2. Obtain a mathematical model of the overall system to be controlled, including important nonlinearities such as actuator limits, disturbance sources, parameter variations and low-level embedded controls.
3. Validate the mathematical models with empirical data or relevant standards.
4. Express the model in a state-space representation that is applicable to controller design methods.
5. Determine the ideal ‘inverse dynamics’ of the system to obtain knowledge of the complex cause and effect relationships between the system, the controlled inputs, and the external disturbances.
6. Develop a robust control strategy to allow the system to approach the behaviour of the ideally controlled system in the presence of modelling inaccuracy and unknown disturbances.
7. Measure the performance of the control strategy to case study problems in a numerical simulation environment.

### **3.1.1** *Controller test case*

The controller test case looks at controlling the mCHP device alone to fulfil the thermal and electrical demands of the building. That is, there is no support from solar PV or electrical- or thermal-energy storage. This case is concerned with constructing a controller for the following MIMO problem:

#### **Control Goal**

Design a control system to track a desired load-supply water temperature set-point while simultaneously tracking a demand-response signal from the LEN. In the absence of a signal from the LEN, the control system will regulate the utilisation of the electrical grid to zero.





From this control goal, it is possible to identify the variables to be controlled as

**cv 1** Load-supply water temperature, which is the bulk exit temperature of the encapsulated mCHP cooling water.

**cv 2** Measured electrical grid power.

By removing the building dynamics, solar PV and energy storage from the control problem allows for significant model order reduction. In this case, it is possible to conduct algebraic manipulation to illustrate the fundamental mathematical application of the controller developed in this work. This case is utilised in the controller development chapters 6 and 7 to facilitate discussion without excessive model order. Furthermore, if the controller is unable to control the mCHP device alone, then it would not be able to tackle the complete control problem illustrated in figs. 3.1 and 3.2.

When this case is used throughout this work, the *dynamics* of the model used for the controller design and the building and system performance models are the same. This is to demonstrate the applicability of this type of control to energy systems without introducing modelling error. However, the effect that the uncertainty in the model parameter values has on the control system performance is evaluated in § 8.2.

### 3.1.2 Overview of case studies

The case study for the control of the system (as shown in fig. 8.27) where the system consists of an mCHP in combination with solar PV, electrical energy storage and a stratified TES tank. Then, this example is concerned with constructing a controller for the following MIMO problem:

#### Control Goal

Regulate the internal air temperature to any desired set-point and maintain the prescribed set-point while simultaneously minimising the utilisation of the electrical grid – in the presence of disturbances and process uncertainties.

From this control goal, it is possible to identify the variables to be controlled as:

**vc 1** Zone dry-bulb (air) temperature.

**vc 2** Electrical grid power.

The primary difficulty in the control of this system is that the air temperature is only indirectly related to the input fuel flow rate – which must first influence the engine, cooling water, TES tank and finally radiator temperatures before changes to the internal air temperature will be seen. The case study is split into two problems: controlling the system without the TES tank and with a TES tank from a cold start.



In these cases, the *dynamics* of the energy system models used for the controller design and system performance models are the same. The controller design uses a reduced-order model for the building while the performance analysis uses a high-resolution model (the difference in the building models is explored in §§ 5.2.3).

In the first case, it examines if the controller can fulfil the thermal demands of the building from the mCHP alone. In the second case, the controller will have to generate and maintain a thermocline within the tank while being simultaneously charged by the mCHP and discharged by the loads from the radiators to the zone. The performance of the controller will be assessed using the metrics discussed in § 3.5.

### **3.2** Developing models of the system to be controlled

Quantitative mathematical models allow control engineers to understand and control complex systems (1, p. 50). The term model, as it is used and understood in this work, means a set of differential equations that describe the dynamic behaviour of the process. Models utilised for the purposes of controller design can be obtained using knowledge and principles of the underlying physics or by testing a prototype of the device. The latter involves measuring the device's response to inputs, and using the data to construct a mathematical model. This method of obtaining models is sometimes called 'System Identification'. The models employed in this work use the former approach. This allows the control algorithms developed to be applicable to generic systems and not only a specific device modelled via System Identification. Where possible the models used here are sourced from or based on physics-based models that have been verified experimentally to ensure accuracy of the model's dynamic response. These models facilitate the development of the control algorithms in chapters 6 and 7 that can exploit the synergy of multiple energy systems to simultaneously fulfil the electrical and thermal demands of a building, regardless of the variance in the demands and despite any external disturbance or any changes in the dynamics of the process.

#### **3.2.1** *State-space modelling*

This work utilises the *state-space* approach<sup>1</sup> for modelling, analysing and designing the control algorithms for the microgeneration systems and the environment in which they operate. This modelling method uses differential equations to represent the dynamic performance of the physical systems and is equally applicable to modelling mechanical, hydraulic and electrical systems (1, p. 50).

State-space can be used to represent nonlinear systems dynamics, as well as discontinuities such as backlash, friction, dead zone, relays, and saturation/rate limits.

---

<sup>1</sup>Also referred to as the *modern*, or *time-domain*, approach (2, p. 112).



Also, it can handle time-varying systems (one or more of the parameters of the system may vary as a function of time) and systems with non-zero initial conditions. And finally, the systems do not have to be SISO, as multi-input multi-output (MIMO) systems can be equally well represented in state-space form, typically employing compact vector-matrix notation that allows large, complex systems to be expressed in a manageable form.

In the state-space modelling approach, each physical system will be described by a set of  $n$  simultaneous first-order differential equations based on a (non-unique) set of variables known as the **state variables** and an array of system inputs. Knowledge of the value of the state of the system, the system inputs, and the equations describing the dynamics will provide the future state and output of the system.

To produce the dynamic model for numerical analysis and simulation requires knowledge of the system parameter values, such as heat transfer coefficients, heat capacities, resistances etc. which is often not easy to obtain. For this reason this work strives to keep the system parameters in algebraic form for both the dynamic models and the resulting control algorithms, which has the added benefit of generalising the overall system. Where necessary system parameters are sourced either from vendors/manufacturers data sheets or experimental data.

The state-space approach is also easy to manipulate in order to utilise implicit and explicit iterative methods used in temporal discretisation for the approximate solutions to the set of differential equations. These methods are used in software packages such as MATLAB/Simulink in order to digitally simulate the behaviour of the dynamic models and their control.

### 3.2.2 Modelling resolution

In the process of developing models suitable for controller design, it is often necessary to make several simplifying assumptions on the dynamic behaviour of the system in order to keep the resulting model manageable and still approximate physical reality (2, p. 34). Without the assumptions the system model could be of very high order or described with complex nonlinearities, or partial differential equations. However, all assumptions must be checked and all simplifications justified through analysis or testing.

Even with suitable assumptions, the differential equations of motion often remain nonlinear. As nonlinear systems are significantly more challenging to solve than linear ones and because linear models are usually adequate for controller design, the emphasis is based on developing linear models, where possible.

There are three levels or ‘resolutions’ of modelling microgeneration technologies,



each with a purpose:

1. Detailed: models the individual components within a microgeneration device ( $t_{\text{step}} < 1 \text{ s}$ );
2. Systems-level: models the microgeneration device as a simplified theoretical-, grey- or black-box model that characterises the overall dynamic performance ( $1 \text{ s} \leq t_{\text{step}} \leq 1 \text{ h}$ );
3. Strategic: used for the long-term performance assessment of microgeneration deployment such as life-cycle assessment or to inform government policy on their impact on long-term emissions reductions ( $t_{\text{step}} > 1 \text{ h}$ ).

Where  $t_{\text{step}}$  represents the temporal discretisation at which the model is typically utilised.

A comprehensive review of modelling resolution for simulation and optimisation of MGTs was conducted by Kelly et al. (3) and not repeated here. The models developed and utilised in this work are primarily at the systems-level which is deemed appropriate for development of control algorithms as they facilitate simulation of the microgeneration technologies, the energy delivery network, and the building model in which they operate.

Where any internal components/processes would result in the previously mentioned constraints on system performance, then these elements should be modelled within the scope of the systems-level models to ensure simulation of sensible control strategy performance and potential implementation of the controller in practice.

Chapter 4 establishes models of the energy systems in § 3.1, of appropriate resolution, to be used for the purposes of controller design. These models are drawn together from various sources and converted into state-space representations. Advancements are made to the models where necessary in order to ensure that the mathematical models of the physical systems adequately approximate reality so that all important dynamic characteristics are captured.

The environment in which the energy systems operate dictates the thermal and electrical demands that must be fulfilled by the control system. Chapter 5 establishes a general state-space model of the thermodynamics of a building zone that is suitable for the application of controller design and integration with the models of the previous chapter.

### **3.3** Inverse dynamics of systems

While it is sometimes possible to adjust a single system parameter in an existing control system in order to improve performance, it is often found that it is not sufficient to

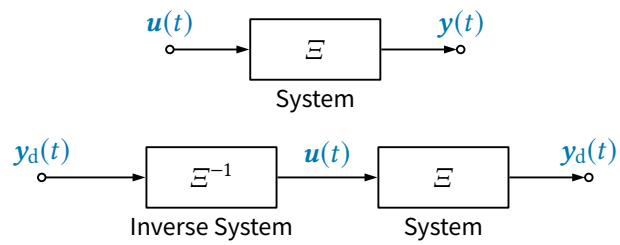


**Figure 3.3 | Inverse dynamics concept.** Block diagram representation of the concept of inverting the dynamics of the system: **(a)** Original system; **(b)** Inverse system used to compute the control input  $u(t)$  required to produce the desired output  $y_d(t)$ .



alter a single or even a group of parameters in order to achieve the desired system operational performance (1, p. 744). Instead, it is often necessary to consider the overall structure of the system and how it can be reconfigured/redesigned to obtain a system that can be controlled to achieve the desired performance. To assess the system structure and the potential interconnection of the various energy systems for control purposes, this work utilises the concept of the inverse dynamics of the system.

The fundamental concept of an inverse system is a straightforward, appealing and logical one (4, § 4.1). Consider a general continuous system with control inputs  $\mathbf{u}$  and outputs  $\mathbf{y}$

$$\Xi : \begin{cases} \dot{\mathbf{x}}(t) = \mathbf{f}(\mathbf{x}(t), \mathbf{u}(t)) \\ \mathbf{y}(t) = \mathbf{h}(\mathbf{x}(t), \mathbf{u}(t)) \end{cases}$$

If the dynamics of  $\Xi$  are known it may be possible to design an inverse system  $\Xi^{-1}$  such that the control input  $\mathbf{u}(t)$  can be computed given a desired output  $\mathbf{y}_d(t)$  from  $\Xi$ . The inverse-dynamics based control concept is illustrated in fig. 3.3.

Chapter 6 of this work will explore the application of inverse dynamics concept and controllers to the problem specified in § 3.1. The controller development in chapter 6 uses the same model for the controller design and systems performance analysis. This is to demonstrate the applicability of this type of control to energy systems without introducing modelling error. However, as discussed in § 1.3, in reality, the system being controlled will be subject to parameter changes, unmodelled dynamics and unmeasured disturbances. These uncertainties in the system models are addressed in the chapter 7 and are introduced in the following section.

### 3.4 Robust inversion-based control

The **robust control** problem is defined as: The overall energy system – and the external environment in which it operates – cannot be modelled precisely, may change in an unpredictable manner, and may be subject to significant disturbances (1, p. 910). The design of a control system in the presence of significant uncertainty requires the development of a robust controller.

However, control systems designed using inverse dynamics methods and concepts as in § 3.3 assume complete knowledge of the energy systems and building model and constant parameters. Unfortunately, a model – no matter how detailed – is never a completely accurate representation of a real physical system. Analytical or computational models cannot truly characterise and emulate all physical phenomena observed in practice. These systems-level models will always be an inaccurate representation of the actual physical system because of

- parameter changes



- unmodelled dynamics
- unmodelled time delays
- changes in equilibrium point (or operating point)
- sensor noise
- unpredicted disturbance inputs e.g. human activity, in the case of buildings

Recent advances in robust control design methodologies can address stability robustness and performance robustness in the presence of uncertainty in the models. The idea of robust control is then that some level of performance of the controlled system is guaranteed irrespective of these effects and that stability is assured in all cases. The robustness of the controller is then measured by the low sensitivity to those effects *not* considered in the analysis and design phase i.e. the system should be able to withstand these neglected effects when performing the tasks for which it was designed. A system can then be declared 'robust' when the system has acceptable changes in performance (as specified by the designer) due to model changes or inaccuracies.

Robust controllers are typically comprised of two parts (5, p. 276):

1. A nominal part – the inner model reduction component – commonly a feedback linearisation or inverse control law, and
2. An outer component used to account for model uncertainties and disturbances

A block diagram schematic of the proposed robust controller structure that will be used in this work is given in fig. 3.4.

The inverse dynamic concept in fig. 3.3 only showed *control* inputs. However, systems will have a multiple of different types of inputs as shown in fig. 3.4. In general, all inputs to the model are collectively called the *system* inputs, denoted  $\boldsymbol{\mu}$ . The system inputs can be first sub-divided into those which are manipulable and those that are not i.e.  $\boldsymbol{\mu} = (\boldsymbol{u}^T, \boldsymbol{\psi}^T)^T$ , where  $\boldsymbol{\psi}$  are designated as exogenous inputs.

The exogenous inputs are a generalised input vector that contains all the inputs originating from outside the model and are unexplained by the model e.g. outside ambient temperature, electrical demand loads, metabolic gains, process noise, measurement noise, are all are examples of system inputs that can affect the controlled process that are not modelled by the system itself.

The exogenous inputs can be further split into those inputs that are measured and those that are not. The measured exogenous inputs  $\boldsymbol{w}$  are comprised of all the measurements that are available to the controller but cannot be manipulated. The unmeasured inputs are typically considered as the 'disturbance' inputs  $\boldsymbol{d}$  and are comprised of the process noise, measurement noise, modelling error, unmeasured system inputs etc.

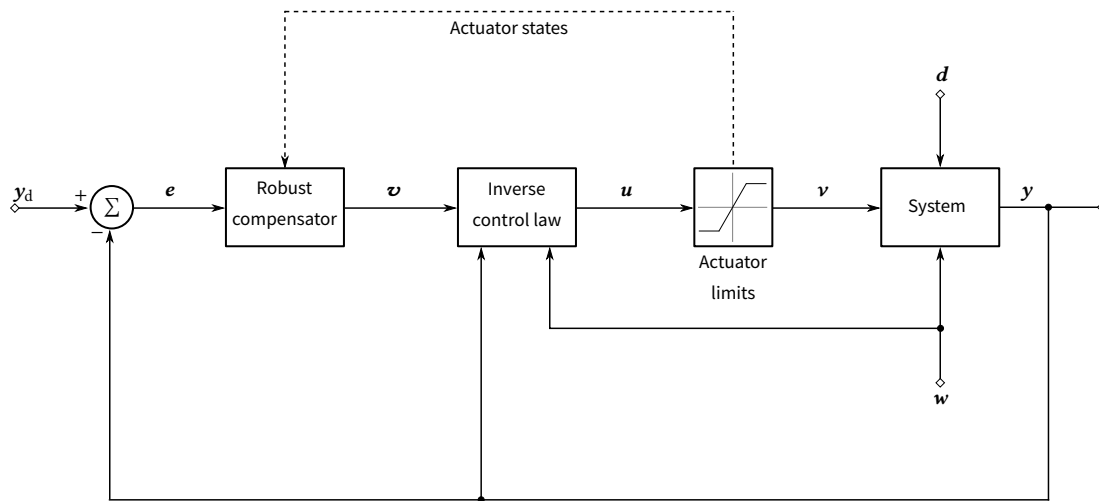


**Figure 3.4** | Block diagram of proposed controller structure.

Therefore, without loss of generality, the system input vector can be split into sub-vectors as  $\boldsymbol{\mu} = (\mathbf{u}^T, \boldsymbol{\psi}^T)^T = (\mathbf{u}^T, \mathbf{w}^T, \mathbf{d}^T)^T$ .

This work addresses the robustness to parameter changes, unmoderated dynamics, changes in operating point and unpredicted disturbance inputs in the form of unknown small power loads, internal heat gains and changes in external climate. How these uncertainties are characterised is described in the following section.

#### 3.4.1 Characterising the uncertainties

A robust controller allows the models to be imprecise, where the imprecision in the system stems from two major areas:

- *System uncertainty*: it is not possible to know precisely the system parameters. For example, the exact heat capacity of the building structure, or the heat transfer coefficients, or the vast array of distances to the system cannot be known with absolute certainty, and may also change over time.
- *Simplified dynamics*: the models used in the study of control systems performance are often a *purposefully* simplified representation of the dynamics of the overall system – using a reduced model of the building structure or stratified thermal storage tank, modelling the radiation heat transfer as linear, neglecting the modelling of the high frequency dynamical modes, such as internal mechanisms of the mCHP plant.

In control literature, these two areas of imprecision are known as **structured** uncertainties (related to the parametric uncertainties) and **unstructured** uncertainties (the unmodelled or reduced-order dynamics) (5). The assessment of control systems performance to each type of uncertainty is treated separately, as different modelling approaches are required to characterise the effect of each type.

#### Structured uncertainties

All of the models developed following the procedure in § 3.2 will be constructed in terms of parameters: heat transfer coefficients, specific heat capacities, mass flow rates, to name but a few. However, it is impossible to measure these parameters with absolute precision, and even if you could, they are likely to change over time when the actual system is built or has been in operation (2). Accordingly, the performance of the control system will also change over time and will not be consistent with the performance metrics attained during the design stage. Unfortunately, the relationship between parameter changes and their effect on performance is not linear. In some cases, especially in nonlinear systems, small changes in parameter values can lead to



large changes in performance, depending on the system's nominal operating point and the type of controller design employed.

Therefore, to capture the variations in the parameters in the controller design stage, these structured uncertainties are modelled using confidence intervals on the values of the parameters. Consider a general model parameter,  $\varrho$ . Instead of defining a single constant value, define its value to be between known bounds  $\varrho_{\min} \leq \varrho \leq \varrho_{\max}$  i.e.  $\varrho \in [\varrho_{\min}, \varrho_{\max}]$ . Also define a nominal value for the parameter, denoted  $\varrho_0$  (which in this work is always taken as the mean value between the bounds). Then it is possible to describe the parameter in terms of a perturbation from its nominal value as

$$\varrho = \varrho_0(1 + \chi_\varrho \Delta), \quad |\Delta| \leq 1, \quad (3.1)$$

where  $\varrho_0 = (1/2)(\varrho_{\min} + \varrho_{\max})$ ,  $\chi_\varrho = (\varrho_{\min} - \varrho_{\max})/(\varrho_{\min} + \varrho_{\max})$  and  $\Delta$  defines the amount perturbation from its nominal value. When  $\Delta = 0$  in this representation the parameter takes on its nominal value, as you would expect. While the relation in (3.1) is useful for the mathematical analysis of these uncertainties, there is an alternative representation that is useful for computer implementation. The parameter can also be expressed as

$$\varrho = (\varrho_{\max} - \varrho_{\min})S + \varrho_{\min}, \quad (3.2)$$

where  $S \in [0, 1]$ . In this form, it is straightforward to generate a random sample,  $\varrho_i$ , from its permissible values by taking  $S$  as a random number in the open interval  $(0, 1)$ . This is particularly useful for generating a number of samples for use in Monte Carlo simulations.

In the buildings industry, the certainty to which parameters are known are often expressed as percentages of the nominal value e.g. “the thermal conductivity of 304 stainless steel is accurate to  $\pm 5\%$ ” (6) i.e.  $\lambda = \lambda_0 \times (1 \pm 5\%)$ . Therefore, it is possible to express (3.2) as

$$\varrho = \varrho_0((2S - 1)Z + 1), \quad (3.3)$$

where  $Z$  is the given percentage accuracy of the parameter. Equation (3.3) provides a convenient relation to generate a sample of a parameter given its nominal value and percentage accuracy.

Due to the lack of information on the uncertainty in the majority of the model parameters (7), it is assumed throughout the rest of this work (unless stated otherwise) that the variation is taken from the uniform distribution i.e.  $S \sim \mathcal{U}(0, 1)$ . There are, however, some studies available that describe the variation as a different distribution e.g. the uncertainty in the thermal conductivity of insulation materials (7) where a normal distribution better characterises the variation in parameter value.





To determine the nominal values of the parameters, studies have been made to identify and collate the nominal thermal properties of building materials (8), while for the energy systems models, methods such those detailed in Arndt et al. (9) can be used to estimate the nominal model parameters.

### Unstructured uncertainties

The second type of uncertainty is related to the *simplified dynamics* of the majority of models used for controller design. In the process of developing models suitable for controller design, simplifications are made to the model describing the dynamic behaviour of the system in order to keep the resulting model manageable and still approximate physical reality (2, p. 32). Without the assumptions the system model could be of very high order or described with complex nonlinearities, or partial differential equations. However, these neglected dynamics may cause the system to become unstable or cause the performance to degrade below acceptable limits. Furthermore – in almost all cases – as time and the environment change, even the best of models will be in error because the system dynamics have changed (10, p. 524).

In energy systems, these unstructured uncertainties can take many forms:

- *Elements not captured/neglected in the systems-level models:* sensors, pumps, valves, piping, and the inner workings of grey-box models that were not captured in the dynamics at the time, but could be excited during operation.
- *Effect of model's reduced-order dynamics and linearisation:* the dynamics of the elements that *are* modelled are often simplified and linearised from the true dynamic behaviour of the system. If the system is asked to perform out with the scope of the linearisation point the dynamics can be significantly different and can be detrimental to controller performance and stability.
- *Unmeasured disturbances:* Changes in the external climate (air temperature, wind speed, solar radiation etc), occupant behaviour, internal gains, among others will effect the performance of the controller.
- *Nonlinearities:* Systems can have unknown and unmodelled time delays, parasitic coupling between elements, hysteresis, dead bands, backlash on the actuators to name but a few.
- *Unstructured parametric uncertainties:* These can take the form of wear and tear effects on the plant components, shifting operating points and manufacturing defects (11, p. 17). While these can technically be characterised in the same way as structured uncertainties knowledge of the range of uncertainty in the



parameters due to these effects is very difficult to determine ahead of time and will likely be environment and unit specific.

These types of uncertainty are more difficult to quantify compared to structured uncertainties and frequency domain techniques are often used to quantify their behaviour. Their effects are lumped together into ‘blocks’ and are applied as bounded perturbations (additive, multiplicative, inverse etc. as applicable) on the nominal transfer function of the system (12). In each case it is then possible to determine the stability and dynamic response due to each type of uncertainty. However such methods are only applicable to LTI representations of the systems while the majority of the energy systems models encountered in this work are nonlinear.

Instead – following the work of Macdonald (13) who quantified the effect of uncertainty in building simulation – this work utilises Monte Carlo simulations in the case study problems to subject the controlled system to a range of relevant unmodelled dynamics to assess the stability robustness and performance robustness of the chosen control strategy.

### **3.5** Assessment of control systems performance

“ A robust control system provides stable, consistent performance as specified by the designer in spite of the wide variation of plant parameters and disturbances. It also provides a highly robust response to command inputs and a steady-state tracking error equal to zero. ”

Richard C. Dorf - *Modern Control Systems* (1, p. 912)

From this definition of a robust control system this section describes how this statement can be represented as quantitative measures of performance.

#### **3.5.1** Stability

The first and basic requirement of the system is that it is stable. That is, the natural response of the system from its initial conditions will be to decay towards equilibrium. There are two causes for instability, either the open-loop system is already unstable or by adding feedback control the system becomes unstable. The control system must be designed to be stable at all times and this must be assessed for every permutation of system parameters and possible disturbances.

#### **3.5.2** Time-domain specifications

The controller developed in this work is concerned with the following control problems:



*Asymptotic Stabilisation Problem.* For a given a dynamic energy system find a control law  $\mathbf{u}$  such that, starting from anywhere in a region in  $\Omega$ , the output  $\mathbf{y}$  tends to  $\mathbf{0}$  as  $t \rightarrow \infty$  while the whole state  $\mathbf{x}$  remains bounded.

In many cases the problems in this work can be described as asymptotic stabilisation problems e.g. the control goals are to drive the electrical grid power use to zero and the zone air temperature to some non-zero set-point. For the latter case the problem can be reformulated as a zero-point regulation problem by taking the output as the error dynamics i.e.  $\mathbf{e}(t) = \mathbf{y}_d - \mathbf{y}(t)$ .

When the reference trajectory is time-varying, the control goal is modified slightly and is termed *asymptotic tracking* and can be defined as:

*Asymptotic Tracking Problem.* For a given dynamic energy system and its desired output trajectory  $\mathbf{y}_d(t)$ , find a control law for the input  $\mathbf{u}$  such that, starting from any initial state in a region  $\Omega$ , the tracking errors  $\mathbf{y}_d(t) - \mathbf{y}(t)$  go to zero, while the whole state  $\mathbf{x}$  remains bounded.

Examples of tracking problems in the control of energy systems would be following ramp-command temperature signals for the warm-up of mCHP systems or time-varying load signals from the local electrical network. The problem in either case is to keep the error small when disturbances are present.

Broadly speaking, the time-domain response of a controller can be split into two parts: the *transient* response, and the *steady-state* response. The transient response is the initial period of the response due to its initial conditions or a sudden change in set-point. The following metrics can be used to assess its performance during this time:

- *Peak time,  $T_p$* : The time required to reach the first, or maximum peak.
- *Overshoot,  $\overline{OS}$* : The amount that the response overshoots the steady-state (or final) value at the peak time.
- *Settling time,  $T_s$* : The time required for the transient's oscillations to reach and stay within a prescribed amount of the steady-state (or final) value.

The use of these metrics will allow for the adjustment/trade-off for obtaining an admissible or acceptable design and to discriminate between acceptable and unacceptable departures from the ideal performance.

These metrics are also important when designing a controller with respect to the thermal comfort of the occupants of the building – the heating system cannot take too long to reach and remain at the desired temperature, and also cannot initially overshoot the desired temperature by an amount that would become uncomfortable.



Similarly, when controlling the flow or bulk temperature in a hydronic heating system it is important to keep the flow temperature below the permissible limits of the mCHP or the unit could shut-down prematurely.

After the transient response has completed the system a stable system will settle at (or around) a constant value. The analysis is then concerned with the correctness of this value, as the thermal and electrical demands must be met within acceptable tolerances.

### 3.5.3 Control effort

The control effort is fundamentally the amount of energy or power needed for the controller to accomplish its task. However, especially when dealing with uncertain systems, there will be a trade-off between the amount of effort the controller uses and the accuracy to which it tracks the desired trajectory in the presence of disturbances.

To assign a metric to this trade-off, a performance index for the controller is given by

$$\mathcal{J} = \int_0^{\infty} \left( (\mathbf{y} - \mathbf{y}_d)^T \mathbf{Y} (\mathbf{y} - \mathbf{y}_d) + \mathbf{u}^T \mathbf{U} \mathbf{u} \right) dt. \quad (3.4)$$

where the selection of  $\mathbf{Y}$  and  $\mathbf{U}$  can place emphasis on the tracking error and controller effort respectively.

An additional measure of the controller action is the root-mean-square (RMS) value of the control. The RMS value of the control may be computed as

$$\|u\|_{\text{rms}} = \left( \frac{1}{T} \int_0^T u(t)^2 dt \right)^{(1/2)} \quad (3.5)$$

where  $T$  is the time period under consideration. For systems that have excessive noise or fast acting disturbances the control variable may need to change rapidly in order to maintain the set-point. A larger value of RMS in eq. (3.5) indicates there could be excessive wear of the actuator. Even if it is within their capabilities, generally do not want valves and pumps changing their value rapidly in order to maintain control of the system.

## 3.6 Monte Carlo experiments

To assess the stability robustness and performance robustness of the controllers this works uses the Monte Carlo simulation method. This method is “simple, universally applicable, and does not require any modification to the available (deterministic) computational tools” (14).





Monte Carlo (MC) experiments are extensively used for assessing the performance of a system or a computational method by generating a random sample of typical inputs (15, p. 1065). The aim of these case studies is to assess the performance of each candidate controller in the presence of uncertainty in the system modelling.

The idea behind the method is straightforward.

1. Randomly generate  $n_s$  sets of input parameters (also known as *scenarios*).
2. Run a simulation for each of the  $n_s$  sets of input parameters.
3. Aggregate and assess the outputs from the simulations using suitable performance metrics.

The design of a MC experiment with  $n_s$  scenarios and  $n_v$  variable (uncertain) parameters is written as a  $n_s \times n_v$  matrix

$$\mathbf{P} = \left[ \boldsymbol{\rho}_1^T, \boldsymbol{\rho}_2^T, \dots, \boldsymbol{\rho}_{n_s}^T \right]^T$$

where each row  $\boldsymbol{\rho}_i = (\rho_{i1}, \rho_{i2}, \dots, \rho_{in_v})$  represents a scenario and each column represents a variable parameter. Note that each variable parameter is taken from its permissible range of values i.e. for each unknown parameter  $k$ , select  $\rho_k \in [\rho_{k,\min}, \rho_{k,\max}]$ .

Each scenario  $i$  will result in a system model  $\Xi_i$ . Denote the set of all models as  $\mathcal{P}$  then  $\Xi_i$  is an admissible model with parameter set  $\boldsymbol{\rho}_i$ . Further denote  $\Xi_0$  in  $\mathcal{P}$  as the model with the nominal value of the parameters. In this work,  $\Xi_0$  is used for the controller design in each case study and will be referred to as the **design model**.

With the sets of parameters calculated and the controller design completed for the design model, the MC simulations can be performed. Because the simulations are independent from each other, this work makes use of parallel computing techniques, which can significantly reduce the computation time (16).

For the control system to be acceptable, the design must be internally stable for every model in the set  $\mathcal{P}$  – this is the robust stability property discussed in §§ 3.5.1. Once stability & robustness are assured the time-domain response of the system in each scenario is assessed using the performance metrics discussed in §§ 3.5.2.

### 3.6.1 Sampling method

It is well known that truly random numbers are impossible to generate on a ‘deterministic’ computer (15, p. 1070). Instead, in the vast majority of cases *pseudo-random number* generators are used.<sup>2</sup> This work makes use of the Mersenne Twister algorithm (17)

<sup>2</sup>The additional benefit of these generators is that the sequence of random numbers are repeatable by setting a ‘seed’ – allowing the results to be repeated.



that is available in MATLAB and is the preferred random number generator for MC simulations (15, p. 1071).

There are issues, however, with using truly random sampling of the parameter ranges; a large number of scenarios may be required to encompass the entire range of each parameter. Standard random sampling has a tendency to produce “clusters and holes in the samples” (14, p. 11). Several sampling techniques have been developed to address this issue (18, § 4). This work makes use of one of the most prevalent: Latin Hypercube Sampling (LHS). In LHS, the range of each uncertain parameter  $\varrho_i \in [\varrho_{i,\min}, \varrho_{i,\max}]$  is sub-divided into non-overlapping intervals of equal probability. One value from each interval is selected at random with respect to the probability distribution in the interval. The  $n_s$  values obtained for  $\varrho_1$  are paired randomly with  $n_s$  values of  $\varrho_2$ . These  $n_s$  values are then combined with  $n_s$  values of  $\varrho_3$  to form  $n_s$ -triplets, and so on, until  $n_s$   $k$ -tuplets are formed (19). Note that here LHS does not enforce uniformity when sampling across the variables as it samples each variable independently and then combines the dimensions randomly (20).

The design of the MC experiments first generates all sets of random numbers on the open interval  $(0, 1)$  then maps that random number to the permissible parameter ranges. The LHS of random numbers with  $n_s$  samples for  $n_v$  variables is written as an  $n_s \times n_v$  matrix

$$\mathbf{S} = \left[ \mathbf{s}_1^T, \mathbf{s}_2^T, \dots, \mathbf{s}_{n_v}^T \right]$$

where  $\mathbf{S} \in \mathbb{R}^{n_s \times n_v}$  contains a latin hypercube sample of  $n_s$  values of each  $n_v$  variables. For each column of  $\mathbf{S}$ , the  $n_s$  values are randomly distributed with one from each interval  $(0, 1/n_s), (0, 2/n_s), \dots, (1 - 1/n_s, 1)$ , and they are randomly permuted. The Latin hypercube is iteratively generated to find the best one according to a specific criterion. In this work, the ‘maximin’ criterion is used, which maximises the minimum distance between points.

As each random number is on the open interval  $S \sim (0, 1)$ , the mapping formula from eq. (3.3) can be used to generate the random sample from the range of permissible values:

$$\varrho = \varrho_0((2S - 1)Z + 1) \quad (3.3 \text{ revisited})$$

Equation (3.3) can be applied over all the values as

$$\text{col}_i \mathbf{P} = (\varrho_{1i}, \varrho_{2i}, \dots, \varrho_{n_s i})^T = \bar{\varrho}_i((2 \text{col}_i \mathbf{S} - 1)Z_i + 1)$$

Then, each  $i$ -th scenario uses the parameter values  $\boldsymbol{\varrho}_i = \text{col}_i \mathbf{P}^T$ .



### 3.7 Summary

This chapter has described the research method that will be employed for the remainder of the thesis for addressing the objectives of this work. The system to be controlled was defined and the methods for modelling the system were discussed. The models of the system will be developed in the next two chapters. After obtaining the dynamic models of the system, chapters 6 and 7 will present the controller design. Finally, chapter 8 will provide results and discussion on the case studies detailed in § 3.1, against the metrics specified in § 3.5 across a range of Monte Carlo experiments as laid out in § 3.6.

### References

1. Dorf, R. C., Bishop, R. H. *Modern Control Systems*. 12th ed. Upper Saddle River, New Jersey: Prentice Hall, 2011: 1104. ISBN: 978-0-13-602458-3 (cited pp. 57, 60, 65)
2. Nise, N. S. *Control Systems Engineering*. 5th ed. Hoboken, NJ, USA: John Wiley & Sons, 2008: 861. ISBN: 978-0471-79475-2 (cited pp. 57, 58, 62, 64)
3. Kelly, N., Samuel, A., Hand, J. Testing integrated electric vehicle charging and domestic heating strategies for future UK housing. *Energy and Buildings* **105**: 377–92 (2015). DOI: [10.1016/j.enbuild.2015.07.044](https://doi.org/10.1016/j.enbuild.2015.07.044) (cited p. 59)
4. Zaher, O. S. Advanced Control, Identification and Optimisation of Energy Systems. PhD thesis. University of Strathclyde, 2013: 205. URL: [http://oleg.lib.strath.ac.uk/R/?func=dbin-jump-full%7B%5C%7Dobject%7B%5C\\_%7Ddid=22632](http://oleg.lib.strath.ac.uk/R/?func=dbin-jump-full%7B%5C%7Dobject%7B%5C_%7Ddid=22632) (cited p. 60)
5. Slotine, J.-J. E., Li, W. *Applied Nonlinear Control*. New Jersey: Prentice Hall, 1991: 461. ISBN: 0-13-040890-5 (cited pp. 61, 62)
6. Blackwell, B. F., Gill, W., Dowding, K. J., Easterling, R. G. Uncertainty estimation in the determination of thermal conductivity of 304 stainless steel. In *Proceedings of IMECE '00*. Washington, DC, United States, 2000: 1–10 (cited p. 63)
7. Domínguez-Muñoz, F., Anderson, B., Cejudo-López, J. M., Carrillo-Andrés, A. Uncertainty in the thermal conductivity of insulation materials. *Energy and Buildings* **42**(11): 2159–68 (2010-11). DOI: [10.1016/j.enbuild.2010.07.006](https://doi.org/10.1016/j.enbuild.2010.07.006) (cited p. 63)
8. Clarke, J. A., Yaneske, P. P., Pinney, A. A. The harmonisation of thermal properties of building materials. *BEPAC Research Report* **2**(July): 1–87 (1990) (cited p. 64)
9. Arndt, U. et al. *Experimental Investigation of Residential Cogeneration Devices and Calibration of Annex 42 Models*. Tech. rep. Annex 42 of the International Energy Agency Energy Conservation in Buildings and Community Systems Programme, 2007: 255 (cited p. 64)
10. Franklin, G. F., Powell, J. D., Emami-Naeini, A. *Feedback Control of Dynamic Systems*. 6th ed. Upper Saddle River, New Jersey: Pearson Education, Inc., 2010: 837. ISBN: 978-0-13-500150-9 (cited p. 64)
11. Gu, D. W., Petkov, P. H., Konstantinov, M. M. *Robust Control Design with MATLAB*. Second. London: Springer, 2005: 392. ISBN: 9781852339838. DOI: [10.1007/b135806](https://doi.org/10.1007/b135806). arXiv: [arXiv:1011.1669v3](https://arxiv.org/abs/1011.1669v3) (cited p. 64)



12. GU, D.-W., Petkov, P. H., Konstantinov, M. M. Modelling of Uncertain Systems. In *Robust Control Design with MATLAB*. 2005: 13–23 (cited p. 65)
13. Macdonald, I. Quantifying the Effects of Uncertainty in Building Simulation. PhD. University of Strathclyde, 2002: 267. URL: [http://www.strath.ac.uk/media/departments/mechanicalengineering/esru/research/phdmphilprojects/macdonald%7B%5C\\_%7Dthesis.pdf](http://www.strath.ac.uk/media/departments/mechanicalengineering/esru/research/phdmphilprojects/macdonald%7B%5C_%7Dthesis.pdf) (cited p. 65)
14. Iaccarino, G. *Quantification of uncertainty in flow simulations using probabilistic methods*. Tech. rep. NATO RESEARCH and TECHNOLOGY ORGANIZATION NEUILLY-SUR-SEINE (FRANCE), 2009 (cited pp. 67, 69)
15. Cemgil, A. T. A Tutorial Introduction to Monte Carlo Methods, Markov Chain Monte Carlo and Particle Filtering. In. Vol. 1. Elsevier, 2014-01: 1065–114. DOI: [10.1016/B978-0-12-396502-8.00019-X](https://doi.org/10.1016/B978-0-12-396502-8.00019-X) (cited pp. 68, 69)
16. The MathWorks, I. *Monte Carlo Simulation - MATLAB & Simulink*. 2017. URL: <https://uk.mathworks.com/discovery/monte-carlo-simulation.html> (visited on 2017-10-31) (cited p. 68)
17. Matsumoto, M., Nishimura, T. Mersenne Twister: A 623-dimensionally Equidistributed Uniform Pseudo-random Number Generator. *ACM Trans. Model. Comput. Simul.* **8**(1): 3–30 (1998-01). DOI: [10.1145/272991.272995](https://doi.org/10.1145/272991.272995) (cited p. 68)
18. Janssen, H. Monte-Carlo based uncertainty analysis: Sampling efficiency and sampling convergence. *Reliability Engineering and System Safety* **109**: 123–32 (2013-01). DOI: [10.1016/j.ress.2012.08.003](https://doi.org/10.1016/j.ress.2012.08.003) (cited p. 69)
19. McKay, M. D., Beckman, R. J., Conover, W. J. A Comparison of Three Methods for Selecting Values of Input Variables in the Analysis of Output from a Computer Code. *Technometrics* **21**(2): 239–45 (1979). DOI: [10.2307/1268522](https://doi.org/10.2307/1268522) (cited p. 69)
20. Owen, A. B. Advanced variance reduction. In *Monte Carlo theory, methods and examples*. Stanford, California, 2013. Chap. 10: 1–63. ISBN: 0787987999. URL: <http://statweb.stanford.edu/%7B~%7Dowen/mc/Ch-var-adv.pdf> (cited p. 69)





*“...energy systems are complex.  
To pretend otherwise is to design for  
certain failure.”*

---

—JOSEPH CLARKE, *Energy  
Simulation in Building Design*

# 4

## Dynamic modelling of energy systems

THE aim of this chapter is to establish mathematical models of the microgeneration and energy storage devices to be used for the purposes of controller design. The chapter details the development of dynamic models of combustion-based mCHP units (§ 4.1), water-based stratified TES tanks (§ 4.2), the heat emitters (§ 4.3), and the electrical energy storage (§ 4.4).

The models are drawn together from various sources, with all models having origins from building simulation tools.

### 4.1 Combustion cogeneration

The model of the combustion-based (SE/ICE) cogeneration device utilised in this work is the model that was developed and validated as part of the Annex 42 research project (1) that aimed to create “A Generic Model for Combustion-Based Cogeneration Devices”. The project developed a generic ‘grey-box’ mathematical model of a cogeneration device (2), where the parameters of the system dynamics were calibrated with experimental studies (3), and then the model was validated and integrated into existing, publically available building simulation programs (4). This model is suitable for this work since the ‘grey-box’ model approximates the fundamental underlying physical processes of the device to a resolution suitable for controller design.

The model encompasses the following energy exchange / heat transfer mechanisms across thermo-chemical, thermo-fluid, mechanical and electrical domains:

- Heat transfer (via convection and radiation) from the fuel combustion to the air;
- Energy storage in the engine block and cooling water heat exchanger;
- Heat transfer from the engine block to the cooling water heat exchanger;



- Electrical power produced by the device's alternator.

This section details the thermal model of the cogeneration device, the low-level controls that dictate the operational mode of the mCHP unit, the digital limits imposed on its operation, and its implementation and validation within the MATLAB/Simulink environment.

#### 4.1.1 Energy conversion

The principle energy conversion in a cogeneration device is the transformation of the energy in the input fuel to thermal energy and electrical power. The simplified physical processes within the unit consist of the combustion of the fuel which generates mechanical work to drive a piston mechanism that produces power. The heat generated from the combustion is captured in the exhaust gases and the cooling fluid and then is transferred to cooling water via a heat exchanger. Instead of modelling the physical engine components, the systems-level mCHP model characterises the performance as a function of the total energy input to the device given by

$$P_{\text{net}}(t) = \eta_E(\dot{m}_{\text{cw}}(t), \Theta_{\text{cw},i}(t), P_{\text{gen}}(t)) \cdot \Phi_{\text{gross}}(t), \quad (4.1)$$

$$\Phi_{\text{gen}}(t) = \eta_Q(\dot{m}_{\text{cw}}(t), \Theta_{\text{cw},i}(t), P_{\text{gen}}(t)) \cdot \Phi_{\text{gross}}(t), \quad (4.2)$$

$$\Phi_{\text{gross}}(t) = \overline{LHV} \dot{m}_{\text{fuel}}(t), \quad (4.3)$$

where

- $t$  is the time (s);
- $P_{\text{net}}$  is the net electrical power of the system (W);
- $P_{\text{gen}}$  is the electrical power output of the unit (W);
- $\Phi_{\text{gen}}$  is the rate of heat generation within the engine (W);
- $\eta_E$  is the electrical conversion efficiency of the engine (1);
- $\eta_Q$  is the thermal efficiency of the engine (1);
- $\Phi_{\text{gross}}$  is the gross heat input to the system (W);
- $\overline{LHV}$  is the lower heating value of the fuel ( $\text{J kg}^{-1}$  or  $\text{J kmol}^{-1}$ );
- $\dot{m}_{\text{fuel}}$  is the fuel flow rate ( $\text{kg s}^{-1}$  or  $\text{kmol s}^{-1}$ );
- $\dot{m}_{\text{cw}}$  is the flow rate of the cooling water through the heat exchanger ( $\text{kg s}^{-1}$ );
- $\Theta_{\text{cw},i}$  is the temperature of the cooling water entering the unit (K).

In reality, in a combustion engine, the efficiency is a function of many factors that are not modelled, such as the expansion/compression ratio and engine speed. The use of the externally measurable variables ( $\dot{m}_{\text{cw}}(t)$ ,  $\Theta_{\text{cw},i}(t)$ ,  $P_{\text{gen}}(t)$ ) allows for the empirical calculation of the efficiencies from field trials and laboratory experiments.



The function of the measured variables forms a ‘performance map’ describing the efficiencies of the cogeneration device as a function of the boundary and operating conditions of the system.

The model uses the gross lower heating value (LHV) efficiency, which ignores self-consumption by the unit and losses in the production of water vapour. As the efficiency is calculated as a function of output power, the efficiency equations intrinsically captures these losses within the model.

#### 4.1.2 Thermal model

The model consists of two thermal masses each with a single state variable. The ‘engine block’ state represents the thermal mass of the engine block, the encapsulated working fluid, and part of the heat exchanger. The ‘cooling water heat exchanger’ state represents the cooling water within the heat exchanger and the elements of the heat exchanger in immediate thermal contact with the water.

The energy balance of the engine block control volume is

$$C_{\text{eng}}\dot{\Theta}_{\text{eng}}(t) = \Phi_{\text{gen}}(t) - \Phi_{\text{HX}}(t) - \Phi_{\text{env}}(t), \quad (4.4)$$

where

- $C_{\text{eng}}$  is the heat capacity of the engine block ( $\text{J K}^{-1}$ );
- $\Theta_{\text{eng}}$  is the bulk temperature of the engine block (K);
- $\Phi_{\text{HX}}$  is the rate of heat transfer between the engine block and the cooling water heat exchanger (W);
- $\Phi_{\text{env}}$  is the rate of heat transfer between the engine block and the surrounding environment (W).

The heat transfer between the engine block and cooling water,  $\Phi_{\text{HX}}$ , will occur via a heat exchanger. In reality, this will be governed by the geometry of the heat exchanger, the flow profile of the cooling water, and heat will be exchanged via convection, conduction and radiation heat transfer as a function of the log-mean temperature difference between the inlet and outlet cooling water temperatures. This model describes the heat transfer by combining the multiple modes of heat transfer into a single heat transfer coefficient and uses the linear difference in temperature between the engine block control volume and cooling-water control volume given by

$$\Phi_{\text{HX}}(t) = H_{\text{HX}}(\Theta_{\text{eng}}(t) - \Theta_{\text{cw,o}}(t)), \quad (4.5)$$

where



$\Theta_{cw,o}$  is the bulk exit temperature of the cooling water and shell (K);  
 $H_{HX}$  is the thermal conductance between the engine block and the cooling water heat exchanger ( $W K^{-1}$ ).

There is heat exchange between the mCHP unit and the environment it is in. The model assumes that the heat transfer between the engine block control volume and the environment is proportional to their difference in temperature given by

$$\Phi_{env}(t) = H_{env}(\Theta_{eng}(t) - \Theta_{env}(t)) \quad (4.6)$$

where

$\Theta_{env}$  is the temperature of the surrounding environment (K);  
 $H_{env}$  is the thermal conductance between the engine block and the surrounding environment ( $W K^{-1}$ ).

The energy balance of the cooling water control volume is

$$C_{cw}\dot{\Theta}_{cw,o}(t) = (c_p\dot{m}(t))_{cw}(\Theta_{cw,i}(t) - \Theta_{cw,o}(t)) + \Phi_{HX}(t), \quad (4.7)$$

where

$C_{cw}$  is the heat capacity of the encapsulated cooling water and the heat exchanger shell ( $JK^{-1}$ );  
 $(\dot{m}c_p)_{cw}$  is the thermal capacity flow rate of the cooling water ( $WK^{-1}$ ).

Combining eqs. (4.2) to (4.7) results in the overall thermal system model,  $\Xi_{CHP}$ , for a combustion based cogeneration device given as

$$\Xi_{CHP} : \begin{cases} C_{eng}\dot{\Theta}_{eng}(t) = H_{HX}(\Theta_{cw,o}(t) - \Theta_{eng}(t)) + H_{env}(\Theta_{env}(t) - \Theta_{eng}(t)) \\ \quad + \eta_Q \overline{LHV} \dot{m}_{fuel}(t) & (4.8a) \\ C_{cw}\dot{\Theta}_{cw,o}(t) = (c_p\dot{m}(t))_{cw}(\Theta_{cw,i}(t) - \Theta_{cw,o}(t)) \\ \quad + H_{HX}(\Theta_{eng}(t) - \Theta_{cw,o}(t)) & (4.8b) \end{cases}$$

#### 4.1.3 Operational modes

The thermal dynamics of  $\Xi_{CHP}$  correspond to the mCHP unit in its *normal* mode of operation. However, these systems can display markedly different behaviour during its other modes of operation: standby, warm-up, and cool-down. It is important to model these modes of operation as they can have a detrimental effect on the overall operational efficiency of the system. The deficiency comes from the fact that mCHP





units consume electrical power during these other modes. During warm-up and cool-down the use of pumps, low-level controls, and sensors will consume electricity. In standby, there will be an additional small 'base-load' of electrical power consumption to supply the electronics to ensure it is ready to respond to demands.

As the device is not generating its electrical power at these times, then this electricity must come from another source. This lack of power generation is an important consideration for buildings operating with limited availability of a local electrical network as the building must be able to supply this energy or the device will not be able to start-up, or able to complete its cool-down procedure.

### Standby

The unit is in standby when there is no demand input, i.e.  $\dot{m}_{\text{fuel}} = 0$ . The electrical power consumed during standby will not conform to eq. (4.1) as there is no fuel input. Instead the electrical power consumption is given by

$$P_{\text{net}} = P_{\text{standby}}, \quad (4.9)$$

where

$P_{\text{standby}}$  is the electrical power consumed by the mCHP unit during standby (W).

### Start-up/Warm-up

**INTERNAL COMBUSTION ENGINES** Some ICE-based mCHP units exhibit a static time-delay between fuel input and the production of electrical power each time the mCHP unit is activated from standby. This is computed as

$$P_{\text{net}}(t) = \begin{cases} 0 & \text{if } (t - t_0) < t_{\text{warm-up}} \\ \eta_E(\cdot) \overline{LHV} \dot{m}_{\text{fuel}}(t) & \text{if } (t - t_0) \geq t_{\text{warm-up}} \end{cases} \quad (4.10)$$

where  $t$  is the current time,  $t_{\text{warm-up}}$  is the duration of the warm-up period and  $t_0$  is the time at which the engine is started. It is worth highlighting that this time-delay does not work in the traditional way observed in control systems literature. The typical time-delay is a *transport* delay, where the signal input to the delay is seen in its entirety after the time delay period has elapsed. Here the delay is only observed when the unit switches from standby to warm-up. The electrical power output is zero until the time delay period has elapsed, after which the electrical power output will correspond to  $\eta_E(\cdot) \overline{LHV} \dot{m}_{\text{fuel}}(t)$  until there is no longer fuel input and the electrical power output instantaneously switches off.



Mathematically, then, the net electrical power can be written as

$$P_{\text{net}}(t) = \eta_E(\cdot) \overline{LHV} \dot{m}_{\text{fuel}}(t) \sum_i \mathbb{1}(t - t_{\text{CHP,on},i} - t_{\text{warm-up}}) \cdot \mathbb{1}(t_{\text{CHP,off},i} - t - \epsilon) \quad (4.11)$$

where  $t_{\text{CHP,off},i} > t_{\text{CHP,on},i}$  and

- $\mathbb{1}(\cdot)$  is the Heaviside step function whose value is 0 for a negative argument and 1 for a positive argument;
- $t_{\text{CHP,on},i}$  is the  $i$ th switch-on demand time of the unit, which corresponds to the  $i$ th time that  $\dot{m}_{\text{fuel}}(t) \neq 0$ ;
- $t_{\text{CHP,off},i}$  is the  $i$ th switch-off demand time of the unit, which corresponds to the  $i$ th time that  $\dot{m}_{\text{fuel}}(t) = 0$ ;
- $\epsilon$  is a very small positive number.

Equation (4.11) ensures that the electrical power output from the device at time  $t$  is proportional to the fuel input at time  $t$  as soon as the warm-up period has elapsed. The instant there is no longer demand the power output is zero.

**STIRLING ENGINES** Unlike ICE-based mCHP units, Stirling engines display a dynamic warm-up period that correlates with its *nominal* engine temperature, which is the observed engine temperature while the engine is operating at its maximum operating point.

Combustion-based cogeneration devices typically have low-level electronic controls that limit the maximum fuel flow rate,  $\dot{m}_{\text{fuel,max}}$ , below what is physically permissible through the fuel valve. However, during the warm-up procedure of Stirling engines, this limitation is relaxed so that extra fuel can be delivered to get to the ideal operational engine temperature as quickly as possible. The relative increase in fuel flow rate above the maximum flow rate under the normal operating mode is given by

$$\dot{m}_{\text{fuel,warm-up}}(t) = \dot{m}_{\text{fuel,max}} + \kappa_{\text{fuel}} \dot{m}_{\text{fuel,max}} \frac{\Theta_{\text{eng,nom}} - \Theta_{\text{env}}(t)}{\Theta_{\text{eng}}(t) - \Theta_{\text{env}}(t)} \quad (4.12)$$

where

- $\dot{m}_{\text{fuel,max}}$  is the maximum fuel flow rate imposed by the electronic limiters during the normal operating mode ( $\text{kg s}^{-1}$ );
- $\dot{m}_{\text{fuel,warm-up}}$  is the fuel flow rate during the warm-up mode ( $\text{kg s}^{-1}$ );
- $\Theta_{\text{eng,nom}}$  is the nominal engine temperature for the Stirling engine (K);
- $\kappa_{\text{fuel}}$  is an empirical coefficient used to characterise an individual Stirling engine's performance during warm-up (1).



There are several issues with direct implementation of the relation in eq. (4.12). From a cold start, the engine temperature will be very close to or the same as the environment it is in, i.e. in eq. (4.12) as  $\Theta_{\text{eng}}(t) \rightarrow \Theta_{\text{env}}(t) \implies \dot{m}_{\text{fuel,warm-up}}(t) \rightarrow \infty$ . The second scenario is where eq. (4.12) becomes invalid. When the environmental temperature is greater than the current engine temperature, it will cause the maximum fuel flow rate during the warm-up to either be less than the nominal maximum fuel rate or worse cause it to become negative. In either case, a second electronic limit is imposed on the fuel flow rate during the warm-up mode:

$$\dot{m}_{\text{fuel,warm-up}}(t) = \begin{cases} \dot{m}_{\text{fuel,warm-up}}(t) & \text{if } \dot{m}_{\text{fuel,warm-up}}(t) \leq \kappa_{\text{warm-up}} \dot{m}_{\text{fuel,max}} \\ \kappa_{\text{warm-up}} \dot{m}_{\text{fuel,max}} & \text{if } \dot{m}_{\text{fuel,warm-up}}(t) > \kappa_{\text{warm-up}} \dot{m}_{\text{fuel,max}} \end{cases} \quad (4.13)$$

where

$\kappa_{\text{warm-up}}$  is an empirical coefficient ( $\kappa_{\text{warm-up}} \geq 1$ ) used to determine the maximum fuel flow rate during warm-up (1).

In a similar fashion to the standby mode, the electrical power consumed during warm-up does not utilise eq. (4.1) and instead is correlated to the nominal engine temperature as

$$P_{\text{warm-up}}(t) = P_{\text{max}} \kappa_{\text{power}} \frac{\Theta_{\text{eng,nom}} - \Theta_{\text{env}}(t)}{\Theta_{\text{eng}}(t) - \Theta_{\text{env}}(t)} \quad (4.14)$$

where

$P_{\text{warm-up}}$  is the electrical power generation of the Stirling engine during warm-up (W);

$P_{\text{max}}$  is the maximum electrical power generation of the unit (W);

$\kappa_{\text{power}}$  is an empirical coefficient used to used to characterise an individual Stirling engine's electrical power generation during warm-up (1).

### Cool-down

When there is no longer a demand from the mCHP unit, it will enter its cool-down mode of operation. The cool-down mode is to allow the cooling water to continue circulating through the hydronic system which will typically reduce its temperature. The cool-down mode of the mCHP is functionally similar to the standby mode where the unit consumes no fuel ( $\dot{m}_{\text{fuel}} = 0$ ) but will consume electrical power from the available resources. In cool-down mode the electrical power consumed will not conform to



eq. (4.1) and instead is given by

$$P_{\text{net}} = P_{\text{cool-down}} , \quad (4.15)$$

where

$P_{\text{cool-down}}$  is the electrical power consumed by the device during cool-down (W).

Instead of switching from cool-down mode based on a measured temperature, the cool-down mode is based on a cool-down period  $t_{\text{cool-down}}$ , where the model allows for two different cool-down types:

1. *Optional*: if there is demand from the unit during cool-down and the properties of the cooling water are acceptable then the unit may be reactivated;
2. *Mandatory*: the mCHP unit must remain in the cool-down mode until the cool-down period has elapsed.

### Mode switching

There are two low-level fault detection based controls that can override the high-level controller and change the operating mode of the mCHP unit to ensure safe operation:

1. *High cooling water temperature*: if the temperature of the cooling water is too high the device can overheat. The sensor is placed at the outlet of the heat exchanger,  $\Theta_{\text{cw,o}}$ , and if it is detected to be too high then the unit is deactivated.
2. *Low cooling water flow rate*: at low cooling-water flow rates there will be limited heat transfer from the cooling water at the inlet to the heat exchanger and engine block causing the unit to overheat. A sensor measures the cooling water flow rate,  $\dot{m}_{\text{cw}}$ , and if it is detected as being too low then the unit is deactivated.

These fault detections can be represented in the following logical functions

$$\check{b}_{\text{isCool}} := \Theta_{\text{cw,o}} < \Theta_{\text{cw,o,max}} , \quad (4.16a)$$

$$\check{b}_{\text{isFlow}} := \dot{m}_{\text{cw}} > \dot{m}_{\text{cw,min}} , \quad (4.16b)$$

where

$\Theta_{\text{cw,o,max}}$  is the maximum temperature bound of the cooling water measured at the outlet (K);

$\dot{m}_{\text{cw,min}}$  is the minimum flow rate bound of the cooling water through the heat exchanger ( $\text{kg s}^{-1}$ ).

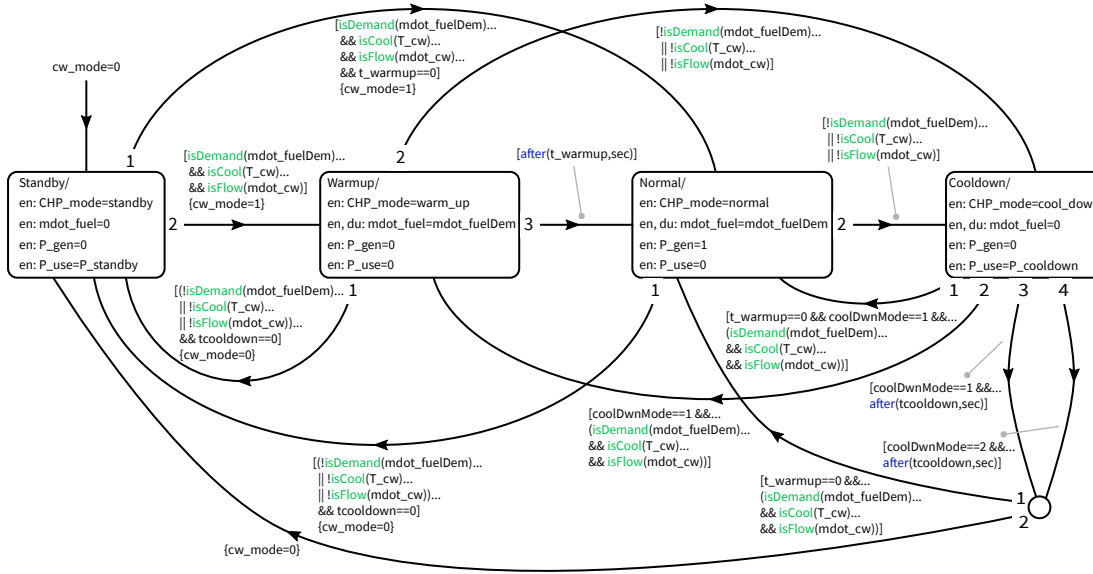


**Figure 4.1 | Stateflow logic diagram for mode switching of an internal combustion based CHP unit.** Each operating mode is designated as a state on the chart. Transition logic is marked on the lines connecting each mode state. When the logic is true the unit will transition from the current operating mode to the connecting state. Transitions are numbered according to their evaluation order, as soon as one transition branch is true the operating mode will switch.

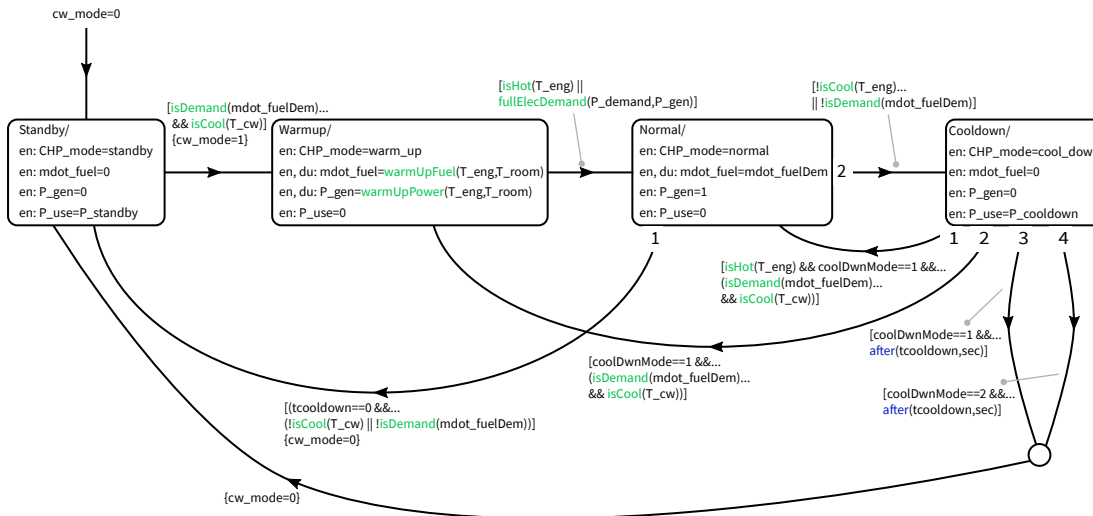


**Figure 4.2 | Stateflow logic diagram for mode switching of a Stirling engine based CHP unit.** Each operating mode is designated as a state on the chart. Transition logic is marked on the lines connecting each mode state. When the logic is true the unit will transition from the current operating mode to the connecting state. Transitions are numbered according to their evaluation order, as soon as one transition branch is true the operating mode will switch. On the chart the warm-up functions are  $warmUpFuel(\cdot) = \dot{m}_{fuel,warm-up}(t)$  and  $warmUpPower(\cdot) = P_{net,warm-up}(t)$ .



There is an additional logical function required to complete the mode switching logic of the mCHP unit:

$$\check{b}_{\text{isDemand}} := \dot{m}_{\text{fuel,dem}}(t) > 0 \quad (4.17)$$

$\dot{m}_{\text{fuel,dem}}(t)$  is the fuel flow rate demand from the high-level controller ( $\text{kg s}^{-1}$ ).

The description of all the permutations of when and under what conditions the mCHP unit can switch between modes would become convoluted. Instead, the mode switching logic has been implemented in a state transition digram and is provided in fig. 4.1 for a ICE-based mCHP device, and fig. 4.2 for a SE-based mCHP device. On both charts  $\text{coolDwnMode} = 0$  indicates the *mandatory* cool-down mode, and  $\text{coolDwnMode} = 1$  indicates the *optional* cool-down mode. Also  $\text{cw\_mode} = 0$  indicates that the internal pump is switched off, whereas  $\text{cw\_mode} = 1$  indicates that the internal pump is switched on.

#### 4.1.4 Digital limits

As alluded to in the previous section, there are restrictions placed on the fuel flow rate by electronic limiters to ensure safe operation of the device. These will likely be less than the physical limits of the fuel value so that the controller is not able to ask more of the device than it is capable of delivering. There is a minimum and maximum permitted fuel flow rate, denoted in this work as the ‘saturation limits’, and also a constraint on the rate of change of the flow rate, denoted as the ‘rate limits’.

#### Saturation limits

The saturation limits can be computed as

$$\dot{m}_{\text{fuel}}(t) = \begin{cases} \dot{m}_{\text{fuel,max}} & \text{if } \dot{m}_{\text{fuel,dem}}(t) > \dot{m}_{\text{fuel,max}} \\ \dot{m}_{\text{fuel,min}} & \text{if } \dot{m}_{\text{fuel,dem}}(t) < \dot{m}_{\text{fuel,min}} \\ \dot{m}_{\text{fuel,dem}}(t) & \text{otherwise} \end{cases} \quad (4.18)$$

The limits in eq. (4.18) can be re-expressed as a single mathematical expression given as

$$\dot{m}_{\text{fuel}}(t) = \max(\min(\dot{m}_{\text{fuel,dem}}(t), \dot{m}_{\text{fuel,max}}), \dot{m}_{\text{fuel,min}}) \quad (4.19a)$$

or

$$\dot{m}_{\text{fuel}}(t) = \max(-\max(-\dot{m}_{\text{fuel,dem}}(t), -\dot{m}_{\text{fuel,max}}), \dot{m}_{\text{fuel,min}}) \quad (4.19b)$$

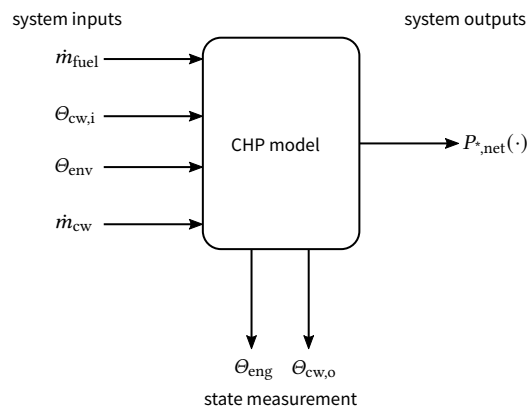


**Figure 4.3 |** Input-output block diagram for the cogeneration model.

where

$\dot{m}_{\text{fuel},\text{min}}$  is the minimum fuel flow rate imposed by the electronic limiters ( $\text{kg s}^{-1}$ ).

Expressing the limits mathematically as in eq. (4.19) can be exploited in the controller design later in this work to allow the control system to be ‘intelligent’ to the restrictions imposed on the fuel flow rate into the mCHP unit.

### Rate limits

The non-limited rate of change of the fuel flow rate is given as

$$\frac{d\dot{m}_{\text{fuel}}(t)}{dt} = \frac{\dot{m}_{\text{fuel},\text{dem}}(t) - \dot{m}_{\text{fuel}}(t - \Delta t)}{\Delta t} \quad (4.20)$$

where

$\Delta t$  is the duration between evaluations, otherwise known as the time-step (s).

The rate limits can be computed as

$$\dot{m}_{\text{fuel}}(t) = \begin{cases} \Delta t \ddot{m}_{\text{fuel},\text{rising}} + \dot{m}_{\text{fuel}}(t - \Delta t) & \text{if } \frac{d\dot{m}_{\text{fuel}}(t)}{dt} > \ddot{m}_{\text{fuel},\text{rising}} \\ \Delta t \ddot{m}_{\text{fuel},\text{falling}} + \dot{m}_{\text{fuel}}(t - \Delta t) & \text{if } \frac{d\dot{m}_{\text{fuel}}(t)}{dt} < \ddot{m}_{\text{fuel},\text{falling}} \\ \dot{m}_{\text{fuel},\text{dem}}(t) & \text{otherwise} \end{cases} \quad (4.21)$$

where

$\ddot{m}_{\text{fuel},\text{rising}}$  is the rising rate limit of the fuel flow rate ( $\text{kg s}^{-2}$ );

$\ddot{m}_{\text{fuel},\text{falling}}$  is the falling rate limit of the fuel flow rate ( $\text{kg s}^{-2}$ ).

The rate limits in eq. (4.21) allows for a different rate limit depending on whether the input is rising or falling.

#### 4.1.5 Model synthesis

The components in the previous sections can be combined to form the complete mathematical model of a combustion-based mCHP device. The thermal system  $\Xi_{\text{CHP}}$  in eq. (4.8) can be represented by the state differential equation:

$$\dot{\mathbf{x}}(t) = \mathbf{A}\mathbf{x}(t) + \mathbf{g}(\mathbf{x}(t), \boldsymbol{\mu}(t)), \quad (4.22)$$

where  $\mathbf{x}(t) \subset \mathcal{X} \in \mathbb{R}^2$  is the state vector,  $\boldsymbol{\mu}(t) \subset \mathcal{U} \in \mathbb{R}^4$ , is the input vector,  $\mathbf{A} \in \mathbb{R}^{2 \times 2}$  is the system matrix, and  $\mathbf{g} : \mathbb{R}^2 \times \mathbb{R}^4 \rightarrow \mathbb{R}^2$  are vector fields. The state and input vectors are given as  $\mathbf{x}(t) = (\Theta_{\text{eng}}(t), \Theta_{\text{cw},\text{o}}(t))^{\mathcal{T}}$  and  $\boldsymbol{\mu}(t) = (\dot{m}_{\text{fuel}}(t), \Theta_{\text{cw},\text{i}}(t), \Theta_{\text{env}}(t), \dot{m}_{\text{cw}}(t))^{\mathcal{T}}$ . An input-output block diagram for the model (4.22) is given in fig. 4.3. Then for the



system  $\Xi_{\text{CHP}}$ :

$$\mathbf{A} = \begin{bmatrix} -\frac{H_{\text{HX}} + H_{\text{env}}}{C_{\text{eng}}} & \frac{H_{\text{HX}}}{C_{\text{eng}}} \\ \frac{H_{\text{HX}}}{C_{\text{cw}}} & -\frac{H_{\text{hx}}}{C_{\text{cw}}} \end{bmatrix}, \quad \mathbf{g}(\mathbf{x}(t), \boldsymbol{\mu}(t)) = \begin{pmatrix} \frac{\eta_Q \overline{\text{LHV}} \mu_1(t) + H_{\text{env}} \mu_3(t)}{C_{\text{eng}}} \\ \frac{c_p \mu_4(t) (\mu_2(t) - x_2(t))}{C_{\text{cw}}} \end{pmatrix}$$

The electrical system of the mCHP unit is formed as a variable structure system that depends on the operating mode of the unit. For an ICE based mCHP the net electrical power is given as

$$P_{\text{ICE,net}}(t) = \begin{cases} P_{\text{standby}} & \text{if mode} = 0 \\ P_{\text{cool-down}} & \text{if mode} = 3 \\ \eta_E(\cdot) \overline{\text{LHV}} \mu_1(t) \cdot \sum_i \mathbb{1}(t - t_{\text{CHP,on},i} - t_{\text{warm-up}}) \cdot \mathbb{1}(t_{\text{CHP,off},i} - t - \epsilon) & \text{otherwise} \end{cases} \quad (4.23)$$

For an SE based mCHP the net electrical power is given as

$$P_{\text{SE,net}}(t) = \begin{cases} P_{\text{standby}} & \text{if mode} = 0 \\ P_{\text{max}} \kappa_{\text{power}} \frac{\Theta_{\text{eng,nom}} - \mu_3(t)}{x_1(t) - \mu_3(t)} & \text{if mode} = 1 \\ \eta_E(\cdot) \overline{\text{LHV}} \mu_1(t) & \text{if mode} = 2 \\ P_{\text{cool-down}} & \text{if mode} = 3 \end{cases} \quad (4.24)$$

The system inputs are constrained as

$$\mu_1(t) \in [\dot{m}_{\text{fuel,min}}, \dot{m}_{\text{fuel,max}}] \quad (4.25a)$$

$$\mu_2(t) \in (0, \infty) \quad (4.25b)$$

$$\mu_3(t) \in (0, \infty) \quad (4.25c)$$

$$\mu_4(t) \in (\dot{m}_{\text{cw,min}}, \dot{m}_{\text{cw,max}}) \quad (4.25d)$$

with additional limits on the rate of change of the fuel flow rate,  $\dot{\mu}_1(t)$ , given in eq. (4.21).

There are also constraints on the permissible values of the states given as

$$x_1(t) \in (0, \infty) \quad (4.26a)$$

$$x_2(t) \in (0, \Theta_{\text{cw,o,max}}) \quad (4.26b)$$



The overall model of a combustion-based mCHP unit is formed from eqs. (4.22) to (4.24) and eqs. (4.25) and (4.26) and in control systems terminology is a variable structure MIMO, input-nonaffine,<sup>1</sup> state-constrained, input-constrained system.

#### 4.1.6 Validation

The model in §§ 4.1.5 was implemented in Simulink, which is a graphical programming environment for modelling, simulating, and analysing multidomain dynamic systems (5). Simulink is widely used for the analysis of the implementation of automatic control systems. In contrast to building simulation environments such as EnergyPlus, ESP-r, and TRNSYS, Simulink allows for sub-secondly time-steps and provides numerical solvers for the solution of ‘stiff’ dynamical systems – roughly defined as systems where the time constants of different elements within the system differ by several orders of magnitude (6).

The Annex 42 research project put forth a set of validation tests (4) to complete when the model is implemented in a new environment to ensure there are no errors in the mathematical solution or coding errors. The validation of the model’s implementation in Simulink is provided in appendix B.1. The model exhibits no discernible difference in results from those calculated in ESP-r, TRNSYS, or EnergyPlus.

#### 4.1.7 Systems control remarks

The implementation of the Annex 42 model in this work differs most significantly from the building energy simulation (BES) implementations with regard to the control of the mCHP unit. The Annex model is defined so that the device operates as electrically-led i.e. it will follow a set demand for electrical power,  $P_{\text{demand}}$ , provided the model constraints be satisfied. The Annex 42 model calculates the control input as follows: From the known demand for electrical power, it will calculate the required operational efficiencies ( $\eta_E, \eta_Q$ ) from the performance map. The efficiencies are then used to determine the necessary gross heat input to the system, and finally, the fuel flow rate is calculated from the computed gross heat input.

While this control interface is suitable for building simulation, the real-time efficiencies of the cogeneration device cannot be known precisely, which makes it difficult to implement this type of control in practice. Also, the unit is controlled only considering the electrical demands of the building and doesn’t provide a control interface for thermal demands. The aim of the control of the mCHP unit in this work are that they are led-agnostic and utilise the current thermal and electrical demands of the building to calculate the necessary fuel flow rate to the device.

---

<sup>1</sup>nonaffine in the context of a dynamic system means that the input does not appear linearly.





Another issue is the loss of ‘manipulative control’ of the electrical power during non-normal modes: In standby and cool-down the unit *consumes* electrical power instead of generating it, and for an SE based unit in the warm-up mode the electrical power generation is only a function of the engine and environment temperatures. Consideration for these factors is important in the development of the control algorithms especially for buildings that have limited or restricted access to a local electrical network to balance the building electrical demands with the electrical power generation within the building.

## 4.2 Thermal energy storage

TES systems are used to store heat that can be deployed at a later stage depending on the demands of the building. As discussed in chapters 1 and 2 a TES can be used to store the heat generated from the mCHP unit. This has been demonstrated as useful at overcoming the mismatch between the thermal demands of the building and the heat generated from the mCHP unit (7).

There are three main types of TES (8):

**Sensible heat storage** energy is stored by increasing the temperature of the storage material. Typical materials are water, brick, concrete, and clay (8, table 1.4)

**Latent heat storage** energy is stored by exploiting the phase transition of a material. Normally from a solid→liquid, where heat is stored when the material melts and can be released when the material solidifies. Materials used are known as phase change material (PCM) and typical PCMs used are water, salt hydrates, paraffins, sugar alcohols, and nitrates (9, fig. 2.2)

**Thermochemical storage** energy is stored after a dissociation reaction (a thermochemical material absorbs heat energy and is converted chemically into two components that are stored separately) and then recovered in a chemically reversible reaction (by recombining the two components from the initial reaction) (10, 11)

This work is concerned solely with (sensible) water-based TES tanks. Water has the highest volumetric thermal capacity compared to the other typically used sensible heat storage materials (8), and can be easily integrated with the cooling water output from the mCHP heat exchanger. It is also far and away the most common form of thermal storage currently available.

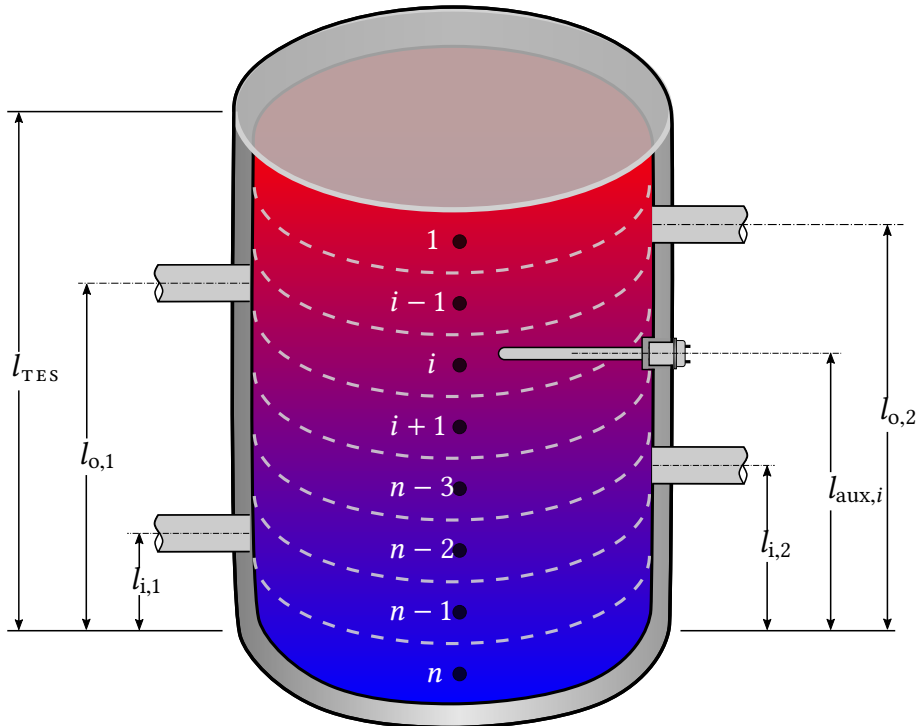


**Figure 4.4 | Schematic of cylindrical thermal energy storage tank.** The tank of volume  $V_{TES}$  is discretised into  $n$  nodes along the length of the tank. The model has two inlet and two outlet pipes that can be placed at arbitrary positions along the length of the tank. The schematic shows a tank with uniform cross-section but the model allows for a non-uniform cross-section at any node. Only one auxiliary electrical heater placed at  $l_{aux,i}$  is shown, but the model allows for  $n_{aux}$  auxiliary heaters.

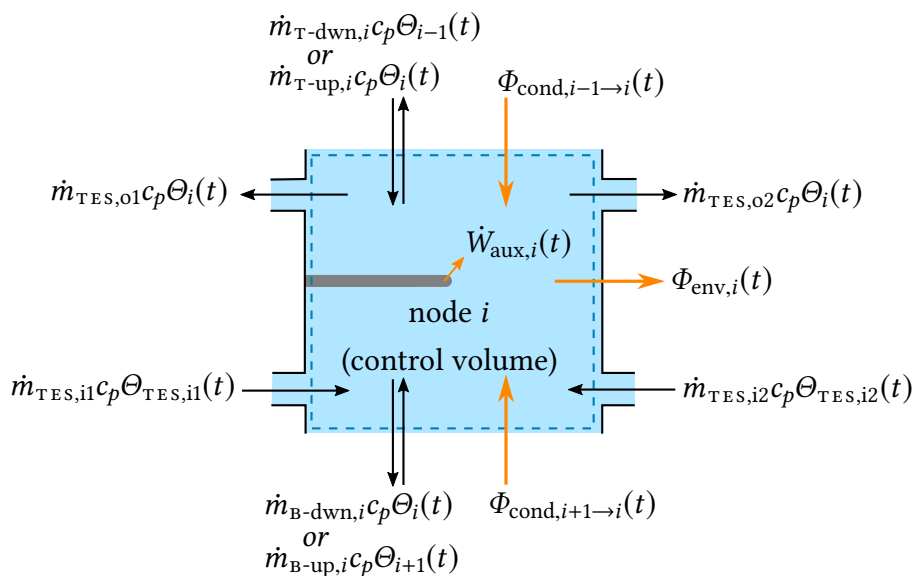


**Figure 4.5 | Energy and mass flows in a node  $i$  of the thermal energy storage tank.** Mass flow heat transfers shown in black while conduction, convection, radiation heat transfer shown in orange. It is assumed that the mass within the control volume is constant i.e.  $m_i = \text{const}$ .

#### 4.2.1 Modelling approach

The model utilised in this work is based on the computer model developed by Newton (12). However, Newton's model is specifically designed to be implemented in the energy simulation software TRNSYS. The computer model is constructed using loops and conditional statements, and its dynamic behaviour is solved using iterative solution techniques. The development of the nonlinear inversion based MIMO control algorithms in this work requires a *continuous* dynamic mathematical model (in the same way that many optimisation algorithms do (13)) that are represented in a set of ODEs. Therefore, the following section is concerned with reconstructing and modifying the TRNSYS computer model to a fully nonlinear continuous differential state model of the TES suitable for the application of advanced control theory techniques.

Figure 4.4 provides a schematic of the TES tank, where the volume of water contained in the tank has been discretised into  $n$  nodes of equal volume. The nodes are arranged so that the first node is at the top of the tank, and the  $n$ -th node is at the bottom. The model allows for two inlet and two outlet pipes that can be placed at arbitrary positions along the length of the tank. The schematic shows a tank with uniform cross-section but the model allows for a non-uniform cross-section at any node. The model includes auxiliary electrical heaters that can be placed in any node. These elements use electrical power to heat up the water in the TES when there is demand for thermal energy from the store that is not available. The figure only shows one auxiliary electrical heater but the model allows for  $n_{\text{aux}}$  auxiliary heaters.

The model is comprised of the following energy transfer mechanisms:

- *Heat conduction*: between the nodes through the water and along the tank wall
- *Environmental heat transfer*: between the nodes – through the tank wall – to the surrounding environment
- *Mass flow*: enters and exits via the inlet and outlet pipes, and also occurs through the body of water depending on the mass flow balance among the connected pipes
- *Electrical element heaters*: placed within the tank can directly heat the node(s) in which they are contained

The amount of energy stored in each node  $i$  is calculated as

$$Q_i(t) = m_i c_p \Delta \Theta_i(t) \quad (4.27)$$

where



- $Q_i$  is the amount of heat stored in the water contained in the control volume  $i$  (J);
- $m_i$  is the mass of the water contained in the control volume  $i$  (kg);
- $\Delta\Theta_i$  is the change in temperature of the water contained in the control volume  $i$  (K).

The energy balance for a node  $i$  is represented pictorially in fig. 4.5 considering the scenario when every possible energy flow is occurring at the node simultaneously. Taking the rate form of eq. (4.27) and considering the energy balance for a node  $i$  given in fig. 4.5, the state differential equation for the energy balance in node  $i$  is given as

$$\begin{aligned}
m_i c_p \frac{d\Theta_i(t)}{dt} = & \underbrace{\frac{\lambda_{\text{eff}} A_{T,i}}{\Delta x_{i-1 \rightarrow i}} (\Theta_{i-1}(t) - \Theta_i(t))}_{\substack{\text{conductance heat transfer,} \\ \Phi_{\text{cond}, i-1 \rightarrow i}(t)}} + \underbrace{\frac{\lambda_{\text{eff}} A_{B,i}}{\Delta x_{i+1 \rightarrow i}} (\Theta_{i+1}(t) - \Theta_i(t))}_{\substack{\text{conductance heat transfer,} \\ \Phi_{\text{cond}, i+1 \rightarrow i}(t)}} \\
& - \underbrace{H_{\text{env},i} (\Theta_i(t) - \Theta_{\text{env}}(t))}_{\substack{\text{environmental heat transfer,} \\ \Phi_{\text{env},i}(t)}} \\
& + \underbrace{\dot{m}_{T\text{-dwn},i}(\cdot) c_p \Theta_{i-1}(t) - \dot{m}_{T\text{-up},i}(\cdot) c_p \Theta_i(t)}_{\text{mass flow through top of the node}} \\
& - \underbrace{\dot{m}_{B\text{-dwn},i}(\cdot) c_p \Theta_i(t) + \dot{m}_{B\text{-up},i}(\cdot) c_p \Theta_{i+1}(t)}_{\text{mass flow through bottom of the node}} \\
& + \underbrace{\dot{m}_{\text{TES},i1,i}(t) c_p \Theta_{\text{TES},i1}(t) + \dot{m}_{\text{TES},i2,i}(t) c_p \Theta_{\text{TES},i2}(t)}_{\text{mass flow entering the TES}} \\
& - \underbrace{\dot{m}_{\text{TES},o1,i}(t) c_p \Theta_i(t) - \dot{m}_{\text{TES},o2,i}(t) c_p \Theta_i(t)}_{\text{mass flow exiting the TES}} + \underbrace{\dot{W}_{\text{aux},i}(t)}_{\text{auxiliary heater}}
\end{aligned} \tag{4.28}$$

where



$\lambda_{\text{eff}}$	is the effective thermal conductivity ( $\text{W m}^{-1} \text{K}^{-1}$ );
$A_{\text{T},i}, A_{\text{B},i}$	are the cross-sectional areas of the top and bottom of the control volume $i$ ( $\text{m}^2$ );
$\Delta x_{i+1 \rightarrow i}, \Delta x_{i-1 \rightarrow i}$	are the centre-to-centre distances between node $i$ and the node below and above it, respectively (m);
$H_{\text{env},i}$	is the overall heat transfer coefficient from the node $i$ to the surrounding environment ( $\text{W K}^{-1}$ );
$\dot{m}_{\text{T-dwn},i}, \dot{m}_{\text{T-up},i}$	are the mass flow rates entering/exiting the top of node $i$ ( $\text{kg s}^{-1}$ );
$\dot{m}_{\text{B-dwn},i}, \dot{m}_{\text{B-up},i}$	are the mass flow rates exiting/entering the bottom of node $i$ ( $\text{kg s}^{-1}$ );
$\dot{m}_{\text{TES},i1}, \Theta_{\text{TES},i1}$	is the mass flow rate and temperature of fluid entering inlet 1;
$\dot{m}_{\text{TES},i2}, \Theta_{\text{TES},i2}$	is the mass flow rate and temperature of fluid entering inlet 2;
$\dot{m}_{\text{TES},o1}$	is the mass flow rate of fluid exiting outlet pipe 1 ( $\text{kg s}^{-1}$ );
$\dot{m}_{\text{TES},o2}$	is the mass flow rate of fluid exiting outlet pipe 2 ( $\text{kg s}^{-1}$ );
$\dot{W}_{\text{aux},i}$	is the work input by an auxiliary heater to node $i$ (W).

#### 4.2.2 Heat transfer via conduction

As discussed in § 2.3, the use of TES coupled with external energy systems often employ thermal stratification of the fluid within the tank for improving the storage- and operational-efficiency of the overall system. However, the fluid in the tank will not remain stratified forever, so it is important to model how this stratification decays in the absence of fluid flow. Experimental analysis of such tanks has concluded that the temperature distribution is largely one-dimensional (14), with variation in the vertical direction. Number of nodes required to accurately model stratification 15 to 50 (12, p. 103). Increasing  $n$  increases stratification modelling resolution.

The de-stratification of the fluid is modelled as one-dimensional heat conduction between adjacent nodes through the fluid in the tank and along the tank wall, which will eventually cause the nodes to reach thermal equilibrium. Considering only the heat conduction between the nodes in eq. (4.28), the energy balance for the  $i$ th node in the tank would be given by

$$m_i c_p \frac{d\Theta_i(t)}{dt} = \underbrace{\frac{\lambda_{\text{eff}} A_{\text{T},i}}{\Delta x_{i-1 \rightarrow i}}}_{H_{i(i-1)}} (\Theta_{i-1}(t) - \Theta_i(t)) + \underbrace{\frac{\lambda_{\text{eff}} A_{\text{B},i}}{\Delta x_{i+1 \rightarrow i}}}_{H_{i(i+1)}} (\Theta_{i+1}(t) - \Theta_i(t))$$

where





$H_{ij}$  represents the thermal conductance between node  $i \leftrightarrow j$  ( $\text{W K}^{-1}$ ).

The effective thermal conductivity,  $\lambda_{\text{eff}} = \lambda + \Delta\lambda$ , accounts for both the thermal conductivity of the fluid ( $\lambda$ ) and the thermal conductivity along the tank wall ( $\Delta\lambda$ ). Fluid thermal conductivity for many elements is readily available from several handbooks, but the conduction along the tank wall is often best determined experimentally (see 12, § 2.2.2). In the absence of experimental data, a theoretical estimate of the tank wall conductivity is given by

$$\Delta\lambda = \lambda_{\text{wall}} \frac{A_{\text{wall}}}{A_{\text{fluid}}},$$

where

$\lambda_{\text{wall}}$  is the thermal conductivity of the tank wall ( $\text{W m}^{-1} \text{K}^{-1}$ );  
 $A_{\text{wall}}, A_{\text{fluid}}$  are the cross-sectional areas of the tank wall and tank fluid respectively, perpendicular to the direction of heat flow (m).

Note that the cross-sectional area of the fluid can be different at the top and the bottom of the node, denoted by  $A_{\text{T},i}, A_{\text{B},i}$ . This is due to the fact that horizontal cylindrical tanks do not have a uniform cross-section in the direction of flow. However, the majority of tanks encountered in practice will be vertical cylinders with uniform cross-section such that  $A_{\text{T},i} = A_{\text{B},i} = A_i = A$ .

Not every node in the tank will contain both upwards and downwards heat conduction. The node at the top of the tank will conduct heat only with the node below it, while the node at the bottom of the tank will only conduct heat with the node above it. All interior nodes will conduct heat with the nodes directly above and below it. This directional thermal conductance between two nodes can be defined as

$$H_{ij} = \begin{cases} \frac{\lambda_{\text{eff}} A_{\text{B},i}}{\Delta x_{j \rightarrow i}} & \text{for } i \in [1, n-1], \text{ where } j = i+1, \\ \frac{\lambda_{\text{eff}} A_{\text{T},i}}{\Delta x_{j \rightarrow i}} & \text{for } i \in [2, n], \text{ where } j = i-1. \end{cases}$$

Assembling the heat conduction transfer between all the nodes in an  $n$ th-order TES model will result in

$$\begin{bmatrix} m_1 c_p \dot{\Theta}_1(t) \\ m_2 c_p \dot{\Theta}_2(t) \\ m_3 c_p \dot{\Theta}_3(t) \\ \vdots \\ m_n c_p \dot{\Theta}_n(t) \end{bmatrix} = \underbrace{\begin{bmatrix} -H_{12} & H_{12} & & & \\ H_{21} & -(H_{21} + H_{23}) & H_{23} & & \\ & H_{32} & \ddots & \ddots & \\ & & \ddots & \ddots & H_{(n-1)n} \\ & & & H_{n(n-1)} & -H_{n(n-1)} \end{bmatrix}}_{H_{\text{TES}}} \begin{bmatrix} \Theta_1(t) \\ \Theta_2(t) \\ \Theta_3(t) \\ \vdots \\ \Theta_n(t) \end{bmatrix}.$$



where it is evident that  $\mathbf{H}_{\text{TES}}$  is a tridiagonal matrix. It can be recognised that the elements along the subdiagonal represent the heat conduction ‘upwards’ from the bottom of the tank to the top, while the superdiagonal contains the terms ‘downwards’ from the top of the tank to the bottom. These can be gathered into vectors  $\mathbf{h}_{\text{up}}, \mathbf{h}_{\text{down}} \in \mathbb{R}_{>0}^{n-1}$ , where  $\mathbf{h}_{\text{up}} = (H_{21}, H_{32}, \dots, H_{n(n-1)})$  and  $\mathbf{h}_{\text{down}} = (H_{12}, H_{23}, \dots, H_{(n-1)n})$ . The main diagonal elements contain the negative of the sum of the adjacent elements in that row in order to ensure an energy balance for that node via heat conduction. Therefore, the main diagonal can also be written in a vector  $\mathbf{h}_{\text{tank}} \in \mathbb{R}_{>0}^n$ ,  $\mathbf{h}_{\text{tank}} = (-H_{12}, -(H_{21} + H_{23}), \dots, -H_{n(n-1)})$ . Now, the complete description for heat conduction between the nodes of an  $n$  node TES tank is given by

$$\boxed{C_{\text{TES}} \dot{\boldsymbol{\theta}}_{\text{TES}}(t) = \mathbf{H}_{\text{TES}} \boldsymbol{\theta}_{\text{TES}}(t)}, \quad (4.29)$$

where  $C_{\text{TES}} = \text{diag}(m_i c_p)$ ,  $i = 1, \dots, n$  is a diagonal matrix where the entries along the diagonal are the heat capacities of the nodes.  $\boldsymbol{\theta}_{\text{TES}}(t) = (\theta_1(t), \dots, \theta_n(t))^T$  is a vector containing all of the nodal temperatures in the TES. The heat conduction matrix is given by  $\mathbf{H}_{\text{TES}} = \text{tridiag}(\mathbf{h}_{\text{up}}, \mathbf{h}_{\text{tank}}, \mathbf{h}_{\text{down}})$ .

#### 4.2.3 Environmental heat transfer

Considering only the heat transfer between the node and the surrounding environment from eq. (4.28), the energy balance for the  $i$ th node in the tank is given by

$$m_i c_p \frac{d\theta_i(t)}{dt} = -H_{\text{env},i} (\theta_i(t) - \theta_{\text{env}}(t)).$$

The overall heat transfer coefficient from the node  $i$  to the surroundings can be calculated as

$$H_{\text{env},i} = (H_{\text{tank}} + \Delta H_{\text{tank},i}),$$

where

$H_{\text{tank}}$  is the heat transfer coefficient between the fluid in the tank and the surrounding environment ( $\text{W K}^{-1}$ );

$\Delta H_{\text{tank},i}$  is the additional heat transfer coefficient between the fluid in node  $i$  and the surrounding environment ( $\text{W K}^{-1}$ ).

The additional heat transfer coefficient is used to account for differences from the ‘base’ heat transfer coefficient for each  $i$ -th node. These variations can be to accommodate varying thickness of insulation along the length of the tank, extra losses at the pipe connections, or to allow for additional losses via the top or bottom of the tank.



Gathering the environmental heat transfers from all nodes in vector-matrix form

$$\begin{bmatrix} m_1 c_p \dot{\Theta}_1(t) \\ m_2 c_p \dot{\Theta}_2(t) \\ \vdots \\ m_n c_p \dot{\Theta}_n(t) \end{bmatrix} = - \underbrace{\begin{bmatrix} H_{\text{env},1} & 0 & \dots & 0 \\ 0 & H_{\text{env},2} & \dots & 0 \\ \vdots & \vdots & \ddots & \vdots \\ 0 & 0 & \dots & H_{\text{env},n} \end{bmatrix}}_{\mathbf{H}_{\text{env}}} \begin{bmatrix} \Theta_1(t) \\ \Theta_2(t) \\ \vdots \\ \Theta_n(t) \end{bmatrix} + \underbrace{\begin{bmatrix} H_{\text{env},1} \\ H_{\text{env},2} \\ \vdots \\ H_{\text{env},n} \end{bmatrix}}_{\mathbf{h}_{\text{env}}} \Theta_{\text{env}}(t)$$

Or in compact form

$$\mathbf{C}_{\text{TES}} \dot{\boldsymbol{\theta}}_{\text{TES}}(t) = - \underbrace{\text{diag}(\mathbf{h}_{\text{env}})}_{\mathbf{H}_{\text{env}}} \boldsymbol{\theta}_{\text{TES}}(t) + \mathbf{h}_{\text{env}} \Theta_{\text{env}}$$

or

$$\boxed{\mathbf{C}_{\text{TES}} \dot{\boldsymbol{\theta}}_{\text{TES}}(t) = -\mathbf{H}_{\text{env}} \boldsymbol{\theta}_{\text{TES}}(t) + \mathbf{h}_{\text{env}} \Theta_{\text{env}}(t)} \quad (4.30)$$

#### 4.2.4 Mass flow network

Consider only the mass flow network for the fluid entering, leaving and flowing within the TES tank. The energy balance for the  $i$ th node in the tank is then given by

$$\begin{aligned} m_i c_p \frac{d\Theta_i(t)}{dt} = & \underbrace{+\dot{m}_{\text{T-dwn},i}(\cdot) c_p \Theta_{i-1}(t) - \dot{m}_{\text{T-up},i}(\cdot) c_p \Theta_i(t)}_{\text{mass flow through top of the node}} \\ & \underbrace{-\dot{m}_{\text{B-dwn},i}(\cdot) c_p \Theta_i(t) + \dot{m}_{\text{B-up},i}(\cdot) c_p \Theta_{i+1}(t)}_{\text{mass flow through bottom of the node}} \\ & \underbrace{+\dot{m}_{\text{TES},i1}(t) c_p \Theta_{\text{TES},i1}(t) + \dot{m}_{\text{TES},i2}(t) c_p \Theta_{\text{TES},i2}(t)}_{\text{mass flow entering the TES}} \\ & \underbrace{-\dot{m}_{\text{TES},o1}(t) c_p \Theta_i(t) - \dot{m}_{\text{TES},o2}(t) c_p \Theta_i(t)}_{\text{mass flow exiting the TES}} \end{aligned} \quad (4.31)$$

#### Bulk flow rates

Unlike the heat transfer via condition, the mass flow network is uni-directional. That means for each node only one of the ‘up’ or ‘dwn’ terms at the top and bottom of the node will be non-zero (or both will be zero for the case of zero mass flow). To determine the direction of the flow it is necessary to first compute the **bulk flow** in and out of each node. A mass balance is taken for each node, where the sign convention is that if flow is leaving the node the bulk flow is negative, and positive if the flow is



entering the node. This can be computed as

$$\dot{m}_{T,i} = \begin{cases} 0 & \text{for } i = 1 \\ -\dot{m}_{B,i-1} & \text{for } i \in [2, n] \end{cases}, \quad (4.32a)$$

$$\dot{m}_{B,i} = \begin{cases} \dot{m}_{TES,o1,i} + \dot{m}_{TES,o2,i} - \dot{m}_{TES,i1,i} - \dot{m}_{TES,i2,i} - \dot{m}_{T,i} & \text{for } i \in [1, n-1] \\ 0 & \text{for } i = n \end{cases}. \quad (4.32b)$$

The bulk flow rates for all nodes in the TES tank can be placed into **bulk flow vectors** given by

$$\dot{\mathbf{m}}_T(t) = \left[ \dot{m}_{T,1}(t) \quad \dot{m}_{T,2}(t) \quad \dots \quad \dot{m}_{T,n}(t) \right]^T \quad (4.33a)$$

$$\dot{\mathbf{m}}_B(t) = \left[ \dot{m}_{B,1}(t) \quad \dot{m}_{B,2}(t) \quad \dots \quad \dot{m}_{B,n}(t) \right]^T. \quad (4.33b)$$

The calculation of the bulk flow vectors are given by

$$\dot{\mathbf{m}}_T(t) = \mathbf{P}_T \dot{\mathbf{m}}_{i/o}(t), \quad (4.34)$$

$$\dot{\mathbf{m}}_B(t) = \mathbf{P}_B \dot{\mathbf{m}}_{i/o}(t), \quad (4.35)$$

where

$$\mathbf{P}_T = \mathbf{L}_T \begin{bmatrix} \gamma_{i1} & \gamma_{i2} & -\gamma_{o1} & -\gamma_{o2} \end{bmatrix},$$

$$\mathbf{P}_B = \mathbf{L}_B \begin{bmatrix} -\gamma_{i1} & -\gamma_{i2} & \gamma_{o1} & \gamma_{o2} \end{bmatrix}.$$

The matrices  $\mathbf{P}_T, \mathbf{P}_B$  compute the combinations of the mass flow rates in order to determine the bulk flow through the top and bottom of each node.

The derivation of eq. (4.34) is provided in appendix A.1.

### Directional flow rates

With knowledge of the bulk flow to each node, it is possible to compute the mass flow rates entering/exiting through the top or bottom of each node in eq. (4.31). These flow rates are designated as the nodal **directional flows** given by

$$\dot{m}_{T,up,i} = \begin{cases} 0 & \text{if } \dot{m}_{T,i} \geq 0 \\ -\dot{m}_{T,i} & \text{if } \dot{m}_{T,i} < 0 \end{cases} \quad (4.36a)$$

$$\dot{m}_{T,dwn,i} = \begin{cases} \dot{m}_{T,i} & \text{if } \dot{m}_{T,i} > 0 \\ 0 & \text{if } \dot{m}_{T,i} \leq 0 \end{cases} \quad (4.36b)$$





$$\dot{m}_{B,\text{up},i} = \begin{cases} \dot{m}_{B,i} & \text{if } \dot{m}_{B,i} > 0 \\ 0 & \text{if } \dot{m}_{B,i} \leq 0 \end{cases} \quad (4.36c)$$

$$\dot{m}_{B,\text{dwn},i} = \begin{cases} 0 & \text{if } \dot{m}_{B,i} \geq 0 \\ -\dot{m}_{B,i} & \text{if } \dot{m}_{B,i} < 0 \end{cases} \quad (4.36d)$$

Simply, the mass flow parameters are switched so that flow only occurs in one direction through the top and bottom of each node, determined by the sign of the bulk flow at that end.

The directional flow terms can also be re-expressed in terms of the max function e.g.  $\dot{m}_{T\text{-up},i} = \max(-\dot{m}_{T,i}, 0)$ . The maximum function can be applied in vector form, such that

$$\dot{\mathbf{m}}_{T,\text{up}} = \max(-\dot{\mathbf{m}}_T, \mathbf{0}_n), \quad (4.37a)$$

$$\dot{\mathbf{m}}_{T,\text{dwn}} = \max(\dot{\mathbf{m}}_T, \mathbf{0}_n), \quad (4.37b)$$

$$\dot{\mathbf{m}}_{B,\text{up}} = \max(\dot{\mathbf{m}}_B, \mathbf{0}_n), \quad (4.37c)$$

$$\dot{\mathbf{m}}_{B,\text{dwn}} = \max(-\dot{\mathbf{m}}_B, \mathbf{0}_n), \quad (4.37d)$$

where  $\dot{\mathbf{m}}_{T\text{-up}} = (\dot{m}_{T,1}, \dot{m}_{T,2}, \dots, \dot{m}_{T,n})$  and similarly for the other directional flow vectors.

Note that the switching of these parameters has introduced discontinuous terms into the model equations. In this case the occurrence of the discontinuous terms in system dynamics can be approximated using a continuously differentiable ( $C^\infty$ ) function that approximates the max function. There are a number of possible functions that can be used and 4 such functions will be compared in order to assess which one is most appropriate for this application.

There is the so-called **softmax** function used in computer graphics and optimization problems (15):

$$\max(a, b) \approx \underbrace{\ln(e^{ka} + e^{kb})/k}_{A1}, \quad (4.38)$$

where  $k$  sets the scaling factor for the approximation such that for large  $k$ ,  $\ln(e^{ka} + e^{kb})/k \rightarrow \max(a, b)$ . However, when  $a$  and  $b$  are equal:

$$\ln(e^{ka} + e^{ka})/k = \ln(2e^{ka})/k = a + \ln(2)/k,$$

this shows that the approximation will be off by  $\ln(2)/k$  when the two parameters are equal. Since in this case  $b$  is always zero, the approximation will be off when

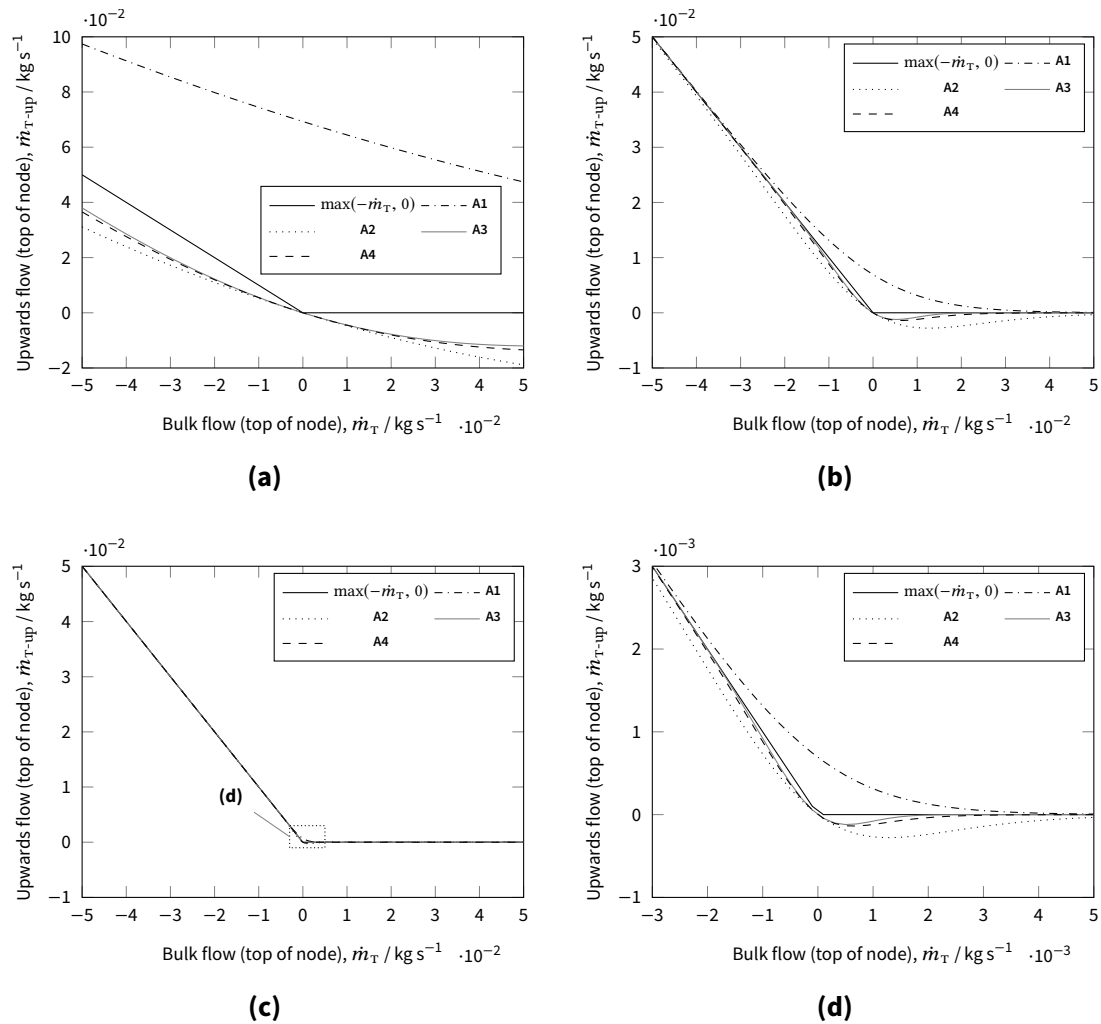


**Figure 4.6 | Comparison of max function approximations for continuous mass flow rates.** In the approximations the following scaling factors are used in each subfigure: **(a)**  $k = 10$  **(b)**  $k = 100$  **(c)**  $k = 1000$  **(d)**  $k = 1000$  with the axis rescaled to show approximations around zero.

either bulk mass flow rate is zero. Since this is less than ideal, take (4.38) and add its derivative with respect to  $k$  divided by  $k$ , results in a new function (16)

$$\max(a, b) \approx \underbrace{\frac{ae^{ka} + be^{kb}}{e^{ka} + e^{kb}}}_{\text{A2}}. \quad (4.39)$$

Now (4.39) will be exact when the bulk mass flow rate is zero.

The final two approximations utilises the fact that the max function can be written in terms of absolute values as  $\max(a, b) = (1/2)(a + b + |a - b|)$ . Recognising that  $b$  is always zero, then  $\max(a, 0) = (1/2)(a + |a|)$ . A smooth approximation of the absolute value function utilises the error function (17) as

$$|a| \approx a \operatorname{erf}(ka), \quad \text{where } \operatorname{erf}(ka) = \frac{2}{\sqrt{\pi}} \int_0^{ka} e^{-t^2} dt.$$

It follows that letting  $1/k \rightarrow 0$  gives better approximations. This works because feeding large positive numbers to the error function returns +1 and large negative numbers  $-1$ , essentially returning the sign of  $a$  for large  $k$ . Now, the max function can be given by

$$\max(a, 0) \approx \underbrace{\frac{a}{2}(1 + \operatorname{erf}(ka))}_{\text{A3}}. \quad (4.40)$$

The final approximation is constructed by recognising that  $|a| = a \operatorname{sgn}(a)$ , where  $\operatorname{sgn}$  denotes the signum function, which returns a number's sign irrespective of its value. An approximation of the signum function is given by  $\operatorname{sgn} a \approx \tanh(ka)$ , where for large  $k$ ,  $\tanh(ka) \rightarrow \operatorname{sgn}(a)$ . The final approximation of the maximum function is now given by

$$\max(a, 0) \approx \underbrace{\frac{a}{2}(1 + \tanh(ka))}_{\text{A4}}. \quad (4.41)$$

In order to compare the different approximations, consider the flow rate through the top of a node in the TES tank, given by  $\dot{m}_{\text{T-up},i} = \max(-\dot{m}_{\text{T},i}, 0)$ . Figure 4.6 shows the curves for the different approximations of this function for a wide range of bulk flow rates and varying  $k$ .

As can be seen from the figures, increasing the scaling factor increases the accuracy of the approximation. It is not until  $k = 1000$  that a very close approximation is reached.<sup>2</sup> It is also evident that of the 4 approximations of the max function, A3, the

<sup>2</sup>This is dependent on the units of the input variable. For  $\text{kg s}^{-1}$   $k = 1000$  yields a good approximation. Alternative units will require different values of  $k$  for a suitable approximation.



function utilising the error function, provides the best approximation of the control mass flow rate: It has no error at the discontinuity crossover point, and both its overshoot and settling time either side of the discontinuity are the lowest. However, the error function – while continuous – is not an elementary function and as such would still have to be numerically approximated. Therefore in this work the second best approximation is used, which is **A4** that utilises the hyperbolic tangent.<sup>3</sup>

The continuous approximations,  $\widehat{m}$ , of the directional mass flow rates are now given by

$$\begin{aligned}\widehat{m}_{T\text{-up},i} &= -\frac{\dot{m}_{T,i}}{2}(1 + \tanh(-k\dot{m}_{T,i})), \\ \widehat{m}_{T\text{-down},i} &= \frac{\dot{m}_{T,i}}{2}(1 + \tanh(k\dot{m}_{T,i})), \\ \widehat{m}_{B\text{-up},i} &= \frac{\dot{m}_{B,i}}{2}(1 + \tanh(k\dot{m}_{B,i})), \\ \widehat{m}_{B\text{-down},i} &= -\frac{\dot{m}_{B,i}}{2}(1 + \tanh(-k\dot{m}_{B,i})),\end{aligned}$$

where  $\widehat{m} \rightarrow m$  for  $k \rightarrow \infty$ .

### Mass flow matrix

Recalling the (mass flow) energy balance for the TES tank given by (4.31), this can be written in vector-matrix form for all nodes in the tank as

$$\begin{aligned}\begin{bmatrix} m_1 c_p \dot{\Theta}_1(t) \\ m_2 c_p \dot{\Theta}_2(t) \\ \vdots \\ m_n c_p \dot{\Theta}_n(t) \end{bmatrix} &= c_p \begin{bmatrix} \dot{m}_{\text{TES},i1,1}(t) \\ \dot{m}_{\text{TES},i1,2}(t) \\ \vdots \\ \dot{m}_{\text{TES},i1,n}(t) \end{bmatrix} \Theta_{\text{TES},i1}(t) + c_p \begin{bmatrix} \dot{m}_{\text{TES},i2,1}(t) \\ \dot{m}_{\text{TES},i2,2}(t) \\ \vdots \\ \dot{m}_{\text{TES},i2,n}(t) \end{bmatrix} \Theta_{\text{TES},i2}(t) \\ &\quad - c_p \begin{bmatrix} \dot{m}_{\text{TES},o1,1}(t) & 0 & \dots & 0 \\ 0 & \dot{m}_{\text{TES},o1,2}(t) & \dots & 0 \\ \vdots & \vdots & \ddots & \vdots \\ 0 & 0 & \dots & \dot{m}_{\text{TES},o1,n}(t) \end{bmatrix} \begin{bmatrix} \Theta_1(t) \\ \Theta_2(t) \\ \vdots \\ \Theta_n(t) \end{bmatrix} \\ &\quad - c_p \begin{bmatrix} \dot{m}_{\text{TES},o2,1}(t) & 0 & \dots & 0 \\ 0 & \dot{m}_{\text{TES},o2,2}(t) & \dots & 0 \\ \vdots & \vdots & \ddots & \vdots \\ 0 & 0 & \dots & \dot{m}_{\text{TES},o2,n}(t) \end{bmatrix} \begin{bmatrix} \Theta_1(t) \\ \Theta_2(t) \\ \vdots \\ \Theta_n(t) \end{bmatrix}\end{aligned}$$

<sup>3</sup>There is a related discussion on how tanh can produce a very accurate approximation of erf found here (18).



$$\begin{aligned}
& + c_p \begin{bmatrix} 0 & 0 & 0 & 0 \\ \dot{m}_{T,dwn,2}(\cdot) & 0 & 0 & 0 \\ 0 & \ddots & 0 & 0 \\ 0 & 0 & \dot{m}_{T,dwn,n}(\cdot) & 0 \end{bmatrix} \begin{bmatrix} \Theta_1(t) \\ \Theta_2(t) \\ \vdots \\ \Theta_n(t) \end{bmatrix} \\
& - c_p \begin{bmatrix} \dot{m}_{T,up,1}(\cdot) & 0 & \dots & 0 \\ 0 & \dot{m}_{T,up,2}(\cdot) & \dots & 0 \\ \vdots & \vdots & \ddots & \vdots \\ 0 & 0 & \dots & \dot{m}_{T,up,n}(\cdot) \end{bmatrix} \begin{bmatrix} \Theta_1(t) \\ \Theta_2(t) \\ \vdots \\ \Theta_n(t) \end{bmatrix} \\
& + c_p \begin{bmatrix} 0 & \dot{m}_{B,up,1}(\cdot) & 0 & 0 \\ 0 & 0 & \ddots & 0 \\ 0 & 0 & 0 & \dot{m}_{B,up,n-1}(\cdot) \\ 0 & 0 & 0 & 0 \end{bmatrix} \begin{bmatrix} \Theta_1(t) \\ \Theta_2(t) \\ \vdots \\ \Theta_n(t) \end{bmatrix} \\
& - c_p \begin{bmatrix} \dot{m}_{B,dwn,1}(\cdot) & 0 & \dots & 0 \\ 0 & \dot{m}_{B,dwn,2}(\cdot) & \dots & 0 \\ \vdots & \vdots & \ddots & \vdots \\ 0 & 0 & \dots & \dot{m}_{B,dwn,n}(\cdot) \end{bmatrix} \begin{bmatrix} \Theta_1(t) \\ \Theta_2(t) \\ \vdots \\ \Theta_n(t) \end{bmatrix}
\end{aligned}$$

Or in compact notation:

$$\begin{aligned}
C_{TES} \dot{\boldsymbol{\theta}}_{TES}(t) &= c_p \boldsymbol{\gamma}_{i1} \dot{m}_{TES,i1}(t) \boldsymbol{\theta}_{TES,i1}(t) + c_p \boldsymbol{\gamma}_{i2} \dot{m}_{TES,i2}(t) \boldsymbol{\theta}_{TES,i2}(t) \\
& - c_p \text{diag}(\boldsymbol{\gamma}_{o1}) \dot{m}_{TES,o1}(t) \boldsymbol{\theta}_{TES}(t) - c_p \text{diag}(\boldsymbol{\gamma}_{o2}) \dot{m}_{TES,o2}(t) \boldsymbol{\theta}_{TES}(t) \\
& + c_p \underbrace{\text{diag}(\dot{\mathbf{m}}_{T-dwn,2 \rightarrow n}(\cdot), -1)}_{\mathbf{M}_{T-dwn}(\cdot)} \boldsymbol{\theta}_{TES}(t) - c_p \underbrace{\text{diag}(\dot{\mathbf{m}}_{T-up}(\cdot))}_{\mathbf{M}_{T-up}(\cdot)} \boldsymbol{\theta}_{TES}(t) \\
& + c_p \underbrace{\text{diag}(\dot{\mathbf{m}}_{B-up,1 \rightarrow (n-1)}(\cdot), 1)}_{\mathbf{M}_{B-up}(\cdot)} \boldsymbol{\theta}_{TES}(t) - c_p \underbrace{\text{diag}(\dot{\mathbf{m}}_{B-dwn}(\cdot))}_{\mathbf{M}_{B-dwn}(\cdot)} \boldsymbol{\theta}_{TES}(t)
\end{aligned}$$

$$\begin{aligned}
C_{TES} \dot{\boldsymbol{\theta}}_{TES}(t) &= c_p \underbrace{\begin{bmatrix} \boldsymbol{\gamma}_{i1} \dot{m}_{TES,i1}(t) & \boldsymbol{\gamma}_{i2} \dot{m}_{TES,i2}(t) \end{bmatrix}}_{\mathbf{M}_i(t)} \underbrace{\begin{bmatrix} \boldsymbol{\theta}_{TES,i1}(t) \\ \boldsymbol{\theta}_{TES,i2}(t) \end{bmatrix}}_{\boldsymbol{\theta}_{TES,i}(t)} \\
& - c_p \underbrace{(\text{diag}(\boldsymbol{\gamma}_{o1}) \dot{m}_{TES,o1}(t) + \text{diag}(\boldsymbol{\gamma}_{o2}) \dot{m}_{TES,o2}(t))}_{\mathbf{M}_o(t)} \boldsymbol{\theta}_{TES}(t) \\
& + c_p \underbrace{(\mathbf{M}_{T-dwn}(\cdot) - \mathbf{M}_{T-up}(\cdot) - \mathbf{M}_{B-dwn}(\cdot) + \mathbf{M}_{B-up}(\cdot))}_{\mathbf{M}_{tank}(\cdot)} \boldsymbol{\theta}_{TES}(t)
\end{aligned}$$





$$C_{\text{TES}}\dot{\theta}_{\text{TES}}(t) = c_p(\mathbf{M}_{\text{tank}}(\dot{\mathbf{m}}_{i/o}(t)) - \mathbf{M}_o(\dot{\mathbf{m}}_o(t)))\theta_{\text{TES}}(t) + c_p\mathbf{M}_i(\dot{\mathbf{m}}_i(t))\theta_{\text{TES},i}(t) \quad (4.42)$$

where

$$\mathbf{M}_i = \begin{bmatrix} \gamma_{i1} & \gamma_{i2} \end{bmatrix} \text{diag}(\dot{\mathbf{m}}_i(t))$$

$$\mathbf{M}_o = \text{diag} \left( \begin{bmatrix} \gamma_{o1} & \gamma_{o2} \end{bmatrix} \dot{\mathbf{m}}_o(t) \right)$$

The inner-tank mass flow rate matrix,  $\mathbf{M}_{\text{tank}}$ , is determined as a discontinuous function of the bulk mass flow rates:

$$\mathbf{M}_{\text{tank}} = \text{diag}(\dot{\mathbf{m}}_{\text{T-dwn},2 \rightarrow n}, -1) - \text{diag}(\dot{\mathbf{m}}_{\text{T-up}}) \\ - \text{diag}(\dot{\mathbf{m}}_{\text{B-dwn}}) + \text{diag}(\dot{\mathbf{m}}_{\text{B-up},1 \rightarrow (n-1)}, 1)$$

where the control flows are given by

$$\dot{\mathbf{m}}_{\text{T-up}} = \max(-\mathbf{P}_T \dot{\mathbf{m}}_{i/o}(t), 0_n),$$

$$\dot{\mathbf{m}}_{\text{T-dwn}} = \max(\mathbf{P}_T \dot{\mathbf{m}}_{i/o}(t), 0_n),$$

$$\dot{\mathbf{m}}_{\text{B-up}} = \max(\mathbf{P}_B \dot{\mathbf{m}}_{i/o}(t), 0_n),$$

$$\dot{\mathbf{m}}_{\text{B-dwn}} = \max(-\mathbf{P}_B \dot{\mathbf{m}}_{i/o}(t), 0_n).$$

In order to provide a continuous mathematical model, the inner-tank mass flow rate matrix can be approximated by letting  $\mathbf{M}_{\text{tank}} \approx \widehat{\mathbf{M}}_{\text{tank}}$ , where

$$\widehat{\mathbf{M}}_{\text{tank}} = \text{diag}(\widehat{\dot{\mathbf{m}}}_{\text{T-dwn},2 \rightarrow n}, -1) - \text{diag}(\widehat{\dot{\mathbf{m}}}_{\text{T-up}}) - \text{diag}(\widehat{\dot{\mathbf{m}}}_{\text{B-dwn}}) + \text{diag}(\widehat{\dot{\mathbf{m}}}_{\text{B-up},1 \rightarrow (n-1)}, 1)$$

and

$$\widehat{\dot{\mathbf{m}}}_{\text{T-up}} = -\frac{1}{2}\mathbf{P}_T \dot{\mathbf{m}}_{i/o}(t)(1 + \tanh(-k\mathbf{P}_T \dot{\mathbf{m}}_{i/o}(t))),$$

$$\widehat{\dot{\mathbf{m}}}_{\text{T-dwn}} = \frac{1}{2}\mathbf{P}_T \dot{\mathbf{m}}_{i/o}(t)(1 + \tanh(k\mathbf{P}_T \dot{\mathbf{m}}_{i/o}(t))),$$

$$\widehat{\dot{\mathbf{m}}}_{\text{B-up}} = \frac{1}{2}\mathbf{P}_B \dot{\mathbf{m}}_{i/o}(t)(1 + \tanh(k\mathbf{P}_B \dot{\mathbf{m}}_{i/o}(t))),$$

$$\widehat{\dot{\mathbf{m}}}_{\text{B-dwn}} = -\frac{1}{2}\mathbf{P}_B \dot{\mathbf{m}}_{i/o}(t)(1 + \tanh(-k\mathbf{P}_B \dot{\mathbf{m}}_{i/o}(t))).$$



#### 4.2.5 Auxiliary heaters

Many TES tanks have auxiliary electric heaters placed at varying heights within the tank in order to heat the fluid in the tank when the external energy systems have not provided enough heat to the fluid in the tank to fulfil the demand. The use/control of these heaters is not considered in this section, only their modelling.

As before, considering only the auxiliary heaters the energy balance for the  $i$ th node in the tank would be given by

$$m_i c_p \frac{d\Theta_i(t)}{dt} = \dot{W}_{\text{aux},i}(t). \quad (4.43)$$

In vector-matrix form for all nodes in the tank:

$$\begin{bmatrix} m_1 c_p \dot{\Theta}_1(t) \\ m_2 c_p \dot{\Theta}_2(t) \\ \vdots \\ m_n c_p \dot{\Theta}_n(t) \end{bmatrix} = \underbrace{\begin{bmatrix} \boldsymbol{\gamma}_{\text{aux},1} & \boldsymbol{\gamma}_{\text{aux},2} & \cdots & \boldsymbol{\gamma}_{\text{aux},n_{\text{aux}}} \end{bmatrix}}_{\boldsymbol{\Gamma}_{\text{aux}}} \begin{bmatrix} \dot{W}_{\text{aux},1}(t) \\ \dot{W}_{\text{aux},2}(t) \\ \vdots \\ \dot{W}_{\text{aux},n_{\text{aux}}}(t) \end{bmatrix}$$

where each  $k$ -th column of  $\boldsymbol{\Gamma}_{\text{aux}}$  (denoted  $\boldsymbol{\gamma}_{\text{aux},k}$ ) defines the effect the  $k$ -th auxiliary heater has on the nodes within the tank. For example,

$$\boldsymbol{\gamma}_{\text{aux},2} = \begin{bmatrix} 0 & 0 & 0 & \frac{1}{2} & \frac{1}{2} & 0 & 0 & 0 & 0 & 0 \end{bmatrix}^T.$$

defines that the 2nd auxiliary heater's output affects the 4th and 5th node equally but doesn't directly effect any other node in the tank.

In compact form,

$$\boxed{\mathbf{C}_{\text{TES}} \dot{\boldsymbol{\theta}}_{\text{TES}}(t) = \boldsymbol{\Gamma}_{\text{aux}} \boldsymbol{\phi}_{\text{aux}}(t)} \quad (4.44)$$

In this form the auxiliary heaters could be modelled and/or controlled continuously i.e. the amount of heat input by the  $k$ th auxiliary heater is modelled by directly varying the value of  $\dot{W}_{\text{aux},k}$ . However, often the auxiliary heaters are a simple electric element that is only either on or off. In this case the controlled signal is either on or off. Then a simple modification can be made to (4.44) as

$$\mathbf{C}_{\text{TES}} \dot{\boldsymbol{\theta}}_{\text{TES}}(t) = \boldsymbol{\Gamma}_{\text{aux}} \text{diag}(\boldsymbol{\phi}_{\text{aux}}) \boldsymbol{\mu}_{\text{aux}}(t) \quad (4.45)$$

Where the control signals  $\mu_{\text{aux},k} \in [0, 1]$ .  $\boldsymbol{\mu}_{\text{aux}} = (\mu_{\text{aux},1}, \mu_{\text{aux},2}, \dots, \mu_{\text{aux},n_{\text{aux}}})$  and  $\boldsymbol{\phi}_{\text{aux}} \in \mathbb{R}^{n_{\text{aux}}}$ . The alternative form of (4.44) is then

$$\boxed{\mathbf{C}_{\text{TES}} \dot{\boldsymbol{\theta}}_{\text{TES}}(t) = \boldsymbol{\Phi}_{\text{aux}} \boldsymbol{\mu}_{\text{aux}}(t)} \quad (4.46)$$

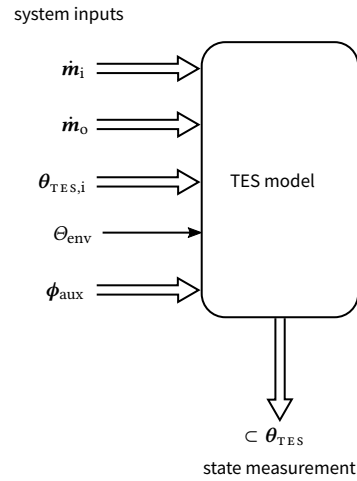


**Figure 4.7** | Input-output block diagram for the TES model.

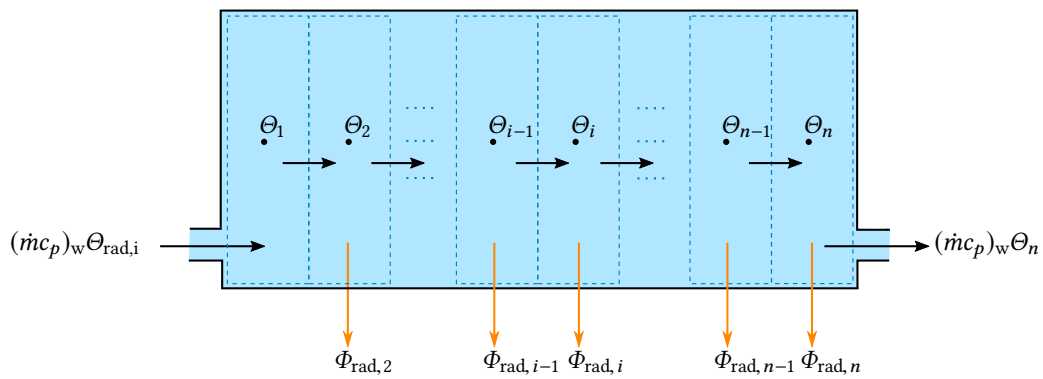


**Figure 4.8** | Schematic of hydronic radiator model. Energy flows (orange) and mass flows (black) are shown for the dynamic model that has been spatially discretised into control volumes  $1, \dots, n$  (blue dashed areas).

The overall mathematical model of the stratified TES tank combines the heat transfer via conduction (4.29), environmental heat transfer (4.30), mass flow network (4.42), and auxiliary heaters (4.44) into a single vector-matrix equation given by

$$\boxed{C_{\text{TES}}\dot{\theta}_{\text{TES}}(t) = \left( H_{\text{TES}} - H_{\text{env}} + c_p \left( \widehat{M}_{\text{tank}}(\dot{m}_{i/o}(t)) - M_o(\dot{m}_o(t)) \right) \right) \theta_{\text{TES}}(t) + c_p M_i(\dot{m}_i(t)) \theta_{\text{TES},i}(t) + h_{\text{env}} \Theta_{\text{env}}(t) + \Gamma_{\text{aux}} \phi_{\text{aux}}(t)} \quad (4.47)$$

An input-output block diagram for the model (4.47) is given in fig. 4.7.

### 4.3 Heat emitters

This work primary utilises hydronic systems with radiators to deliver the heat to the building. The model of the radiator is based on Hensen (19)'s PhD thesis that provides BES models for many of the components that dictate the thermal interaction between the building structure and the heating systems. This specific model was empirically validated in the same work (19, § 6.2.4) based on experimental tests.

#### 4.3.1 Modelling approach

This section takes the 8-node BES model from (19, § 5.4.9) and constructs a general  $n$ -th order dynamic radiator model. The model is spatially discretised into  $n$  segments with each  $i$ -th segment assigned a state-variable,  $\Theta_i(t)$ . Heat transfer takes place between each radiator segment to the environment ( $\Phi_{\text{rad},i}$ ). As the heat transfer occurs between the nodes it is assumed that the energy balance with the environment occurs on each of the  $i \geq 2$  nodes, with the magnitude of the heat transfer being a function of both the supply ( $\Theta_{i-1}$ ) and exit ( $\Theta_i$ ) nodal temperatures of each radiator segment. The energy balance schematic for each node in the dynamic radiator model is given in fig. 4.8.

From fig. 4.8 the differential equations governing the behaviour of the radiator are given by

$$(m_i c_p)_{\text{rad}} \dot{\Theta}_i(t) = (\dot{m}(t) c_p)_{\text{w}} (\Theta_{\text{rad},i}(t) - \Theta_i(t)) \quad \text{for } i = 1 \quad (4.48a)$$

$$(m_i c_p)_{\text{rad}} \dot{\Theta}_i(t) = (\dot{m}(t) c_p)_{\text{w}} (\Theta_{i-1}(t) - \Theta_i(t)) - \Phi_{\text{rad},i}(\Theta_{i-1}(t), \Theta_i(t), \Theta_{\text{env}}(t)) \quad \text{for } i = 2, \dots, n \quad (4.48b)$$



- $(m_i c_p)_{\text{rad}}$  is the mass weighted average heat capacity of the radiator and encapsulated water ( $\text{J K}^{-1}$ );
- $(\dot{m} c_p)_w$  is the thermal capacity flow rate of the water through the radiator ( $\text{W K}^{-1}$ );
- $\Theta_{\text{rad},i}$  is the supply temperature at the inlet of the radiator (K);
- $\Theta_{i-1}$  is the temperature of the supply water into radiator segment  $i$  (K);
- $\Theta_i$  is the temperature of the exit water from radiator segment  $i$  (K);
- $\Phi_{\text{rad}}$  is the heat emitted by radiator segment  $i$  to the environment (W).

#### 4.3.2 Heat transfer to environment

An exponential relationship is assumed between the heat emitted by each radiator segment to the environment:

$$\Phi_{\text{rad},i}(\Theta_{i-1}(t), \Theta_i(t), \Theta_{\text{env}}(t)) = H_{\text{rad}}^* (\Delta\Theta_i(\Theta_{i-1}(t), \Theta_i(t), \Theta_{\text{env}}(t)))^{\kappa_{\text{rad}}}$$

- $H_{\text{rad}}^*$  is the exponential heat transfer coefficient between the radiator segment and the environment ( $\text{W K}^{-\kappa_{\text{rad}}}$ );
- $\Delta\Theta_i(\cdot)$  is the temperature difference between the radiator segment  $i$  and the environment (K);
- $\kappa_{\text{rad}}$  is an empirical coefficient called the radiator exponent (-).

The radiator exponent,  $\kappa_{\text{rad}}$ , depends on the geometry and material of the radiator as well as on the characteristics of the room it is situated in (19, p. 5.39). Typically the empirical values range  $1.25 \leq \kappa_{\text{rad}} \leq 1.6$ , with a nominal value of 1.3 often assumed (19, p. 5.39).

The exponential heat transfer coefficient,  $H_{\text{rad}}^*$ , is determined from the radiator heat emission under nominal temperature conditions:

$$\frac{\Phi_{\text{rad},i}(\cdot)}{\Phi_{\text{nom}}} = \left( \frac{\Delta\Theta_i(\cdot)}{\Delta\Theta_{\text{nom}}} \right)^{\kappa_{\text{rad}}}$$

or

$$\Phi_{\text{rad},i}(\cdot) = \underbrace{\frac{\Phi_{\text{nom}}}{(\Delta\Theta_{\text{nom}})^{\kappa_{\text{rad}}}}}_{H_{\text{rad}}^*} (\Delta\Theta_i(\cdot))^{\kappa_{\text{rad}}} \quad (4.49)$$

where

- $\Phi_{\text{nom}}$  is the radiator heat emission at the nominal temperature difference (W);
- $\Delta\Theta_{\text{nom}}$  is the nominal temperature difference condition (K).

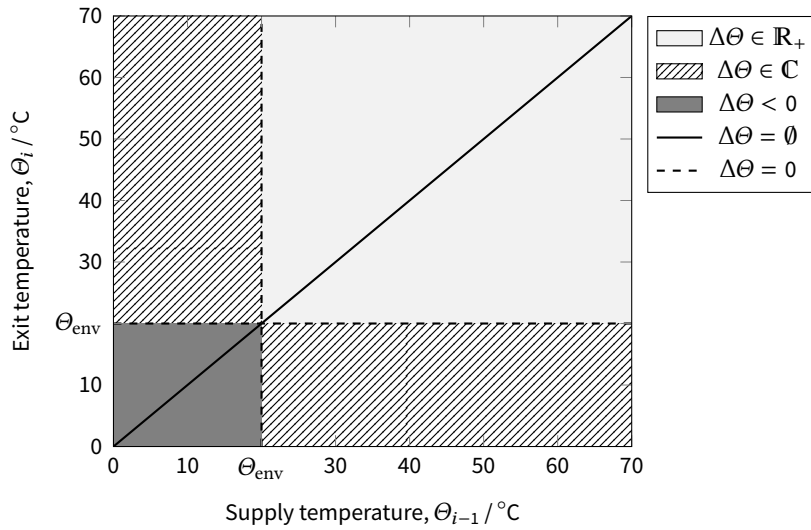


**Figure 4.9 | Logarithmic temperature difference for varying supply & exit temperatures.** Surface plot that shows the variance in  $\Delta\theta$ , where the environmental temperature is fixed at  $\theta_{\text{env}} = 20\text{ }^\circ\text{C}$ . The light grey areas shows the region for which the log-mean temperature difference is valid. For the other regions: When the supply and exit temperatures are equal  $\Delta\theta$  is undefined (black line). When one of either the supply or exit temperature is greater than the environmental temperature, but the other is less than the environmental temperature then  $\Delta\theta$  will be a complex number (north east lined areas). When either the supply or exit temperature is equal to the environmental temperature  $\Delta\theta = 0$  (dashed lines). When both the supply and exit temperatures are less than the environmental temperature  $\Delta\theta < 0$  (dark grey area).



Both  $\Phi_{\text{nom}}$  and  $\Delta\Theta_{\text{nom}}$  are normally provided in the manufacturer's data sheets for a specific radiator type.

The temperature difference between the radiator segment  $i$  and the environment,  $\Delta\Theta_i$ , is normally calculated using the logarithmic mean temperature difference:

$$\Delta\Theta_{\text{LM},i}(t) = \frac{\Theta_{i-1}(t) - \Theta_i(t)}{\ln\left(\frac{\Theta_{i-1}(t) - \Theta_{\text{env}}(t)}{\Theta_i(t) - \Theta_{\text{env}}(t)}\right)} \quad (4.50)$$

The experiments conducted by (19) support the use of this relation as it results in the most accurate reflection of reality. However, by examining eq. (4.50) it can be seen that there are several numerical issues with implementing eq. (4.50) when considering all permissible values of the supply and exit temperatures:

1. When the supply and exit temperatures are equal  $\Delta\Theta_{\text{LM},i}$  is undefined ( $\Delta\Theta_{\text{LM},i} = 0/\ln(1) = 0/0$ ).
2. When one of either the supply or exit temperature is greater than the environmental temperature, but the other is less than the environmental temperature then  $\Delta\Theta_{\text{LM},i}$  will require the natural logarithm of a negative number, which is undefined.<sup>4</sup>
3. When either the supply or exit temperature is equal to the environmental temperature  $\Delta\Theta_{\text{LM},i} = 0$ .
4. When both the supply and exit temperatures are less than the environmental temperature  $\Delta\Theta_{\text{LM},i} < 0$ .

The variance of  $\Delta\Theta_{\text{LM},i}$  as a function of the supply and exit temperatures is reflected in fig. 4.9. To avoid the numerical issues in items 1 to 3 the arithmetic temperature difference is used under these circumstances. The arithmetic temperature difference is given by

$$\Delta\Theta_{\text{AM},i}(t) = (\Theta_{i-1}(t) + \Theta_i(t))/2 - \Theta_{\text{env}}(t)$$

The temperature difference is then determined by

$$\Delta\Theta_i(t) = \begin{cases} \Delta\Theta_{\text{AM},i}(t) & \text{if } \check{b}_1 \vee \check{b}_2 \vee (\Theta_{i-1}(t) = \Theta_i(t)) \\ \Delta\Theta_{\text{LM},i}(t) & \text{otherwise} \end{cases} \quad (4.51)$$

where  $\check{b}_1 := \Theta_{i-1} \geq \Theta_{\text{env}} \wedge \Theta_i \leq \Theta_{\text{env}}$ , and  $\check{b}_2 := \Theta_i \geq \Theta_{\text{env}} \wedge \Theta_{i-1} \leq \Theta_{\text{env}}$ .

---

<sup>4</sup>or becomes a complex number if the complex logarithm function is used

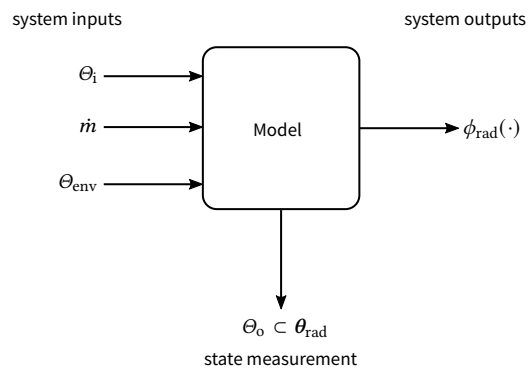


**Figure 4.10** | Input-output block diagram for the radiator model.

The last numerical consideration is for the scenario when  $\Delta\Theta_i < 0$  (item 4). Normally this would imply that the direction of heat transfer is reversed so that heat is transferred from the environment to the radiator. However, numerical issues arise due to the radiator exponent. Assuming the radiator exponent is expressed as a rational number i.e.  $\kappa_{\text{rad}} = a/b$ , for even values of  $b$  the heat emission  $\Phi_{\text{rad},i}$  will be a complex number. For this reason the model ignores the (unlikely) situation where the environment is warmer than the radiator so that when  $\Delta\Theta_i < 0 \rightarrow \Delta\Theta_i = 0$ .

### 4.3.3 Model synthesis

Assembling the differential equations for all the nodes results in an  $n$ th-order dynamic radiator model given in vector-matrix form as

$$\begin{bmatrix} (m_1 c_p)_{\text{rad}} \dot{\Theta}_1(t) \\ (m_2 c_p)_{\text{rad}} \dot{\Theta}_2(t) \\ (m_3 c_p)_{\text{rad}} \dot{\Theta}_3(t) \\ \vdots \\ (m_n c_p)_{\text{rad}} \dot{\Theta}_n(t) \end{bmatrix} = (\dot{m}(t) c_p)_w \begin{bmatrix} -1 & 0 & 0 & \cdots & 0 \\ 1 & -1 & 0 & \ddots & 0 \\ 0 & 1 & -1 & \ddots & 0 \\ \vdots & \ddots & \ddots & \ddots & \ddots \\ 0 & 0 & 0 & \cdots & -1 \end{bmatrix} \begin{bmatrix} \Theta_1(t) \\ \Theta_2(t) \\ \Theta_3(t) \\ \vdots \\ \Theta_n(t) \end{bmatrix} + \begin{bmatrix} (\dot{m}(t) c_p)_w \\ 0 \\ 0 \\ \vdots \\ 0 \end{bmatrix} \Theta_{\text{rad},i}(t) - \begin{bmatrix} 0 & \Phi_{\text{rad},2}(\cdot) & \Phi_{\text{rad},3}(\cdot) & \cdots & \Phi_{\text{rad},n}(\cdot) \end{bmatrix}^T$$

Or in compact notation the dynamic radiator model is given by

$$\boxed{C_{\text{rad}} \dot{\theta}_{\text{rad}}(t) = c_p \mathbf{M}_{\text{rad}} (\dot{m}(t)) \theta_{\text{rad}}(t) + c_p \mathbf{M}_i (\dot{m}(t)) \Theta_{\text{rad},i}(t) - \phi_{\text{rad}}(\theta_{\text{rad}}(t), \Theta_{\text{env}}(t))} \quad (4.52)$$

An input-output block diagram for the model (4.52) is given in fig. 4.10.

## 4.4 Electrical energy storage

The model of the EES utilised in this work is the generic battery model originally developed by Tremblay et al. (20), that was extended and validated in Tremblay, Dessaint (21). The battery model was initially developed for dynamic simulation of batteries in hybrid electric vehicles, but has since been successfully utilised in studies on microgrid control (22), wind energy supply systems (23), evening and peak support for PV systems (24), and many more. It also forms the basis of the generic battery model in the Simscape Power Systems toolbox in Simulink, which is used to model and simulate electrical power systems. The battery model can be used for four types of battery chemistries: Lead-Acid, Lithium-Ion (Li-Ion), Nickel-Cadmium (NiCd) and Nickel-Metal-Hydride (NiMH).

This section describes the battery model and how it has been mathematically



structured into a state-space representation as opposed to the original model designed for computer simulation provided in Tremblay, Dessaint (21). In addition, Tremblay's model assumes that the charging and drawing of current from the battery is 100 % efficient when temperature effects are not modelled. The model in this section amends the model in order to allow for varying charging and drawing efficiencies.

#### 4.4.1 Dynamic model

The model functions as a simple 'bucket' model which accounts for the flow of current/power into and out of the battery. As the internal chemistry is not modelled the dynamic model is subject to a number of limitations and modelling assumptions:

- *Constant internal resistance:* The battery's internal resistance is not a function of the current flow through the battery;
- *Capacity doesn't change with amplitude of current:* Some batteries exhibit reduced capacity when charged/discharged at a high rate (i.e. no modelling of Peukert's law (25));
- *No temperature effects:* Li-Ion cell's power and capacity can vary in different temperature environments;<sup>5</sup>
- *No self-discharge:* A observed phenomenon in batteries where internal chemical reactions reduce the stored charge of the battery;
- *No memory effect:* NiCd batteries can exhibit a reduction in maximum capacity if they are repeatedly charged after only being partially discharged.

The state-of-charge (SOC) of a battery is calculated as:

$$\overline{SOC}(t) = 100 \left( 1 - \frac{1}{q_{\text{cap}}} \int_0^t \eta_{\text{bat}}(I_{\text{dem}}(\tau)) I_{\text{dem}}(\tau) d\tau \right). \quad (4.53)$$

where

- $q_{\text{cap}}$  is the maximum battery capacity (A s or C);
- $\eta_{\text{bat}}(\cdot)$  is the electrical efficiency of the battery;
- $\tau$  is the variable of integration; takes on values of 0 to the present  $t$ ;
- $I_{\text{dem}}(t)$  is the instantaneous demand on battery current (A).

The output of the integration operation in eq. (4.53) is limited so that the SOC of the battery is constrained between 0 % to 100 %. Therefore, at 0 % SOC the output from the integrator will be  $q_{\text{cap}}$  and at 100 % it will be zero.

<sup>5</sup>Studies have shown that this relationship is weak over the cycle life of the battery (26).



From eq. (4.53) it is clear that the electrical efficiency of the battery is a function of the instantaneous demand on current from the battery. In this simplified model, the function is given by the following piecewise function:

$$\eta_{\text{bat}}(I_{\text{dem}}(t)) = \begin{cases} \eta_{\text{charge}} & \text{if } I_{\text{dem}}(t) < 0 \\ \frac{1}{\eta_{\text{discharge}}} & \text{if } I_{\text{dem}}(t) > 0 \end{cases}$$

where

$\eta_{\text{charge}}$  is the energetic efficiency of charging (fraction from 0 to 1 where 1 indicates no losses);

$\eta_{\text{discharge}}$  is the energetic efficiency of drawing (fraction from 0 to 1 where 1 indicates no losses).

The actual current through the battery is then given by  $I(t) = \eta_{\text{bat}}(I_{\text{dem}}(t)) I_{\text{dem}}(t)$ .

In order to reconstruct eq. (4.53) as a differential equation, introduce a state-variable  $q_{\text{bat}}(t)$  that represents the actual battery charge:  $q_{\text{bat}}(t) = \int_0^t I(\tau) d\tau$ . Then the differential equation describing the battery charge is given by

$$\dot{q}_{\text{bat}}(t) = I(t) = \eta_{\text{bat}}(I_{\text{dem}}(t)) I_{\text{dem}}(t), \quad (4.54)$$

where

$q_{\text{bat}}$  is the charge in the battery (A s or C);

$I$  is the battery current (A).

The SOC of the battery is then given as a function of the battery charge as

$$\overline{\text{SOC}}(t) = 100 \left( 1 - \frac{1}{q_{\text{cap}}} q_{\text{bat}}(t) \right). \quad (4.55)$$

#### 4.4.2 State-of-charge limits & integrator wind-up

The state-variable,  $q_{\text{bat}}$ , must be constrained in order to model the limits on the SOC of the battery. The mapping of SOC to battery charge is found from eq. (4.55) as

$$q_{\text{bat}}(t) = (1 - \overline{\text{SOC}}(t)/100)q_{\text{cap}}.$$

Then the battery charge for the minimum and maximum permissible SOC is given by

$$q_{\text{bat,UL}} = (1 - \overline{\text{SOC}}_{\text{min}}/100)q_{\text{cap}}, \quad (4.56a)$$

$$q_{\text{bat,LL}} = (1 - \overline{\text{SOC}}_{\text{max}}/100)q_{\text{cap}}, \quad (4.56b)$$

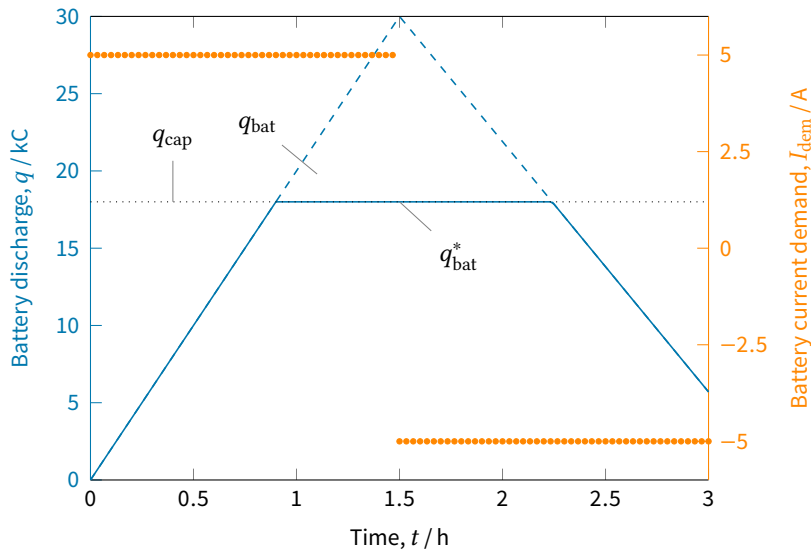


**Figure 4.11 | Integrator wind-up for constrained battery charge.** The demand on the battery  $I_{dem}$  (solid marks) is a constant discharge of 5 A from 0 h to 1.5 h then a constant charge of  $-5$  A from 1.5 h to 3 h. The battery is depleted by 0.9 h, but the state-variable  $q_{bat}$  (dashed line) continues to increase while there is still a current demand of  $+5$  A while the actual battery charge,  $q_{bat}^*$  (solid line) is restricted to the capacity of the battery. It is not until the sign of the battery current demand changes at 1.5 h that the state-variable begins to decrease. The effect of this is that the actual battery charge should have begun to change at 1.5 h but instead was delayed  $\approx 0.74$  h due to the overdriven integrator.

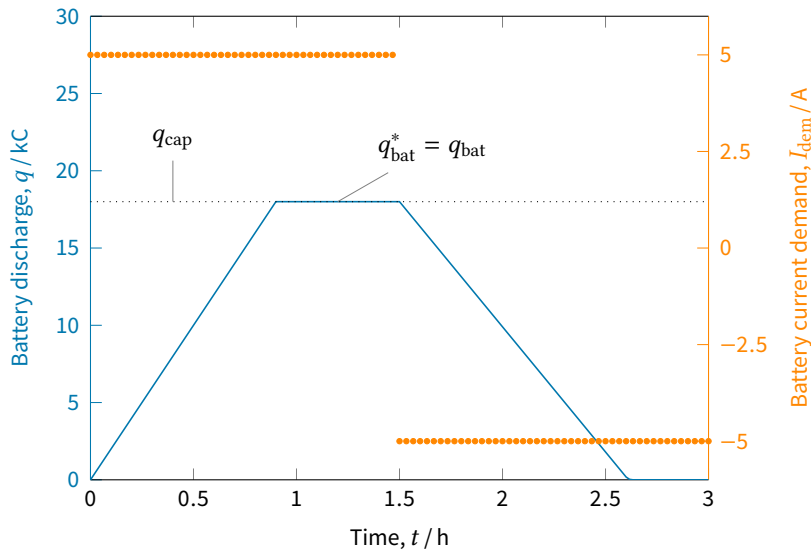


**Figure 4.12 | Constrained battery charge with anti-windup logic.** The state-variable for the battery  $q_{bat}$  (dashed line), now follows the actual battery charge,  $q_{bat}^*$  (solid line), and exhibits no wind-up. The battery current demand,  $I_{dem}$  (solid marks), remains the same as in fig. 4.11.



then the state-variable in the state differential equation (4.54) is constrained as

$$q_{\text{bat}}(t) \in [q_{\text{bat,LL}}, q_{\text{bat,UL}}]. \quad (4.57)$$

Applying the constraints in eqs. (4.56) and (4.57) while there is still demand for charging or drawing from the battery will cause a phenomenon known as integrator wind-up to occur in eq. (4.54).<sup>6</sup>

The ‘wind-up’ of the integrator can be explained as follows: Consider the integral form of eq. (4.54) in its linear range given as

$$q_{\text{bat}}^*(t) = q_{\text{bat}}(t) = \int_0^t I(\tau) d\tau.$$

where

$q_{\text{bat}}^*$  is the actual (limited) battery charge (A s or C).

However, when a state-limit (4.56) has been reached the system is ‘overdriven’ and now

$$q_{\text{bat}}^* = q_{\text{bat,LL}} \vee q_{\text{bat,UL}},$$

but still

$$q_{\text{bat}}(t) = \int_0^t I(\tau) d\tau.$$

The integrator will continue to increase the value of  $q_{\text{bat}}(t)$  as long as the sign of the current demand does not change. This can be made clearer in a simple simulation, with resultant curves provided in fig. 4.11. For the purposes of results duplication the model parameters are given in table 4.2.

The behaviour exhibited in fig. 4.11 can be overcome by implementing a ‘limited integrator’ with anti-windup logic. The basic principle is that when the integrator is in overdriven operation the integration is switched off. Assign two logical variables to determine if the state-variable is out with the constraints:

$$\check{b}_{\text{LL}} := q_{\text{bat}}(t) \leq q_{\text{bat,LL}}$$

$$\check{b}_{\text{UL}} := q_{\text{bat}}(t) \geq q_{\text{bat,UL}}$$

where  $\check{b}$  is a logical boolean variable such that  $\check{b} \in \mathbb{Z} : \check{b} \in [0, 1]$ . Then the variable

---

<sup>6</sup>This will be covered in detail with regards to control in § 7.3.



structure state differential equation in eq. (4.54) becomes

$$\dot{q}_{\text{bat}}(t) = \begin{cases} I(t) & \text{if } (\neg \check{b}_{\text{LL}} \wedge \neg \check{b}_{\text{UL}}) \vee (\check{b}_{\text{LL}} \wedge I(t) > 0) \vee (\check{b}_{\text{UL}} \wedge I(t) < 0) \\ 0 & \text{otherwise} \end{cases} \quad (4.58)$$

The implementation of the anti-windup logic to the example simulation case is given in fig. 4.12. The results demonstrate that the mathematical model of the battery now operates as would be expected.

#### 4.4.3 Charging/drawing limits

Just as with the limits on the fuel flow and hydronic valves in the mCHP unit and TES tank, there are limits placed on the amount of current that can be delivered to or drawn from the battery. These limits are computed as

$$I^*(t) = \begin{cases} I_{\text{max}} & \text{if } I(t) > I_{\text{max}} \\ I_{\text{min}} & \text{if } I(t) < I_{\text{min}} \\ I(t) & \text{otherwise} \end{cases} \quad (4.59)$$

#### 4.4.4 Conversion to power-based model

While the model provided in (21) provides equations to resolve the voltage in the battery as a function of the battery charge and current, this work does not utilise those relations. A DC-DC converter is utilised alongside a battery to ensure the required voltage for charging and discharging the battery. It is assumed that the dynamics of the DC-DC converter occur on a much higher frequency than any of the other system components so that it can be modelled as a set efficiency to account for the changes in battery voltage.

Recalling the simple electrical circuit relations  $E(t) = U(t)q(t)$  and  $P(t) = U(t)I(t)$ , the state-variable can be modified to

$$E_{\text{bat}}(t) = \int P(\tau) d\tau \quad (4.60)$$

where  $E_{\text{bat}}$  is the energy in the battery (J) and  $P$  is the power to/from the battery (W), which is given by

$$P(t) = \eta_{\text{bat}}(P_{\text{dem}}(t)) P_{\text{dem}}(t)$$

where  $P_{\text{dem}}$  is the instantaneous power demand from the battery, and  $\eta_{\text{bat}}$  is the instantaneous efficiency of the battery as a function of the power demand.

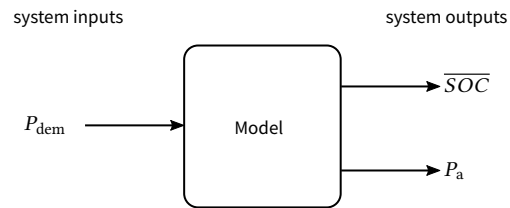


**Figure 4.13** | Input-output block diagram for the battery model.

**Table 4.2** | Model parameters for battery wind-up example.

Parameter	Value
$\eta_{\text{charge}}$	0.9
$\eta_{\text{discharge}}$	0.9
$q_{\text{cap}}$	18 kC
$\overline{SOC}_{\text{min}}$	0
$\overline{SOC}_{\text{max}}$	100

The variable structure state differential equation for the dynamic battery model is

$$\dot{E}_{\text{bat}}(t) = \begin{cases} P(t) & \text{if } (\neg \check{b}_{\text{LL}} \wedge \neg \check{b}_{\text{UL}}) \vee (\check{b}_{\text{LL}} \wedge P(t) > 0) \vee (\check{b}_{\text{UL}} \wedge P(t) < 0) \\ 0 & \text{otherwise} \end{cases} \quad (4.61)$$

where the logical variables  $\check{b}_{\text{LL}}$ ,  $\check{b}_{\text{UL}}$  have also undergone similar unit conversions. An input-output block diagram for the model (4.61) is given in fig. 4.13.

## 4.5 Summary

Developing dynamic models of the systems to be controlled is the first step in devising, developing and analysing the required system controls. This chapter described the development of dynamic state-space models – based on already verified BES models – of combustion-based mCHP units, stratified TES tanks, the water-based heat emitters, and the electrical battery storage. A specific effort was made to develop *continuous* models of the systems where possible. When a system would demonstrate markedly different behaviour – such as during the various operating modes of the mCHP unit or when the EES is full or depleted – the systems are defined as variable structure models that will switch between dynamic models as a function of measured conditions.

The aim of this work is to design MIMO control algorithms for the microgeneration devices and energy storage within a building with the primary objectives of meeting the thermal and electrical demands of the building while minimising the interaction with the local electrical network. With the development dynamic models of the MGTs and energy storage completed, the next step is to gain an understanding of the thermal and electrical demands of the building. Therefore, the focus of the following chapter is to develop a model of the thermal and electrical requirements of a building.

## References

1. Beausoleil-Morrison, I. *An experimental and simulation-based investigation of the performance of small-scale fuel cell and combustion-based cogeneration devices serving residential buildings*. Tech. rep. 2008: 70. URL: [http://www.ecbcs.org/docs/Annex%7B%5C\\_%7D42%7B%5C\\_%7DFinal%7B%5C\\_%7DReport.pdf](http://www.ecbcs.org/docs/Annex%7B%5C_%7D42%7B%5C_%7DFinal%7B%5C_%7DReport.pdf) (cited p. 72)
2. Beausoleil-Morrison, I., Ferguson, A., Griffith, B., Kelly, N., Maréchal, F., Weber, A. *Specifications for Modelling Fuel Cell and Combustion-Based Residential Cogeneration Devices within Whole-Building Simulation Programs*. Tech. rep. Annex 42 of the International Energy Agency Energy Conservation in Buildings and Community Systems Programme, 2007: 111. URL: [www.cogen-sim.net](http://www.cogen-sim.net) (cited p. 72)
3. Arndt, U. et al. *Experimental Investigation of Residential Cogeneration Devices and Calibration of Annex 42 Models*. Tech. rep. Annex 42 of the International Energy Agency Energy Conservation in Buildings and Community Systems Programme, 2007: 255 (cited p. 72)



4. Beausoleil-Morrison, I., Ferguson, A. *Inter-model Comparative Testing and Empirical Validation of Annex 42 Models for Residential Cogeneration Devices*. Tech. rep. Annex 42 of the International Energy Agency Energy Conservation in Buildings and Community Systems Programme, 2007 (cited pp. 72, 83)
5. The MathWorks, Inc. *Simulink - Simulation and Model-Based Design*. 2016. URL: <http://uk.mathworks.com/products/simulink/> (visited on 2016-04-17) (cited p. 83)
6. Thohura, S., Rahman, A. Numerical Approach for Solving Stiff Differential Equations : A Numerical Approach for Solving Stiff Differential Equations A Comparative Study Numerical Approach for Solving Stiff Differential Equations : A Comparative Study. *Global Journal of Science Frontier Research F: Mathematics and Decision Sciences* **13**(6) (2013) (cited p. 83)
7. Ding, Y., Riffat, S. B. Thermochemical energy storage technologies for building applications: a state-of-the-art review. *International Journal of Low-Carbon Technologies* **8**(2): 106–16 (2012). DOI: [10.1093/ijlct/cts004](https://doi.org/10.1093/ijlct/cts004) (cited p. 84)
8. Cabeza, L., Martorell, I., Miró, L., Fernández, A., Barreneche, C. *Introduction to thermal energy storage (TES) systems*. Elsevier, 2015: 1–28. ISBN: 9781782420880. DOI: [10.1533/9781782420965.1](https://doi.org/10.1533/9781782420965.1). URL: <http://www.sciencedirect.com/science/article/pii/B9781782420880500018> (cited p. 84)
9. Mehling, H., Cabeza, L. F. *Heat and cold storage with PCM: An up to date introduction into basis and applications*. Ed. by Mewes, D., Mayinger, F. Berlin, Germany: Springer-Verlag, 2008. 308 pp. ISBN: 978-3-540-68557-9. Google Books: [N8LGwUNYWX8C](https://books.google.com/books?id=N8LGwUNYWX8C) (cited p. 84)
10. Abedin, A., Rosen, M. A Critical Review of Thermochemical Energy Storage Systems. *Open Renewable Energy Journal*: 42–6 (2011). DOI: [10.2174/1876387101004010042](https://doi.org/10.2174/1876387101004010042) (cited p. 84)
11. Abedin, A. H., Rosen, M. A. Closed and open thermochemical energy storage: Energy- and exergy-based comparisons. *Energy* **41**(1): 83–92 (2012-05). DOI: [10.1016/j.energy.2011.06.034](https://doi.org/10.1016/j.energy.2011.06.034) (cited p. 84)
12. Newton, B. J. Modeling of Solar Storage Tanks. Master's thesis. University of Wisconsin-Madison, 1995: 228. URL: <http://digital.library.wisc.edu/1793/7803> (cited pp. 85, 87, 88)
13. Wetter, M., Wright, J. A comparison of deterministic and probabilistic optimization algorithms for nonsmooth simulation-based optimization. *Building and Environment* **39**(8): 989–99 (2004-08). DOI: [10.1016/J.BUILDENV.2004.01.022](https://doi.org/10.1016/J.BUILDENV.2004.01.022) (cited p. 85)
14. Jaluria, Y., Gupta, S. Decay of thermal stratification in a water body for solar energy storage. *Solar Energy* **28**(2): 137–43 (1982). DOI: [10.1016/0038-092X\(82\)90292-4](https://doi.org/10.1016/0038-092X(82)90292-4) (cited p. 87)
15. Wnoise (<http://math.stackexchange.com/users/7882/wnoise>). *Is there an analytic approximation to the minimum function?* Mathematics Stack Exchange. URL: <http://math.stackexchange.com/q/30921> (cited p. 92)
16. Alfc (<http://math.stackexchange.com/users/11546/alfc>). *Is there an analytic approximation to the minimum function?* Mathematics Stack Exchange. URL: <http://math.stackexchange.com/q/601130> (cited p. 93)
17. (<http://math.stackexchange.com/users/940/byron-schmuland>), B. S. *Is there an analytic approximation to the minimum function?* Mathematics Stack Exchange. URL: <http://math.stackexchange.com/q/30881> (cited p. 93)





18. (<http://math.stackexchange.com/users/18993/nikolajk>), N. *Approximating the error function erf by analytical functions*. Mathematics Stack Exchange. URL: <http://math.stackexchange.com/q/321569> (cited p. 94)
19. Hensen, J. L. M. *On the thermal interaction of building structure and heating and ventilating system*. 1991: 197. ISBN: 903860081X (cited pp. 98–100)
20. Tremblay, O., Dessaint, L. A., Dekkiche, A. I. A Generic Battery Model for the Dynamic Simulation of Hybrid Electric Vehicles. In *2007 IEEE Vehicle Power and Propulsion Conference*. 2007-09: 284–9.  
DOI: [10.1109/VPPC.2007.4544139](https://doi.org/10.1109/VPPC.2007.4544139) (cited p. 101)
21. Tremblay, O., Dessaint, L.-A. Experimental validation of a battery dynamic model for EV applications. *World Electric Vehicle Journal* **3**: 1–10 (2009) (cited pp. 101, 102, 105)
22. Xu, L., Chen, D. Control and operation of a DC microgrid with variable generation and energy storage. *IEEE Transactions on Power Delivery* **26**(4): 2513–22 (2011).  
DOI: [10.1109/TPWRD.2011.2158456](https://doi.org/10.1109/TPWRD.2011.2158456) (cited p. 101)
23. Bhende, C. N., Mishra, S., Malla, S. G. Permanent Magnet Synchronous Generator-Based Standalone Wind Energy Supply System. *IEEE Transactions on Sustainable Energy* **2**(4): 361–73 (2011-10).  
DOI: [10.1109/TSTE.2011.2159253](https://doi.org/10.1109/TSTE.2011.2159253) (cited p. 101)
24. Alam, M. J. E., Muttaqi, K. M., Sutanto, D. Mitigation of Rooftop Solar PV Impacts and Evening Peak Support by Managing Available Capacity of Distributed Energy Storage Systems. *IEEE Transactions on Power Systems* **28**(4): 3874–84 (2013-11).  
DOI: [10.1109/TPWRS.2013.2259269](https://doi.org/10.1109/TPWRS.2013.2259269) (cited p. 101)
25. SmartGauge Electronics. *An in depth analysis of the maths behind Peukert's Equation (Peukert's Law)*. 2013-04-08. URL: [http://www.smartgauge.co.uk/peukert\\_depth.html](http://www.smartgauge.co.uk/peukert_depth.html) (visited on 2016-05-08) (cited p. 102)
26. Belt, J. R., Ho, C. D., Miller, T. J., Habib, M. A., Duong, T. Q. The effect of temperature on capacity and power in cycled lithium ion batteries. *Journal of Power Sources* **142**(1-2): 354–60 (2005-03).  
DOI: [10.1016/j.jpowsour.2004.10.029](https://doi.org/10.1016/j.jpowsour.2004.10.029) (cited p. 102)



*“Once I got home, I sulked for a while.  
All my brilliant plans foiled by  
thermodynamics.  
Damn you, Entropy!”*

---

—ANDY WEIR, *The Martian*

5

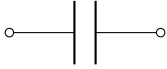
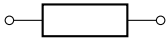
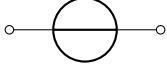
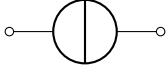
## Dynamic modelling of buildings

THE overarching goal of this work was to develop a control strategy applicable to building-integrated energy systems that would minimise the interaction with the grid while fulfilling the thermal and electrical demands of the building. The thermodynamic model constructed in this chapter is intended for controller design and initial-stage performance evaluation. It strives to strike a balance between minimising the order of the system – so that rapid prototyping, controller design, and optimisation can be performed quickly – and encapsulating the full dynamic response of the building. The model, therefore, should represent the short- and long-term dynamic fluctuations in response. Furthermore, it is formulated as a wholly general model, where the control designer is free to increase the order of the model and/or allow for a conceivably infinite array of disturbance and controllable heat inputs to the model without having to re-formulate the system of equations directly. Research by Achterbosch et al. (1), Riederer et al. (2), Khalid (3), Murphy et al. (4) among others has all contributed towards the idea of producing simplified, convenient, and generalised building models. The objective of this chapter is to build upon and synthesise this work and provide new approximations of the heat transfer and fluid flow processes occurring within the building, where there are gaps in the existing work.

This chapter details the construction of the base thermodynamic model, which is a general explicit state-space representation of the thermodynamics within, and acting upon, the building. The following mechanisms are considered:

1. Convective and conductive exchange between the air and [building components](#)
2. Radiative exchange between the building components
3. Heat gains (from internal sources and solar irradiation)

**Table 5.1 | Thermal-electrical network analogy** with equivalent characteristic equation for each component.

Component	Represents	Mathematical relation
 Capacitor	Thermal capacitance	$\Phi(t) = C \frac{d\theta(t)}{dt}$
 Resistor	Thermal resistance	$\Phi(t) = \frac{1}{R} \theta(t)$
 Voltage source	Temperature source	$\theta(t)$
 Current source	Heat flow source	$\Phi(t)$

The remainder of this chapter considers each one of these in turn (after defining the overall extent and assumptions of the model). Finally, these heat transfer processes are combined into a generalised state-space representation of a **building zone**. The validation of the energy predictions of this new model is provided in appendix B.3.

## 5.1 Model structure and assumptions

There is a vast array of building modelling techniques, which are broadly separated into three categories (5): computational fluid dynamics (CFD), the zonal approach, and the nodal approach. For this work, the nodal approach will be used, which commonly makes use of an electrical network analogy of the heat transfer mechanisms within a zone, originally developed by Rumianowski et al. (6). Table 5.1 provides the fundamental relations between the thermal and electrical network analogy.

There are numerous building and integrated energy modelling software tools available that use the nodal approach, such as ESP-r (7), EnergyPlus (8), and TRNSYS (9). However, they run at a time resolution that is too large to properly assess controller operation. The model developed here is compatible with the MATLAB/Simulink environment, which is one of the most common software packages used for control system modelling, design, and analysis and can be used to complement building simulation. The model makes several limiting assumptions that make it unable to be directly compared with many of these software packages. However, despite these assumptions, what it does provide is a complete set of ODEs in state-space form that act as a ‘controller test bed’.

This controller test bed allows for the development of a control scheme with the knowledge that the predicted energy performance and thermodynamic response will be *reasonably* accurate, as it has been validated with “EN 15265: Energy performance of buildings. Calculation of energy needs for space heating and cooling using dynamic methods. General criteria and validation procedures” (10) (provided in appendix B.3).

The following heat transfer mechanisms comprise the energy (heat) balance at the building zone level:

- Heat transfer between the conditioned zone and the external environment – via convective heat transfer between the air and the surface of the enclosure, and conduction heat transfer between the layers;
- Radiation heat transfer between the internal surfaces of the conditioned space, governed by the difference between the temperature of respective surfaces;
- Heat gains for persons, appliances, and lighting;



- Solar heat gains (which can be direct, e.g. through windows, or indirect, e.g. via absorption in opaque building elements), which includes the offset of radiation to the atmosphere from external-facing surfaces;
- Energy need for space heating and cooling: if the zone is conditioned, a heating/cooling system supplies or extracts heat to raise/lower the internal air temperature to the required set-point.

The general modelling assumptions are

- The air temperature is uniform throughout the zone.
- The convective and radiative heat transfer coefficients are constant.
- The thermophysical properties of all materials are constant and isotropic.
- The heat conduction through the components is one-dimensional.
- Fixed distribution of the solar radiation on the component surfaces.
- The radiative heat flow is uniform over the surface of the components.

The majority of all real world processes are nonlinear ([11](#), p. 49, [12](#), p. 620, [13](#), p. 53) – but to widely varying degrees. In the case of building zone thermodynamics, for the majority of the time these tend to operate at stable temperatures based on occupant thermal comfort. It is, therefore, reasonable to assume that a linear system model exists that encapsulates the majority of the thermodynamics of the zone, considering that these zones often only encounter small deviations from this equilibrium condition. Also, considering the continual improvements to building regulations, whereby buildings (specifically their envelope) are being constructed to higher standards year on year, this continual effort decreases the heat loss and attenuates the fluctuations seen internally due to changes in the external environment. Considering these heat transfer mechanisms and related assumptions, the mathematical model developed in this chapter will be a continuous explicit state-space representation of a building zone thermodynamics that is ideally suited to the development of time-domain controller design methods.

## **5.2** Building component heat transfer

This section develops models for the convective and conductive heat transfer between building components (that can be walls, floor, ceiling and glazing), the outside environment and the internal air.

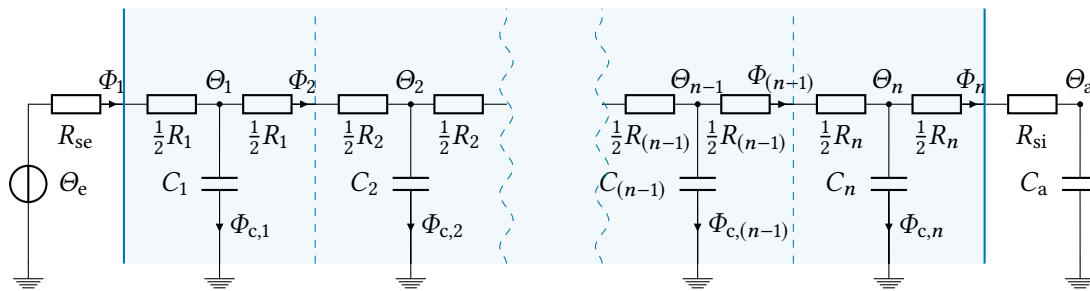


**Figure 5.1** | Equivalent electrical network for an  $n$ -layer building component. The dashed lines indicate the separation between the material layers that comprise the building component.



The method employed for the modelling of the building components is an extended and generalised network representation of two different modelling techniques. The inverse dynamics based energy assessment and simulation (IDEAS) method developed by the author and Murphy et al. (4) and a similar approach that is known as the dominant layer method (DLM) developed by Ramallo-González et al. (14). These are reduced-order lumped parameter models (LPMs) where there are two thermal masses per component and three thermal resistances separating the internal and external air. The difference between the two methods lies in the determination of the parameters for the equivalent capacitances and thermal resistances of the reduced-order models.

Both the IDEAS model and the DLM aim to scale down the number of nodes per component while retaining representative transient thermodynamic behaviour and steady-state characteristics under typical building zone fluctuations on either side of the element. Since the difference between the models lie in the determination of the parameters of the reduced-order model and not in the underlying differential equations that represent the thermodynamics, the models will be referred to together as the reduced order models (ROMs).

### 5.2.1 Lumped parameter component modelling

Lumped component parameter modelling (LPM) utilises the electrical network analogy by discretising the component so that each layer of material has a capacitance (i.e. thermal mass represented by a node) at its centre of mass and two resistances (half of the layer's conductive thermal resistance which connects the node to its neighbours). Figure 5.1 shows a general  $n$ -layer component equivalent electrical network. Note that this method still assumes perfect (ideal) thermal contact between the layers i.e. no thermal contact resistance. The magnitude of the contact resistance is negligible in most cases (15, p. 183). However, if it were necessary to include the thermal contact resistance, it could be added to either resistance across the layer boundary, ideally appearing first following the general direction of heat flow for the zone.

Assuming (for example) each building component in a cuboid enclosure were comprised of 6 layers of material, a direct state-space model of the resulting LPM would result in 36 state variables. Therefore, ROMs were devised to reduce the required number of nodes per component to reduce the overall order of the model. While it is possible to use numerical methods to minimise the order of a known system e.g. using model order reduction procedures, these rely on already having the LPM of the component, and are then also only valid for that particular component with its predefined thermophysical properties. Furthermore, these are optimised for either a better steady-state response or transient time-domain response behaviour. Both the

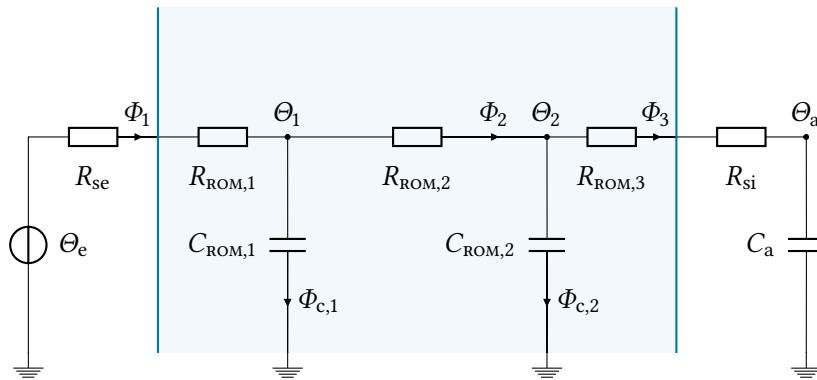


**Figure 5.2** | Equivalent electrical network for a reduced-order model building component.

IDEAS component model and the DLM are analytical approaches to reducing the order of the model while balancing the frequency and time-domain responses. However, each ROM was conceived for different purposes.

The IDEAS method was developed to calibrate a combined thermal zone and controller design model with empirical data, with an emphasis on creating a dynamic model from the typical (limited) data available on a building's construction. The DLM was developed to reduce the computational time of building simulation software for the purpose of design optimisation routines. The DLM assumes that the full thermo-physical properties of the components are known so that the effect of each layer of the component on the overall dynamic response can be found and utilised within the model. The stage of the design process at which the controller is being developed will dictate the level of information available to the control engineer.

### 5.2.2 Reduced-order model methodology

Figure 5.2 shows a ROM of a building component. The concept of the ROMs is that the effect of the fluctuations on either side of the multi-layered component can be approximated by the existence of an internal and external thermal capacitance or 'mass', each represented by a capacitor. The two capacitors allow for the modelling of differing fluctuations on either side of the component – where proper selection of parameters for the elements in the network allows for the approximation of the resultant time-delays and attenuation of the heat flow through the component in each direction.

The IDEAS component model first determines an equivalent thermal conductivity of the component based on its known  $U$ -value and the convective heat transfer coefficient of the inside and outside surfaces, by treating the whole component as a single layer (e.g. a plane wall). This is achieved by noting that the inverse of the  $U$ -value is approximately<sup>1</sup> equal to the total thermal resistance between the inside and outside environments. The unit thermal resistance of a conductive layer  $i$  is given by  $d_i/\lambda_i$ , and for a convective layer by  $1/h_i$ . Therefore, the equivalent thermal resistance network is given by

$$\frac{1}{U} = \frac{1}{h_{c,e}} + \frac{d_{\text{tot}}}{\lambda_{\text{eq}}} + \frac{1}{h_{c,i}}. \quad (5.1)$$

Assuming that all parameters in eq. (5.1) are real and positive the equivalent thermal

---

<sup>1</sup>The determination of a  $U$ -value of a component in accordance with BS EN ISO 6946:2007 (16) contains several correction factors that are not accounted for here.

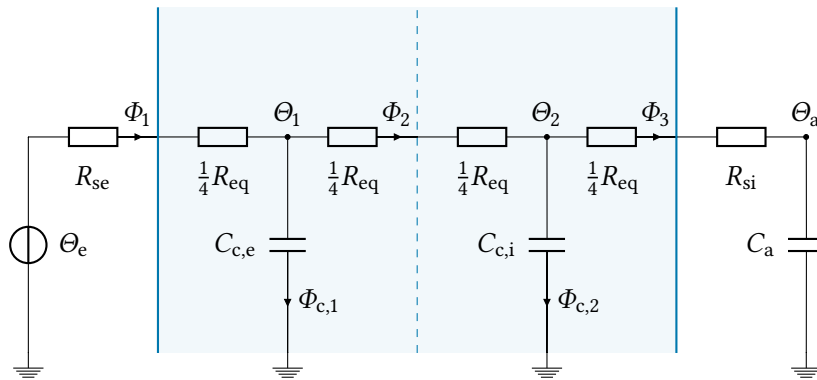


**Figure 5.3** | Equivalent electrical network for the IDEAS component model.

conductivity of the wall can be expressed as

$$\lambda_{\text{eq}} = \begin{cases} \frac{U d_{\text{tot}} h_{\text{c,e}} h_{\text{c,i}}}{h_{\text{c,e}} h_{\text{c,i}} - U(h_{\text{c,e}} + h_{\text{c,i}})} & \text{if } h_{\text{c,e}} h_{\text{c,i}} > U(h_{\text{c,e}} + h_{\text{c,i}}) \\ \emptyset & \text{if } h_{\text{c,e}} h_{\text{c,i}} \leq U(h_{\text{c,e}} + h_{\text{c,i}}). \end{cases} \quad (5.2a)$$

If the inequality from eq. (5.2b),  $h_{\text{c,e}} h_{\text{c,i}} \leq U(h_{\text{c,e}} + h_{\text{c,i}})$ , were true it would either result in an infinite or negative equivalent thermal conductivity, both of which are not realisable. For the first case, where  $h_{\text{c,e}} h_{\text{c,i}} \approx U(h_{\text{c,e}} + h_{\text{c,i}})$ , examination of eq. (5.1) shows that this would require that the wall separating the internal and external environment to not only be of very small thickness, but of extremely high thermal conductivity – akin to a very thin sheet of metal between the zones. If this were the case, then the thermal heat capacity of this component would also be close to zero. Therefore, in order to avoid numerical errors in dealing with numbers very close to zero, the two zones separated by such a component should be considered as a single zone. It is acknowledged that this is a very rare if not improbable occurrence in real-world application of this theory, but is included for completeness. The second case, where  $h_{\text{c,e}} h_{\text{c,i}} < U(h_{\text{c,e}} + h_{\text{c,i}})$ , is simply not realisable since the wall thickness and thermal conductivity are real and positive. Therefore, it is assumed that  $\lambda_{\text{eq}}$  is always given by eq. (5.2a).

Now that  $\lambda_{\text{eq}}$  can be determined, the equivalent thermal resistance is given by

$$R_{\text{eq}} = \frac{d_{\text{tot}}}{\lambda_{\text{eq}} A}. \quad (5.3)$$

Since the IDEAS component model does not assume knowledge of the composition of the layers for the purposes of the thermal resistance parameters, the equivalent thermal resistance is split equality over the constituent thermal resistances. This can be visualised in the IDEAS component model schematic in fig. 5.3. The downside of this is that valid through-surface temperature profiles cannot be obtained.

Comparing figs. 5.2 and 5.3, this results in the following ROM resistances for the IDEAS component model:

$$R_{\text{ROM},1} = \frac{1}{4} R_{\text{eq}}, \quad R_{\text{ROM},2} = \frac{1}{2} R_{\text{eq}}, \quad R_{\text{ROM},3} = \frac{1}{4} R_{\text{eq}},$$

where  $R_{\text{eq}}$  is calculated using eq. (5.3). This allows for the determination of the reduced-order resistance parameters of the ROM using the IDEAS method, with only knowledge of the construction  $U$ -value (typically available from architects drawings, energy performance certificates etc.) and inside and external convective heat transfer coefficients, of which there is a multitude of sources for nominal values, such as BS EN ISO



6946:2007 (16), CIBSE (17) etc.

The thermal mass calculations follow those detailed in BS EN ISO 13786:2007 (18), which is the International Standard for calculating the dynamic thermal performance of building components. The standard provides two methods for calculation – a detailed method, and a simplified method. The simplified method is given in its Annex A and is typically used only for energy estimation purposes. The method detailed in Annex A is used by the UK government’s National Calculation Methodology (NCM) in both Standard Assessment Procedure (SAP) (the tool for generating domestic Energy Performance Certificates (EPCs)) and Simplified Building Energy Model (SBEM) (the tool used for non-domestic building building regulation compliance checks and EPC generation).

In order to provide fair comparison between the IDEAS component model and the DLM, it is assumed that the thermophysical properties of the layers of the component are available for the calculation detailed in BS EN ISO 13786:2007 (18). The full calculation procedure is available within the Standard, which is based upon the solution of the one dimensional transient heat conduction equation with no heat generation (diffusion equation) given by

$$\frac{\partial^2 \Theta}{\partial d^2} = \frac{\rho c_p}{\lambda} \frac{\partial \Theta}{\partial t}.$$

For a finite plane component this can be solved using matrix algebra as opposed to analytic or numerical (e.g. via finite-difference) methods. This method was detailed by Pipes (19). This is adapted to estimate the heat capacity of the multi-layered component based upon sinusoidal fluctuations on each side of the component. The method results in two heat capacities per building component – one internal and one external. This lends itself to the IDEAS component model as these calculated parameters can be used directly.

### 5.2.3 Inter-model performance comparison

In order to assess the thermal performance of these modelling methods, a state-space model of the complete LPM and the ROMs can be constructed. Taking the state variables as the voltage (temperature) across the capacitors (thermal masses) and treating the external temperature as a voltage source (since the external temperature can be considered an ‘ideal’ source of thermal energy, which is capable of maintaining its temperature regardless of the heat flow to/from the zone). The generalised state-space model of each is given in appendix A.2.

The comparisons will be performed by considering a typical building construction for a 3.08 m<sup>2</sup> external wall, consisting of (from external to internal) an outer layer, an

**Table 5.2 | Thermophysical properties of the example external wall.**

	$d$ / m	$\lambda$ / W m <sup>-1</sup> K <sup>-1</sup>	$\rho$ / kg m <sup>-3</sup>	$c_p$ / kJ kg <sup>-1</sup> K <sup>-1</sup>
outer layer	0.115	0.99	1 800	0.84
insulating layer	0.06	0.04	30	0.84
masonry	0.175	0.79	1 600	1.00
internal plastering	0.015	0.70	1 400	0.92

**Table 5.3 | Calculated parameters of the example wall for reduced-order models.**

ROM	Thermal resistance / 10 <sup>-3</sup> K W <sup>-1</sup>			Thermal capacitance / kJ K <sup>-1</sup>	
	$R_1$	$R_2$	$R_3$	$C_1$	$C_2$
DLM	21.119	539.57	42.918	540.21	862.40
IDEAS	150.90	301.80	150.90	459.74	426.58

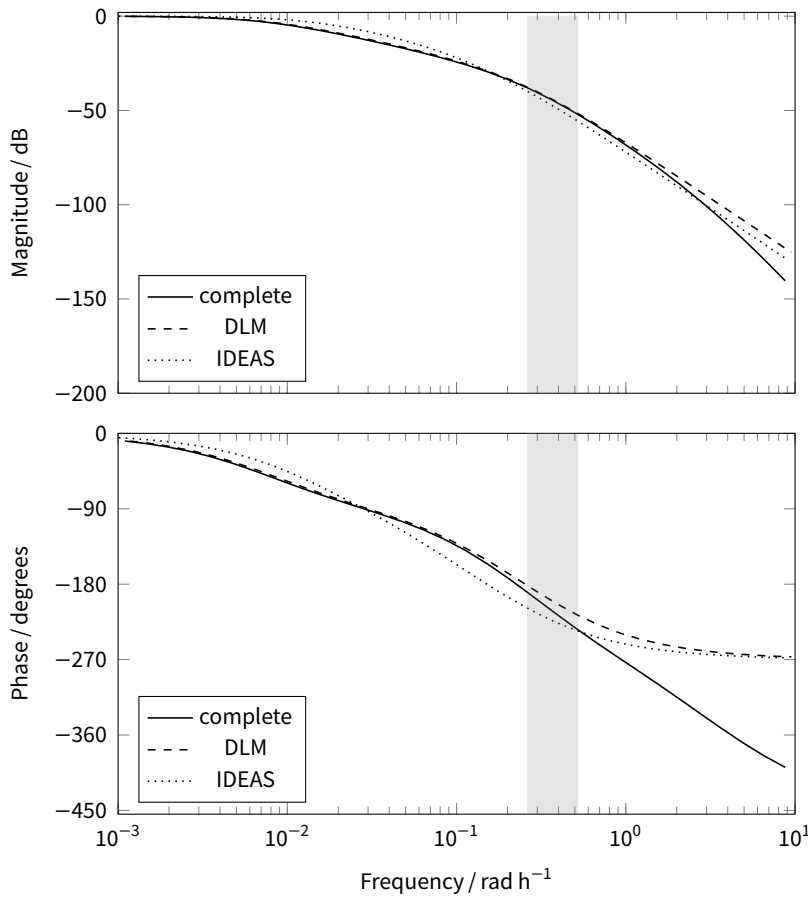


**Figure 5.4 | Frequency response of component models.** The highlighted segment corresponds to the typical range of frequency of the period of variations of the outside temperature (12 h to 24 h): **(a)** Bode gain plot of the magnitude of response; **(b)** Bode phase plot of model responses indicating the phase-shift of the fluctuation; as a function of the frequency of the period of variations.



insulating layer, a masonry layer and a layer of internal plastering (thermophysical properties as given in table 5.2). Additionally, the resistance and capacitance values calculated for the ROMs are given table 5.3. For all tests, a convective surface heat transfer coefficient of  $2.5 \text{ W m}^{-2} \text{ K}^{-1}$  for an internal surface, and  $17.5 \text{ W m}^{-2} \text{ K}^{-1}$  for an external surface are used (10, p. 10). The heat capacity of the internal air is  $68.2 \text{ kJ K}^{-1}$ .

A series of tests were performed in order to assess the dynamic performance of the ROMs. These tests consider the following:

**100 Series tests** These assess the frequency response of the models, which is a measure of the reduced-order models' steady-state response to sinusoidal changes, of varying frequency, in outside temperature versus that of the complete LPM.

**200 Series tests** These investigate the zone air temperature response under equilibrium and non-equilibrium initial conditions.

**300 Series tests** These investigate the zone wall surface temperature response under equilibrium and non-equilibrium initial conditions.

#### 100 Series tests

The state-space model of the test wall were constructed for the complete, DLM and IDEAS component models, and subjected to frequency response tests shown in fig. 5.4. The highlighted segment on the graph corresponds to the typical range of frequency of outside temperature. This ranges from the nominal diurnal cycle (24 h) to an 'extreme' of 12 h period of variations. As can be seen from fig. 5.4, the magnitude of the response on the zone side of the component for all models show a high level of agreement within the range of interest, with a root-mean-square error (RMSE)<sup>2</sup> of 0.408 dB for the DLM, and 2.88 dB for the IDEAS component model. These correspond to relatively small errors in zone temperature since the maximum magnitude within the range of interest is already 38 dB. The ROMs diverge from the complete model at  $3.26 \text{ rad h}^{-1}$  at a magnitude of  $-103 \text{ dB}$ . At this point the frequency of variations of the outside temperature would be 2 h, which is improbable. Furthermore, at a magnitude of  $-103 \text{ dB}$  the fluctuations would be highly attenuated as a  $1 \text{ }^\circ\text{C}$  change in outside temperature would result in a  $10 \times 10^{-6} \text{ }^\circ\text{C}$  change in inside temperature.

Investigating the bode phase plot in fig. 5.4, within the range of interest, again the ROMs are good approximations of the complete model. The DLM has an RMSE of  $12.6^\circ$  while the IDEAS component model has an RMSE of  $12.2^\circ$ . For reference, a  $12^\circ$  error

---

<sup>2</sup>RMSE is an often used measure of how closely an estimate model is to the actual observed data or, in this case, a high-order model.

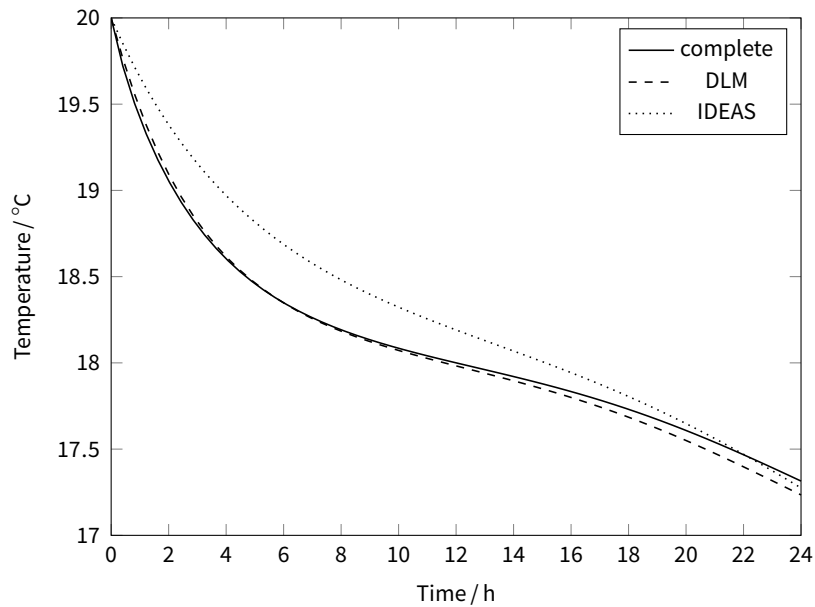


**Figure 5.5 | Non-equilibrium zone-air temperature response of component models.** This test simulates the dynamic response of the zone-air of each model once the heating has been switched off.

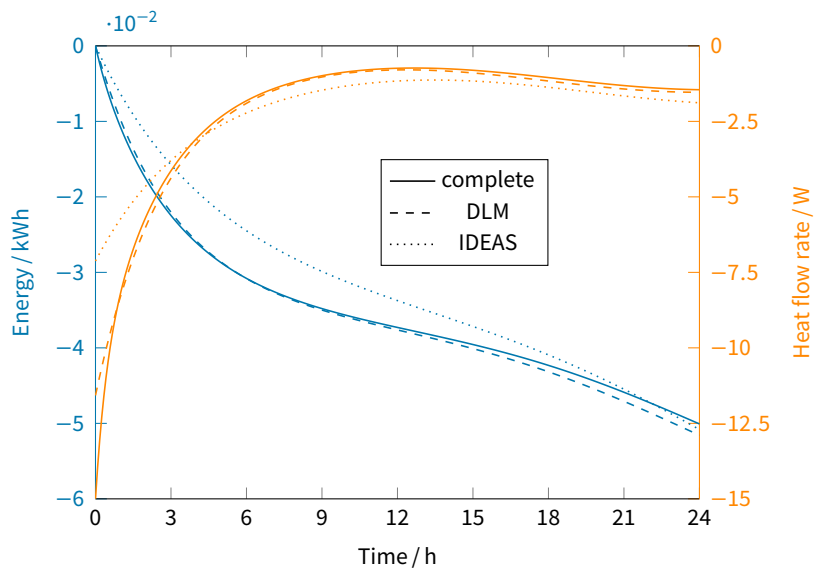


**Figure 5.6 | Non-equilibrium heat flow & energy loss response of component models.**

would result in a *steady-state* time-delay error of 24 min to 48 min depending on the period of variations (12 h to 24 h).

While the frequency response graph has been useful in determining the steady-state response of the component models (i.e. after all transients have decayed), it is important to investigate the time-domain transient response of the ROMs.

### 200 Series tests

Two conditions for the zone air transient response are considered:

**Test case 201** Transient decay immediately after the zone heating is switched-off.

**Test case 202** Transient response during free-float conditions.

In each case, there exists a sinusoidal outside temperature of

$$\Theta_e = \bar{\Theta}_e + \hat{\Theta}_e \quad \text{where } \hat{\Theta}_e = a \sin((2\pi/T)t)$$

$\bar{\Theta}_e$  is the mean outside temperature and  $\hat{\Theta}_e$  is the sinusoidal fluctuations from the mean outside temperature. The angular frequency of the sinusoid is given by  $2\pi/T$ , where  $T$  is the period of variations. For these tests, the period of variations has been set to the nominal diurnal variations of 24 h. Additionally, the mean outside temperature has been set to 8.7 °C, which coincides with the mean yearly temperature of Glasgow from the CIBSE TRY (test reference years) WCo8GLA. Similarly, the amplitude of the sinusoid has been set to 5.4 °C, which is the standard-deviation of the same CIBSE TRY weather data.

**TEST CASE 201** For test 201, at the beginning of the simulation, the nodes of the construction are set to 18 °C, while the zone air is initially at the zone set-point of 20 °C. This is a non-equilibrium initial condition. The system is then simulated while being subjected to the variations in outside temperature as an input. This test mimics the response of the zone with intermittent heating immediately after the heating is switched off, since the zone air temperature had reached the set-point, but the component temperatures had not reached equilibrium with the inside and outside air. Figure 5.5 shows the results of this simulation over a 24 h period.

The RMSE of the DLM for test 201 is 0.0357 °C, while the RMSE of the IDEAS model is 0.2136 °C. Both models show similar behaviour in the dynamic response with the DLM outperforming the IDEAS model. The speed of decay of the IDEAS model is less than that of the complete and DLM model, caused by its equal distribution of thermal resistance throughout the component – in the complete model once the heating is

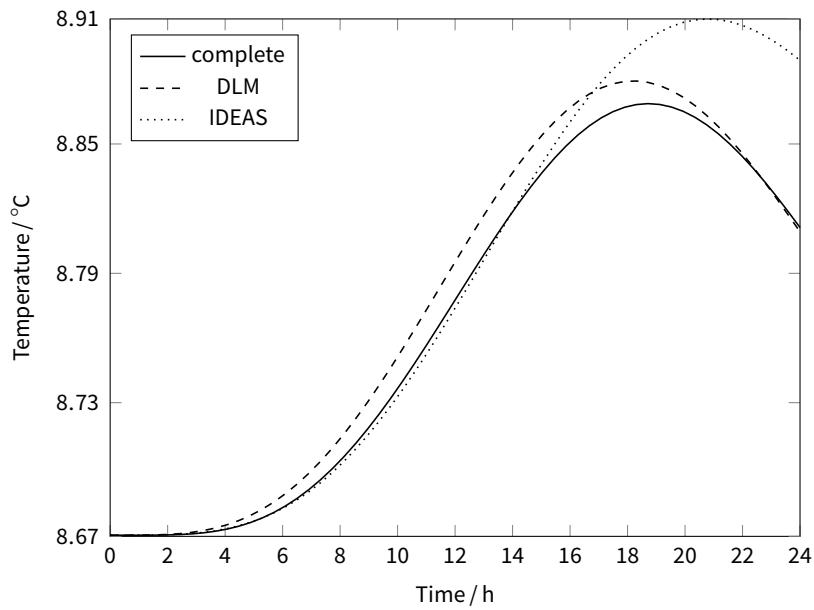


**Figure 5.7 | Equilibrium zone-air temperature response of component models.** This test simulates the dynamic response of the zone-air of each model from free-float conditions.

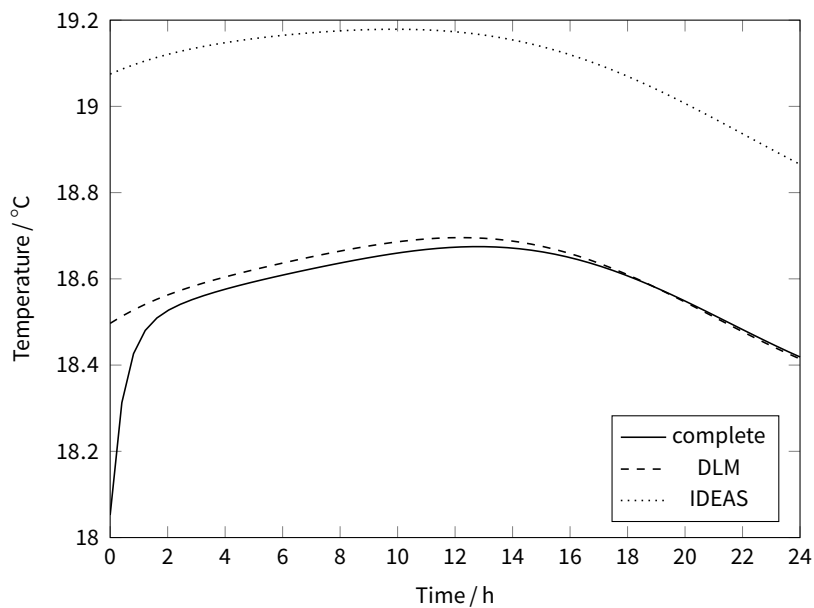


**Figure 5.8 | Non-equilibrium zone-facing surface temperature response of component models.** This test simulates the dynamic response of the temperature of the zone-facing surface while zone air held at 20 °C and external surface is subjected to sinusoidal variations.

switched off, heat will be quickly lost from the air to the low-mass inner layer before diffusing throughout the rest of the layers. The DLM captures this behaviour as its inner resistance is equal to that of the complete model up until the dominant layer. The IDEAS model will show the appropriate temperature response after this initial transient behaviour.

It is also possible to model the heat flow rate and associated energy loss through the component from the air during the simulation. Figure 5.6 shows that the energy lost through the component is directly proportional to the transient temperature loss, with all three models converging as the system approaches steady-state equilibrium conditions. Therefore for energy estimation purposes either ROM method will be able to predict the heat loss through the component as well as the complete LPM, especially over longer term averaging of the zone. Note that for the rest of the tests the heat and energy analysis have been omitted. It is clear from comparing figs. 5.5 and 5.6 that the heat flow rate is proportional to the change in temperature and would display the same transient response as seen in the temperature responses.

**TEST CASE 202** For test 202, the initial conditions are set so that the air and components are in equilibrium with the outside temperature. This represents the ‘free-float’ conditions of the zone. The system is then subjected to the same outside temperature fluctuation as in test 201. Results from this simulation are given in fig. 5.7.

The RMSE of the DLM for test 202 is  $0.0096^{\circ}\text{C}$ , while the RMSE of the IDEAS model is  $0.0358^{\circ}\text{C}$ . As is evident from these results, the dynamic response of the IDEAS model is much improved over the non-equilibrium test 201, but is still outperformed by the DLM. Figure 5.7 highlights the time-delay and magnitude error from the frequency response results. However, both models have minimal error under free-float conditions, with a RMSEs that would be imperceptible in many cases.

### 300 Series tests

Two conditions for the zone facing surface temperature response are considered:

**Test case 301** Dynamic response of the surface while the zone air is held at set-point ( $20^{\circ}\text{C}$ ) and the external surface is subjected to sinusoidal fluctuations in outside temperature – component has not reached equilibrium.

**Test case 302** Same as test 301 but the component begins at equilibrium with the inside and outside air.

The same sinusoidal excitation from the 200 series tests is used in these tests.

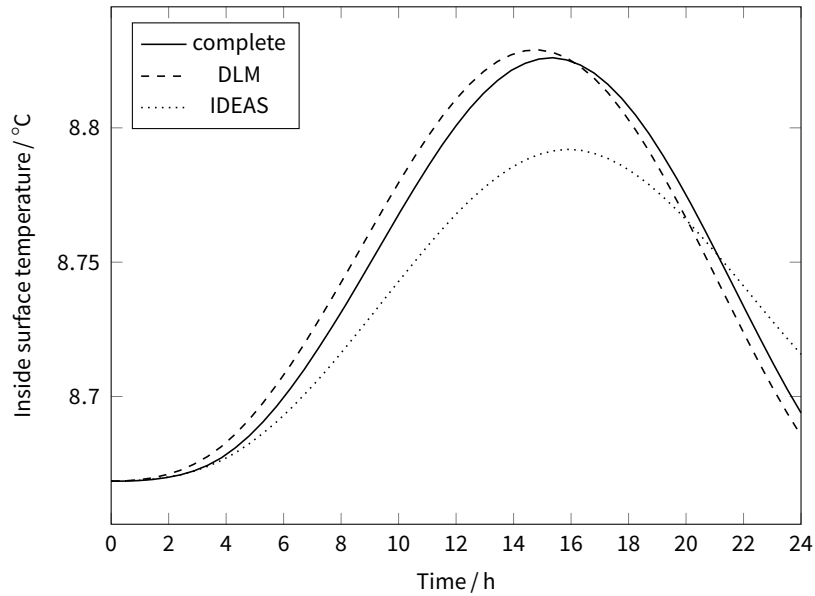


**Figure 5.9 | Equilibrium zone-facing surface temperature response of component models.** This test simulates the dynamic response of the temperature of the zone-facing surface from equilibrium.

**Table 5.4 | Precision of reduced-order methods for dynamic temperature calculations.**

ROM	200 Series		300 Series	
	201	202	301	302
RMSE (°C)				
DLM	0.035 7	0.009 6	0.074 6	0.007 0
IDEAS	0.213 6	0.035 8	0.543 7	0.012 3

**TEST CASE 301** For test 301, at the beginning of the simulation, the nodes of the construction are set to 18 °C, while the zone air is held at the zone set-point of 20 °C. This is a non-equilibrium initial condition. The system is then simulated while being subjected to the variations in outside temperature as an input, with the output of the model being the zone facing surface temperature. This test shows the influence of the change in external temperature during the occupied/controlled period as the zone air is held at a steady set-point. Figure 5.8 shows the results of this simulation over a 24 h period.

The RMSE of the DLM for test 301 is 0.0746 °C, while the RMSE of the IDEAS model is 0.5437 °C. As is evident from the graph and these statistics that the DLM true to the dynamic response of the complete LPM while the IDEAS model suffers from over-prediction of the surface temperature. Once again this is related to the even distribution of thermal conductivity throughout the component in the IDEAS model compared to the complete model where the resistance to heat flow through the component in the inner layers is much less than that of the overall component. Since the dominant layer of the DLM is the masonry, it uses the actual thermal conductivity of the inner layers from this point as its outer resistance which results in superior dynamic response matching.

**TEST CASE 302** For test 302, the same test is performed as 301 but the components are in equilibrium with the inside and outside temperature at the beginning of the simulation. This represents the same occupied/controlled period but conditions have remained the same for a sufficient enough time for the component to reach equilibrium. Figure 5.9 shows the results of this simulation over a 24 h period.

The RMSE of the DLM for test 302 is 0.0070 °C, while the RSME of the IDEAS model is 0.0122 °C. Once again, both ROM methods show close transient response in comparison with the complete model. As expected, the IDEAS model shows a small attenuation of the peak temperature fluctuation shown on the inside surface of the component compared to the complete model, however the magnitude of this difference can be considered negligible.

### Results summary

Table 5.4 collates the results from the four tests. These results indicate that the ROM methods provide good approximations of the dynamic transient response of the component in comparison with the high-order ‘complete’ model. The DLM method generally outperforms the IDEAS model over the range of tests conducted, mainly attributed to its variable thermal conductivity throughout the component. The average RMSE of





the DLM over the four tests was  $0.0315^\circ\text{C}$ , while the IDEAS model was  $0.199^\circ\text{C}$ . The IDEAS model shows improved transient response when excited from equilibrium conditions with an average RMSE over the two equilibrium tests of  $0.0243^\circ\text{C}$  – indicating a very close approximation of the complete model in line with those predicted by the DLM. Therefore, when sufficient information is available, the DLM method should be used, but when limited information is available the IDEAS method will provide satisfactory dynamic response for temperature and energy performance.

#### 5.2.4 Component heat transmission

Now that the performance of the ROMs have been validated, the generalised state-space equations can be formulated. Utilising the equivalent electrical network for a ROM building component, the state equations for the  $k$ -th component in an enclosure of  $m$  components are given by

$${}^k C_1 {}^k \dot{\Theta}_1(t) = - (H_{\text{ext},k} + H_{\text{cp},k}) {}^k \Theta_1(t) + H_{\text{cp},k} {}^k \Theta_2(t) + H_{\text{ext},k} \Theta_{\text{env,ext}}(t) \quad (5.4a)$$

$${}^k C_2 {}^k \dot{\Theta}_2(t) = - (H_{\text{int},k} + H_{\text{cp},k}) {}^k \Theta_2(t) + H_{\text{cp},k} {}^k \Theta_1(t) + H_{\text{int},k} \Theta_{\text{env,int}}(t) \quad (5.4b)$$

where

- $C_1, C_2$  are the external and internal heat capacities of the component ( $\text{J K}^{-1}$ );
- $\Theta_1, \Theta_2$  are the external and internal nodal temperatures of the component (K);
- $H_{\text{ext}}$  is the heat transfer coefficient from the external node to the external environment ( $\text{W K}^{-1}$ );
- $H_{\text{int}}$  is the heat transfer coefficient from the internal node to the internal environment ( $\text{W K}^{-1}$ );
- $H_{\text{cp}}$  is the heat transfer coefficient between the component's nodes ( $\text{W K}^{-1}$ );
- $\Theta_{\text{env,ext}}$  are the external and internal environment temperatures either side of the
- $\Theta_{\text{env,int}}$  component (K).

The heat transfer coefficients are calculated by

$$H_{\text{int},k} = \frac{1}{R_{\text{ROM},3,k} + R_{\text{si},k}} \quad H_{\text{cp},k} = \frac{1}{R_{\text{ROM},2,k}} \quad H_{\text{ext},k} = \frac{1}{R_{\text{se},k} + R_{\text{ROM},1,k}}$$

If the exterior or interior surface is adiabatic, then  $R_{\text{ROM},1,k} = \infty$  or  $R_{\text{ROM},3,k} = \infty$ . Therefore, if the external or internal surface of the  $k$ -th component is adiabatic  $H_{\text{ext},k} = 0$  or  $H_{\text{int},k} = 0$ .



### 5.2.5 Low-mass & infiltration/ventilation heat transmission

The heat transfer via infiltration/ventilation, thermal bridges and heat transmission through components with negligible thermal inertia are collectively called ‘no mass’ components in the model. The generalised heat transmission through such a component  $k$  is denoted  $H_{nm,k}$ , where it is understood that appropriate heat transfer coefficient is substituted for  $H_{nm,k}$  in each case. Therefore, the heat transmission through a ‘no mass’ component is given by

$$\Phi_{nm,k} = H_{nm,k}(\Theta_{env,ext}(t) - \Theta_{env,int}(t)).$$

For heat transfer by ventilation,  $H_{nm} = H_{ve}$  and is connected directly to the inside air node,  $\Theta_{env,int} = \Theta_a$ , and to a node representing the supply air temperature  $\Theta_{env,ext} = \Theta_{sup}$ . For ventilation directly from the outside,  $\Theta_{env,ext} = \Theta_{out}$ .

For heat transfer by infiltration,  $H_{nm} = H_{infl}$  and is connected directly to the inside air node,  $\Theta_{env,int} = \Theta_a$ , and to the outside air node  $\Theta_{env,ext} = \Theta_{out}$ .

### 5.2.6 Heat transmission matrix module

Taking eq. (5.4) for all components in a building zone, it is possible to represent the generalised transmission network in vector-matrix form. The heat transmission coefficients are placed into vectors, as

$$\begin{aligned} \mathbf{h}_{int} &= \begin{bmatrix} H_{int,1} & \cdots & H_{int,m} \end{bmatrix} & \mathbf{h}_{cp} &= \begin{bmatrix} H_{cp,1} & \cdots & H_{cp,m} \end{bmatrix} \\ \mathbf{h}_{ext} &= \begin{bmatrix} H_{ext,1} & \cdots & H_{ext,m} \end{bmatrix} & \mathbf{h}_{nm} &= \begin{bmatrix} H_{nm,1} & \cdots & H_{nm,l} \end{bmatrix} \end{aligned}$$

The heat transmission for all component nodes in the building zone is given by

$$\begin{bmatrix} {}^1C_1 \frac{d^1\Theta_1(t)}{dt} \\ \vdots \\ {}^mC_1 \frac{d^m\Theta_1(t)}{dt} \\ {}^1C_2 \frac{d^1\Theta_2(t)}{dt} \\ \vdots \\ {}^mC_2 \frac{d^m\Theta_2(t)}{dt} \end{bmatrix} = \begin{bmatrix} -(H_{ext,1} + H_{cp,1}) & \cdots & 0 & H_{cp,1} & \cdots & 0 \\ \vdots & \ddots & \vdots & \vdots & \ddots & \vdots \\ 0 & \cdots & -(H_{ext,m} + H_{cp,m}) & 0 & \cdots & H_{cp,m} \\ H_{cp,1} & \cdots & 0 & -(H_{int,1} + H_{cp,1}) & \cdots & 0 \\ \vdots & \ddots & \vdots & \vdots & \ddots & \vdots \\ 0 & \cdots & H_{cp,m} & 0 & \cdots & -(H_{int,m} + H_{cp,m}) \end{bmatrix} \begin{bmatrix} {}^1C_1 {}^1\Theta_1(t) \\ \vdots \\ {}^mC_1 {}^m\Theta_1(t) \\ {}^1C_2 {}^1\Theta_2(t) \\ \vdots \\ {}^mC_2 {}^m\Theta_2(t) \end{bmatrix}$$

or in compact notation

$$\mathbf{C}_{com} \begin{bmatrix} \dot{\boldsymbol{\theta}}_{ext}(t) \\ \dot{\boldsymbol{\theta}}_{int}(t) \end{bmatrix} = \begin{bmatrix} -\text{diag}(\mathbf{h}_{ext} + \mathbf{h}_{cp}) & \text{diag}(\mathbf{h}_{cp}) \\ \text{diag}(\mathbf{h}_{cp}) & -\text{diag}(\mathbf{h}_{int} + \mathbf{h}_{cp}) \end{bmatrix} \begin{bmatrix} \boldsymbol{\theta}_{ext}(t) \\ \boldsymbol{\theta}_{int}(t) \end{bmatrix} \quad (5.5)$$



where  $C_{\text{com}} = \text{diag}({}^1C_1, \dots, {}^mC_1, {}^1C_2, \dots, {}^mC_2)$ ,  $\boldsymbol{\theta}_{\text{ext}}(t) = ({}^1\theta_1(t), \dots, {}^m\theta_1(t))^T$ , and  $\boldsymbol{\theta}_{\text{int}}(t) = ({}^1\theta_2(t), \dots, {}^m\theta_2(t))^T$ .

Equation (5.5) represents the conductive and convective heat transfer between all nodes in the  $m$ -component enclosure. It is relatively trivial to augment eq. (5.5) in order to account for the heat transmission from the external and internal environments. The following assumes that a controlled voltage source models the outside air i.e.  $\Theta_{\text{env,ext}}(t) = \Theta_{\text{out}}(t)$ , and a capacitor models the inside air, where  $\Theta_{\text{env,int}}(t) = \Theta_a(t)$ . It should be obvious how this can be further augmented for components separating two modelled environments. The state equation for the internal air node is given by

$$C_a \dot{\Theta}_a(t) = \sum_{k=1}^m H_{\text{int},k} ({}^k\dot{\Theta}_2(t) - \Theta_a(t)) + \sum_{k=1}^l H_{\text{nm},k} (\Theta_{\text{out}}(t) - \Theta_a(t)) \quad (5.6)$$

Combining eqs. (5.5) and (5.6) the vector-matrix equation for the heat transmission for the zone is now given by

$$\begin{bmatrix} C_{\text{com}} & \mathbf{0}_m \\ \mathbf{0}_m^T & C_a \end{bmatrix} \begin{bmatrix} \dot{\boldsymbol{\theta}}_{\text{ext}}(t) \\ \dot{\boldsymbol{\theta}}_{\text{int}}(t) \\ \dot{\Theta}_a(t) \end{bmatrix} = \begin{bmatrix} -\text{diag}(\mathbf{h}_{\text{ext}} + \mathbf{h}_{\text{cp}}) & \text{diag}(\mathbf{h}_{\text{cp}}) & \mathbf{0}_m \\ \text{diag}(\mathbf{h}_{\text{cp}}) & -\text{diag}(\mathbf{h}_{\text{int}} + \mathbf{h}_{\text{cp}}) & \mathbf{h}_{\text{int}}^T \\ \mathbf{0}_m^T & \mathbf{h}_{\text{int}} & -(\mathbf{h}_{\text{int}}\mathbf{1}_m + \mathbf{h}_{\text{nm}}\mathbf{1}_l) \end{bmatrix} \begin{bmatrix} \boldsymbol{\theta}_{\text{ext}}(t) \\ \boldsymbol{\theta}_{\text{int}}(t) \\ \Theta_a(t) \end{bmatrix} + \begin{bmatrix} \mathbf{h}_{\text{ext}}^T \\ \mathbf{0}_m \\ \mathbf{h}_{\text{nm}}\mathbf{1}_m \end{bmatrix} \Theta_{\text{out}}(t)$$

or

$$\boxed{\begin{bmatrix} C_{\text{com}} & \mathbf{0}_m \\ \mathbf{0}_m^T & C_a \end{bmatrix} \begin{bmatrix} \dot{\boldsymbol{\theta}}_{\text{ext}}(t) \\ \dot{\boldsymbol{\theta}}_{\text{int}}(t) \\ \dot{\Theta}_a(t) \end{bmatrix} = \mathbf{H}_{\text{tr}} \begin{bmatrix} \boldsymbol{\theta}_{\text{ext}}(t) \\ \boldsymbol{\theta}_{\text{int}}(t) \\ \Theta_a(t) \end{bmatrix} + \mathbf{h}_{\text{tr,ext}} \Theta_{\text{out}}(t)} \quad (5.7)$$

Using eq. (5.7) it is possible model the convective and conductive heat transfer between the air, components and external environment for a zone of a building in a single linear vector-matrix equation.

### 5.3 Radiation heat transfer

The inclusion of radiation exchange between the surfaces of the zone has an affect on the energy estimation capabilities of the model. It is most significant when considering the following:

- *Control of internal temperature:* The internal temperature of a zone can be approximated by the operative temperature of the zone (20). The operative temperature of a zone is a function of air temperature and mean radiant temperature within

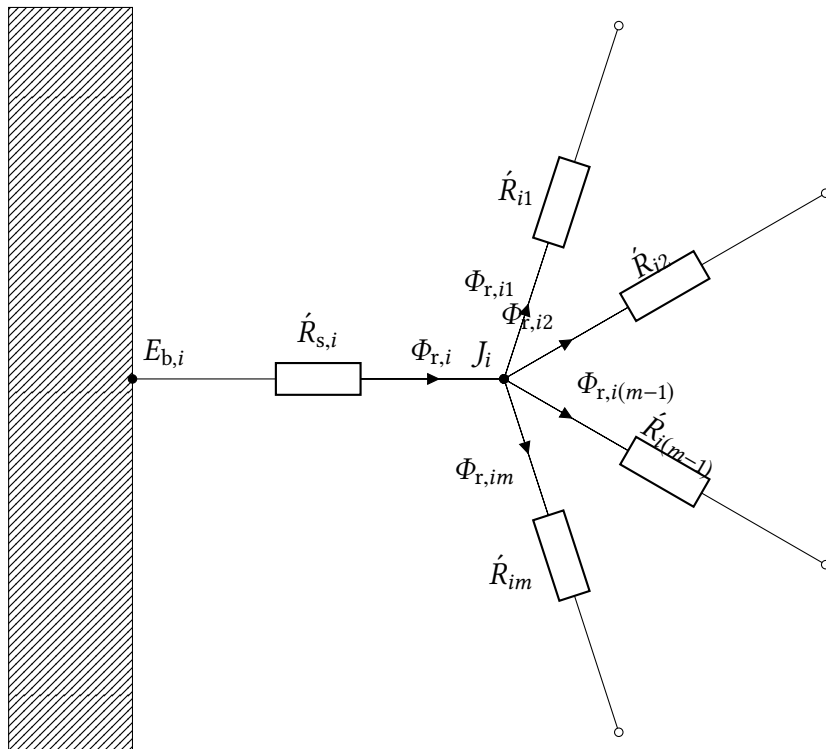


**Figure 5.10** | Schematic of the network method of radiation exchange from a surface  $i$  to the remaining surfaces of an  $m$ -surface enclosure.

the zone:

$$\Theta_{\text{op}} = f_a \Theta_a + (1 - f_a) \Theta_{\text{mrt}}$$

where for internal air speeds  $< 0.2 \text{ m s}^{-1}$ ,  $f_a = 0.5$  (17, p. 177). The mean radiant temperature in turn is a function of the surface temperatures of the enclosing elements within the zone. Therefore, since the surface temperatures are affected by the radiation exchange between the surface of the components it follows that the (controlled) internal temperature is as well.

- *Adiabatic internal components:* When the outer surface of components are assumed to be adiabatic then radiation heat transfer becomes a more dominant mode of heat transmission since there is no convective heat transfer across the external boundary of the component.

### 5.3.1 Radiation network method

Similar to the heat transfer by convection from § 5.2, an electrical network analogy can be used to solve the radiation heat transfer problem. The following analysis uses the **network method** introduced by Oppenheim (21) and provides a simpler solution to the problem of net radiation transfer in enclosures as opposed to the **direct method** which must account for the direct interreflections of radiation beams between all internal surfaces.

In the network method, there are two different types of resistance:

- **surface resistance**,  $\hat{R}_{s,i}$ , which represents the ability of the surface of component  $i$  to resist the flow of radiative heat.
- **space resistance**,  $\hat{R}_{ij}$ , where the reciprocal represents the radiation thermal conductance between two surfaces  $i$  and  $j$  within the enclosure.

The method is utilised by drawing a surface resistance associated with each component surface within the enclosure and connecting them with space resistances. Then solve the radiation problem by treating it as an electrical network where the radiation heat flow rate replaces the current and radiosity<sup>3</sup> replaces the potential. The schematic of the network method of radiation exchange from a surface  $i$  to the remaining surfaces of an  $m$ -surface enclosure is shown in fig. 5.10.

---

<sup>3</sup>Radiosity is the total radiation (reflected plus emitted) leaving a surface.





### Surface resistance to radiation

The *net* rate of radiation heat transfer from a surface  $i$  of surface area  $A_i$  is denoted by  $\Phi_{r,i}$  and is expressed as

$$\Phi_{r,i} = \frac{E_{bi} - J_i}{\dot{R}_{s,i}} \quad \text{where } \dot{R}_{s,i} = \frac{1 - \varepsilon_i}{A_i \varepsilon_i}$$

where

$\dot{R}_{s,i}$  is the surface resistance to radiation ( $\text{m}^{-2}$ );

$\varepsilon_i$  is the emissivity of the surface (1);

$E_{bi}$  is the blackbody emissive power ( $\text{W m}^{-2}$ );

$J_i$  is the radiosity of the surface ( $\text{W m}^{-2}$ ).

In some cases, some components are said to be modelled as *adiabatic* as it is assumed that the net heat transfer through them is zero.<sup>4</sup> Under these conditions, the surface must lose as much radiation energy as it gains, thus  $\Phi_{r,i} = 0$ . In such cases, the surface is said to *reradiate* all the radiation energy it receives, and as such is called a **reradiating surface**.<sup>5</sup> Therefore, in this radiation analysis, if a component is defined as adiabatic, then the surface resistance of that component is disregarded since there is no heat transfer through it.

### Space resistance to radiation

Consider a radiation interaction between two surfaces  $i$  and  $j$ , where the radiosity  $J$  represents the rate of radiation leaving a surface per unit surface area and that the **view factor**  $F_{i \rightarrow j}$  (detailed in the following section) represents the fraction of radiation leaving surface  $i$  that strikes surface  $j$ , the *net* rate of radiation heat transfer from surface  $i$  to surface  $j$  can be expressed as

$$\Phi_{r,i \rightarrow j} = A_i F_{i \rightarrow j} (J_i - J_j)$$

or

$$\phi_{r,ij} = \frac{J_i - J_j}{\dot{R}_{ij}} \quad \text{where } \dot{R}_{ij} = \frac{1}{A_i F_{ij}}$$

where

$\dot{R}_{ij}$  is the space resistance to radiation ( $\text{m}^{-2}$ ).

<sup>4</sup>This is often the case for internal partitions where the temperature difference between the sides of the component is assumed to be zero (since each zone is tracking the same set-point).

<sup>5</sup>These are also known as “no-flux surfaces” in some literature.



### View factors

The view factor is a measure the proportion of the radiation which leaves a surface  $i$  and strikes a surface  $j$ . The formula to calculate the diffuse view factor between two planer polygonal surfaces placed at arbitrary orientations relative to each other, denoted  $F_{i \rightarrow j}$  (or simply  $F_{ij}$ ) is given by (21)

$$F_{ij} = \frac{1}{A_i} \int_{A_j} \int_{A_i} \frac{\cos \beta_1 \cos \beta_2}{\pi r^2} dA_1 dA_2. \quad (5.8)$$

where

$\beta$  is the angle between the surface normal and a ray between the two differential areas;

$r$  is the distance between the surfaces (m).

From eq. (5.8) it can be seen that the view factor between the two surfaces  $i$  and  $j$  depends on their relative orientation and the distance between them. It is a fair assumption that the geometry of the building does not change during the simulation, and it is also assumed that the surfaces are gray and diffuse<sup>6</sup> In order to evaluate the double contour integral in eq. (5.8), this work uses a numerical procedure developed by Mazumder, Ravishankar (22). The only required inputs are the coordinates of the vertices that define the outline of each building component *in situ* – this is called the parametric vector representation of the surface.<sup>7</sup>

The number of view factors in an  $m$ -surface enclosure is given by the variation equation, since the order of the surfaces is important (as  $F_{ij} \neq F_{ji}$ ), with repetition allowed (to account for a concave surface where  $F_{ii} \neq 0$ ). Therefore the number of view factors is simply  $N_{vf} = {}^R V_m^2 = m^2$ .

#### 5.3.2 Radiation network analysis

Now that the surface and space resistances can be calculated from knowledge of the properties of the components used within the enclosure, it is possible to analyse the radiation network and determine relations for the unknown heat transfer or temperature at each node.

In an  $m$ -surface enclosure, from the conservation of energy principle, the net heat transfer from surface  $i$  is equal to the sum of the heat transfers from surface  $i$  to each of the  $m$  surfaces of the enclosure, as shown schematically in fig. 5.10. Mathematically,

<sup>6</sup>The properties of the components are independent of wavelength and that the radiation is reflected equally in all directions.

<sup>7</sup>The method detailed in (22) has been converted into a MATLAB function which was based on code written by Lauzier (23).



that is

$$\Phi_{r,i} = \sum_{\substack{j=1 \\ j \neq i}}^m \Phi_{r,ij}.$$

This is mathematically equivalent to applying Kirchhoff's current law to each node in the network.

Networks such as this can be analysed using the Kron method (24). This allows for the representation of a mesh network in such a way that it solves for the equivalent admittance between any two node pairs by utilising matrix algebra. The method used to solve for the radiative heat flow to/from each node in the network is an adaptation of the methods detailed by Oppenheim (21) for the mesh network in this problem.

The radiation heat transfer at the inside surface of a component  $i$  is given by

$$\Phi_{r,i} = \sum_{j=1}^m \frac{1}{\bar{R}_{ij}} (E_{b,j} - E_{b,i}).$$

where

$\bar{R}_{ij}$  is the equivalent radiative resistance between surface  $i$  and  $j$  in a grey enclosure ( $\text{m}^{-2}$ ).

Solving for the equivalent radiative resistance between all the surfaces in an  $m$  surface enclosure involves a rather mathematically dense process and is produced in appendix A.3 for reference. The result of which is that the radiation heat transfer at the inside surface of all components in an  $m$ -surface enclosure is given by

$$\phi_r(t) = -T^{\mathcal{T}} (\mathbf{R}_{\text{mesh}} + T \mathbf{R}_s T^{\mathcal{T}})^{-1} T \mathbf{e}_b(\theta_s(t)) \quad (5.9)$$

where

$T$  is a matrix that relates the branch potential differences with the node potentials;

$\mathbf{R}_{\text{mesh}}$  is a diagonal matrix comprised of the  $\binom{m}{2}$  space resistances;

$\mathbf{R}_s$  is a diagonal matrix comprised of the  $m$  surface resistances;

$\mathbf{e}_b(\cdot)$  is a vector containing the blackbody emissive power of all surfaces.

The blackbody emissive power of a surface can be written as a function of the surface's temperature as

$$E_{b,i} = \sigma \Theta_{s,i}^4. \quad (5.10)$$

where  $\sigma = 5.6704 \times 10^{-8} \text{ W/m}^2\text{K}^4$  is the Stefan-Boltzmann constant. Substituting eq. (5.10) into eq. (5.9) gives

$$\phi_r(t) = \sigma Y f(\theta_s(t)) \quad (5.11)$$



where  $f : \mathbb{R}^m \rightarrow \mathbb{R}^m$  is a vector function and each element  $f_i = \Theta_{s,i}(t)^4$ , and  $Y = -T^T(R_{\text{mesh}} + TR_s T^T)^{-1}T$  is the  $m \times m$  radiative admittance matrix. Equation (5.11) is then a single vector-matrix equation that calculates the net long-wave radiative heat transfer at each surface in an  $m$  surface enclosure.

Equation (5.11) is a nonlinear function due to the  $f_i$  elements. It is possible to obtain a linear approximation of eq. (5.11) by truncating the Taylor series expansion of  $\phi_r$  around an equilibrium point above the first-order term. The linear approximation is then given by (see appendix A.3.1 for working)

$$\hat{\phi}_r(t) = h_{r,i} Y \theta_s(t) \quad (5.12)$$

where  $h_{r,i}$  is the long-wave radiative heat transfer coefficient at the internal surface ( $\text{W m}^{-2} \text{K}^{-1}$ ).

### 5.3.3 Remarks

This section has detailed the formation of a network method to solve for the radiative heat flow between all surface components that enclosure a building zone. The methods specified allow for the straightforward construction of the system of equations representing the radiative heat flow for a general  $m$ -surface zone enclosure that is readily implementable in state-space and/or for deployment in computer simulations.

Other simplified dynamic building models often exclude radiative heat exchange, however, it is worth calling attention to past literature from Achterbosch et al. (1) that has used a simplified method to the one presented here with good success. This method showed admirable correlation with empirical data from two Dutch semi-detached dwellings. However, that model was developed for domestic housing, where they only considered the mutual radiative heat exchange between two surfaces<sup>8</sup>: The internal surfaces (internal walls, floor and ceiling all lumped into a single node) and the external wall node. The assumption being that the dominant heat exchange occurs between these inner and outer surfaces and therefore neglects the radiative heat exchange between the inner surfaces themselves. As a consequence of this assumption, all internal wall temperatures are approximated as the internal air temperature. While this assumption holds for lightweight constructions it breaks down when internal surfaces have appreciable mass.

The method presented in this work can account for all the radiative exchange within a zone: This allows not only for the internal surfaces to have their own dynamic temperature and radiation exchange with the rest of the enclosure, but allows the

<sup>8</sup>The radiative analysis presented in this work produces the same nonlinear and linear models as Achterbosch et al. if  $m = 2$ .





calculation of the mean radiant temperature of the internal surfaces – an important aspect of operative/comfort temperature calculation. For this reason the radiative heat analysis is a key aspect of the control of indoor conditions of a zone and will also affect the energy use of a controlled zone.

#### **5.4** Internal heat gains

Internal heat gains (also known as casual gains) are considered to be any source or sink of heat generated within, or entering into, the zone that is not heat deliberately (i.e. via control) introduced or extracted from the zone. Furthermore, if an internal heat source is determined to be a function of the temperature difference between itself and the internal temperature and/or temperature of any surface within the zone, then it is *not* considered an internal heat gain i.e. only sources that are not (or only weakly) dependent on any internal/surface temperature are considered internal heat gains.<sup>9</sup> In this case, it would be accounted for as a transmission or radiative heat transfer as discussed earlier in this chapter.

The main sources of internal heat gains considered throughout this work are

- Heat dissipated from lighting
- Heat dissipated from appliances
- Metabolic heat from occupants

all of which constitute the dominant sources of internal heat gains within buildings currently (17), and likely towards the future (25, 26). It should, however, be acknowledged that these are not the only internal heat gains within buildings, with heat gains such as hot water, sewage, residual heat from HVAC systems, cooking equipment etc. all having some impact on the building zone thermodynamics. Nonetheless, for the purposes of controller design and model development only these sources are considered in this work.

If any one of the dominant internal heat gains are considered as a disturbance input – and the control strategy is designed to be robust to any reasonable disturbance input from these sources – then it follows that these additional parasitic disturbances will be rejected by the controller if it can account for the dominant internal heat gains (if it has sufficient capacity to do so). Furthermore, for the purposes of this work, none of these additional internal heat gains are considered as a controllable input, so their absence from the model is reasonable.

---

<sup>9</sup>If a change in any temperature within the zone would result a proportional increase/decrease to the magnitude of the heat flow from an internal source then it is not an internal heat gain.



As discussed in chapter 2, energy demand management can be useful investigating automatic control of the lighting and appliances within the a building in order to improve the efficiency, reliability, economics, and sustainability of the overall system. This is especially important as information and communications technology (ICT) and lighting equipment are ubiquitous within offices. At the same time, advancing building standards are rapidly improving the heat loss characteristics of buildings whereby the internal heat gains are becoming one of the dominant mechanisms for heat exchange within the zone (26). Being able to control not only the electrical power consumption of ICT and lighting equipment, as a type of dynamic demand management, but their impact on the thermodynamic conditions of the zone is an intriguing prospect, which this dynamic building model should incorporate.

If or when not being directly controlled, an internal heat gain is essentially a disturbance, where it is important to define the magnitude, schedule and type of heat output from each. The type of heat output is first split between sensible heat – the heat output that will cause a change in temperature, and latent heat – the heat output that will cause a change in substance state e.g. water to vapour. The most common source of latent heat will be from a human body, which will cause an increase in the moisture content of the air. Sensible heat into the zone is split between three fundamental modes of heat transfer: conduction, convection, and radiation. For the analyses throughout this work, convection gains have an instantaneous gain to the air of the zone, whereas radiative gains are absorbed by the building mass and dissipated back into the zone air over time. It is assumed that the conductive gains have no ‘direct’ impact on the air temperature and is dominated by the heat transfer via convection.

Based on the information available on the building modelled, it is possible to either estimate the internal heat gain via a ‘model’ (typically a series of equations), or in the absence of sufficient information, base it on nominal/benchmark values typical for the zone and its intended use – this latter approach is typically used within the buildings industry. The specific method used to estimate/capture/define this data is not relevant at this stage but will be fully described in the case study in chapter 8.

#### 5.4.1 *Modelling assumptions*

For all internal heat gains, the heat delivered to the zone is split between a convective portion which acts directly on the internal air node, and a radiative portion which is absorbed by the building components and re-released into the zone over time (17, 27). The ratio of convective to radiative heat flux differs from source to source, and often for an individual element of a source e.g. within appliances a desktop computer will have a notable difference in convective/radiative heat ratio from that of an LED-backlit



monitor. In each following section that represents one of the internal heat gain sources there contains a discussion of the convective/radiative split with respect to that source.

Due to the conservation of energy principle, it is assumed that the electrical power input to both the lighting and appliances is converted into heat. It is further assumed that this will be comprised of sensible heat only i.e. that the latent heat from these sources is negligible.

Although care is taken throughout to assure a reasonable and literature supported modelling procedure for each of these internal heat gains, it should be noted that each of these could be considered an entire research area on its own, and the methods presented here are often a considerable simplification over the actual processes at hand. However, for the purposes of controller design focussed on fulfilling the electrical and thermal demands of the building, the methods detailed here are considered sufficient.

#### 5.4.2 Lighting heat gains

The amount of energy required to fulfil the lighting requirements of the building, and type of heat generated, can vary considerably due to the different lighting technology used within the zone. Regardless of the chosen technology, it is important to consider lighting energy as a heat gain, not only a visible light source. Furthermore, the affect of lighting heat gains on the required heating and cooling loads within an office can be significant, due to the large amounts of artificial lighting often used within these zones.

The type of heat generated is not only affected by the technology used, but the way in which the light fixture is installed. For example, if the luminaire is suspended from the ceiling, more heat will be emitted into the zone compared to if the luminaire is mounted in a recess in the ceiling – where a proportion of heat will be ‘lost’ to the ceiling void or to another zone.

Therefore, considering these points, the heat flux from a single lighting fixture is given by

$$\Phi_{\text{int,L}}(t) = f_{\text{L,zone}} P_{\text{int,L}}(t), \quad (5.13)$$

where  $f_{\text{L,zone}}$  is the fraction of heat emitted that enters the zone, and  $P_{\text{int,L}}$  is the *total* power demand of the lighting fixture (including the lamps and control gear).<sup>10</sup>

A recent study (28) has shown that it is possible to use a control strategy to control the heat sink on LED lighting in order to change the thermal effect the heat gains have on the zone, by redirecting the convective output either towards the zone during the

---

<sup>10</sup>Note that for light-emitting diode (LED) lighting the LED control gear is often known as the LED driver

**Table 5.5** | Power conversion for 'white' light sources (29).

	Incandescent (%)	Fluorescent (%)	Metal Halide (%)	LED (%)
Visible light	8	21	27	15-25
Infrared	73	37	17	0
Ultraviolet	0	0	19	0
Radiant	81	58	63	15-25
Convective	19	42	37	75-85

heating period, or outside during cooling periods. The study shows that such a control strategy can reduce the total building energy consumption. It would be possible to model the affect of this control strategy in this model by using  $f_{L,zone}$  as a control input to the system.  $P_{int,L}$  can either be determined from metered data, considered as a control input, or estimated.

### Convective and radiative components

The heat output of a lighting fixture is a mix of convective and radiative heat transfer. Radiative heat is considered to be the combination of the visible, infrared (IR) and ultraviolet (UV) electromagnetic radiation emitted by the lamp. The U.S. Department of Energy reports (29) the typical thermal energy and electromagnetic radiation split of the major lighting technologies: incandescent, fluorescent, metal halide and LED lighting. These are given in table 5.5.

As can be seen from the data, the primary emitter of radiative heat is incandescent lamps<sup>11</sup> where they convert 81 % of their power input into radiative heat, while at the other end of range LED light only convert 15 % to 25 % of their power input into radiative heat.<sup>12</sup> It follows that these technologies will have a considerably different affect on the thermodynamic performance of the building, since radiative heat is first absorbed by the surfaces of the internal components before being emitted back into the zone. Therefore, the highly convective output of LED lights will likely have a more instantaneous affect on the internal temperature of the zone compared to an incandescent bulb with the same *power input*. This highlights the need to account for the different convective/radiative split of heat generation of lighting within the building model. Note that, for the purposes of energy performance, International Standard BS EN ISO 13790:2008 assumes that the radiative and convective portions are each 50 %.

It should be emphasised, however, that these are still only indicative values, as the optical properties of the luminaire can greatly affect the convective/radiant split – indeed luminaires can be designed to specifically alter the heat output from the lamps. However, these values will serve as useful benchmark values in the absence of manufacturer's data.

The modelling procedure given in §§ 5.4.5 allows for the input of individual convective/radiative ratios for each internal heat gain source, allowing for the possibility of having multiple and different light fixtures and/or lamps within a single office zone.

---

<sup>11</sup>Incandescent lamps are being phased out in Europe leaving fluorescent as the majority radiative light source.

<sup>12</sup>Recent advances in LED technology are reported to deliver up to 40 % visible light, slightly increasing their radiative heat output.

**Table 5.6 | Components of heat gain dissipated from office equipment. (30)**

Device	Heat gain component (%)	
	Convective	Radiant
Desktop computer	90	10
Laptop computer	75	25
Flat panel monitor	60	40
Laser printer	70	30
Copy machine	100	0



### 5.4.3 Appliance heat gains

Just as with the lighting, all electrical power input to the appliances within the zone is eventually converted into heat. However, for appliances there are no losses to other zones as they are all considered to be contained within the building zone under consideration. Therefore, the most accurate method to determine the total internal heat gain from appliances within the building is by measuring the total electrical power input to the equipment (30). It follows that the heat flow from an appliance within the zone is given by

$$\Phi_{\text{int,A}} = P_A \quad (5.14)$$

where  $P_A$  is the input power to the appliance.

This power consumption is not static – it can vary depending on diversity of use, idle/sleep-mode operation and the effects of energy saving features built-in to most modern equipment (17). The power consumption of appliances within buildings can be determined from measured data, considered as a control input, or estimated.

#### Convective and radiative components

The number of studies on the convective and radiant loads from appliances is limited. However, Hosni *et al.* has conducted several research projects that aimed to quantify the total heat gain and convective/radiant split for office equipment (30, 31).

As office equipment has evolved, the convective and radiant split has changed to due technological improvements to fans, heat sinks, and materials used within the devices. Furthermore, the convective/radiant split for different appliances within a single office can vary from 100% convective for multi-user commercial-size copy machines to 60/40 split for modern flat-panel monitors. Table 5.6 shows the convective/radiant split reported by Hosni *et al.*

Frequently individual breakdown of appliances within the controlled building zone are not readily available, or control may be being considered at the building design stage before the zone use has been finalised. As such, Hosni *et al.* suggests that

*Where no other information is available, total heat loss can be estimated as 20% by radiation and 80% by convection.*

which is what can be deduced by averaging the data in table 5.6. As with the lighting gains, for the purposes of energy performance, International Standard BS EN ISO 13790:2008 assumes that the radiative and convective portions are each 50 %.

Although this set convective/radiative ratio is often assumed for all of the office equipment taken together the modelling procedure given in §§ 5.4.5 allows for the input of individual convective/radiative ratios for each internal heat gain source.



#### 5.4.4 Metabolic heat gains

Metabolic heat gains are the sensible and latent heat emitted from a human body in order for the body's cells to maintain the human body temperature of 37 °C while performing necessary bodily functions.

The metabolic heat gain from a single occupant of a zone is given by

$$\Phi_{Oc} = f_{cl}A_{Oc,s}\varphi_{met}, \quad (5.15)$$

where  $A_{Oc,s}$  is the surface area of a nude body and  $f_{cl}$  is the clothing correction factor, to account for the actual surface area that is giving off heat into the zone. For simplification, a clothing correction factor of 1.2 is assumed.

The calculation of human body surface area (BSA) most often used in literature is the formula proposed by DuBois and DuBois in 1916. However, with recent advancements in 3D scanning and software technology, Yu et al. (32) have refined the BSA formula to reduce estimation errors compared to the other studies' proposed formulas. This is given as

$$A_{Oc,s} = 71.3989l_{Oc}^{0.7437}m^{0.4040} \quad (\text{cm}^2)$$

where  $m$  is the mass of the person in kg and  $l_{Oc}$  is their height in cm. This can be converted into pure SI units which gives

$$A_{Oc,s} = 0.219327l_{Oc}^{0.7437}m^{0.4040} \quad (\text{m}^2) \quad (5.16)$$

where  $m$  is still the mass of the person in kg and  $l_{Oc}$  is now their height in m.

$\varphi_{met}$  is the metabolic heat production of the person, which is largely dependent on activity.<sup>13</sup> Throughout the day, peoples activity levels are likely to fluctuate based on their daily routine. Since physically modelling  $\varphi_{met}$  is highly improbable, a weighted-average metabolic rate is commonly used to calculate internal heat gains from people within a zone. In addition, a single value of  $A_{Oc,s}$  can be assumed corresponding to the measurements of the average person in the office zone.

The discussion of the specifics of the metabolic heat gain (such as predicted occupant schedules, occupant density and activity levels within a chosen building zone) is not pertinent to the development of the thermodynamic model, since it will behave purely as a disturbance heat input to the model,  $\Phi_{Oc}(t)$ .

<sup>13</sup>For typical office work, this can vary between 55 W m<sup>-2</sup> to 130 W m<sup>-2</sup> (33).



### Sensible, latent, convective and radiative components

Of the total  $\Phi_{Oc}$  per person, the entire energy released during metabolism is assumed to occur as *heat* – in both sensible and latent forms. Therefore, the metabolic heat gain is split between sensible and latent heat. This ratio typically varies from 70/30 sensible to latent heat ratio at low activity levels to 40/60 at high activity levels (due to the higher rate of perspiration). Since the activity levels in offices tend towards the lower end of the scale, a 60/40 sensible to latent heat ratio is assumed throughout this work. Between 20 % to 60 % (17) of the sensible heat emission can be radiant – depending on type of clothing and activity of the occupants and the mean radiant temperature and air velocity within the zone. Similar to the sensible/latent heat ratio, a nominal ratio of 40/60 (15) can be chosen for the convective/radiative split to simplify the analyses.

#### 5.4.5 Modelling internal heat gains

As with the other modes of heat exchange discussed in previous sections, the aim is to represent the internal heat gains in vector-matrix form as part of a dynamic model of a building in a state-space representation. The matrix will be built up by considering first the generalised heat input from each internal heat gain source on each individual node. With that in mind, the heat from an internal heat gain  $k$  imparted on a node  $i$  of the model is given by

$$\Phi_{int,i,k} = f_{int,c,k} \Phi_{HG,k} \quad (5.17a)$$

for an air node, or

$$\Phi_{int,i,k} = f_{int,df,s,i} (1 - f_{int,c,k}) \Phi_{HG,k} \quad (5.17b)$$

for a surface node.  $f_{int,c,k}$  is the fraction of heat flow from the internal heat gain that is convective.<sup>14</sup>  $\Phi_{HG,k}$  is the total heat flow from the internal heat source  $k$ , e.g. metabolic, lighting etc.  $f_{int,df,s,i}$  is the internal heat gain distribution factor, which is fraction of radiative heat from source  $k$  that acts on a surface node  $i$ . This distribution factor is assumed to be time invariant and is defined for each surface as the area weighted fraction of internal heat gain that is absorbed by that surface. The internal heat gain distribution factor can be calculated using the following equation

$$f_{int,df,s,i} = \frac{A_i}{\sum_{j=1}^m A_j} \quad (5.18)$$

<sup>14</sup>The choice of convective here is arbitrary since the sum of convective and radiative fractions are always unity – a fact that can be exploited in the matrix construction since there is no internal heat gain loss.



i.e. the distribution factor is the surface area associated with node  $i$  divided by the total surface area of the zone enclosure.

It follows that, the total heat flow from the internal heat gains on a node  $i$  is the sum of all  $k$  internal heat gains given from eq. (5.17) i.e.

$$\Phi_{\text{int},i} = \sum_k^p \Phi_{\text{int},i,k}. \quad (5.19)$$

If the nodes are arranged in the state vector such that the air node follows the internal surface nodes,

$$\boldsymbol{\theta} = [\theta_{s,1} \quad \cdots \quad \theta_{s,m} \quad \theta_a]^\mathcal{T}$$

or

$$\boldsymbol{\theta} = [\boldsymbol{\theta}_s \quad \theta_a]^\mathcal{T}$$

then the internal heat gain matrix is given by

$$\begin{bmatrix} \Phi_{\text{int},s,1} \\ \vdots \\ \Phi_{\text{int},s,m} \\ \Phi_{\text{int},a} \end{bmatrix} = \begin{bmatrix} f_{\text{int,df},s,1}(1 - f_{\text{int,c},1}) & \cdots & f_{\text{int,df},s,1}(1 - f_{\text{int,c},p}) \\ \vdots & & \vdots \\ f_{\text{int,df},s,m}(1 - f_{\text{int,c},1}) & \cdots & f_{\text{int,df},s,m}(1 - f_{\text{int,c},p}) \\ f_{\text{int,c},1} & \cdots & f_{\text{int,c},p} \end{bmatrix} \begin{bmatrix} \Phi_{\text{HG},1} \\ \vdots \\ \Phi_{\text{HG},p} \end{bmatrix} \quad (5.20a)$$

or in vector-matrix form,

$$\boldsymbol{\phi}_{\text{int}} = \begin{bmatrix} f_{\text{int},s} \\ f_{\text{int},a} \end{bmatrix} \boldsymbol{\phi}_{\text{HG}} \quad (5.20b)$$

$f_{\text{int},s} = f_{\text{int,df},s}(1 - f_{\text{int},a})$ ,  $f_{\text{int},a} = (f_{\text{int,c},1}, \dots, f_{\text{int,c},p})$ ,  $f_{\text{int,df},s} = (f_{\text{int,df},s,1}, \dots, f_{\text{int,df},s,m})^\mathcal{T}$ . Equation (5.20b) incorporates all internal heat gains and convective/radiative fractions into a single vector-matrix equation.

This section provides a dynamic state-space model to the internal heat gains within an building zone, with specific considerations for lighting, appliance, and metabolic heat gains. Due to the modular block matrix form of the equations, it is infinitely expandable for any  $p$  number of internal heat gains within the building, each with its own convective/radiative split amongst the zone nodes.

## 5.5 Solar heat gains

Solar gains arise from short-wave radiation impinging on the glazing and external surfaces of the building zone. In general, the radiation reaching a surface consists of three components: direct radiation, diffuse radiation, and reflected radiation. The





direct radiation is the solar radiation from the sun that reaches the earth's surface without being scattered or absorbed by the atmosphere, whereas the diffuse radiation is solar radiation re-emitted or scattered by parts of the atmosphere (clouds, dust particles etc.) towards the surface of the earth. The reflected radiation is the radiation from surrounding surfaces e.g. grass, trees, other buildings etc. that has been reflected towards the glazing or external surface of the zone under consideration.

The direct radiation follows a straight path from the sun, whereas it is assumed that the diffuse radiation reaches the earth's surface uniformly from all directions in the sky. Determining the solar position for prediction of the direct radiation requires knowledge of the solar altitude, solar azimuth, time of day, latitude of the building etc. Therefore the amount of solar radiation on a surface varies as a complex time-varying function of solar geometry and sun position.

This can be predicted using detailed tracing of rays from the sun, from tables of typical solar gains depending on orientation & location of the surface under consideration, or available from measured data via sensors deployed at the building. For the entirety of this work, regardless of the aforementioned method used to procure the data, for the modelling of solar heat gains within the building it is assumed that the irradiation on the outside surface of the glazing and external surfaces is available as an input to the model – typically denoted as  $\varphi_{\text{sol}}$ , in  $\text{W m}^{-2}$ . Only this solar heat flux can be controlled or considered as a disturbance into the building, therefore the modelling of the solar heat gains is only considered once it has reached the envelope of the outside surface of the glazing or external surface of the building.

In addition to these solar heat gains that come from the sun in various forms, it is also necessary to consider the radiation exchange with the atmosphere itself. Although often this can be neglected in thermodynamic models of buildings (27), for the case of a well-insulated building or (in the limiting case) the zone has many components assumed to be adiabatic, the radiation exchange with the atmosphere (i.e. sky) is not insignificant, especially with regards to the heating loads during winter. This radiation exchange is due to the fact that the gas molecules and suspended particles in the atmosphere emit radiation as well as absorbing it. Although not an actual solar heat gain, this extra heat flow due to thermal radiation to the atmosphere can be considered as a reduction in the effective internal solar heat gain into the zone.

#### 5.5.1 Modelling solar radiation

The majority of the modelling procedure utilised for the solar gains in this model takes cues from BS EN ISO 13790:2008 (27, § 11), which details the calculation method suggested for the determination of energy use for space heating and cooling due to



heat gains from solar heat sources. Although a similar procedure is used, the solar heat gain does not act in steady-state in this model, as such elaboration on the effect that constituent terms have on the thermodynamics of the zone is considered.

There are many factors to consider which affect the amount of solar gain that will have an effect on the thermodynamics of the office zone:

1. External shading devices
2. Indoor shading devices
3. Type of glazing system
4. Thermophysical properties of external structural components

Each of these factors is included in the following modelling procedure.

This work considers solar heat gains as a external thermal disturbance to the control of the microgeneration and energy supply systems. Therefore, while it is important that these are modelled correctly in the dynamic simulations, the mathematical derivation and elaboration of precisely how the solar heat gains are modelled are relegated to appendix A.4.

From appendix A.4.2, the net solar heat flow rate to building element  $k$  is dependant on whether the element is a glazing system or an opaque component. For an element  $k$  representing a glazing system the net solar heat flow rate given as

$$\Phi_{\text{sol,net,tr},k} = A_k(f_{\text{sh,e},k}f_{\text{sh,in},k}g_k(1 - f_{\text{r},k})\varphi_{\text{sol},k} - R_{\text{se},k}A_kU_kF_{\text{r},k}h_{\text{lr,e}}\Delta\Theta_{\text{er},k}) \quad (5.21)$$

Similarly for an opaque building element the net solar heat flow rate is given by

$$\Phi_{\text{sol,net,op},k} = \frac{R_{\text{se},k}}{R_{\text{se},k} + R_{1,k}}A_k(f_{\text{sh,e},k}\alpha_k\varphi_{\text{sol},k} - F_{\text{r},k}h_{\text{lr,e}}\Delta\Theta_{\text{er},k}). \quad (5.22)$$

where



- $f_{sh,e,k}$  is the external shading reduction factor, varying from 0 for completely shaded to 1 for no external shading;
- $f_{sh,in,k}$  is the internal shading reduction factor, varying from 0 for completely shaded to 1 for no internal shading;
- $f_{f,k}$  is the frame area fraction, where a value of 0 indicates no window frame;
- $A_k$  is the overall projected area of the element ( $m^2$ );
- $\alpha_k$  is the absorptivity of the opaque element  $k$  (1);
- $F_{r,k}$  is the form factor between the external surface and the sky (i.e. 1 for horizontal surface, 0.5 for vertical surface);
- $g_k$  is the solar heat gain coefficient (a.k.a. solar energy transmittance), varying between 0 and 1, with 1 corresponding to an opening with no glazing;
- $h_{lr,e}$  is the external radiative heat transfer coefficient ( $W m^{-2} K^{-1}$ );
- $\Delta\Theta_{er,k}$  is the average difference between the temperature of external surface  $k$  and the apparent sky temperature (K);
- $U$  is the thermal transmittance of the glazing system ( $W m^{-2} K^{-1}$ ).

### 5.5.2 State-space representation of solar radiation

The net solar heat flow rate from a glazed building element given by eq. (5.21) can be re-written considering both  $\varphi_{sol,k}$  and  $\Delta\Theta_{er,k}$  together as a disturbance input vector to the model.  $\Phi_{sol,tr,k}$  now becomes

$$\Phi_{sol,net,tr,k} = \begin{bmatrix} f_{sh,e,k}A_{sol,tr,k} & f_{sky,nm,k}H_{lr,e,k} \end{bmatrix} \begin{bmatrix} \varphi_{sol,k} \\ \Delta\Theta_{er,k} \end{bmatrix} \quad (5.23)$$

where  $f_{nm,k} = R_{se,k}A_kU_k$ ,  $f_{sky,nm,k} = -f_{nm,k}F_{r,k}$ ,  $H_{lr,e,k} = h_{lr,e,i}A_k$ .

Assume that there are  $p_{sol}$  sources of solar gain i.e. a total of  $p_{sol}$  external-facing glazing components. Then from eq. (5.23) and assuming that the average difference between the temperature of each external surface and the apparent sky temperature is the same (i.e.  $\Delta\Theta_{er,k} = \Delta\Theta_{er}$ ), gives

$$\Phi_{sol,net,tr} = \underbrace{\begin{bmatrix} f_{sh,e,1}A_{sol,tr,1} & \cdots & f_{sh,e,p_{sol}}A_{sol,tr,p_{sol}} \end{bmatrix}}_{\mathbf{a}_{sol}} \underbrace{\begin{bmatrix} \sum_k^{p_{sol}} f_{sky,nm,k}H_{lr,e,k} \end{bmatrix}}_{H_{sky,a}} \begin{bmatrix} \varphi_{sol,1} \\ \vdots \\ \varphi_{sol,p_{sol}} \\ \Delta\Theta_{er} \end{bmatrix} \quad (5.24)$$

Equation (5.24) must be partitioned to account for the distribution of the solar gain amongst the air and internal surface nodes. Substituting eq. (5.24) into eq. (A.60) gives



at once the net solar radiation gain on the air and internal surface nodes in the model in a single vector-matrix equation given by

$$\begin{bmatrix} \Phi_{\text{sol},a} \\ \phi_{\text{sol},si} \end{bmatrix} = \begin{bmatrix} f_{sa} \mathbf{a}_{\text{sol}} & H_{\text{sky},a} \\ f_{\text{sol},si} \mathbf{a}_{\text{sol}} & 0 \end{bmatrix} \begin{bmatrix} \boldsymbol{\varphi}_{\text{sol}} \\ \Delta\Theta_{\text{er}} \end{bmatrix} \quad (5.25)$$

Similarly, utilising eq. (5.22) for each external-facing opaque component the solar radiation matrix for the external mass nodes is given by

$$\begin{bmatrix} \Phi_{\text{sol},em,1} \\ \Phi_{\text{sol},em,2} \\ \vdots \\ \Phi_{\text{sol},em,m} \end{bmatrix} = \begin{bmatrix} f_{em,1} f_{sh,e,1} A_{\text{sol},op,1} & 0 & \cdots & 0 & f_{\text{sky},1} H_{lr,e,1} \\ 0 & f_{em,2} f_{sh,e,2} A_{\text{sol},op,2} & \cdots & 0 & f_{\text{sky},2} H_{lr,e,2} \\ \vdots & \vdots & \ddots & \vdots & \vdots \\ 0 & 0 & \cdots & f_{em,m} f_{sh,e,m} A_{\text{sol},op,m} & f_{\text{sky},m} H_{lr,e,m} \end{bmatrix} \begin{bmatrix} \varphi_{\text{sol},1} \\ \varphi_{\text{sol},2} \\ \vdots \\ \varphi_{\text{sol},q} \\ \Delta\Theta_{\text{er}} \end{bmatrix}$$

or

$$\boldsymbol{\phi}_{\text{sol},em} = \begin{bmatrix} \mathbf{A}_{\text{sol},em} & \mathbf{h}_{\text{sky},em} \end{bmatrix} \begin{bmatrix} \boldsymbol{\varphi}_{\text{sol}} \\ \Delta\Theta_{\text{er}} \end{bmatrix} \quad (5.26)$$

where  $f_{em,k} = R_{se,k}/(R_{se,k} + R_{1,k})$ ,  $f_{\text{sky},k} = -f_{em,k} F_{r,k}$ ,  $H_{lr,e,k} = h_{lr,e,k} A_k$ , and

$$\begin{aligned} \mathbf{A}_{\text{sol},em} &= \text{diag}(f_{em,1} f_{sh,e,1} A_{\text{sol},op,1}, \dots, f_{em,m} f_{sh,e,m} A_{\text{sol},op,m}) \\ \mathbf{h}_{\text{sky},em} &= (f_{\text{sky},1} H_{lr,e,1}, \dots, f_{\text{sky},q} H_{lr,e,m})^T. \end{aligned}$$

Finally, combining Equations (5.25) and (5.26) gives at once the net solar radiation gain on all nodes in the model in a single vector-matrix equation, given by

$$\begin{bmatrix} \Phi_{\text{sol},a} \\ \boldsymbol{\phi}_{\text{sol},si} \\ \boldsymbol{\phi}_{\text{sol},em} \end{bmatrix} = \begin{bmatrix} f_{sa} \mathbf{a}_{\text{sol}} & H_{\text{sky},a} \\ f_{\text{sol},si} \mathbf{a}_{\text{sol}} & 0_m \\ \mathbf{A}_{\text{sol},em} & \mathbf{h}_{\text{sky},em} \end{bmatrix} \begin{bmatrix} \boldsymbol{\varphi}_{\text{sol}} \\ \Delta\Theta_{\text{er}} \end{bmatrix} \quad (5.27)$$

Equation (5.27) contains all the parameters to account for the solar gain into the zone, due to the orientation of the collecting areas, the external and movable shading, the solar transmittance and absorption and thermal heat transfer characteristics of each surface. It accounts for the radiation exchange with the particles that comprise the atmosphere. It also determines the distribution of the net solar gain amongst the nodes of a general  $n$ -node,  $m$ -surface building zone model.

## 5.6 State-space building zone model

Now recall the previous work of this chapter, where the following thermodynamic processes were determined, along with their respective state-space representation:





1. *Building component heat transfer*: the convective and conductive heat transfer between the air node, building components, and the external environment:

$$\begin{bmatrix} C_{\text{com}} & \mathbf{0}_m \\ \mathbf{0}_m^T & C_a \end{bmatrix} \begin{bmatrix} \dot{\theta}_{\text{ext}}(t) \\ \dot{\theta}_{\text{int}}(t) \\ \dot{\Theta}_a(t) \end{bmatrix} = \mathbf{H}_{\text{tr}} \begin{bmatrix} \theta_{\text{ext}}(t) \\ \theta_{\text{int}}(t) \\ \Theta_a(t) \end{bmatrix} + \mathbf{h}_{\text{tr,ext}} \Theta_{\text{out}}(t) \quad (5.7 \text{ revisited})$$

2. *Radiation heat transfer*: the long-wave radiation exchange between the internal surfaces:

$$\hat{\phi}_r(t) = h_{\text{lr,i}} Y \theta_s(t) \quad (5.12 \text{ revisited})$$

3. *Internal heat gains*: the internal heat gains to the air and internal surfaces from occupants, lighting, & equipment:

$$\phi_{\text{int}}(t) = \begin{bmatrix} f_{\text{int,s}} \\ f_{\text{int,a}} \end{bmatrix} \phi_{\text{HG}}(t) \quad (5.20b \text{ revisited})$$

4. *Solar heat gains*: the net solar gains to the air, internal surfaces, and external (opaque) masses:

$$\begin{bmatrix} \phi_{\text{sol,em}}(t) \\ \phi_{\text{sol,si}}(t) \\ \Phi_{\text{sol,a}}(t) \end{bmatrix} = \begin{bmatrix} \mathbf{A}_{\text{sol,em}} & \mathbf{h}_{\text{sky,em}} \\ f_{\text{sol,si}} \mathbf{a}_{\text{sol}} & \mathbf{0}_m \\ f_{\text{sa}} \mathbf{a}_{\text{sol}} & H_{\text{sky,a}} \end{bmatrix} \begin{bmatrix} \phi_{\text{sol}}(t) \\ \Delta \Theta_{\text{er}}(t) \end{bmatrix} \quad (5.27 \text{ revisited})$$

Using these modules, and their respective parameters, the thermodynamics of the building zone can be represented in state-space form.

The state-variables are the the air, internal, and external component nodes i.e.  $\mathbf{x} = (\theta_{\text{ext}}^T, \theta_{\text{int}}^T, \Theta_a)^T$ . The system inputs are  $\boldsymbol{\mu} = (\Theta_{\text{out}}, \phi_{\text{HG}}^T, \phi_{\text{sol}}^T, \Delta \Theta_{\text{er}})^T$ . Finally, the state differential equation for the building zone is then given by combining eqs. (5.7), (5.12), (5.20b) and (5.27) to give a LTI explicit state-space model:

$$\dot{\mathbf{x}}(t) = \mathbf{A}\mathbf{x}(t) + \mathbf{B}\boldsymbol{\mu}(t) \quad (5.28)$$

where

$$\mathbf{A} = \mathbf{C}^{-1}(\mathbf{H}_{\text{tr}} + \mathbf{H}_r) \quad \mathbf{B} = \mathbf{C}^{-1} \begin{bmatrix} \mathbf{h}_{\text{ext}}^T & \mathbf{0}_{mp_{\text{HG}}} & \mathbf{A}_{\text{sol,em}} & \mathbf{h}_{\text{sky,em}} \\ \mathbf{0}_m & f_{\text{int,si}} & f_{\text{sol,si}} \mathbf{a}_{\text{sol}} & \mathbf{0}_{mp_{\text{sol}}} \\ \mathbf{h}_{\text{nm}} \mathbf{1}_m & f_{\text{int,a}} & f_{\text{sa}} \mathbf{a}_{\text{sol}} & H_{\text{sky,a}} \end{bmatrix}$$

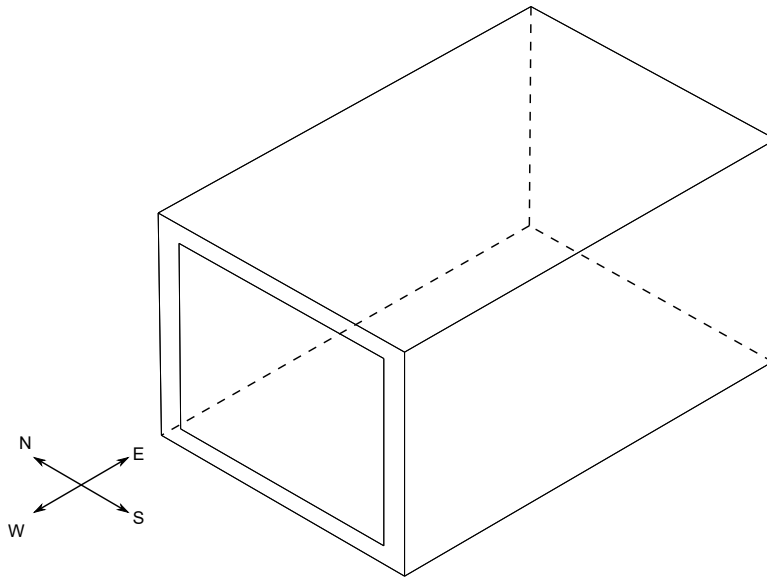


**Figure 5.11** | Wire-frame of building zone with orientation.

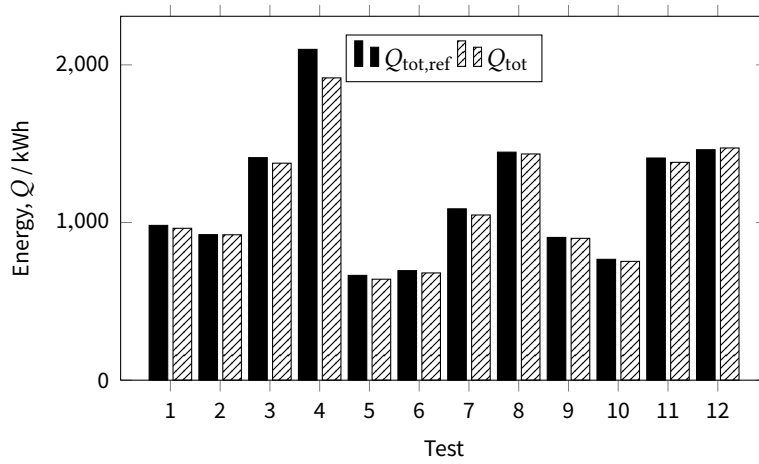


**Figure 5.12** | Yearly total energy needs compared with the reference results.

## 5.7 Validation

The energy use for heating and cooling loads for the building model in eq. (5.28) have been validated using BS EN 15265:2007 (10) and the full details of the validation test report are provided in appendix B.3. A short summary of the results is presented here. Validation of the model with the Standard requires the comparison of yearly calculated results for both heating and cooling loads with given reference values over eight test cases. There are an additional four test cases that are not mandatory, these are provided as informative tests in order to check the basic operation of the model.

The zone modelled is a small office located in Trappes, France for which the climatic data (external air temperature and solar radiation) are provided. Figure 5.11 shows the wire-frame drawing of the office zone modelled, which has dimensions  $3.6\text{ m} \times 5.5\text{ m} \times 2.8\text{ m}$ . Additionally, the thermophysical properties of each material layer of the opaque building components (external wall, internal walls, roof/ceiling and floor) are also provided for each of the test cases. There is ventilation (1 air change per hour) by external air between 08:00 and 18:00 during weekdays. The heating and cooling is intermittent and are only in effect from 08:00 to 18:00 during weekdays. The set point for heating is  $20\text{ }^{\circ}\text{C}$  and cooling is  $26\text{ }^{\circ}\text{C}$ , using air temperature as the controlled variable. For each of the test cases, a major element of the building model is changed in order to assess the model's performance. These involve changing the inertia of the building, removing the internal gains, altering the solar protection and adding an external roof. Full details of each test case can be found in appendix B.3.

The yearly total energy needs for each of the test cases are given in fig. 5.12. The model is able to achieve a level of accuracy classification of Level A, indicating the highest level of agreement with the reference results.

## 5.8 Summary

### 5.8.1 General remarks & review

This chapter has discussed and developed models of the various heat transfer mechanisms within a building zone – with specific considerations throughout for the implementation and utilisation of controller design. The concept of an electrical network analogy was used throughout to model each of the heat transfer mechanisms. Each of the following state-space modules were defined that together comprise the overall thermodynamic model:

- A reduced-order model of the building components was presented that retained the dynamic behaviour of a full order model while offering a reduction in the number of nodes (and therefore differential equations) per component.



- A method to model the radiative heat flow between all surfaces that enclose a building zone was detailed in a linear state-space form, that includes the effects of surface and space resistance.
- The interaction of the internal heat gains (from lighting, appliances, and people) with the zone were defined, and the individual radiative and convective heat flow of each was considered. In addition, the coupling with the electrical network for the lighting and appliances was introduced.
- The solar radiation to through transparent (glazing) and opaque components was defined, as well as the distribution of the solar radiation that enters via the transparent components among the internal surfaces. As well as the radiative heat exchange with the atmosphere from external-facing components.

The model developed is a simplified, convenient, model in a general LTI explicit state-space representation. It has a modular structure so that it can be modified to include servicing systems and added dynamics without having to re-formulate the entire state-space representation, as the state matrices can be concatenated to, or partitioned, without affecting the overall system due to the linear time-invariant nature of the model.

#### 5.8.2 *Impact on this work*

The goal of the model is to act as the base thermodynamic model for the *development* of control strategies for use within buildings, that is capable of rapid processing, while still being adequate for robustness and controller design and analysis, as well as thermodynamic and energy performance.

This ‘controller test bed’ will allow for the design and analysis of control strategies developed for the utilisation of renewable and micro-generation technologies within a building, as it will provide adequate thermal and energy performance computation in order to assess the chosen renewable and micro-generation configuration with a proposed control scheme.

The presentation of this model in an analytical and symbolic manner allows better understanding of the interaction between the heat transfer mechanisms and the input/output relationships within the zone. This will become even more evident in subsequent chapters when considering the its use in inverse-dynamics based control of the building-integrated energy systems.



## References

1. Achterbosch, G., de Jong, P., Krist-Spit, C., van der Meulen, S., Verberne, J. The development of a convenient thermal dynamic building model. *Energy and Buildings* **8**(3): 183–96 (1985-08). DOI: [10.1016/0378-7788\(85\)90003-9](https://doi.org/10.1016/0378-7788(85)90003-9) (cited pp. 109, 127)
2. Riederer, P., Marchio, D., Visier, J., Husaunndee, a., Lahrech, R. Room thermal modelling adapted to the test of HVAC control systems. *Building and Environment* **37**(8-9): 777–90 (2002-08). DOI: [10.1016/S0360-1323\(02\)00052-5](https://doi.org/10.1016/S0360-1323(02)00052-5) (cited p. 109)
3. Khalid, Y. A. Controllability of Building Systems. PhD thesis. University of Strathclyde, 2011: 364 (cited p. 109)
4. Murphy, G. B., Counsell, J., Allison, J., Brindley, J. Calibrating a combined energy systems analysis and controller design method with empirical data. *Energy* **57**: 484–94 (2013-08). DOI: [10.1016/j.energy.2013.06.015](https://doi.org/10.1016/j.energy.2013.06.015) (cited pp. 109, 112)
5. Foucquier, A., Robert, S., Suard, F., Stéphan, L., Jay, A. State of the art in building modelling and energy performances prediction: A review. *Renewable and Sustainable Energy Reviews* **23**: 272–88 (2013-07). DOI: [10.1016/j.rser.2013.03.004](https://doi.org/10.1016/j.rser.2013.03.004) (cited p. 110)
6. Rumianowski, P., Brau, J., Roux, J. J. An adapted model for simulation of the interaction between a wall and the building heating system. In *Proceedings of the thermal performance of the exterior envelopes of buildings IV*. Orlando, USA: Oak Ridge National Laboratory (ORNL), 1989: 224–33. URL: <http://web.ornl.gov/sci/buildings/2012/1989%20B4%20papers/020.pdf> (cited p. 110)
7. ESP-r [computer program]. *Version X*. Glasgow, UK: Energy Systems Research Unit | University of Strathclyde. 2014. URL: <http://www.esru.strath.ac.uk/Programs/ESP-r.htm> (cited p. 110)
8. EnergyPlus [computer program]. *Version 8.1.0*. U.S. Department of Energy. 2013. URL: [www.eere.energy.gov/buildings/energyplus](http://www.eere.energy.gov/buildings/energyplus) (cited p. 110)
9. Et al Klein, S. *TRNSYS 17: A Transient System Simulation Program*. Madison, USA: Solar Energy Laboratory | University of Wisconsin, 2010. URL: <http://sel.me.wisc.edu/trnsys> (cited p. 110)
10. BS EN 15265:2007. *Energy performance of buildings. Calculation of energy needs for space heating and cooling using dynamic methods. General criteria and validation procedures*. 1st ed. London, UK: British Standards Institution, 2007. ISBN: 978-0-580-55627-2. DOI: [10.3403/30136887](https://doi.org/10.3403/30136887) (cited pp. 110, 116, 141)
11. Dorf, R. C., Bishop, R. H. *Modern Control Systems*. 12th ed. Upper Saddle River, New Jersey: Prentice Hall, 2011: 1104. ISBN: 978-0-13-602458-3 (cited p. 111)
12. Franklin, G. F., Powell, J. D., Emami-Naeini, A. *Feedback Control of Dynamic Systems*. 6th ed. Upper Saddle River, New Jersey: Pearson Education, Inc., 2010: 837. ISBN: 978-0-13-500150-9 (cited p. 111)
13. Slotine, J.-J. E., Li, W. *Applied Nonlinear Control*. New Jersey: Prentice Hall, 1991: 461. ISBN: 0-13-040890-5 (cited p. 111)
14. Ramallo-González, A. P., Eames, M. E., Coley, D. A. Lumped parameter models for building thermal modelling: An analytic approach to simplifying complex multi-layered constructions. *Energy and Buildings* **60**: 174–84 (2013-05). DOI: [10.1016/j.enbuild.2013.01.014](https://doi.org/10.1016/j.enbuild.2013.01.014) (cited p. 112)





15. Çengel, Y. A. *Heat and mass transfer: A practical approach*. third. New York, NY: McGraw-Hill, 2007: 901. ISBN: 978-0-07-312930-3 (cited pp. 112, 134)
16. BS EN ISO 6946:2007. *Building components and building elements. Thermal resistance and thermal transmittance. Calculation method*. 2nd ed. London, UK: British Standards Institution, 2007. ISBN: 978-0-580-54937-3.  
DOI: 10.3403/30127651. URL: <https://bsol.bsigroup.com/Bibliographic/BibliographicInfoData/000000000030127651> (cited pp. 113, 114)
17. CIBSE. *CIBSE Guide A: Environmental Design*. 7th ed. London, UK: Chartered Institution of Building Services Engineers, 2006: 323. ISBN: 978-1-903287-66-8 (cited pp. 115, 123, 128, 129, 132, 134)
18. BS EN ISO 13786:2007. *Thermal performance of building components. Dynamic thermal characteristics. Calculation methods*. 2nd ed. London, UK: British Standards Institution, 2007. ISBN: 978-0-580-67099-2.  
DOI: 10.3403/30129545. URL: <https://bsol.bsigroup.com/Bibliographic/BibliographicInfoData/000000000030200150> (cited p. 115)
19. Pipes, L. Matrix analysis of heat transfer problems. *Journal of the Franklin Institute* **263**(3): 195–206 (1957).  
DOI: 10.1016/0016-0032(57)90927-4 (cited p. 115)
20. BS EN ISO 7726:2001. *Ergonomics of the thermal environment. Instruments for measuring physical quantities*. 2nd ed. 1. London, UK: British Standards Institution, 2001. ISBN: 0-580-38651-1.  
DOI: 10.3403/02509505. URL: <https://bsol.bsigroup.com/Bibliographic/BibliographicInfoData/000000000030066593> (cited p. 122)
21. Oppenheim, A. K. Radiation analysis by the network method. *Transactions of the ASME*: 725–35 (1956) (cited pp. 123, 125, 126)
22. Mazumder, S., Ravishankar, M. General procedure for calculation of diffuse view factors between arbitrary planar polygons. *International Journal of Heat and Mass Transfer* **55**(23-24): 7330–5 (2012-11).  
DOI: 10.1016/j.ijheatmasstransfer.2012.07.066 (cited p. 125)
23. Lauzier, N. *View Factors*. 2004. URL: <http://www.mathworks.co.uk/matlabcentral/fileexchange/5664-view-factors> (cited p. 125)
24. Kron, G. A set of principles to interconnect the solutions of physical systems. *Journal of Applied Physics* **24**(8): 965–80 (1953).  
DOI: 10.1063/1.1721447 (cited p. 126)
25. Korolija, I., Marjanovic-Halburd, L., Zhang, Y., Hanby, V. I. UK office buildings archetypal model as methodological approach in development of regression models for predicting building energy consumption from heating and cooling demands. *Energy and Buildings* **60**: 152–62 (2013-05).  
DOI: 10.1016/j.enbuild.2012.12.032 (cited p. 128)
26. Johnston, J., Counsell, J. M., Strachan, P. A. Trends in office internal gains and the impact on space heating and cooling demands. In *CIBSE Technical Symposium 2011*. Leicester, UK: Chartered Institution of Building Services Engineers, 2011 (cited pp. 128, 129)
27. BS EN ISO 13790:2008. *Energy performance of buildings. Calculation of energy use for space heating and cooling*. 2nd ed. London, UK: British Standards Institution, 2008: 172. ISBN: 978-0-580-55359-2.  
DOI: 10.3403/30133624. URL: <https://bsol.bsigroup.com/Bibliographic/BibliographicInfoData/000000000030133624> (cited pp. 129, 131, 132, 136)



28. Ahn, B.-L., Jang, C.-Y., Leigh, S.-B., Yoo, S., Jeong, H. Effect of LED lighting on the cooling and heating loads in office buildings. *Applied Energy* **113**: 1484–9 (2014-01).  
DOI: [10.1016/j.apenergy.2013.08.050](https://doi.org/10.1016/j.apenergy.2013.08.050) (cited p. 130)
29. U.S. Department of Energy | Office of Energy Efficiency & Renewable Energy. *Thermal Management of White LEDs*. PNNL-SA-51901. 2007-02. URL: [http://apps1.eere.energy.gov/buildings/publications/pdfs/ssl/thermal%7B%5C\\_%7Dled%7B%5C\\_%7Dfeb07%7B%5C\\_%7D2.pdf](http://apps1.eere.energy.gov/buildings/publications/pdfs/ssl/thermal%7B%5C_%7Dled%7B%5C_%7Dfeb07%7B%5C_%7D2.pdf) (cited p. 131)
30. Hosni, M. H., Beck, B. *Update to measurements of office equipment heat gain data*. ASHRAE Research Project RP-1482. 2011 (cited p. 132)
31. Hosni, M. H., Jones, B. W., Xu, H. Experimental results for heat gain and radiant/convective split from equipment in buildings. In *ASHRAE Transactions*. Vol. 105. 2. Seattle, WA: American Society of Heating, Refrigerating and Air-Conditioning Engineers, 1999: 527–39. URL: <http://www.techstreet.com/ashrae/products/1703542> (cited p. 132)
32. Yu, C.-Y., Lin, C.-H., Yang, Y.-H. Human body surface area database and estimation formula. *Burns* **36**(5): 616–29 (2010-08).  
DOI: [10.1016/j.burns.2009.05.013](https://doi.org/10.1016/j.burns.2009.05.013) (cited p. 133)
33. BS EN ISO 8996:2004. *Ergonomics of the thermal environment. Determination of metabolic rate*. 2nd ed. London, UK: British Standards Institution, 2004. ISBN: 0-580-45322-7.  
DOI: [10.3403/03205220](https://doi.org/10.3403/03205220). URL: <https://bsol.bsigroup.com/Bibliographic/BibliographicInfoData/000000000030092320> (cited p. 133)



*“Usually in Mathematics you have an equation and you want to find a solution. Here you are given a solution and you have to find the equation. I liked that.”*

---

—JULIA ROBINSON, *Julia: A Life in Mathematics*

6

## Inversion-based control of MIMO energy systems

THE objective of this research – as specified in chapter 1 – is to design a control strategy for hybrid building-integrated energy systems that can make the building more energy autonomous while adhering to requirements on building environmental conditions. While the quantitative measures of controller performance will be covered in chapter 7, the minimal requirements of an acceptable controller design are a satisfactory response to the building demands (internal air temperature, electrical load demand etc.), less sensitive to changes in building operation and/or modelling inaccuracies, and is able to attenuate the effect of undesirable disturbances on the building/plant operation.

In order to develop a control strategy that will fulfil these requirements, it was necessary to develop mathematical models of the systems in the previous two chapters 4 and 5, which allows the complex interaction between the various elements to be understood and analysed. However, these dynamic mathematical models utilise what is known as **internal** representations of the systems i.e. the models are state-space models where the physical system is characterised by a set of state-variables, each of which describes how energy is stored in the system. In this form, however, the dynamical behaviour between the inputs and outputs is not explicit, which means designing the structure of the control system for complex interconnected energy systems can become very difficult.

This chapter first describes how to transform the models from an internal representation to an **external** representation where the dynamic system model is a set of higher-order differential equations in the inputs and outputs. Subsequently a control strategy is developed that utilises this representation in order to develop an ‘ideal’



energy systems control algorithm suitable for determining the feasibility of a proposed control structure. Finally a similar control strategy is developed that is the first stage in making the identified ideal control realisable in practice.

### 6.1 External differential representation

Consider a general continuous system with control inputs  $\mathbf{u}$  and outputs  $\mathbf{y}$

$$\Xi : \begin{cases} \dot{\mathbf{x}}(t) = \mathbf{f}(\mathbf{x}(t), \mathbf{u}(t)) \\ \mathbf{y}(t) = \mathbf{h}(\mathbf{x}(t), \mathbf{u}(t)) \end{cases}$$

If the dynamics of  $\Xi$  are known it may be possible to design an inverse system  $\Xi^{-1}$  such that the control input  $\mathbf{u}(t)$  can be computed given a desired output  $\mathbf{y}_d(t)$  from  $\Xi$ .

Note that the system representation is not an explicit expression relating the inputs to the outputs as the output is also expressed as a function of the internal states  $\mathbf{x}$ . The following section describes an approach to eliminating the states in  $\Xi$  and to obtain a direct expression between the system inputs and outputs.

In energy systems it can be difficult to obtain on-line measurement of important state variables (e.g. inner tank temperatures in TES tanks, bulk engine block temperature in mCHP engines, radiator temperatures) because of limitations in the sensor technology, access restrictions, and infrastructure costs. Therefore, inverse dynamics based controllers that rely on knowledge of these measurements must rely on state estimation techniques. An alternative scheme is a mathematical approach called the External Differential Representation (EDR) that allows for the prediction of the time evolution of the measured outputs based on only the measurement of the outputs and the system inputs. i.e. an EDR allows for the output of a process to be reconstructed from only part knowledge of the overall system.

For example, consider a system consisting of a mCHP unit, hydronic network and radiators, where the control goal is to manipulate the fuel flow rate into the engine to regulate the air temperature of the building. The energy demand will vary depending on the intermediate temperatures of the engine block, cooling water inlet and outlet temperatures, pump pressure, radiator inlet and outlet temperatures, internal surface temperatures within the building, among other state variables. From a reasonable model of the overall system (including bounded estimates of the system parameters) the EDR of the same system would enable a continuous prediction of air temperature based only on the feedback of the prior input of fuel and previous measurements of the air temperature. As will be shown, this facilitates the application of superior controllers with the capability of regulating the process within a narrow range about the set point.





Mathematically then, the EDR of an  $n$ -th order SISO system in general form is given by the following higher-order differential equation:

$$y^{(n)}(t) = \varphi(y(t), \dots, y^{(n-1)}(t), u(t), \dots, u^{(\beta)}(t)),$$

where it is clear the time evolution of  $y$  is based only on knowledge of the output, the input, and their derivatives. This section describes an algorithm that can transform the models developed in the previous chapters into EDRs suitable for inverse dynamics controller design.

Consider a general multi-variable nonlinear system described in a state-space representation as

$$\Xi : \begin{cases} \dot{\mathbf{x}}(t) = \mathbf{f}(\mathbf{x}(t), \boldsymbol{\mu}(t)) & (6.1a) \\ \mathbf{y}(t) = \mathbf{h}(\mathbf{x}(t), \boldsymbol{\mu}(t)) & (6.1b) \end{cases}$$

where  $\mathbf{x}(t) \in \mathbb{R}^n$  is the state vector (comprised of the state-variables),  $\boldsymbol{\mu}(t)$  is the system input vector (comprised of all inputs to the system including the control inputs, disturbances, command signals etc.),  $\mathbf{y}(t)$  is the output vector (comprised of all the measured/controlled variables), and  $\mathbf{f} : \mathbb{R}^n \times \mathbb{R}^m \rightarrow \mathbb{R}^n$ ,  $\mathbf{h} : \mathbb{R}^n \times \mathbb{R}^m \rightarrow \mathbb{R}^p$  are assumed to be smooth continuous functions over the range of interest.

The system  $\Xi$  in eq. (6.1) is nonlinear, just as very nearly all real world processes that are controlled are nonlinear (1, p. 49, 2, p. 620, 3, p. 53). However, for small perturbations from a set operating point a nonlinear system's behaviour will correspond to an equivalent linear model. If the selected operating point is a stable equilibrium point of the nonlinear system, then Lyapunov's linearisation theory (4)<sup>1</sup> proves that there is a region around this point for which the real nonlinear system is stable. The result of that work is that if a sufficient linear model is designed so that it approximates the nonlinear one, then both the analysis and control design methods applicable to the linear model will be valid for the real nonlinear system (in the region of the equilibrium).

Taking the Taylor series expansion about an equilibrium point of  $\Xi$  for each multivariable function in (6.1) and truncating the series above the first order terms results in the set of LTI differential equations in state-space that approximate the dynamics of the nonlinear system  $\Xi$  as (see appendix D.2 for the derivation)

$$\dot{\mathbf{x}}(t) = \mathbf{A}\mathbf{x}(t) + \mathbf{B}\boldsymbol{\mu}(t), \quad (6.2a)$$

$$\mathbf{y}(t) = \mathbf{C}\mathbf{x}(t) + \mathbf{D}\boldsymbol{\mu}(t), \quad (6.2b)$$

---

<sup>1</sup>Reference is an English translation of Lyapunov's original 1892 memoir which was published in Russian by the Mathematical Society of Kharkov.



where  $\mathbf{x}(t) \in \mathbb{R}^n$  is the state vector,  $\boldsymbol{\mu}(t) \in \mathbb{R}^m$  is the input vector,  $\mathbf{y}(t) \in \mathbb{R}^p$  is the output vector,  $\mathbf{A} = (a_{ij}) \in \mathbb{R}^{n \times n}$  is the plant matrix,  $\mathbf{B} = (b_{ij}) \in \mathbb{R}^{n \times m}$  is the input matrix,  $\mathbf{C} = (c_{ij}) \in \mathbb{R}^{p \times n}$  is the output matrix and  $\mathbf{D} = (d_{ij}) \in \mathbb{R}^{p \times m}$  is the feedforward matrix.

In this work this method of obtaining a linear approximation of the nonlinear system is called the **Jacobian linearisation** of system  $\Xi$  around the equilibrium  $(\mathbf{x}_o, \boldsymbol{\mu}_o)$  in order to make a distinction between this and the more ‘exact’ linearisation techniques utilised later in this work.

### 6.1.1 External representation algorithm

For continuous LTI state-space systems, it is possible to obtain the the dynamic input-output response of the system by beginning with the general equations of state (6.2) and considering the problem in the frequency domain. In the frequency domain linear constant-coefficient differential equations are transformed into algebraic equations. The algebraic equation can be solved and then transformed back to find the solution of the differential equation.

The Laplace transform of a function  $f(t)$  can be used for this purpose and is given as

$$\mathcal{L}\{f(t)\} = f(s) = \int_0^{\infty} f(t)e^{-st} dt$$

where  $s$  is a complex variable. It is assumed that the reader is familiar with the concept of Laplace transforms and transfer functions of LTI systems and their relation to control systems, however there are several good textbooks for reference (5, ch. 2, 1, ch. 2). The Laplace transform of the derivative  $f^{(k)}$  is given by (see 6, ch. 5, thm. 2):

$$\begin{aligned} \mathcal{L}(f^{(k)}) &= s^k \mathcal{L}(f) - s^{k-1}f(0) - s^{k-2}\dot{f}(0) - \dots - f^{(k-1)}(0), \\ \mathcal{L}(f^{(k)}) &= s^k \mathcal{L}(f) - \sum_{j=1}^k s^{k-j} f^{(j-1)}(0). \end{aligned} \quad (6.3)$$

where it is assumed that  $f$  is a minimum of  $n$ -times differentiable. Taking the Laplace transform of the state and output equations by utilising eq. (6.3)

$$\begin{aligned} \mathcal{L}(\dot{\mathbf{x}}) &= \mathcal{L}\{\mathbf{A}\mathbf{x}(t) + \mathbf{B}\boldsymbol{\mu}(t)\}, \\ \implies s\mathbf{x}(s) - \mathbf{x}(0) &= \mathbf{A}\mathbf{x}(s) + \mathbf{B}\boldsymbol{\mu}(s), \end{aligned} \quad (6.4a)$$

$$\begin{aligned} \mathcal{L}(\mathbf{y}) &= \mathcal{L}\{\mathbf{C}\mathbf{x}(t) + \mathbf{D}\boldsymbol{\mu}(t)\}, \\ \implies \mathbf{y}(s) &= \mathbf{C}\mathbf{x}(s) + \mathbf{D}\boldsymbol{\mu}(s). \end{aligned} \quad (6.4b)$$

The system (6.4) is now comprised of algebraic equations. Then, solving for  $\mathbf{x}(s)$  in



eq. (6.4a),<sup>2</sup>

$$(s\mathbf{I}_n - \mathbf{A})\mathbf{x}(s) = \mathbf{B}\boldsymbol{\mu}(s) + \mathbf{x}(0),$$

premultiplying both sides by  $(s\mathbf{I}_n - \mathbf{A})^{-1}$  gives

$$\mathbf{x}(s) = (s\mathbf{I}_n - \mathbf{A})^{-1}(\mathbf{B}\boldsymbol{\mu}(s) + \mathbf{x}(0)). \quad (6.5)$$

Substituting eq. (6.5) into eq. (6.4b) yields

$$\begin{aligned} \mathbf{y}(s) &= \mathbf{C}(s\mathbf{I}_n - \mathbf{A})^{-1}(\mathbf{B}\boldsymbol{\mu}(s) + \mathbf{x}(0)) + \mathbf{D}\boldsymbol{\mu}(s), \\ \mathbf{y}(s) &= \underbrace{(\mathbf{C}(s\mathbf{I}_n - \mathbf{A})^{-1}\mathbf{B} + \mathbf{D})}_{{}^{\mu}\mathbf{G}(s)}\boldsymbol{\mu}(s) + \underbrace{\mathbf{C}(s\mathbf{I}_n - \mathbf{A})^{-1}}_{{}^0\mathbf{G}(s)}\mathbf{x}(0) \end{aligned} \quad (6.6)$$

$$\mathbf{y}(s) = {}^{\mu}\mathbf{G}(s)\boldsymbol{\mu}(s) + {}^0\mathbf{G}(s)\mathbf{x}(0),$$

where  ${}^{\mu}\mathbf{G}(s)$  is a  $p \times m$  transfer function matrix that relates the output vector,  $\mathbf{y}(s)$ , to the input vector,  $\boldsymbol{\mu}(s)$ , and  ${}^0\mathbf{G}(s)$  is a  $p \times n$  transfer function matrix that relates the output to the initial conditions of state.

Define the **fundamental matrix** as

$$(s\mathbf{I}_n - \mathbf{A})^{-1} = \frac{\text{adj}(s\mathbf{I}_n - \mathbf{A})}{\det(s\mathbf{I}_n - \mathbf{A})}, \quad (6.7)$$

where  $\det(s\mathbf{I}_n - \mathbf{A}) = \delta(s)$  and when evaluated yields an  $n$ th-order monic polynomial in  $s$ , i.e.  $\delta(s) = s^n + \alpha_2 s^{n-1} + \dots + \alpha_{n+1}$ . When this is set to zero, it is known as the **characteristic equation** of the LTI state-space system.<sup>3</sup> The matrix  $\text{adj}(s\mathbf{I}_n - \mathbf{A}) = \mathbf{N}(s)$ , where the  $n \times n$  matrix  $\mathbf{N}(s)$  is the adjoint of  $(s\mathbf{I}_n - \mathbf{A})$ .<sup>4</sup> Equation (6.7) can now be expressed as

$$(s\mathbf{I}_n - \mathbf{A})^{-1} = \frac{1}{\delta(s)}\mathbf{N}(s). \quad (6.8)$$

Substituting eq. (6.8) into eq. (6.6) yields

$$\mathbf{y}(s) = \left( \mathbf{C} \frac{1}{\delta(s)} \mathbf{N}(s) \mathbf{B} + \mathbf{D} \right) \boldsymbol{\mu}(s) + \mathbf{C} \frac{1}{\delta(s)} \mathbf{N}(s) \mathbf{x}(0)$$

<sup>2</sup> $\mathbf{I}$  is the identity matrix, with ones on the main diagonal and zeros elsewhere.

<sup>3</sup>The roots of this equation (commonly called the **poles**) are frequently used in the analysis of LTI systems to give an indication of the qualitative characteristic behaviour of the response i.e. to assess the stability of the system and determine the time response.

<sup>4</sup>The adjoint of a matrix  $\mathbf{X}$ , denoted  $\text{adj}(\mathbf{X})$  is the transpose of the matrix formed by taking the cofactor of each element of  $\mathbf{X}$ . If the determinant of  $\mathbf{X}$ ,  $\det(\mathbf{X}) \neq 0$ , then  $\mathbf{X}^{-1} = \text{adj}(\mathbf{X})/\det(\mathbf{X})$  as utilised in (6.7).



or

$$\begin{aligned}\delta(s)\mathbf{y}(s) &= \underbrace{(\mathbf{C}\mathbf{N}(s)\mathbf{B} + \delta(s)\mathbf{D})}_{\mathbf{N}(s)} \boldsymbol{\mu}(s) + \underbrace{\mathbf{C}\mathbf{N}(s)}_{\mathbf{N}(s)} \mathbf{x}(0) \\ \delta(s)\mathbf{y}(s) &= {}^{\mu}\mathbf{N}(s)\boldsymbol{\mu}(s) + {}^0\mathbf{N}(s)\mathbf{x}(0),\end{aligned}\quad (6.9)$$

where  ${}^{\mu}\mathbf{N}(s)$  is a  $p \times m$  polynomial matrix and  ${}^0\mathbf{N}(s)$  is a  $p \times n$  polynomial matrix i.e. each element of the matrices  $({}^{\mu}\mathbf{N}(s), {}^0\mathbf{N}(s))$  is a polynomial in  $s$  of the form  $v_1 + v_2s + v_3s^2 + \dots + v_{\beta_{ij}+1}s^{\beta_{ij}}$ .

In order to best understand the structure of eq. (6.9) consider its expanded form as

$$\delta(s) \begin{bmatrix} y_1(s) \\ \vdots \\ y_p(s) \end{bmatrix} = \begin{bmatrix} {}^{\mu}N_{11}(s) & \dots & {}^{\mu}N_{1m}(s) \\ \vdots & \vdots & \vdots \\ {}^{\mu}N_{p1}(s) & \dots & {}^{\mu}N_{pm}(s) \end{bmatrix} \begin{bmatrix} \mu_1(s) \\ \vdots \\ \mu_m(s) \end{bmatrix} + \begin{bmatrix} {}^0N_{11}(s) & \dots & {}^0N_{1n}(s) \\ \vdots & \vdots & \vdots \\ {}^0N_{p1}(s) & \dots & {}^0N_{pn}(s) \end{bmatrix} \begin{bmatrix} x_1(0) \\ \vdots \\ x_n(0) \end{bmatrix} \quad (6.10)$$

Extracting the  $i$ th output channel from eq. (6.10) gives the linear external differential representation (LEDR) of the  $i$ th output of eq. (6.2) in the frequency-domain:

$$s^n y_i(s) = - \sum_{j=1}^n \alpha_{j+1} s^{n-j} y_i(s) + \sum_{j=1}^m {}^{\mu}N_{ij}(s) \mu_j(s) + \sum_{j=1}^n {}^0N_{ij}(s) x_j(0). \quad (6.11)$$

It is now possible to utilise the inverse Laplace transform of eq. (6.11) to obtain the LEDR of output  $y_i$  in the time-domain.

First begin by expanding the  $N_{ij}(s)$  polynomials into their constituent coefficients. Each polynomial  $N_{ij}(s)$  can be expressed as  $N_{ij}(s) = {}^{ij}v_1 + {}^{ij}v_2s + \dots + {}^{ij}v_{\beta_{ij}+1}s^{\beta_{ij}}$  or in compact notation  $N_{ij}(s) = \sum_{k=1}^{\beta_{ij}+1} {}^{ij}v_k s^{k-1}$ , where  ${}^{ij}v_k$  denotes the  $k$ th coefficient of the polynomial  $N_{ij}(s)$  for the  $i$ th output to the  $j$ th input. Then eq. (6.11) becomes

$$s^n y_i(s) = - \sum_{j=1}^n \alpha_{j+1} s^{n-j} y_i(s) + \sum_{j=1}^m \sum_{k=1}^{\beta_{ij}+1} {}^{ij}v_k s^{k-1} \mu_j(s) + \sum_{j=1}^n \sum_{k=1}^{\beta_{ij}+1} {}^{ij}v_k s^{k-1} x_j(0). \quad (6.12)$$

Utilising eq. (6.3) the inverse Laplace transform of eq. (6.12) is given by

$$y_i^{(n)}(t) = - \sum_{j=1}^n \alpha_{j+1} y_i^{(n-j)}(t) + \sum_{j=1}^m \sum_{k=1}^{\beta_{ij}+1} {}^{ij}v_k \mu_j^{(k-1)}(t), \quad (6.13a)$$

$$y_i^{(n)}(t) = \varphi_i(\tilde{\mathbf{y}}, \tilde{\boldsymbol{\mu}}). \quad (6.13b)$$

where  $\tilde{\mathbf{y}} = (y_1, \dots, y_1^{(n-1)}, \dots, y_p, \dots, y_p^{(n-1)})^T$  and the highest-order derivative of each system input  $\mu_i$  that appears in eq. (6.13) is denoted  $\beta_i$ , where for matrix  $\boldsymbol{\beta}_{\text{idx}} = (\beta_{ij})$ ,





$\beta_i = \max(\text{col}_i \boldsymbol{\beta}_{\text{idx}})$  so that  $\tilde{\boldsymbol{\mu}} = (\mu_1, \dots, \mu_1^{(\beta_1)}, \dots, \mu_m, \dots, \mu_m^{(\beta_m)})$  and the initial conditions resolve to zero (see appendix C.1). Equation (6.13) is a higher-order differential equation that explicitly relates the system inputs  $\boldsymbol{\mu}$  to the output  $y_i$ . In vector-matrix form for all outputs of the system:

$$\begin{bmatrix} y_1^{(n)}(t) \\ \vdots \\ y_p^{(n)}(t) \end{bmatrix} = \begin{bmatrix} \varphi_1(\tilde{\mathbf{y}}, \tilde{\boldsymbol{\mu}}) \\ \vdots \\ \varphi_p(\tilde{\mathbf{y}}, \tilde{\boldsymbol{\mu}}) \end{bmatrix}, \quad (6.14)$$

this has now produced a set of higher-order differential equations in the inputs and outputs that forms the so-called EDR of the LTI state-space system  $\Xi$  in eq. (6.4).

While the idea of constructing an LEDR from the state-space representation of a system has been mentioned in several works (7, ch. 4), to the author's knowledge no such algorithm has been explicitly defined. Furthermore, the author has developed a set of functions for MATLAB<sup>®</sup> that leverages the Symbolic Math Toolbox<sup>™</sup> to implement the algorithm in this section that will transform any<sup>5</sup> nonlinear system into its LEDR representation.

### 6.1.2 Identification of models from monitored data

The last two chapters have focused on the development of the mathematical models that are used to represent the energy system and the environment in which they operate. While effort was made to simplify the dynamics, the resulting mathematical models are still complex and require a number of parameters to characterise the behaviour of a specific system. Even then, the mCHP model used was still a grey-box model as the dynamics of the inner workings of the engine and heat exchangers are difficult to derive from first principles. Therefore, it would be particularly useful if the controller designs developed in this work are also suitable for models obtained from experimental data. For example, given a mCHP unit, by measuring the fuel input and the resulting outputs there are techniques to develop a mathematical model based on only these measurements. The resulting identified model is usually expressed in an EDR. The controller design based on a general EDR system can then be applied directly to the identified system.

It would also be possible to construct a neural network for the system model that would continually update the identified dynamical system model in real-time, from which the control could not only continually improve, but could also adapt to changes in system use and changes in operational performance (e.g. changes in unit efficiency

<sup>5</sup>For purely symbolic models of high-order this could result in significant computational expense so “any” will be limited to the resources available to the computer.



due to wear/age). This concept and its applicability to this work is explored further in the future work § 9.3.

## 6.2 Inverse dynamics controller design

In § 3.3 it was shown that in order to develop a system inverse it was necessary to transform the system from its internal state-space representation to an EDR, an algorithm for which was developed in § 6.1. It is now possible to construct an inverse dynamics controller for MIMO energy systems such as heat and power supplied by mCHP.

Note that while this work utilises the LEDR, the controller design is equally applicable to a nonlinear EDR if it is available. Indeed, all the controller design methods in this work are applicable to nonlinear systems. Furthermore, while the LEDR algorithm resulted in each output differential equation being of order  $n$ , models acquired via identification techniques or from nonlinear EDR models may have differing orders for each output. Therefore, the control algorithm has been designed for systems represented in the following locally equivalent differential input-output (IO) form:

$$\begin{aligned} y_1^{(n_1)}(t) &= \varphi_1(\tilde{\mathbf{y}}, \tilde{\boldsymbol{\mu}}) \\ &\vdots \\ y_p^{(n_p)}(t) &= \varphi_p(\tilde{\mathbf{y}}, \tilde{\boldsymbol{\mu}}) \end{aligned} \tag{6.15}$$

where  $\tilde{\mathbf{y}} = (y_1, \dots, y_1^{(n_1-1)}, \dots, y_p, \dots, y_p^{(n_p-1)})^T$ ,  $\tilde{\boldsymbol{\mu}} = (\mu_1, \dots, \mu_1^{(\beta_1)}, \dots, \mu_m, \dots, \mu_m^{(\beta_m)})$ .

### 6.2.1 Controllability conditions

In order to obtain an inverse dynamic controller the system must be **square**, that is there are an equal number of ( $m_0$ ) control inputs (manipulated variables) to the  $p$  system outputs (controlled variables). A system with an excess of control inputs ( $m_0 > p$ ) is known as a **fat system** while a system with additional output measurements ( $p > m_0$ ) is known as a **tall system** (8). These are explored further in §§ 6.2.3.

Up until now the system representations have only considered the *system* inputs. However, not all of the system inputs will be candidates for control inputs. For example, in the absence of variable shading, the amount of incident solar radiation received through the glazing of a building is a system input but could not be considered as a control input since it is not directly manipulable by the control engineer. Similarly, the amount of available energy from a static PV array will be considered a system input but not a control input since that amount of energy is injected into the system



and must be dealt with. However, if the PV array had a solar tracker to orientate the panels (either directly at the sun or even away from the sun) then axis tilt *could* be a control input. It is, therefore, essential that the division of the system inputs into potential control inputs be considered on a case-by-case basis. The remaining subset of system inputs that are not control candidates are designated as exogenous inputs.

The exogenous inputs are a generalised input vector  $\boldsymbol{\psi} \in \mathbb{R}^{m_1+m_2}$  that contains all the inputs originating from outside the model and are unexplained by the model e.g. outside ambient temperature, electrical demand loads, metabolic gains, process noise, measurement noise, are all examples of system inputs that can affect the controlled process that are not modelled by the system itself.

The exogenous inputs can be further split into those inputs that are measured and those that are not. The measured exogenous inputs are comprised of all the measurements that are available to the controller but cannot be manipulated, this includes the command/deterministic inputs. The unmeasured inputs are typically considered as the ‘disturbance’ inputs and are comprised of the process noise, measurement noise, modelling error, and unmeasured system inputs. It is worth noting that in the control of energy systems not all disturbances are inherently bad: metabolic heat gains and solar irradiation are essentially ‘free heat’, it is all relative to the magnitude and at what time these disturbances occur whether they should be rejected or captured within the controlled system.

Now, without loss of generality, the system input vector can be split into sub-vectors as  $\boldsymbol{\mu} = (\mathbf{u}^T, \boldsymbol{\psi}^T)^T = (\mathbf{u}^T, \mathbf{w}^T, \mathbf{d}^T)^T$ , where  $\mathbf{u} \in \mathbb{R}^{m_0}$  is the **control** input vector and  $\mathbf{w} \in \mathbb{R}^{m_1}$  is the **measured** input vector, and  $\mathbf{d} \in \mathbb{R}^{m_2}$  is the **disturbance** input vector.

For the time being it is assumed that the subset of remaining system inputs that are not controlled inputs are all measured exogenous signals. Chapter 7 addresses the issues of modelling error, unmeasured disturbance inputs etc.

### 6.2.2 Symbolic computation of inverse dynamics controller

Assume now that the system is square so that  $m_0 = p$  and  $(\varphi_1, \dots, \varphi_p)$  are continuously differentiable. The set of higher-order differential equations (6.15) representing the system can be re-written as a set of implicit equations:

$$\begin{aligned} P_i(y_1, \dots, y_1^{(n_1)}, \dots, y_p, \dots, y_p^{(n_p)}, \\ \mu_1, \dots, \mu_1^{(\beta_1)}, \dots, \mu_m, \dots, \mu_m^{(\beta_m)}) = y_i^{(n_i)} - \varphi_i(\tilde{\mathbf{y}}, \tilde{\boldsymbol{\mu}}) = 0, \quad i = 1, \dots, p \end{aligned} \quad (6.16)$$

Now in eq. (6.16) split the  $m$  system inputs into  $m_0 = p$  control inputs and  $m_1$  measured exogenous inputs i.e.  $m = m_0 + m_1 = p + m_1$ . In order to construct the inverse dynamics



controller instead of considering the system output  $y_i(t)$  in eq. (6.16) recall fig. 3-3 where the system output is replaced with the desired output of the system and is fed as an ‘input’ to the inverse system. That is, assume that each system output  $y_i(t)$  is identical to the reference output  $y_{d,i}$ , i.e.  $y_i(t) \equiv y_{d,i}(t), \forall t \geq 0$ , which implies that

$$y_i^{(k)}(t) = y_{d,i}^{(k)}(t) \quad k = 0, \dots, n \quad \forall t \geq 0. \quad (6.17)$$

With these substitutions eq. (6.16) can be expressed as

$$\begin{aligned} P_i(y_{d,1}, \dots, y_{d,1}^{(n_1)}, \dots, y_{d,p}, \dots, y_{d,p}^{(n_p)}, \\ u_1, \dots, u_1^{(\beta_1)}, \dots, u_p, \dots, u_p^{(\beta_p)}, \\ w_1, \dots, w_1^{(\beta_1)}, \dots, w_{m_1}, \dots, w_{m_1}^{(\beta_{m_1})}) = 0, \quad i = 1, \dots, p \end{aligned} \quad (6.18)$$

where it is understood that each  $\beta_i$  for a  $(u, w)$  corresponds to the appropriate system input.

The goal of the inverse dynamics controller is to solve for the control inputs from eq. (6.18). To achieve this it is possible to utilise the implicit function theorem (9), which simply stated is a tool that allows a set of  $p$  variables from  $P_i, i = 1, \dots, p$  in eq. (6.18) to be expressed in terms of the remaining variables as long as a set of conditions on their partial derivatives is satisfied. In this case the objective is to solve for the highest-order derivatives of the control  $(u_1^{(\beta_1)}, \dots, u_p^{(\beta_p)})$ , then from which the solution is the inverse dynamics controller.

The set of conditions on the partial derivatives is known as the **regulatory condition** and is given by

$$\Psi = \det \left[ \frac{\partial(P_1, \dots, P_p)}{\partial(u_1^{(\beta_1)}, \dots, u_p^{(\beta_p)})} \right] \neq 0, \quad (6.19)$$

where  $\Psi$  is the determinant of the Jacobian matrix of  $P_i, i = 1, \dots, p$  with respect to the highest-order derivatives of the control inputs. As long as  $\Psi \neq 0$  then the highest-order derivatives of the control can be solved out from eq. (6.18) by the implicit function theorem as

$$\begin{aligned} u_i^{(\beta_i)} = R_i(y_{d,1}, \dots, y_{d,1}^{(n_1)}, \dots, y_{d,p}, \dots, y_{d,p}^{(n_p)}, \\ u_1, \dots, u_1^{(\beta_1-1)}, \dots, u_p, \dots, u_p^{(\beta_p-1)}, \\ w_1, \dots, w_1^{(\beta_1)}, \dots, w_{m_1}, \dots, w_{m_1}^{(\beta_{m_1})}), \quad i = 1, \dots, p \end{aligned} \quad (6.20)$$

The solution of eq. (6.20) for each  $u_1, \dots, u_p$  are then the inverse-dynamics control inputs for the system  $\Xi$  in eq. (6.2).

In order to solve eq. (6.20) for the inverse dynamic control inputs  $(u_1, \dots, u_p)$  the set





of higher-order equations can be re-expressed as a set of first-order ODEs. Introducing the following pseudo-state variables (inspired by 10)  ${}^i z_1 = u_i$ ,  ${}^i z_2 = \dot{u}_i$ ,  $\dots$ ,  ${}^i z_{\beta_i} = u_i^{(\beta_i-1)}$  the control can be realised as

$$\begin{aligned}
 {}^1 \dot{z}_1 &= {}^1 z_2 \\
 &\vdots \\
 {}^1 \dot{z}_{\beta_1-1} &= {}^1 z_{\beta_1} \\
 {}^1 \dot{z}_{\beta_1} &= R_1(\mathbf{z}, \tilde{\mathbf{y}}_d, \tilde{\mathbf{w}}) \\
 &\vdots \\
 {}^p \dot{z}_1 &= {}^p z_2 \\
 &\vdots \\
 {}^p \dot{z}_{\beta_p-1} &= {}^p z_{\beta_p} \\
 {}^p \dot{z}_{\beta_p} &= R_p(\mathbf{z}, \tilde{\mathbf{y}}_d, \tilde{\mathbf{w}})
 \end{aligned} \tag{6.21}$$

where  ${}^i \mathbf{z} = ({}^i z_1, \dots, {}^i z_{\beta_i})^T = (u_i, \dots, u_i^{(\beta_i-1)})^T$ ,  $i = 1, \dots, p$  and  $\mathbf{z} = ({}^1 \mathbf{z}^T, \dots, {}^p \mathbf{z}^T)^T$ ,  $\tilde{\mathbf{y}}_d = (y_{d,1}, \dots, y_{d,1}^{(n_1)}, \dots, y_{d,p}, \dots, y_{d,p}^{(n_p)})^T$ ,  $\tilde{\mathbf{w}} = (w_1, \dots, w_1^{(\beta_1)}, \dots, w_{m_1}, \dots, w_{m_1}^{(\beta_{m_1})})$ .

The inverse dynamic control system can now be realised in state-space form as

$$\dot{\mathbf{z}} = \mathbf{E}\mathbf{z} + \mathbf{G}\mathbf{r}(\mathbf{z}, \tilde{\mathbf{y}}_d, \tilde{\mathbf{w}}), \tag{6.22a}$$

$$\mathbf{u} = \mathbf{H}\mathbf{z}, \tag{6.22b}$$

where  $\mathbf{E} = \text{diag}(\mathbf{E}_1, \dots, \mathbf{E}_p)$  and each sub-matrix  $\mathbf{E}_i \in \mathbb{R}^{\beta_i \times \beta_i}$  is an upper shift matrix;<sup>6</sup>  $\mathbf{G} = \text{diag}(\mathbf{g}_1, \dots, \mathbf{g}_p)$  and  $\mathbf{g}_i \in \mathbb{R}^{\beta_i \times 1}$  is the vector  $\mathbf{g}_i = (0, \dots, 0, 1)^T$ ; and  $\mathbf{H} \in \mathbb{R}^{p \times \sum^p \beta_i}$  where  $\mathbf{H}$  has entries of 1 for each  ${}^i z_1$  in  $\mathbf{z}$  and zeros everywhere else. The ‘output’ of the dynamic control system eq. (6.22) is the inverse dynamic control input  $\mathbf{u} = (u_1, \dots, u_p)$ .

### Numerical solution of inverse dynamics control system

After the inverse dynamics controller has been designed it must also be possible to solve the resulting control system for the actual control inputs. Being that the inverse dynamics controller can be expressed as a set of first-order ODEs as in (6.22), this lends itself to implementation/solution in computer simulation. The majority of building performance simulation (BPS) tools have the capability of solving a system of equations in this form via a multitude of numerical integration techniques. The goal of this work, however, is not to integrate this control into the existing BPS tools but to

<sup>6</sup>An upper shift matrix is a matrix with ones only on the superdiagonal, and zeroes elsewhere. The elements of an upper shift matrix  $(\mathbf{U})_{ij} = \delta_{i+1,j}$ , where  $\delta_{ij}$  is the Kronecker delta symbol.



provide enough detail so that those tools with sufficient capabilities and the flexibility to integrate new control algorithms can choose to do so. It is also desirable that the controller can be implemented on dedicated embedded hardware for real-time control of physical systems.

An issue that can arise with this type of control is oft-needed requirement of the computation of the derivative of an input signal. As can be seen in eq. (6.22) the computation of the inverse dynamics controller may need the derivative(s) of a demand signal  $y_{d,i}(t)$  and/or measured exogenous signal  $w_i(t)$ . While computation of the derivative of a continuous function *algebraically* for a known function is generally straightforward, problems can appear numerically when an input (a) is non-continuous (b) possesses a large value derivative upon control activation (i.e. at  $t = 0$ ) (c) exhibits abrupt changes in amplitude (11). Examples commonly encountered in practice are noisy measurement signals or demand inputs with a rapid or discontinuous change in set-point.

This work uses the classical fourth-order Runge-Kutta method (12, § 25.4) for solving the system of equations in eq. (6.22). The frequency of evaluation ('time step') should at a minimum be one-tenth of smallest time constant in the system for safe and robust control (13). For highly nonlinear inverse dynamics based controllers the limiting size may need to be determined iteratively.

### 6.2.3 Control structure design/selection

Now that the inverse dynamics control theory has been developed, it is useful to examine how the scheme or plan of the interconnected energy systems can be constructed into a suitable system to which the control can be applied.

As stated previously, the first requirement is that the system must be square i.e. equal number of controlled variables ( $p$ ) to manipulated variables ( $m_0$ ). The discussion of the control of non-square systems is typically confined to the study of industrial and chemical processes (14). This is because in chemical processes there are good arguments to be made that 'squaring' a system results in inferior control as opposed to control methods that are applicable to non-square systems (15). The relevance of directly controlling non-square energy systems is left as future work, as well as research into modifying the inverse dynamics control theory for direct application to non-square systems.

Assuming that the overall system can be made square, there are many controllability analysis techniques that can be used for control structure design (CSD). These tools are able to assess each candidate selection of measurements outputs and manipulated inputs from all the combinatorial combinations in a system. Based on a set of feasibil-



ity criteria, the tools will return a set of practical IO combinations. A survey of the literature regarding CSD is given by de Wal, Jager (16). However, (16) conclude that the current methods for CSD show severe shortcomings (assumption that it is possible to control the selected outputs based on the control of intermediate measured outputs or are analysed based on the steady-state response) and that for their application to nonlinear control systems “almost nothing is known”.

This section introduces a new method of control input ‘screening’ for nonlinear MIMO systems that leverages the inverse dynamics controller developed in the previous section. In this work, a new system input pre-screening technique has been developed for control structure selection. It is possible to use the regularity condition (6.19) to determine the possible subsets of the system inputs that can be used as control inputs. For a system with  $m$  system inputs, the inverse dynamics controller dictates that  $p$  control inputs (square system requirement) must be selected from the  $m_0$  available manipulable inputs. Mathematically then, the number of combinations of control inputs from the available candidate inputs is

$${}^p C_{m_0} = \binom{m_0}{p} = \frac{m_0!}{p!(m_0 - p)!}. \quad (6.23)$$

By evaluating the regularity condition for each candidate control set it is possible to investigate the feasibility of a chosen control structure i.e. given a set of controlled variables and known ‘process interactions’ what subsets of the manipulable variables within the system can be employed as control inputs to achieve the control goals. This input-screening technique is illuminated in the example of §§ 6.2.4 and the case study in chapter 8.

Just as with the LEDR algorithm, the author has implemented the inverse dynamics control algorithm in MATLAB® that makes use of the Symbolic Math Toolbox™. Given a general dynamic system described by a nonlinear differential equation in state-space form, the toolbox will construct the LEDR of the system, determine the feasible control inputs from which the user can select, and then construct the inverse dynamics controller. When the inverse dynamics controller evaluates symbolically it illuminates the control structure design/selection process by demonstrating not only what combinations of manipulated variables would result in a realisable controller, but also what *system parameters* are important to the control i.e. what are the set of parameters of the system that have the greatest influence over the performance of the control. The example of §§ 6.2.4 and the case study in chapter 8 will demonstrate this.



#### 6.2.4 Example application of inverse dynamics control

Consider the combustion-based cogeneration device model from § 4.1:

$$C_{\text{eng}}\dot{\Theta}_{\text{eng}}(t) = H_{\text{HX}}(\Theta_{\text{cw,o}}(t) - \Theta_{\text{eng}}(t)) + H_{\text{env}}(\Theta_{\text{env}}(t) - \Theta_{\text{eng}}(t)) + \eta_Q \overline{LHV} \dot{m}_{\text{fuel}}(t) \quad (4.8 \text{ revisited})$$

$$C_{\text{cw}}\dot{\Theta}_{\text{cw,o}}(t) = (c_p \dot{m}(t))_{\text{cw}}(\Theta_{\text{cw,i}}(t) - \Theta_{\text{cw,o}}(t)) + H_{\text{HX}}(\Theta_{\text{eng}}(t) - \Theta_{\text{cw,o}}(t))$$

The electrical grid utilisation is a simple energy balance between the electrical load demand and the electrical generation of the cogeneration device:

$$P_{\text{grid}}(t) = P_{\text{load}}(t) - P_{\text{gen}}(t),$$

where  $P_{\text{grid}}(t) > 0$  represents import from the grid.

If the mass flow rate of the cooling water through the heat exchanger is considered as a constant system parameter<sup>7</sup>, then (4.8) can be expressed as an explicit LTI state-space representation:

$$\Xi : \begin{cases} \dot{\mathbf{x}}(t) = \mathbf{A}\mathbf{x}(t) + \mathbf{B}\boldsymbol{\mu}(t) \\ \mathbf{y}(t) = \mathbf{C}\mathbf{x}(t) + \mathbf{D}\boldsymbol{\mu}(t) \end{cases}$$

where the state-vector  $\mathbf{x} = (\Theta_{\text{eng}}(t), \Theta_{\text{cw,o}}(t))^T$ , and the system input vector  $\boldsymbol{\mu}(t) = (\mu_1(t), \dots, \mu_4(t))^T = (\dot{m}_{\text{fuel}}(t), \Theta_{\text{cw,i}}(t), \Theta_{\text{env}}(t), P_{\text{load}}(t))^T$ . The system matrices are

$$\mathbf{A} = \begin{bmatrix} -\frac{H_{\text{HX}} + H_{\text{env}}}{C_{\text{eng}}} & \frac{H_{\text{HX}}}{C_{\text{eng}}} \\ \frac{H_{\text{HX}}}{C_{\text{cw}}} & -\frac{H_{\text{HX}} + (c_p \dot{m})_{\text{cw}}}{C_{\text{cw}}} \end{bmatrix} \quad \mathbf{B} = \begin{bmatrix} \frac{\overline{LHV}\eta_Q}{C_{\text{eng}}} & 0 & \frac{H_{\text{env}}}{C_{\text{eng}}} & 0 \\ 0 & \frac{(c_p \dot{m})_{\text{cw}}}{C_{\text{cw}}} & 0 & 0 \end{bmatrix}$$

$$\mathbf{C} = \begin{bmatrix} 0 & 1 \\ 0 & 0 \end{bmatrix} \quad \mathbf{D} = \begin{bmatrix} 0 & 0 & 0 & 0 \\ -\overline{LHV}\eta_E & 0 & 0 & 1 \end{bmatrix} \quad (6.24)$$

This example is concerned with constructing the inverse-dynamics control for the following MIMO control problem:

#### Control Goal

Design a system to track a desired load-supply water temperature set-point while simultaneously regulating the utilisation of the electrical grid to zero.

From this control goal, it is possible to identify the variables to be controlled as

<sup>7</sup>This is not always the case and is compensated for by the robust control method detailed in § 7.2

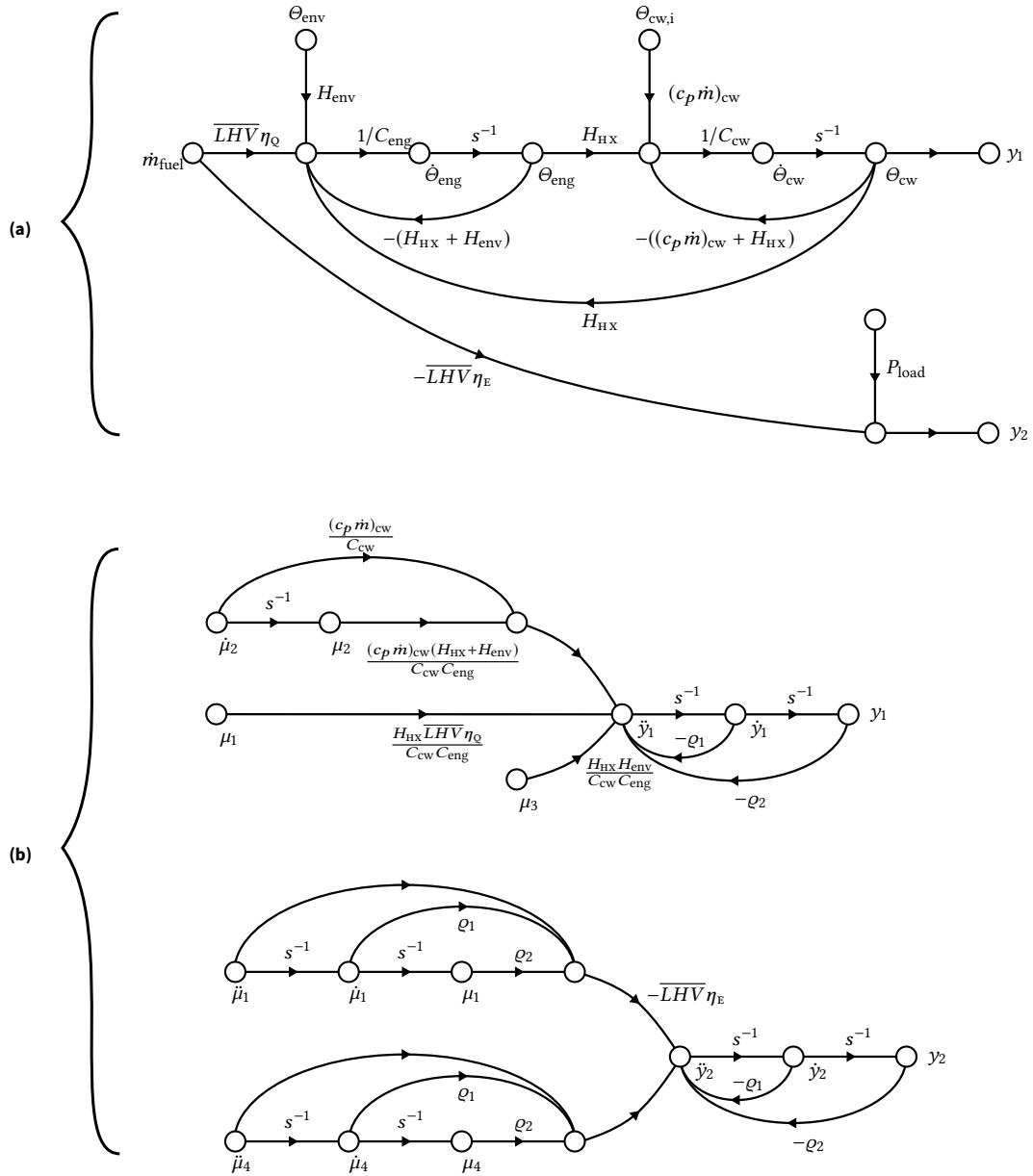


**Figure 6.1 | Signal-flow graphs for inverse dynamics control example. (a) Original internal state-space representation. (b) External differential representation.**



**cv1** Load-supply water temperature, which is the bulk exit temperature of the encapsulated mCHP cooling water,  $\Theta_{\text{cw,o}}$ .

**cv2** Electrical grid power,  $P_{\text{grid}}$ .

Therefore  $\mathbf{y}(t) = (y_1(t), y_2(t))^T = (\Theta_{\text{cw,o}}(t), P_{\text{grid}}(t))^T$ , and the system inputs are the fuel flow rate, heat exchanger inlet temperature, air temperature surrounding the mCHP unit, and the electrical load demand.

The EDR for the system (6.24) is constructed by using the symbolic algorithm developed in §§ 6.2.2 (see appendix C.1 for full derivation).

$$\begin{aligned}\ddot{y}_1(t) &= (-\varrho_2)y_1(t) + (-\varrho_1)\dot{y}_1(t) + \frac{H_{\text{HX}}\overline{LHV}\eta_{\text{Q}}}{C_{\text{cw}}C_{\text{eng}}}\mu_1(t) \\ &\quad + \frac{(c_p\dot{m})_{\text{cw}}(H_{\text{HX}} + H_{\text{env}})}{C_{\text{cw}}C_{\text{eng}}}\mu_2(t) + \frac{(c_p\dot{m})_{\text{cw}}}{C_{\text{cw}}}\dot{\mu}_2(t) + \frac{H_{\text{HX}}H_{\text{env}}}{C_{\text{cw}}C_{\text{eng}}}\mu_3(t) \\ \ddot{y}_1(t) &= \varphi_1(\tilde{\mathbf{y}}, \tilde{\boldsymbol{\mu}})\end{aligned}$$

$$\begin{aligned}\ddot{y}_2(t) &= (-\varrho_2)y_2(t) + (-\varrho_1)\dot{y}_2(t) + (-\overline{LHV}\eta_{\text{E}}\varrho_2)\mu_1(t) + (-\overline{LHV}\eta_{\text{E}}\varrho_1)\dot{\mu}_1(t) \\ &\quad + (-\overline{LHV}\eta_{\text{E}})\ddot{\mu}_1(t) + \varrho_2\mu_4(t) + \varrho_1\dot{\mu}_4(t) + \ddot{\mu}_4(t) \\ \ddot{y}_2(t) &= \varphi_2(\tilde{\mathbf{y}}, \tilde{\boldsymbol{\mu}})\end{aligned}$$

the generalised system parameters are

$$\varrho_1 = \frac{C_{\text{cw}}(H_{\text{HX}} + H_{\text{env}}) + C_{\text{eng}}(H_{\text{HX}} + (c_p\dot{m})_{\text{cw}})}{C_{\text{cw}}C_{\text{eng}}}, \quad \varrho_2 = \frac{H_{\text{HX}}H_{\text{env}} + (H_{\text{HX}} + H_{\text{env}})(c_p\dot{m})_{\text{cw}}}{C_{\text{cw}}C_{\text{eng}}}$$

$$\Xi_{\text{EDR}} : \begin{cases} \ddot{y}_1(t) = \varphi_1(\tilde{\mathbf{y}}, \tilde{\boldsymbol{\mu}}) \\ \ddot{y}_2(t) = \varphi_2(\tilde{\mathbf{y}}, \tilde{\boldsymbol{\mu}}) \end{cases} \quad (6.25)$$

where  $\tilde{\mathbf{y}} = (y_1, \dot{y}_1, y_2, \dot{y}_2)^T$ , and  $\tilde{\boldsymbol{\mu}} = (\mu_1, \dot{\mu}_1, \ddot{\mu}_1, \mu_2, \dot{\mu}_2, \mu_3, \mu_4, \dot{\mu}_4, \ddot{\mu}_4)^T$ .

Figure 6.1 gives signal-flow graphs for the original internal state-space representation (6.24) and the new external differential representation (6.25). The dynamics of these models are identical, with the graphs illustrating the input-output pathways of each model structure. This shows the benefit of the EDR representation as the input options available for each output are clear as opposed to the internal state-space representation, where it is difficult to assess the effect each input has on each output.

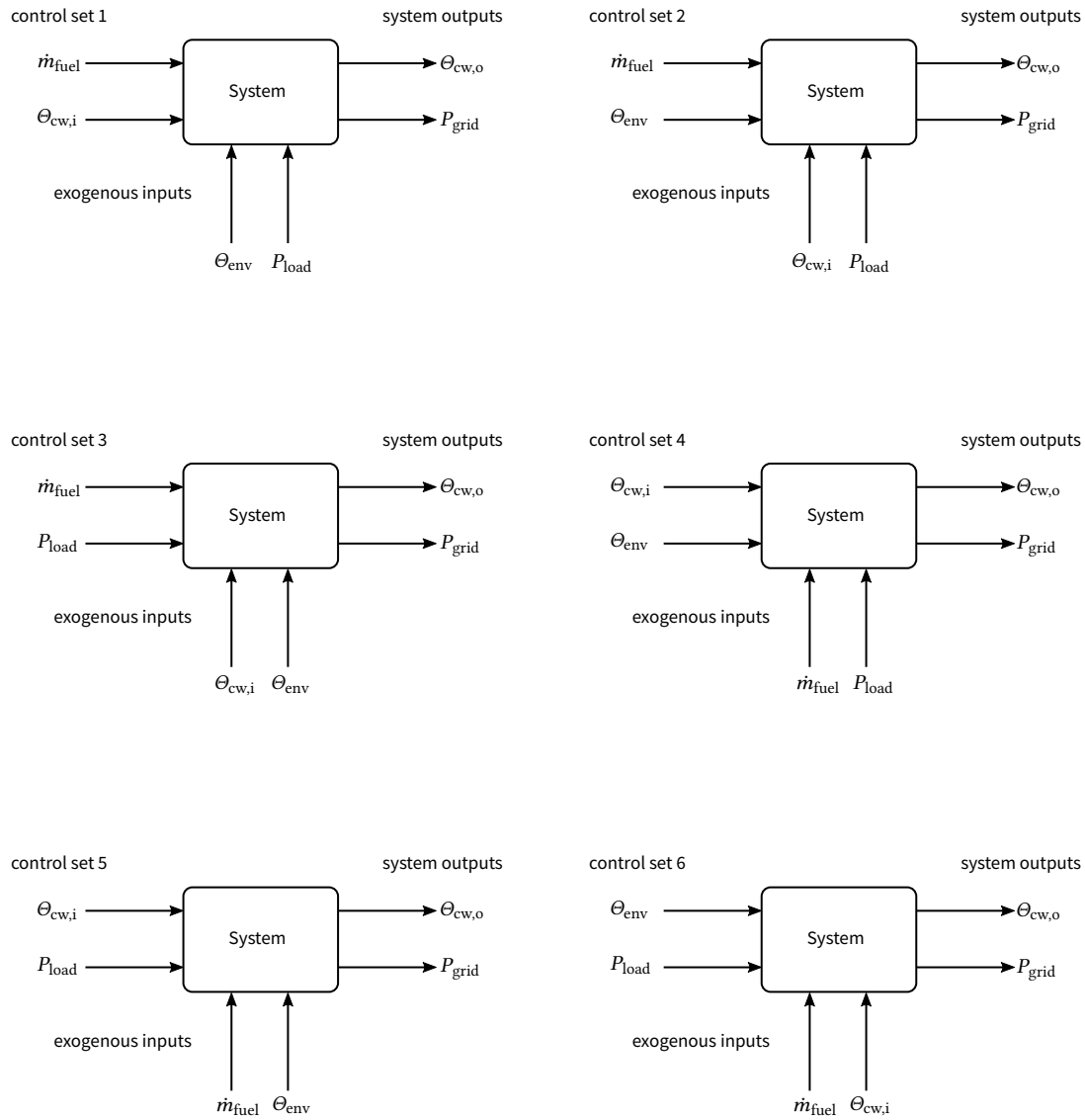


**Figure 6.2** | Input-output block diagrams for control structure design sets.

### Control structure design

Now that the differential IO system representation has been established, the next step is to map the general system inputs to the control inputs and exogenous inputs. The selection of the control inputs can be supported by utilising the previously derived inverse dynamic controllability conditions (6.2.1):

1. The number of control inputs must be equal to the number of system outputs, therefore must select  $p = 2$  control inputs
2. The highest-order derivatives of the control inputs can be solved out by the implicit function theorem.

To fulfil these requirements and select the control structure it is possible to utilise the regularity condition (6.19) such that

$$\Psi = \det \left[ \frac{\partial(\varphi_1, \dots, \varphi_p)}{\partial(u_1^{(\beta_1)}, \dots, u_p^{(\beta_p)})} \right] = \det \begin{bmatrix} \frac{\partial\varphi_1}{\partial u_1^{(\beta_1)}} & \frac{\partial\varphi_1}{\partial u_2^{(\beta_2)}} \\ \frac{\partial\varphi_2}{\partial u_1^{(\beta_1)}} & \frac{\partial\varphi_2}{\partial u_2^{(\beta_2)}} \end{bmatrix} \neq 0. \quad (6.26)$$

In this example it is assumed that all system inputs are candidate control inputs i.e.  $m_0 = m$  to facilitate discussion of the input-screening technique using the regularity condition. There are  ${}^pC_m = {}^2C_4 = 6$  potential combinations of system inputs that can be selected as the control inputs. Therefore,  $(u_1, u_2) =$

1.  $(\mu_1, \mu_2) = (\dot{m}_{\text{fuel}}, \Theta_{\text{cw,i}})$
2.  $(\mu_1, \mu_3) = (\dot{m}_{\text{fuel}}, \Theta_{\text{env}})$
3.  $(\mu_1, \mu_4) = (\dot{m}_{\text{fuel}}, P_{\text{load}})$
4.  $(\mu_2, \mu_3) = (\Theta_{\text{cw,i}}, \Theta_{\text{env}})$
5.  $(\mu_2, \mu_4) = (\Theta_{\text{cw,i}}, P_{\text{load}})$
6.  $(\mu_3, \mu_4) = (\Theta_{\text{env}}, P_{\text{load}})$

Figure 6.1(b) shows that combinations 3 and 4 can be excluded since the highest-order derivatives of the selected system inputs for each case appear only in a single differential IO equation and not the other. This will cause the a zero determinant ( $\implies \Psi = 0$ ). The remaining control combinations are discussed in the following sections, with simple I/O block diagrams provided in fig. 6.2 to illustrate the control inputs in each control set.



**CONTROL SET #1** The control inputs are the supply fuel flow rate to the cogeneration device and the input water temperature to the cogeneration heat exchanger.

$$\Psi_{cs1} = \det \begin{bmatrix} \frac{\partial \varphi_1}{\partial \dot{\mu}_1} & \frac{\partial \varphi_1}{\partial \dot{\mu}_2} \\ \frac{\partial \varphi_2}{\partial \dot{\mu}_1} & \frac{\partial \varphi_2}{\partial \dot{\mu}_2} \end{bmatrix} = \det \begin{bmatrix} 0 & \frac{(c_p \dot{m})_{cw}}{C_{cw}} \\ -LHV \eta_E & 0 \end{bmatrix} = \frac{LHV_{fuel} (c_p \dot{m})_{cw} \eta_e}{C_{cw}}.$$

The regulatory condition shows that the inverse dynamics controller exists as long as the electrical efficiency of the cogeneration device is non-zero, and the water mass flow rate through the heat exchanger is non-zero, while the lower-heating value of the fuel can always be assumed to be non-zero. Note that as the heat capacity of the heat exchanger gets very large the regulatory condition will approach zero. This can be interpreted as that as the heat capacity of the heat exchanger becomes larger the more ‘effort’ the control will have to put in to remain in control due to the increased thermal inertia of the system.

**CONTROL SET #2** The control inputs are the supply fuel flow rate to the cogeneration device and the air temperature surrounding the cogeneration device.

$$\Psi_{cs2} = \det \begin{bmatrix} \frac{\partial \varphi_1}{\partial \dot{\mu}_1} & \frac{\partial \varphi_1}{\partial \mu_3} \\ \frac{\partial \varphi_2}{\partial \dot{\mu}_1} & \frac{\partial \varphi_2}{\partial \mu_3} \end{bmatrix} = \det \begin{bmatrix} 0 & \frac{H_{HX} H_{env}}{C_{cw} C_{eng}} \\ -LHV \eta_E & 0 \end{bmatrix} = \frac{H_{HX} H_{env} LHV_{fuel} \eta_e}{C_{cw} C_{eng}}$$

The regulatory condition is similar to that of control set #1, except the total thermal inertia of the heat exchanger and the engine block affects the controllability of the system. As the product of the heat capacities of the engine block and heat exchanger becomes larger the more effort the control will have to exert to remain in control. If the heat transfer between the engine block and heat exchanger were to become zero then control would be lost. Conversely, the greater the heat transfer between them the less effort the control would have to exert to achieve complete inverse dynamics. Finally, if the heat transfer between the engine block and the environment were to become zero then control would be lost.

At first glance this control set may seem ridiculous as manipulating the environmental temperature surrounding the cogeneration device in order to control the system is infeasible. At the design stage this may have been excluded as a candidate control input. While that is generally true for the system in this example, it is used in many practical cases such as the cooling of ICT equipment in server rooms where the room temperature is manipulated to regulate the temperature of the equipment to a safe and efficient operating temperature. In this case, the heat transfer coefficient



between the air and the server ( $H_{\text{env}}$ ) would be maximised via utilisation of fins, forced convection etc. to increase the  $\Psi$  of the system. This shows that not only can the regulatory condition be used to determine the existence of an inverse dynamics controller, but can also contribute the design of the system to maximise the ‘controllability’ of the system.

**CONTROL SET #5** The control inputs are the inlet water temperature to the cogeneration heat exchanger and the electrical load demand.

$$\Psi_{\text{cs5}} = \det \begin{bmatrix} \frac{\partial \varphi_1}{\partial \dot{\mu}_2} & \frac{\partial \varphi_1}{\partial \dot{\mu}_4} \\ \frac{\partial \varphi_2}{\partial \dot{\mu}_2} & \frac{\partial \varphi_2}{\partial \dot{\mu}_4} \end{bmatrix} = \det \begin{bmatrix} \frac{(c_p \dot{m})_{\text{cw}}}{C_{\text{cw}}} & 0 \\ 0 & 1 \end{bmatrix} = \frac{(c_p \dot{m})_{\text{cw}}}{C_{\text{cw}}}$$

The regulatory condition is the simplest of all the control sets, whereby the inverse dynamics control exists as long as the mass flow rate of the water through the heat exchanger is non-zero. This control set is the most obvious choice that is selected in practice since it amounts to demand-side management of the electrical loads in tandem with manipulating the inlet water temperature of the cogeneration heat exchanger. Even if there is a limit to the amount of demand-side management that can be utilised in the system, in practice the electrical load demand is ‘controlled’ via load-shedding and an external energy system can be used to manipulate the inlet water temperature to the cogeneration device. This highlights the fact that traditional control approaches to fulfilling the heat and electrical demands in a building can also result from this control theory, but it isn’t the only choice available to the control engineer.

**CONTROL SET #6** The control inputs are the air temperature surrounding the cogeneration device and the electrical load demand.

$$\Psi_{\text{cs6}} = \det \begin{bmatrix} \frac{\partial \varphi_1}{\partial \mu_3} & \frac{\partial \varphi_1}{\partial \dot{\mu}_4} \\ \frac{\partial \varphi_2}{\partial \mu_3} & \frac{\partial \varphi_2}{\partial \dot{\mu}_4} \end{bmatrix} = \det \begin{bmatrix} \frac{H_{\text{HX}} H_{\text{env}}}{C_{\text{cw}} C_{\text{eng}}} & 0 \\ 0 & 1 \end{bmatrix} = \frac{H_{\text{HX}} H_{\text{env}}}{C_{\text{cw}} C_{\text{eng}}}$$

For the final control set the inverse dynamics controller exists only if the heat transfer coefficient between the engine block and heat exchanger is non-zero and the heat transfer coefficient between the engine block and the environment in which the device is situated is non-zero. The same discussion applies as that for control set #2, except the existence of the inverse dynamics control is not contingent on the electrical efficiency of the cogeneration device.

From analysis of the potential control sets, if it is assumed that the environmental





air temperature is non-manipulable, and that demand-side management of the electrical demands is not possible, then the manipulated/control-input variables are selected as control set #1:

**MV1** Fuel flow rate,  $\dot{m}_{\text{fuel}}$

**MV2** Cooling water inlet temperature,  $\Theta_{\text{cw},i}$

For the purposes of the example it is assumed that the inlet water temperature is directly manipulable. In reality it is obvious that this would itself be controlled by an external energy system such as a boiler, a thermal energy store, or as the return temperature from the loads the mCHP is supplying. However, note that if the dynamics of the external energy system were much faster than those of the system being controlled then this would effectively be the case in practicality. Nevertheless, the application here will demonstrate the inverse dynamic control without excessive model order.

Now for the system  $\Xi_{\text{EDR}}$  described by (6.25), it is possible to find the initial conditions  $\mathbf{x}(0)$  and control input vector  $\mathbf{u}$  in order for the system output to track a reference output  $\mathbf{y}_d(t)$  perfectly.

Following the procedure of §§ 6.2.2, assume that each system output  $y_i(t)$  is identical to the reference output  $y_{d,i}$ , i.e.  $y_i(t) \equiv y_{d,i}(t), \forall t \geq 0$ , which implies that

$$y_i^{(k)}(t) = y_{d,i}^{(k)}(t) \quad k = 0, 1, 2 \quad \forall t \geq 0.$$

Substituting  $(\mu_1, \dot{\mu}_1, \ddot{\mu}_1, \mu_2, \dot{\mu}_2) = (u_1, \dot{u}_1, \ddot{u}_1, u_2, \dot{u}_2)$ ,  $(\mu_3, \mu_4, \dot{\mu}_4, \ddot{\mu}_4)^T = (w_1, w_2, \dot{w}_2, \ddot{w}_2)^T$  and eq. (6.17) into eq. (6.25), and solving for the highest-order derivatives of the control inputs results in the following inverse dynamics controller for the system:

$$\begin{aligned} \ddot{u}_1(t) &= (-\varrho_2) u_1(t) + (-\varrho_1) \dot{u}_1(t) - \frac{1}{LHV\eta_E} (\varrho_2 y_{d,2}(t) + \varrho_1 \dot{y}_{d,2}(t) + \ddot{y}_{d,2}(t)) \\ &\quad + \frac{1}{LHV\eta_E} (\varrho_2 w_2(t) + \varrho_1 \dot{w}_2(t) + \ddot{w}_2(t)) \\ \ddot{u}_1(t) &= R_1(\cdot) \\ \ddot{u}_2(t) &= \left( -\frac{H_{\text{HX}} \overline{LHV} \eta_Q}{C_{\text{eng}} (c_p \dot{m})_{\text{cw}}} \right) u_1(t) + \left( -\frac{(H_{\text{HX}} + H_{\text{env}})}{C_{\text{eng}}} \right) u_2(t) \\ &\quad + \frac{C_{\text{cw}}}{(c_p \dot{m})_{\text{cw}}} (\varrho_2 y_{d,1}(t) + \varrho_1 \dot{y}_{d,1}(t) + \ddot{y}_{d,1}(t)) + \left( -\frac{H_{\text{HX}} H_{\text{env}}}{C_{\text{eng}} (c_p \dot{m})_{\text{cw}}} \right) w_1(t) \\ \ddot{u}_2(t) &= R_2(\cdot) \end{aligned} \tag{6.27}$$

Introducing the control state-variables as  ${}^1z_1 = u_1, {}^1z_2 = \dot{u}_1, {}^2z_1 = u_2$  then from eq. (6.22)

**Table 6.1** | Model parameters for inverse dynamics controller example.

Cogeneration device		Fuel composition		Hydronic system	
$C_{\text{eng}}$	$18.5 \times 10^3 \text{ J K}^{-1}$	$\text{H}_2$	0.00 %	$c_p$	$4192 \text{ J kg}^{-1} \text{ K}^{-1}$
$C_{\text{cw}}$	$28.1 \times 10^3 \text{ J K}^{-1}$	$\text{CH}_4$	94.76 %	$\dot{m}_{\text{cw}}$	$0.2 \text{ kg s}^{-1}$
$H_{\text{HX}}$	$31.8 \text{ W K}^{-1}$	$\text{C}_2\text{H}_6$	2.70 %		
$H_{\text{env}}$	$4.64 \text{ W K}^{-1}$	$\text{C}_3\text{H}_8$	0.23 %		
$\eta_{\text{E}}$	0.0929	$\text{N}_2$	1.76 %		
$\eta_{\text{Q}}$	0.970	$\text{CO}_2$	0.55 %		
		$\overline{\text{LHV}}$	$35.16 \text{ MJ m}^{-3}$		

the inverse dynamics control system is:

$$\begin{bmatrix} {}^1\dot{z}_1 \\ {}^1\dot{z}_2 \\ {}^2\dot{z}_1 \end{bmatrix} = \underbrace{\begin{bmatrix} 0 & 1 & 0 \\ 0 & 0 & 0 \\ 0 & 0 & 0 \end{bmatrix}}_E \begin{bmatrix} {}^1z_1 \\ {}^1z_2 \\ {}^2z_1 \end{bmatrix} + \underbrace{\begin{bmatrix} 0 & 0 \\ 1 & 0 \\ 0 & 1 \end{bmatrix}}_G \begin{bmatrix} R_1(z, \tilde{y}_d, \tilde{w}) \\ R_2(z, \tilde{y}_d, \tilde{w}) \end{bmatrix}$$

where  $z = ({}^1z_1, {}^1z_2, {}^2z_1)^T$ ,  $\tilde{y}_d = (y_{d,1}, \dot{y}_{d,1}, \ddot{y}_{d,1}, y_{d,2}, \dot{y}_{d,2}, \ddot{y}_{d,2})^T$ ,  $\tilde{w} = (w_1, w_2, \dot{w}_2, \ddot{w}_2)^T$ .

### Simulation

The model parameters used for the cogeneration device for purpose of this example were obtained from the dynamic calibration work of the Annex 42 project (Annex 42 of the International Energy Agency's Energy Conservation in Buildings and Community Systems Programme) (see 17, tab. V-4). The calibration was conducted with a WhisperGen unit, which is a Stirling-engine based cogeneration device. It is assumed that the unit is capable of modulating its output. Also acquired from the Annex 42 work was the assumed composition and pressure of the natural gas supply to the cogeneration device, which was used to determine the Lower Heating Value of the fuel. It is assumed that the flow of liquid water through the cogeneration device's heat exchanger is supplied using an external pump and is fixed at the manufacturer's recommended flow rate of  $12 \text{ l min}^{-1}$ . These model parameters are collectively given for the purposes of reproduction in table 6.1.

In the following example simulation, the same model (6.24) has been used for the controller design (6.27) and systems performance analysis (see fig. 6.3). This is to demonstrate the applicability of this type of control to energy systems without introducing modelling error. However, as discussed in § 1.3, in reality, the system being controlled will be subject to parameter changes, unmodelled dynamics and unmeasured disturbances. These uncertainties in the system models are addressed in the following chapter.

The control goal was to design a system to track a desired load-supply water temperature set-point while simultaneously regulating the utilisation of the electrical grid to zero. The load-supply water temperature is to be held initially at  $16^\circ\text{C}$  until 6 a.m. when over the duration on an hour it is ramped up to the supply temperature of  $70^\circ\text{C}$ , it is held at  $70^\circ\text{C}$  until 6 p.m., after which it is ramped down to the setback temperature of  $40^\circ\text{C}$  over the course of an hour, and then held there until the end of the simulation. The electrical grid power demand set-point is set to zero for the

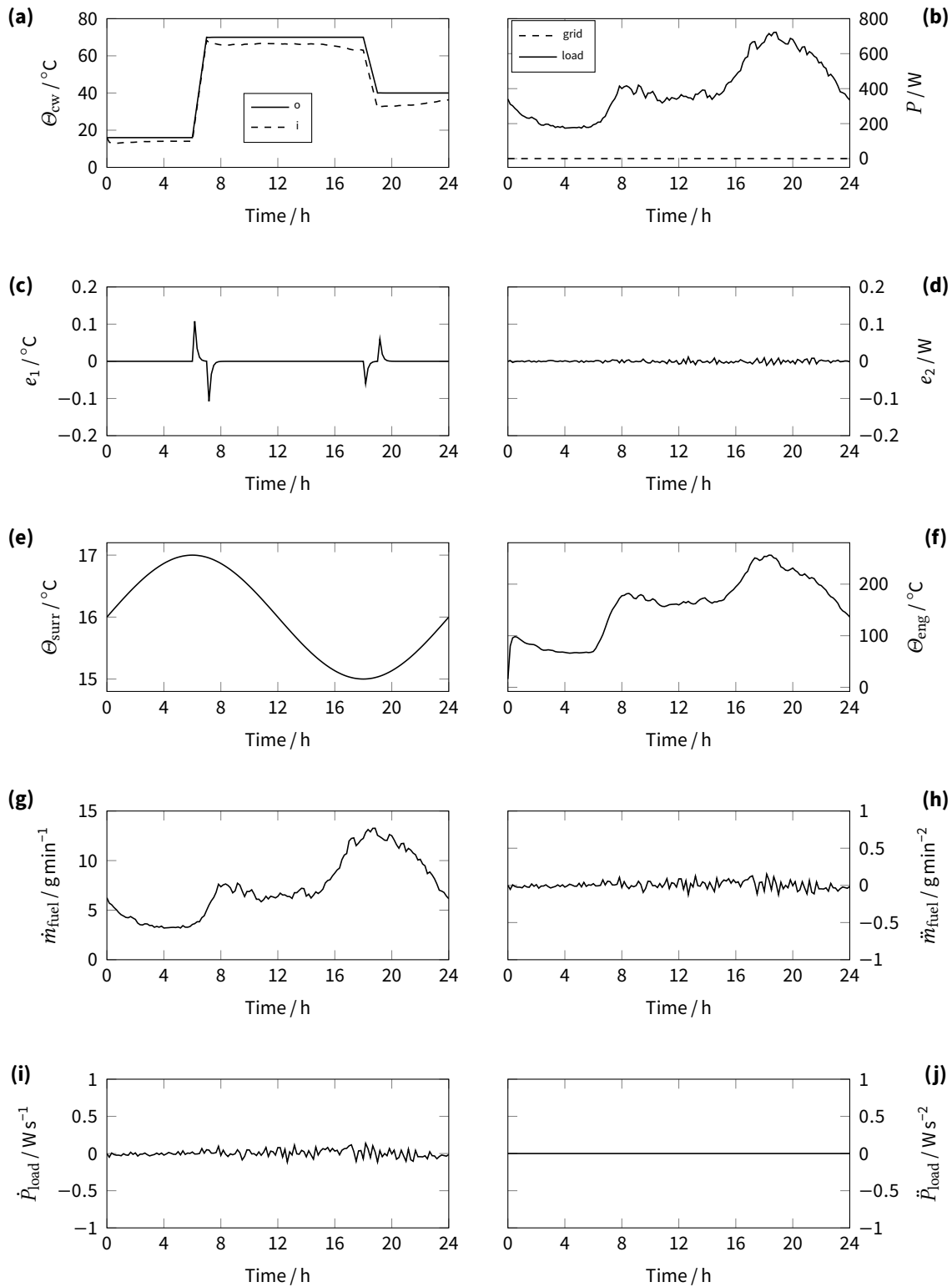


**Figure 6.3 | Simulation results for inverse dynamics controller. (a)** Inlet (dashed) and outlet (solid) cooling water temperature. **(b)** Electrical power demand (solid) and grid use (dashed). **(c)** Cooling water outlet temperature error. **(d)** Electrical grid power error. **(e)** Environmental temperature. **(f)** Engine temperature. **(g)** Manipulated fuel flow rate. **(h)** Rate-of-change of manipulated fuel flow rate. **(i)** Rate-of-change of power demand. **(j)** Acceleration of power demand.

duration. Therefore, mathematically the reference trajectories are defined as

$$y_{d,1}(t) = \begin{cases} 16 & t \in [0, 21600) \\ 0.015t - 308 & t \in [21600, 25200) \\ 70 & t \in [25200, 64800) \\ -(1/120)t + 610 & t \in [64800, 68400) \\ 40 & t \in [68400, \infty) \end{cases}$$

$$y_{d,2}(t) = 0, \forall t \geq 0$$

The electrical load demand profile that was used is the ‘Standard European Electric Profile’ for a winter weekday, which was created from the average electricity consumption of 69 homes in the UK (18).

As the environment in which the cogeneration device is situated was not explicitly modelled in this case, the temperature of the air surrounding the cogeneration device was assumed to be approximated as a sine wave:

$$w_1(t) = \sin((2\pi/T)t) + 16,$$

where the period is one day i.e.  $T = 86\,400$  s.

Substituting the values from table 6.1 into the system matrices (6.24), the poles are located at  $(-1.90 \times 10^{-3}, -31.0 \times 10^{-3})$ . This corresponds to time constants of  $\tau = -1/\mathbf{R}[\mathbf{p}] = (526, 32.2)$ . From the rule-of-thumb established in §§ 6.2.2, the control loop sample time is then set to  $t_c = \min(\tau/10) \approx 3$  s. The reporting sample time was set to 10 min. Initial conditions are chosen as  $\mathbf{x}(0) = (16, 16)$ ;  $\mathbf{z}(0) = (1.0417 \times 10^{-4}, 0, 16)$  to ensure  $y_{d,i}^{(k)}(0) = y_i^{(k)}(0)$ ,  $k = 0, \dots, n$ . All figures are in the original state variables  $(u_1, \dot{u}_1, u_2) = (\dot{m}_{\text{fuel}}, \ddot{m}_{\text{fuel}}, \Theta_{\text{cw},i})$ , and output variables  $(y_1, y_2) = (\Theta_{\text{cw},o}, P_{\text{grid}})$ .

Simulation results are shown in fig. 6.3.

The control inputs can be seen in figs. 6.3a, 6.3g and 6.3h. The inputs are smooth and the fuel flow rate and rate-of-change of fuel flow rate are well within the limits of the capabilities of the unit. The engine temperature is provided in fig. 6.3f for reference and is in-line with expected engine temperatures since the nominal engine temperature at maximum load for this unit is  $257^\circ\text{C}$  (17, tab. V-3).

The spikes in the error of the cooling water temperature seen in fig. 6.3c are due to the demand function  $y_{d,1}(t)$ , which is only piecewise continuously differentiable, with the derivative undefined at the switch-over points between a constant reference set-point and ramping up the temperature. The magnitude of the error, however, is insignificant.



It is clear from figs. 6.3a to 6.3d that the application of the inverse dynamics controller to the cogeneration device has been successful in achieving the control goals.

### Remarks

This example is only intended to demonstrate the basic dynamic controller performance as it relates to the **Control Goal**. The results could, of course, be produced for each and every valid control set with identical outcome: fulfilment of the control goal via manipulation of the chosen control inputs. The discussion of its performance and application to a large MIMO control problem for a building-integrated hybrid energy supply system is found in chapter 8, before which several necessary modifications are made to the control theory.

This example, while simplified, demonstrates the usefulness of the inverse dynamics controller and the control structure design via the regulatory condition, where it was possible to determine the combinations of inputs that could achieve simultaneous control of the system outputs.

The regulatory condition could also be utilised for fault detection in large interconnected systems. If control is lost for one or more of the system outputs, then an element that would cause  $\Psi = 0$  would be the first point of inspection. For example, in the control set chosen in the previous example, if control were lost either the mass flow rate through the cogeneration device has dropped to zero, or the electrical efficiency of the device has become zero.

There are, of course, drawbacks to attempting to implement this control as-is in practice. In reality the generalised parameters ( $\rho_1, \rho_2$ ) cannot possibly be known with absolute certainty and will result in imperfect control. There were also unmodelled dynamics excluded from the example such as the external pump, the actuating values, and the dependence of the unit's thermal/electrical efficiency on cooling water flow rate / temperature. These elements (and several more) are tackled in the following chapter.

Excluding these points of concern for now, there are two aspects to the *inversion* that should be addressed. While the inverse dynamic controller and design methodology is wholly applicable to nonlinear EDRs of systems, obtaining the EDR in this work was accomplished by first linearising the system around an operating point. While a number of energy systems can be well represented as a linear model over their entire range of operation, for certain energy system configurations it is feasible that the use of the system(s) may stray far from the design specifications where the linearisation is no longer valid. The obvious approach in this case would be to use





a form of gain scheduling, where a family of inverse dynamic controllers (based on linear EDRs obtained at different operating points) could be used to provide satisfactory control by switching between them (see 19, for an overview of the approach).

Another ‘ideal’ approach would be to obtain a general nonlinear EDR of the interconnected energy systems. To this end van der Schaft’s paper (20) has essentially developed an algorithm for this purpose, with an extract of the abstract reading:

“An algorithm is presented for transforming a nonlinear state space system into a threefold set of equations; the first subset describing the dynamics of the unobservable part of the system the second subset representing the remaining state variables as functions of inputs and outputs and their derivatives, and the last subset defining the external behaviour of the system.”

While this would result in a completely nonlinear EDR of the system, and its use would therefore result in an inverse controller design that is valid for the entire range of operation, its applicability to large systems is limited. In the author’s experience attempting to implement the algorithm of (20) for systems with  $\approx 5$  or more state-variables (contingent of the extent of the nonlinear behaviour) results in an enormous amount of algebraic manipulation. The investigation of efficient computer implementation is currently left for future work.

The second point of concern is the fact that the LEDR always results in a set of higher-order differential equations of order  $n$ , while there may exist a reduced-order system that will result in equally performing control. Even though model-order-reduction techniques could be used to reduce the order of the resulting EDR before the application of the inverse dynamics controller, there is fortunately a branch of nonlinear control theory that is able to ‘cancel’ the nonlinearities in the original system and renders the system to be controlled as a set of linear differential equations, often with total order  $< n$ .

The central idea of the approach is to algebraically transform a nonlinear system dynamics into a (fully or partly) linear one, so that linear control techniques can be applied. This differs entirely from conventional linearisation (i.e. Jacobian linearisation as in eq. (D.14)) in that feedback linearisation is achieved by exact state transformations and feedback, rather than by linear approximations of the dynamics. Feedback linearisation techniques can be viewed as ways of *transforming original system models into equivalent models of a simpler form* i.e. it amounts to cancelling the nonlinearities in a nonlinear system so that the closed-loop dynamics is in a linear form.



### 6.3 Feedback linearisation

The general concept of feedback-linearisation based control and its application to a wide variety of control problems in the field of energy systems was covered in § 2.4. The aim of this section is to illustrate the substantive theory and provide an example of its application to the problem at hand, so as to demonstrate its applicability to the control of a system of building-integrated interconnected hybrid energy supply systems. To that end, the theory will be expanded as much as is necessary for its utilisation in this work. The theoretical basis for the control approach in this section is based on the work of Cheng et al. (21) – and influenced by the clear presentation in Lin (22) – and is known as input-output feedback linearisation. The design procedure is briefly outlined here with more detailed description of the mathematical theory available elsewhere (23, 24). The application of feedback linearisation will be first demonstrated via an example before generalising the approach so that it is applicable to many configurations of energy systems.

#### 6.3.1 SISO application of feedback linearisation

Once again consider the combustion-based cogeneration device model from § 4.1:

$$\begin{aligned} C_{\text{eng}}\dot{\Theta}_{\text{eng}}(t) &= H_{\text{HX}}(\Theta_{\text{cw,o}}(t) - \Theta_{\text{eng}}(t)) + H_{\text{env}}(\Theta_{\text{env}}(t) - \Theta_{\text{eng}}(t)) \\ &\quad + \eta_Q \overline{LHV} \dot{m}_{\text{fuel}}(t) \quad (4.8 \text{ revisited}) \\ C_{\text{cw}}\dot{\Theta}_{\text{cw,o}}(t) &= (c_p \dot{m}(t))_{\text{cw}}(\Theta_{\text{cw,i}}(t) - \Theta_{\text{cw,o}}(t)) + H_{\text{HX}}(\Theta_{\text{eng}}(t) - \Theta_{\text{cw,o}}(t)) \end{aligned}$$

Consider the nonlinear SISO control problem of controlling the temperature of the outlet cooling water temperature during the cool-down phase of the mCHP operation cycle. Assume that the cooling water entering the inlet of the mCHP heat exchanger is the return feed from supplying a hydronic heat supply system (e.g. return feed from radiators). In this case the cooling water temperature at the inlet is a measured exogenous signal as it is external to the controlled system. Controlling the outlet temperature is then achieved by manipulating the mass flow rate of the external pump.

With these specifications the system can be expressed as:

$$\begin{aligned} \dot{x}_1(t) &= \left( -\frac{H_{\text{HX}} + H_{\text{env}}}{C_{\text{eng}}} \right) x_1(t) + \frac{H_{\text{HX}}}{C_{\text{eng}}} x_2(t) + \frac{H_{\text{env}}}{C_{\text{eng}}} w_2(t) \\ \dot{x}_2(t) &= \frac{H_{\text{HX}}}{C_{\text{cw}}} x_1(t) + \frac{c_p}{C_{\text{cw}}} u(t) w_1(t) + \left( -\frac{c_p}{C_{\text{cw}}} \right) u(t) x_2(t) + \left( -\frac{H_{\text{HX}}}{C_{\text{cw}}} \right) x_2(t) \\ y(t) &= x_2(t) \end{aligned}$$

where the state-vector  $\mathbf{x}(t) = (\Theta_{\text{eng}}(t), \Theta_{\text{cw,o}}(t))^T$ , the control input  $u(t) = \dot{m}_{\text{cw}}(t)$ ,



and the measured exogenous input  $\mathbf{w}(t) = (w_1(t), w_2(t))^T = (\Theta_{\text{cw},i}(t), \Theta_{\text{env}}(t))^T$ . It is evident that the output is not directly related to the input. However taking the first time derivative of  $y(t)$  yields

$$\dot{y}(t) = \frac{H_{\text{HX}}}{C_{\text{cw}}}x_1(t) + \frac{c_p}{C_{\text{cw}}}u(t)w_1(t) + \left(-\frac{c_p}{C_{\text{cw}}}\right)u(t)x_2(t) + \left(-\frac{H_{\text{HX}}}{C_{\text{cw}}}\right)x_2(t)$$

By investigation it can be seen that a feedback control law of

$$u(t) = \frac{C_{\text{cw}}v(t) + H_{\text{HX}}(x_2(t) - x_1(t))}{c_p(w_1(t) - x_2(t))}, \quad (6.28)$$

will result in

$$\dot{y}(t) = v(t), \quad (6.29)$$

where  $v(t)$  is considered as a new ‘synthetic’ control input. The control in eq. (6.28) has used part of the control effort to cancel the nonlinear terms and can now design the remainder of the control  $v(t)$  based on linear theory. As opposed to controllers based on linear models, this control law is valid everywhere except for singularity points such as when  $w_1(t) = x_2(t)$  i.e. when the inlet and outlet temperatures are exactly the same.

Note that eq. (6.29) is now a first-order linear ODE. The control of a system in this form is trivial and any number of linear control approaches can be applied. For example, consider a simple proportional controller

$$v(t) = K_p(y_d(t) - y(t)), \quad (6.30)$$

then the resulting system transfer function is

$$\frac{y(s)}{y_d(s)} = \frac{1}{(1/K_p)s + 1} \quad (6.31)$$

where  $K_p$  is a positive constant and  $1/K_p$  is the time constant of the resulting system. This example has shown how it is possible to transform a nonlinear SISO energy system control problem into a simple first-order linear one, where the controller design is valid over a much wider range than that of an inverse dynamic controller based on an LEDR. Also note that contrary to the inverse dynamics controller developed in the previous section, the control is applied at the first-derivative of the output, and does not require an EDR of the output of order  $n$ . Although this is generally beneficial from a computational point-of-view when controlling large systems of high-order, notice that (6.31) only accounts for part of the closed-loop dynamics. It is of order one, while



the system (4.8) is second-order. Therefore, a part of the system dynamics has been rendered “unobservable” (3, p. 218) in the IO system eq. (6.29) by the control law (6.28). This part of the dynamics is called the **internal dynamics**, because its behaviour is not visible from the external IO system.

In this example, the internal dynamics is represented by  $x_1(t)$  (the engine temperature) and is given by

$$\dot{x}_1(t) = \left( -\frac{H_{\text{HX}} + H_{\text{env}}}{C_{\text{eng}}} \right) x_1(t) + \frac{H_{\text{HX}}}{C_{\text{eng}}} y(t) + \frac{H_{\text{env}}}{C_{\text{eng}}} w_2(t)$$

Provided these internal dynamics are stable, the control law (6.28) is valid.

Assuming the goal is for the cooling water temperature at the outlet to reach a desired set-point temperature  $y_d = \Theta_{\text{cool}}$ , then the solution to eq. (6.29) is given by  $y(t) = \Theta_{\text{cool}} + (y(0) - \Theta_{\text{cool}})e^{-K_p t}$  and the internal dynamics are now

$$\dot{x}_1(t) + \left( \frac{H_{\text{HX}} + H_{\text{env}}}{C_{\text{eng}}} \right) x_1(t) = \frac{H_{\text{HX}}}{C_{\text{eng}}} \left( \Theta_{\text{cool}} + (y(0) - \Theta_{\text{cool}})e^{-K_p t} \right) + \frac{H_{\text{env}}}{C_{\text{eng}}} w_2(t)$$

Assuming that the environmental temperature is bounded such that  $|w_2(t)| \leq D$ , then the engine temperature will exhibit a stable bounded response.

Alternatively, it is possible to investigate the stability of the entire closed-loop system. Consider again the control law (6.28), this time in the original state variables  $(x_1, x_2)$ :

$$u(t) = \frac{C_{\text{cw}} K_p (y_d(t) - x_2(t)) + H_{\text{HX}} (x_2(t) - x_1(t))}{c_p (w_1(t) - x_2(t))}, \quad (6.32)$$

Substituting eq. (6.32) into the original system yields the closed-loop system

$$\begin{aligned} \dot{x}_1(t) &= \left( -\frac{H_{\text{HX}} + H_{\text{env}}}{C_{\text{eng}}} \right) x_1(t) + \frac{H_{\text{HX}}}{C_{\text{eng}}} x_2(t) + \frac{H_{\text{env}}}{C_{\text{eng}}} w_2(t) \\ \dot{x}_2(t) &= (-K_p) x_2(t) + K_p y_d(t) \end{aligned}$$

To investigate the stability of this system, take the Jacobian linearisation (as in appendix D.2) around an equilibrium point of the system which results in the following LTI state-space system matrix

$$\mathbf{A} = \begin{bmatrix} -\frac{H_{\text{HX}} + H_{\text{env}}}{C_{\text{eng}}} & \frac{H_{\text{HX}}}{C_{\text{eng}}} \\ 0 & -K_p \end{bmatrix}$$





From eq. (6.7) the characteristic equation of the system is given by

$$\delta(s) = \det(s\mathbf{I}_n - \mathbf{A}) = s^2 + \frac{H_{\text{HX}} + H_{\text{env}} + C_{\text{eng}}K_p}{C_{\text{eng}}}s + \frac{K_p(H_{\text{HX}} + H_{\text{env}})}{C_{\text{eng}}}$$

The roots of which are  $s = -K_p$  and  $s = -(H_{\text{HX}} + H_{\text{env}})/C_{\text{eng}}$ . Therefore, for any real positive values of  $(C_{\text{eng}}, H_{\text{HX}}, H_{\text{env}}, K_p)$  the resulting closed-loop system is *always* stable.

The example in §§ 6.3.1 showed (for a SISO system) how the internal dynamics of the engine temperature were stable under the inversion-based control law (eqs. (6.28) and (6.30)). Analysis of the closed-loop system dynamics has shown that the entire system is stable for any positive constant  $K_p$ .

While it was possible to determine the internal dynamics for this relatively simple example, a large interconnected energy system could have internal dynamics of high order, and exhibit nonlinear behaviour. Moreover, as was shown in this example the internal dynamics can be a function of the external dynamics and the chosen control law. Note that an advantage of the inverse dynamics controller is that it has no such internal dynamics but is computationally more expensive.

### 6.3.2 Relative degree of energy systems

The general control objective is to make any output  $y_i(t)$  (such as internal air temperature, or electrical grid power use) track a desired trajectory while keeping the system stable. The difficulty with this, as demonstrated in the example, is that any output is only indirectly related to a controlled input, through the state variables and the nonlinear state equations. For example, a direct convective air heater will have a more deliberate effect on the air temperature than a hydronic radiator. The inability to quickly see a change in the output based upon a change in the controlled input often results in poor control and inefficient utilisation of the energy systems. In buildings a common result of this is over-heating/cooling. A measure of this ‘indirectness’ is known as the **relative order/degree** of the output. In the example of this section the relative degree of the output is  $\rho = 1$ , since the control appears after one time derivative of the output. Another way of thinking of the relative degree of an output in interconnected energy systems is that it is generally equivalent to the number of *inertial* or energy storage elements ‘downstream’ of the manipulated input in reference to a controlled output. Essentially the relative degree represents the delay existing between a manipulated input and controlled output.

It is generally understood that the higher the relative degree between an input and an output, the more difficult it will be to control. Indeed, (25) has shown that



for systems with  $r > 2$  the higher the relative degree the harder the system is to control (25, p. 202). As reviewed in § 2.3, this is typically why the traditional approach to control is to control energy systems in cascade, with the relative degree being  $r \leq 2$  between each element so that closed-loop feedback mechanisms such as PI control can be utilised (this ensures that there is an equal number of ‘degrees of freedom’ - proportional and integral gains - to sub-system order).

However, there are several reasons why controlling the systems in cascade may not be feasible. Beyond the additional complexity of having multiple interacting sub-control-systems, the sub-systems being controlled may not behave satisfactorily as an individual IO system, or it may simply not be possible to break the system into separate parts each with its own demand signal, controlled variable, and manipulated variable. Due to the MIMO nature of the systems and the fact that they can have an effect on both the thermal and electrical networks in the building, it is assumed that it is not possible to control the interconnected energy systems in cascade while still being able to achieve the best possible performance of the systems while retaining robust control.

To control the overall network of systems the concept of the relative degree of each controlled output will be exploited. Consider the general differential equations that govern the dynamics of the energy systems and the environment in which they operate. These can be written in state-space form as the class of nonlinear MIMO control-affine systems described by

$$\begin{aligned}\dot{\mathbf{x}}(t) &= \mathbf{f}(\mathbf{x}(t)) + \mathbf{G}(\mathbf{x}(t))\mathbf{u}(t), \\ \mathbf{y}(t) &= \mathbf{h}(\mathbf{x}(t)),\end{aligned}\tag{6.33}$$

where  $\mathbf{x}(t) \in \mathbb{R}^n$  is the state vector,  $\mathbf{y}(t) \in \mathbb{R}^p$  are the measured outputs,  $\mathbf{u}(t) \in U \subset \mathbb{R}^p$ , are the controlled inputs,  $\mathbf{f} : \mathbb{R}^n \rightarrow \mathbb{R}^n$  and  $\mathbf{h} : \mathbb{R}^n \rightarrow \mathbb{R}^p$  are smooth vector fields, and  $\mathbf{G} : \mathbb{R}^n \rightarrow \mathbb{R}^n \times \mathbb{R}^p$  is a matrix whose columns  $\mathbf{g}_j : \mathbb{R}^n \rightarrow \mathbb{R}^n$ ,  $j = 1, \dots, p$  are smooth vector fields. Also, for notational compactness from now on the time-dependence is implied so that  $\mathbf{x} := \mathbf{x}(t)$ ,  $\mathbf{u} := \mathbf{u}(t)$ ,  $\mathbf{y} := \mathbf{y}(t)$ .

From the mathematical representation of the system (6.33), it is possible to calculate the relative degree of each output in relation to the controlled input. This is determined by continually differentiating the output of the system until the control appears. Then, the order of differentiation which has to be applied to the output to have explicit dependence on a manipulated input is defined as the relative degree of that output. Since this involves partial derivatives of the nonlinear system (6.33), extra notation is borrowed from differential geometry to reduce conceptual and notational



complexity (3, p. 229). Readers unfamiliar with the notation of a Lie derivative<sup>8</sup> are referred to appendix D.3 for a more thorough derivation of the following. Continuously taking time-derivatives of a single output  $y_i(t)$  in eq. (6.33) produces

$$\begin{aligned}
 \dot{y}_i &= \frac{dh_i}{dt} = \frac{\partial h_i}{\partial \mathbf{x}} \frac{d\mathbf{x}}{dt} = \mathcal{L}_f h_i \\
 \ddot{y}_i &= \frac{\partial \mathcal{L}_f h_i}{\partial \mathbf{x}} \frac{d\mathbf{x}}{dt} = \mathcal{L}_f^2 h_i \\
 &\vdots \\
 y_i^{(k)} &= \mathcal{L}_f^k h_i, \quad \text{for } k < \rho_i \\
 y_i^{(\rho_i)} &= \mathcal{L}_f^{\rho_i} h_i + \sum_{j=1}^p \mathcal{L}_{g_j} \mathcal{L}_f^{\rho_i-1} h_i u_j
 \end{aligned} \tag{6.34}$$

where  $\mathcal{L}$  denotes the Lie derivative, and for at least one  $j$ ,  $\mathcal{L}_{g_j} \mathcal{L}_f^{\rho_i-1} h_i \neq 0$ , and  $\rho_i$  denotes the relative degree of output  $y_i$  i.e. the relative degree corresponds to the lowest order derivative of the output that depends explicitly on an input.

### 6.3.3 Input-output inversion of MIMO energy systems

The same method that results in (6.34) can be applied to each output of the system (6.33) and written together in a single compact vector-matrix equation as

$$\underbrace{\begin{bmatrix} y_1^{(\rho_1)} \\ y_2^{(\rho_2)} \\ \vdots \\ y_p^{(\rho_p)} \end{bmatrix}}_{\hat{\mathbf{y}}} = \underbrace{\begin{bmatrix} \mathcal{L}_f^{\rho_1} h_1 \\ \mathcal{L}_f^{\rho_2} h_2 \\ \vdots \\ \mathcal{L}_f^{\rho_p} h_p \end{bmatrix}}_{P(\mathbf{x})} + \underbrace{\begin{bmatrix} \mathcal{L}_{g_1} \mathcal{L}_f^{\rho_1-1} h_1 & \dots & \mathcal{L}_{g_p} \mathcal{L}_f^{\rho_1-1} h_1 \\ \mathcal{L}_{g_1} \mathcal{L}_f^{\rho_2-1} h_2 & \dots & \mathcal{L}_{g_p} \mathcal{L}_f^{\rho_2-1} h_2 \\ \vdots & \dots & \vdots \\ \mathcal{L}_{g_1} \mathcal{L}_f^{\rho_p-1} h_m & \dots & \mathcal{L}_{g_p} \mathcal{L}_f^{\rho_p-1} h_p \end{bmatrix}}_{Q(\mathbf{x})} \mathbf{u}$$

or

$$\hat{\mathbf{y}} = P(\mathbf{x}) + Q(\mathbf{x})\mathbf{u}. \tag{6.35}$$

If the matrix  $Q(\mathbf{x})$  in (6.35) is invertible, then utilising feedback control of the form

$$\mathbf{u} = (Q(\mathbf{x}))^{-1}(-P(\mathbf{x}) + \mathbf{v}), \tag{6.36}$$

<sup>8</sup>The Lie derivative of a function is defined as the directional derivative of a function.



results in the simple linear system

$$\begin{bmatrix} y_1^{(\rho_1)} \\ y_2^{(\rho_2)} \\ \vdots \\ y_p^{(\rho_p)} \end{bmatrix} = \begin{bmatrix} v_1 \\ v_2 \\ \vdots \\ v_p \end{bmatrix} \quad (6.37a)$$

$$\hat{\mathbf{y}} = \mathbf{v} \quad (6.37b)$$

where as was in (6.29), each  $v_i$  is an outer-loop control law to be defined in order to achieve the required performance tracking on  $y_i$ . It can be seen that utilising (6.36) has resulted in an input-output relation that is linearised *and* decoupled, such that each output  $y_i$  is a linear function of a single input  $v_i$ . For this reason (6.36) is called a **decoupling control law**, and the invertible matrix  $\mathbf{Q}(\mathbf{x})$  is called the **decoupling matrix** of the system (6.33) (3). The system is said to have a vector relative degree  $\boldsymbol{\rho} = (\rho_1, \dots, \rho_p)$ , and the total relative degree of this new system is  $\rho = \boldsymbol{\rho}\mathbf{1} = \rho_1 + \dots + \rho_p$ . If  $\rho < n$  then there exists internal dynamics.

Due to the nature of the control law of (6.36) involving the inversion of  $\mathbf{Q}(\mathbf{x})$ , the author prefers the name **nonlinear feedback inversion** control law as opposed to feedback linearisation. The term ‘linearisation’ can be a misnomer considering that the same procedure is equivalently applicable to systems that are already approximately linear in nature or applied to systems obtained via Jacobian linearisation of the original nonlinear system.

Note that this ‘exact’ linearisation method has resulted in what appears to be **noninteracting control** where the  $i$ th output is affected only by the  $i$ th input. However, recall that these are only ‘synthetic inputs’ the total control action for the  $i$ th control input may be comprised of multiple synthetic inputs. However, expressing the system in this fashion allows the control engineer the freedom to specify the performance of each output channel independently of the others. For this reason it is also called **input-output decoupling** in some literature.

### Special theory: linear systems

Although all real systems are nonlinear, there are systems which either predominately perform as linear systems the system operates around a local equilibrium point. This is true for a subset of building control problems, such as well insulated buildings or energy systems which have only a limited range of ‘movement’ around their operation points. For these cases, small signal analysis applies and the behaviour of the system can be well approximated as a linear system. In any case, a general nonlinear system





can be linearised via the Jacobian linearisation approach. Recall from § 6.1 that the Jacobian linearised system can be expressed as

$$\begin{aligned}\dot{\mathbf{x}}(t) &= \mathbf{A}\mathbf{x}(t) + \mathbf{B}\boldsymbol{\mu}(t), \\ \mathbf{y}(t) &= \mathbf{C}\mathbf{x}(t) + \mathbf{D}\boldsymbol{\mu}(t),\end{aligned}\tag{6.2 revisited}$$

where  $\mathbf{x}(t) \in \mathbb{R}^n$  is the state vector,  $\boldsymbol{\mu}(t) \in \mathbb{R}^m$  is the input vector,  $\mathbf{y}(t) \in \mathbb{R}^p$  is the output vector,  $\mathbf{A} \in \mathbb{R}^{n \times n}$  is the plant matrix,  $\mathbf{B} \in \mathbb{R}^{n \times m}$  is the input matrix,  $\mathbf{C} \in \mathbb{R}^{p \times n}$  is the output matrix and  $\mathbf{D} \in \mathbb{R}^{p \times m}$  is the feedforward matrix.

Now as with the inverse dynamics controller, the system input vector can be split into sub-vectors as  $\boldsymbol{\mu} = (\mathbf{u}^T, \mathbf{w}^T)^T$ , where  $\mathbf{u} \in \mathbb{R}^p$  is the **control** input vector and  $\mathbf{w} \in \mathbb{R}^{m_1}$  is the **exogenous** input vector. Note that it is already assumed that the system is square – that is – there is the same number of control inputs as system outputs. The system (6.2) can now be expressed as

$$\begin{aligned}\dot{\mathbf{x}}(t) &= \mathbf{A}\mathbf{x}(t) + \mathbf{B}_1\mathbf{u}(t) + \mathbf{B}_2\mathbf{w}(t), \\ \mathbf{y}(t) &= \mathbf{C}\mathbf{x}(t) + \mathbf{D}_1\mathbf{u}(t) + \mathbf{D}_2\mathbf{w}(t),\end{aligned}\tag{6.38}$$

The general  $k$ -th derivative of an output  $y_i$  of the system (6.38) is given by

$$y_i^{(k)}(t) = \mathbf{c}_i \mathbf{A}^k \mathbf{x}(t) + {}^2\mathbf{d}_i \mathbf{w}^{(k)}(t) + \sum_j^k \mathbf{c}_i \mathbf{A}^{k-j} \mathbf{B}_1 \mathbf{u}^{(j-1)}(t) + \sum_j^k \mathbf{c}_i \mathbf{A}^{k-j} \mathbf{B}_2 \mathbf{w}^{(j-1)}(t)\tag{6.39}$$

where  $\mathbf{c}_i$  is the  $i$ th row vector of  $\mathbf{C}$ , and  ${}^2\mathbf{d}_i$  is the  $i$ th row vector of  $\mathbf{D}_2$ .

Applying the method (6.34) to the linear system (6.38) is straightforward and by utilising the general derivative of (6.39) results in

$$\begin{aligned}\dot{y}_i(t) &= \mathbf{c}_i \mathbf{A} \mathbf{x}(t) + {}^2\mathbf{d}_i \dot{\mathbf{w}}(t) + \mathbf{c}_i \mathbf{B}_2 \mathbf{w}(t) \\ \ddot{y}_i(t) &= \mathbf{c}_i \mathbf{A}^2 \mathbf{x}(t) + {}^2\mathbf{d}_i \ddot{\mathbf{w}}(t) + \mathbf{c}_i \mathbf{A} \mathbf{B}_2 \mathbf{w}(t) + \mathbf{c}_i \mathbf{B}_2 \dot{\mathbf{w}}(t) \\ &\vdots \\ y_i^{(k)}(t) &= \mathbf{c}_i \mathbf{A}^k \mathbf{x}(t) + {}^2\mathbf{d}_i \mathbf{w}^{(k)}(t) + \sum_j^k \mathbf{c}_i \mathbf{A}^{k-j} \mathbf{B}_2 \mathbf{w}^{(j-1)}(t), \quad \text{for } k < \rho_i \\ y_i^{(\rho_i)}(t) &= \mathbf{c}_i \mathbf{A}^{\rho_i} \mathbf{x}(t) + {}^2\mathbf{d}_i \mathbf{w}^{(\rho_i)}(t) + \mathbf{c}_i \mathbf{A}^{\rho_i-1} \mathbf{B}_1 \mathbf{u}(t) + \sum_j^{\rho_i} \mathbf{c}_i \mathbf{A}^{\rho_i-j} \mathbf{B}_2 \mathbf{w}^{(j-1)}(t)\end{aligned}\tag{6.40}$$

Then, the subsystem of relative order  $\rho_i$  that directly relates an input to the output  $y_i$  is given by

$$y_i^{(\rho_i)}(t) = \mathbf{c}_i \mathbf{A}^{\rho_i} \mathbf{x}(t) + \mathbf{c}_i \mathbf{A}^{\rho_i-1} \mathbf{B}_1 \mathbf{u}(t) + f_i(\tilde{\mathbf{w}}).\tag{6.41}$$



where  $f_i : \mathbb{R}^n \rightarrow \mathbb{R}$  is a scalar function of the measured exogenous inputs  $\tilde{\mathbf{w}} = (\mathbf{w}, \dots, \mathbf{w}^{(n)})^T$ .

Utilising the same feedback control as (6.36) results in the decoupling control law for linear systems where the elements  $P(\mathbf{x}(t)) = P\mathbf{x}(t)$  and  $Q$  are defined as

$$P\mathbf{x}(t) = \begin{bmatrix} \mathbf{c}_1 \mathbf{A}^{\rho_1} \\ \mathbf{c}_2 \mathbf{A}^{\rho_2} \\ \vdots \\ \mathbf{c}_p \mathbf{A}^{\rho_p} \end{bmatrix} \mathbf{x}(t) \quad Q = \begin{bmatrix} \mathbf{c}_1 \mathbf{A}^{\rho_1-1} \mathbf{B}_1 \\ \mathbf{c}_2 \mathbf{A}^{\rho_2-1} \mathbf{B}_1 \\ \vdots \\ \mathbf{c}_p \mathbf{A}^{\rho_p-1} \mathbf{B}_1 \end{bmatrix} \quad (6.42)$$

As before, if the matrix  $Q$  is invertible, then utilising feedback control of the form

$$\mathbf{u}(t) = Q^{-1}(-P\mathbf{x}(t) - \mathbf{f}(\tilde{\mathbf{w}}) + \mathbf{v}(t)), \quad (6.43)$$

will result in a linear system of the form of eq. (6.37a). Note that for linear systems, the decoupling matrix  $Q$  is static and is not a function of the state. Therefore, provided reasonable estimates of the system parameters, the system can be decoupled without state measurement or estimation.

### Output filtering for non-proper systems

Unlike the inverse dynamics controller, the dynamic inversion cannot be applied directly to systems with a non-zero feedforward matrix i.e. where the control input affects the output directly as in the case of electrical grid power control seen in the example of §§ 6.2.4. Said otherwise, nonlinear inversion is not directly applicable to outputs with a relative degree of zero.

In order to utilise the nonlinear inversion controller for systems with a relative degree zero output, the output-redefinition method can be used, whose principle is to redefine the output function so that the original control theory can be utilised. Provided that the new output function is defined in such a way that it is essentially the same as the original output function in the frequency range of interest, exact tracking of the new output function then also implies good tracking of the original output  $y_i(t)$ .

The output-redefinition method is achieved by introducing an additional state for the output of interest, given by

$$\dot{x}_{y_i}(t) = \frac{1}{\tau_{y_i}}(y_i(t) - x_{y_i}(t)), \quad (6.44)$$



with the new output function given by

$${}^*y_i(t) = x_{y_i}(t)$$

This increases the relative degree of the output by one, so that (6.36) can be implemented directly. The time constant  $\tau_{y_i}$  dictates how quickly the output filter will estimate the actual system output.

#### 6.3.4 Asymptotic control law

The example in §§ 6.3.1 showed that the control of the cooling water temperature in the cogeneration device could be reduced to a first-order linear system as

$$\dot{y}(t) = v(t) \quad (6.29 \text{ revisited})$$

with a simple proportional error controller used for  $v(t)$  to allow for asymptotic tracking of a set-point temperature. However, if the relative degree of the output is greater than one ( $\rho_i > 1$ ) then this would not result in satisfactory control as the order of the system is higher than the number of degrees of freedom. Recall that the feedback linearised output will reduce the the dynamics of an output to

$$y_i^{(\rho_i)}(t) = v_i(t). \quad (6.45)$$

The typical approach in the literature (see e.g. 3, p. 210, 22, p. 266) is to now consider instead of the single demand trajectory  $y_{d,i}(t)$ , consider the demand trajectory up to the relative degree of the system i.e.  $\tilde{y}_{d,i}(t) = (y_{d,i}(t), \dot{y}_{d,i}(t), \dots, y_{d,i}^{(\rho_i)}(t))^T$ . Then asymptotic tracking can be achieved by extending the proportional control to the higher-derivatives. Define the error as  $e_i(t) = y_i(t) - y_{d,i}(t)$ , then if

$$e_i^{(\rho_i)}(t) + K_{\rho_i} e_i^{(\rho_i-1)}(t) + \dots + K_2 \dot{e}_i(t) + K_1 e_i(t) = 0 \quad (6.46)$$

can be satisfied then asymptotic tracking of a reference trajectory  $\tilde{y}_{d,i}(t)$  can be accomplished. Substituting eq. (6.46) into eq. (6.45) results in a synthetic control

$$v_i(t) = y_{d,i}^{(\rho_i)}(t) - \sum_{j=1}^{\rho_i} K_j e_i^{(j-1)}(t). \quad (6.47)$$

The control law (6.47) has resulted in a new system (6.46) where the characteristic



polynomial of its transfer function is

$$s^{\rho_i} + K_{\rho_i} s^{\rho_i-1} + K_{\rho_i-1} s^{\rho_i-2} + K_{\rho_i-2} s^{\rho_i-3} + \dots + K_1. \quad (6.48)$$

If the controller gains  $\mathbf{k} = (K_1, \dots, K_{\rho_i})$  are selected so that eq. (6.48) is a Hurwitz polynomial<sup>9</sup> then the system will be asymptotically stable.

### 6.3.5 Computation of control law

As the calculation of the Lie derivatives and the subsequent solving for the control law (6.36) can be algebraically involved, as before the author has implemented the computation of the control law in MATLAB<sup>®</sup> that makes use of the Symbolic Math Toolbox<sup>™</sup>. Given a general dynamic system described by a nonlinear differential equation in input-affine form (as in eq. (6.33)), the function will construct the input-output inversion-based control law, and evaluate the stability of the internal dynamics. The design of the controller for the synthetic control input(s) is performed separately.

## 6.4 Limitations of inversion-based control laws

While it has been demonstrated that the inversion-based control laws can achieve ‘idealised’ control; this is only feasible when the complete dynamics of the system are known, the parameters are known with absolute certainty, and the all other system inputs are measurable. However, energy systems and the environment in which they operate are complex, highly volatile, and modelling every element in the system is infeasible. These limitations can be broadly separated into the following four categories as they relate to energy systems.

### 6.4.1 Imperfect models

§§ 3.2.2 discussed that the models of the energy systems used in this work are ‘systems level’ models, where the resulting models are manageable and *approximate* physical reality. Although these models will provide a good estimate of the dynamic behaviour of the system they will not be exact. This is because these systems have complex fluid and electrochemical dynamics, 3D heat transfer mechanisms, mechanical vibrations, and many other processes that are challenging to model. Furthermore, the building is subject to unpredictable presence and behaviour of its occupants, and it is impossible to model the climate & its interaction with the building envelope with 100 % accuracy. In fact, even if detailed models of the energy systems were to be used where each of the individual components within a microgeneration device were highly-detailed

<sup>9</sup>A Hurwitz polynomial is a polynomial for which the real part of every root is negative.





models valid at sub-secondly resolution, they would still only provide a close but ultimately flawed model of the actual real-time behaviour of the system.

There will also be several elements in the overall system that are not modelled explicitly within the control laws as their dynamics occur on a short time-scale as opposed to the larger energy systems e.g. fuel valves, water pumps, TRVs. In buildings, the individual items within the zone are not usually modelled discretely but their presence lumped together. This is convenient for energy use estimation but will result in an imperfect model of the thermodynamic behaviour within the zone. In addition, the thermophysical properties of the construction elements cannot be known precisely and are functions of their temperature which is not explicitly modelled.

Finally, even if the models were incredibly accurate, the nonlinear feedback required to render the system behaviour linear (as in eq. (6.36)) may be very mathematically complex and/or very sensitive to parameter uncertainties (7, p. 177).

It is important then that the models used are of sufficient resolution to capture the main dynamical modes of operation of the system, while the control laws are designed to accommodate for the inaccuracies in the modelling.

#### 6.4.2 *Input constraints*

Thus far the physical limits of the inputs have not been considered. All of the control inputs in energy systems controller design and analysis will have constraints on the amount of energy or substance that they are able to transport. These are typically known as the **actuator limitations** and will effect the magnitude and rate of change of the supply of energy from each system. Since the systems are coupled MIMO processes if one of the control inputs has reached its limit, it may not be possible to completely decouple the control channels using the inversion-based control laws. Under these circumstances it is important to robustly handle the input constraints to ensure optimal and safe control.

Furthermore, if the actual control signals  $(u_1, \dots, u_p)$  are bounded i.e. constrained to  $u_i \in [u_{i,\min}, u_{i,\max}]$ , then the bounds for the synthetic inputs  $(v_1, \dots, v_p)$  may become complicated functions of the states and other system parameters (7, p. 177).

#### 6.4.3 *Insufficient measurements*

The nonlinear input-output inversion control (6.36) can require full state measurement in some cases in order to render the overall system linear. While pervasive sensor technology is becoming more commonplace, it is still not guaranteed that all of the necessary state variables in the system will be monitored and available as feedback to the control system. Thus in order to facilitate the coordinated control and operation



of the energy systems it is important to either be able to estimate these measurements as a function of the actual measured outputs, or to be able to compensate for the lack of available measurement signals within the control law itself.

#### 6.4.4 Energy system operational bounds

All of the energy systems have different operational bounds that are not inherently captured in a single model or system of equations. Examples of this are: the different operational modes of the mCHP unit (standby, warm-up, normal, cool-down) where the system dynamics can be considerably different during each; the imposed ‘capacity’ of the TES whereby it is dangerous to attempt to store hot water over a certain temperature throughout the tank; and embedded low-level controls within the energy systems that may impose restrictions on the use of the unit if attempting to control the unit in a way for which it was not designed. It is possible to identify such operational bounds and design controllers that can switch modes depending on the current mode of the energy system.

## 6.5 Summary

This chapter has applied the inversion-based control techniques of inverse dynamics and nonlinear inversion to the control microgeneration-based energy systems. The main contributions of this chapter are

- A algorithm to transform the state-space energy systems models to linear external differential representations that are not only useful for the inversion-based control techniques but can be used for identification of model parameters from monitored data.
- Developed an inverse dynamics controller that can achieve perfect tracking for MIMO nonlinear systems as long as the system model is accurate.
- The existence of an inverse dynamics based controller relies on the regularity condition. It was shown how this regularity condition can be used for control structure design of interconnected energy systems with multiple inputs and outputs.
- Application of nonlinear inversion with asymptotic tracking to the control of energy systems.
- The limitations of inversion-based control techniques were discussed and highlighted the need for robust control techniques.



While conditions are obvious for a simple system, for a complex system of interconnected energy systems the controllability condition could prove most useful in control structure design, building simulation and feasibility studies.

The idealised, inverse dynamics approach to the balance of the energy systems can be considered as a sort of ‘benevolent decision maker’ where the whole system is optimised in real-time i.e. how should the system be operating at any moment in time in order to meet the design objectives (tracking etc.). The next chapter explores how to make these types of control laws applicable in practice with full awareness of their inherent limitations.

## References

1. Dorf, R. C., Bishop, R. H. *Modern Control Systems*. 12th ed. Upper Saddle River, New Jersey: Prentice Hall, 2011: 1104. ISBN: 978-0-13-602458-3 (cited pp. 148, 149)
2. Franklin, G. F., Powell, J. D., Emami-Naeini, A. *Feedback Control of Dynamic Systems*. 6th ed. Upper Saddle River, New Jersey: Pearson Education, Inc., 2010: 837. ISBN: 978-0-13-500150-9 (cited p. 148)
3. Slotine, J.-J. E., Li, W. *Applied Nonlinear Control*. New Jersey: Prentice Hall, 1991: 461. ISBN: 0-13-040890-5 (cited pp. 148, 171, 174, 175, 178)
4. Lyapunov, A. M. *General Problem of the Stability of Motion*. London, UK: Taylor & Francis, 1992: 270. ISBN: 0-7484-0062-1 (cited p. 148)
5. Nise, N. S. *Control Systems Engineering*. 5th ed. Hoboken, NJ, USA: John Wiley & Sons, 2008: 861. ISBN: 978-0471-79475-2 (cited p. 149)
6. Kreyszig, E. *Advanced Engineering Mathematics*. Ed. by Holland, B. 8th ed. Hoboken: John Wiley & Sons, 1999: 1156. ISBN: 0-471-33328-X (cited p. 149)
7. Nijmeijer, H., Van Der Schaft, A. *Nonlinear Dynamical Control Systems* (1989) (cited pp. 152, 180)
8. Goodwin, G. C., Graebe, S. F., Salgado, M. E. *Control System Design*. 1st ed. Prentice Hall, 2000: 908. ISBN: 0139586539 (cited p. 153)
9. (<http://math.stackexchange.com/users/5191/zhen-lin>), Z. L. *What is the 'implicit function theorem'?* Mathematics Stack Exchange. URL: <http://math.stackexchange.com/q/26240> (cited p. 155)
10. Lu, X.-Y., Spurgeon, S. K. Asymptotic stabilisation of multiple input nonlinear systems via sliding modes. *Dynamics and Control* **8**(3): 231–54 (1998). DOI: [10.1023/A:1008206419550](https://doi.org/10.1023/A:1008206419550) (cited p. 156)
11. MathWorks Support Team. *What are the implications of using the Derivative block in Simulink?* The MathWorks, Inc. 2013-10-18. URL: <http://uk.mathworks.com/matlabcentral/answers/95614-what-are-the-implications-of-using-the-derivative-block-in-simulink> (visited on 2016-03-13) (cited p. 157)
12. Chapra, S. C., Canale, R. P. *Numerical Methods for Engineers*. 5th ed. New York, NY, USA: McGraw-Hill, 2006. ISBN: 0-07-291873-X (cited p. 157)
13. Hartley, T. T., Beale, G. O., Chicatelli, S. P. *Digital Simulation of Dynamic Systems: A Control Theory Approach*. Prentice-Hall, Inc., 1994 (cited p. 157)



14. Cao, Y., Rossiter, D. An input pre-screening technique for control structure selection. *Computers & Chemical Engineering* **21**(6): 563–9 (1997-02).  
DOI: [10.1016/S0098-1354\(96\)00296-7](https://doi.org/10.1016/S0098-1354(96)00296-7) (cited p. 157)
15. Loh, E. J., Chiu, M.-S. Robust decentralized control of non-square systems. *Chemical Engineering Communications* **158**(1): 157–80 (1997).  
DOI: [10.1080/00986449708936586](https://doi.org/10.1080/00986449708936586) (cited p. 157)
16. De Wal, M. V., Jager, B. D. Control structure design: A survey. *Proceedings of the American control ...* 5–9 (1995) (cited p. 158)
17. Arndt, U. et al. *Experimental Investigation of Residential Cogeneration Devices and Calibration of Annex 42 Models*. Tech. rep. Annex 42 of the International Energy Agency Energy Conservation in Buildings and Community Systems Programme, 2007: 255 (cited pp. 165, 166)
18. IEA / ECBCS Annex 42. *Standard European Electrical Profiles*. 2006-09. URL: [http://www.ecbcs.org/docs/Annex\\_42\\_European\\_Electrical\\_Standard\\_Profiles\\_Annex\\_42\\_September\\_2006.zip](http://www.ecbcs.org/docs/Annex_42_European_Electrical_Standard_Profiles_Annex_42_September_2006.zip) (visited on 2016-03-14) (cited p. 166)
19. Leith, D. J., Leithead, W. E. Survey of gain-scheduling analysis and design. *International Journal of Control* **73**(11): 1001–25 (2000).  
DOI: [10.1080/002071700411304](https://doi.org/10.1080/002071700411304) (cited p. 168)
20. Van der Schaft, A. J. Representing a nonlinear state space system as a set of higher-order differential equations in the inputs and outputs. *Systems & Control Letters* **12**: 151–60 (1989).  
DOI: [10.1016/0167-6911\(89\)90008-X](https://doi.org/10.1016/0167-6911(89)90008-X) (cited p. 168)
21. Cheng, D., Isidori, A., Respondek, W., Tarn, T. J. Exact linearization of nonlinear systems with outputs. *Mathematical systems theory* **21**(1): 63–83 (1988).  
DOI: [10.1007/BF02088007](https://doi.org/10.1007/BF02088007) (cited p. 169)
22. Lin, C.-F. *Advanced Control Systems Design*. Englewood Cliffs, NJ, USA: Prentice Hall, 1994. ISBN: 0-13-006305-3 (cited pp. 169, 178)
23. Isidori, A., Ruberti, A. On the synthesis of linear input-output responses for nonlinear systems. *Systems & Control Letters* **4**(1): 17–22 (1984-02).  
DOI: [10.1016/S0167-6911\(84\)80046-8](https://doi.org/10.1016/S0167-6911(84)80046-8) (cited p. 169)
24. Isidori, A. *Nonlinear Control Systems*. New York, NY, USA: Springer-Verlag, 1989 (cited p. 169)
25. Phelan, R. M. *Automatic control systems*. London, UK: Cornell University Press, 1977: 280. ISBN: 0-8014-1033-9 (cited pp. 172, 173)





*“...PID control is extremely tolerant of even gross approximations and, therefore, our inability to model the system exactly will be of relatively little consequence in a real situation.”*

---

—RICHARD PHELAN, *Automatic Control Systems*

7

## Robust inversion-based control

THE previous chapter demonstrated that, for a given energy system, an inversion-based controller design can be used to cause the system to exhibit the desired response provided that the dynamic model of the system is known with certainty. However – as discussed in § 6.4 – models are never perfect and the manipulated control inputs are always subject to limitations. As explored in the review of current approaches to the control of energy systems in chapter 2, typically on/off or some type of PID control is used in practice to attempt to counteract (or allow the controlled system to tolerate some amount of) disturbances and uncertainties – with varying levels of success.

The purpose of this chapter is to describe the robust control theory used in the rest of this work to address stability robustness and performance robustness in the presence of uncertainty. The method is based on the RIDE controller methodology discussed in § 2.6. This theory was used as the base structure for the various advancements developed in this thesis in order to make the theory applicable to the whole range of energy supply systems established in chapters 4 and 5. The methodology provides a way to augment the inversion-based control developed in the previous chapter with an outer-loop controller that can compensate for modelling uncertainties and disturbances.

It should be acknowledged that control engineering design is not a linear process. It is an iterative, nonlinear, creative process. However, for the purposes of this work, the controller design is presented as the final design rather than the iterative process that the author endured to conceive the final designs. The case studies in the following chapter will provide comparisons between the proposed controller, those typically used in practice (such as on/off and PID), and modern robust controller design methods ( $H_\infty$  synthesis).



## 7.1 Equivalent control via nonlinear inversion

The concept of fast and slow modes of a system can be directly related to the concept of the relative degree of a system, as explored in the feedback linearisation control in §§ 6.3.2. Recall the feedback linearising control for a LTI system from §§ 6.3.3:

$$\mathbf{u}(t) = \mathbf{Q}^{-1}(-\mathbf{P}\mathbf{x}(t) - \mathbf{f}(\tilde{\mathbf{w}}) + \mathbf{v}(t)) \quad (6.43 \text{ revisited})$$

where

$$\mathbf{P}\mathbf{x}(t) = \begin{bmatrix} \mathbf{c}_1 \mathbf{A}^{\rho_1} \\ \mathbf{c}_2 \mathbf{A}^{\rho_2} \\ \vdots \\ \mathbf{c}_p \mathbf{A}^{\rho_p} \end{bmatrix} \mathbf{x}(t), \quad \mathbf{Q} = \begin{bmatrix} \mathbf{c}_1 \mathbf{A}^{\rho_1-1} \mathbf{B}_1 \\ \mathbf{c}_2 \mathbf{A}^{\rho_2-1} \mathbf{B}_1 \\ \vdots \\ \mathbf{c}_p \mathbf{A}^{\rho_p-1} \mathbf{B}_1 \end{bmatrix},$$

and  $f_i(\tilde{\mathbf{w}}) = {}^2 d_i \mathbf{w}^{(\rho_i)}(t) + \sum_j \mathbf{c}_i \mathbf{A}^{\rho_i-j} \mathbf{B}_2 \mathbf{w}^{(j-1)}(t)$ . Setting the relative degree of the system to  $\boldsymbol{\rho} = (1, \dots, 1)$  and assuming for the moment that the additional synthetic control  $\mathbf{v}$  is zero, then  $\mathbf{P}\mathbf{x}(t) = \mathbf{C}\mathbf{A}\mathbf{x}(t)$ ,  $\mathbf{Q} = \mathbf{C}\mathbf{B}_1$ ,  $\mathbf{f}(\tilde{\mathbf{w}}) = \mathbf{D}_2 \dot{\mathbf{w}}(t) + \mathbf{C}\mathbf{B}_2 \mathbf{w}(t)$  and (6.43) becomes

$$\mathbf{u}(t) = -(\mathbf{C}\mathbf{B}_1)^{-1} (\mathbf{C}\mathbf{A}\mathbf{x}(t) + \mathbf{D}_2 \dot{\mathbf{w}}(t) + \mathbf{C}\mathbf{B}_2 \mathbf{w}(t)). \quad (7.1)$$

Comparing (7.1) obtained from feedback linearisation and the equivalent control (2.4) from the original RIDE methodology it is clear that they are *identical* for systems with a vector relative degree  $\boldsymbol{\rho} = (1, \dots, 1)$  (as  $\mathbf{D}_1$  is zero for systems where  $\forall i : \rho_i > 0$ ).

Therefore, we can see that the equivalent control in the RIDE methodology is the feedback linearising control for LTI systems with a vector relative degree of  $\boldsymbol{\rho} = (1, \dots, 1)$ . Recognising this allows us to immediately create a new equivalent control that is applicable to control affine nonlinear systems by recalling the feedback linearisation control law (6.36)

$$\mathbf{u}(t) = (\mathbf{Q}(\mathbf{x}(t), \mathbf{w}(t)))^{-1} (-\mathbf{P}(\mathbf{x}(t), \mathbf{w}(t)) + \mathbf{v}(t)) \quad (6.36 \text{ revisited})$$

or

$$\mathbf{u}(t) = \mathbf{u}_{\text{eq}}(\mathbf{x}(t), \mathbf{w}(t)) + \boldsymbol{\beta}(\mathbf{x}(t), \mathbf{w}(t))\mathbf{v}(t), \quad (7.2)$$

where

$$\mathbf{u}_{\text{eq}}(\mathbf{x}(t), \mathbf{w}(t)) = -(\mathbf{Q}(\mathbf{x}(t), \mathbf{w}(t)))^{-1} \mathbf{P}(\mathbf{x}(t), \mathbf{w}(t)) \quad (7.3a)$$

$$\boldsymbol{\beta}(\mathbf{x}(t), \mathbf{w}(t)) = (\mathbf{Q}(\mathbf{x}(t), \mathbf{w}(t)))^{-1} \quad (7.3b)$$

The use of this new equivalent control  $\mathbf{u}_{\text{eq}}$  in (7.3a) and dynamic decoupling matrix  $\boldsymbol{\beta}$



in (7.3b) reduces the system to the following simple linear system

$$\begin{bmatrix} y_1^{(\rho_1)}(t) \\ y_2^{(\rho_2)}(t) \\ \vdots \\ y_p^{(\rho_p)}(t) \end{bmatrix} = \begin{bmatrix} v_1(t) \\ v_2(t) \\ \vdots \\ v_p(t) \end{bmatrix} \quad (7.4a)$$

$$\hat{\mathbf{y}}(t) = \mathbf{v}(t) \quad (7.4b)$$

Therefore we have extended the concept of the equivalent control in the RIDE methodology to the control of control-input-affine nonlinear systems of any relative degree  $\forall i : \rho_i \geq 1$ .

## 7.2 Generalised outer-loop controller design

The general control theory principle is to design the controller so that the resulting closed-loop transfer function between the reference input and the controlled variable is unity, and that the closed-loop transfer function between the disturbance loads and controlled variable is zero. Said otherwise, we want to completely reject all disturbances and for the controlled variable to follow the reference input under all circumstances.

### 7.2.1 Control structure

The new equivalent control (7.3) has resulted in a reduced system of the form (7.4a). Applying the typical PDF control structure to a single channel in (7.4a) results in the following input-output transfer function

$$\frac{y(s)}{y_d(s)} = \frac{K_I}{s^{\rho+1} + K_D s + K_I},$$

which has characteristic equation  $\delta(s) = s^{\rho+1} + K_D s + K_I$ . For systems with relative degree  $\rho > 1$  there will be a missing powers of  $s$  in the characteristic equation. From the Routh-Hurwitz stability criterion (1), there must exist a coefficient for all powers of  $s$  and they must all be of the same sign for the system to be stable. Therefore, the structure of the PDF control will need to be extended to systems with  $\rho > 1$ . Fortunately, Phelan specified a generalised PDF structure that is applicable to system of any order, known simply as the generalised PDF control system for controlling the basic  $n$ th-order controlled system (2, p. 243):

$$v_i(t) = K_{I,i} \int (y_{d,i}(t) - y_i(t)) dt - \sum_{q=1}^{\rho_i} {}^i K_{Dq} y_i^{(q-1)}(t). \quad (7.5)$$



This structure has introduced extra derivatives of the output up to  $\rho - 1$ . Substituting (7.5) into (7.4a) and taking the Laplace transform results in the following transfer function between the demand trajectory and the output:

$$G_{ii}(s) = \frac{y_i(s)}{y_{d,i}(s)} = \frac{K_{I,i}}{s^{\rho_i+1} + \sum_{q=1}^{\rho_i} {}^i K_{Dq} s^q + K_{I,i}}. \quad (7.6)$$

Note that the introduction of the integral action has increased the order of the system by one. Now provided the controller gains of each channel  $\mathbf{k}_i = (K_{I,i}, {}^i K_{D1}, \dots, {}^i K_{D\rho})$  are selected so that the denominator of (7.6) forms a Hurwitz polynomial – that ensures all the poles are in the left-half plane – results in a stable system. System performance can then be tuned to get the required tracking performance.

It is possible to determine the steady-state value for  $y$  due to the use of the PDF control by invoking the final value theorem, which is given as

$$y_{ss} = \lim_{t \rightarrow \infty} y(t) = \lim_{s \rightarrow 0} s y(s). \quad (7.7)$$

For a set change in demand set-point of  $y_{d,i}(s) = y_{d,i}/s$ , (7.7) gives

$$y_{ss,i} = \frac{K_{I,i}}{0^{\rho_i+1} + \sum_{q=1}^{\rho_i} {}^i K_{Dq} 0^q + K_{I,i}} = y_{d,i}$$

Therefore, after the transient response of the system has completed the output will track the demand set-point exactly.

In order to differentiate this new generalised controller from the original RIDE controller, and for lack of a better name, from this point forward this controller will be referred to as the nonlinear inversion plus pseudo-derivative-feedback (NI+PDF) controller.

### 7.2.2 Performance specification via controller gains

With the stability and the steady-state tracking of the control system guaranteed, this section is concerned with the transient performance of the controller. For the majority of cases considered in this work, the controlled system will be asked to respond to step changes in set-point or to regulate the output to zero. As discussed in § 3.5 the transient performance of a controller with reference to a step change in set-point is characterised in terms of tracking/regulation metrics: rise time, overshoot & peak time, and settling time.

There are an infinite possible selection of controller gains  $\mathbf{k}_i$ , and methods for tuning controllers is still an active area of research. In order for the controller to be

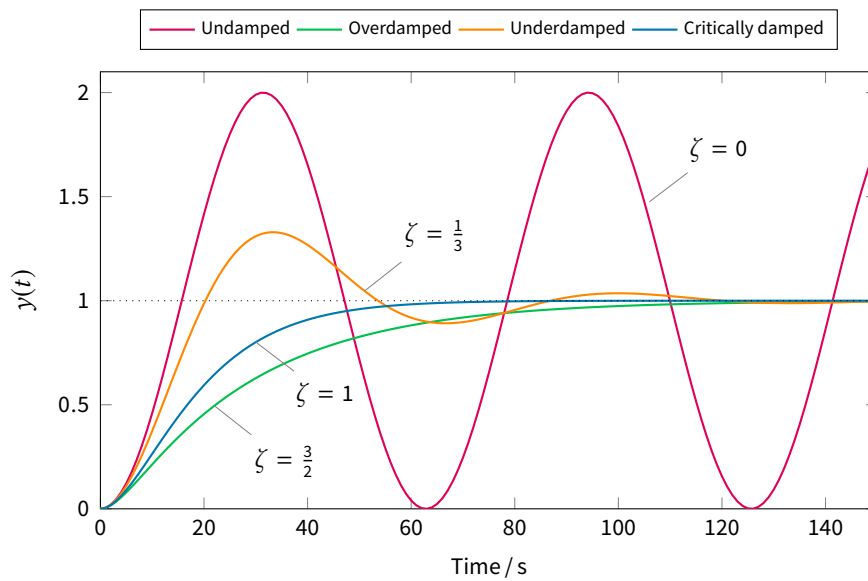


**Figure 7.1 | Second-order system response types.** All systems have the same natural frequency,  $\omega_n = 0.1 \text{ rad s}^{-1}$ . Each form of response corresponds to a different value of the damping ratio,  $\zeta$ , as indicated on the figure.



implemented in practice as easily as possible an objective of this work was to determine a method to tune the controller gains simply and effectively. In the past, tuning the gains of the RIDE controller has been performed via pole-placement techniques (3), and more recently via constrained genetic algorithms (4). These techniques were developed for the original RIDE methodology, where each channel had two gains i.e. there are the same number of gains as the desired order of response. This work has developed a method to tune the  $(\rho_i + 1)$  gains of each PDF controller for systems of any relative degree (order).

The use of the nonlinear inversion reduces the system to a linear system of *fixed* structure. This makes it possible to construct a method of controller tuning that is applicable to any energy system (provided the nonlinear inversion exists). This section shows how the controller gains of the PDF controller can be algebraically determined from a given set of desired tracking/regulation metrics.

### Background

As shown by (2.6), an output with relative degree of 1 will result in the following closed-loop second-order system for that channel:

$$G(s) = \frac{K_I}{s^2 + K_D s + K_I} = \frac{\omega_n^2}{s^2 + 2\zeta\omega_n s + \omega_n^2}.$$

where the roots of its characteristic equation are given by  $s_{1,2} = -\zeta\omega_n \pm j\omega_n\sqrt{1 - \zeta^2}$ . A second-order closed-loop system such as this can exhibit 4 types (or forms) of response: undamped, underdamped, critically damped, and overdamped. Each relating to the damping ratio,  $\zeta$ , of the system. Figure 7.1 summarises the types of response.

- *Undamped*: An undamped response is also known as a *marginally* stable response as its response is that of a sinusoid that does not decay. These type of response are unsatisfactory and will be avoided.  
Poles at  $s_{1,2} = \pm j\omega_n$  and  $\zeta = 0$ .
- *Overdamped*: Overdamped systems have zero overshoot but have excess energy absorption in the response causing the response to appear ‘sluggish’ in contrast to the other types of response. Poles at  $s_{1,2} = -\zeta\omega_n \pm \omega_n\sqrt{\zeta^2 - 1}$  and  $\zeta > 1$ .
- *Underdamped*: Underdamped systems always exhibit overshoot of their final steady-state value and will have a decaying oscillation after the peak value due to the imaginary roots. Poles at  $s_{1,2} = -\zeta\omega_n \pm j\omega_n\sqrt{1 - \zeta^2}$  and  $0 < \zeta < 1$ .



- *Critically damped*: Critically damped responses have zero overshoot without the excess energy absorption of overdamped systems. They are also the quickest response for zero overshoot compared to underdamped systems.

Poles at  $s_{1,2} = -\zeta\omega_n$  and  $\zeta = 1$ .

### Tuning for underdamped response

First, the selection of controller gains for a second-order closed-loop system (i.e. relative degree of 1) are considered before extending the method to systems of any relative degree.

The output of the general second-order system is in the Laplace domain as

$$y(s) = G(s)y_d(s) = \frac{K_I}{s^2 + K_D s + K_I} \frac{y_d(s)}{s}.$$

Taking the inverse Laplace transform and simplifying produces

$$y(t) = y_d \left( 1 - \frac{\sqrt{K_I}}{\sigma} e^{-\frac{K_D t}{2}} \sin(\sigma t + \phi) \right), \quad (7.8)$$

where  $\sigma = \sqrt{K_I - K_D^2/4}$  and  $\phi = \tan^{-1}(2\sigma/K_D)$ . Equation (7.8) is the exact solution of the second-order closed-loop system in terms of the PDF controller gains. This exact solution can now be used to determine the time-domain performance metrics as functions of the PDF controller gains.

For underdamped systems this results in the following performance metrics (see appendix C.2 for derivation):

Peak time:

$$T_p = \frac{2\pi}{\sqrt{4K_I - K_D^2}} \quad (7.9a)$$

Overshoot fraction:

$$\overline{OS} = e^{(-\pi K_D / \sqrt{4K_I - K_D^2})} \quad (7.9b)$$

Settling time:

$$T_s = -\frac{1}{K_D} \ln \left( \frac{c_s^2(4K_I - K_D^2)}{4K_I} \right) \quad (7.9c)$$

where  $c_s$  is the settling time criterion i.e. the settling time will be the time for the response to reach and stay within  $\pm c_s(\%)$  of the steady-state value. By selecting any two performance metrics from (7.9), it is possible to solve for  $(K_I, K_D)$ .

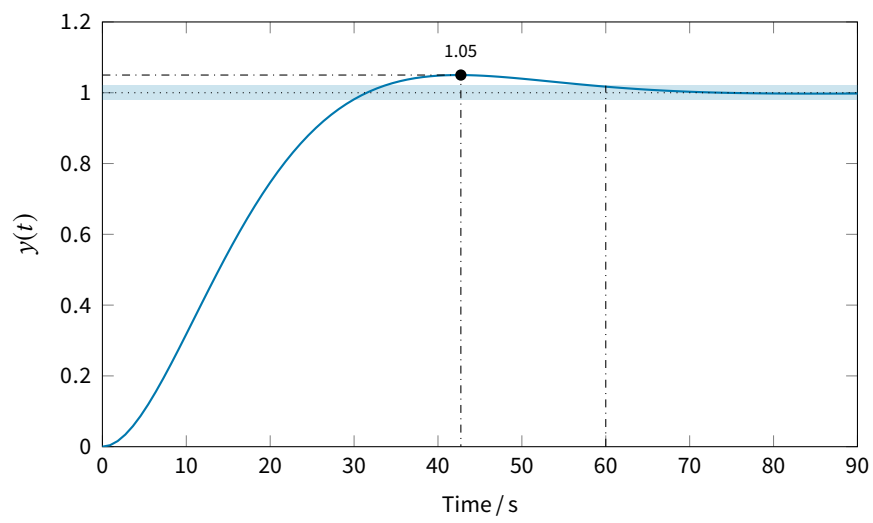


**Figure 7.2** | Underdamped second-order system with desired response. Shaded area indicates the 2% settling time criterion.

**EXAMPLE** For a given output channel the desired settling time is 60 s with a maximum overshoot of 5%. Substituting these values into eqs. (7.9b) and (7.9c) yields gains of  $(K_I, K_D) = (0.0105, 0.1412)$ . Figure 7.2 shows the response curve for the output of the system with these gains, which has achieved the specified performance metrics.

### Tuning for critically damped response – the optimum

Critically damped responses are the fastest possible without overshoot and are considered the optimum response of the controller. Recall again that the output of the general second-order system in the Laplace domain is given by

$$G = \frac{K_I}{s^2 + K_D s + K_I},$$

which has a characteristic equation of  $\delta(s) = s^2 + K_D s + K_I$ . The roots of this equation are given by

$$r_{1,2} = -\frac{K_D}{2} \pm \frac{\sqrt{K_D^2 - 4K_I}}{2}.$$

As discussed in the background section, critically damped systems have poles with equal real parts and zero imaginary parts. Therefore, critically damped systems require that  $\sqrt{K_D^2 - 4K_I} = 0$ , which results in a pseudo-derivative gain of

$$K_D = 2\sqrt{K_I}. \quad (7.10)$$

The system now has the form

$$G = \frac{K_I}{s^2 + 2\sqrt{K_I}s + K_I}, \quad (7.11)$$

and the design poles are located at  $r_{1,2} = -\sqrt{K_I}$ .

Taking the inverse Laplace transform of (7.11) that is subject to a set change in set-point  $y_d(s) = y_d/s$  and simplifying produces

$$y(t) = y_d \left( 1 - e^{-\sqrt{K_I}t} \left( 1 + \sqrt{K_I}t \right) \right). \quad (7.12)$$

Equation (7.12) gives the exact response of a critically damped second-order closed loop system, which is a function of a single gain,  $K_I$ . This can now be used to determine the appropriate gain from the desired performance metrics. As a critically damped system has no peak time or overshoot, the only remaining criteria on its performance is the settling time. This corresponds to the time at which the decaying exponential in

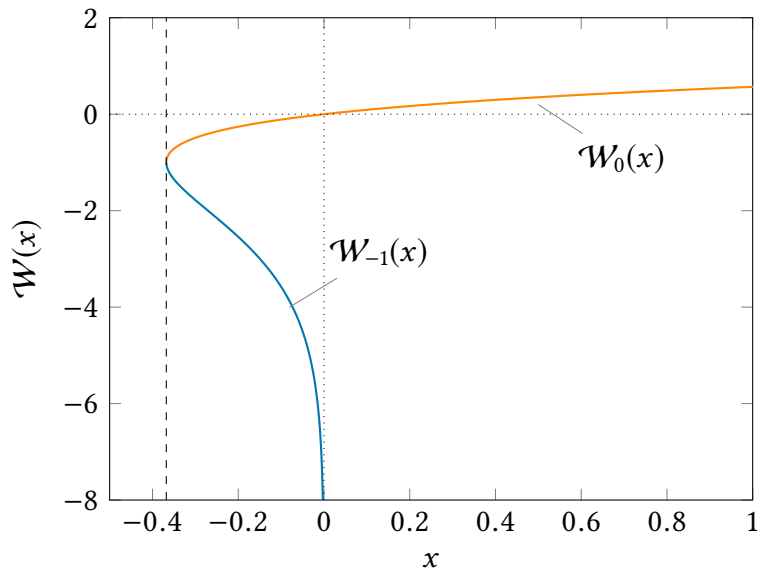


**Figure 7.3** | Plot of two main branches of Lambert-W function. Dashed line indicates the left-extreme of the function at  $-1/e$ .

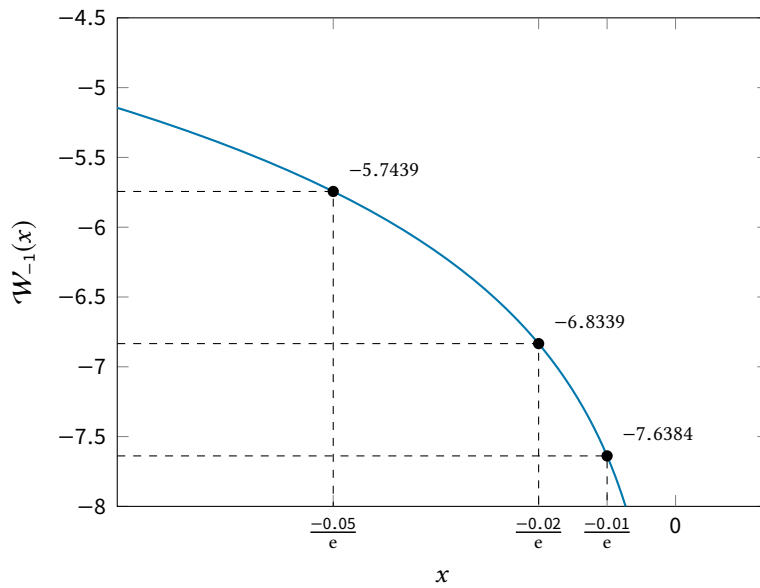


**Figure 7.4** | Plot of  $W_{-1}(x)$  with settling time criteria.

(7.12) is

$$e^{-\sqrt{K_I}t} \left( 1 + \sqrt{K_I}t \right) = c_s, \quad (7.13)$$

where  $c_s$  is the settling time criterion i.e. the settling time will be the time for the response to reach and stay within  $\pm c_s(\%)$  of the steady-state value. Solving (7.13) at  $t = T_s$  for the integral gain yields

$$K_{I,c_s\%} = \frac{1}{T_s^2} (\mathcal{W}_{-1}(-c_s/e) + 1)^2, \quad (7.14)$$

where  $\mathcal{W}(x)$  is the Lambert-W function, which is a set of solutions of the equation  $x = \mathcal{W}(x)e^{\mathcal{W}(x)}$  and  $\mathcal{W}_k(x)$  corresponds to the  $k$  branch of the solution. Figure 7.3 shows a plot of the two main branches of the Lambert-W function.

To simplify the problem, only a select few values of the settling time criterion are now considered. Therefore, the only requirement is to find the value of the Lambert-W function corresponding to the specific settling time criteria. Figure 7.4 shows the values of the Lambert-W function for 1%, 2%, and 5% settling time criteria. Using the corresponding values from the figure results in the following simple algebraic equations for the integral gain of the PDF control for specific settling time criteria:

$$K_{I,5\%} = \left( \frac{4.7439}{T_s} \right)^2, \quad K_{I,2\%} = \left( \frac{5.8339}{T_s} \right)^2, \quad K_{I,1\%} = \left( \frac{6.6384}{T_s} \right)^2. \quad (7.15)$$

Therefore, using (7.15) and recalling that  $K_D = 2\sqrt{K_I}$  from (7.10) the controller gains for each channel of the PDF controller can be determined via simple algebraic equations that will cause the response of each output to respond to a step change in set-point as a critically damped system with a prescribed settling time.

**EXAMPLE** Using the relations of eqs. (7.10) and (7.15) and a desired settling time of 60 s results in gains ( $K_D, K_I$ ) of (0.2213, 0.0122), (0.1945, 0.0095), and (0.1581, 0.0063) for 1%, 2%, and 5% settling time criterion respectively. Figure 7.5 shows the response of each respective second-order system. These response curves show the system is critically damped and achieves the prescribed settling time for each criteria.

These figures demonstrate that the eqs. (7.10) and (7.15) are able to determine the gains for a second-order closed-loop system that will cause it to be critically damped with a prescribed settling time. Figure 7.8 illustrates that having a stricter criteria for settling time will increase the maximum value of the actuator input, but will not increase the overall energy requirements to move the system from its initial conditions to the set-point when the magnitude of the settling time demand remains the same.





### Dominant pole technique for NI+PDF control

The previous section has developed a method for pole placement for PDF control applied to the resulting linear subsystem after the application of equivalent control obtained via nonlinear inversion. However, the system will only exhibit the desired response provided that the relative degree of the system is one. When the relative degree is larger than one there are  $(\rho_i - 1)$  excess poles in the characteristic equation of each output, which also results in extra  $(\rho_i - 1)$  controller gains that must be computed.

This work uses what is known as the *dominant pole placement* method to assign the location of the other poles, and therefore determine the values for the extra controller gains. Pole placement is a well-established design method for linear control systems (5) and is widely used in PID controller tuning (SISO: 6, MIMO: 7).

The method is conceptually straightforward – choose the desired location of a pair of poles that represent the desired performance metrics of the closed-loop response, and make them ‘dominant’, that is, the other poles are placed far to the left of the dominant poles, so that the amplitude of the transients due to these poles are small.

This work extends the concept to PDF control structures with specific consideration to the application to the fixed structure linear subsystem obtained after nonlinear inversion of the original nonlinear system.

Mathematically the idea of the dominant pole placement methods can be considered as follows. First consider a general transfer function with no zeros:

$$G(s) = \frac{1}{(s + r_1)(s + r_2)(s + r_3) \cdots (s + r_n)}.$$

The output in general terms for a unit step input is given by

$$y(t) = \kappa_0 + \kappa_1 e^{-r_1 t} + \kappa_2 e^{-r_2 t} + \kappa_3 e^{-r_3 t} + \cdots + \kappa_n e^{-r_n t}.$$

It can be seen that if the magnitude of  $r_{3 \rightarrow n}$  are much larger than that of the ‘designed’ poles  $r_{1,2}$  the transient response due to the additional poles will occur much faster than for the ones for which the system is designed. Therefore, the further the poles are placed from the design poles the response will approach that of the second-order system.

Then by placing the excess poles at some distance  $W$  from the primary design poles will allow the system to respond as an approximately second-order system. However, moving such poles can require large control effort – the further away the poles are moved the closer the system will respond as a second-order system, but the larger the control effort will be. When this method is used in state-space pole placement

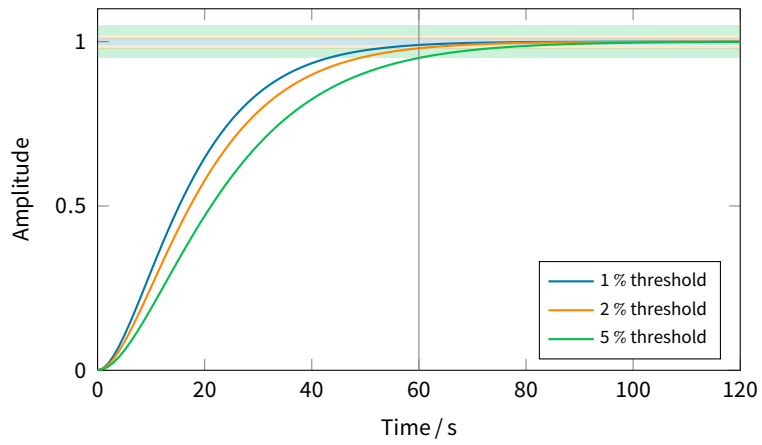


**Figure 7.5 | Comparison of settling time criterion for critically damped RIDE control (1).** Response curves show the response is critically damped with a prescribed settling time. Shaded areas indicate the settling time bands.

or traditional PID, the system to which it is applied is different each time, and the distance  $W$  becomes yet another variable that the controller designer can manipulate until the response is satisfactory.

However, as was exploited in the previous section for the controller gains, the equivalent control reduces the system to an LTI input-output system with a *fixed* structure. As will now be shown, this can be used to determine an optimal distance for the NI+PDF controller based on the relative degree of each output. This optimal distance aims to strike a balance between how much the system can respond as a second-order system and the resulting control effort required to do so.

As was done in the previous section, first place the design poles at  $r_{1,2} = -\sqrt{K'_I}$ , where  $K'_I$  is the integral gain of the target second-order system response from (7.15). Then place the excess poles at a distance  $W$  from the design poles i.e.  $r_{3 \rightarrow n} = -W\sqrt{K'_I}$ . Now the corresponding transfer function becomes

$$G(s) = \frac{W^{\rho-1}(K'_I)^{\frac{1}{2}(\rho+1)}}{(s + \sqrt{K'_I})^2(s + W\sqrt{K'_I})^{\rho-1}}.$$

To determine an optimal distance for  $W$ , two performance indexes were defined:

$$\mathcal{J}_u = \int_0^{\infty} |u| dt$$

and

$$\mathcal{J}_e = \int_0^{\infty} |y' - y| dt$$

where  $\mathcal{J}_u$  is a measure of the controller effort and  $\mathcal{J}_e$  is a measure of the error between the target response  $y'$  and the observed response  $y$ . A series of simulations were conducted where the relative degree of the system was increased from 2 to 10 and for each value of relative degree the distance  $W$  from was moved from 2 to 100 times away from the design poles. The performance indices were normalised to the unit square so that the systems of different relative degree are on the same figure and the results are shown in fig. 7.9.

Each of the curves have a 'knee' point, which corresponds to the optimal trade-off between controller effort and response. It can be seen that increasing the distance past a certain point will rapidly increase the control effort and will no longer be worth the corresponding performance benefit. In order to find this knee point algorithmically, the 'Kneedle' method by Satopää et al. (8) was used that provides a general approach to knee detection for data sets. Figure 7.10 shows the knee-detection for the design trade-off curve for a system of relative degree of 4. The corresponding response curves in figs. 7.11 and 7.12 show that based on detected optimal distance the system has an



approximately second-order response with reasonable control effort.

Figure 7.13 shows the response for the considered range of relative degree with the optimal pole placement distance. This demonstrates that regardless of relative degree the system will respond as an approximately 2nd order system.

In fact, a remarkable result can be found by plotting the relative degree of the system against the optimal excess pole placement distance as shown in fig. 7.14. This demonstrates that it is possible to determine the optimal excess pole placement distance from the following linear regression equation:

$$W = 7.785\rho - 10.843. \quad (7.16)$$

Therefore, regardless of the relative degree of the system, for the response of the NI+PDF controller to be critically damped with a prescribed settling time, the excess poles should be placed at a distance:

$$r_{3 \rightarrow \rho-1} = -(7.785\rho - 10.843)\sqrt{K'_1}$$

In addition, if this dominant pole technique is used without consideration for constraints on the inputs, this can be used as a sizing method to know how large pumps, valves, or energy supply systems would have to be in order to have the desired response.

### **7.3** Input constrained control system

The performance of all real systems is limited by the capabilities of the actuators that are responsible for the transfer of energy from the control system to the process being controlled. So far the control theory developed in this chapter has considered dynamic systems which are continuous, however, all of the energy systems considered in this work have discontinuous dynamics in their actuating systems: The actuating control value that supplies fuel to the mCHP engine has a maximum and minimum fuel supply, as well as restricted rate at which the fuel can be delivered. Electrical energy storage also has low-level electronics that restricts the maximum permissible current that can be transferred to the device to avoid overheating and to protect their inner circuitry. Depending on the type of thermal energy store, these can have mechanical/hydraulic actuators that have physical limits on the magnitude or flow rate of water entering/exiting from the tank. A hydronic heating system will have pumps which also have physical limits on the magnitude of the flow rate of water through the system. Many of these discontinuous limits are designed to ensure safe performance of the energy system, and so the controller should be respectful of these

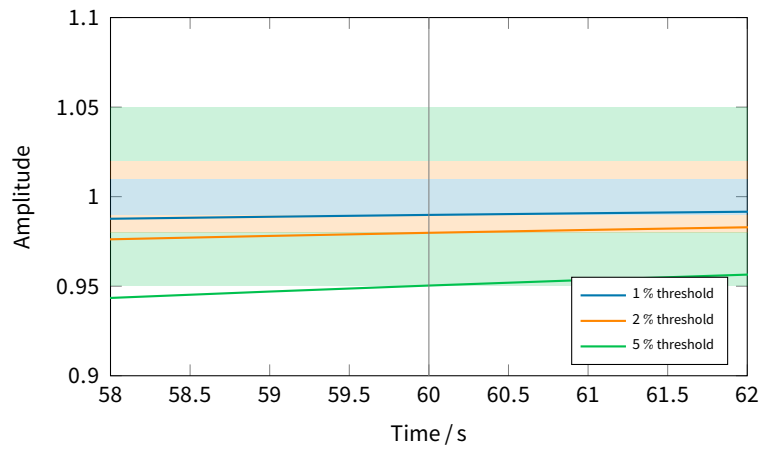


**Figure 7.7** | Comparison of settling time criterion for critically damped RIDE control (2). Zoomed axis range with response curves showing the desired settling time of 60 s is achieved with respect to different settling time criteria.

system limitations to ensure optimal and safe control.

There are many cases when a system may reach the limits of the actuator; this can be when there is a large change in set-point such that the system must drive as hard as possible to reach its target. There is also the case where a large disturbance may cause the actuator to saturate. A well-designed controller should be capable of handling *exceptional* disturbances, i.e. disturbances of intensity higher than the predicted bounds of the uncertainties discussed in §§ 3.4.1. If integral control is used in such cases, the integral term in the control action may become unreasonably large, so that once the disturbance stops, the system goes through large amplitude oscillations in order to return to the desired trajectory.

### 7.3.1 Overdriven system performance

When any of the physical limits of any one of the actuators have been reached, the system is said to be in overdriven operation. Predicting the response of an overdriven system is much more complicated, since under these circumstances even a linear system will have been forced into nonlinear behaviour (2). This nonlinear behaviour is especially prevalent in systems which include integral action.

For this discussion, denote the controller output as  $\mathbf{u}$  as before, and the actual process input from the actuators as  $\mathbf{v}$  as shown in fig. 7.6.

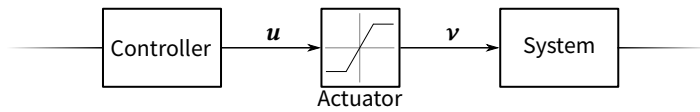


**Figure 7.6** | Input constrained control system.

Further, denote the actuator saturation with a general limit  $\mathbf{v}_{\text{limit}}$ .

For the NI+PDF control system eqs. (7.2) and (7.5), for a single control variable  $u_i$  while the controller output is within the actuator limit,

$$v_i = u_i = u_{\text{eq},i}(\cdot) + \sum_{j=1}^p \beta_{ij}(\cdot) v_j \quad (7.17a)$$

$$= u_{\text{eq},i}(\cdot) + \sum_{j=1}^p \beta_{ij}(\cdot) \left( K_{I,j} \int \underbrace{(y_{d,j} - y_j)}_{e_j} dt - \underbrace{\sum_{q=1}^{\rho_j} {}^j K_{Dq} y_j^{(q-1)}}_{u_{D,j}} \right) \quad (7.17b)$$

$$= u_{\text{eq},i}(\cdot) + \sum_{j=1}^p \beta_{ij}(\cdot) \left( K_{I,j} \int e_j dt - u_{D,j} \right) . \quad (7.17c)$$





However, when an actuator limit has been reached the system is overdriven and now

$$v_i = v_{\text{limit},i},$$

but still

$$u_i = u_{\text{eq},i}(\cdot) + \sum_{j=1}^p \beta_{ij}(\cdot) \left( K_{I,j} \underbrace{\int e_j dt}_{\text{continues to increase}} - u_{D,j} \right)$$

The integration will continue to increase rapidly the value of  $u_i$  as long as the sign of  $(e_j, \beta_{ij})$  do not change, since the magnitude of the error is no longer decreasing. However, note that this control contains additional elements  $u_{D,j}$  and  $u_{\text{eq},i}$ . Each integral term will increase in the direction of the error signal as  $e_j = y_{d,j} - y_j$ , however, as  $u_{D,j}$  is only a function of the output and its derivatives, each  $-u_{D,j}$  term will act in the opposite direction to attempt to alleviate the problem.<sup>1</sup> Unfortunately, this effect is slight, because the integral builds up a lot faster than the magnitude of the output changes. Recall that the equivalent control attempts to drive the rate-of-change of  $y_i$  to zero i.e.  $\dot{y}_i = 0$ . Therefore, once at the limit, the equivalent control will act to remain at the value of the output when the system entered the saturation region. This has the same helping effect as the PDF term but is even less pronounced, since the amount of controller effort required to remain steady will almost always be less than the amount required to move toward the set-point.

Also it should be recognised that the ‘decoupling’ provided by the nonlinear inversion does not imply that the limitations on each control variable  $u_i$  can be assessed separately. The limitations are imposed on the actual control  $u_i$  not the independent synthetic control  $v_i$ . Therefore, any of the synthetic control signals can cause the control to saturate i.e. the saturation of one control input  $u_i$  can actually cause one of the other synthetic controls  $u_j$  to wind-up. The control inputs are only truly independent if  $\beta$  is a diagonal matrix i.e.  $\forall i, j \in \{1, 2, \dots, p\}, i \neq j \implies \beta_{ij} = 0$ .

### Example

The following is an example of this so-called **integrator wind-up** phenomenon, as seen when attempting to control the engine temperature of the mCHP engine. A Stirling mCHP engine does not produce electricity at maximum efficiency until the engine has reached a nominal temperature. Therefore, from a cold start the system will enter the saturation region as the fuel flow rate will be at actuator’s maximum permissible

<sup>1</sup>This is another reason why PDF control should be favoured over PID control – since the proportional term in PID is also error actuated, it would exacerbate the situation.

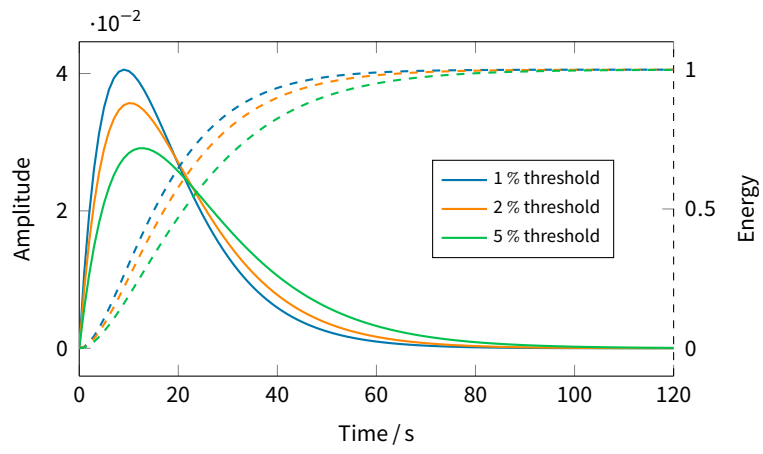


**Figure 7.8** | Comparison of control effort for different settling time criteria.

value in order to reach the nominal temperature – and thereby be generating power at maximum efficiency – as quickly as possible.

In the following example, the fuel flow rate is limited to  $v_{\min} = 0$  and  $v_{\max} = 18.4 \text{ g min}^{-1}$  and has been tuned – in the non-limit case – to be critically damped (system *should* respond with zero overshoot). The response curves of the engine from an initial condition of  $15^\circ\text{C}$  to a step command of  $257^\circ\text{C}$  (the nominal temperature of the engine) are plotted in fig. 7.15. Both the fuel flow rate restrictions and nominal engine temperature are based on the WhisperGEN mCHP engine, with empirical data taken from (9).

As can be seen, the engine temperature increases while  $v = v_{\max}$  and there is severe overshoot. There is also a negative overshoot because the first overshoot was great enough to overdrive the system towards the lower limit  $v_{\min} = 0$ . This is due to the integral increasing rapidly and the  $u$  quickly reaches the actuator limit  $v_{\max}$ . The only way  $u$  can decrease is when the error becomes negative and the integration operation begins to decrease. Consequently,  $v$  cannot start to pull away from the saturation value until the value of  $u$  decreases to the level of  $v_{\max}$ . Note that the level of wind-up is dependent upon the length of time an error exists as well as upon the magnitude of the error.

It is important to note that while  $y$  eventually follows the set-point closely as a linear system, there is a time delay in recovering from being overdriven, and  $y$  fails to follow the set-point at all until recovery has been completed. This general type of behaviour is always present when the control algorithm contains the operation of integration and the system is driven beyond its linear operating range. This is a well-known source of degradation of performance, and can at times lead to a complete loss of control and force the system into an unstable response. This can be seen to be of particular concern at the process start-up since the system will likely be far from the requested set-point.

From this example it is clear that the nonlinear dynamics of the actuator can be detrimental to the performance and has to be somehow taken into account in the design of the controller. The following section will introduce the RIDE methodology's procedure for dealing with actuator saturation and the resulting integrator windup, and will then offer an amendment to the current method that can eliminate all problems associated with integrator windup when utilising the NI+PDF controller.

### 7.3.2 Constraint handling techniques

If the system is well designed, the final control elements will be capable of supplying the energy required by the controlled system to ensure that the controlled variable

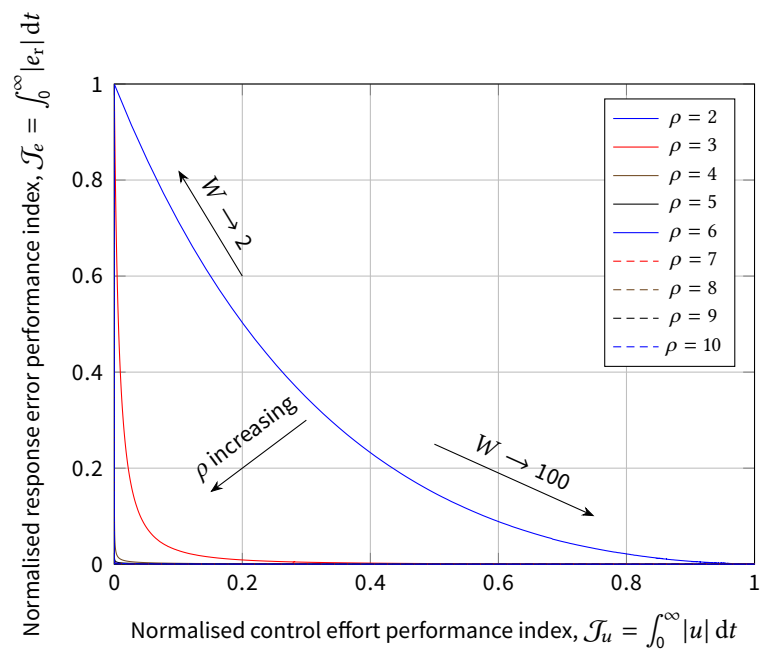


**Figure 7.9** | Design trade-off curves for excess-poles placement distance.

follows the reference set-point within the performance specifications over the specified range of operation. Under such circumstances, the only way a reasonably well tuned system can get into trouble is for it to be driven into the saturation region.

There have been numerous studies into integrator wind-up compensation, the majority of which are designed for PID controllers (10, 11). However, the key element to all techniques is to simply ensure that the output of the controller never asks the actuators to do anything they cannot do, by controlling the value of the output of the integrator.

A common and potentially obvious way to avoid integrator wind-up is to avoid saturating the actuator in the first place. This can be achieved by appropriately sizing the energy supply systems and their actuators so that it is always able to supply any potential demand for energy. However, this will often not be practical or efficient, since maximum/peak demand may only occur for a limited time during the lifetime of the system if they were to be sized this way. And as discussed previously, most energy supply systems are at their most efficient when running at full load, so operating at (but not beyond) the actuator limits can actually be the most energy efficient control option.

Another option is to ‘de-tune’ the control system, so that its response to large errors is slower, which will in turn smooth the changes in the control signal such that it avoids entering the saturation region. Obviously this will lead to a downturn in controller performance that will almost always be unacceptable or fall far from the performance specifications. Again, this is especially true for the control of energy supply systems since they must react quickly to the electrical and thermal demands of the building.

An interesting approach has been proposed by Kurtz, Henson (12) for a constrained SISO nonlinear system (specifically for a continuously stirred chemical reactor) using an input-output linearisation strategy. It first applies the input-output linearisation on the original system. Then, it uses a constraint mapping algorithm to transform the constraints on  $u$  onto constraints on  $v$ . A MPC is then used as the synthetic control  $v$ , which looks ahead over a future (short) time-horizon to determine if the actuators may saturate, and then make corrections to the controller input to stop it from saturating. However, this method requires an accurate model of the disturbances in order to be effective (12, p. 11). Were an unstructured uncertainty to happen in this time frame it could saturate the actuators anyway and potentially cause instability in the system. Furthermore it is only designed for a SISO system, with multiple inputs and outputs the solving of the MPC – especially if the inputs are highly coupled – could lead to significant computational expense for every update period of the controller.

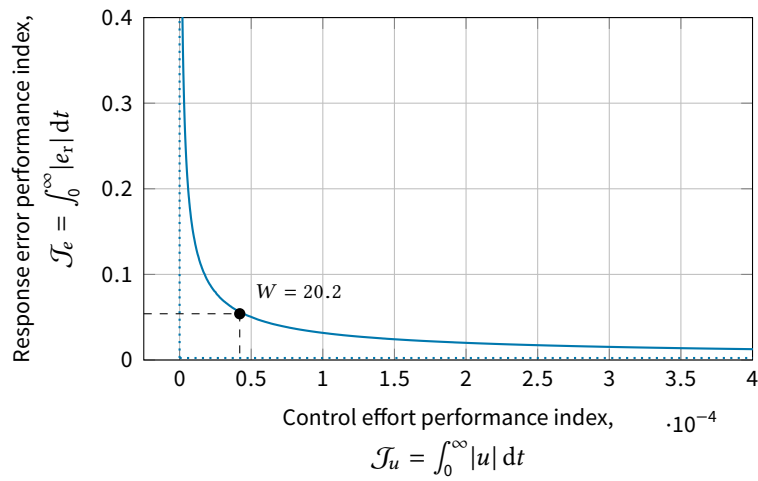


**Figure 7.10** | Design trade-off curve for  $\rho = 4$ .

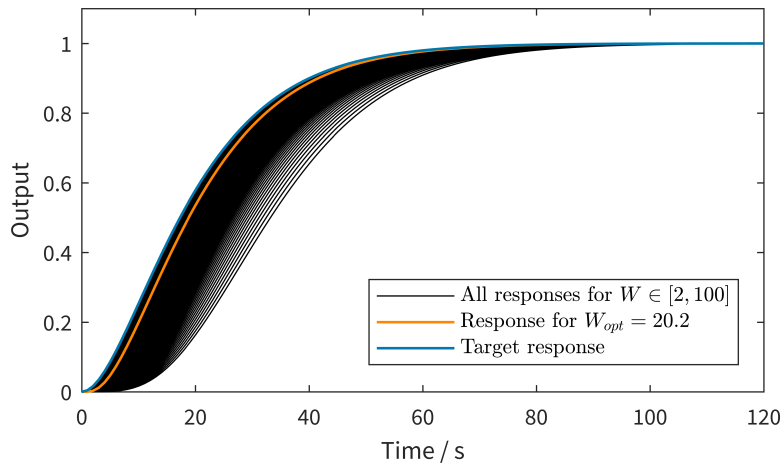


**Figure 7.11** | Family of responses for output of system with  $\rho = 4$ .

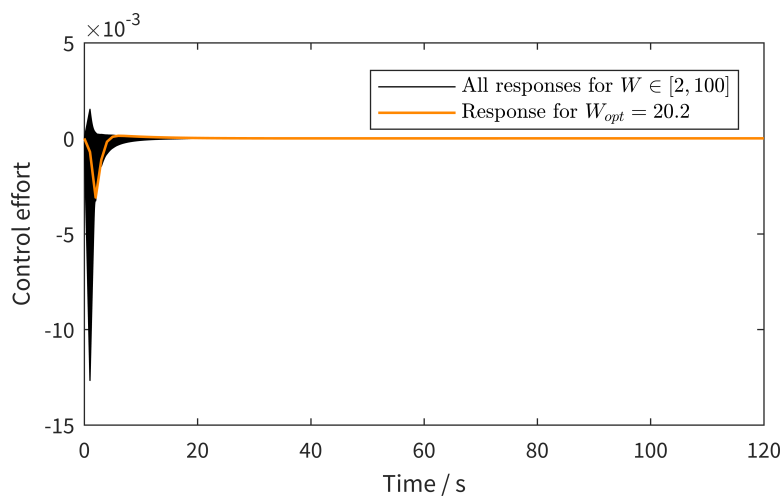


**Figure 7.12** | Family of responses for control effort of system with  $\rho = 4$ .

Nevertheless, the author considers this an interesting area of study and is discussed in future work § 9.3 as to how it may be used with the control strategy proposed in this work in the future.

The final, and most robust way to cope with input constraints and the resulting integrator wind-up is to design a variable structure controller so that when the controller output has reached either limit, any future control action must either keep  $u_i$  constant or reduce it so that it will continue its normal mode of operation (3).

### 7.3.3 New anti-lock integrator wind-up compensation

The constraints on the control input vector are then  $\mathbf{u} \in U$  with the set

$$U = \left\{ \mathbf{u} = (u_1, \dots, u_p)^T \in \mathbb{R}^p : u_{LL,i} \leq u_i \leq u_{UL,i}, i = 1, \dots, p \right\}$$

and  $u_{LL,i} \geq v_{\min,i}$  and  $u_{UL,i} \leq v_{\max,i}$ . Here  $(u_{LL,i}, u_{UL,i})$  are the lower and upper limits of the controller output  $u_i$  respectively and  $(v_{\min,i}, v_{\max,i})$  are the minimum and maximum limits of the actuator  $v_i$ . Note here the distinction between the limits of the controller output  $\mathbf{u}$  and the actuator output / system input  $\mathbf{v}$ .  $\mathbf{v}$  represent the physical limits on the actuators, while the limits  $\mathbf{u} \in U$  are imposed on the controller. This allows the controller to have constraints on the magnitude of the control output that are less than the physical constraints. This is especially useful for systems with mechanical actuators such as valves and pumps, where it may cause damage to the physical actuator if it were to strike up against its limits. Note that in a ‘commercially useful’ system it will be desirable to set the limit values without measurement or calculations. So the values of the actuator limits should be taken from manufacturers specifications. Implementing these dynamic limits ensures safe operation as the controller will never ask the actuator to do something it isn’t capable of.

Mathematically to ensure that when the controller output has reached either limit, any future control action must either keep  $u_i$  constant or reduce it so that it will continue its normal mode of operation can be expressed as:

$$u_i \dot{u}_i \leq 0 \quad \text{when } u_i \geq u_{UL,i} \vee u_i \leq u_{LL,i}. \quad (7.18)$$

If (7.18) can be guaranteed, then the controller output  $u_i$  will always tend to remain at or move away from a saturation limit.

To enforce this behaviour, the traditional RIDE methodology proposes a switching

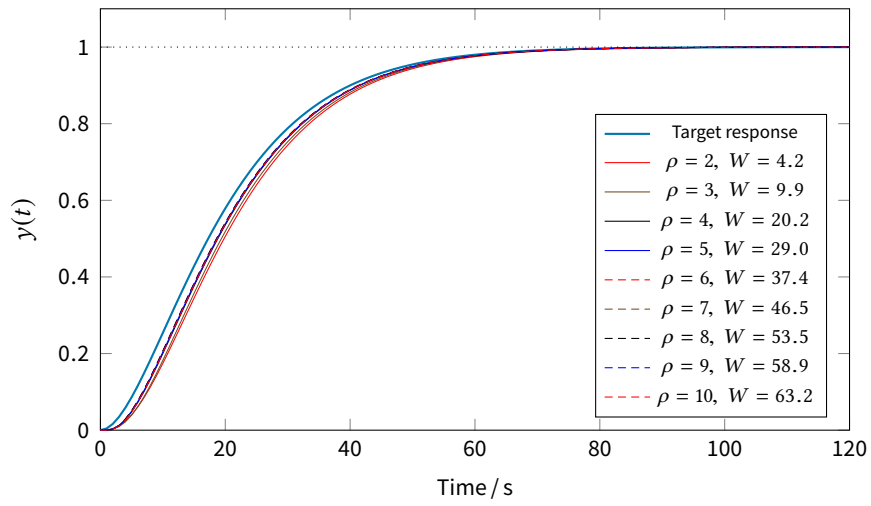


**Figure 7.13** | Response of systems for a range of relative degree with optimal excess pole placement.

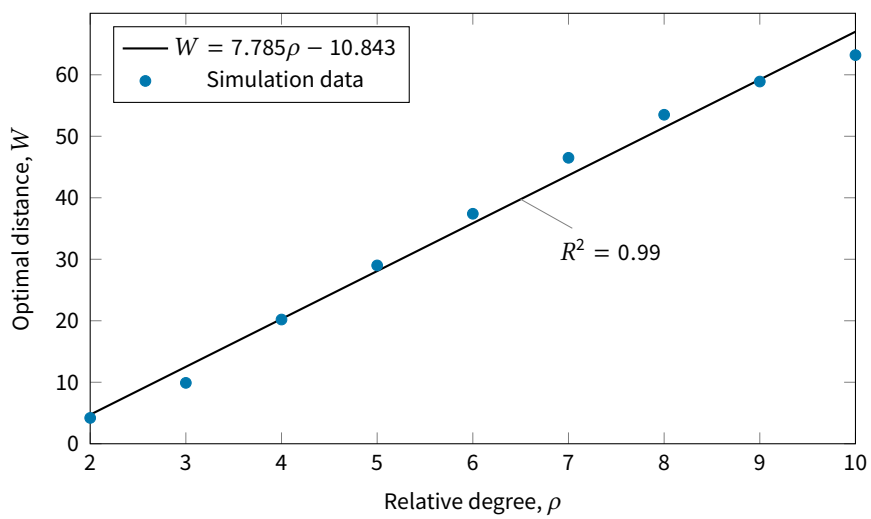


**Figure 7.14** | Linear regression fit for relative degree vs optimal excess pole distance.



surface given as

$$\dot{z} = \begin{cases} \mathbf{0} & \text{if any } u_i \geq u_{UL,i} \vee u_i \leq u_{LL,i}, \\ K_I \mathbf{e} & \text{otherwise,} \end{cases}, \quad i = 1, \dots, p \quad (7.19)$$

where  $z_i$  denotes the state variable of the integrator  $i$ . This is commonly known as conditional integration, where the error signal to the integrator is switched off under the specified conditions. Since under these circumstances the output from the integrator will be constant, it is also known as **integrator clamping**.

This method has shown to be remarkably effective in eliminating integrator wind-up in previous applications of the RIDE methodology. However, it is global in its action. Whereby *all* integrators are switched off when *any one* of the control outputs saturates. While this is the most pragmatic solution, it is possible to switch off only those integrators affected by a specific output saturating, which can improve controller performance. Also, switching off all integrators can cause an output of the controller to ‘lock up’ as it is not aware when the control error could cause it to begin to move away from the saturation limit.

The optimal anti-windup technique is that integration is stopped when a control variable saturates *and* when the current control action would push further into the saturation region. Consider again the NI+PDF controller:

$$u_i = u_{eq,i}(\cdot) + \sum_{j=1}^p \beta_{ij}(\cdot) \left( K_{I,j} \int e_j dt - u_{D,j} \right)$$

If the control variable  $u_i$  were to reach its maximum value  $u_{UL,i}$ , then only when both  $\beta_{ij} > 0$  and  $e_j > 0$  will the control variable continue to rapidly increase above its upper limit. Conversely, if the control variable  $u_i$  were to reach its minimum value  $u_{LL,i}$ , then only when both  $\beta_{ij} < 0$  and  $e_j < 0$  will the control variable continue to rapidly decrease below its lower limit.

Therefore, when a control variable  $u_i$  saturates and both  $\beta_{ij}$  and  $e_j$  act to move further into the saturation region the corresponding integrator  $j$  should be clamped. The addition of this logic will cause the other integrators to not be inhibited when they would help push the control variable away from the saturation. This will speed up the response of the controller returning from saturation as a change in the sign of any error signal  $e_{ij}$  or  $\beta_{ij}$  will cause the system to move from the saturation limit instantaneously.

To implement this new anti-windup logic with the NI+PDF controller, first define the following nonlinear piecewise ‘dead zone’ function, where for an given control



variable  $u_i$ , the output  $\tilde{u}_i$  is given by

$$\tilde{u}_i = \begin{cases} 0 & \text{if } u_{LL,i} \leq u_i \leq u_{UL,i} \\ u_i - u_{UL,i} & \text{if } u_i > u_{UL,i} \\ u_i - u_{LL,i} & \text{if } u_i < u_{LL,i} \end{cases} \quad (7.20)$$

Then from (7.20), when  $\tilde{u}_i \neq 0$  then the system has been overdriven as the controller output,  $u_i$ , is out with the constraints ( $u_{LL,i} \leq u_i \leq u_{UL,i}$ ).

Now introduce two logical variables to detect what limit the control has hit:

$$\check{b}_{UL,i} := \tilde{u}_i > 0, \quad (7.21)$$

$$\check{b}_{LL,i} := \tilde{u}_i < 0, \quad (7.22)$$

where a true value for  $\check{b}_{UL,i}$  indicates that the control variable  $u_i$  is above the upper limit and a true value for  $\check{b}_{LL,i}$  indicates that the control variable  $u_i$  is below the lower limit.

The other aspect of the integrator clamping logic is determined by the direction of each control variable – if  $\beta_{ij}$  and  $e_j$  would cause the system to move further into the saturation region then the integrator should be clamped. This is determined by realising that when the sign of the error,  $\text{sgn}(e_j)$ , is the same as that of  $\text{sgn}(\beta_{ij})$  then the system will be pushed further into the saturation region. Therefore, defining a pair of logical matrices to detect the direction of each control:

$$\check{\mathbf{B}}_{\text{inc}} := \text{sgn}(\boldsymbol{\beta}) \text{sgn}(\text{diag}(\mathbf{e})) > 0$$

$$\check{\mathbf{B}}_{\text{dec}} := \text{sgn}(\boldsymbol{\beta}) \text{sgn}(\text{diag}(\mathbf{e})) < 0$$

where  $\check{\mathbf{B}}_{\text{inc}}$  is an  $(p \times p)$  matrix of logical values where each  $(\check{b}_{\text{inc}})_{ij}$  indicates if the  $j$ -th integrator is increasing the value of the  $i$ -th control variable and  $\check{\mathbf{B}}_{\text{dec}}$  is an  $(p \times p)$  matrix of logical values where each  $(\check{b}_{\text{dec}})_{ij}$  indicates if the  $j$ -th integrator is decreasing the value of the  $i$ -th control variable.

Then the new integrator clamping logic can be implemented as

$$\dot{z}_j = \begin{cases} 0 & \left( \check{b}_{UL,i} \wedge (\text{any } j : \text{row}_i \check{\mathbf{B}}_{\text{inc}}) \right) \vee \left( \check{b}_{LL,i} \wedge (\text{any } j : \text{row}_i \check{\mathbf{B}}_{\text{dec}}) \right) \\ K_{I,j} e_j & \text{otherwise} \end{cases} \quad (7.23)$$

Equation (7.23) is then the new anti-windup technique for the NI+PDF controller that will speed up the recovery response and to stop any control variable  $u_i$  locking up due to cross-coupling between inputs.



### Example – revisited

In order to demonstrate the performance of the new anti-windup technique, the example from the previous section is revisited but with the anti-windup circuits in place. The response curves are given in fig. 7.16.

Figure 7.16 also shows that the addition of the limiters has resulted in a system that responds with zero overshoot even though overdriven. There is no way for this controller to wind-up; it knows what the actuators are capable of and never asks them at any time to perform out with their capabilities. It also can be seen that there is no drawbacks to this implementation of the input constraints: the temperature rises at the same rate as the unconstrained case but is more efficient and effective. It puts into the controlled system exactly the amount of energy required to change the controlled variable the desired amount.

## 7.4 Variable-structure-system control

The previous sections have developed a robust nonlinear control algorithm that can be readily applied to any one configuration of energy supply systems. However, when any configuration features multiple energy supply systems within the building, the resulting system being controlled is a complex *hybrid* dynamic system – where the system is a mixture of continuous-time and discrete-time dynamical systems. The discrete behaviour is caused by the varying modes of the mCHP engine (standby, warm-up, normal, and cool-down) and the quasi-modes of the energy storage elements: *quasi* denotes the fact that although not a strict operational mode, the change in state caused when an energy storage element has available capacity or is full are considered as discrete modes in this sense.

Unlike servicing systems such as condensing boilers, the mCHP engine is not well suited to oscillating between ON/OFF states, in fact, as demonstrated in §§ 4.1.3, the mCHP engine has in-built low-level controls which prohibit such action. Furthermore, the mCHP can cause operational mode switchings based based on events in the continuous dynamics, such as the temperature of the return water being over a set safety limit. At this time, the mCHP engine would transition to cool-down, which changes the continuous dynamics of the overall system as the mCHP engine is effectively removed from the system until the predetermined cool-down period completes – at which time another event would occur causing the mCHP engine to return to standby and once again be available to the controller. Moreover, during standby and cool-down modes, the mCHP actually acts as an electrical demand, since its circulatory pumps require electricity in these modes, but the unit isn't generating any supply.

Another example is the state-of-charge regulation within the embedded electronics

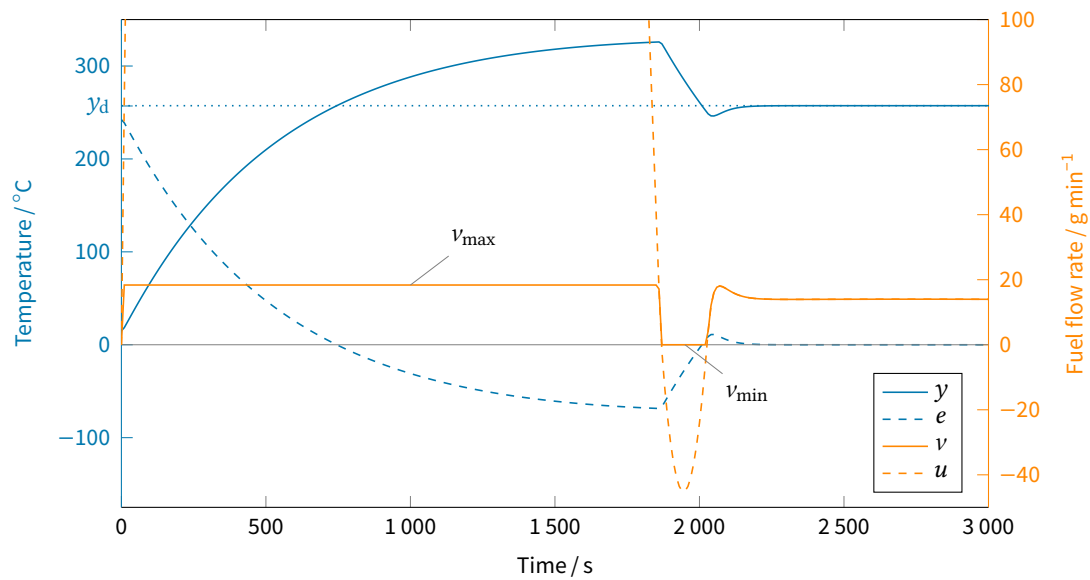


**Figure 7.15 | Engine temperature control.** Response of a critically damped system with PDF control of the basic first-order controlled system when overdriven by a step change in reference input. Numerical simulation over a period of 50 min at a sampling frequency of 100 Hz and output frequency of 100 mHz.

of the thermal and electrical storage elements. When the discrete low-level controllers within these storage elements consider the store full, the continuous dynamics change since they can no longer be used to store energy, and similarly for the case when the storage element is depleted – they can no longer be utilised as an energy source. These events can be thought of as the discrete-time transmission zeros of the system since the controller output will have no effect on the system.

In order to somewhat alleviate the complexity of such a system, it will be considered in *modular* form; that is, as the interconnection of several continuous subsystems depending on the availability of each energy supply system. Then a controller is designed for each permutation of the operational modes for all energy systems under consideration. It is possible to consider the overall system as several individual autonomous systems corresponding to the mCHP engine's operational mode and energy storage availability. This leads to a variable structure controller with a differing nonlinear inversion for each of these permutations. The switching between modes is handled by a hard-logic, with safe-guards in place to ensure smooth state transitions between the operational modes. The mode switching logic are created on an ad hoc basis for each case study considered in chapter 8. The switching between operational modes of the controller is thought to be an appealing area of future work as a more 'intelligent' governing controller could decide to switch between operational modes before an energy system has hit an operational limit or when a particular combination will be more energy efficient based on predictions of future climate, electrical and/or thermal demands, and occupant behaviour. This is considered again in § 9.3.

## 7.5 Controller design synthesis

The purpose of this section is to consolidate the robust nonlinear inversion-based controller design method detailed in the current and previous chapter into a design procedure that will be followed for the case studies in chapter 8.

### 7.5.1 Problem setup

Recall the definition of a general multi-variable nonlinear system described in a state-space representation as

$$\Xi : \begin{cases} \dot{\mathbf{x}}(t) = \mathbf{f}(\mathbf{x}(t), \boldsymbol{\mu}(t)) & (6.1a \text{ revisited}) \\ \mathbf{y}(t) = \mathbf{h}(\mathbf{x}(t), \boldsymbol{\mu}(t)) & (6.1b \text{ revisited}) \end{cases}$$

where  $\mathbf{x}(t) \in \mathbb{R}^n$  is the state vector (comprised of the state-variables),  $\boldsymbol{\mu}(t) \in \mathbb{R}^m$  is the system input vector (comprised of all inputs to the system including the control inputs, disturbances, command signals etc.),  $\mathbf{y}(t) \in \mathbb{R}^p$  is the output vector (comprised





of all the controlled variables), and  $f : \mathbb{R}^{n+m} \rightarrow \mathbb{R}^n$ ,  $h : \mathbb{R}^{n+m} \rightarrow \mathbb{R}^p$  are assumed to be smooth continuous functions over the range of interest. Also, for notational compactness from now on the time-dependence is implied so that  $\mathbf{x} := \mathbf{x}(t)$ ,  $\boldsymbol{\mu} := \boldsymbol{\mu}(t)$ ,  $\mathbf{y} := \mathbf{y}(t)$ .

To utilise the nonlinear inversion control law, it must be possible to represent the system  $\Xi$  as a control-affine system, that is, the control signal enters the system linearly in the state differential equation and that there is no direct feed-through from  $\mathbf{u}$  to  $\mathbf{y}$  in the output equation i.e.  $h$  is not a direct function of  $\mathbf{u}$ . However, this second restriction can often be circumvented by redefinition of the output, as demonstrated in §§ 6.3.3.

First, without loss of generality, partition the system input vector  $\boldsymbol{\mu} = (\mathbf{u}^\mathcal{T}, \boldsymbol{\psi}^\mathcal{T})^\mathcal{T} = (\mathbf{u}^\mathcal{T}, \mathbf{w}^\mathcal{T}, \mathbf{d}^\mathcal{T})^\mathcal{T}$ , where  $\mathbf{u} \in \mathbb{R}^{m_0}$  is the control input vector and  $\mathbf{w} \in \mathbb{R}^{m_1}$  is the measured input vector, and  $\mathbf{d} \in \mathbb{R}^{m_2}$  is the disturbance input vector. Now, assuming that there is no measurement or estimation of the disturbances into the system, or alternatively, that there is an estimate or measurement for each *modelled* disturbance then the input vector reduces to  $\boldsymbol{\mu} = (\mathbf{u}^\mathcal{T}, \mathbf{w}^\mathcal{T})^\mathcal{T}$ .

For control-affine systems, the target form for  $\Xi$  would now be

$$\Xi : \begin{cases} \dot{\mathbf{x}} = \mathbf{f}(\mathbf{x}, \mathbf{w}) + \mathbf{G}(\mathbf{x}, \mathbf{w})\mathbf{u}, & (7.25a) \\ \mathbf{y} = \mathbf{h}(\mathbf{x}), & (7.25b) \end{cases}$$

where  $\mathbf{f} : \mathbb{R}^{n+m_1} \rightarrow \mathbb{R}^n$  and  $\mathbf{h} : \mathbb{R}^n \rightarrow \mathbb{R}^p$  are smooth vector fields, and  $\mathbf{G} : \mathbb{R}^{n+m_1} \rightarrow \mathbb{R}^n \times \mathbb{R}^p$  is a matrix whose columns  $\mathbf{g}_j : \mathbb{R}^n \rightarrow \mathbb{R}^n$ ,  $j = 1, \dots, p$  are smooth vector fields. Now, recognise that it is possible to transform the system from the form in (6.1) to (7.25) as

$$\dot{\mathbf{x}} = \underbrace{\mathbf{f}(\mathbf{x}, \mathbf{u}, \mathbf{w})|_{\mathbf{u}=0}}_{\mathbf{f}(\mathbf{x}, \mathbf{w})} + \underbrace{\frac{\partial \mathbf{f}(\mathbf{x}, \mathbf{u}, \mathbf{w})}{\partial \mathbf{u}}}_{\mathbf{G}(\mathbf{x}, \mathbf{w})} \mathbf{u}, \quad (7.26)$$

where the new representation must be algebraically equivalent to the original system i.e.  $\mathbf{f}(\mathbf{x}, \mathbf{w}) + \mathbf{G}(\mathbf{x}, \mathbf{w})\mathbf{u} \equiv \mathbf{f}(\mathbf{x}(t), \boldsymbol{\mu}(t))$ , otherwise the system  $\Xi$  cannot be represented in control affine form and an alternative control strategy should be used.

### 7.5.2 Nonlinear inversion

For each output  $i$  in (7.25b), calculate its relative degree  $\rho_i$  using the method detailed in §§ 6.3.2. Assuming the system has a well-defined relative degree such that there exists a set of integers  $\mathbf{r} = (r_1, \dots, r_p)$ , then using the outputs of the system, their



derivatives and the values of the relative degree  $\mathbf{r}$  to form the input-output system

$$\underbrace{\begin{bmatrix} y_1^{(\rho_1)} \\ y_2^{(\rho_2)} \\ \vdots \\ y_p^{(\rho_p)} \end{bmatrix}}_{\hat{\mathbf{y}}} = \underbrace{\begin{bmatrix} \mathcal{L}_f^{\rho_1} h_1 \\ \mathcal{L}_f^{\rho_2} h_2 \\ \vdots \\ \mathcal{L}_f^{\rho_p} h_p \end{bmatrix}}_{P(\mathbf{x}, \mathbf{w})} + \underbrace{\begin{bmatrix} \mathcal{L}_{g_1} \mathcal{L}_f^{\rho_1-1} h_1 & \dots & \mathcal{L}_{g_p} \mathcal{L}_f^{\rho_1-1} h_1 \\ \mathcal{L}_{g_1} \mathcal{L}_f^{\rho_2-1} h_2 & \dots & \mathcal{L}_{g_p} \mathcal{L}_f^{\rho_2-1} h_2 \\ \vdots & \dots & \vdots \\ \mathcal{L}_{g_1} \mathcal{L}_f^{\rho_p-1} h_m & \dots & \mathcal{L}_{g_p} \mathcal{L}_f^{\rho_p-1} h_p \end{bmatrix}}_{Q(\mathbf{x}, \mathbf{w})} \mathbf{u}$$

or

$$\hat{\mathbf{y}} = P(\mathbf{x}, \mathbf{w}) + Q(\mathbf{x}, \mathbf{w})\mathbf{u}. \quad (7.27)$$

If the matrix  $Q(\mathbf{x}, \mathbf{w})$  in (7.27) is invertible, then utilising feedback control of the form

$$\mathbf{u} = \mathbf{u}_{\text{eq}}(\mathbf{x}, \mathbf{w}) + \boldsymbol{\beta}(\mathbf{x}, \mathbf{w})\mathbf{v}, \quad (7.28)$$

where  $\mathbf{u}_{\text{eq}}(\mathbf{x}, \mathbf{w}) = -(Q(\mathbf{x}, \mathbf{w}))^{-1}P(\mathbf{x}, \mathbf{w})$  and  $\boldsymbol{\beta}(\mathbf{x}, \mathbf{w}) = (Q(\mathbf{x}, \mathbf{w}))^{-1}$ . This feedback control results in the simple linear system

$$\begin{bmatrix} y_1^{(\rho_1)} \\ \vdots \\ y_p^{(\rho_p)} \end{bmatrix} = \begin{bmatrix} v_1 \\ \vdots \\ v_p \end{bmatrix} \quad (7.29)$$

**CONTROLLABILITY** The existence of this input-output inversion control law is reliant on the condition that  $Q(\mathbf{x}, \mathbf{w})$  is invertible. Therefore, for all  $\mathbf{x}$  in the neighbourhood of some  $\mathbf{x}^\circ$ , and bounded measured inputs  $\mathbf{w}$ ,

$$\det(Q(\mathbf{x}, \mathbf{w})) \neq 0. \quad (7.30)$$

The input-output controllability condition (7.30) should be evaluated algebraically at the design stage to check the controllability for any values of the system parameters. When physical components of the system have been selected and nominal values (and their associated uncertainties) are known, the non-singularity of  $Q(\mathbf{x}, \mathbf{w})$  should be confirmed for the range of possible parameters and estimates for the range of the inputs  $\mathbf{w}$ .

### 7.5.3 Normal form

Introducing a new set of state-variables for the system as the phase-variables of each output and its successive derivatives up to  $\rho_i - 1$ :  ${}^i\xi_1 = y_i(t)$ ,  ${}^i\xi_2 = \dot{y}_i(t)$ ,  $\dots$ ,  ${}^i\xi_{\rho_i} = y_i^{(\rho_i-1)}(t)$  where  ${}^i\xi_j$  indicates the  $j$ th phase-variable of the  $i$ th output. Then (7.29) may



be expressed in the following **normal form**:

$$\begin{aligned}
 {}^1\dot{\xi}_1 &= {}^1\xi_2 \\
 &\dots \\
 {}^1\dot{\xi}_{\rho_1-1} &= {}^1\xi_{\rho_1} \\
 {}^1\dot{\xi}_{\rho_1} &= v_1 \\
 &\dots \\
 {}^p\dot{\xi}_{\rho_p-1} &= {}^p\xi_{\rho_p} \\
 {}^p\dot{\xi}_{\rho_p} &= v_p
 \end{aligned} \tag{7.31}$$

where  ${}^i\xi = ({}^i\xi_1, \dots, {}^i\xi_{\rho_i}) = (y_i, \dots, y_i^{(\rho_i-1)})$ ,  $i = 1, \dots, p$  and  $\xi = ({}^1\xi, \dots, {}^p\xi)^T$ .

This results in a new linear subsystem of the dynamics given as

$$\begin{aligned}
 \dot{\xi} &= A_n \xi + B v, \\
 y &= C_n \xi,
 \end{aligned} \tag{7.32}$$

where  $A_n = \text{diag}(A_1, \dots, A_p)$  and  $A_i$  is an  $\rho_i \times \rho_i$  upper shift matrix;  $b_i$  is a  $\rho_i \times 1$  vector  $b_i = (0, \dots, 0, 1)^T$  that gives  $B_n = \text{diag}(b_1, \dots, b_p)$ ; and  $c_i$  is a  $1 \times \rho_i$  vector  $c_i = (1, 0, \dots, 0)$  that gives  $C_n = \text{diag}(c_1, \dots, c_p)$ .

The new sub-state vector  $\xi$  is comprised of the derivatives of the measured outputs. However, in practice it is not practical to differentiate any signal more than once (2, p. 185), so there is a limiting factor to directly calculating the feedback vector required by the outer-loop controller. Therefore, it is possible to leverage the Lie derivatives of the output before the input appears in each channel to determine the derivatives of the output as functions of the state:

$$\xi = \begin{bmatrix} y_1 \\ \dot{y}_1 \\ \vdots \\ y_1^{(\rho_1-1)} \\ \vdots \\ y_p \\ \dot{y}_p \\ \vdots \\ y_p^{(\rho_p-1)} \end{bmatrix} = \begin{bmatrix} h_1 \\ \mathcal{L}_f^{l-1} h_1 \\ \vdots \\ \mathcal{L}_f^{\rho_1-1} h_1 \\ \vdots \\ h_p \\ \mathcal{L}_f^{l-1} h_p \\ \vdots \\ \mathcal{L}_f^{\rho_1} h_p \end{bmatrix} = \Phi(x, w) \tag{7.33}$$

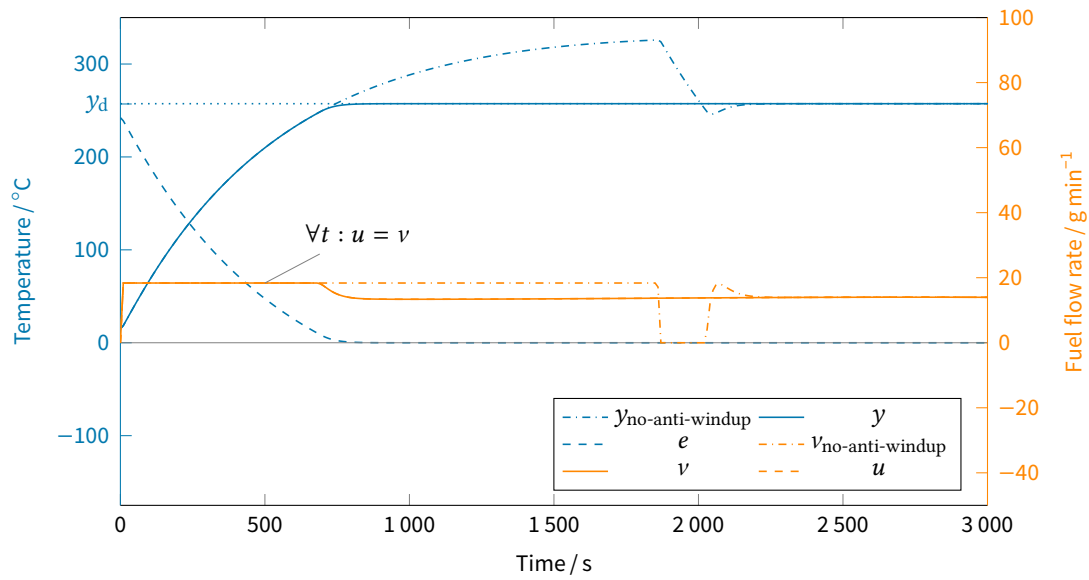


**Figure 7.16 | Engine temperature control with anti-windup.** Response of a critically damped system with PDF control of the basic first-order controlled system when overdriven by a step change in reference input. Numerical simulation over a period of 25 min at a sampling frequency of 100 Hz and output frequency of 100 mHz.

The remaining states are the **internal dynamics** given by

$$\dot{\eta} = \mathbf{q}(\xi, \eta) + \mathbf{p}(\xi, \eta)\mathbf{u} \quad (7.34)$$

#### 7.5.4 PDF control

From § 7.2 the generalised PDF controller for each synthetic output is given by

$$v_i = z_i - \sum_{q=1}^{\rho_i} {}^i K_{d,q} y_i^{(q-1)}, \quad i = 1, \dots, p \quad (7.35)$$

where  $z_i = K_{I,i}(y_{d,i} - y_i)$  and  $\mathbf{k}_{d,i} = ({}^i K_{d,1}, \dots, {}^i K_{d,\rho_i})$  are the pseudo-derivative feedback controller gains for the  $i$ -th control input. Equation (7.35) can be written in vector-matrix form for all  $v_1, \dots, v_p$  using the normal form notation from the previous section:

$$\dot{\mathbf{z}} = \mathbf{K}_I(\mathbf{y}_d - \mathbf{C}_n \xi), \quad (7.36a)$$

$$\mathbf{v} = \mathbf{z} - \mathbf{K}_D \xi, \quad (7.36b)$$

where  $\mathbf{K}_I \in \mathbb{R}^{p \times p} = \text{diag}(K_{I,1}, \dots, K_{I,p})$  and  $\mathbf{K}_D \in \mathbb{R}^{p \times \rho^1} = \text{diag}(\mathbf{k}_{d,1}, \dots, \mathbf{k}_{d,p})$ . The dynamics of the closed-loop linear subsystem as then given as

$$\begin{bmatrix} \dot{\xi} \\ \dot{\mathbf{z}} \end{bmatrix} = \begin{bmatrix} \mathbf{A}_n - \mathbf{B}_n \mathbf{K}_D & \mathbf{B}_n \\ -\mathbf{K}_I \mathbf{C}_n & \mathbf{0} \end{bmatrix} \begin{bmatrix} \xi \\ \mathbf{z} \end{bmatrix} + \begin{bmatrix} \mathbf{0} \\ \mathbf{K}_I \end{bmatrix} \mathbf{y}_d \quad (7.37)$$

$$\mathbf{y} = \begin{bmatrix} \mathbf{C}_n & \mathbf{0} \end{bmatrix} \begin{bmatrix} \xi \\ \mathbf{z} \end{bmatrix} \quad (7.38)$$

and the coordinate transformation  $\xi = \Phi(\mathbf{x}, \mathbf{w})$  in (7.33) can be used to determine the sub-state feedback.

For all integrators in the PDF controller, the integrator wind-up compensation should be implemented as described in §§ 7.3.3.

#### 7.5.5 Performance specification via gain selection

For each output in the MIMO system, assume that an optimum response is desired i.e. zero overshoot for a step change in set-point, then the ideal integral gain is determined by any one of

$$K'_{I,5\%} = \left( \frac{4.7439}{T_s} \right)^2, \quad K'_{I,2\%} = \left( \frac{5.8339}{T_s} \right)^2, \quad K'_{I,1\%} = \left( \frac{6.6384}{T_s} \right)^2, \quad (7.15 \text{ revisited})$$





where  $T_s$  is the desired settling time of the output. Then, form the generalised transfer function of the reduced linear subsystem with respect to the output's relative degree:

$$G_{ii}(s) = \frac{W^{\rho_i-1}(K'_{1,i})^{\frac{1}{2}(\rho_i+1)}}{\left(s + \sqrt{K'_{1,i}}\right)^2 \left(s + W\sqrt{K'_{1,i}}\right)^{\rho_i-1}} = \frac{K_{1,i}}{s^{\rho_i+1} + \sum_{q=1}^{\rho_i} {}^i K_{Dq} s^q + K_{1,i}}, \quad (7.39)$$

where the optimal excess pole distance can be determined by  $W = 7.785\rho - 10.843$ . The coefficients of  $s$  in the characteristic equation of the transfer functions in (7.39) yields the controller gains  $\mathbf{k}_i = (K_{1,i}, {}^i K_{D1}, \dots, {}^i K_{D\rho})$  that will correspond to a critically damped response with desired settling time  $T_{s,i}$ .

### 7.5.6 Variable-structure-system control

The overall system being controlled has  $n$  energy systems, each with  $m$  modes of operation. Then the total combination of configurations is given as

$$N = \prod_{i=1}^n m_i.$$

Each energy system's set of modes can be written as  $A_i = \{\text{mode } 1, \dots, \text{mode } m_i\}$ . The Cartesian product of these sets would be

$$A_{\text{sys}} = \prod_{i=1}^n A_i,$$

where  $A_{\text{sys}}$  contains the  $N$  possible configurations of all the energy systems being controlled. Therefore, for each  $i$ -th set of  $A_{\text{sys}}$  a nonlinear inversion is computed. Switching between each control configuration is then handled by logic that is determined ad hoc for the hybrid energy system under consideration.

**EXAMPLE** The hybrid system being controlled consists of an mCHP plant and a TES, where  $A_{\text{CHP}} = \{\text{standby, warm-up, normal, cool-down}\}$  and  $A_{\text{TES}} = \{\text{empty, normal, full}\}$ . There are then  $N = 4 \times 3 = 12$  possible mode configurations:

$$A_{\text{sys}} = \{(\text{standby, empty}), (\text{warm-up, empty}), (\text{normal, empty}), (\text{cool-down, empty}), \\ (\text{standby, normal}), (\text{warm-up, normal}), (\text{normal, normal}), (\text{cool-down, normal}), \dots \\ (\text{standby, full}), (\text{warm-up, full}), (\text{normal, full}), (\text{cool-down, full})\}$$

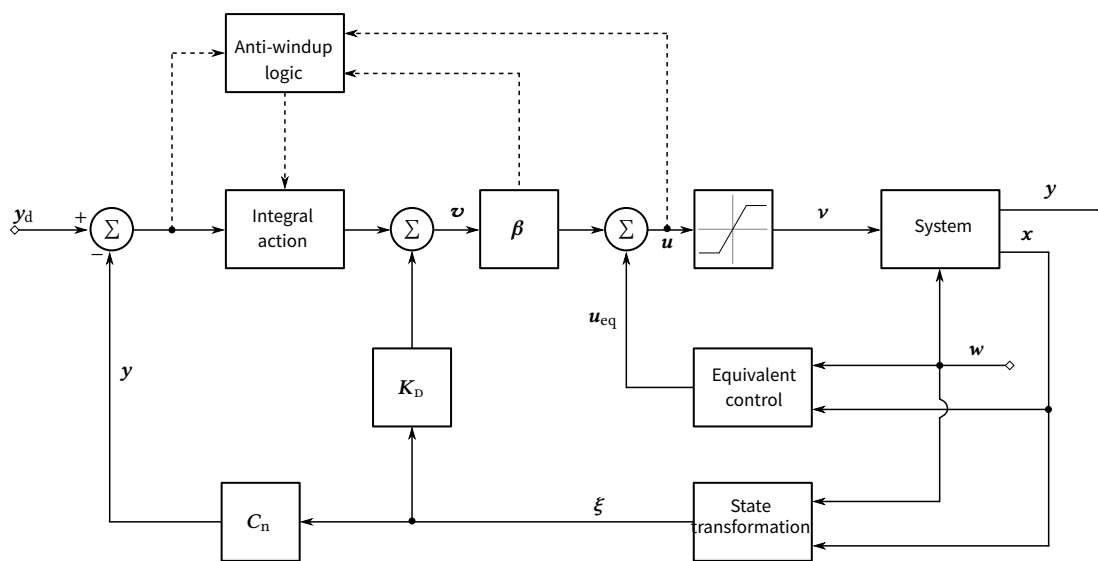


**Figure 7.17** | Block diagram of new NI+PDF structure.

### 7.5.7 Testing design for robustness

Once the controller has been designed, the following procedure should be followed to ensure robust control for each operational mode:

1. Stability
  - (a) input-output stability
  - (b) internal stability
2. Disturbance rejection
  - (a) input disturbance
  - (b) output disturbance
3. Sensor (measurement) noise rejection
4. Handling of actuator saturation
5. Performance robustness – the tracking performance should not deteriorate to unacceptable level when the system changes due to uncertainties

If all steps are completed the resulting controller design can be considered robust.

## 7.6 Summary

This chapter has explored how the inversion-based control techniques can be combined with robust control methods and applied to the control of hybrid building-integrated energy systems. The final controller design is shown in fig. 7.17.

The main features of this chapter are

- Generalisation of the RIDE methodology to a so-called NI+PDF controller:
  - Range of applicable systems extended from LTI systems with relative degree  $\rho \leq 1$  to control-affine nonlinear systems with relative degree of any order.
  - Analytical determination of controller gains from desired system performance.
  - Novel anti-windup scheme for nonlinear inversion coupled with pseudo-derivative feedback that achieves better performance than existing windup methods.
- Controller design methodology for the application of NI+PDF to the control of control-input-affine nonlinear energy systems.



The next chapter presents case studies for the application of the controller design methodology of chapters 6 and 7 to the models developed in chapters 4 and 5.

## References

1. Hurwitz, A. Ueber die Bedingungen, unter welchen eine Gleichung nur Wurzeln mit negativen reellen Theilen besitzt. *Mathematische Annalen* **46**(2): 273–84 (1895-06).  
DOI: [10.1007/BF01446812](https://doi.org/10.1007/BF01446812) (cited p. 186)
2. Phelan, R. M. *Automatic control systems*. London, UK: Cornell University Press, 1977: 280. ISBN: 0-8014-1033-9 (cited pp. 186, 195, 206)
3. Bradshaw, A., Counsell, J. M. Design of autopilots for high performance missiles. *Proceedings of the Institution of Mechanical Engineers, Part I: Journal of Systems and Control Engineering* **206**(2): 75–84 (1992-05) (cited pp. 188, 199)
4. Counsell, J. M., Zaher, O. S., Brindley, J. Auto-tuning for high performance autopilot design. In *AIAA Guidance, Navigation, and Control Conference*. Toronto, Canada: American Institute of Aeronautics and Astronautics, 2010 (cited p. 188)
5. Wang, Q. G., Zhang, Z., Astrom, K. J., Chek, L. S. Guaranteed dominant pole placement with PID controllers. *Journal of Process Control* **19**(2): 349–52 (2009-02).  
DOI: [10.1016/j.jprocont.2008.04.012](https://doi.org/10.1016/j.jprocont.2008.04.012) (cited p. 192)
6. Persson, P., Åström, K. Dominant Pole Design - a Unified View of Pid Controller Tuning. *Adaptive Systems in Control and Signal Processing 1992* **25**(14): 377–82 (1993-07).  
DOI: [10.1016/B978-0-08-041717-2.50066-5](https://doi.org/10.1016/B978-0-08-041717-2.50066-5) (cited p. 192)
7. Zhang, Y., Wang, Q. G., Astrom, K. J. Dominant pole placement for multi-loop control systems. *Automatica* **38**(7): 1213–20 (2002-07).  
DOI: [10.1016/S0005-1098\(02\)00009-2](https://doi.org/10.1016/S0005-1098(02)00009-2) (cited p. 192)
8. Satopää, V., Albrecht, J., Irwin, D., Raghavan, B. Finding a "kneedle" in a haystack: Detecting knee points in system behavior. *Proceedings - International Conference on Distributed Computing Systems*: 166–71 (2011).  
DOI: [10.1109/ICDCSW.2011.20](https://doi.org/10.1109/ICDCSW.2011.20) (cited p. 193)
9. Arndt, U. et al. *Experimental Investigation of Residential Cogeneration Devices and Calibration of Annex 42 Models*. Tech. rep. Annex 42 of the International Energy Agency Energy Conservation in Buildings and Community Systems Programme, 2007: 255 (cited p. 197)
10. Rundquest, L. Anti-reset windup for PID controllers. Ph.D. Lund Institute of Technology, 1991 (cited p. 198)
11. Hansson, A., Gruber, P., Tödtli, J. Fuzzy anti-reset windup for PID controllers. *Control Engineering Practice* **2**(3): 389–96 (1994-06).  
DOI: [10.1016/0967-0661\(94\)90775-7](https://doi.org/10.1016/0967-0661(94)90775-7) (cited p. 198)
12. Kurtz, M. J., Henson, M. A. Input-output linearizing control of constrained nonlinear processes. *Journal of Process Control* **7**(1): 3–17 (1997-02).  
DOI: [10.1016/S0959-1524\(96\)00006-6](https://doi.org/10.1016/S0959-1524(96)00006-6) (cited p. 198)



*“They say no plan survives first contact with implementation...”*

—ANDY WEIR, *The Martian*

8

## Results & discussion

THE case studies in this chapter will provide comparisons between the proposed controller developed in chapter 7, those typically used in practice (such as on/off and PID variants), and modern robust controller design methods ( $H_\infty$  synthesis).

The chapter will first describe the overall control problem being considered in the case studies in § 3.1. Each subsequent section presents the final controller designs and results of each case study in turn.

### 8.1 Systems specifications

The zone modelled is a small office located in Trappes, France, for which the climatic data is available (1). Figure 8.1 shows the wire-frame drawing of a single office zone, with major dimensions indicated. The thermophysical properties of the constructions are provided in table B.3. The overall office controlled consists of five of these zones in parallel, joined along their length so that all windows are facing west giving a total floor area of 99 m<sup>2</sup>. The thermal demands of the zone are served by a hydronic radiator system supplied by either a Stirling-engine based mCHP system or water-based TES tank. The electrical demands are served by the electrical generation of the mCHP, PV, electrical energy storage and a connection to the local electrical network.

The electrical power demands for the zone were generated using a model developed by Menezes et al. (2) for estimating the power demand of equipment in office buildings. This work uses ‘Model 2’ of the work that generates the demand using a ‘bottom-up’ approach to establish the likely power demands as opposed to ‘Model 1’, which relies on having existing monitoring data for a specific building. A power load density of 12 W m<sup>-2</sup> is assumed, which corresponds to ‘good practice’ for open plan office spaces (2, tab. 1). A workstation density of 10.9 m<sup>2</sup>/workstation was chosen, which

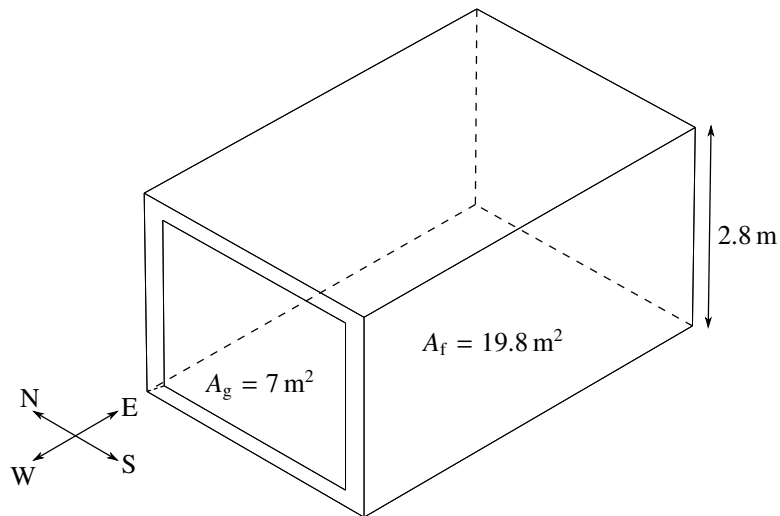


**Figure 8.1** | Wire frame drawing of building zone modelled.

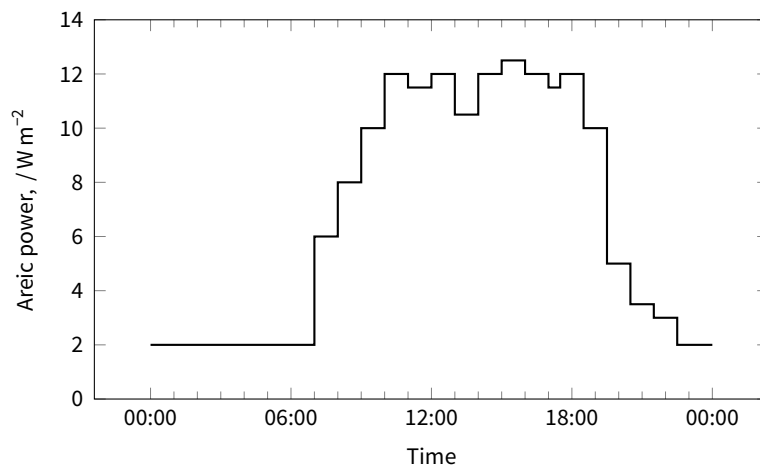


**Figure 8.2** | Small power demand profile for case study.



is the average office space density in the UK (3) and is assumed to be applicable in this case study. The equipment operation and usage patterns were left as the model defaults provided in (2, tab. 4). A typical day's half-hourly electrical power demand generated by the model is shown in fig. 8.2. Note that the model does not account for occupant plug loads e.g. mobile phone chargers, desk fans/lamps.

The mCHP specifications are based upon a WhisperGEN mCHP engine, with model parameters given in table 8.1. The engine has an external pump, and a permissible water flow rate of  $1.5 \text{ l min}^{-1}$  to  $12 \text{ l min}^{-1}$ . This particular engine has a small electrical capacity of 750 W (nominal) – equivalent to 698 W once the parasitic electrical consumption of the mCHP is subtracted – and large thermal output 6.5 kW (nominal). The typical application is residential mCHP, but is shown here to be applicable to a small office. These engines are typically controlled by heat demand (heat-led) rather than electrical demand.

The unit also has several low-level controls: The unit will shut-down if the cooling water temperature at the outlet of the system exceeds  $85 \text{ }^\circ\text{C}$ . The cool-down period of the unit was 25 min, but is assumed that the cool-down period is *optional*, that is if the unit receives demand while in cool-down mode it will switch to warm-up before completing the entire cool-down period. For the purpose of control demonstration, it is assumed that the unit can also modulate down to as low as 3 kW, while still generating electricity. Furthermore, a fixed efficiency and heat-to-power ratio is also assumed.

The hydronic system contains 4 radiators, based on the Kudox Premium Type 21 double-panel single convactor radiator, with model parameters given in table 8.3.

The energy production from photovoltaics is calculated using PVWatts (4). The PV system characteristics consist of a standard 4 kW solar array, with full specifications given in table 8.2.

The electrical power storage is based on the Tesla Powerwall, which is a battery system designed for residential or light commercial use. This battery is designed to be used for “solar self-consumption, load shifting and backup power” making it ideal for use in this hybrid energy supply system. The specifications required for modelling the battery are provided in table 8.4.

The stratified thermal storage tank is built from carbon steel, with a capacity of 210 l. The tank is insulated with polyurethane ( $\lambda = 0.038 \text{ W m}^{-1} \text{ K}^{-1}$ ) at a thickness of 100 mm. The connections and full dimensional characteristics are provided in (5).

## 8.2 Controller test case

The first case study for the control of the system (as specified in § 3.1) looks at controlling the mCHP device alone to fulfil the thermal and electrical demands of the

**Table 8.1 | mCHP model parameters for case study.** All values obtained from experimental investigation and calibration by Arndt et al. (8).

Parameter		Nominal value	Uncertainty
$C_{\text{eng}}$	heat capacity of the engine block	$18.5 \times 10^3 \text{ J K}^{-1}$	11 %
$C_{\text{cw}}$	heat capacity of the encapsulated cooling water and the heat exchanger shell	$28.1 \times 10^3 \text{ J K}^{-1}$	11 %
$H_{\text{HX}}$	rate of heat transfer between the engine block and the cooling water heat exchanger	$31.8 \text{ W K}^{-1}$	3.5 %
$H_{\text{env}}$	rate of heat transfer between the engine block and the surrounding environment	$4.64 \text{ W K}^{-1}$	20 %
$\eta_{\text{E}}$	electrical conversion efficiency of the engine	0.0929	2.15 % <sup>a</sup>
$\eta_{\text{Q}}$	thermal efficiency of the engine	0.970	4.12 % <sup>b</sup>
$\overline{LHV}$	lower heating value of the fuel	$35.16 \text{ MJ kg}^{-1}$	0.55 %
$c_p$	Specific heat of water	$4192 \text{ J kg}^{-1} \text{ K}^{-1}$	3 %

<sup>a</sup> Uncertainty given as  $\eta_{\text{E}}(\%) \pm 0.2 \%$ , which can be converted into standard relative uncertainty as  $0.002/0.0929 = 2000/929 \% \approx 2.15 \%$ .

<sup>b</sup> Uncertainty given as  $\eta_{\text{Q}}(\%) \pm 4 \%$ , which can be converted into standard relative uncertainty as  $0.04/0.97 = 400/97 \% \approx 4.12 \%$ . Where upper uncertainty bounds would result in an efficiency > 100 %, it is limited to 100 %

**Table 8.2 | Solar PV system specifications.**

<b>Location and station identification</b>	
Requested location	Trappes
Weather data source	(INTL) Paris, France
Latitude	48.73° N
Longitude	2.4° E
<b>PV system specifications</b>	
DC system size	4 kW
Module type	Standard
Array type	Fixed (roof mount)
Array tilt	20°
Array azimuth	180°
System losses	14 %
Inverter efficiency	96 %
DC to AC size ratio	1.1

building. That is, there is no support from photovoltaics or electrical- or thermal-energy storage. Then, this example is concerned with constructing a robust controller for the following MIMO problem:

### Control Goal

Design a control system to track a desired load-supply water temperature set-point while simultaneously tracking a demand-response signal from the LEN. In the absence of a signal from the LEN, the control system will regulate the utilisation of the electrical grid to zero.

From this control goal, it is possible to identify the variables to be controlled as

**cv1** Load-supply water temperature, which is the bulk exit temperature of the encapsulated mCHP cooling water.

**cv2** Measured electrical grid power.

#### 8.2.1 Problem formulation

The WhisperGen unit is designed for flow temperatures of 60 °C to 75 °C (6). A study by Kuhn et al. determined that the greatest performance and efficiency of Stirling Engine based mCHP engines is maximised by running at minimum flow temperature (7, Fig. 2). Therefore, the initial demand set-point for the mCHP supply temperature is set to 60 °C. From on/off tests conducted on the unit, from a cold start it can generate maximum power after 40 min (8, pp. V-16) and minimum power generation after approximately half this time.<sup>1</sup> Therefore, in order to generate power as quickly as possible, the controller should have a settling time of 20 min.

The mCHP has a maximum outlet temperature of 85 °C, if the temperature exceeds this it will automatically enter cool-down operation. Therefore, the system should have a maximum percentage overshoot of less than 41 % for a set-point of 60 °C and 13 % for a set-point of 75 °C. And finally, for uninterrupted load regulation, for a step change in power demand the delivered power should be within  $\pm 1$  %.

The summary of the design specifications are given as

**ds1** Attain a percentage overshoot of less than 41 % for a step change in supply temperature set-point to 60 °C and less than 13 % for a set-point of 75 °C.

**ds2** Reach and maintain the supply temperature set-point – within a 2 % error band – in a period less than or equal to 20 min from start-up.

---

<sup>1</sup>The exact value is not provided but can be inferred from (8, Fig. V-5).

**Table 8.3 | Radiator parameters for case study.** Specifications obtained from manufacturer's datasheet (9).

Parameter		Value
$m$	mass of the radiator and encapsulated water	20.76 kg <sup>a</sup>
$c_p$	mass weighted average specific heat	1 350 J kg <sup>-1</sup> K <sup>-1</sup>
$\kappa_{\text{rad}}$	radiator exponent	1.3
$\phi_0$	nominal heat emission of radiator	898 W
$\Theta_{s,0}$	nominal supply temperature	75 °C
$\Theta_{x,0}$	nominal exit temperature	65 °C
$\Theta_{e,0}$	nominal environmental temperature	20 °C

<sup>a</sup> Dry weight of 16.96 kg plus 3.8 l water content.

**Table 8.4 | Battery parameters for case study.** Specifications obtained from manufacturer's datasheet (10).

Parameter		Value
$E_{\text{bat}}$	usable capacity	13.2 kWh
	depth of discharge	100 % <sup>a</sup>
$\eta_{\text{bat}}$	round-trip efficiency	89.0 %
$P_{\text{max,cont.}}$	Max continuous charge and discharge real power	5 kW
$P_{\text{max,peak}}$	Max peak (10 s) discharge power	7 kW

<sup>a</sup> Depth of discharge of 100 % indicates  $\overline{SOC}_{\text{min}} = 0\% \implies E_{\text{bat,UL}} = E_{\text{bat}} \wedge E_{\text{bat,LL}} = 0$ .

- DS3** Respond to a step change in electrical demand as quickly as possible within a  $\pm 1\%$  error band.
- DS4** Minimisation of electrical grid utilisation at all times unless responding to a demand signal from the LEN.
- DS5** Fulfilment of all electrical demands within the building at all times.
- DS6** Minimum sensitivity to process parameter changes.
- DS7** Robust stability.

### 8.2.2 Control law design

Once again consider the combustion-based cogeneration device model from § 4.1:

$$\begin{aligned}
 C_{\text{eng}}\dot{\Theta}_{\text{eng}}(t) &= H_{\text{HX}}(\Theta_{\text{cw,o}}(t) - \Theta_{\text{eng}}(t)) + H_{\text{env}}(\Theta_{\text{env}}(t) - \Theta_{\text{eng}}(t)) \\
 &\quad + \eta_{\text{Q}}\overline{LHV}\dot{m}_{\text{fuel}}(t) \qquad (4.8 \text{ revisited}) \\
 C_{\text{cw}}\dot{\Theta}_{\text{cw,o}}(t) &= (c_p\dot{m}(t))_{\text{cw}}(\Theta_{\text{cw,i}}(t) - \Theta_{\text{cw,o}}(t)) + H_{\text{HX}}(\Theta_{\text{eng}}(t) - \Theta_{\text{cw,o}}(t))
 \end{aligned}$$

The electrical grid utilisation is a simple energy balance between the electrical load demand and the electrical generation of the cogeneration device:

$$P_{\text{grid}}(t) = P_{\text{load}}(t) - P_{\text{gen}}(t) = P_{\text{load}}(t) - \eta_{\text{E}}\overline{LHV}_{\text{fuel}}(t),$$

where  $P_{\text{grid}}(t) > 0$  represents import from the grid. Assume that there is a sensor on the measurement of the electrical power use of the grid with a time constant  $\tau_{\text{grid}}$  such that an extra state is introduced and the electrical network model is given by

$$\hat{P}_{\text{grid}}(t) = (1/\tau_{\text{grid}})(P_{\text{grid}}(t) - \hat{P}_{\text{grid}}(t)),$$

Therefore  $\mathbf{y}(t) = (y_1(t), y_2(t))^{\mathcal{T}} = (\Theta_{\text{cw,o}}(t), \hat{P}_{\text{grid}}(t))^{\mathcal{T}}$ , and the system inputs are the external pump flow rate, fuel flow rate, heat exchanger inlet temperature, air temperature surrounding the mCHP unit, and the electrical load demand i.e. the system input vector  $\boldsymbol{\mu}(t) = (\mu_1(t), \dots, \mu_5(t))^{\mathcal{T}} = (\dot{m}_{\text{cw}}(t), \dot{m}_{\text{fuel}}(t), \Theta_{\text{cw,i}}(t), \Theta_{\text{env}}(t), P_{\text{load}}(t))^{\mathcal{T}}$ . The state-vector  $\mathbf{x}(t) = (x_1(t), \dots, x_3(t))^{\mathcal{T}} = (\Theta_{\text{eng}}(t), \Theta_{\text{cw,o}}(t), \hat{P}_{\text{grid}}(t))^{\mathcal{T}}$ . Also, for notational compactness for the remainder of this section the time-dependence is implied so that  $\mathbf{x} := \mathbf{x}(t)$ ,  $\mathbf{u} := \mathbf{u}(t)$ ,  $\mathbf{y} := \mathbf{y}(t)$ .

The system also includes temperature sensors with time delay and discretisation to accuracy of  $0.1^\circ\text{C}$ . These are 'unmodelled' by the controller i.e. they are unstructured uncertainties.



Assume that the cooling water entering the inlet of the micro-combined heat and power (CHP) heat exchanger is the return feed from supplying a hydronic heat supply system (e.g. return feed from radiators). In this case the cooling water temperature at the inlet is a measured exogenous signal as it is external to the controlled system. Also assume that measurement of the electrical load is available. Therefore,  $\mathbf{w} = (\mu_3, \mu_5) = (\Theta_{\text{cw,i}}, P_{\text{load}})$ . Controlling the system is then achieved by manipulating the mass flow rate of the external pump and the fuel flow rate into the mCHP i.e.  $\mathbf{u} = (u_1, u_2) = (\mu_1, \mu_2) = (\dot{m}_{\text{cw}}, \dot{m}_{\text{fuel}})$ . The remaining system input is then an unmeasured disturbance, given as  $d = \mu_4 = \Theta_{\text{env}}$ .

With these specifications the system can be expressed as a control-affine system

$$\Xi : \begin{cases} \dot{\mathbf{x}} = \mathbf{f}(\mathbf{x}, \mathbf{w}, d) + \mathbf{G}(\mathbf{x}, \mathbf{w})\mathbf{u}, \\ \mathbf{y} = \mathbf{h}(\mathbf{x}), \end{cases}$$

where

$$\mathbf{f}(\mathbf{x}, \mathbf{w}, d) = \begin{pmatrix} (1/C_{\text{eng}})(H_{\text{env}}(d - x_1) - H_{\text{HX}}(x_1 - x_2)) \\ (1/C_{\text{cw}})H_{\text{HX}}(x_1 - x_2) \\ (1/\tau_{\text{grid}})(w_2 - x_3) \end{pmatrix}, \quad (8.1)$$

$$\mathbf{G}(\mathbf{x}, \mathbf{w}) = \begin{pmatrix} 0 & (1/C_{\text{eng}})\overline{\text{LHV}}\eta_{\text{Q}} \\ (1/C_{\text{cw}})c_p(w_1 - x_2) & 0 \\ 0 & -(1/\tau_{\text{grid}})\overline{\text{LHV}}\eta_{\text{E}} \end{pmatrix}, \quad (8.2)$$

$$\mathbf{h}(\mathbf{x}) = (x_2, x_3)^{\mathcal{T}}. \quad (8.3)$$

The variable speed pump is always in operation when the demand from the mCHP is non-zero. When activated, it can modulate its output between  $1.5 \text{ l min}^{-1}$  and  $12 \text{ l min}^{-1}$ , which was taken from (8, pp. III-18). Therefore, assuming a nominal water density of  $1000 \text{ kg m}^{-3}$ , the mass flow rate is constrained as  $u_1 \in [0.025, 0.2] \text{ kg s}^{-1}$ . The operating bounds of the electrical power generation are  $P_{\text{gen}} \in [0, 698] \text{ W}$  and the fuel flow rate is constrained as a function of these operating bounds.

### Nonlinear inversion + PDF

The NI+PDF controller is designed using the procedure detailed in § 7.5.

Taking the Lie derivatives of each output in (8.3) until the control appears results





in the following system

$$\underbrace{\begin{bmatrix} \dot{y}_1 \\ \dot{y}_2 \end{bmatrix}}_{\dot{\mathbf{y}}} = \underbrace{\begin{bmatrix} \frac{1}{C_{cw}} H_{HX}(x_1 - x_2) \\ \frac{1}{\tau_{grid}}(w_2 - x_3) \end{bmatrix}}_{P(\mathbf{x}, \mathbf{w})} + \underbrace{\begin{bmatrix} \frac{1}{C_{cw}} c_p(w_1 - x_2) & 0 \\ 0 & -\frac{1}{\tau_{grid}} \overline{LHV} \eta_E \end{bmatrix}}_{Q(\mathbf{x}, \mathbf{w})} \underbrace{\begin{bmatrix} u_1 \\ u_2 \end{bmatrix}}_{\mathbf{u}} \quad (8.4)$$

with vector relative degree  $\boldsymbol{\rho} = (1, 1)$ .

**CONTROLLABILITY** The existence of an input-output inversion is reliant on the condition that  $Q(\mathbf{x}, \mathbf{w})$  in (8.4) is invertible. Therefore, for all  $\mathbf{x}$  in the neighbourhood of some  $\mathbf{x}^\circ$ , and bounded measured inputs  $\mathbf{w}$  (in the original notation)

$$\det(Q(\mathbf{x}, \mathbf{w})) = -\frac{\overline{LHV} c_p \eta_E (\Theta_{cw,i} - \Theta_{cw,o})}{C_{cw} \tau_{grid}} \neq 0. \quad (8.5)$$

By investigation of (8.5), assuming the parameters  $(\overline{LHV}, C_{cw}, c_p) \neq 0$ , the condition is satisfied as long as  $T_{cw,i} \neq T_{cw,o} \wedge \eta_E \neq 0$ .

**NONLINEAR INVERSION** The nonlinear inversion of eq. (8.4) is given by

$$\mathbf{u} = \mathbf{u}_{eq}(\mathbf{x}, \mathbf{w}) + \boldsymbol{\beta}(\mathbf{x}, \mathbf{w})\mathbf{v},$$

$$\begin{bmatrix} u_1 \\ u_2 \end{bmatrix} = \begin{bmatrix} -\frac{H_{HX}(x_1 - x_2)}{c_p(\Theta_{cw,i} - x_2)} \\ -\frac{(-P_{load} + x_3)}{\overline{LHV} \eta_E} \end{bmatrix} + \begin{bmatrix} \frac{C_{cw}}{c_p(\Theta_{cw,i} - x_2)} & 0 \\ 0 & -\frac{\tau_{grid}}{\overline{LHV} \eta_E} \end{bmatrix} \begin{bmatrix} v_1 \\ v_2 \end{bmatrix}$$

**PDF CONTROLLER** The PDF controllers are given by

$$\dot{\mathbf{z}} = \mathbf{K}_I(\mathbf{y}_d - \mathbf{y}),$$

$$\mathbf{v} = \mathbf{z} - \mathbf{K}_D \mathbf{y},$$

$$\mathbf{K}_D = \text{diag}(9.7232 \times 10^{-3}, 1.1668) \quad \mathbf{K}_I = \text{diag}(23.635 \times 10^{-6}, 340.34 \times 10^{-3}).$$

The anti-windup technique for this controller is implemented exactly as in eq. (7.23).

### H-infinity loop shaping

The design of the  $H_\infty$  loop shaping controller for this case study is detailed in appendix C.3 and only the final design is produced here. The  $H_\infty$  controller is implemented in the following state-space representation:

$$K_{H_\infty} : \begin{cases} \dot{\mathbf{z}}(t) = \mathbf{A}\mathbf{z}(t) + \mathbf{B}(\mathbf{e}(t) - K_{\text{sat}}(\mathbf{v}(t) - \mathbf{u}(t))), \\ \mathbf{u}(t) = \mathbf{C}\mathbf{z}(t) + \mathbf{D}(\mathbf{e}(t) - K_{\text{sat}}(\mathbf{v}(t) - \mathbf{u}(t))), \end{cases}$$



$$\mathbf{A} = \begin{bmatrix} -0.70828 & 2.3955 & 1.3913 & -3.5287 & 0 & 0 \\ 2.531 & -8.5864 & 0.41013 & 12.645 & 0 & 0 \\ 0.13363 & 0.041602 & -4.096 & 1.3334 \times 10^{-5} & 0 & 0 \\ 3.5332 & -12.645 & -6.6004 \times 10^{-5} & -4.096 & 0 & 0 \\ 0 & 0 & 0 & 0 & 0 & 1.571 \times 10^{-14} \\ 0 & 0 & 0 & 0 & -8.4655 \times 10^{-15} & -2.2737 \times 10^{-13} \end{bmatrix}$$

$$\mathbf{C} = \begin{bmatrix} 0.0057888 & 0.0016171 & -2.1718 & -3.1521 \times 10^{-7} & -0.00053083 & -6.4168 \times 10^{-5} \\ -0.11265 & 0.38212 & 2.4608 \times 10^{-6} & -0.28105 & 1.9326 \times 10^{-13} & -0.010054 \end{bmatrix}$$

$$\mathbf{B} = \begin{bmatrix} -0.00092146 & 0.11279 \\ -0.00027166 & -0.38212 \\ 2.1718 & -3.1122 \times 10^{-7} \\ -2.2834 \times 10^{-8} & -0.28105 \\ 0.065039 & -0.0041777 \\ -1.4581 \times 10^{-9} & 0.58665 \end{bmatrix}$$

$$\mathbf{D} = \begin{bmatrix} 0 & -1.2925 \times 10^{-26} \\ -2.068 \times 10^{-25} & -4.8704 \times 10^{-21} \end{bmatrix}$$

It is evident that the final controller design has resulted in an additional 6 states as opposed to the 2 states in the NI+PDF and PI controllers, which increases the computation and implementation time of the  $H_\infty$  controller as opposed to the other two methods.

A suitable back calculation gain of  $K_{\text{sat}} = 1.5 \times 10^4$  was determined via trial-and-error for the back calculation anti-windup scheme.

### Robustly-tuned MIMO PI

A pair of PI controllers were used given by

$$\mathbf{u}(t) = \mathbf{K}_p \mathbf{e}(t) + \mathbf{z}(t),$$

where the integral action with a clamping anti-windup scheme is given by

$$z_i(t) = \begin{cases} 0 & \text{if } (\tilde{u}_i(t) \neq 0) \wedge (\text{sgn}(\tilde{u}_i(t)) = \text{sgn}(K_{i,i}e_{ii}(t))) \\ K_{i,ii}e_i(t) & \text{otherwise} \end{cases}$$

where  $\tilde{u}_i$  is the piecewise ‘dead zone’ function as defined in eq. (7.20). To obtain robustly-tuned PI control, the controller is formed as a fixed-structure  $H_\infty$  controller and then the gains were determined by applying the work of Apkarian, Noll (11). Apkarian, Noll uses a specialised optimisation technique to ensure closed-loop stability and minimises the  $H_\infty$  norm of the linear closed-loop transfer function model. This resulted in the

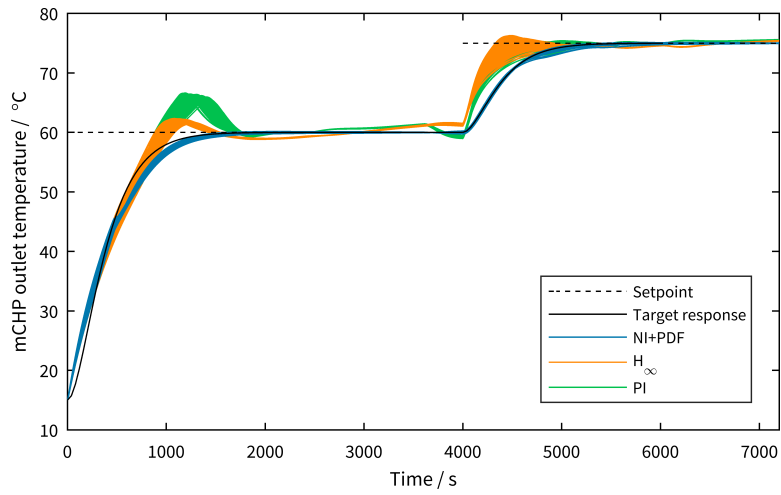


**Figure 8.3** | Comparison of dynamic response of mCHP outlet temperature for case 1.

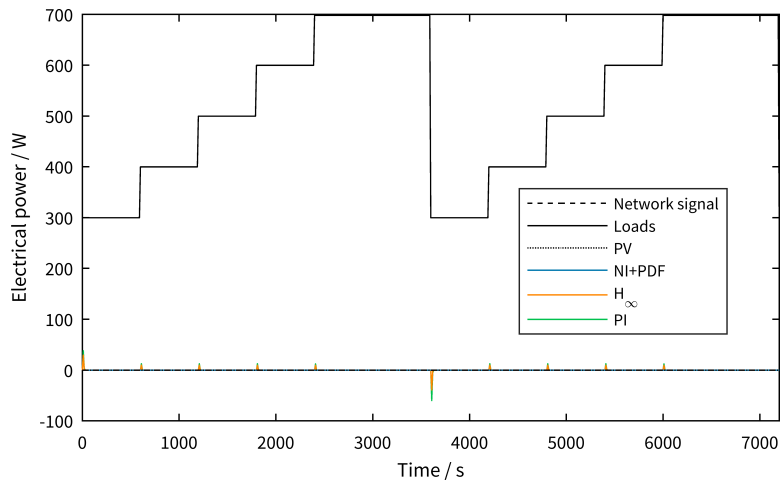


**Figure 8.4** | Comparison of all electrical power interactions for case 1.

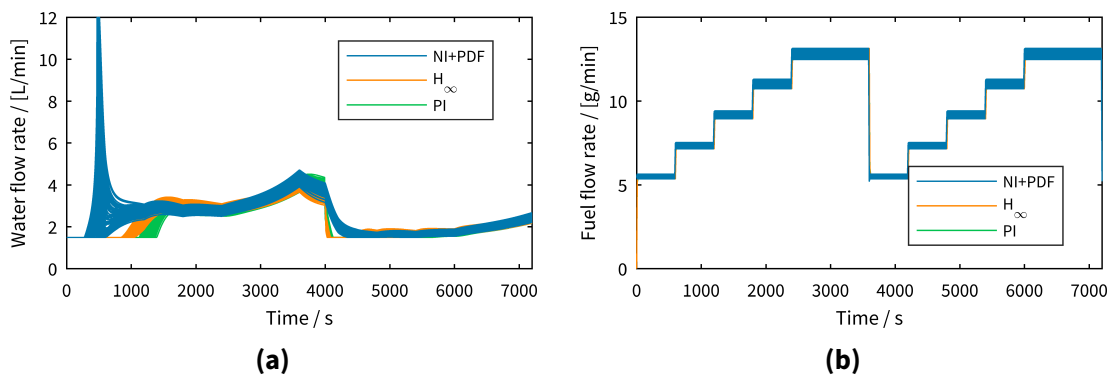


**Figure 8.5** | Comparison of manipulated control inputs for case 1: **(a)** Water flow rate. **(b)** Fuel flow rate.

following gains for the PI controller:

$$K_p = \text{diag}(-1.207 \times 10^{-3}, -18.87 \times 10^{-3}), K_i = \text{diag}(-23.12 \times 10^{-6}, -6.053 \times 10^{-3}).$$

### 8.2.3 Controls performance assessment: Minimise grid interaction

The first test case is to assess the controller performance to the thermal and electrical demands shown in figs. 8.3 and 8.4 while minimising electrical grid utilisation at all times. Note that the power demand ramps up every 600 s in this case study in order to ‘stress test’ the controllers. In this first case there is no demand signal from the LEN. A series of 100 Monte Carlo simulations were performed using the sampling method described in §§ 3.6.1 based on the parameter uncertainties given in table 8.1.

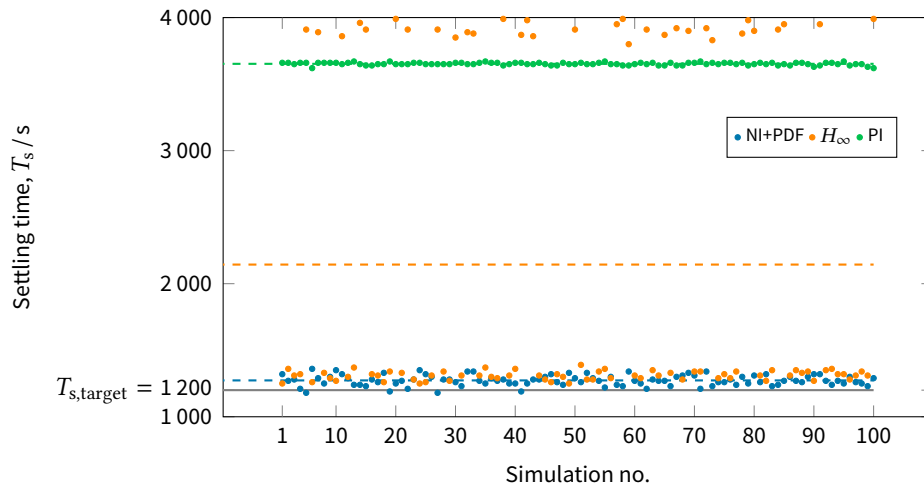
#### Time-domain response

Figure 8.3 shows the response curves for the control of the mCHP outlet temperature across all simulations. The thermal demands constitute a fixed set-point of 60 °C during warm-up and then at 4 000 s the set-point changes to the maximum design flow temperature of 75 °C. It can be seen that the NI+PDF controller closely follows the desired temperature trajectory at all times while both the  $H_\infty$  and PI controllers overshoot the set-point on both occasions. The NI+PDF controller is able to better regulate the set-point temperature, while both the  $H_\infty$  and PI controllers exhibit oscillations below and then above the set-point.

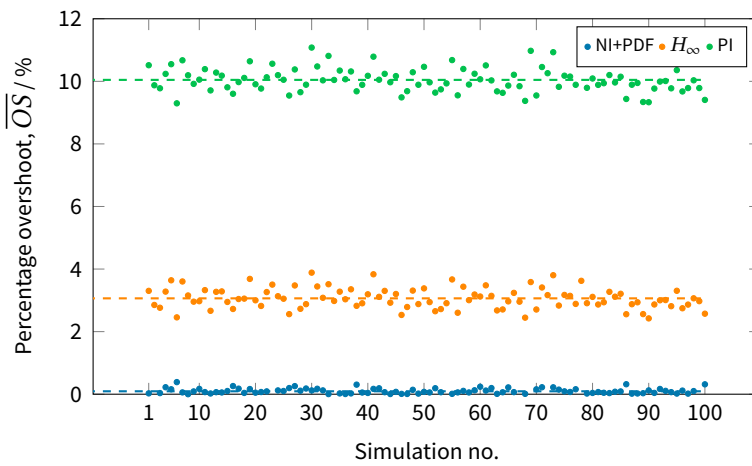
Figure 8.6 shows the corresponding settling time due to the initial set-point change. This demonstrates that the PI controller (on average) takes more than double the design settling time to fall within the required 2 % error band of set-point. The  $H_\infty$  controller achieves the desired settling time  $\approx 70\%$  of the time, but there are parameter combinations that cause the  $H_\infty$  controller to oscillate around the set-point causing an increased settling time.

Figure 8.7 show the corresponding percentage overshoot due to the initial set-point change. The NI+PDF controller exhibits minimal overshoot for all parameter permutations, while the  $H_\infty$  controller attains an average overshoot of 3 % and the PI an average of 10 %. While none of the overshoots of the set-point will violate the maximum allowable outlet temperature, they have a negative effect on the efficiency of the system. Overall, the  $H_\infty$  and PI controllers have performance degradation for some parameter combinations, with poorly damped oscillations and a long settling time.

Figure 8.5 shows the response curves for the manipulated control inputs. As shown in fig. 8.5a all controllers instinctively uses the minimum permissible water flow rate



**Figure 8.6** | Comparison of settling time due to first step-change in thermal reference setpoint for case 1. Dashed lines indicate the mean settling time across all simulations.



**Figure 8.7** | Comparison of overshoot due to first step-change in thermal reference setpoint for case 1. Dashed lines indicate the mean overshoot across all simulations.

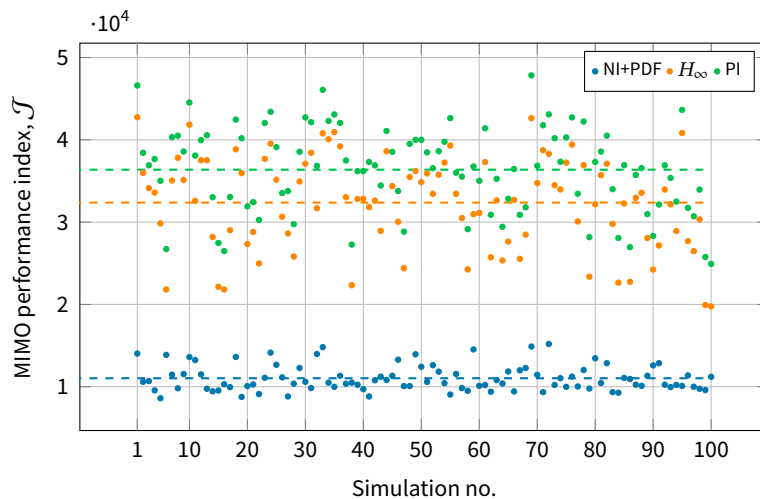


**Figure 8.8** | Comparison of control systems performance for case 1. Dashed lines indicate the mean performance index across all simulations.

when the unit is switched on to allow the heat exchanger and encapsulated water to heat up. After which the NI+PDF controller momentarily ramps up the water flow rate to the maximum for a short period before reducing it again. This behaviour is due to the inverse dynamics that provide the controller with ‘knowledge’ of the inertia in the system – by briefly ramping up the water flow rate it is able to adjust the ramp rate of the outlet temperature and avoids overshooting the set-point. On the other hand, both the  $H_\infty$  and PI controllers remain at the minimum flow rate for too long causing them to overshoot the set-point.

Figure 8.4 shows all the electrical power interactions in the system. This figure shows that both the  $H_\infty$  and PI exhibit unwanted ‘spikes’ in the measured grid power at every step change in power demand while the NI+PDF controller has no interaction with the LEN across all simulations. The absence of spikes in the NI+PDF response is due to the inverse dynamics part of the controller, which makes use of the measurement of the electrical demands of the building, whereas the  $H_\infty$  and PI controllers can only respond after the change in demand is ‘seen’ through the error in grid interaction.

### Desired closed-loop response performance indices

Recall that the performance of the MIMO control system is determined using

$$\mathcal{J} = \int_0^\infty \left( (\mathbf{y} - \mathbf{y}_d)^T \mathbf{Y} (\mathbf{y} - \mathbf{y}_d) + \mathbf{u}^T \mathbf{U} \mathbf{u} \right) dt. \quad (3.4 \text{ revisited})$$

For this case study, the magnitude of both control inputs have been mapped to the unit square such that when either control is at their maximum permissible value,  $u_{UL,i} \implies u_i = 1$  and similarly when at its minimum value  $u_{LL,i} \implies u_i = 0$ .<sup>2</sup> Then, set  $\mathbf{U} = \mathbf{I}_p$  so that the performance of each control channel was assessed with equal weighting.

The selection of  $\mathbf{Y}$  determines the weighting given to the system errors. The selection for the weighting for the system error  $(\mathbf{y} - \mathbf{y}_d)$  is more difficult as the thermal and electrical errors are not equivalent i.e. an identity matrix  $\mathbf{Y} = \mathbf{I}_p$  implies that an outlet temperature error of 1 °C is weighted equal to an electrical power error of 1 W. Therefore, an equivalence between the errors had to be calculated to determine the overall performance of the MIMO controller.

The amount of energy required to raise the outlet temperature by 1 °C during one simulation output is

$$E = C_{cw} \frac{\Delta\theta}{t} = C_{cw} \frac{1}{10} = 0.1 C_{cw} = 1.85 \text{ kW}$$

<sup>2</sup>Mapping the inputs between 0 and 1 is achieved by  $u_{[0,1]} = (u - \min(u)) / (\max(u) - \min(u))$ .

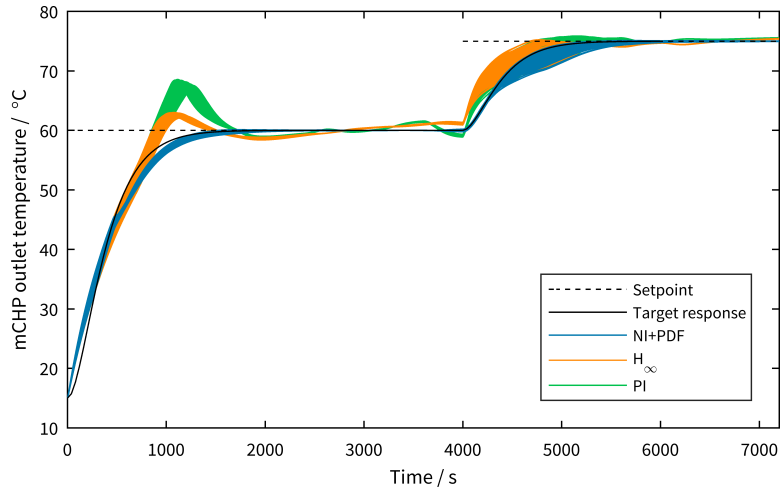


**Figure 8.9** | Comparison of dynamic response of mCHP outlet temperature for case 2.

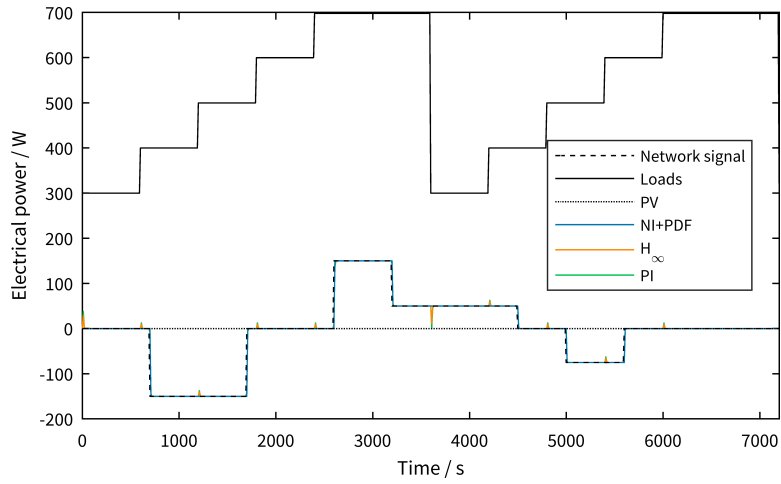


**Figure 8.10** | Comparison of all electrical power interactions for case 2.

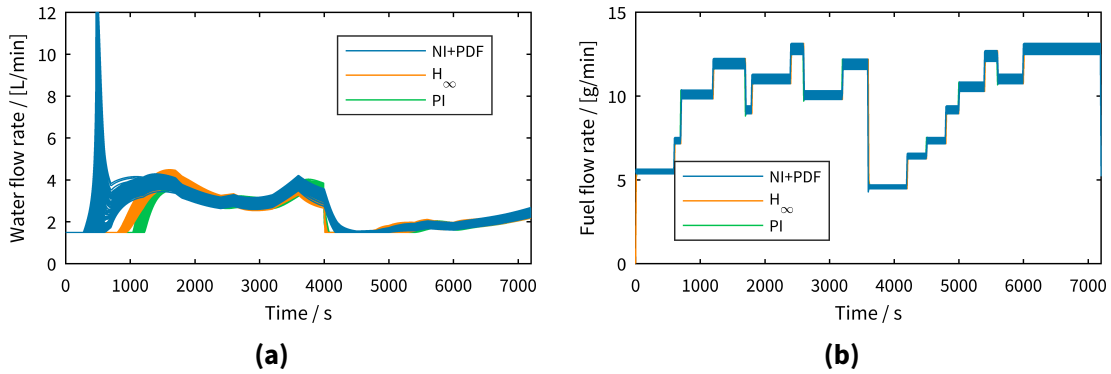


**Figure 8.11** | Comparison of manipulated control inputs for case 2: **(a)** Water flow rate. **(b)** Fuel flow rate.



Then an error weighting matrix of  $Y = \text{diag}(1, 1/(1.85 \times 10^3)^2)$  will cause the errors to be assessed with equal weighting based on energy. Figure 8.8 shows the performance index for each controller across all 100 simulations. Figure 8.8 demonstrates that the NI+PDF controller exhibits superior performance across all 100 simulations. The  $H_\infty$  controller performs (on average) better than the PI controller. Both the  $H_\infty$  and PI controllers show a greater sensitivity to the parameter variations in comparison to the NI+PDF controller as the variation in the performance index is greater across all simulations.

#### 8.2.4 Controls performance assessment: Demand-side response

This scenario analyses the performance of the control systems to DSR signals from the LEN. DSR asks the controlled system to have an immediate or almost immediate change in demand (decrease or increase) in response to an unplanned variation. That is, the LEN can ask the control system to pick up excess generation from the network by reducing the self-generation of the system. Conversely, the LEN can ask the control system to increase its generation above what is required to fulfil the internal loads to export electrical power to the network.

This case retains the same thermal and electrical loads as the previous case, however, there is the additional DSR signals from the LEN shown in fig. 8.10. As before, a series of 100 Monte Carlo simulations were performed using the sampling method described in §§ 3.6.1 based on the parameter uncertainties given in table 8.1.

#### Time domain response

Figure 8.9 shows the response curves for the control of the mCHP outlet temperature across all simulations. The thermal demands are the same as the previous case. The response of all three controllers is similar to the previous case, however, the overshoot exhibited by the  $H_\infty$  and PI is more severe in this case. This is because of the signal from the LEN to generate an extra 150 W for 1 000 s. This causes an increase in the heat generation inside the engine that the  $H_\infty$  and PI controllers do not compensate for. The NI+PDF controller is able to better regulate the set-point temperature, while both the  $H_\infty$  and PI controllers exhibit oscillations below and then above the set-point. All three controllers display variation in the response between simulations due to the second set-point change up to 75 °C. This is caused by the flow rate limits of the external pump – to match the target response during this time would require the pump to operate at a slower speed than it is capable of (see fig. 8.11a). The anti-windup compensators applied to all controllers are capable of handling these limitations and there is minimal overshoot of the second set-point change.

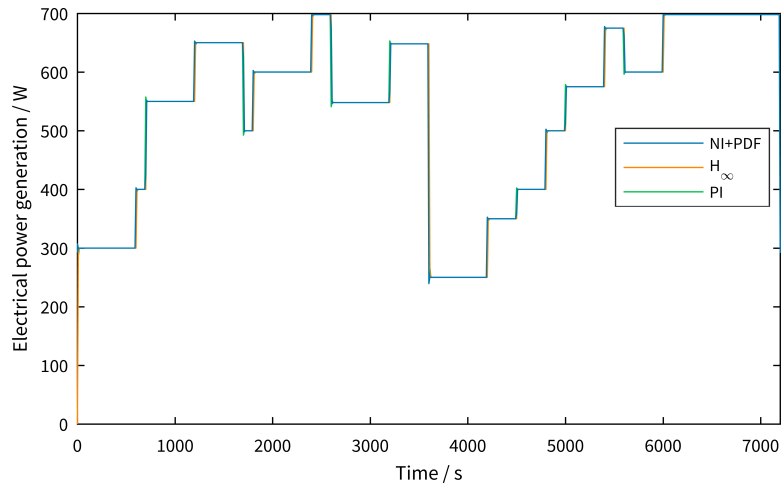


**Figure 8.12 | Comparison of electrical power generation for case 2.**

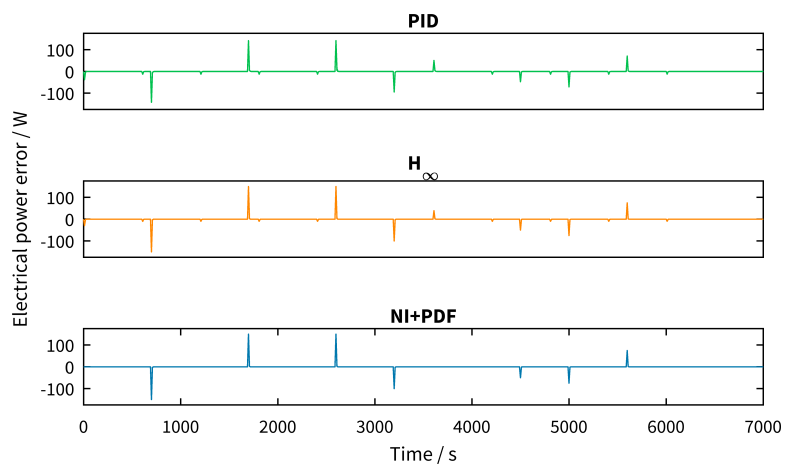


**Figure 8.13 | Comparison of electrical power error for case 2.**

Figure 8.14 shows the corresponding settling time due to the initial set-point change. This demonstrates that the PI controller (on average) takes three times the design settling time to fall within the required 2 % error band of set-point. The  $H_\infty$  controller (on average) takes twice as long to settling than what was desired. The NI+PDF controller, however, manages to settle around the set-point close to the desired time. In fact, the NI+PDF controller is (on average) only 1 min slower than the design settling time across all simulations.

Figure 8.15 show the corresponding percentage overshoot due to the initial set-point change. The NI+PDF controller exhibits minimal overshoot for all parameter permutations, while the  $H_\infty$  controller attains an average overshoot of 4 % and the PI an average of 13 %. Again, none of the overshoots of the set-point will violate the maximum allowable outlet temperature, but they have a negative effect on the efficiency of the system. Overall, the  $H_\infty$  and PI controllers have performance degradation for some parameter combinations, with poorly damped oscillations and a long settling time.

Figure 8.10 shows all the electrical power interactions in the system and fig. 8.12 shows the associated electrical power generation. Figure 8.13 illustrates that both the  $H_\infty$  and PI exhibit unwanted ‘spikes’ in the measured grid power at every step change in internal loads while the NI+PDF controller does not. However, all three controllers have unwanted ‘spikes’ due to the requests from the LEN. These are unavoidable due to the measurement delay from the time the signal is sent by the LEN and the time it is seen by the control system.

### Desired closed-loop response performance indices

This case uses the same performance metrics discussed in §§ 8.2.3. Figure 8.16 shows the performance index for each controller across all 100 simulations. Figure 8.16 demonstrates that the NI+PDF controller exhibits superior performance across all 100 simulations. The  $H_\infty$  controller performs (on average) better than the PI controller.

## 8.3 Case study without thermal storage

The second case study for the control of the system (as specified in fig. 8.17) where the system consists of an mCHP in combination with solar PV and electrical energy storage. Then, this example is concerned with constructing a robust controller for the following MIMO problem:

### Control Goal

Regulate the internal air temperature to any desired set-point and maintain the prescribed set-point while simultaneously minimising the utilisation of the electrical grid – in the presence of disturbances and process uncertainties.

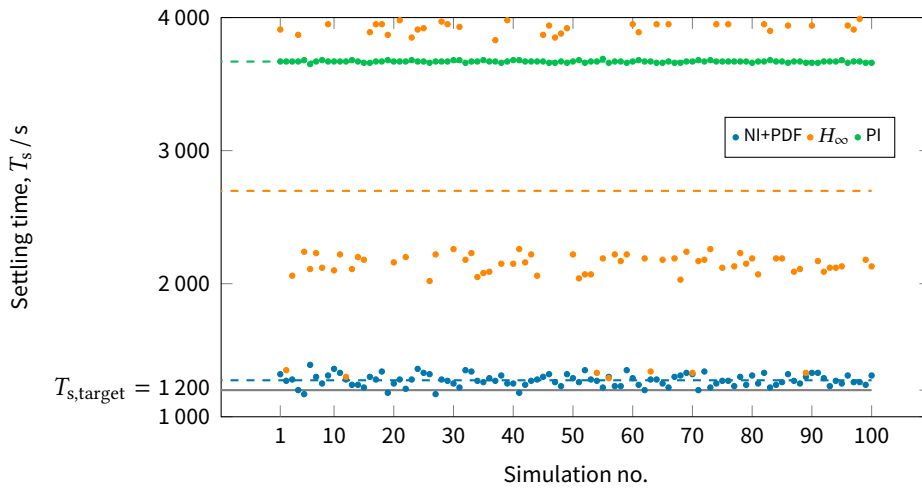


**Figure 8.14** | Comparison of settling time due to first step-change in thermal reference setpoint for case 2. Dashed lines indicate the mean settling time across all simulations.

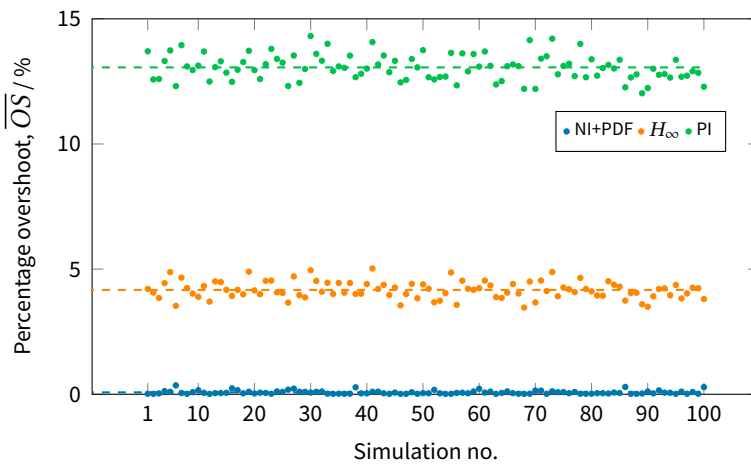


**Figure 8.15** | Comparison of overshoot due to first step-change in thermal reference setpoint for case 2. Dashed lines indicate the mean overshoot across all simulations.

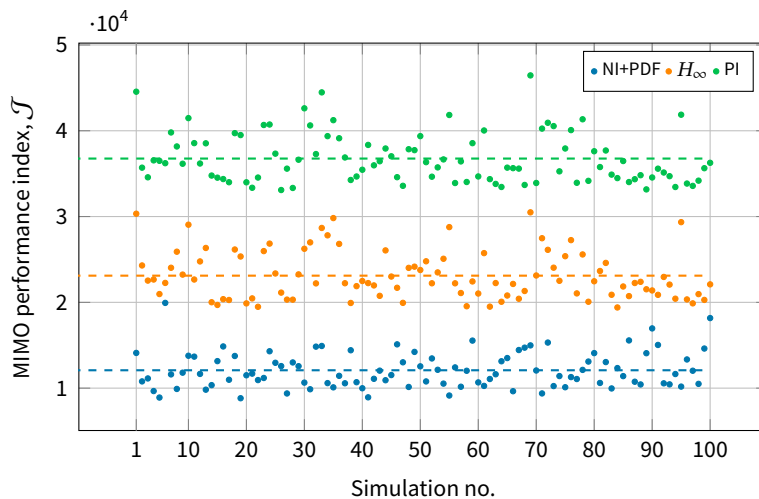


**Figure 8.16** | Comparison of control systems performance for case 2. Dashed lines indicate the mean performance index across all simulations.

From this control goal, it is possible to identify the variables to be controlled as:

**vc1** Zone dry-bulb (air) temperature.

**vc2** Electrical grid power.

The primary difficulty in the control of this system is that the air temperature is only indirectly related to the input fuel flow rate – which must first influence the engine, cooling water, and radiator temperatures before changes to the internal air temperature will be seen.

### 8.3.1 Problem formulation

The heating set-point is 21 °C between 08:00 and 18:00 on weekdays, with a night time and weekend setback temperature of 16 °C. The heating set-point corresponds to a Category I<sup>3</sup> comfort level for offices according to BS EN 15251:2007 (12, p. 26). Once the set-point has been reached, the control should be able to regulate the air temperature as best as possible within a 5 % error band to ensure comfort is maintained. The electrical grid power set-point is set to zero. This means that the controller will strive to neither import or export from or to the LEN, thereby minimising the interaction with the LEN.

The summary of the design specifications are given as

- ds1** Achieve a percentage overshoot of less than 5 % for a step change in air temperature set-point.
- ds2** Reach and maintain the air temperature set-point – within a 5 % error band – in a period less than or equal to 20 min from a change in set-point.
- ds2** Minimisation of electrical grid utilisation at all times unless responding to a demand signal from the LEN.
- ds3** Fulfilment of all electrical demands within the building at all times.
- ds4** Disturbance attenuation with the ultimate boundedness of the tracking error lower than a prescribed tolerance.
- ds5** Minimum sensitivity to process parameter changes.
- ds6** Robust stability.

---

<sup>3</sup>Comfort is ranked at I, II, III where I signifies the best.

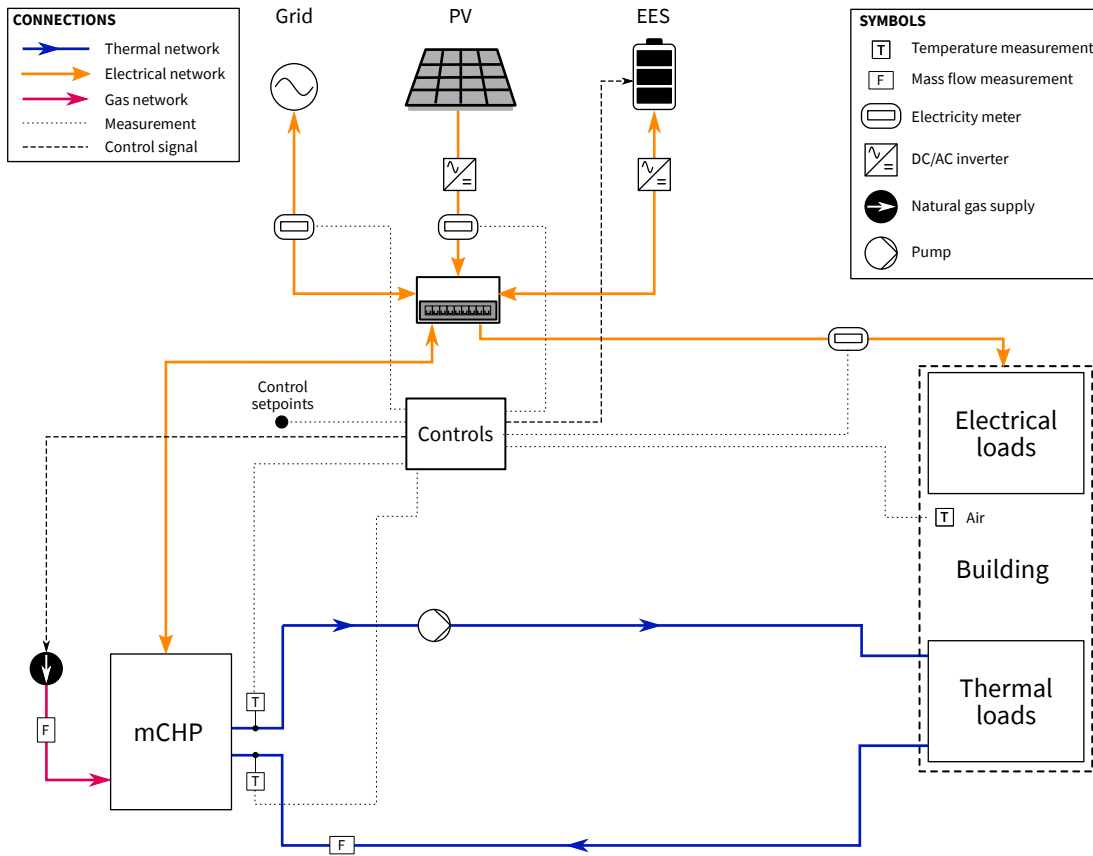


Figure 8.17 | Schematic of case study system with no dedicated thermal energy storage.

### 8.3.2 Control law design

The control model of the system is constructed by concatenating the state-space models of the system together and having the heat flux from each radiator connected to the air and inner surface nodes of the building model. Then the outlet of the mCHP is connected to the inlet of the radiators and the outlet of the radiators feeds into the inlet of the mCHP. That is, the building model in eq. (5.28) with DLM construction model, hydronic radiators in eq. (4.52) with 2 nodes per radiator and the mCHP model from eq. (4.8). The model of the electrical storage is implemented as in eq. (4.61).

The Electrical grid use is based upon an energy balance with all demand and supply elements given by:

$$P_{\text{grid}} = P_{\text{load}} - P_{\text{bat}} - P_{\text{PV}} - P_{\text{CHP}} \quad (8.6)$$

where  $P_{\text{grid}}(t) > 0$  represents import from the grid. It can be seen from (8.6) that the availability of PV is considered a disturbance. In this way, priority is given to utilising as much of the PV-generated electricity as possible, while the combined efforts of the mCHP unit and battery storage can contribute-to/fulfil the remaining demand. Assume that there is a sensor on the measurement of the electrical power use of the grid with a time constant  $\tau_{\text{grid}}$  such that an extra state is introduced and the electrical network model is given by

$$\dot{\hat{P}}_{\text{grid}}(t) = (1/\tau_{\text{grid}})(P_{\text{grid}}(t) - \hat{P}_{\text{grid}}(t)),$$

Therefore  $\mathbf{y}(t) = (y_1(t), y_2(t))^T = (\Theta_a, \hat{P}_{\text{grid}})^T$ , and the system inputs are the air temperature surrounding the mCHP unit, fuel flow rate, electrical demand on the battery, electrical power from photovoltaics, external air temperature, electrical load demand, and solar heat gains i.e. the system input vector  $\boldsymbol{\mu}(t) = (\mu_1(t), \dots, \mu_m(t))^T = (\Theta_{\text{env}}, \dot{m}_{\text{fuel}}, P_{\text{bat}}, P_{\text{PV}}, \Theta_{a,e}, P_{\text{load}}, \phi_{\text{sol}})^T$ . The state-vector  $\mathbf{x}(t) = (x_1(t), \dots, x_n(t))^T = (\Theta_{\text{eng}}, \Theta_{\text{cw,o}}, \Theta_{\text{rad},1}, \Theta_{\text{rad},2}, E_{\text{bat}}, \Theta_{\text{ext},1}, \dots, \Theta_{\text{ext},7}, \Theta_{\text{int},1}, \dots, \Theta_{\text{int},7}, \Theta_a)^T$ . In the remainder of this section the time-dependence is implied so that  $\mathbf{x} := \mathbf{x}(t)$ ,  $\mathbf{u} := \mathbf{u}(t)$ ,  $\mathbf{y} := \mathbf{y}(t)$ .

The system also includes temperature sensors with time delay and discretisation to accuracy of 0.1 °C. These are 'unmodelled' by the controller i.e. they are unstructured uncertainties.

The only measurements that are available to the controller is the electrical power generated by the PV and the electrical power demands of the building. Therefore,  $\mathbf{w} = (w_1, w_2) = (\mu_4, \mu_6) = (P_{\text{PV}}, P_{\text{load}})$ . For this case study, it is assumed that the mCHP unit is making use of its internal pump therefore the speed of the flow through the system is not controllable. Controlling the system is then only achieved by manipulating the fuel flow rate into the mCHP and the power demand on the battery i.e.  $\mathbf{u} = (u_1, u_2) = (\mu_2, \mu_3) = (\dot{m}_{\text{fuel}}, P_{\text{bat}})$ . The remaining system input is then an unmeasured disturbance,

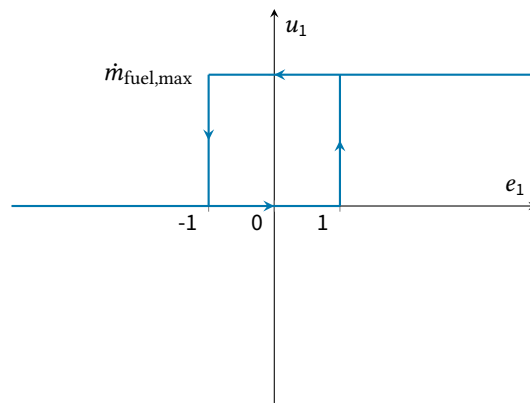


**Figure 8.18** | On/off controller for case study 2.



given as  $\mathbf{d} = (\Theta_{\text{env}}, \Theta_{\text{a,e}}, \phi_{\text{sol}})$ .

With these specifications the system can be expressed as a control-affine system

$$\Xi : \begin{cases} \dot{\mathbf{x}} = \mathbf{f}(\mathbf{x}, \mathbf{w}, \mathbf{d}) + \mathbf{G}(\mathbf{x}, \mathbf{w})\mathbf{u}, & (8.7a) \\ \mathbf{y} = \mathbf{h}(\mathbf{x}), & (8.7b) \end{cases}$$

where the system functions are provided in appendix C for the sake of clarity.

The operating bounds of the electrical power generation are  $P_{\text{gen}} \in [0, 698]$  W and the fuel flow rate is constrained as a function of these operating bounds. The limits on the charge and discharge rate of the battery are implemented as given in table 8.4.

This case study compares the performance of the NI+PDF controller with a robustly-tuned PI controller and a more standard on/off controller. Due to the complexity of the controlled system and the high relative degree, the design of an  $H_{\infty}$  optimal controller for comparison resulted in a numerically ill-conditioned controller and could not achieve the desired loop-shape. The author's attempts at reducing the order and complexity of the controller model did not prove fruitful in computing a stable  $H_{\infty}$  controller for the system in eq. (8.7a).

### Nonlinear inversion + PDF

The NI+PDF controller is designed using the procedure detailed in § 7.5. Taking the Lie derivatives of each output in (8.7a) until the control appears results in the following system

$$\hat{\mathbf{y}} = \mathbf{P}(\mathbf{x}, \mathbf{w}) + \mathbf{Q}(\mathbf{x}, \mathbf{w})\mathbf{u}. \quad (8.8)$$

with vector relative degree  $\boldsymbol{\rho} = (4, 1)$ . Again, the system functions are provided in appendix C for the sake of clarity.

**CONTROLLABILITY** The existence of an input-output inversion is reliant on the condition that  $\mathbf{Q}(\mathbf{x}, \mathbf{w})$  in (8.8) is invertible. Therefore, for all  $\mathbf{x}$  in the neighbourhood of some  $\mathbf{x}^{\circ}$ , and bounded measured inputs  $\mathbf{w}$  (in the original notation)

$$\det(\mathbf{Q}(\mathbf{x}, \mathbf{w})) = \dot{m}_{\text{cw}}((\Theta_{\text{cw,o}} + \Theta_{\text{cw,i}})/2 - \Theta_{\text{a}})^{0.3} \neq 0. \quad (8.9)$$

By investigation of (8.9) the condition is satisfied as long as water is moving through the system ( $\dot{m}_{\text{cw}} \neq 0$ ) and the average temperature between the inlet and outlet temperatures of the mCHP is not equal to the room air temperature. The first condition is obvious as water needs to move through the system to move heat from the mCHP to

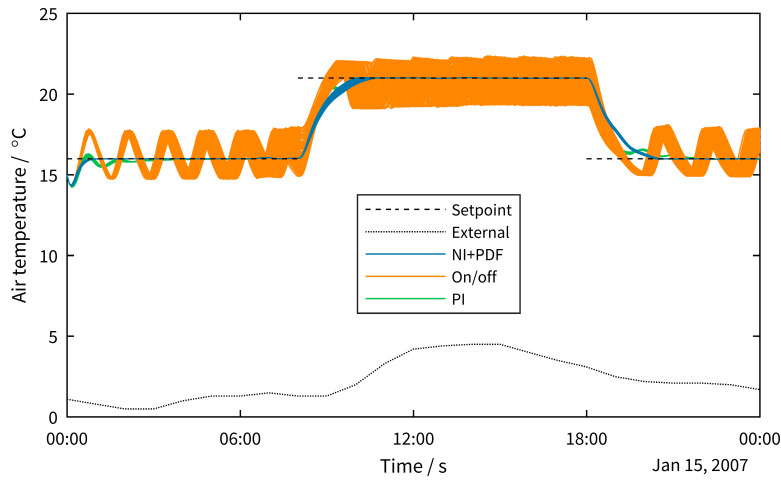


**Figure 8.19** | Comparison of dynamic response of air temperature for case study 2.

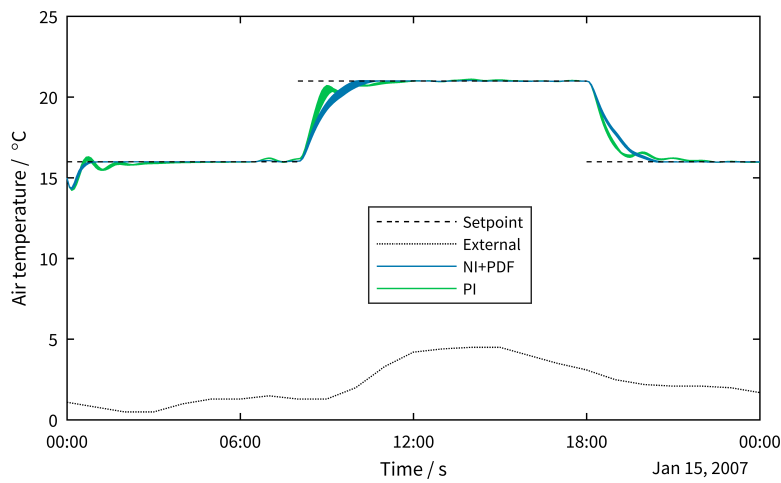


**Figure 8.20** | Comparison of dynamic response of air temperature for case study 2. On/off control removed from figure for clarity

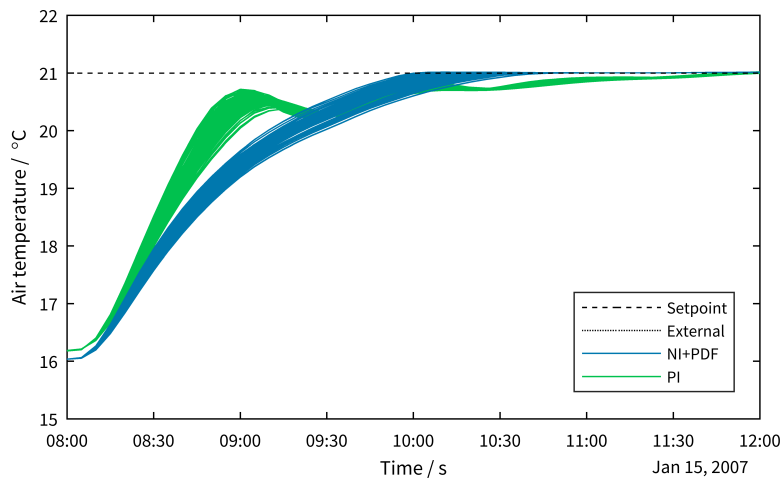


**Figure 8.21** | Comparison of dynamic response of air temperature for case study 2. Figure axis refined to transient period to illustrate response to a positive set-point change at the beginning of the occupied period.

the radiators. The second condition is a result of the fact that were the temperatures equal, the radiators would have no  $\Delta\theta$  across the inlet and outlets and resulting in no heat exchange with the room air meaning the room air temperature is then uncontrollable.

**NONLINEAR INVERSION** The nonlinear inversion of eq. (8.8) is given by

$$\mathbf{u} = \mathbf{u}_{\text{eq}}(\mathbf{x}, \mathbf{w}) + \boldsymbol{\beta}(\mathbf{x}, \mathbf{w})\mathbf{v},$$

$$\begin{bmatrix} u_1 \\ u_2 \end{bmatrix} = \begin{bmatrix} \hat{u}_{\text{eq},1}(\mathbf{x}, \mathbf{w}) \\ \hat{u}_{\text{eq},2}(\mathbf{x}, \mathbf{w}) \end{bmatrix} + \begin{bmatrix} \frac{\varrho_1}{\dot{m}_{\text{cw}}((\theta_{\text{cw},o} + \theta_{\text{cw},i})/2 - \theta_a)^{0.3}} & 0 \\ -\frac{\varrho_2}{\dot{m}_{\text{cw}}((\theta_{\text{cw},o} + \theta_{\text{cw},i})/2 - \theta_a)^{0.3}} & -\varrho_3 \end{bmatrix} \begin{bmatrix} v_1 \\ v_2 \end{bmatrix}$$

where  $\hat{u}_{\text{eq},i}$  are estimates of the equivalent control based on the available measurements and  $\varrho_i$  are positive constants that are functions of the nominal values of the system parameters.

**PDF CONTROLLER** The PDF controllers are given by

$$\dot{\mathbf{z}} = \mathbf{K}_I(\mathbf{y}_d - \mathbf{y}),$$

$$\mathbf{v} = \mathbf{z} - \mathbf{K}_D\mathbf{y},$$

$$\mathbf{K}_I = \text{diag}(22.708 \times 10^{-9}, 340.34 \times 10^{-3}), \quad \mathbf{K}_D = \text{diag}(\mathbf{k}_{D,1}, \mathbf{k}_{D,2}),$$

$$\mathbf{k}_{D,1} = (10.032 \times 10^{-6}, 1.2518 \times 10^{-3}, 32.113 \times 10^{-3}, 305.75 \times 10^{-3}), \quad \mathbf{k}_{D,2} = 1.1668.$$

The anti-windup technique for this controller is implemented exactly as in eq. (7.23).

### Robustly-tuned PI

A pair of PI controllers were used given by

$$\mathbf{u}(t) = \mathbf{K}_p\mathbf{e}(t) + \mathbf{z}(t),$$

where the integral action with a clamping anti-windup scheme is given by

$$z_i(t) = \begin{cases} 0 & \text{if } (\tilde{u}_i(t) \neq 0) \wedge (\text{sgn}(\tilde{u}_i(t)) = \text{sgn}(K_{i,i}e_{ii}(t))) \\ K_{i,ii}e_i(t) & \text{otherwise} \end{cases}$$

where  $\tilde{u}_i$  is the piecewise ‘dead zone’ function as defined in eq. (7.20) as before. The PI controller gains are calculated in the same way as § 8.2 and resulted in the following

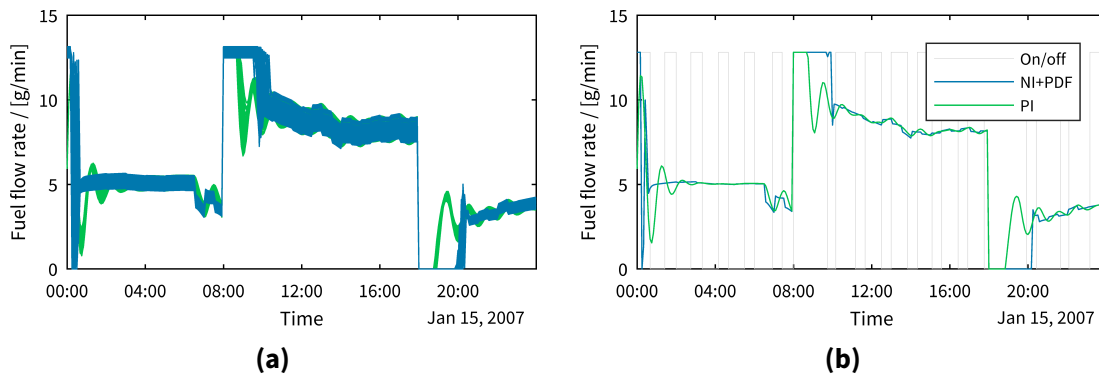


**Figure 8.22** | Comparison of manipulated fuel flow rate for case study 2: **(a)** 100 Monte Carlo simulations with parameter uncertainty. **(b)** Response for nominal parameters.

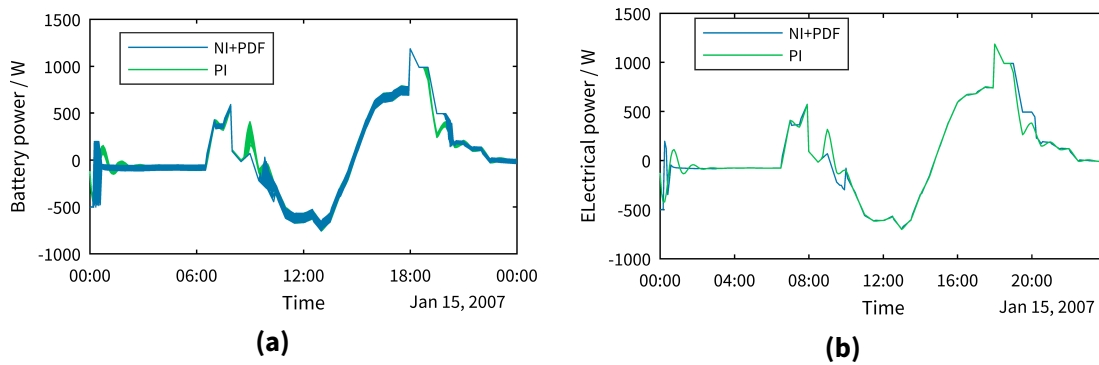


**Figure 8.23** | Comparison of manipulated battery power for case study 2: **(a)** 100 Monte Carlo simulations with parameter uncertainty. **(b)** Response for nominal parameters.

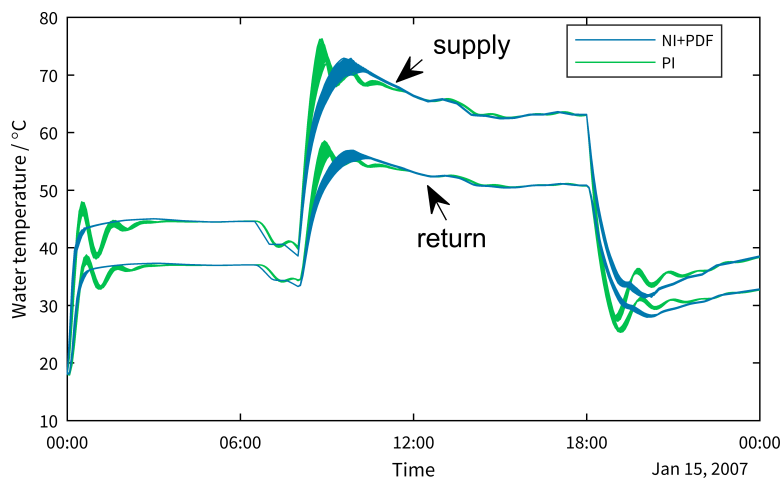


**Figure 8.24** | Comparison of dynamic response of hydronic system inlet and outlet temperatures.

gains for the PI controller:

$$K_p = \text{diag}(9.8598 \times 10^{-5}, -33.769), K_i = \text{diag}(1.9454 \times 10^{-8}, -51.692).$$

### On/off

In the on/off case, the mCHP is purely thermally-led and uses a two-position relay as shown in fig. 8.18 to switch the unit on and off.

#### 8.3.3 Controls performance assessment

A series of 100 Monte Carlo simulations were performed using the sampling method described in §§ 3.6.1 based on the parameter uncertainties given in table 8.1.

#### Time-domain response

Figures 8.19–8.26 show the dynamic results from the model for a cold, bright day. The sampling frequency of the controller was set to 1 Hz with an output frequency of 3.33 mHz.

As can be seen in fig. 8.20 and fig. 8.21, the NI+PDF control is able, after a stable transient period, to maintain the set-point temperature with no oscillation or ‘ringing’ around the set-point typically associated with thermally-led mCHP switching on and off to fulfil the demand (as shown in fig. 8.19). The discussion going forward will only be concerned with comparing the PI and NI+PDF controllers due to the evidently poor performance of the on/off control.

The PI control undershoots the set-point and takes a long time to converge towards the set-point temperature and is unable to reach the set-point until  $\approx 2.5$  h into the occupied period in all simulations. The PI control also demonstrates large fluctuations in control action on the manipulated fuel flow rate during the beginning of the occupied period (see fig. 8.22), while the NI+PDF controller holds the fuel flow rate at maximum before safely decreasing the fuel input to the minimum permissible value before the valve is closed.

The control of the air-temperature response time was selected to settle within 2% of the set-point after 30 min with no overshoot. However, the mCHP unit and hydronic system are not sufficiently sized to achieve the desired performance and saturates at its maximum output. This leads to a slower response (settling after  $\approx 1.5$  h) but the controller still achieves the set-point temperature with no threat of overshoot or oscillatory response due to the input constraint compensation. The use of a supervisory controller in tandem with the predictable response demonstrated by the NI+PDF controller would be beneficial in this case as it could use an ‘optimum start’ calculation

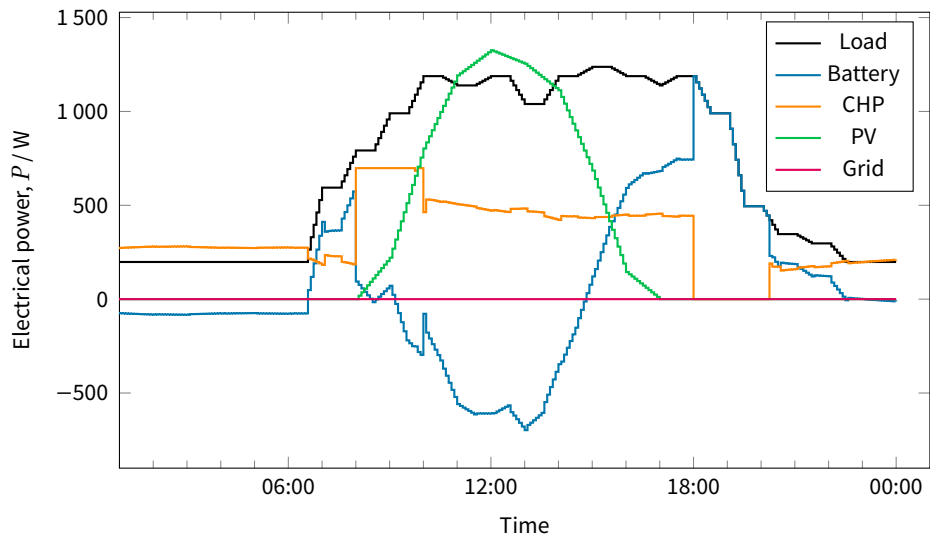


**Figure 8.25 | Comparison of all electrical power interactions over 24 h period.**

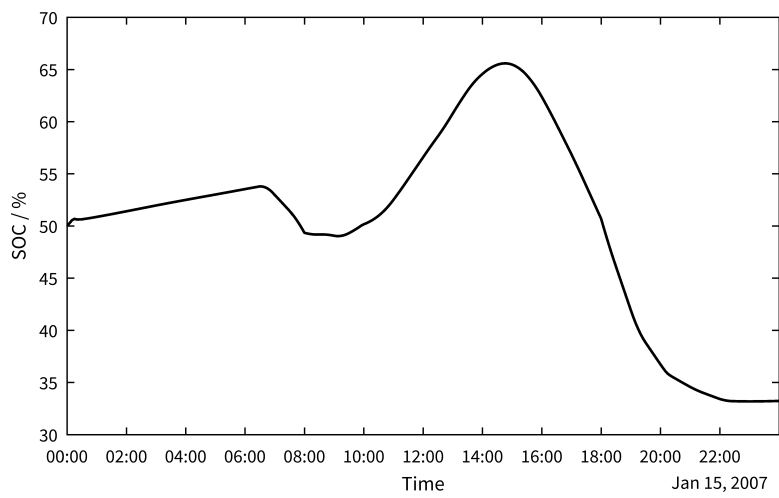


**Figure 8.26 | State-of-charge of battery over 24 h period.**

to shift the set-point earlier in the day to provide sufficient time for the zone to be heated. While the air temperature demonstrated a slower response than for which it was tuned, if the controller were to be re-tuned for a faster response time, the response would be the same, as the fuel flow input remained at its saturation limit as long as possible before safely moving away from the limit until the desired temperature is reached without overshoot.

Figure 8.24 shows the supply and return temperatures from the mCHP unit under both the PI control and NI+PDF controller. The PI controller causes significant oscillation in temperatures at each set-point change, while the NI+PDF controller exhibits no such behaviour. However, the overshoot of supply temperature by the PI controller due to the set-point change could cause the supply temperature to approach the maximum outlet temperature of the mCHP on colder days.

Figure 8.25 shows all of the elements of the electrical network working together to achieve zero electrical grid interaction. This demonstrates the strength of the robust control strategy as it is able to balance both the thermal and electrical networks without any reliance upon the LEN.

It can be seen from fig. 8.26 that the balance of power extracted and supplied to the battery will leave it in a more discharged state at the end of the day compared to its initial state. However, there will be other days where the excess generation from the PV and mCHP would leave the battery in a surplus. Nonetheless, were the battery to be completely depleted the following results can be surmised: The control strategy here only has two manipulable inputs (mCHP fuel flow rate and battery use). When the battery is depleted, the system loses a controllable input. In this case the control law would be dynamically recomputed to a SISO system (see sec. 7.4). It is up to the control engineer to decide whether to control the mCHP to meet the thermal or electrical demand. With no back up thermal heating system, it would control to fulfil the thermal demands and make up the deficit in power generation from the grid.

## **8.4** Case study with thermal storage

The third and final case study for the control of the system (as shown in fig. 8.27) where the system consists of an mCHP in combination with solar PV, electrical energy storage and a stratified TES tank. Then, this example is concerned with constructing a robust controller for the following MIMO problem:

### **Control Goal**

Regulate the internal air temperature to any desired set-point and maintain the prescribed set-point while simultaneously minimising the utilisation of the electrical grid – in the presence of disturbances and process uncertainties.

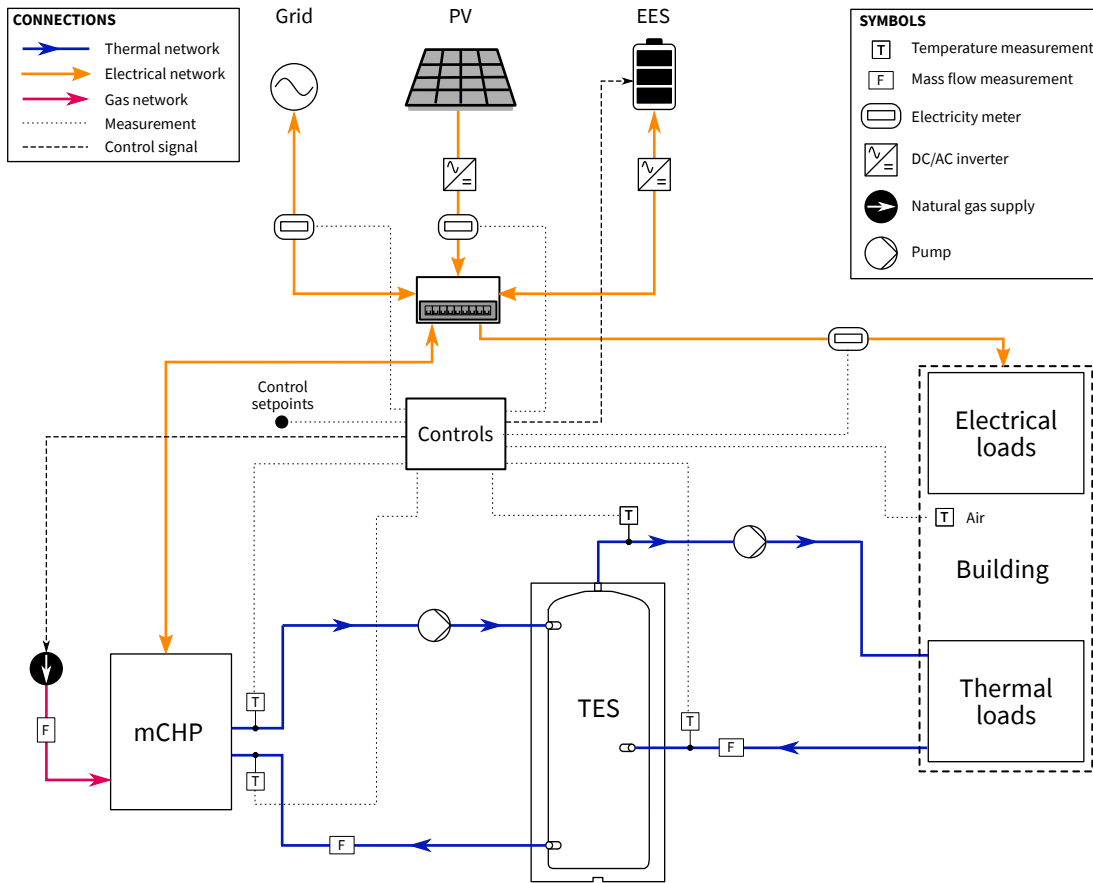


**Figure 8.27** | Schematic of case study system with dedicated thermal energy storage.



From this control goal, it is possible to identify the variables to be controlled as:

**vc1** Zone dry-bulb (air) temperature.

**vc2** Electrical grid power.

The primary difficulty in the control of this system is that the air temperature is only indirectly related to the input fuel flow rate – which must first influence the engine, cooling water, TES tank and finally radiator temperatures before changes to the internal air temperature will be seen.

#### 8.4.1 Problem formulation

The formulation of the problem in this case study has the same objectives as given in §§ 8.3.1. In addition, it is desirable to maintain stratification in the TES tank to reduce mixing in the tank and avoid the destruction of exergy in the system. To maintain the stratification while delivering energy to the loads, there is a charging loop that delivers heat from the mCHP to the top of the tank, while colder water from its bottom is fed back into the inlet of the mCHP unit. The discharging loop takes heat from near the top and is fed to the radiators, while the outlet of the radiators is connected to an inlet pipe near the bottom of the tank. These two loops will allow the TES tank to maintain the thermocline while being simultaneously charged by the mCHP and discharged by the loads from the radiators to the zone.

#### 8.4.2 Control law design

The control model of the system is constructed by concatenating the state-space models of the system together and having the heat flux from each radiator connected to the air and inner surface nodes of the building model. Then the outlet of the mCHP is connected to inlet 2 of the TES tank and outlet 2 of the TES tank is connected back to the return inlet of the mCHP unit. Outlet 1 of the TES tank is connected to the inlet of the radiator network and the outlet of the radiators feeds into the inlet 1 of the TES tank. That is, the building model in eq. (5.28) with DLM construction model, hydronic radiators in eq. (4.52) with 2 nodes per radiator and, mCHP model from eq. (4.8) and the TES tank model from eq. (4.47) with 6 nodes. The model of the electrical storage is implemented as in eq. (4.61).

The Electrical grid use is based upon an energy balance with all demand and supply elements given by:

$$P_{\text{grid}} = P_{\text{load}} - P_{\text{bat}} - P_{\text{PV}} - P_{\text{CHP}} \quad (8.10)$$



where  $P_{\text{grid}}(t) > 0$  represents import from the grid. It can be seen from (8.10) that the availability of PV is considered a disturbance. In this way, priority is given to utilising as much of the PV-generated electricity as possible, while the combined efforts of the mCHP unit and battery storage can contribute-to/fulfil the remaining demand. Assume that there is a sensor on the measurement of the electrical power use of the grid with a time constant  $\tau_{\text{grid}}$  such that an extra state is introduced and the electrical network model is given by

$$\dot{\hat{P}}_{\text{grid}}(t) = (1/\tau_{\text{grid}})(P_{\text{grid}}(t) - \hat{P}_{\text{grid}}(t)),$$

Therefore  $\mathbf{y}(t) = (y_1(t), y_2(t))^{\mathcal{T}} = (\Theta_a, \hat{P}_{\text{grid}})^{\mathcal{T}}$ , and the system inputs are the air temperature surrounding the mCHP unit and TES tank, fuel flow rate, cooling water flow rate, electrical demand on the battery, electrical power from photovoltaics, external air temperature, electrical load demand, solar heat gains and load flow rate i.e. the system input  $\boldsymbol{\mu}(t) = (\mu_1(t), \dots, \mu_m(t))^{\mathcal{T}} = (\Theta_{\text{env}}, \dot{m}_{\text{fuel}}, \dot{m}_{\text{cw}}, P_{\text{bat}}, P_{\text{PV}}, \Theta_{\text{a,e}}, P_{\text{load}}, \phi_{\text{sol}}, \dot{m}_{\text{load}})^{\mathcal{T}}$ . The state-vector  $\mathbf{x}(t) = (x_1(t), \dots, x_n(t))^{\mathcal{T}} = (\Theta_{\text{eng}}, \Theta_{\text{cw,o}}, \Theta_{\text{rad,1}}, \Theta_{\text{rad,2}}, E_{\text{bat}}, \Theta_{\text{ext,1}}, \dots, \Theta_{\text{ext,7}}, \Theta_{\text{int,1}}, \dots, \Theta_{\text{int,7}}, \Theta_a, \Theta_{\text{TES}}^{\mathcal{T}})^{\mathcal{T}}$ . For remainder of this section the time-dependence is implied so that  $\mathbf{x} := \mathbf{x}(t)$ ,  $\mathbf{u} := \mathbf{u}(t)$ ,  $\mathbf{y} := \mathbf{y}(t)$ .

The system also includes temperature sensors with time delay and discretisation to accuracy of 0.1 °C. These are 'unmodelled' by the controller i.e. they are unstructured uncertainties.

The measurements that are available to the controller is the electrical power generated by the PV, the electrical power demands of the building and the flow rates from the mCHP to the TES and from the TES to the radiators. Therefore,  $\mathbf{w} = (w_1, w_2, w_3, w_4) = (\mu_3, \mu_5, \mu_7, \mu_{10}) = (\dot{m}_{\text{cw}}, P_{\text{PV}}, P_{\text{load}}, \dot{m}_{\text{load}})$ . For this case study, it is assumed that the mCHP unit is making use of its internal pump therefore the speed of the flow through the system is not controllable only measurable. Controlling the system is then only achieved by manipulating the fuel flow rate into the mCHP and the power demand on the battery i.e.  $\mathbf{u} = (u_1, u_2) = (\mu_2, \mu_4) = (\dot{m}_{\text{fuel}}, P_{\text{bat}})$ . The remaining system inputs are the unmeasured disturbances, given as  $\mathbf{d} = (d_1, d_2, d_3) = (\Theta_{\text{env}}, \Theta_{\text{a,e}}, \phi_{\text{sol}})$ .

With these specifications the system can be expressed as a control-affine system

$$\Xi : \begin{cases} \dot{\mathbf{x}} = \mathbf{f}(\mathbf{x}, \mathbf{w}, \mathbf{d}) + \mathbf{G}(\mathbf{x}, \mathbf{w})\mathbf{u}, & (8.11a) \\ \mathbf{y} = \mathbf{h}(\mathbf{x}), & (8.11b) \end{cases}$$

where the system functions are provided in appendix C for the sake of clarity.

The operating bounds of the electrical power generation are  $P_{\text{gen}} \in [0, 698]$  W and the fuel flow rate is constrained as a function of these operating bounds. The limits on the charge and discharge rate of the battery are implemented as given in table 8.4.



This case study compares the performance of the NI+PDF controller with a robustly-tuned PI controller and a more standard on/off controller. Due to the complexity of the controlled system and the high relative degree, the design of an  $H_\infty$  optimal controller for comparison resulted in a numerically ill-conditioned controller and could not achieve the desired loop-shape. The author's attempts at reducing the order and complexity of the controller model did not prove fruitful in computing a stable  $H_\infty$  controller for the system in eq. (8.11a).

### Nonlinear inversion + PDF

The NI+PDF controller is designed using the procedure detailed in § 7.5. Taking the Lie derivatives of each output in (8.11a) until the control appears results in the following system

$$\hat{y} = P(\mathbf{x}, \mathbf{w}) + Q(\mathbf{x}, \mathbf{w})\mathbf{u}. \quad (8.12)$$

with vector relative degree  $\boldsymbol{\rho} = (4, 1)$ . Again, the system functions are provided in appendix C for the sake of clarity.

**CONTROLLABILITY** The existence of an input-output inversion is reliant on the condition that  $Q(\mathbf{x}, \mathbf{w})$  in (8.12) is invertible. Therefore, for all  $\mathbf{x}$  in the neighbourhood of some  $\mathbf{x}^\circ$ , and bounded measured inputs  $\mathbf{w}$  (in the original notation)

$$\det(Q(\mathbf{x}, \mathbf{w})) = \dot{m}_{\text{sys}}((\Theta_{\text{tes},01} + \Theta_{\text{tes},i1})/2 - \Theta_a)^{0.3} \neq 0. \quad (8.13)$$

By investigation of (8.13) the condition is satisfied as long as water is moving through the system ( $\dot{m}_{\text{sys}} \neq 0$ ) and the average temperature between the first set of the inlet and outlet temperatures of the TES tank is not equal to the room air temperature. The first condition is obvious as water needs to move through the system to move heat from the TES tank to the radiators. The second condition is a result of the fact that were the temperatures equal, the radiators would have no  $\Delta\Theta$  across the inlet and outlets and resulting in no heat exchange with the room air meaning the room air temperature is then uncontrollable. Therefore, the system is uncontrollable if the tank is fully stratified at the same temperature as the zone.

**NONLINEAR INVERSION** The nonlinear inversion of eq. (8.12) is given by

$$\mathbf{u} = \mathbf{u}_{\text{eq}}(\mathbf{x}, \mathbf{w}) + \boldsymbol{\beta}(\mathbf{x}, \mathbf{w})\mathbf{v},$$



$$\begin{bmatrix} u_1 \\ u_2 \end{bmatrix} = \begin{bmatrix} \hat{u}_{\text{eq},1}(\mathbf{x}, \mathbf{w}) \\ \hat{u}_{\text{eq},2}(\mathbf{x}, \mathbf{w}) \end{bmatrix} + \begin{bmatrix} \frac{\varrho_1}{\dot{m}_{\text{sys}}((\Theta_{\text{tes},01} + \Theta_{\text{tes},i1})/2 - \Theta_a)^{0.3}} & 0 \\ -\frac{\varrho_2}{\dot{m}_{\text{sys}}((\Theta_{\text{tes},01} + \Theta_{\text{tes},i1})/2 - \Theta_a)^{0.3}} & -\varrho_3 \end{bmatrix} \begin{bmatrix} v_1 \\ v_2 \end{bmatrix}$$

where  $\hat{u}_{\text{eq},i}$  are estimates of the equivalent control based on the available measurements and  $\varrho_i$  are positive constants that are functions of the nominal values of the system parameters.

**PDF CONTROLLER** The PDF controllers are given by

$$\dot{\mathbf{z}} = \mathbf{K}_I(\mathbf{y}_d - \mathbf{y}),$$

$$\mathbf{v} = \mathbf{z} - \mathbf{K}_D \mathbf{y},$$

$$\mathbf{K}_I = \text{diag}(709.63 \times 10^{-12}, 340.34 \times 10^{-3}), \quad \mathbf{K}_D = \text{diag}(\mathbf{k}_{D,1}, \mathbf{k}_{D,2}),$$

$$\mathbf{k}_{D,1} = (627.02 \times 10^{-9}, 156.48 \times 10^{-6}, 8.0281 \times 10^{-3}, 152.87 \times 10^{-3}), \quad \mathbf{k}_{D,2} = 1.1668.$$

The anti-windup technique for this controller is implemented exactly as in eq. (7.23).

### Robustly-tuned PI

A pair of PI controllers were used given by

$$\mathbf{u}(t) = \mathbf{K}_p \mathbf{e}(t) + \mathbf{z}(t),$$

where the integral action with a clamping anti-windup scheme is given by

$$z_i(t) = \begin{cases} 0 & \text{if } (\tilde{u}_i(t) \neq 0) \wedge (\text{sgn}(\tilde{u}_i(t)) = \text{sgn}(K_{i,i} e_{ii}(t))) \\ K_{i,ii} e_i(t) & \text{otherwise} \end{cases}$$

where  $\tilde{u}_i$  is the piecewise ‘dead zone’ function as defined in eq. (7.20) as before. The PI controller gains are calculated in the same way as § 8.2 and resulted in the following gains for the PI controller:

$$\mathbf{K}_p = \text{diag}(2.9637 \times 10^{-5}, -33.769), \quad \mathbf{K}_i = \text{diag}(8.9712 \times 10^{-9}, -51.692).$$

### On/off

In the on/off case, the mCHP is purely thermally-led and uses a two-position relay as shown in fig. 8.18 to switch the unit on and off.

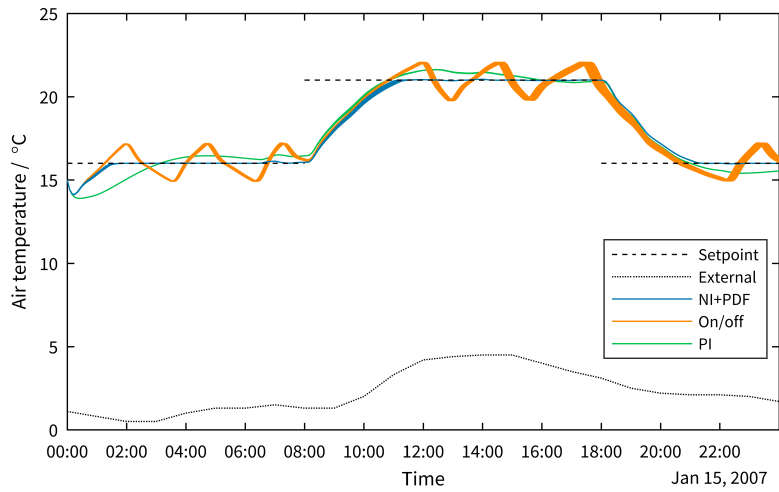


**Figure 8.28** | Comparison of dynamic response of air temperature for case study 3.

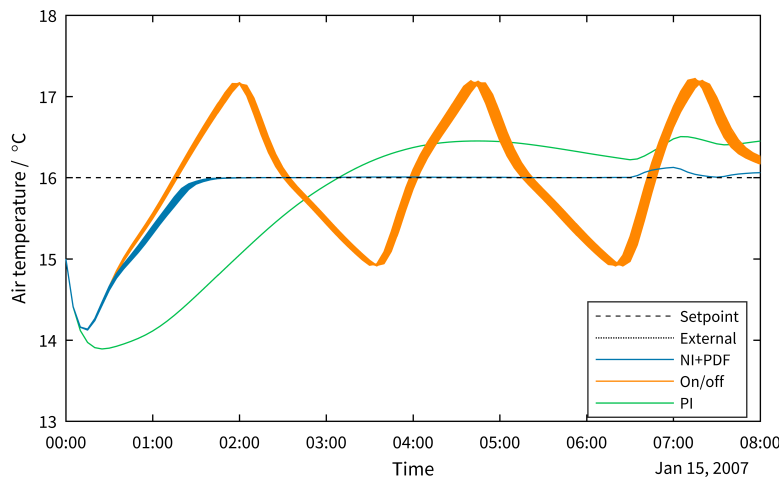


**Figure 8.29** | Comparison of dynamic response of air temperature for case study 3. Figure axis refined to transient period to illustrate response to a positive set-point change at the beginning of the day.

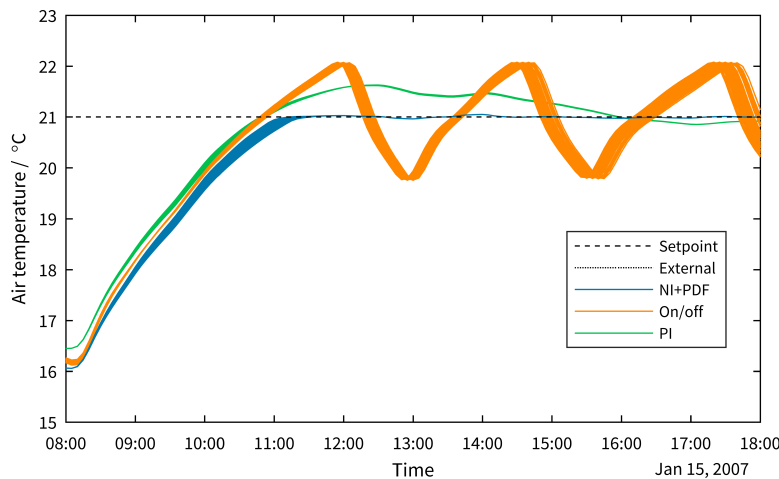


**Figure 8.30** | Comparison of dynamic response of air temperature for case study 3. Figure axis refined to transient period to illustrate response to a positive set-point change at the beginning of the occupied period.



### 8.4.3 Controls performance assessment

A series of 100 Monte Carlo simulations were performed using the sampling method described in §§ 3.6.1 based on the parameter uncertainties given in table 8.1.

#### Time-domain response

Figures 8.28–8.36 show the dynamic results from the model for the same cold, bright day as in § 8.3. The sampling frequency of the controller was set to 1 Hz with an output frequency of 3.33 mHz.

As can be seen in fig. 8.28, the NI+PDF control is able, after a stable transient period, to maintain the set-point temperature with no oscillation or ‘ringing’ around the set-point demonstrated by the thermally-led mCHP switching on and off to fulfil the demand. This is true for both the start-up from equilibrium conditions and for the set-point change at the beginning of the occupied period.

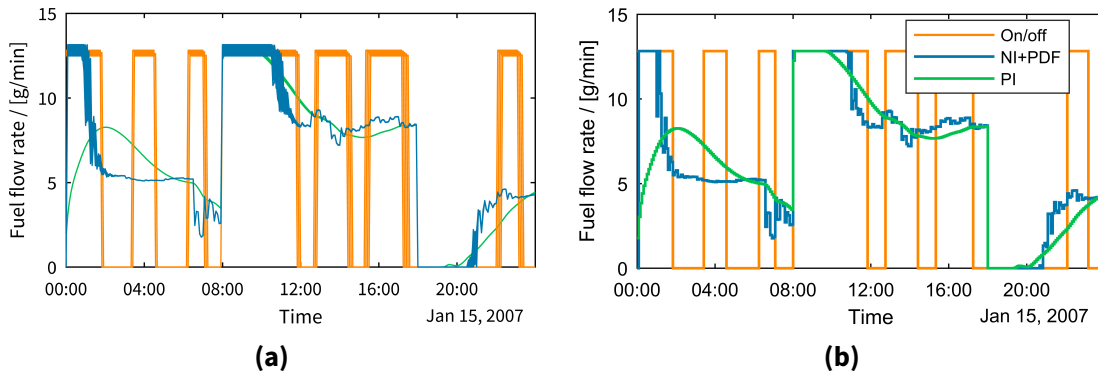
During the transient warm-up period at the beginning of the simulation, fig. 8.29 shows that the PI control is very sluggish and the air temperature takes a long time to begin to move towards the set-point. When the set-point is reached the PI controller overshoots and is unable to converge towards the set-point. Both of these response characteristics can be attributed to the high inertia in the system caused by the introduction of the TES tank. The NI+PDF controller is able to respond as quickly as the on/off controller, but does not overshoot the set-point and is able to regulate the set-point almost perfectly, except for the slight ‘bump’ occurring at approximately 07:00 when the building begins to be occupied, which is quickly attenuated.

Figure 8.30 shows the response of the controllers at the beginning of the occupied period. This time, the PI control overshoots the set-point and takes a long time to converge towards the set-point temperature and is unable to reach the set-point until  $\approx 8$  h into the occupied period in all simulations. This means that the PI control causes either underheating or overheating for almost the entire duration of the occupied period.

It should be noted that regardless of the type of control used, the overall response of the air temperature during the occupied period is slow, with acceptable<sup>4</sup> indoor temperatures not being reached until 09:30 and the set-point not being reached until 11:00. Therefore, it would be beneficial to pair the NI+PDF controller with a supervisory ‘optimal dispatch’ type of MPC to bring the set-point forward in situations where the thermal output of the mCHP is buffered by a TES tank.

---

<sup>4</sup>Minimum acceptable indoor temperature is 19 °C according to category III for office spaces in BS EN 15251:2007 (12).



**Figure 8.31 | Comparison of manipulated fuel flow rate for case study 3: (a)** 100 Monte Carlo simulations with parameter uncertainty. **(b)** Response for nominal parameters.

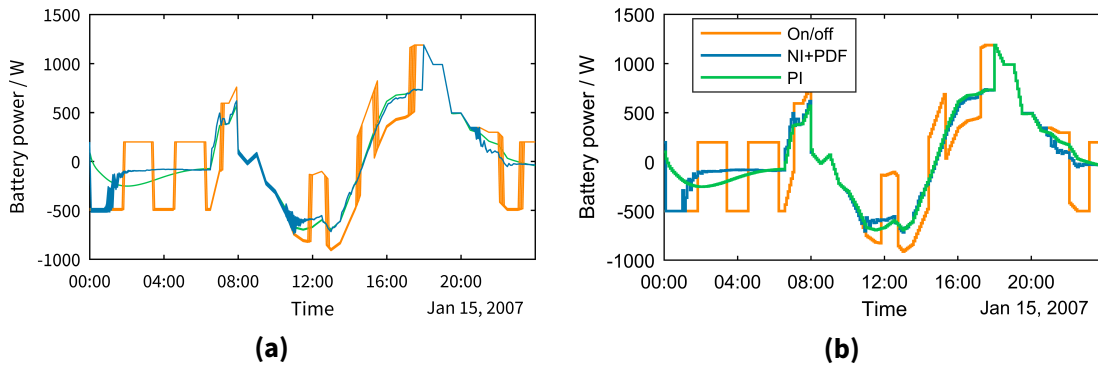


**Figure 8.32 | Comparison of manipulated battery power for case study 3: (a)** 100 Monte Carlo simulations with parameter uncertainty. **(b)** Response for nominal parameters.

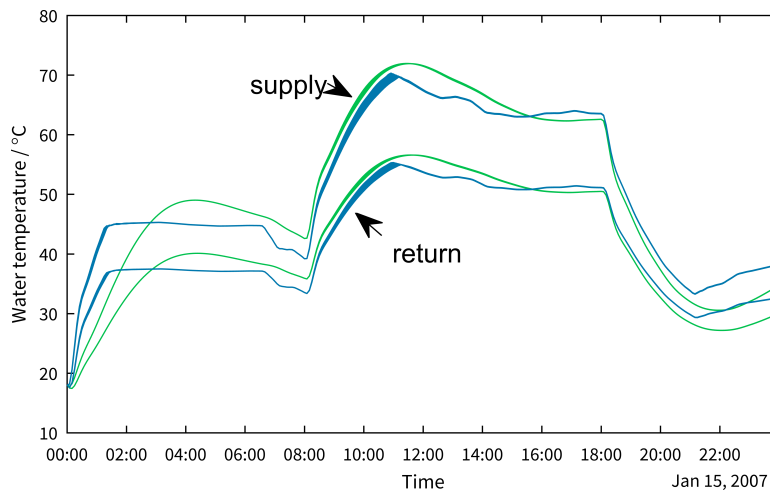


**Figure 8.33 | Comparison of dynamic response of hydronic system inlet and outlet temperatures.**

As in § 8.3, the PI control shows large fluctuations in control action on the manipulated fuel flow rate during the beginning of the simulation (see fig. 8.31), while the NI+PDF controller holds the fuel flow rate at maximum before safely decreasing the fuel input when the set-point is reached.

Figure 8.33 shows the supply and return temperatures from the TES tank to the radiators under both the PI control and NI+PDF controller. The PI controller does not demonstrate as much fluctuation in the hydronic system temperatures as it did without the TES tank, however, the temperatures are too high. The heightened temperatures cause a higher output from the radiators, which coupled with the internal heat gains is causing the high air temperature in the zone during the occupied period. The NI+PDF controller demonstrates more control over the hydronic system temperatures so that there is no overshoot of internal air temperature even in the presence of internal and solar heat gains.

Figure 8.34 shows snapshots of the time evolution of the temperatures inside the TES tank. Figure 8.34a shows that at the beginning of the simulation the TES tank is at a uniform temperature. After 1 h 20 min the air temperature has reached the first set-point (un-occupied setback temperature), and the tank is stratified at low temperatures (fig. 8.34b). After the change in set-point the air temperature has reached the second set-point, and the tank is fully stratified (fig. 8.34c). Figure 8.34d shows that at the end of the day the tank remain stratified but at lower temperatures.

Figure 8.35 shows all of the elements of the electrical network working together to achieve zero electrical grid interaction. This demonstrates the strength of the robust control strategy as it is able to balance both the thermal and electrical networks without any reliance upon the LEN.

It can be seen from fig. 8.36 that the balance of power extracted and supplied to the battery will leave it in a more discharged state at the end of the day compared to its initial state. However, in comparison with the case with no TES tank, the state-of-charge is higher at the end of the day, owed to the increased run time of the mCHP permitted by the addition of the TES tank.

## **8.5** Discussion & reflection

The objective of this research was the design and application of MIMO control algorithms to the problem of controlling microgeneration devices and energy storage within a building. Recall the objectives that the controller should be able to accommodate:

1. The controller can prioritise the use of renewable and low-carbon resources.

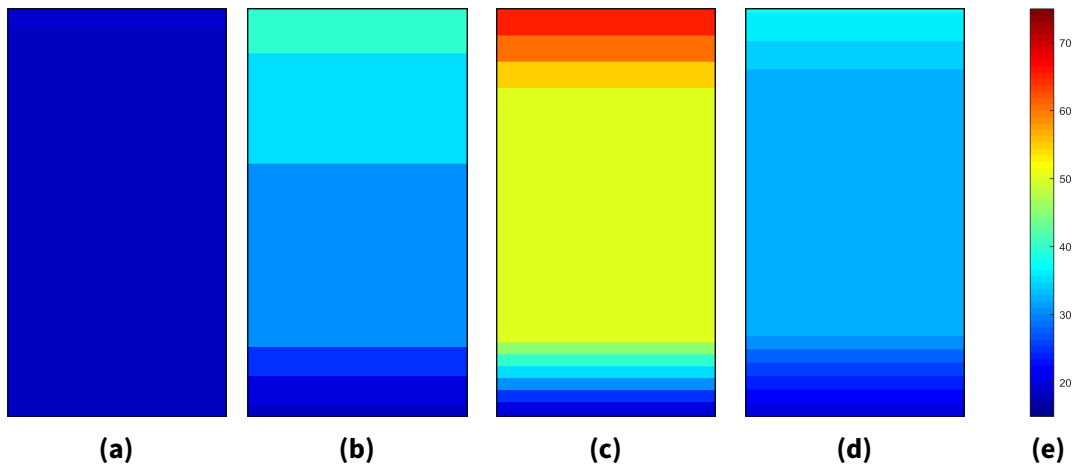


**Figure 8.34** | Time evolution of thermal storage tank temperatures: (a) 00:05 (b) 01:25 (c) 11:00 (d) 23:55 (e) Colour bar showing colour scale of temperatures.

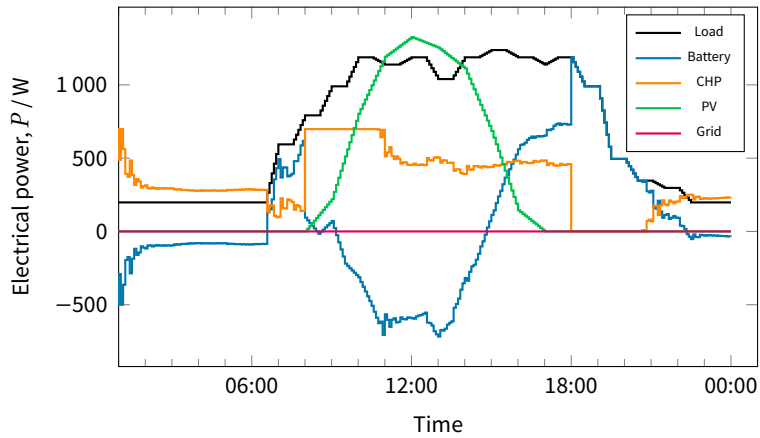


**Figure 8.35** | Comparison of all electrical power interactions over 24 h period for NI+PDF controller.

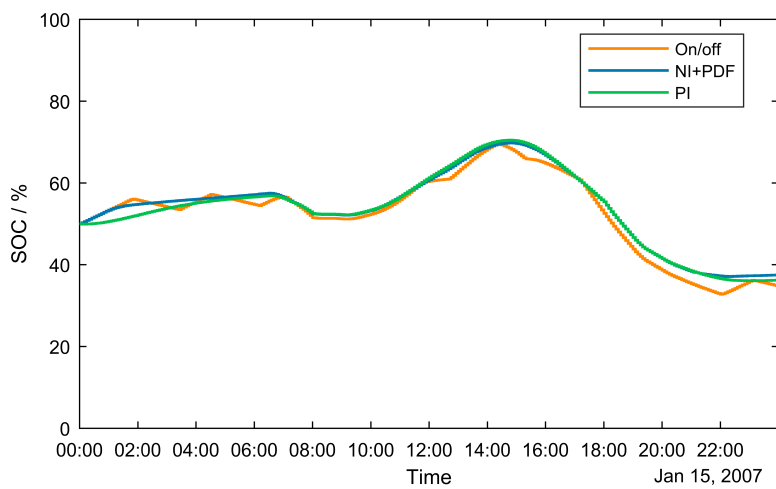


**Figure 8.36** | State-of-charge of battery over 24 h period.

2. To investigate a control structure that would allow for flexible/controllable integration with the local electrical network.
3. The controller can exploit the synergy of multiple energy systems to simultaneously fulfil the thermal and electrical demands of a building.
4. The controller can efficiently operate energy delivery networks with high inertia.
5. The controller is capable of handling multiple simultaneous input constraints.

Each of these objectives are addressed in turn with a critical reflection on the work of this thesis against each.

#### 8.5.1 *Utilisation of intermittent sources and energy storage*

Microgeneration is frequently coupled with energy storage and collectively known as ‘distributed resources’. The work of this chapter has demonstrated that the pairing of these technologies facilitates control of otherwise intermittent resources by storing generated energy and then dispatching it from the storage when called upon from energy demands of the building.

The mCHP specifically benefited from being deployed in tandem with EES. § 8.3 and 8.4 showed that solar PV power output can be stored in banks of batteries during the day, and then the stored energy in the batteries can be used to satisfy electrical demands at night. Another benefit of EES is that – provided it had sufficient charge – it was used to supply the power to the auxiliary components of the mCHP during the modes of operation where the mCHP is not generating its electrical energy (i.e. during start-up/cool-down/standby).

Energy storage was not only advantageous for the intermittent resources, but also allowed for flexible operation of the cogeneration device. Thermal energy storage offers greater flexibility for a building with a mCHP unit as demonstrated in § 8.4:

- It was able to reduce the on/off cycling of the mCHP unit compared to the case of § 8.3 by charging thermal store over time and then utilising the store instantaneously to fulfil the thermal demands as required;
- The mCHP was effectively decoupled from the heat network by passing its thermal output to the storage and operating based on the thermal *and* electrical requirements of the building based on the inverse dynamics of the system.

However, the case study only considered one configuration of mCHP combined with TES. Another useful configuration is where the TES can work in parallel with mCHP to fulfil the heating demands of the building. Such a configuration often allows for a



smaller mCHP unit to be deployed than without storage due to not needing to fulfil peak heating demands with the mCHP alone. Extending the application of the control to more system configurations is considered again in future work §§ 9.3.2.

While the focus of this work is on the performance of the controller itself, the overall efficiency of the system will be a function of the extent of storage available in the system. The case studies provided in this chapter were only for a system which had appropriately sized energy sources and storage. The ability of the controller to reconfigure the balance of plant for an undersized system has not been shown, but only considered conceptually in § 7.4 and from a mathematical perspective in §§ 7.5.6.

### 8.5.2 Flexible electrical grid interaction

The building's connection to the local electrical grid network is the prevalent 'solution' to the mismatch between the electrical power generation in the building and electrical demands of the building. As the local electrical network becomes more dependent on renewable resources, these resources will impact the stability of the grid as it becomes harder for utilities to regulate the supply. As discussed in §§ 1.2.2, while a grid connection may be available in the short term, it is evident that eventually control strategies will need to be devised to cope with the (temporary or not) absence of a local electrical network.

The case study without and with TES demonstrated that the control is capable of determining the real-time balance of plant to fulfil the thermal demand of the building, while neither importing or exporting from or to the LEN i.e., it *minimises* the interaction with the LEN. Its ability to do so was exhibited in all Monte Carlo experiments where the controller had to respond to uncertainties in the model parameters, and changes in climate.

Only the controller test case in §§ 8.2.4, however, showed the controller's ability to re-balance the plant in response to a demand signal from the LEN. The control system was able to pick up excess generation from the network by reducing the self-generation of the system and was able to increase its generation above what is required to fulfil the internal loads to export electrical power to the network. While this case does demonstrate *flexible* interaction – as opposed to the minimisation with the LEN – the system being controlled cannot be considered a 'real' control problem. The extended application of DSR to the case study problem is left as future work.

### 8.5.3 Technology combinations & hybrid systems

In a microgeneration-based future, it will be unlikely that the needs of a building can be met by a single energy resource alone, but requires the adoption and coordinated





operation of a multitude of energy sources. This work demonstrated the synergy between some of the MGTs that can work together to fulfil the thermal and electrical demands of the building; namely mCHP, solar PV, TES and EES. In the case studies in § 8.3 and 8.4 the mCHP can be used to fulfil the majority of the electrical loads of the building with solar PV meeting the deficit in generation for a portion of the occupied period. The EES is then used to fulfil the electrical demand when the heating system switches off in the evening but some electrical demand remains. As the systems were sized appropriately, the system demonstrated complete independence from the electrical network.

No matter the technological combination available at any one time, the controller was able to determine the ideal balance of plant to fulfil the demands of the building *in real time*. This demonstrated that the controller developed in this work was aware of how the technologies interacted with the thermal and electrical loads of the building, but also how they interact with each other.

However, the case study results were only presented for a single day in winter. A more exhaustive study over the whole year would be required to fully assess the controller's ability to balance the plant at all times. In such a study, it would be beneficial to couple the systems-level controller developed in this work with a supervisory controller that was capable of offering additional capabilities such as night cooling and optimum start. This is revisited in the future work section §§ 9.3.4. In addition, the future work §§ 9.3.2 provides further discussion on extending the controller to additional types of energy systems, controlled variables and system configurations.

#### 8.5.4 Efficient control of high inertia systems

The typically slow response of hydronic heating systems coupled with the high thermal inertia of a lot of buildings has traditionally resulted in overshoot of the temperature set-point at the beginning of occupied period. This is because a controlled system with inertia is slow to get moving, and the integral of the error in a PI controller builds up rapidly during the early stage of the response. In PID controllers this can be avoided by measuring the rate of approach to the set-point and reducing the control effort with derivative action. However, as discussed in §§ 2.3.3, the derivative-term in PID controllers can cause problems in practice as noisy measurement feedback can cause the controller to produce an erratic output.

This work makes use of the inverse of the dynamics of the system, which provides the controller with knowledge of the complex cause and effect relationships between the system and the controlled inputs. This knowledge coupled with the PDF control with the addition of a new anti-windup technique has resulted in a system that responds



with zero overshoot even though overdriven: there is no way for this controller to wind-up; it knows what the actuators are capable of and never asks them at any time to perform out with their capabilities.

The case study with thermal energy storage (see § 8.4) clearly demonstrates the efficient control of a system with high thermal inertia. In all Monte Carlo experiments, the air temperature of the building zone never overshoots the temperature set-point, while the two-position and PI controllers exhibit considerable overshoot. Furthermore, it also can be seen that there is no drawbacks to this implementation of the input constraints: the temperature rises at a faster rate than the competing controllers but is more efficient and effective. It puts into the controlled system exactly the amount of energy required to change the controlled variable the desired amount. In this regard, the NI+PDF controller can be considered a success at delivering efficient control of high inertia systems.

#### 8.5.5 Simultaneous control input constraints

It was identified in §§ 1.2.4 that improved handling of multiple input constraints is a requirement for the emerging ‘advanced’ control techniques: As multiple systems are used to fulfil the energy demand of a building, it is likely that several actuators will be active at one time, and many could be operating at full capacity simultaneously. An inherent limitation of inversion-based controllers is there is no straightforward way to imbue them with sufficient intelligence for handling of saturated actuators – as they assume the dynamics of the system are continuous.

The review of the RIDE controller methodology in § 2.6 looked at how these constraints had been handled in previous literature: To ensure that when a controller output has reached its limit, any future control action must either keep the input constant or reduce it so that it will continue its normal mode of operation. To enforce this behaviour, the traditional RIDE methodology proposes a switching technique known as conditional integration, where the error signal to the integrator is switched off under the specified conditions. This method has shown to be effective in eliminating integrator wind-up in previous applications of the RIDE methodology. However, it is global in its action. All integrators are switched off when *any one* of the control outputs saturates.

While this is the most pragmatic solution, it is possible to switch off only those integrators affected by a specific output saturating, which can improve controller performance. A new constraint handling logic was developed in this work so that integration is stopped only when a control variable saturates *and* when the current control action would push further into the saturation region.



The addition of this logic will cause the other integrators to not be inhibited when they would help push the control variable away from the saturation. This should speed up the response of the controller returning from saturation. However, while an algorithm was provided in §§ 7.3.3 on how the theory is implemented in the NI+PDF controller, the example provided in §§ 7.3.3 only demonstrated the constraint handling in terms of eliminating overshoot in high inertial systems as discussed in §§ 8.5.4.

There are multiple simultaneous constraints being handled in the case studies of § 8.2 to 8.4. However, for the time period shown, the charging/drawing limits of the battery are never engaged. Therefore, while the mathematics demonstrate that this new logic should improve handling of multiple inputs saturating simultaneously, the case studies fail to demonstrate the improvement in performance that can be gained by enacting the new ‘anti-lock’ wind-up technique. The future work §§ 9.3.1 provides further discussion on the implication of multiple inputs saturating at the same time.

## References

1. BS EN 15265:2007. *Energy performance of buildings. Calculation of energy needs for space heating and cooling using dynamic methods. General criteria and validation procedures*. 1st ed. London, UK: British Standards Institution, 2007. ISBN: 978-0-580-55627-2. DOI: [10.3403/30136887](https://doi.org/10.3403/30136887) (cited p. 211)
2. Menezes, A. C., Cripps, A., Buswell, R. A., Wright, J., Bouchlaghem, D. Estimating the energy consumption and power demand of small power equipment in office buildings. *Energy and Buildings* **75**: 199–209 (2014). DOI: [10.1016/j.enbuild.2014.02.011](https://doi.org/10.1016/j.enbuild.2014.02.011) (cited pp. 211, 212)
3. Bedford, M., Harris, R., King, A., Hawkeswood, A. *Occupier Density Study 2013*. Tech. rep. September. London, UK: British Council for Offices, 2013: 1–36 (cited p. 212)
4. National Renewable Energy Laboratory. *PVWatts*. 2012. URL: <http://rredc.nrel.gov/solar/calculators/PVWATTS/version1/> (cited p. 212)
5. Angrisani, G., Canelli, M., Roselli, C., Sasso, M. Calibration and validation of a thermal energy storage model: Influence on simulation results. *Applied Thermal Engineering* **67**(1-2): 190–200 (2014-06). DOI: [10.1016/j.applthermaleng.2014.03.012](https://doi.org/10.1016/j.applthermaleng.2014.03.012) (cited p. 212)
6. Fini, L., Busoni, L., Puglisi, A. *AC WhisperGen System - Product Specification 11 June 2013*. Tech. rep. 2003: 13 (cited p. 213)
7. Kuhn, V., Klemeš, J., Bulatov, I. MicroCHP: Overview of selected technologies, products and field test results. *Applied Thermal Engineering* **28**(16): 2039–48 (2008). DOI: <https://doi.org/10.1016/j.applthermaleng.2008.02.003> (cited p. 213)
8. Arndt, U. et al. *Experimental Investigation of Residential Cogeneration Devices and Calibration of Annex 42 Models*. Tech. rep. Annex 42 of the International Energy Agency Energy Conservation in Buildings and Community Systems Programme, 2007: 255 (cited pp. 213, 215)
9. Kudox. *Heat Output Datasheet*. 2017. URL: <https://www.kudox.com/wp-content/uploads/2017/08/2014-04-09-Kudox-Steel-Panel-Radiators-Technical-Data.pdf> (visited on 2017-08-06) (cited p. 214)



10. Tesla. *Tesla Powerwall 2 Datasheet*. 2016. URL: <https://www.energymatters.com.au/wp-content/uploads/2016/11/tesla-powerwall-2-datasheet.pdf> (cited p. 214)
11. Apkarian, P., Noll, D. Nonsmooth H-infinity Synthesis. *IEEE Transactions on Automatic Control* **51**(1): 71–86 (2006) (cited p. 217)
12. BS EN 15251:2007. *Indoor environmental input parameters for design and assessment of energy performance of buildings addressing indoor air quality, thermal environment, lighting and acoustics*. London, UK: British Standards Institution, 2007. ISBN: 978 0 580 55391 2. DOI: [10.3403/30133865](https://doi.org/10.3403/30133865) (cited pp. 222, 232)





*“The world is still a weird place,  
despite my efforts to make clear and  
perfect sense of it.”*

---

—HUNTER S. THOMPSON, *Songs of  
the Doomed*

9

## Perspectives, future work and conclusions

**T**HIS chapter begins with a summary of what has been accomplished in this thesis and highlights the key contributions of this body of work. After which the potential avenues for future work are discussed before giving a final perspective on the future of the control of microgeneration systems in buildings.

### **9.1** Summary

**CHAPTER 1** This chapter provided an overview of the motivations and drivers for the uptake of building-integrated microgeneration. Subsequently, it demonstrates a rationale for the improvement to the control of these systems. It also provides the research objectives, scope, assumptions, and limitations of the research.

**CHAPTER 2** This chapter explored the hierarchy of energy systems controls and highlighted the lack of research in systems-level control of microgeneration. It then investigated the existing control methods for coordinated control across the scale. It presents conventional control methods alongside the emergence of advanced systems-level controls, with  $H_\infty$  and inversion-based controllers highlighted for potential architectures for the control of building-integrated microgeneration.

**CHAPTERS 3 AND 4** These chapters described the development of dynamic continuous state-space models of the energy systems and the environment in which they operate. The energy systems models are based on already verified BES models of combustion-based mCHP units, stratified TES tanks, the water-based heat emitters, and the electrical battery storage. The building model used the concept of an electrical network analogy to generate a simplified, convenient, model of a building zone that provided validated space heating demands.



CHAPTER 5 This chapter applied the inversion-based control techniques of inverse dynamics and nonlinear inversion to the control microgeneration-based energy systems. It demonstrated controllability conditions for MIMO energy systems under inversion-based control that could prove useful in control structure design and feasibility studies. It illustrated the application of nonlinear inversion with asymptotic tracking to the control of energy systems of any relative degree. Finally, the limitations of inversion-based control techniques were discussed and highlighted the need for robust control techniques.

CHAPTER 6 This chapter explored how the inversion-based control techniques can be combined with robust control methods and applied to the control of hybrid building-integrated energy systems. It discusses the uncertainties in the control of energy systems and proposes a control strategy to compensate for modelling inaccuracies. It then establishes a method for the analytical determination of controller gains from desired system performance. It then offers a novel anti-windup scheme for nonlinear inversion coupled with pseudo-derivative feedback. Lastly, it details a controller design methodology for the application of NI+PDF to the control of control-input-affine nonlinear energy systems.

CHAPTER 7 Presents case studies for the application of the controller design methodology of chapter 5–6 to the models developed in chapters 3–4. In each case study, the controller design showed robust, stable control in the presence of modelling deficiencies/uncertainty and unknown disturbances. The physical limitations of the systems were also accounted for via variable structure control whereby the control strategy employed switches depending on the current utilisation and availability of the energy supplies. Results indicate that the control strategy is effective in minimising the electrical grid use while fulfilling the space heating demands of the building.

Across the case studies, as relative degree was increased, the influence of the uncertainty in the grey-box model of the mCHP decreased. However, the high inertia made the regulation of the thermal set-point more difficult for the non-inversion-based controllers. The NI+PDF controller developed in this work showed universally improved control in comparison with the traditional and modern control methods.

The case studies demonstrated that proper application of building-integration microgeneration can be regarded as a move *towards* energy autonomy in buildings, but is designed such that support and coordination from a LEN is also possible. §§ 8.2.4 showed that the control can respond to a signal from the local electricity network so that the building can offer DSR by changing its behaviour via control of the energy systems to consume excess power or that they need extra resource. The controller



achieves this by rebalancing the building-integrated energy systems to match as close as possible to the grid set-point without interfering with the indoor conditions of the building itself.

## 9.2 Contribution review

The main contributions of the research presented in this thesis are outlined as follows:

- Development of dynamic state-space models of combustion-based mCHP units, water-based stratified TES tanks, hydronic radiators, and the electrical energy storage suitable for the application of controller design that were drawn together from validated BES models.
- Development of a state-space model of a building with validated energy consumption predictions that is suitable for controller design and integration with the preceding energy systems models.
- Creation of a system/control structure design selection process for the design of interconnected energy systems with multiple inputs and outputs.
- Generalisation of the RIDE methodology to a so-called NI+PDF controller:
  - Range of applicable systems extended from LTI systems with relative degree less than one to control-affine nonlinear systems with relative degree of any order.
  - Analytical determination of controller gains from desired system performance.
- An improved ‘anti-lock’ anti-windup strategy for MIMO control systems that employ integral action to systems with actuator limits.
- Presentation of a complete controller design methodology for the application of NI+PDF to the control of control-input-affine nonlinear energy systems.
- Demonstration of multiple case studies for the application of all of the previous contributions to a complex multi-objective energy system control problem of maintaining the thermal demands of a building while minimising the use of electricity from the local electrical network.
  - Application of modern  $H_\infty$  control methods to the control of an mCHP unit.

The following is a list of relevant publications by the author that are related to this thesis. The list is sorted by original date of publication:



- Murphy, G. B., Counsell, J., Allison, J., Brindley, J. Calibrating a combined energy systems analysis and controller design method with empirical data. *Energy* 57: 484–94 (2013).
- Allison, J., Murphy, G. B. Control of micro-CHP and thermal energy storage for minimising electrical grid utilisation. *Microgen III: Proceedings of the 3rd International Conference on Microgeneration and Related Technologies*: 38–47 (2013). Naples, Italy, 15–17 April 2013
- Allison, J., Murphy, G. B., Counsell, J. M. Control of micro-CHP and thermal energy storage for minimising electrical grid utilisation. *International Journal of Low-Carbon Technologies* 11(1): 109–18 (2016). [First published online: 2014-08-21]
- Allison, J. Robust control of net-zero offices with integrated hybrid supply system and energy storage. *Microgen IV: Proceedings of the 4th International Conference on Microgeneration and Related Technologies*: 38–47 (2015). Tokyo, Japan, 28–30 October 2015
- Allison, J. Robust control of building-integrated energy systems with energy storage. *Applied Thermal Engineering* 114: 1498–1506 (2017).

Relevant literature that cite the work of this thesis:

- Subject of the section of book “Domestic microgeneration: renewable and distributed energy technologies, policies and economics” (1) on multi-objective control of microgeneration. The authors state that the work of this thesis “demonstrates that the [control] technique can be successfully applied” to the control of a hybrid microgeneration system.
- Hellmers et al. (2) investigate the economics of different operational strategies for a hybrid system of CHP and wind farms. Their work assumes that the thermal and electrical demands are fulfilled by a combination of the systems at each step of their optimisation. This work is cited as a suitable control algorithm “to ensure that these thermal and electrical references are followed at a relevant (finer) time-scale”.
- Kneiske et al. (3) propose a MPC algorithm for PV-CHP hybrid systems and cite this work as “only in [Allison (2017) are] the uncertainties and unpredictable manner of hybrid systems addressed by a robust control algorithm [...] it works for transient processes in the dynamic range”.





### 9.3 Future work

The controller design methodology put forward in this thesis represents a platform on which many different avenues of further work can be conducted. This section explores potential enhancements that can be made to the methodology, and also how it can be incorporated within many other appealing research areas in the control of hybrid energy supply systems to improve its performance and suitability for real-world application further.

#### 9.3.1 *Advancements on NI+PDF methodology*

Throughout the development of the NI+PDF methodology, some areas of potential improvement/advancement to the theory were identified as follows:

##### **Control of non-square systems**

A fundamental requirement of the controller design methodology is that there is an equal number of manipulable inputs to controlled outputs. However, this condition can be restrictive as multiple energy sources can affect a single controlled variable, e.g. a system where the zone air temperature is controlled by a combination of low-temperature underfloor heating and a higher-temperature direct convective or radiative heater. Similarly, the electrical demands of the building could be contributed to by a network of smaller batteries instead of a single battery.

§§ 2.5.1 considered the current approaches to ‘eliminate’ the excess inputs or outputs. However, a recent paper Zhou et al. (4) have shown that inversion-based controls can be modified to include internal model control (IMC) techniques that allow the controller to take advantage of extra manipulable inputs that results in both reduced control costs and increased control performance. While the improvements illustrated were in the application to industrial processes the theory could be modified to apply to the control of hybrid energy supply systems.

##### **Using estimates of disturbance signals**

The nonlinear inversion of the systems in the case studies assumes no knowledge of the disturbance inputs into the system. By using predictions of potential disturbance inputs as measurement signals, it is theorised that the control performance would be further improved. e.g. next-day predicted climate (generated by such models as Rastogi (5)) could be used for estimation of solar gains and solar PV availability. However, caution should be used to ensure that the predictions are trustworthy, as



poor predictions would cause the outer-loop PDF control to work harder to correct the actions of the equivalent control and ensure the desired performance is still met.

### Refinement of gain tuning procedure

From work in this thesis, the controller gains of the NI+PDF controller can be determined analytically, without any iteration or ‘tuning’ of the parameters, as a function of the desired performance. The procedure balanced the control effort required using a dominant pole placement method for the excess poles. However, a useful technique for tuning the gains of linear state-space systems without pre-determined pole locations is known as the LQR. This technique makes use of a performance index (such as (3.4)) to tune the gains of the system. Instead of specifying the performance of the controller regarding settling time and overshoot, the optimal gains of the system can be determined from maximum allowable control effort and values of  $n$ -th time derivatives of the output (6). While this would introduce iteration into the process of the determination of the controller gains, it could further increase the performance of the NI+PDF controller.

### Anti-windup technique

The anti-windup technique developed in this work switches off the integrators in the PDF control when they are affected by a specific output saturating, which improves controller performance. However, this requires a small enough evaluation frequency to avoid the controller switching the integrator off and on that it causes a ‘limit cycle’ to appear in the output of the controller. However, as stated in (7), for the cases of real applications using integrator switching, the switching cannot occur infinitely fast, and imperfect switching occurs. For high-frequency control calculation, the frequency of this limit cycle is much higher than the bandwidth of the actuator dynamics and causes no harm. However, in BEMS, the frequency of the control calculation is sometimes orders of magnitude lower than the bandwidth of the actuator dynamics. The low frequency can, at best, cause a delayed reaction when the system is recovering from being over-driven, and at worst can excite a higher frequency dynamic mode of an actuator – this is especially true for mechanical actuators without embedded low-level controls to filter the oscillating demand signal. For this reason, it would be beneficial to modify the proposed anti wind-up technique to eliminate the limit cycle and slow response to saturation recovery even at low sampling frequencies.

The author believes that two approaches could further improve the anti-windup method:

1. The anti-windup circuit can be modified to use ‘back calculation’ in addition



to the conditional integration (as demonstrated by Visioli (8) for a SISO PID controller). Back-calculation feeds-back the difference between the actual input and the calculated input through a gain and is added to the error signal. Back-calculation leaves the control signal untouched when the controller is not at a limit but will recompute the integral term as a function of the ‘control error’ when saturated. The primary issue with this method is that it introduces an extra gain that can not only be difficult to compute, but the ‘ideal’ value of the gain can change depending on what caused the actuator to saturate in the first place (8, p. 51).<sup>1</sup> Were this approached to be successfully implemented, it should allow for the evaluation of the controller at larger time-steps as the integral term is not switch instantaneously, potentially allowing for the integration into building simulation tools.

2. As discussed in §§ 7.3.2 an exciting solution to the problem is to use MPC to look ahead over a future (short) time-horizon to determine if the actuators may saturate, and then make corrections to the controller input to stop it from saturating. Such a technique would be especially useful when the dynamics of the actuators exhibit complex nonlinear behaviours, such as backlash, coulomb & viscous friction, dynamic rate limits, or quantisation. Provided that the MPC has an appropriately detailed model of such discontinuities, it would allow the controller to compensate for them. In the presence of such nonlinear behaviour, the conditional integration alone may not provide optimal response. However, as noted previously, this method requires an accurate model of the disturbances to be effective (9, p. 11).

### Mu-synthesis

The NI+PDF controller is designed to meet the performance objectives using the *nominal* values of the system parameters. Robust performance is then demonstrated using Monte Carlo simulations in the face of model errors and uncertainty. However, it is not guaranteed that the ‘best’ performance is achieved, only that it satisfied the design criteria.  $\mu$ -synthesis is a procedure from  $H_\infty$  literature where a family of controllers are developed for all uncertainty bounds. Then, using a performance index (such as (3.4)), the best performing controller is selected and used as the controller in practice, as this may not correspond with the controller designed using the nominal parameter values.

---

<sup>1</sup>e.g. a change in set-point or a large disturbance.



### 9.3.2 Extended application

#### Additional energy systems

While the control algorithms and methodology developed in this work are mostly agnostic to the technology used, the technologies covered in this thesis were restricted to combustion-based cogeneration devices, solar PV, TES, and EES. Future work should look to extend the application of the control to heat pumps, which are readily applicable for building integration and linking with the other technologies considered.

Heat pumps use electricity to move heat from an outside source (air/ground) to inside the building and affect the thermal and electrical networks. It is conceivable that heat pumps can be used alongside solar PV and electric batteries to move buildings towards being self-sufficient in heat and power. The amount of power required to run a heat pump entirely from solar PV and electrical batteries may be prohibitive regarding cost and availability of the renewable resource (10) but it is nevertheless an interesting avenue of further study.

In addition, this work did not consider active cooling systems. While it was shown that the mCHP could fulfil the thermal *heat* loads during a typical winter period, there will be many climates where a controllable cooling system will be required in the summer months. Extending the control to building cooling systems such as HVAC systems or simple controllable mechanical ventilation would be beneficial for an all-year hybrid energy supply system applicable to any climate.

#### Controlled variables

The case studies considered only the space heating thermal load of the building. However, as buildings continue to become more energy efficient, the dominant thermal load of the building will be the hot water demand. Extending the controlled system to consider the hot water demand will be important in the near future. In addition to the thermal and electrical demands, the type of control developed in this work could also be applied to HVAC systems where not only is the temperature of the building controlled but the relative humidity and CO<sub>2</sub> concentration as well.

#### System configurations

The case study in § 8.4 considered only one configuration of attaching an mCHP unit to a TES tank. There are many more potential combinations that could further enhance the performance of the overall system. For example, a secondary hydronic loop could be introduced such that the TES tank and mCHP can work in parallel to supply the loads of the building.





The control can also be applied to the control of individual emitters within a single building zone working to different temperature measurements across a single space. By utilising a pervasive sensor network across a large open place office space, it is conceivable that the controller would be able to control the flow of heat from multiple emitters in a single zone to ensure an even temperature distribution across the heated space – avoiding localised temperature gradients often found in large open plan spaces.

### 9.3.3 Adaptive control from system identification

The inversion-based control in this work is based on the nominal model and operating conditions of the system. However, as discussed previously not only are these parameters subject to uncertainty, but they can also change over time (e.g. changes in unit efficiency due to wear/age). While the outer loop PDF controller is designed to compensate for these differences, significant control effort could be required if the inverse dynamics on which the controller is based change significantly from the original design.

By combining the control methodology with an adaptive MPC type design, the inversion could be continually updated from an identified system model in real-time, from which the control could not only continually improve, but could also adapt to changes in system use and changes in operational performance. For example, Li, Wen (11) have developed a state-space model of a commercial building using system identification techniques that update in real-time based on measurements of local climate and lighting/equipment power use. Such a model could be used with the NI+PDF controller to provide robust *and* adaptive control of the building.

### 9.3.4 Combining with supervisory control

To further extend the variable-structure control discussed in § 7.4 the integration of the NI+PDF controller with a ‘supervisory’ control would be beneficial. Currently, the NI+PDF controller will balance the available energy systems to fulfil the thermal and electrical demands with the systems available to it *at that point in time*. The controller switches operational mode depending on the status of the energy storage resources and depending on the current mode of the mCHP (standby, warm-up, normal, and cool-down). However, with the knowledge or prediction of future demands the optimal operation of the systems over a diurnal, daily, or even weekly period may be different from the current ‘operational mode’.

For example, in the case study in § 8.3, by using forecasts of climate and the associated estimates of renewable generation from the solar PV a more economic control solution could be formulated. The most economical solution may have been



to charge the electrical battery from the grid overnight at a lower cost tariff if the predicted amount of available energy from solar PV and mCHP operation would not cover the predicted demand for the following day. Examples of such types of supervisory control (or often called ‘optimisation algorithms’) were discussed in § 2.2.

Therefore, by using the NI+PDF controller as the regulatory controller of a given configuration of a hybrid energy supply system and a supervisory controller with artificial intelligence, the switching between the operational modes could improve the utilisation of the on-site renewable generation and further minimise the import of energy from the LEN. This supervisory control could take many forms, such as fuzzy logic (12), artificial neural networks (13), neuro-fuzzy control (14), or MPC (15), which have all been applied to different types of hybrid energy supply systems. Any of these would make for a compelling avenue of future work.

#### 9.3.5 *Integration with BPS tools*

The models created from detailed BPS tools such as ESP-r, TRNSYS, and EnergyPlus are often very large, complex and detailed; more detailed than is required to compute the inversion-based control techniques used in this work efficiently. Furthermore, the controller design is computed from a system of continuous ODEs with all ‘networks’ (air flow, building, energy systems (i.e. plant), and electrical) being concatenated into a single model of the overall system. These tools often separate the networks into discrete systems where the solution of each is calculated in turn. The discrete networks would make the design of a single regulatory control difficult as the systems could be (and often are) running at different time-steps.

However, by using the system identification methods discussed in §§ 9.3.3, the controller would only have to be connected to the networks that it is controlling, and the model on which the control is based could be generated from input and output data from the BPS tool. Control based on this system identification would allow the control to be assessed and refined in a detailed environment that adheres closely to actual physical systems before being implemented in practice. Additionally, this would facilitate the use of the controller as part of component sizing and feasibility studies in the conceptual building design stage.

#### 9.3.6 *Field trials*

The general principals of Control System Design (6, ch. 10, 16, § 1.5) outlines that the steps of controller design are to establish the required goals of the controller, define models of the systems to be controlled and then to assess the control system design via simulation and analysis. These steps have been undertaken in the work



of this thesis. However, the final step is to then assess the real-world performance of the controller by embedding the controller in hardware/software and testing the performance on a prototype of the system to be controlled, i.e. practical application in an industrial/experimental environment.

Although it would have been preferable to conduct the case studies of chapter 8 on real systems, this was not done due to lack of available resources. In this work instead of a physical prototype, simulation has been used to gauge the performance of the design. While this may diminish the conclusions on the practical realisation of the control, significant effort has been made throughout this work to ensure that the models of the systems cover the dynamic behaviour of the systems. Furthermore, all fundamental limitations of the systems such as actuator limits, operational modes, low-level controls and nonlinear dynamics are accounted for in the simulation models.

Nonetheless, the best avenue for future work is a practical assessment of the controller performance on a prototype system to verify and potentially further improve the controller design methodology of this work.

#### **9.4** Perspective

With the application of the controller design methodology developed in this work microgeneration technologies could now be better positioned to address both the building energy efficiency requirements and an increase of integration of renewables into buildings. By exploiting the synergy between some of the available MGTs it has been demonstrated that they can work together to fulfil the thermal and electrical demands of a building. It has been shown that they can be controlled to not only be less reliant on the LEN but are also able to work in tandem with the LEN in the form of DSR. All of these factors together contribute towards securing a more sustainable, energy secure future.

It is understood that the buildings industry can be slow to accept new or more ‘advanced’ control strategies due to their supposed complexity, or the potential increase in cost and commissioning time. Furthermore, many individual technologies may not allow for their operation to be changed from the manufacturer’s pre-programmed controls for fear of misuse or the uncertainty over the change in performance that could be demonstrated versus what was determined under test conditions. It is hoped that future work on practical implementation and field trials of more advanced control techniques will alleviate these concerns and will see an uptake in the adoption of new methods of control in industry.

However, it is also the responsibility of those designing the controllers that they are relatively simple to implement and the associated costs of implementation remain



competitive with conventional control systems. In that respect, the NI+PDF controller methodology does not require any extra computational expense over that of a traditional PID controller. The NI+PDF controller, however, does rely on the development of a model of the system to utilise the inverse dynamics of the system. Future work on the application of the controller design methodology to models obtained via system identification or from BPS tools will go a long way to mitigate the necessity of developing models from first principles.

This work will conclude with the same quote with which it began:

“ The biggest gap today is between what science allows us to do, and what really happens in the political and economical world that we inhabit. We don't need new inventions to improve the world, we just need proper applications of those we already have. ”

Martin Rees - *A Cosmic Perspective for the 21st Century*

It is hoped that the work in this thesis is a small step towards the proper application and control of building integrated energy systems.

## References

1. Staffell, I., Brett, D. J. L., Brandon, N. P., Hawkes, A. D. *Domestic Microgeneration: Renewable and Distributed Energy Technologies, Policies and Economics*. Abingdon, Oxon, UK: Routledge, 2015. ISBN: 978-1-315-69710-9 (cited p. 243)
2. Hellmers, A., Zugno, M., Skajaa, A., Morales, J. M. Operational Strategies for a Portfolio of Wind Farms and CHP Plants in a Two-Price Balancing Market. *IEEE Transactions on Power Systems* **31**(3): 2182–91 (2016-05). DOI: [10.1109/TPWRS.2015.2439060](https://doi.org/10.1109/TPWRS.2015.2439060) (cited p. 243)
3. Kneiske, T. M., Braun, M., Hidalgo-Rodriguez, D. I. A new combined control algorithm for PV-CHP hybrid systems. *Applied Energy* (2017). DOI: [10.1016/j.apenergy.2017.06.047](https://doi.org/10.1016/j.apenergy.2017.06.047) (cited p. 243)
4. Zhou, Z., Lin, S., Zhang, G., Zhang, W. Block inverted decoupling control with internal model structure for non-square multivariable time delay systems. *IFAC-PapersOnLine* **50**(1): 3617–22 (2017). DOI: <https://doi.org/10.1016/j.ifacol.2017.08.704> (cited p. 244)
5. Rastogi, P. On the sensitivity of buildings to climate: the interaction of weather and building envelopes in determining future building energy consumption. PhD. Lausanne, Switzerland: Ecole polytechnique fédérale de Lausanne, 2016-08. URL: <https://infoscience.epfl.ch/record/220971?ln=en> (cited p. 244)
6. Franklin, G. F., Powell, J. D., Emami-Naeini, A. *Feedback Control of Dynamic Systems*. 6th ed. Upper Saddle River, New Jersey: Pearson Education, Inc., 2010: 837. ISBN: 978-0-13-500150-9 (cited pp. 245, 249)





7. Bradshaw, A., Counsell, J. M. Design of autopilots for high performance missiles. *Proceedings of the Institution of Mechanical Engineers, Part I: Journal of Systems and Control Engineering* **206**(2): 75–84 (1992-05) (cited p. 245)
8. Visioli, A. Modified anti-windup scheme for PID controllers. *IEE Proceedings - Control Theory and Applications* **150**: 49 (2003).  
DOI: [10.1049/ip-cta:20020769](https://doi.org/10.1049/ip-cta:20020769) (cited p. 246)
9. Kurtz, M. J., Henson, M. A. Input-output linearizing control of constrained nonlinear processes. *Journal of Process Control* **7**(1): 3–17 (1997-02).  
DOI: [10.1016/S0959-1524\(96\)00006-6](https://doi.org/10.1016/S0959-1524(96)00006-6) (cited p. 246)
10. Barker-Brown, J. *Three things to consider before running a heat pumps with solar or wind power*. 2011. URL: <http://www.yougen.co.uk/blog-entry/1675/Three+things+to+consider+before+running+a+heat+pumps+with+solar+or+wind+power/> (visited on 2017-12-01) (cited p. 247)
11. Li, X., Wen, J. System identification and data fusion for on-line adaptive energy forecasting in virtual and real commercial buildings. *Energy and Buildings* **129**: 227–37 (2016).  
DOI: [10.1016/j.enbuild.2016.08.014](https://doi.org/10.1016/j.enbuild.2016.08.014) (cited p. 248)
12. Roumila, Z., Rekioua, D., Rekioua, T. Energy management based fuzzy logic controller of hybrid system wind/photovoltaic/diesel with storage battery. *International Journal of Hydrogen Energy* **42**(30): 19525–35 (2017).  
DOI: [10.1016/j.ijhydene.2017.06.006](https://doi.org/10.1016/j.ijhydene.2017.06.006) (cited p. 249)
13. Entchev, E., Yang, L., Ghorab, M., Rosato, A., Sibilio, S. Energy, economic and environmental performance simulation of a hybrid renewable microgeneration system with neural network predictive control. *Alexandria Engineering Journal* (2016).  
DOI: [10.1016/j.aej.2016.09.001](https://doi.org/10.1016/j.aej.2016.09.001) (cited p. 249)
14. Yang, L., Entchev, E. Performance prediction of a hybrid microgeneration system using Adaptive Neuro-Fuzzy Inference System (ANFIS) technique. *Applied Energy* **134**(Supplement C): 197–203 (2014).  
DOI: [10.1016/j.apenergy.2014.08.022](https://doi.org/10.1016/j.apenergy.2014.08.022) (cited p. 249)
15. Tuohy, P. et al. Orchestration of Renewable Generation in Low Energy Buildings and Districts Using Energy Storage and Load Shaping. *Energy Procedia* **78**(Supplement C): 2172–7 (2015).  
DOI: [10.1016/j.egypro.2015.11.311](https://doi.org/10.1016/j.egypro.2015.11.311) (cited p. 249)
16. Dorf, R. C., Bishop, R. H. *Modern Control Systems*. 12th ed. Upper Saddle River, New Jersey: Prentice Hall, 2011: 1104. ISBN: 978-0-13-602458-3 (cited p. 249)



*“I will not deny, but possibly it might be reduced to a narrower Compass than it is; and that some Parts of it might be contracted: The way it has been writ in, by Catches, and many long Intervals of Interruption, being apt to cause some Repetitions. But to confess the Truth, I am now too lazy, or too busy to make it shorter.”*

—JOHN LOCKE, *An Essay Concerning Human Understanding*

A

## Modelling addendum

This appendix is comprised of all of the mathematical modelling material that would have proved unnecessarily lengthy for the main text, and would otherwise distract from the purpose of the work. This appendix is comprised primarily of mathematical derivation of some aspects of the modelling of the energy systems that would otherwise distract from the flow of the main chapter content. Nevertheless, much of the derivations here are not found in other texts and are necessary for the overall understanding of the dynamical modelling of the energy systems and the environment in which they operate.

### A.1 Thermal energy storage tank: Bulk flow rates

For the remainder of this section the time-dependence of the mass flow is implied so that  $\dot{m} := \dot{m}(t)$ .

To determine the direction of the flow within a TES tank, it is necessary to first compute the **bulk flow** in and out of each node. A mass balance is taken for each node, where the sign convention is that if flow is leaving the node the bulk flow is negative, and positive if the flow is entering the node. This can be computed as

$$\dot{m}_{T,i} = \begin{cases} 0 & \text{for } i = 1 \\ -\dot{m}_{B,i-1} & \text{for } i \in [2, n] \end{cases}, \quad (\text{A.1a})$$

$$\dot{m}_{B,i} = \begin{cases} \dot{m}_{TES,01,i} + \dot{m}_{TES,02,i} - \dot{m}_{TES,i1,i} - \dot{m}_{TES,i2,i} - \dot{m}_{T,i} & \text{for } i \in [1, n-1] \\ 0 & \text{for } i = n \end{cases}. \quad (\text{A.1b})$$

Examining eqs. (A.1) it can be seen that calculating  $\dot{m}_{B,i}$  is recursive, that is, explicit determination of bulk flow at the bottom of each node requires knowledge of the bulk



flow through the bottom of the previous nodes. These expressions can be de-recursive by continuously evaluating eqs. (A.1) from node 1 to node  $n$ :

$$\dot{m}_{T,i} = \sum_j^{i-1} \dot{m}_{\text{TES},i1,j} + \sum_j^{i-1} \dot{m}_{\text{TES},i2,j} - \sum_j^{i-1} \dot{m}_{\text{TES},o1,j} - \sum_j^{i-1} \dot{m}_{\text{TES},o2,j}, \quad (\text{A.2})$$

$$\dot{m}_{B,i} = - \sum_j^i \dot{m}_{\text{TES},i1,j} - \sum_j^i \dot{m}_{\text{TES},i2,j} + \sum_j^i \dot{m}_{\text{TES},o1,j} + \sum_j^i \dot{m}_{\text{TES},o2,j}. \quad (\text{A.3})$$

where  $\dot{m}_{T,1} = \dot{m}_{B,n} = 0$ .

In order to express these equations in vector-matrix form, the bulk flows to each node can be placed in the following vectors:

$$\dot{\mathbf{m}}_T = \begin{bmatrix} \dot{m}_{T,1} & \dot{m}_{T,2} & \dots & \dot{m}_{T,n} \end{bmatrix}^T \quad (\text{A.4})$$

$$\dot{\mathbf{m}}_B = \begin{bmatrix} \dot{m}_{B,1} & \dot{m}_{B,2} & \dots & \dot{m}_{B,n} \end{bmatrix}^T. \quad (\text{A.5})$$

Now consider the vector  $\dot{\mathbf{m}}_{\text{TES},i1} \in \mathbb{R}_{\geq 0}^{n \times 1}$  that comprises the inlet 1 mass flow rate to each node:

$$\dot{\mathbf{m}}_{\text{TES},i1} = \begin{bmatrix} \dot{m}_{\text{TES},i1,1} & \dot{m}_{\text{TES},i1,2} & \dots & \dot{m}_{\text{TES},i1,n} \end{bmatrix}^T,$$

with similar vectors constructed for  $\dot{\mathbf{m}}_{\text{TES},o1}$ ,  $\dot{\mathbf{m}}_{\text{TES},i2}$  and  $\dot{\mathbf{m}}_{\text{TES},o2}$ . The summations of these flow rates for each  $i$ th node for the bulk flow into the top of the node can be determined using a strictly lower triangular matrix  $L_T$ :

$$L_T = \begin{bmatrix} 0 & 0 & \dots & 0 \\ 1 & 0 & \dots & 0 \\ \vdots & \vdots & \ddots & 0 \\ 1 & 1 & \dots & 0 \end{bmatrix}$$

i.e.

$$L_T = (l_{ij}), \quad \text{where } l_{ij} = \begin{cases} 0 & \text{if } i \leq j \\ 1 & \text{if } i > j \end{cases}.$$

Now the bulk flow vector (4.33a) for the top of all the nodes is now given by

$$\dot{\mathbf{m}}_T = L_T \dot{\mathbf{m}}_{\text{TES},i1} + L_T \dot{\mathbf{m}}_{\text{TES},i2} - L_T \dot{\mathbf{m}}_{\text{TES},o1} - L_T \dot{\mathbf{m}}_{\text{TES},o2}. \quad (\text{A.6})$$

Similarly for the bulk flow at the bottom of the nodes, the summation can be



replicated with the following matrix

$$\mathbf{L}_B = \begin{bmatrix} 1 & 0 & \dots & 0 \\ 1 & 1 & \dots & 0 \\ \vdots & \vdots & \ddots & \vdots \\ 0 & 0 & \dots & 0 \end{bmatrix}$$

i.e.

$$\mathbf{L}_B = (l_{ij}), \quad \text{where } l_{ij} = \begin{cases} 0 & \text{if } i < j \vee i = n \\ 1 & \text{if } i \geq j \wedge i \neq n \end{cases}.$$

The bulk flow vector (4.33b) for the bottom of all the nodes is now given by

$$\dot{\mathbf{m}}_B = -\mathbf{L}_B \dot{\mathbf{m}}_{\text{TES},i1} - \mathbf{L}_B \dot{\mathbf{m}}_{\text{TES},i1,2} + \mathbf{L}_B \dot{\mathbf{m}}_{\text{TES},o1} + \mathbf{L}_B \dot{\mathbf{m}}_{\text{TES},o2}. \quad (\text{A.7})$$

As an example, consider again the distribution of the mass flow from inlet pipe 1 to the nodes in the tank given by

$$\dot{\mathbf{m}}_{\text{TES},i1} = \left[ \dot{m}_{\text{TES},i1,1} \quad \dot{m}_{\text{TES},i1,2} \quad \dots \quad \dot{m}_{\text{TES},i1,n} \right]^T.$$

The actual magnitude of the flow will be given by  $\dot{m}_{\text{TES},i1}(t)$ . The distribution of  $\dot{m}_{\text{TES},i1}$  among the nodes will be determined by the geometry of tank. The distribution can be defined using a vector  $\boldsymbol{\gamma}_{i1} \in \mathbb{R}_{\geq 0}^n$  where

$$\dot{\mathbf{m}}_{\text{TES},i1} = \boldsymbol{\gamma}_{i1} \dot{m}_{\text{TES},i1}(t)$$

The simplest option is to have all of the flow enter the control volume that has a centroid closest to the centre of the pipe. For example, if inlet pipe 1 was connected to the 4th node in a 10 node TES model,

$$\boldsymbol{\gamma}_{i1} = \left[ 0 \quad 0 \quad 0 \quad 1 \quad 0 \quad 0 \quad 0 \quad 0 \quad 0 \quad 0 \right]^T.$$

A more complex example would be an inlet pipe with a wide diameter such that the flow entered the topmost nodes of the tank. In this case

$$\boldsymbol{\gamma}_{i1} = \left[ \frac{1}{3} \quad \frac{1}{3} \quad \frac{1}{3} \quad 0 \quad 0 \quad 0 \quad 0 \quad 0 \quad 0 \quad 0 \right]^T.$$

Substituting the flow distribution factors ( $\boldsymbol{\gamma}_{i1}, \boldsymbol{\gamma}_{i2}, \boldsymbol{\gamma}_{o1}, \boldsymbol{\gamma}_{o2}$ ) for each pipe into eqs. (A.6)





and (A.7) gives

$$\begin{aligned}\dot{\mathbf{m}}_{\text{T}} &= L_{\text{T}}(\boldsymbol{\gamma}_{i1}\dot{m}_{\text{TES},i1}(t) + \boldsymbol{\gamma}_{i2}\dot{m}_{\text{TES},i2}(t) - \boldsymbol{\gamma}_{o1}\dot{m}_{\text{TES},o1}(t) - \boldsymbol{\gamma}_{o2}\dot{m}_{\text{TES},o2}(t)) \\ \dot{\mathbf{m}}_{\text{B}} &= L_{\text{B}}(-\boldsymbol{\gamma}_{i1}\dot{m}_{\text{TES},i1}(t) - \boldsymbol{\gamma}_{i2}\dot{m}_{\text{TES},i2}(t) + \boldsymbol{\gamma}_{o1}\dot{m}_{\text{TES},o1}(t) + \boldsymbol{\gamma}_{o2}\dot{m}_{\text{TES},o2}(t))\end{aligned}$$

Grouping the mass flow inputs into an ‘mass flow input’ vector

$$\dot{\mathbf{m}}_{i/o}(t) = [\dot{m}_{\text{TES},i1}(t), \dot{m}_{\text{TES},i2}(t), \dot{m}_{\text{TES},o1}(t), \dot{m}_{\text{TES},o2}(t)]^{\mathcal{T}},$$

the bulk mass flow rates are given by

$$\dot{\mathbf{m}}_{\text{T}}(t) = P_{\text{T}}\dot{\mathbf{m}}_{i/o}(t), \quad (\text{A.8})$$

$$\dot{\mathbf{m}}_{\text{B}}(t) = P_{\text{B}}\dot{\mathbf{m}}_{i/o}(t), \quad (\text{A.9})$$

where

$$\begin{aligned}P_{\text{T}} &= L_{\text{T}} \begin{bmatrix} \boldsymbol{\gamma}_{i1} & \boldsymbol{\gamma}_{i2} & -\boldsymbol{\gamma}_{o1} & -\boldsymbol{\gamma}_{o2} \end{bmatrix}, \\ P_{\text{B}} &= L_{\text{B}} \begin{bmatrix} -\boldsymbol{\gamma}_{i1} & -\boldsymbol{\gamma}_{i2} & \boldsymbol{\gamma}_{o1} & \boldsymbol{\gamma}_{o2} \end{bmatrix}.\end{aligned}$$

The matrices  $P_{\text{T}}, P_{\text{B}}$  contain the permutations of the mass flow rates in order to determine the bulk flow through the top and bottom of each node.

## **A.2** Building component state-space models

### **A.2.1** Complete network

The equations governing the dynamics of the electrical network analogy of a general  $n$ -layer building component (as given in fig. 5.1) can be divided into separate entities depending on the location of the capacitor (whose voltage is taken as the state-variable):

1. The capacitor in the outermost layer i.e. facing the external environment
2. The capacitors of the inner layers
3. The capacitor of the innermost layer.

Additionally, depending on whether the inner air node is considered as a capacitor (where the zone air can gain/lose energy through the fabric of the component), as a voltage source (where the air is held at a constant or a known time-varying profile), or as a current source (to model the heat flow rate from internal/solar heat gains on the inner surface of the component) will affect the system of equations.

The state equation for the material layer facing the exterior environment is

$$C_1\dot{\Theta}_1(t) = -\left(\frac{1}{R_{\text{se}} + \frac{R_1}{2}} + \frac{2}{R_1 + R_2}\right)\Theta_1(t) + \left(\frac{2}{R_1 + R_2}\right)\Theta_2(t) + \left(\frac{1}{R_{\text{se}} + \frac{R_1}{2}}\right)\Theta_{\text{env}}(t). \quad (\text{A.10})$$



Similarly the state equation for a material layer  $i$  within a component is

$$C_i \dot{\Theta}_i(t) = - \left( \frac{2}{R_{i-1} + R_i} + \frac{2}{R_i + R_{i+1}} \right) \Theta_i(t) + \left( \frac{2}{R_{i-1} + R_i} \right) \Theta_{i-1}(t) + \left( \frac{2}{R_i + R_{i+1}} \right) \Theta_{i+1}(t). \quad (\text{A.11})$$

The state equation for the material layer facing the interior environment is

$$C_n \dot{\Theta}_n(t) = - \left( \frac{1}{\frac{R_n}{2} + R_{si}} + \frac{2}{R_{n-1} + R_n} \right) \Theta_n(t) + \left( \frac{2}{R_{n-1} + R_n} \right) \Theta_{n-1}(t) + \left( \frac{1}{\frac{R_n}{2} + R_{si}} \right) \Theta_a(t) \quad (\text{A.12})$$

where  $\Theta_a$  is an input when it is a voltage source, or a state-variable when it is the voltage across the capacitor. Furthermore, for the case where  $\Theta_a$  is a state-variable, its state equation is given by

$$C_a \dot{\Theta}_a(t) = - \left( \frac{1}{\frac{R_n}{2} + R_{si}} \right) \Theta_a(t) + \left( \frac{1}{\frac{R_n}{2} + R_{si}} \right) \Theta_n(t) \quad (\text{A.13})$$

This system of equations is used in the analysis of the methods of modelling the thermodynamics of the ‘complete’ building components.

#### A.2.2 ROM network

Similarly for the ROMs (see fig. 5.2), the equations governing the dynamics of the electrical network analogy are given by

$$C_{\text{ROM},1} \dot{\Theta}_{\text{ROM},1}(t) = - \left( \frac{1}{R_{se} + R_{\text{ROM},1}} + \frac{1}{R_{\text{ROM},2}} \right) \Theta_{\text{ROM},1}(t) + \left( \frac{1}{R_{\text{ROM},2}} \right) \Theta_{\text{ROM},2}(t) + \left( \frac{1}{R_{se} + R_{\text{ROM},1}} \right) \Theta_{\text{env}}(t) \quad (\text{A.14})$$

$$C_{\text{ROM},2} \dot{\Theta}_{\text{ROM},2}(t) = - \left( \frac{1}{R_{\text{ROM},2}} + \frac{1}{R_{\text{ROM},3} + R_{si}} \right) \Theta_{\text{ROM},2}(t) + \left( \frac{1}{R_{\text{ROM},2}} \right) \Theta_{\text{ROM},1}(t) + \left( \frac{1}{R_{\text{ROM},3} + R_{si}} \right) \Theta_a(t) \quad (\text{A.15})$$

Again, when  $\Theta_a$  is taken as a state-variable an extra state equation is introduced, given by

$$C_a \dot{\Theta}_a(t) = - \left( \frac{1}{R_{\text{ROM},3} + R_{si}} \right) \Theta_a(t) + \left( \frac{1}{R_{\text{ROM},3} + R_{si}} \right) \Theta_{\text{ROM},2}(t) \quad (\text{A.16})$$

This system of equations is used in the analysis of the methods of modelling the thermodynamics of the reduced-order approximation of the building components.



### A.2.3 Equilibrium initial conditions

The calculation the equilibrium initial conditions for a LTI state-space system can be performed without resorting to a sequential quadratic programming algorithm as long as the inputs to the system at  $t = 0$  are known. This can be achieved by setting the state differential equation equal to zero i.e.  $\dot{\mathbf{x}} = 0$ , resulting in

$$\mathbf{x}(0) = -\mathbf{A}^{-1}\mathbf{B}\boldsymbol{\mu}(0). \quad (\text{A.17})$$

## A.3 Radiation mesh network solution

It follows from fig. 5.10 that there are  $m$  surface resistances in a general grey enclosure, where each surface resistance is denoted  $R_{r,i}$ . From these a **surface resistance vector** is formed, given by

$$\mathbf{r}_s = \begin{bmatrix} R_{r,1} & R_{r,2} & \cdots & R_{r,m} \end{bmatrix}. \quad (\text{A.18})$$

Then, the **surface resistance matrix** is defined as

$$\mathbf{R}_s = \text{diag}(\mathbf{r}_s), \quad (\text{A.19})$$

where  $\mathbf{R}_s$  is an  $m \times m$  diagonal matrix. Furthermore, the heat flow rates (currents) impressed on the nodes along the branch containing each surface resistance is given by

$$\boldsymbol{\phi}_r = \begin{bmatrix} \Phi_{r,1} & \Phi_{r,2} & \cdots & \Phi_{r,m} \end{bmatrix}.$$

The number of space resistances in an  $m$ -surface enclosure is calculated by using the binomial coefficient formula – since the order of the nodes is not important ( $R_{ij} = R_{ji}$ ) and no node can repeat – this results in  $C_m^2 = \binom{m}{2} = m!/(2(m-2)!)$  space resistances in the radiation network. All the space resistances are placed into the **space resistance vector**, defined as

$$\mathbf{r}_{\text{space}} = \{R_{ij} : 1 \leq i < j \leq m\} \in \mathbb{R}^{\binom{m}{2}}, \quad (\text{A.20})$$

and then the following **mesh resistance matrix**,  $\mathbf{R}_{\text{mesh}}$ , takes the form of a diagonal matrix of the elements of eq. (A.20):

$$\mathbf{R}_{\text{mesh}} = \text{diag}(\mathbf{r}_{\text{space}}), \quad (\text{A.21})$$

where  $\mathbf{R}_{\text{mesh}}$  is an  $\binom{m}{2} \times \binom{m}{2}$  diagonal matrix. The heat flow (current) along a branch between a node-pair is denoted as  $\Phi_{ij}$ . All of these ‘mesh currents’ are placed in a



vector defined as

$$\boldsymbol{\phi}_{\text{mesh}} = \{\Phi_{r,ij} : 1 \leq i < j \leq m\} \in \mathbb{R}^{\binom{m}{2}}. \quad (\text{A.22})$$

It is now possible to write Kirchoff's voltage law for the  $\binom{m}{2}$  closed networks in the system in a single vector-matrix equation given by

$$-TR_s\boldsymbol{\phi}_r + \mathbf{R}_{\text{mesh}}\boldsymbol{\phi}_{\text{mesh}} = \mathbf{e}', \quad (\text{A.23})$$

where  $\mathbf{e}' = \{E_{i,j} : 1 \leq i < j \leq m\} \in \mathbb{R}^{\binom{m}{2}}$ , is a vector comprised of all the branch potential differences<sup>1</sup>  $E_{12} = E_1 - E_2$ ,  $E_{13} = E_1 - E_3$  etc. This can be verified by evaluating Kirchoff's voltage law clockwise around the closed network between each node-pair.

The transformation matrix,  $T$ , in eq. (A.23), relates the branch potential differences with the node potentials i.e.

$$\mathbf{e}' = T\mathbf{e}_b \quad (\text{A.24})$$

where  $\mathbf{e}_b = [E_{b1} \ E_{b2} \ \cdots \ E_{bm}]^T$ . The structure of the matrix  $T$  is

$$T = \begin{bmatrix} 1 & -1 & 0 & 0 & \cdots & 0 & 0 \\ 1 & 0 & -1 & 0 & \cdots & 0 & 0 \\ \vdots & & & & \ddots & & \vdots \\ 1 & 0 & 0 & 0 & \cdots & 0 & -1 \\ 0 & 1 & -1 & 0 & \cdots & 0 & 0 \\ 0 & 1 & 0 & -1 & \cdots & 0 & 0 \\ \vdots & & & & \ddots & & \vdots \\ 0 & 1 & 0 & 0 & \cdots & 0 & -1 \\ \vdots & & & & \ddots & & \vdots \\ 0 & 0 & 0 & 0 & \cdots & 1 & -1 \end{bmatrix}. \quad (\text{A.25})$$

This matrix is also related to the fact that each current (heat flow) is a signed ( $\pm$ ) quantity reflecting direction towards or away from a node.

For this analysis, the assumed direction of currents can be seen in fig. 5.10 – where the current is assumed to flow from node  $1 \rightarrow 2 \rightarrow \cdots \rightarrow m$  within the mesh, and from node  $i$  towards the ground along the surface branches. Using this convention it is possible to construct the vector-matrix form of Kirchoff's current law for the radiation network, given by

$$\mathbf{I}_m\boldsymbol{\phi}_r + T^T\boldsymbol{\phi}_{\text{mesh}} = 0 \quad (\text{A.26})$$

<sup>1</sup>Difference in blackbody emissive power between each node-pair





where  $I_m$  is the  $m \times m$  identity matrix. Again, this can be verified by evaluating Kirchoff's current law at each node in the network.

Combining the sets of equations for Kirchoff's voltage and current laws (eqs. (A.23) and (A.26) respectively) gives the  $m + \binom{m}{2}$  equations for all the heat flows in the radiation network:

$$\underbrace{\begin{bmatrix} I_m & T^T \\ -TR_s & R_{\text{mesh}} \end{bmatrix}}_G \begin{bmatrix} \phi_r \\ \phi_{\text{mesh}} \end{bmatrix} = \begin{bmatrix} 0 \\ e' \end{bmatrix} \quad (\text{A.27})$$

Equation (A.27) can be solved to find all the heat flows within the network by inverting the  $G$  matrix. The inverse of a  $2 \times 2$  block matrix can be found in terms of its constituent blocks, i.e. given a block-partitioned matrix  $G$  with blocks  $G_{11}$ ,  $G_{12}$ ,  $G_{21}$ , and  $G_{22}$  its inverse is given by (see appendix D for the proof)

$$G^{-1} = \begin{bmatrix} G_{11}^{-1} + G_{11}^{-1}G_{12}S_D^{-1}G_{21}G_{11}^{-1} & -G_{11}^{-1}G_{12}S_D^{-1} \\ -S_D^{-1}G_{21}G_{11}^{-1} & S_D^{-1} \end{bmatrix} \quad (\text{A.28})$$

where  $S_D = G_{22} - G_{21}G_{11}^{-1}G_{12}$ . Applying the analytic inversion eq. (A.28) to eq. (A.27) gives

$$G^{-1} = \begin{bmatrix} I_m - T^T S^{-1} TR_s & -T^T S^{-1} \\ S^{-1} TR_s & S^{-1} \end{bmatrix} \quad (\text{A.29})$$

where  $S = R_{\text{mesh}} + TR_s T^T$ . This equation gives at once the solution to the radiative heat flow at the surface of each node in the network, and the radiative heat flow between two individual nodes in the network, provided that the blackbody emissive powers at each of these nodes are known. However, the only heat flows of importance are the combined surface heat flow at each node,  $\phi_r$  as these represent the *net* radiative heat flow on a node  $i$  due to the effect of rest of the network on the branch. With this in mind, the benefit of the block inversion should be apparent – it is possible to utilise eqs. (A.27) and (A.29) with the solution vector  $[0 \ e']^T$  to solve for only the node surface heat flows,  $\phi_r$ . The solution is then given by

$$\begin{aligned} \phi_r &= -T^T S^{-1} e' \\ \phi_r &= -T^T (R_{\text{mesh}} + TR_s T^T)^{-1} e'. \end{aligned} \quad (\text{A.30})$$

However, recall that  $e'$  is the branch potential differences. It is beneficial to instead have  $\phi_r$  in terms of the nodes potentials themselves, as it is more readily applied to computational modelling and state-space representations of systems. Substituting eq. (A.24) into eq. (A.30) gives the solution for the net radiative heat flow at the surface



of each node:

$$\boldsymbol{\phi}_r = \boldsymbol{\Gamma} \mathbf{e}_b \quad (\text{A.31a})$$

where

$$\boldsymbol{\Gamma} = -\mathbf{T}^T (\mathbf{R}_{\text{mesh}} + \mathbf{T} \mathbf{R}_s \mathbf{T}^T)^{-1} \mathbf{T}. \quad (\text{A.31b})$$

In eq. (A.31b), the  $m \times m$  matrix  $\boldsymbol{\Gamma}$  is defined as the **radiative conductance matrix**, which relates the blackbody emissive powers of each node to the net radiative heat flow of each node. This can be demonstrated by expanding eq. (A.31) for a single node  $i$  of the network, which results in

$$\Phi_{r,i} = \gamma_{i1} E_{b1} + \gamma_{i2} E_{b2} + \cdots + \gamma_{im} E_{bm}, \quad (\text{A.32})$$

where  $\gamma_{ij}$  is a respective element of  $\boldsymbol{\Gamma}$ . Although this equation gives us a linear relation between the radiative heat flow and the blackbody emissive power of each node, recall that the aim of this building model is to construct a set of linear ODEs where the state variables are the temperatures of the nodes. However, the relation between the blackbody emissive power and temperature of a surface is given by

$$E_{bi} = \sigma \Theta_i^4. \quad (\text{A.33})$$

Substituting eq. (A.33) into eq. (A.32) gives

$$\Phi_{r,i} = \sigma \gamma_{i1} \Theta_1^4 + \sigma \gamma_{i2} \Theta_2^4 + \cdots + \sigma \gamma_{im} \Theta_m^4. \quad (\text{A.34})$$

Clearly, eq. (A.34) is a nonlinear equation since  $\Phi_{r,i}$  cannot be expressed as a linear combination of the state variables. Therefore, in order to obtain a linear relationship between radiative heat flow and node temperatures, the first-term of a Taylor expansion around an equilibrium point can be used.

In vector-matrix form, the nonlinear system of equations are given by

$$\boldsymbol{\phi}_r = \sigma \begin{bmatrix} \gamma_{11} & \gamma_{12} & \cdots & \gamma_{1m} \\ \gamma_{21} & \gamma_{22} & \cdots & \gamma_{2m} \\ \vdots & \vdots & \ddots & \vdots \\ \gamma_{m1} & \gamma_{m2} & \cdots & \gamma_{mm} \end{bmatrix} \begin{bmatrix} \Theta_1^4 \\ \Theta_2^4 \\ \vdots \\ \Theta_m^4 \end{bmatrix}, \quad (\text{A.35})$$

or

$$\boldsymbol{\phi}_r = \mathbf{f}(\boldsymbol{\theta}_s) \quad (\text{A.36})$$

where  $\boldsymbol{\theta}_s = [\Theta_{s,1} \ \Theta_{s,1} \ \cdots \ \Theta_{s,m}]$ .



### A.3.1 Taylor-series linearisation

The linearisation of a function is the first order term of its Taylor expansion around a given equilibrium point. This is given for a general vector-valued function  $f$  as

$$f(\theta_s) \approx f(\theta_s^*) + J|_{\theta_s^*} (\theta_s - \theta_s^*) \quad (\text{A.37a})$$

where

$$J = \begin{bmatrix} \frac{\partial f_1}{\partial \theta_{s,1}} & \cdots & \frac{\partial f_1}{\partial \theta_{s,m}} \\ \vdots & \ddots & \vdots \\ \frac{\partial f_m}{\partial \theta_{s,1}} & \cdots & \frac{\partial f_m}{\partial \theta_{s,m}} \end{bmatrix}. \quad (\text{A.37b})$$

The Jacobian matrix,  $J$ , can be used to find the local (approximate) linearisation of nonlinear systems around a given equilibrium point, which is equivalent to taking the first order Taylor series expansion for each equation with respect to the variables  $\theta_s$ . Evaluating the Jacobian matrix, eq. (A.37b), for eq. (A.35) gives

$$J|_{\theta_s^*} = \begin{bmatrix} 4\sigma\gamma_{11}\Theta_{s,1}^{*3} & 4\sigma\gamma_{12}\Theta_{s,2}^{*3} & \cdots & 4\sigma\gamma_{1m}\Theta_{s,m}^{*3} \\ 4\sigma\gamma_{21}\Theta_{s,1}^{*3} & 4\sigma\gamma_{22}\Theta_{s,2}^{*3} & \cdots & 4\sigma\gamma_{2m}\Theta_{s,m}^{*3} \\ \vdots & \vdots & \ddots & \vdots \\ 4\sigma\gamma_{m1}\Theta_{s,1}^{*3} & 4\sigma\gamma_{m2}\Theta_{s,2}^{*3} & \cdots & 4\sigma\gamma_{mm}\Theta_{s,m}^{*3} \end{bmatrix} \quad (\text{A.38})$$

where  $\Theta_{s,i}^*$  denotes the equilibrium temperature of a surface node  $i$ . For the purposes of this model, it is assumed that all surfaces of a zone enclosure are linearised around a single ‘mean temperature’, denoted  $\bar{\Theta}_s$ .<sup>2</sup> Therefore,  $\Theta_{s,1}^* = \Theta_{s,2}^* = \Theta_{s,m}^* = \bar{\Theta}_s$ . The Jacobian now becomes

$$J|_{\theta_s^*} = 4\sigma\bar{\Theta}_s^3 \begin{bmatrix} \gamma_{11} & \gamma_{12} & \cdots & \gamma_{1m} \\ \gamma_{21} & \gamma_{22} & \cdots & \gamma_{2m} \\ \vdots & \vdots & \ddots & \vdots \\ \gamma_{m1} & \gamma_{m2} & \cdots & \gamma_{mm} \end{bmatrix} \quad (\text{A.39})$$

or

$$J|_{\theta_s^*} = 4\sigma\bar{\Theta}_s^3 \Gamma \quad (\text{A.40})$$

Noting that the term  $f(\theta_s^*)$  of eq. (A.37a) is identically zero, by definition of the equilibrium condition, the linear model describing the network radiative heat flow due to any deviation from the mean surface temperature  $\Delta\theta_s$ , is given by

$$\phi_r \approx 4\sigma\bar{\Theta}_s^3 \Gamma \Delta\theta_s. \quad (\text{A.41})$$

<sup>2</sup>In the absence of national data, a value of 300 K can be assumed (1).



which is a linear vector-matrix differential equation. Commonly in such analyses, the  $\Delta$  notation is dropped and it is understood that  $\theta_s$  refers to the deviation from the equilibrium. Therefore, eq. (A.41) can be expressed as

$$\boxed{\phi_r = \Gamma_{\text{lin}} \theta_s} \quad (\text{A.42})$$

where

$$\Gamma_{\text{lin}} = -4\sigma\bar{\Theta}^3 T^{\mathcal{T}} (R_{\text{mesh}} + TR_s T^{\mathcal{T}})^{-1} T. \quad (\text{A.43})$$

Finally, the vector-matrix eq. (A.42) can be expanded for each node  $i$  as

$$\Phi_{s,i} = Y_{i1}\Theta_{s,1} + Y_{i2}\Theta_{r,2} + \dots + Y_{im}\Theta_{r,m}, \quad (\text{A.44})$$

where  $Y_{ij}$  are the elements of the linear radiation heat transmission matrix  $\Gamma_{\text{lin}}$ .

Equation (A.44) finally represents a linear relationship between the net radiative heat flow at a node  $i$  and the surface temperatures of the zone enclosure components.

## A.4 Modelling of solar heat gains

### A.4.1 Heat flux per building element

The net rate of radiation heat flux to an external surface  $k$ , exposed to solar and atmospheric radiation is determined from an energy balance

$$\begin{aligned} \varphi_{\text{rad},k} &= \sum \varphi_{\text{absorbed},k} - \sum \varphi_{\text{emitted},k} \\ \varphi_{\text{rad},k} &= \varphi_{\text{solar,absorbed},k} + \varphi_{\text{sky,absorbed},k} - \varphi_{\text{sky,emitted},k} \\ \varphi_{\text{rad},k} &= \varphi_{\text{sol},k} + \alpha\sigma\Theta_{\text{sky}}^4 - \varepsilon\sigma\Theta_{e,k}^4 \end{aligned} \quad (\text{A.45})$$

where

- $\alpha$  is the absorptivity of the atmosphere
- $\varepsilon$  is the emissivity of the surface  $k$
- $\Theta_{\text{sky}}$  is the effective sky temperature (K)
- $\Theta_{e,k}$  is the temperature of the external surface of element  $k$

The effective sky temperature allows for a simplification of the radiation exchange with the sky – it acts as a representative temperature assigned to the sky assuming it interacts with the surface as a blackbody at some temperature lower than that of the surface.

From Kirchoff's law<sup>3</sup> it is possible to assume that the absorptivity of the sky is

---

<sup>3</sup> $\varepsilon(\Theta) = \alpha(\Theta)$





equal to the emissivity of the surface. Therefore, eq. (A.45) becomes

$$\varphi_{\text{rad},k} = \varphi_{\text{sol},k} - \varphi_{\text{sky},k} \quad (\text{A.46})$$

where

$$\varphi_{\text{sky},k} = \varepsilon\sigma \left( \Theta_{e,k}^4 - \Theta_{\text{sky}}^4 \right) \quad (\text{A.47})$$

Since the difference between the external temperature and the effective sky temperature is relatively small, it is possible to approximate the radiative heat flux exchange with the sky from element  $k$ ,  $\varphi_{\text{sky},k}$  as a linear equation as opposed to the nonlinear eq. (A.47). This can be achieved by taking the first term of the Taylor series expansion of eq. (A.47), and assuming that at the local equilibrium point around which the expansion takes place is the arithmetic average of the external surface temperature and effective sky temperature,  $\Theta_{\text{ss}}$ . Therefore, eq. (A.47) becomes

$$\varphi_{\text{sky},k} \approx 4\varepsilon\sigma\Theta_{\text{ss}}^3 (\Delta\Theta_{e,k} - \Delta\Theta_{\text{sky}})$$

or

$$\varphi_{\text{sky},k} = h_{\text{lr},e} \Delta\Theta_{\text{er},k} \quad (\text{A.48})$$

where

$$h_{\text{lr},e} = 4\varepsilon\sigma\Theta_{\text{ss}}^3 \quad \text{and} \quad \Delta\Theta_{\text{er},k} = \Delta\Theta_{e,k} - \Delta\Theta_{\text{sky}}$$

$h_{\text{lr},e}$  is the external radiative heat transfer coefficient ( $\text{W m}^{-2} \text{K}^{-1}$ )

$\Delta\Theta_{\text{er},k}$  is the average difference between the temperature of external surface  $k$  and the apparent sky temperature (K)

Equation (A.48) is a linear equation that allows the model to account for the radiative exchange between the external surface of an element  $k$  and the atmosphere. It is assumed that the long-wave radiative heat transfer coefficient  $h_{\text{lr},e}$  is the same for all external surfaces of the zone, and that  $\Delta\Theta_{\text{er},k}$  is a known constant or time-varying disturbance input to the model. Note that since  $\Delta\Theta_{\text{er},k}$  will always be positive, the radiative exchange with the atmosphere results in a loss of heat from the zone, effectively reducing the net solar heat gain into the zone.

#### A.4.2 Heat flow per building element

Now that the net solar heat flux incident on an external surface can be calculated, it is possible to find the approximate net solar heat flow rate *through* a building element. For each building element  $k$ , the solar gain is the product of the incident solar radiation heat flux on that surface, the effective collecting area, and the external



shading reduction factor.

$$\Phi_{\text{sol},k} = f_{\text{sh},e,k} A_{\text{sol},k} \varphi_{\text{sol},k} \quad (\text{A.49})$$

where

$f_{\text{sh},e,k}$  is the external shading reduction factor, varying from 0 for completely shaded to 1 for no external shading.

$A_{\text{sol},k}$  is the effective solar collecting area of surface  $k$ , which is equal to the area of blackbody having the same solar heat gain as the surface considered.

It is assumed that the external shading is passive i.e. a static parameter that is neither controlled or time-varying.

### Effective solar collecting area

$A_{\text{sol}}$  in eq. (A.49) is a term that differs depending on whether the element is an opaque building component or a glazing system. In either case, it is a simplified approach to modelling the transmission of solar thermal radiation incident on a external surface into a building zone. It accounts for any integrated or add-on solar shading provisions *inside* the zone, as well as the absorption and transmission properties of the element. The true solar transmission properties of elements, especially glazing systems, is comprised of several complex heat transfer mechanisms as well as generally time-varying parameters such as the sun's position throughout the day. As such, it is recognised that this is a simplification of the solar transmittance through elements into the zone, but it is suitable for the purposes of heating and cooling load calculation(2), as well as reasonably accurate for related temperature changes within the zone.

When solar radiation strikes a glazed element, part of it is reflected back outdoors, part of it is absorbed within the glass (of which some still flows back outdoors, while some flows into the zone), and the rest is transmitted directly into the zone. The sum of the transmitted solar radiation and the portion of the absorbed radiation that flows indoors comprise the solar heat gain of the glazed element. This is represented by a term,  $g_k$ , which is called the solar heat gain coefficient or solar energy transmittance. The value of  $g_k$  can vary between 0 and 1, with 1 corresponding to an opening with no glazing.<sup>4</sup> For the purposes of this model this is considered to be fixed based on the type of glazing system used in the office zone. Therefore, the effective solar collecting area of a glazed envelope element is given by

$$A_{\text{sol},k} = f_{\text{sh},in,k} g_k (1 - f_{F,k}) A_k \quad (\text{A.50})$$

<sup>4</sup>Typical values are 0.85 for single glazing, to 0.5 for high-performance triple-glazing.



where

$f_{\text{sh,in},k}$  is the internal shading reduction factor, varying from 0 for completely shaded to 1 for no internal shading.

$f_{\text{r},k}$  is the frame area fraction, where a value of 0 indicates no window frame.

$A_k$  is the overall projected area of the element ( $\text{m}^2$ )

The parameter  $f_{\text{sh,in},k}$  can account for movable shading. This can either be a static parameter for fixed internal shading, a time-varying disturbance input to account for unknown manual changes in shading (i.e. due to occupant behaviour), or a controllable input to the model to allow for a control system to alter the internal shading within the zone.

The solar heat gain of external opaque elements (with no transparent part) are indirect solar gains, typically resulting from direct radiation being absorbed by the external walls and roofs. This heat can conduct through the constructions and end up as a solar gain inside the building. These gains often only constitute a small portion of the overall solar radiation from the sun and atmosphere. In a well-insulated building in northern Europe the effect is minor, but in poorly-insulated buildings in sunny climates, as well as zones with large sky facing external surfaces these heat gains can be significant.

The effective solar collecting area of an opaque part of the building envelope is given by

$$A_{\text{sol},k} = A_k \alpha_k \quad (\text{A.51})$$

where  $\alpha_k$  is the absorptivity of the opaque element  $k$ .

### Atmospheric radiation

Equation (A.48) gives a linear relationship for the modelling of radiant heat flux between an *external* surface  $k$  and the atmosphere. However, in order to simplify the analysis, it is possible to approximate the heat loss from the internal zone *through* a no mass (e.g. glazing) component  $k$  to the atmosphere with knowledge of its thermophysical properties and the atmospheric radiant heat flux,  $\varphi_{\text{sky},k}$ . This is given by

$$\Phi_{\text{sky},k} = R_{\text{se},k} A_k U_k F_{\text{r},k} A_k \varphi_{\text{sky},k} \quad (\text{A.52})$$

where  $F_{\text{r},k}$  is the form factor between the external surface and the sky (i.e. 1 for horizontal surface, 0.5 for vertical surface). This formula can be deduced by inspection of the electrical network analogy as if the atmospheric radiation was acting as a heat flow from the external surface node. Similarly for an opaque component with thermal



mass, the heat loss from the external mass node to the sky is given by

$$\Phi_{\text{sky},k} = \frac{R_{\text{se},k}}{R_{\text{se},k} + R_{1,k}} F_{\text{r},k} A_k \varphi_{\text{sky},k} \quad (\text{A.53})$$

### Net solar radiation

The net solar heat flow rate to building element  $k$  is given by

$$\Phi_{\text{sol,net},k} = \Phi_{\text{sol},k} - \Phi_{\text{sky},k} \quad (\text{A.54})$$

Depending on whether the element is a glazing system or an opaque component will dictate the net solar heat flow rate calculation procedure. For an element  $k$  representing a glazing system, substituting eqs. (A.48) to (A.50) and (A.52) into eq. (A.54) gives the net solar heat flow rate from a glazed building element as

$$\Phi_{\text{sol,net},k} = A_k (f_{\text{sh},e,k} f_{\text{sh},\text{in},k} g_k (1 - f_{\text{r},k}) \varphi_{\text{sol},k} - R_{\text{se},k} A_k U_k F_{\text{r},k} h_{\text{lr},e} \Delta\Theta_{\text{er},k}) \quad (\text{A.55})$$

Similarly for an opaque building element, substituting eqs. (A.48), (A.49), (A.51) and (A.53) into eq. (A.54) results in the net solar heat flow rate from an opaque building element, given by

$$\Phi_{\text{sol,net},k} = \frac{R_{\text{se},k}}{R_{\text{se},k} + R_{1,k}} A_k (f_{\text{sh},e,k} \alpha_k \varphi_{\text{sol},k} - F_{\text{r},k} h_{\text{lr},e} \Delta\Theta_{\text{er},k}). \quad (\text{A.56})$$

#### A.4.3 Solar radiation zone distribution

The solar gain into the zone via the glazing will be distributed amongst the zone nodes. When this solar gain is transmitted into the zone, a small fraction will be immediately delivered as a heat flow to the internal air, but almost all of it is absorbed by the internal surfaces. This raises the temperature of each surface, which in turn contributes to the internal radiative heat transfer between the internal surfaces, affecting the energy performance and mean radiant temperature within the zone.

The distribution of the solar gain amongst the internal surfaces is generally time varying since the angle at which the direct radiation beam hits the glazing will differ throughout the day. However, for the purposes of this model and to comply with BS EN 15265:2007, the distribution of the solar radiation is time independent.

With these factors in mind, the solar gain to an internal node  $i$  of the model is given by

$$\Phi_{\text{sol},i} = f_{\text{sa}} \Phi_{\text{sol}} \quad (\text{A.57})$$





for an air node, or

$$\Phi_{\text{sol},i} = f_{\text{df},i}(1 - f_{\text{sa}})\Phi_{\text{sol}} \quad (\text{A.58})$$

for an internal surface node, where

$f_{\text{sa}}$  is the solar to air factor  
 $f_{\text{df},i}$  is the solar distribution factor

$f_{\text{sa}}$  represents the fraction of the solar gain that enters the zone that immediately acts as a heat flow to the internal air node. This depends on the number of surface elements within the zone which have negligible thermal capacity e.g. carpets, furniture etc. since they will almost immediately re-emit the solar gain to the internal air. A default value of  $f_{\text{sa}} = 0.1$  is assumed throughout this work, as defined in BS EN 15265:2007 (1).

Similar to the distribution of the internal heat gains, the solar distribution factor is defined as an area weighted fraction of solar heat gain that is absorbed by that surface. The solar distribution factor for a surface node  $i$  is given by

$$f_{\text{df},i} = \frac{A_i}{\sum_{i=1}^m A_i} \quad (\text{A.59})$$

Note that the total surface area on the denominator of eq. (A.59) *excludes* the internal surface area of the glazing.

Now that the distribution amongst the nodes can be calculated, it is possible to represent this in vector-matrix form for the air and internal surface nodes within the zone. Again assuming the temperature nodes are ordered so that the surface nodes are concatenated to the end of the air node, the solar gain to each node can be written as

$$\begin{bmatrix} \Phi_{\text{sol},a} \\ \Phi_{\text{sol},\text{si},1} \\ \vdots \\ \Phi_{\text{sol},\text{si},m} \end{bmatrix} = \begin{bmatrix} f_{\text{sa}} \\ f_{\text{df},i}(1 - f_{\text{sa}}) \\ \vdots \\ f_{\text{df},m}(1 - f_{\text{sa}}) \end{bmatrix} \Phi_{\text{sol}}, \quad \text{or } \boldsymbol{\phi}_{\text{sol},a-\text{si}} = \begin{bmatrix} f_{\text{sa}} \\ \mathbf{f}_{\text{sol},\text{si}} \end{bmatrix} \Phi_{\text{sol}} \quad (\text{A.60})$$

where  $\mathbf{f}_{\text{sol},\text{si}} = \mathbf{f}_{\text{sol},\text{df}}(1 - f_{\text{sa}})$  and  $\mathbf{f}_{\text{sol},\text{df}} = [f_{\text{df},1} \ \cdots \ f_{\text{df},m}]^T$ .

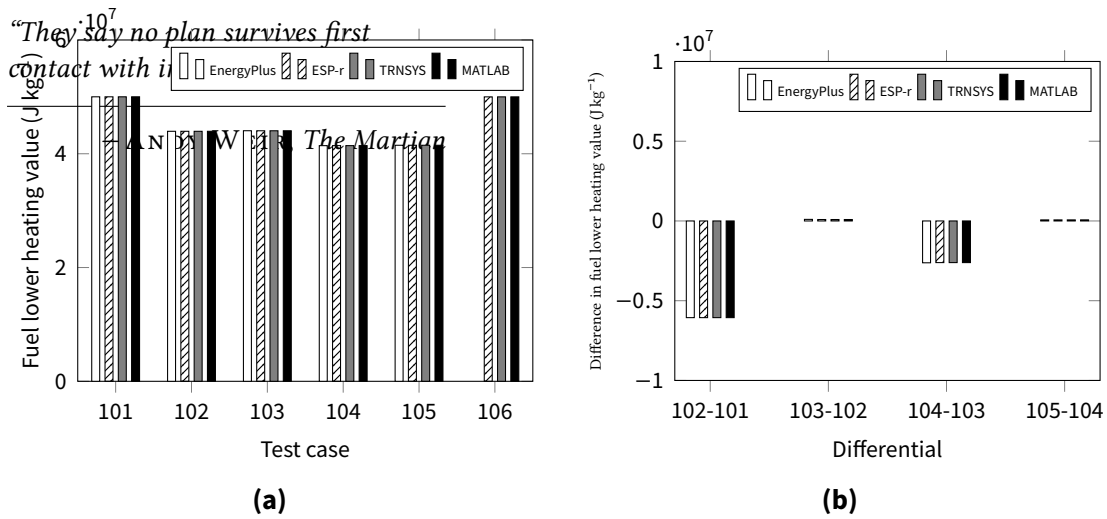


**Figure B.1 | 100 series test case results: (a) reported fuel lower heating value, and (b) differences between fuel lower heating value reported in successive test cases.**

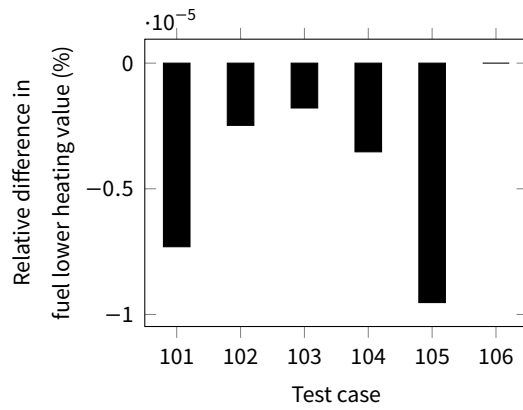


**Figure B.2 | 100 series test case results: relative difference between fuel lower heating values reported by MATLAB and ESP-r/TRNSYS.**

**B**

## Model validation

### **B.1** Combustion cogeneration

The model of the combustion-based (SE/ICE) cogeneration device utilised in this work is the model that was developed and validated as part of the Annex 42 research project (1) that aimed to create “A Generic Model for Combustion-Based Cogeneration Devices”. The Annex 42 research project put forth a set of validation tests (2) to complete when the model is implemented in a new environment to ensure there are no errors in the mathematical solution or coding errors. This section presents the results from the validation of the model’s implementation in the MATLAB/Simulink environment. The document published by Beausoleil-Morrison, Ferguson (2) contains full details of the validation procedure, specifications and results against which the model should be compared. This appendix does not reproduce this information in full, what it does contain is the minimal information required to understand the purpose of each validation test, the results of the validation, and any discrepancy between the MATLAB model and the validation suite.

#### **B.1.1** 100 series tests

The 100 series tests are designed to check the calculations of the fuel heating values from given fuel compositions. Figures B.1 and B.2 shows the results were in agreement with the other calculation methods.

#### **B.1.2** 200 series tests

The 200 series tests are designed to check the model’s calculation of the electrical & thermal efficiency correlations, and fuel, air & cooling water mass flow rates. Each



test varies the boundary conditions and input configurations. Test cases 201–203 use an external cooling pump, while test cases 204–205 use an internal cooling pump.

**Test case 201**

Figures B.3 to B.8 shows the results were in agreement with the other calculation methods.

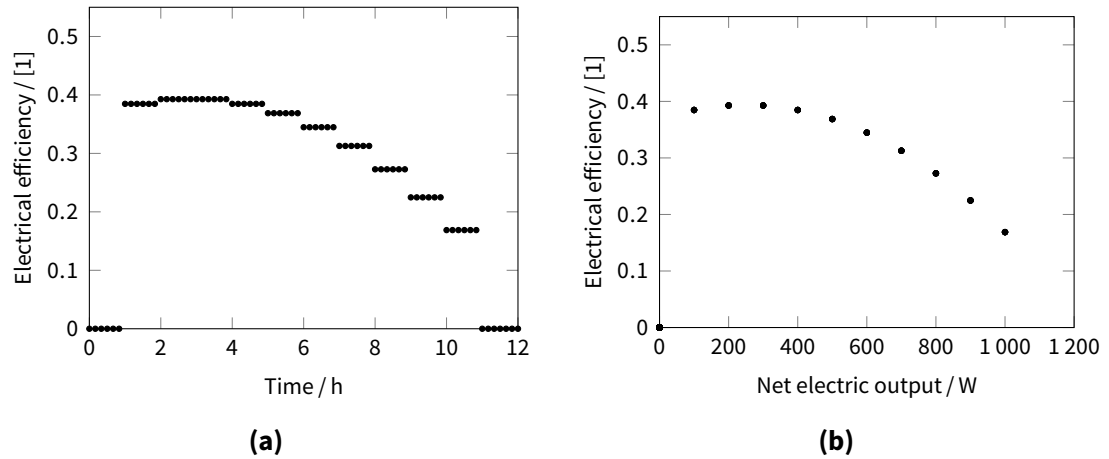


**Figure B.3** | Test case 201 results: electrical efficiency as a function of (a) time, and (b) net electric output

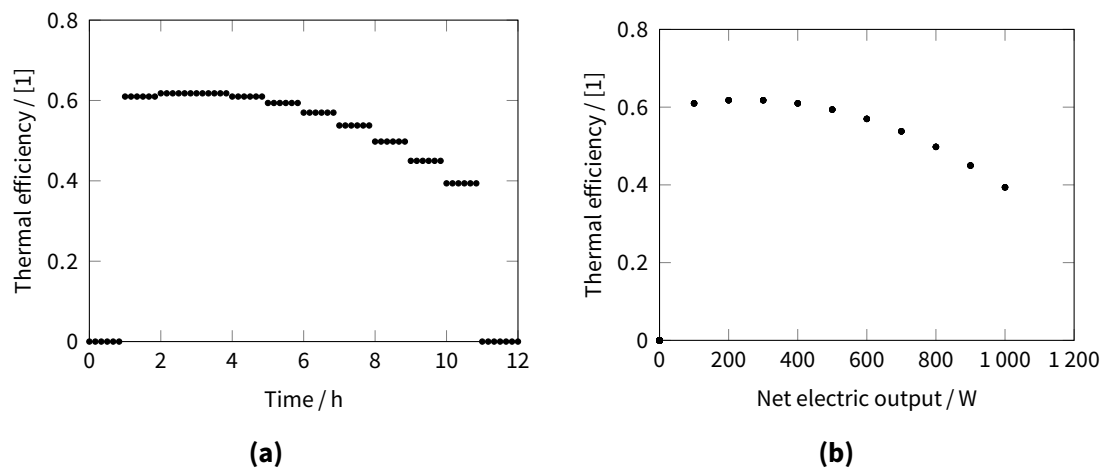


**Figure B.4** | Test case 201 results: thermal efficiency as a function of (a) time, and (b) net electric output



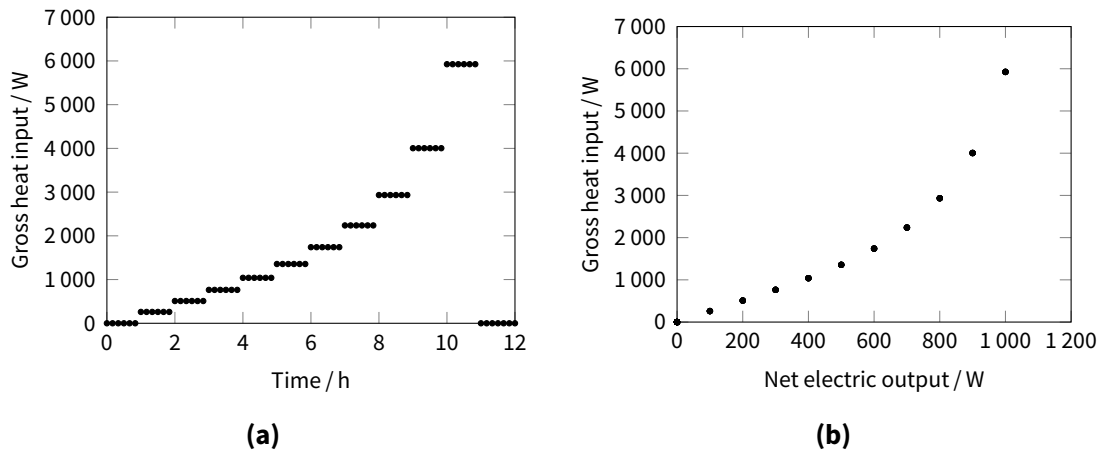


**Figure B.5** | Test case 201 results: gross heat input as a function of (a) time, and (b) net electric output

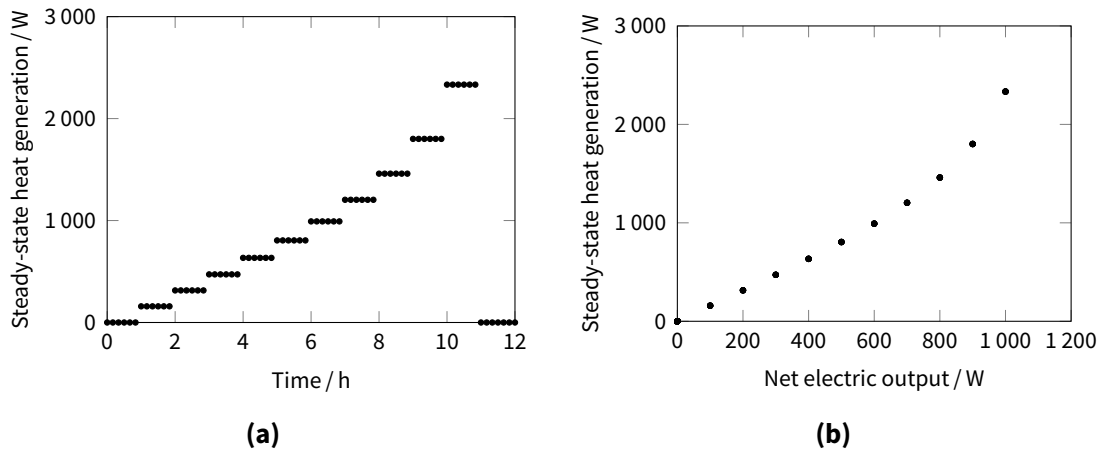


**Figure B.6** | Test case 201 results: heat generation as a function of (a) time, and (b) net electric output

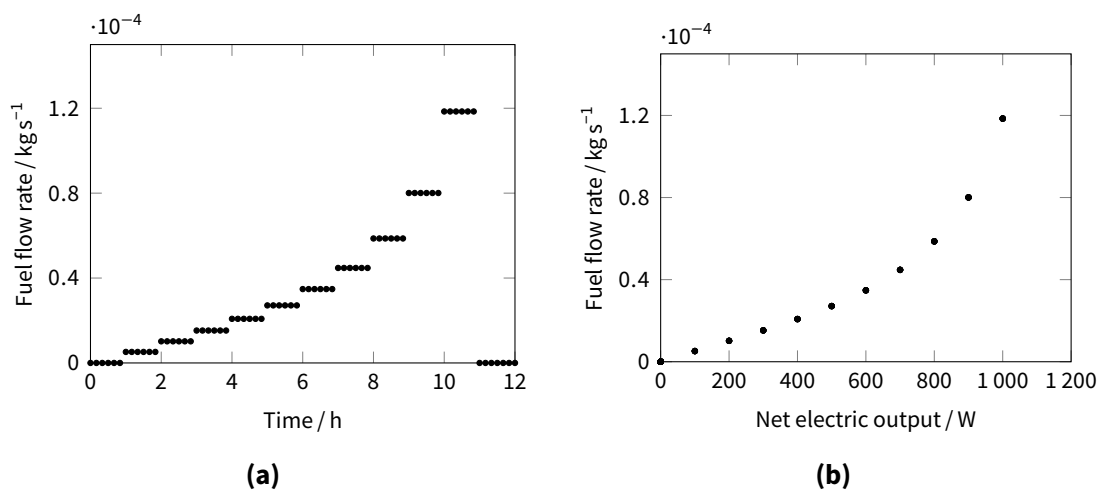


**Figure B.7** | Test case 201 results: fuel flow rate as a function of (a) time, and (b) net electric output





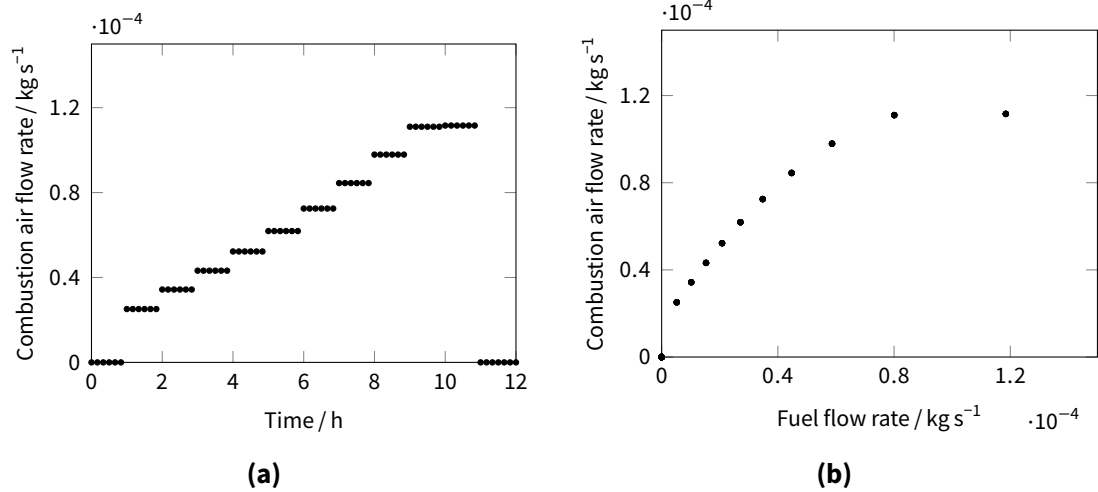


**Figure B.8** | Test case 201 results: combustion air flow rate as a function of (a) time, and (b) fuel flow rate

### Test case 202

Figures B.9 and B.10 shows the results were in agreement with the other calculation methods.

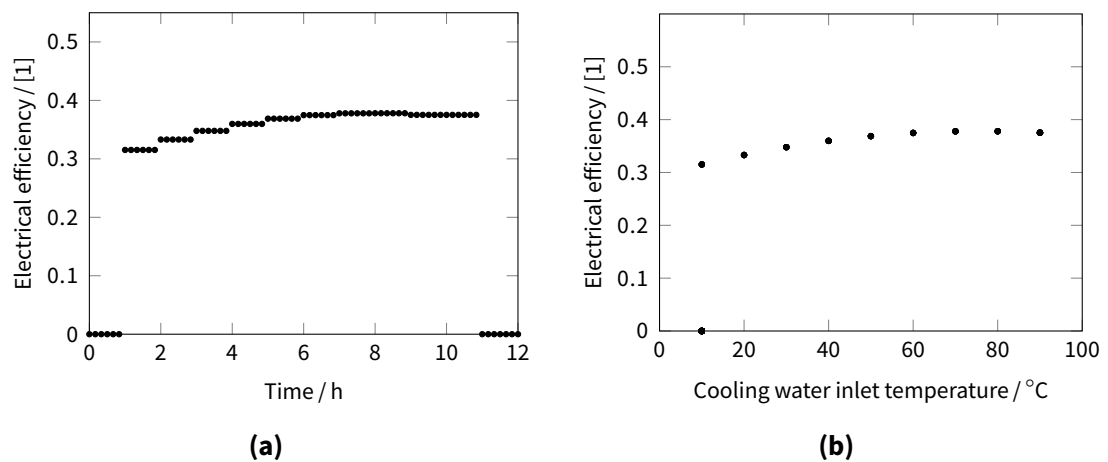


**Figure B.9** | Test case 202 results: electrical efficiency as a function of (a) time, and (b) cooling water inlet temperature



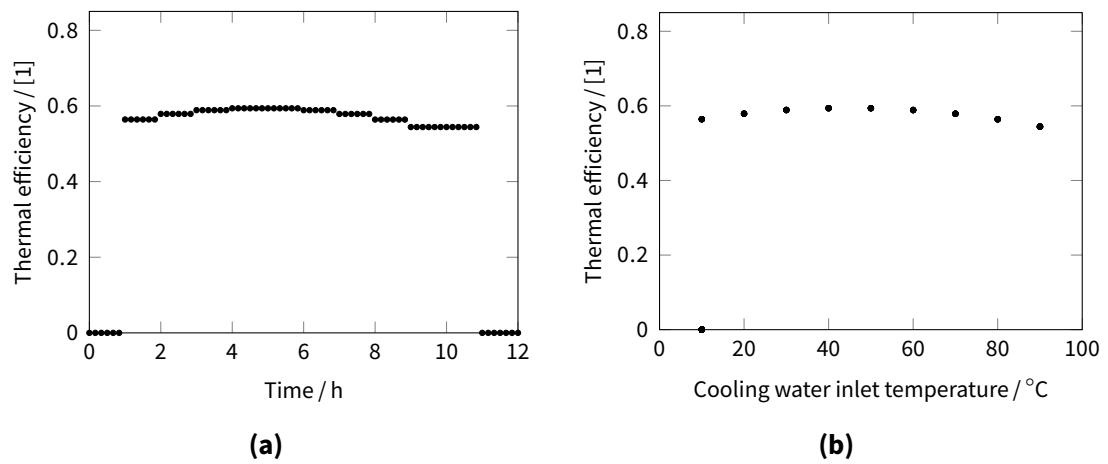


**Figure B.10** | Test case 202 results: thermal efficiency as a function of (a) time, and (b) cooling water inlet temperature

### Test case 203

Figures B.11 and B.12 shows the results were in agreement with the other calculation methods.

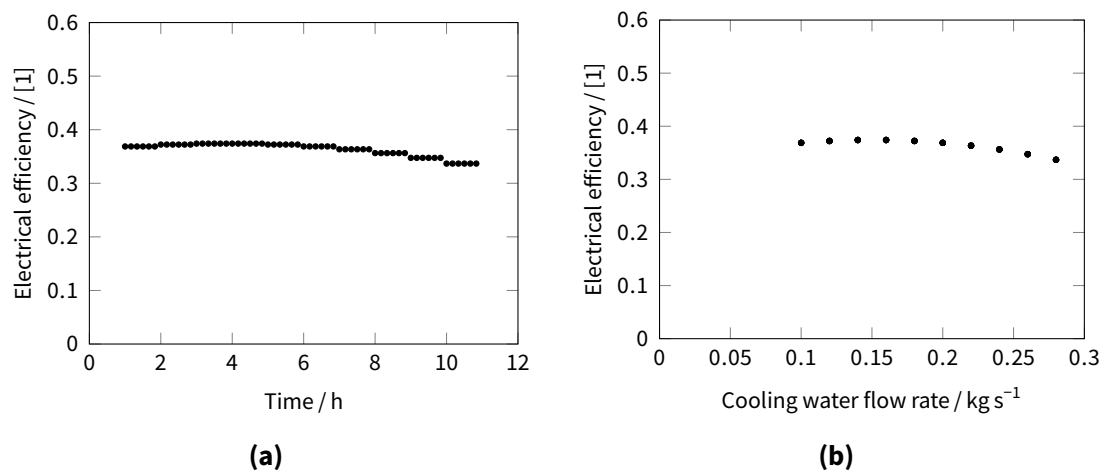


**Figure B.11** | Test case 203 results: electrical efficiency as a function of (a) time, and (b) cooling water flow rate



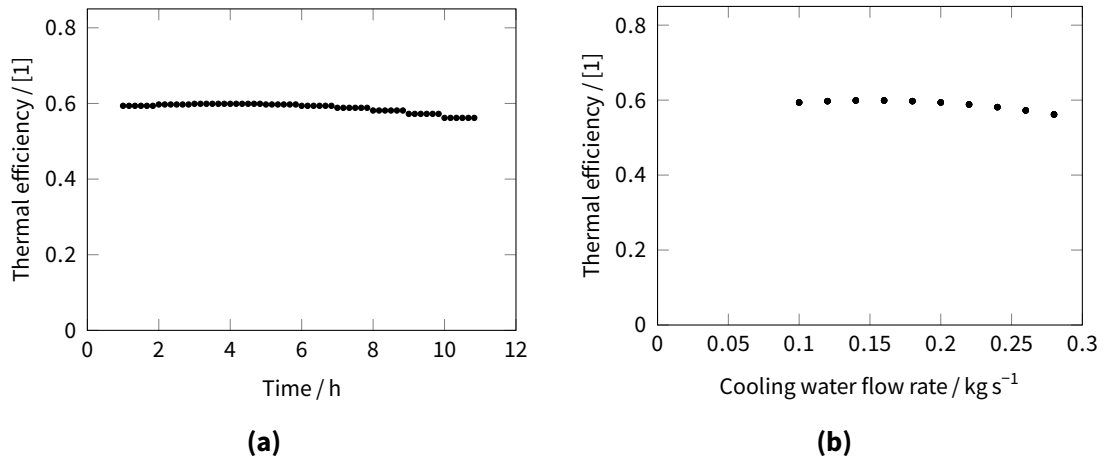


**Figure B.12** | Test case 203 results: thermal efficiency as a function of (a) time, and (b) cooling water flow rate

**Test case 204**

Figure B.13 shows the results were in agreement with the other calculation methods.

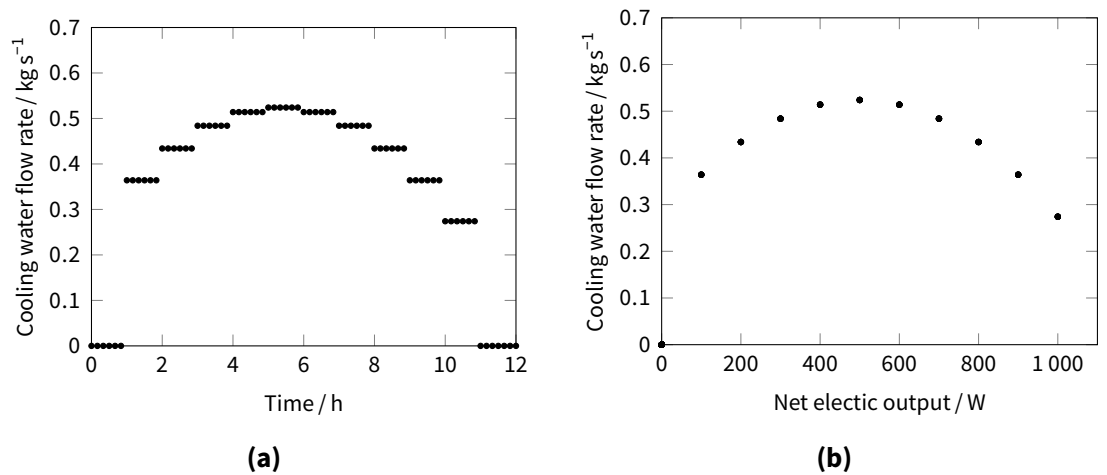


**Figure B.13** | Test case 204 results: cooling water flow rate as a function of (a) time, and (b) net electric output

**Test case 205**

Figure B.14 shows the results were in agreement with the other calculation methods.



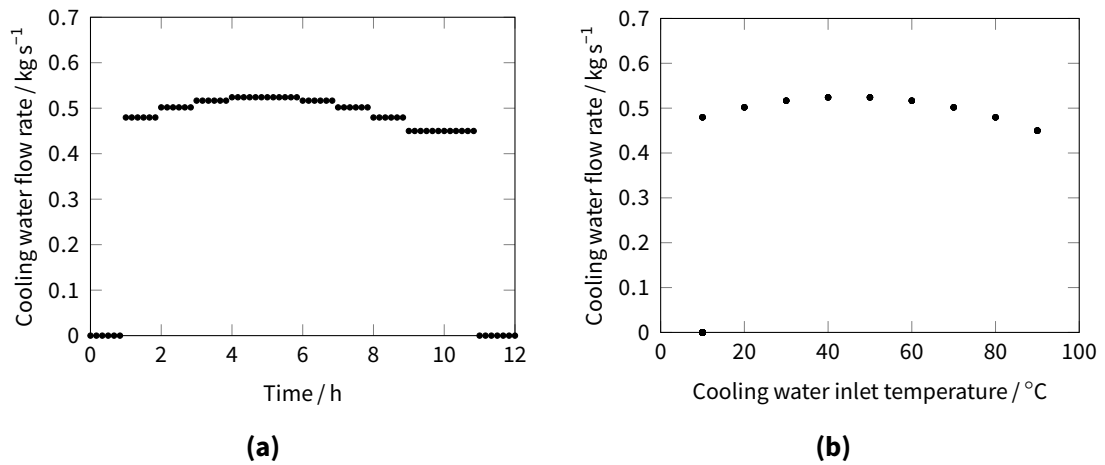


**Figure B.14** | Test case 205 results: cooling water flow rate as a function of (a) time, and (b) cooling water inlet temperature

### B.1.3 300 series tests

The 300 series tests are designed to check the model's calculation of the dynamic thermal model. Each test varies the boundary conditions and input configurations.

#### Test case 301

Figures B.15 and B.16 shows the results were in agreement with the other calculation methods.

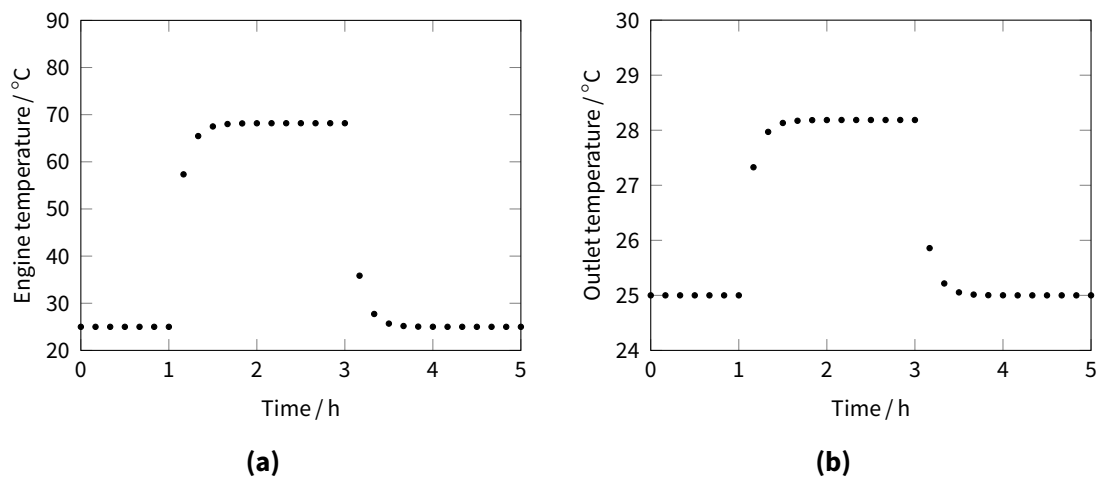


**Figure B.15** | Test case 301 results: (a) engine temperature, and (b) cooling water temperature as functions of time.





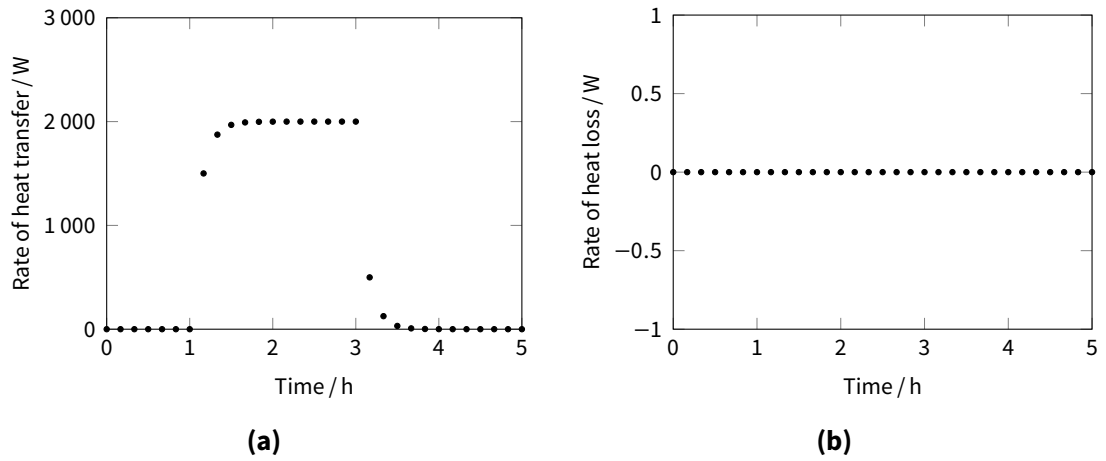


**Figure B.16** | Test case 301 results: Rate of (a) heat transfer and (b) heat loss as functions of time.

### Test case 302

Figures B.17 and B.18 shows the results were in agreement with the other calculation methods.

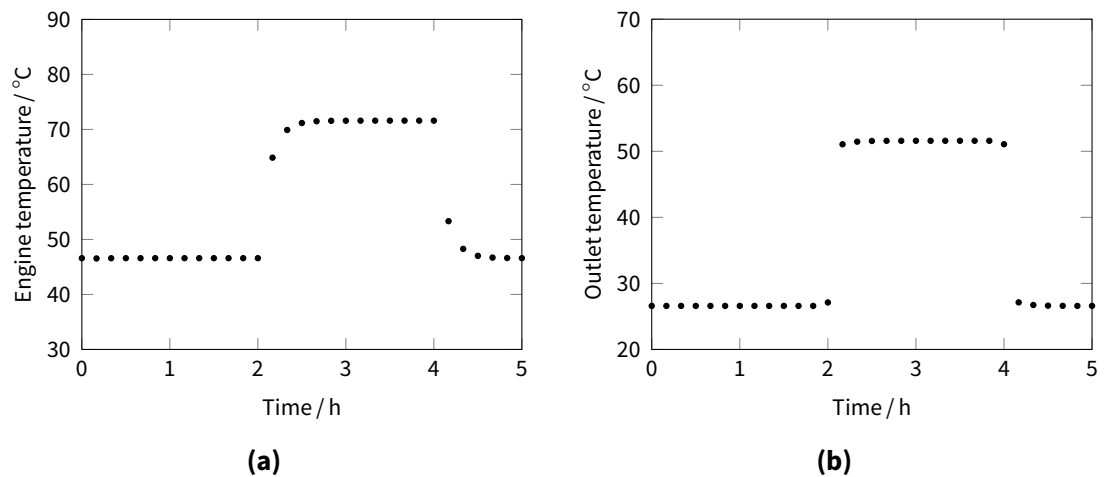


**Figure B.17** | Test case 302 results: (a) engine temperature and (b) cooling water temperature as functions of time.



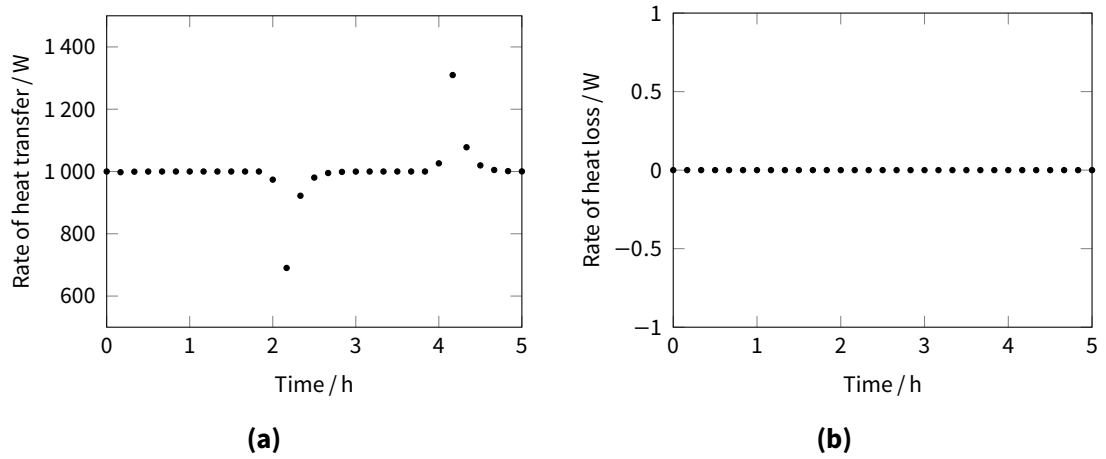


**Figure B.18** | Test case 302 results: rates of (a) heat transfer and (b) heat loss as functions of time.

### Test case 303

Figures B.19 and B.20 shows the results were in agreement with the other calculation methods.

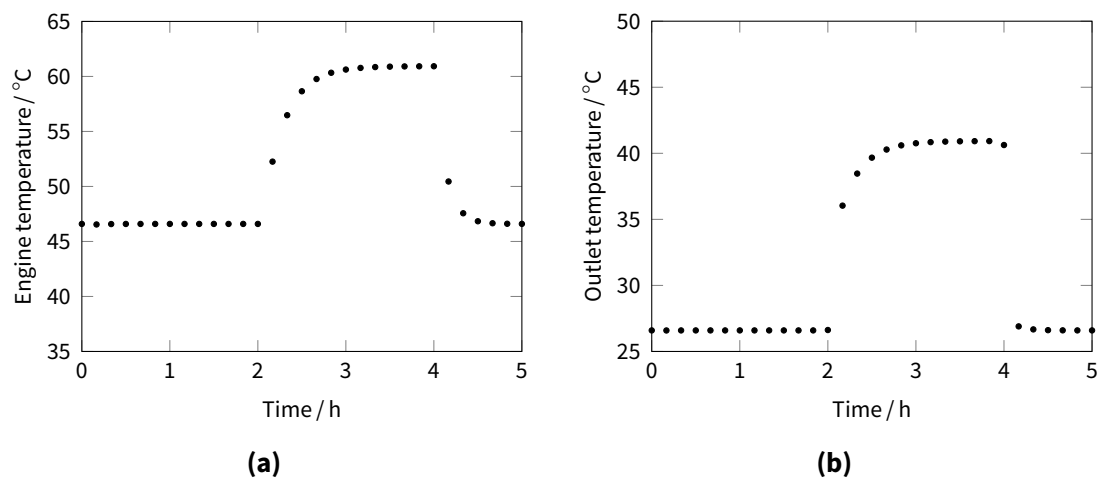


**Figure B.19** | Test case 303 results: (a) engine temperature and (b) cooling water temperature as functions of time.



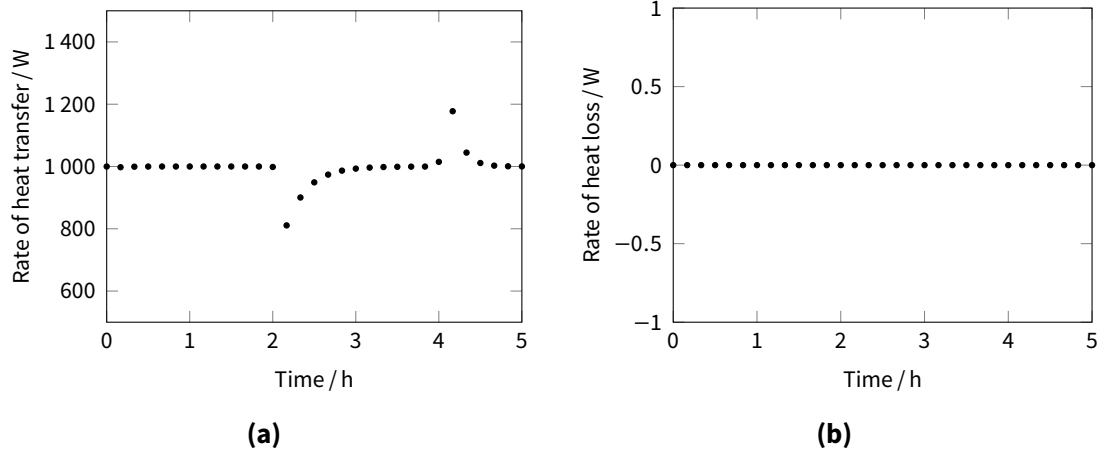


**Figure B.20 | Test case 303 results: rates of (a) heat transfer and (b) heat loss as functions of time.**

**Test case 304**

Figures B.21 to B.24 shows the results were in agreement with the other calculation methods.

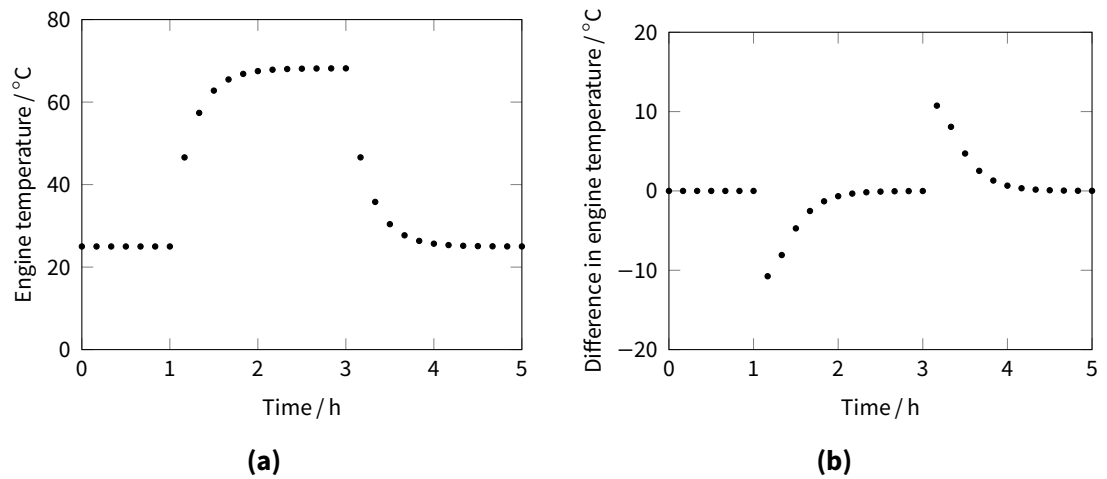


**Figure B.21 | Test case 304 results: engine temperature as a function of time for (a) case 304 and (b) differential between cases 304 and 301.**



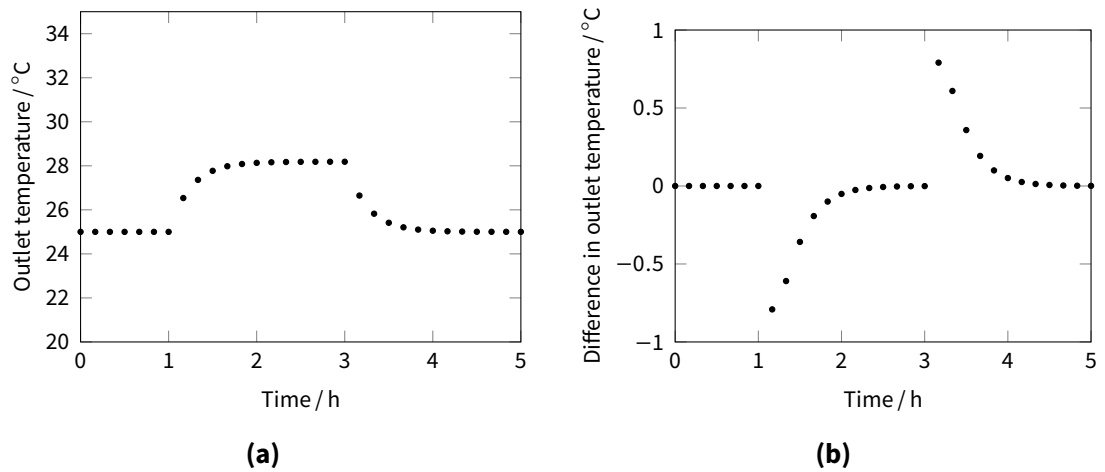


**Figure B.22** | Test case 304 results: cooling water outlet temperature as a function of time for (a) case 304 and (b) differential between cases 304 and 301.

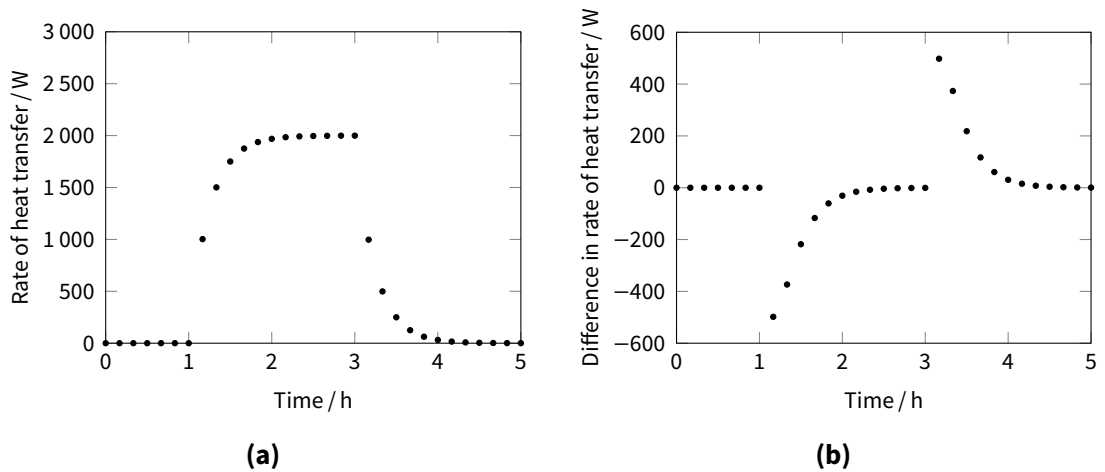


**Figure B.23** | Test case 304 results: heat transfer rate as a function of time for (a) case 304 and (b) differential between cases 304 and 301.

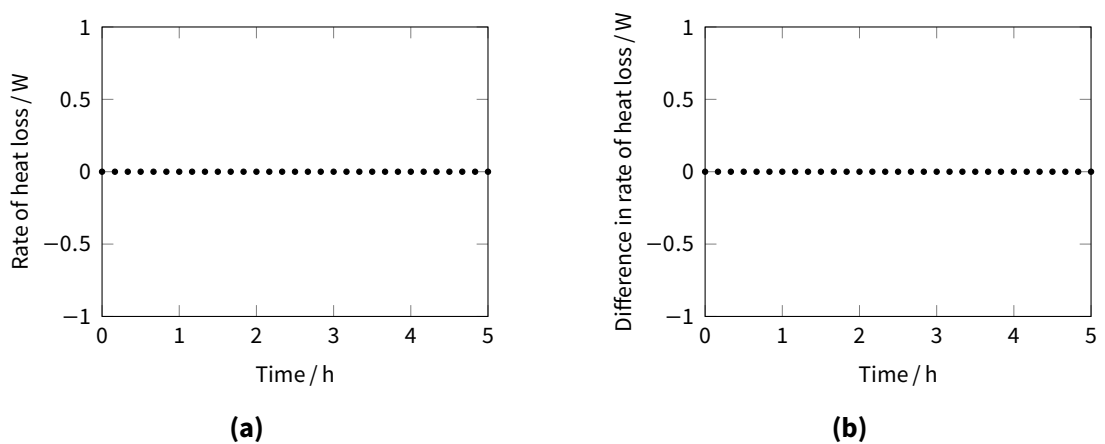


**Figure B.24** | Test case 304 results: heat loss rate as a function of time for (a) case 304 and (b) differential between cases 304 and 301.





### Test case 305

Figures B.25 to B.28 shows the results were in agreement with the other calculation methods.

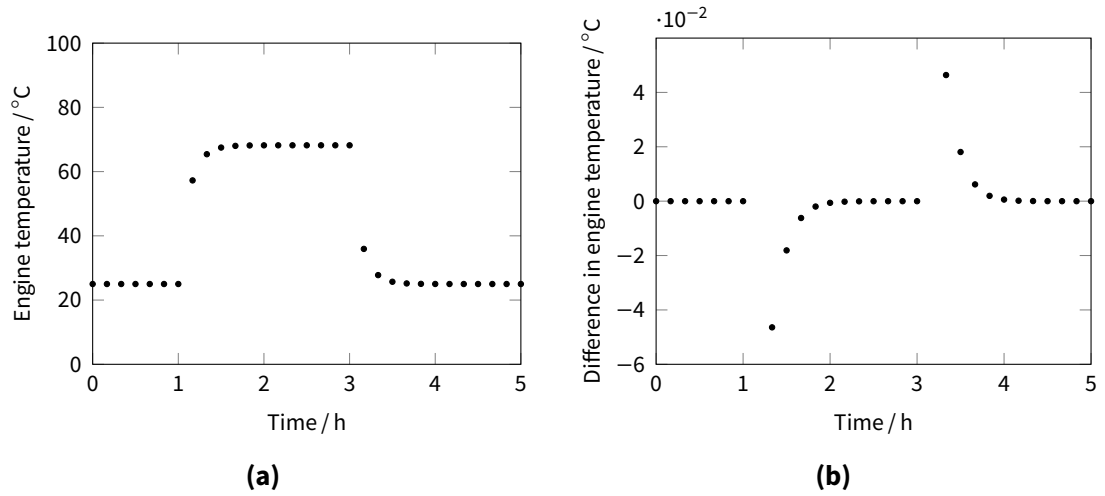


**Figure B.25** | Test case 305 results: engine temperature as a function of time for (a) case 305 and (b) differential between cases 305 and 301.

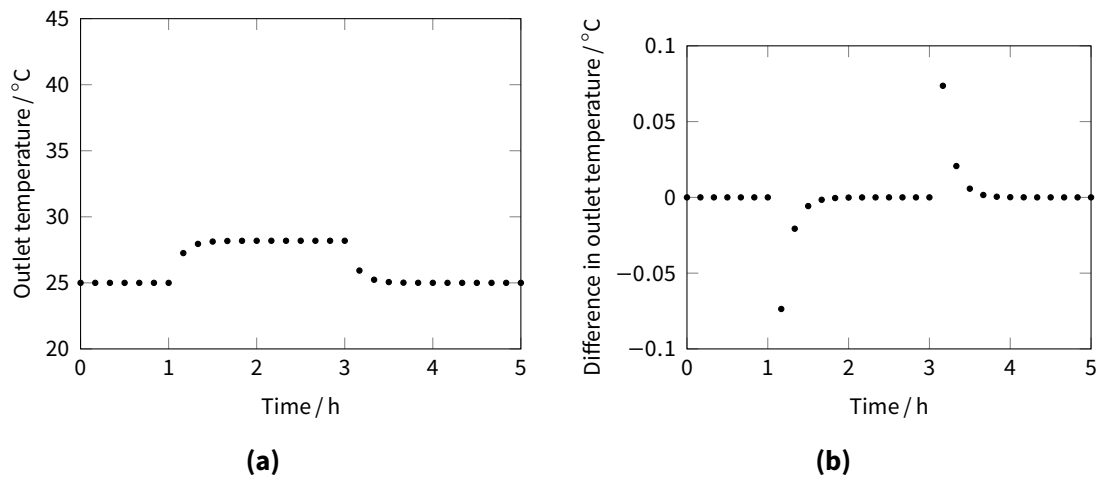


**Figure B.26** | Test case 305 results: cooling water outlet temperature as a function of time for (a) case 305 and (b) differential between cases 305 and 301.



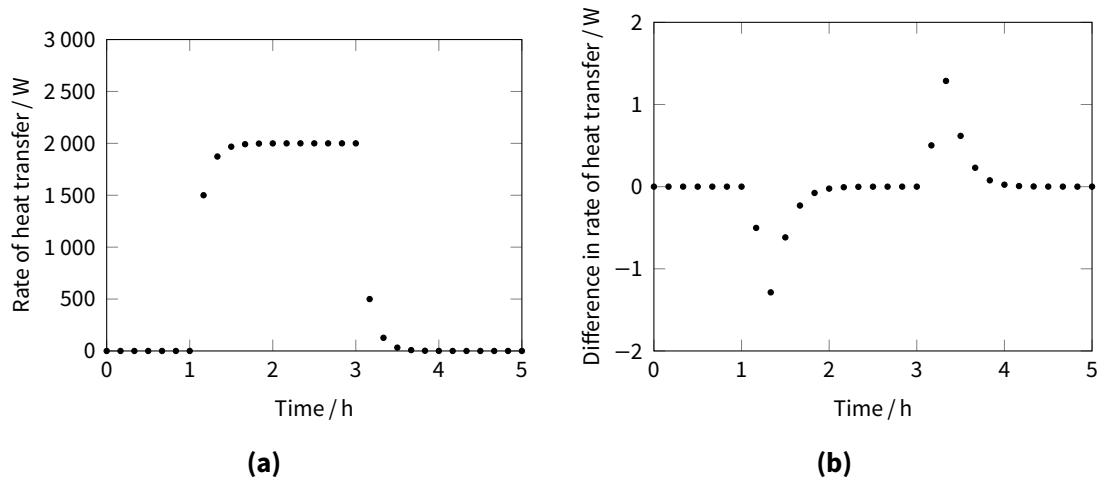


**Figure B.27** | Test case 305 results: heat transfer rate as a function of time for (a) case 305 and (b) differential between cases 305 and 301.

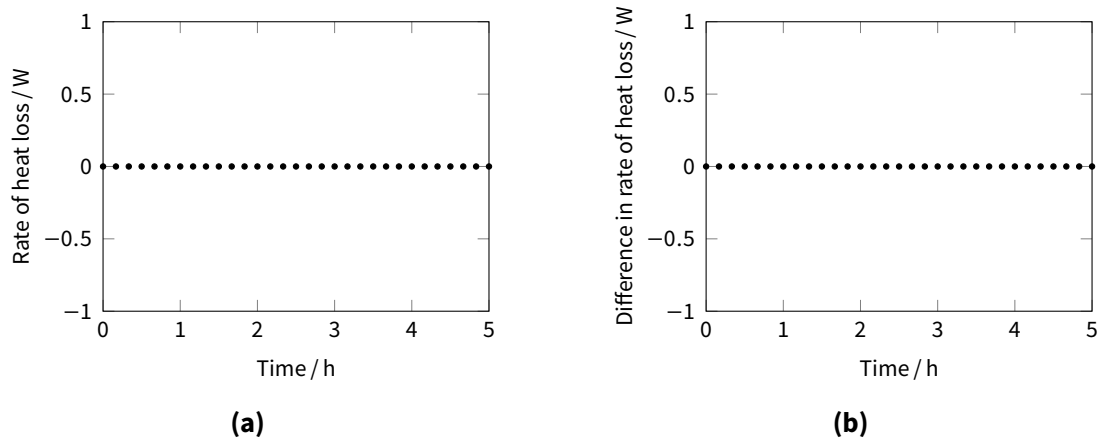
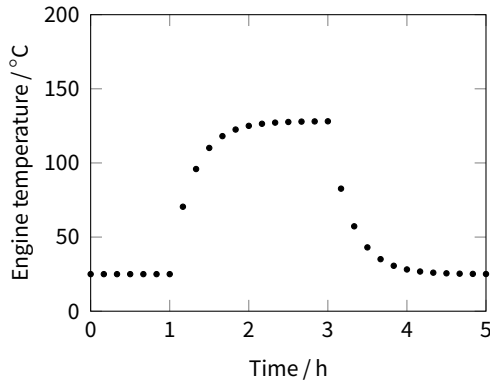


**Figure B.28** | Test case 305 results: heat loss rate as a function of time for (a) case 305 and (b) differential between cases 305 and 301.

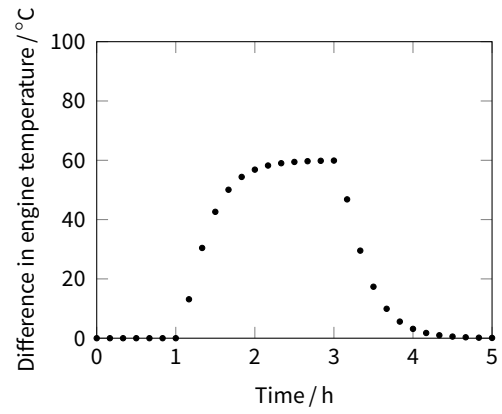
### Test case 306

There is a discrepancy in the specifications for this test. Table III-10 of (2) states that the heat transfer coefficient between the engine and the cooling water control volume should be set to  $20 \text{ W K}^{-1}$  while the text in on page III-60 of (2) states that it should be set to  $100 \text{ W K}^{-1}$ . The model shows exact agreement with the  $20 \text{ W K}^{-1}$  value as shown in Figures B.29 to B.32. It is assumed that this is the intended value for this test case.



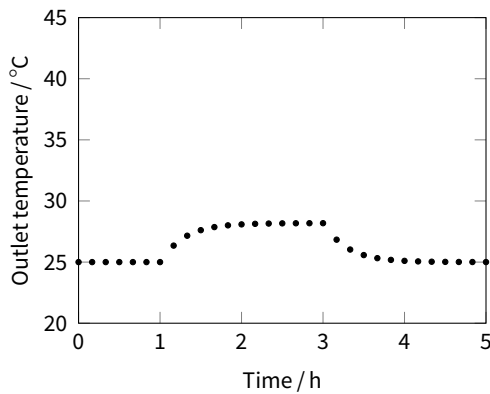


(a)

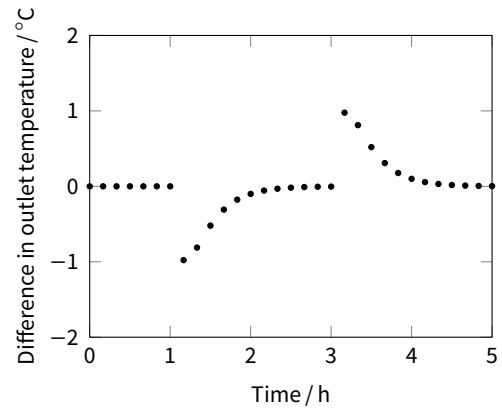


(b)

**Figure B.29** | Test case 306 results: engine temperature as a function of time for (a) case 306 and (b) differential between cases 306 and 301.

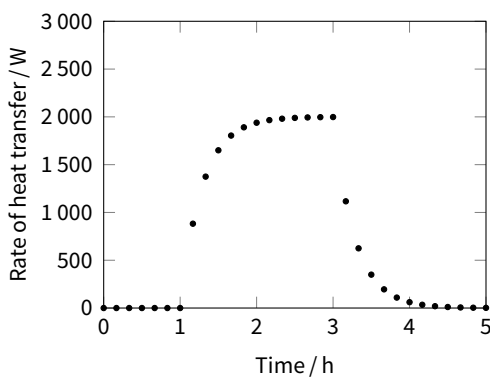


(a)

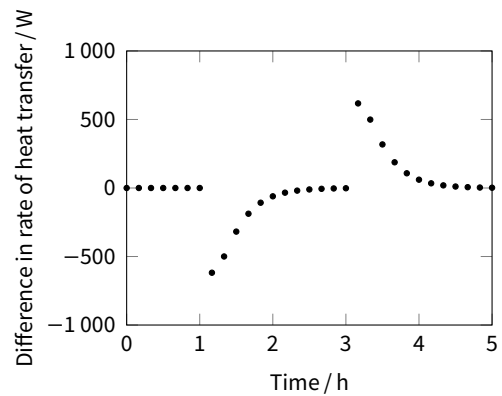


(b)

**Figure B.30** | Test case 306 results: cooling water outlet temperature as a function of time for (a) case 306 and (b) differential between cases 306 and 301.



(a)



(b)

**Figure B.31** | Test case 306 results: heat transfer rate as a function of time for (a) case 306 and (b) differential between cases 306 and 301.



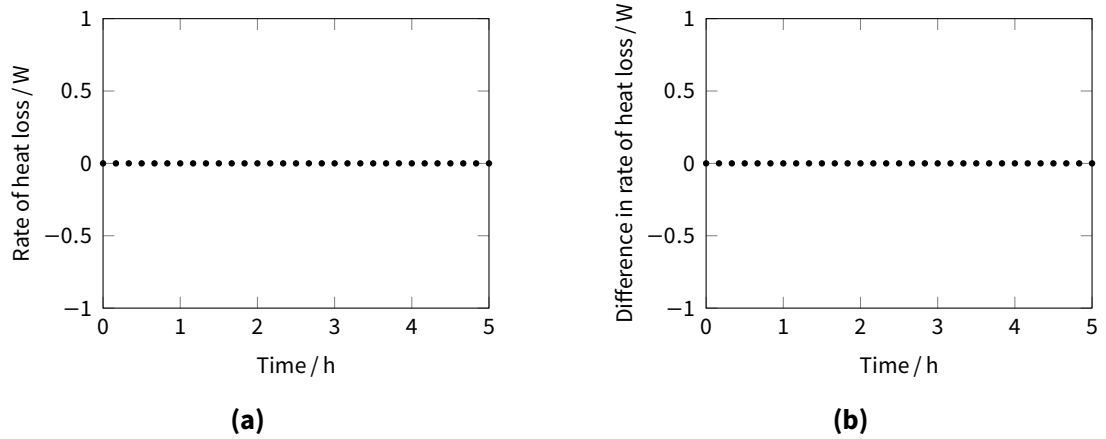


**Figure B.32** | Test case 306 results: heat loss rate as a function of time for (a) case 306 and (b) differential between cases 306 and 301.

### Test case 307

Figures B.33 and B.34 shows the results were in agreement with the other calculation methods.

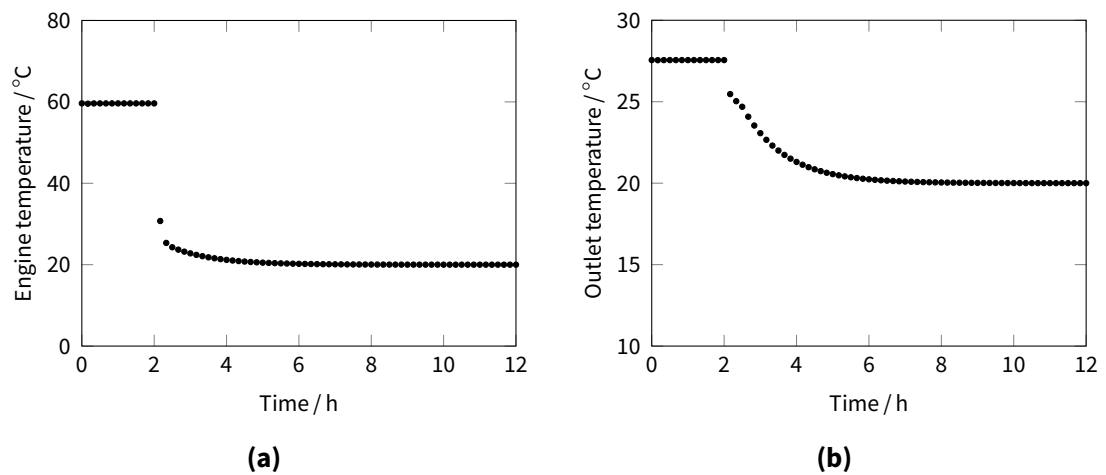


**Figure B.33** | Test case 307 results: (a) engine temperature, and (b) cooling water temperature as functions of time.





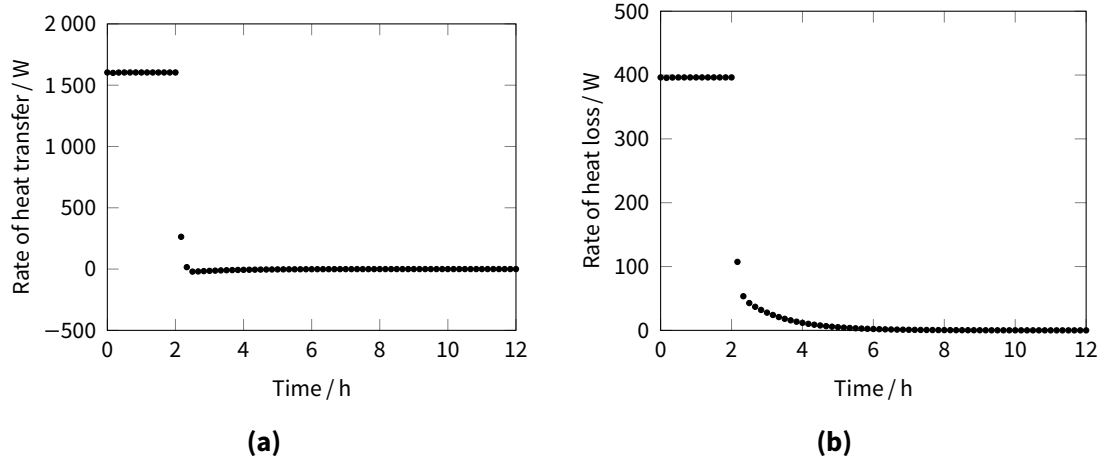


**Figure B.34** | Test case 307 results: Rate of (a) heat transfer and (b) heat loss as functions of time.

### Test case 308

Figures B.35 to B.38 shows the results were in agreement with the other calculation methods.

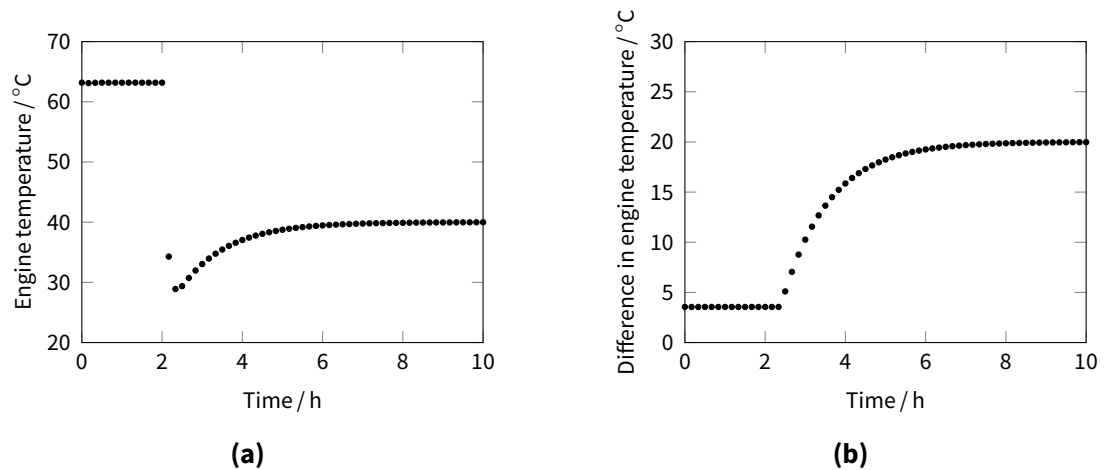


**Figure B.35** | Test case 308 results: engine temperature as a function of time for (a) case 308 and (b) differential between cases 308 and 307.



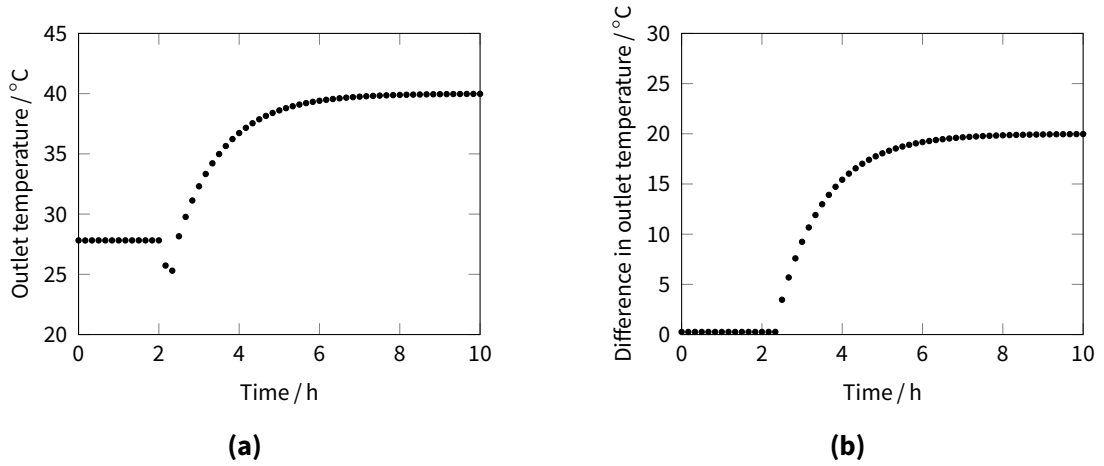


**Figure B.36** | Test case 308 results: cooling water outlet temperature as a function of time for (a) case 308 and (b) differential between cases 308 and 307.

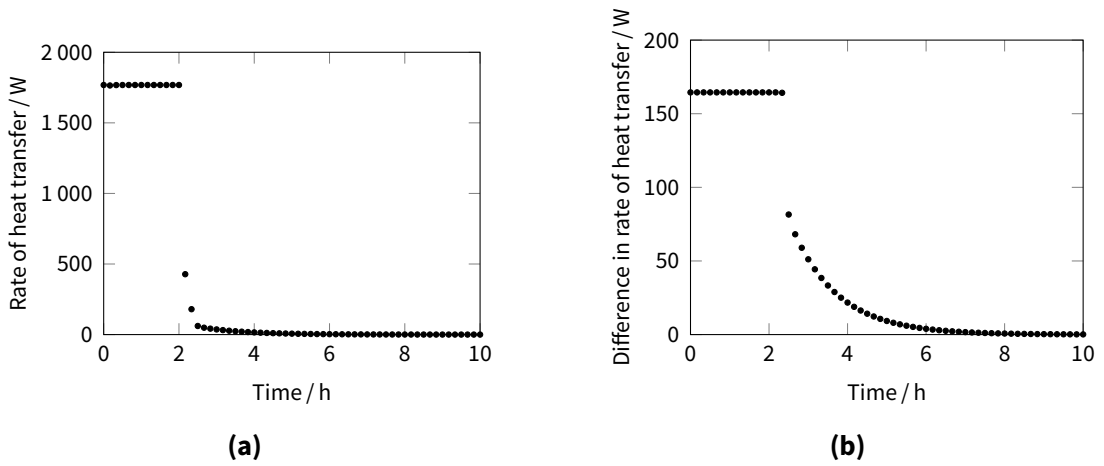


**Figure B.37** | Test case 308 results: heat transfer rate as a function of time for (a) case 308 and (b) differential between cases 308 and 307.

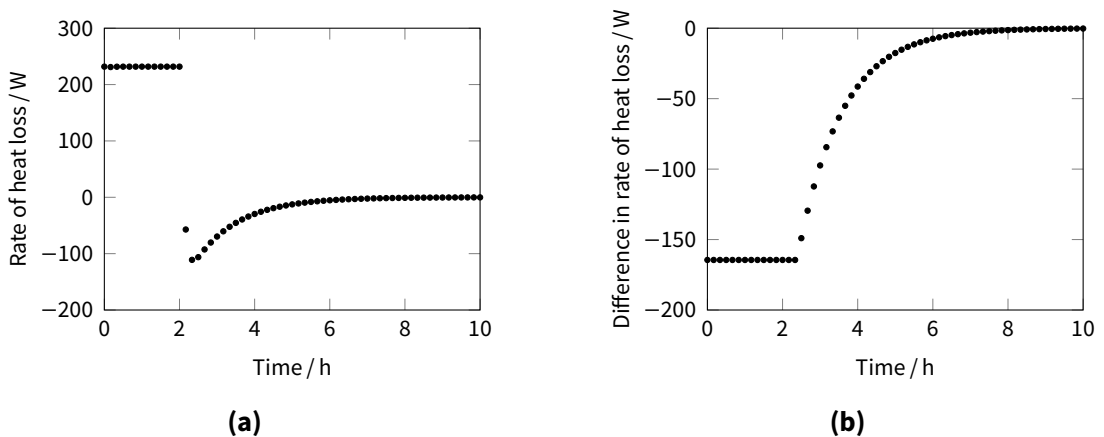


**Figure B.38** | Test case 308 results: heat loss rate as a function of time for (a) case 308 and (b) differential between cases 308 and 307.



**B.1.4 400 series tests**

The 400 series tests are designed to check the model’s treatment of the modes of operation (standby, warm-up, normal, cool-down). In order to directly compare results with ESP-r and TRNSYS, all of these tests use a 10 min time-step and a fixed-step continuous implicit solver to ensure a stable solution at such a large time-step compared to the time constants of the dynamic thermal model.

**Test case 401**

Figures B.39 and B.40 shows the results were in agreement with the other calculation methods.

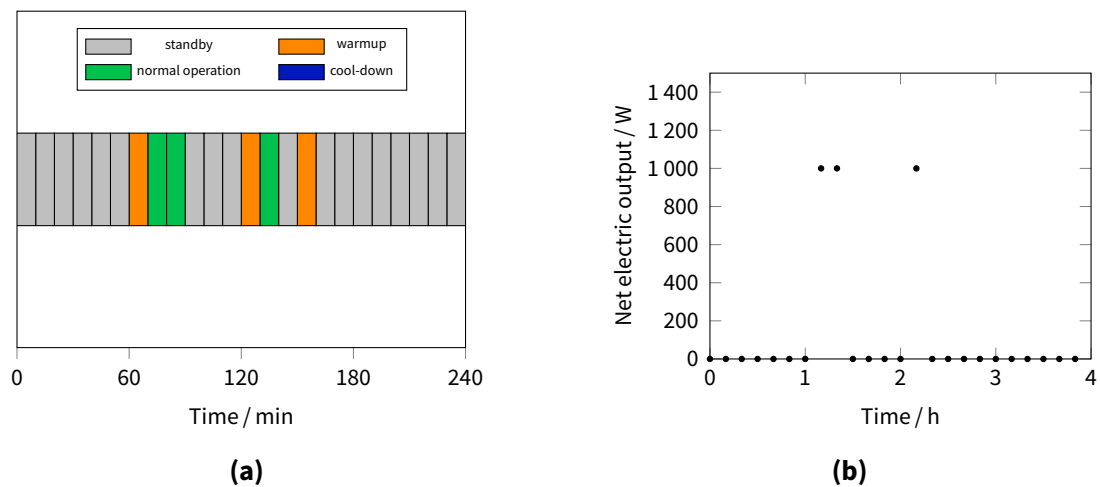


**Figure B.39 | Test case 401 results: (a) time spent in each mode of operation, and (b) net power as a function of time.**

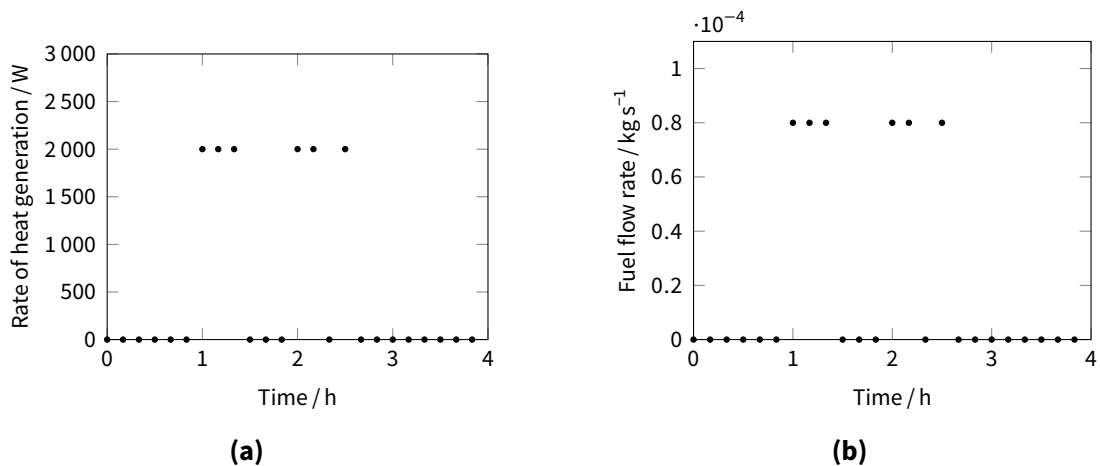


**Figure B.40 | Test case 401 results: (a) rate of heat generation, and (b) fuel flow rate as a functions of time.**



### Test case 402

This test specifies a warm-up period shorter than the simulation time-step. According to the specifications the model may exhibit two possible behaviours: (1) recognise the completion of the warm-up between time steps and calculate a time-averaged rate of fuel consumption, electrical power output and heat generation; (2) assume the unit remains in warm-up for the entire duration of the time step and report the corresponding values. The MATLAB/Simulink implementation here does not support option (1) as continuous mathematical models are used. Therefore the results provided here correspond to behaviour (2). Figures B.41 and B.42 shows the results were in agreement with the other calculation methods with respect to the aforementioned issue.

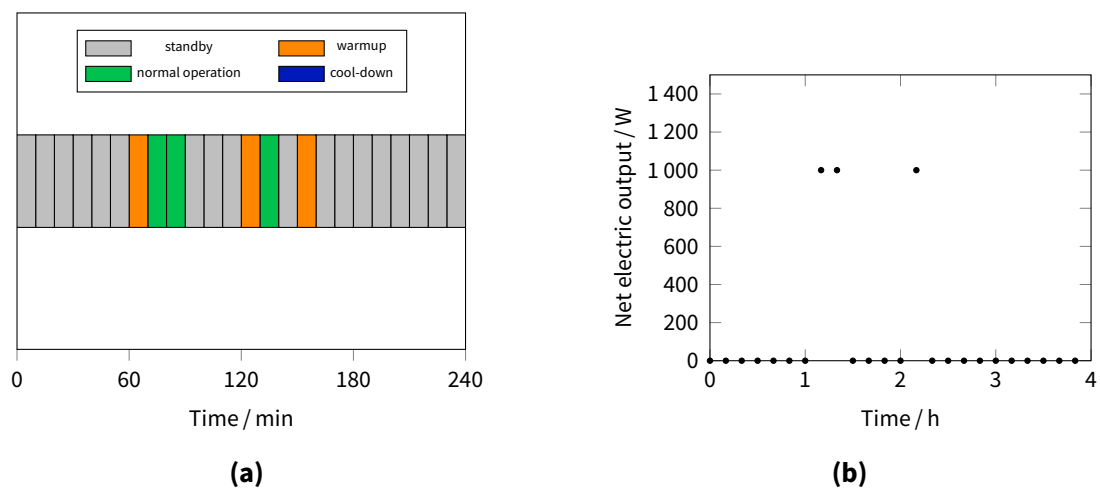


**Figure B.41** | Test case 402 results: (a) time spent in each mode of operation, and (b) net power as a function of time.

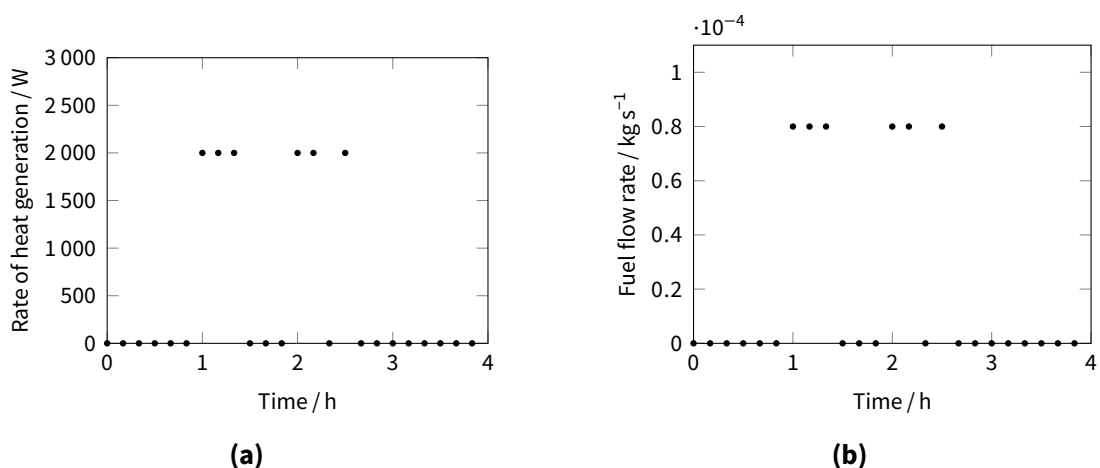


**Figure B.42** | Test case 402 results: (a) rate of heat generation, and (b) fuel flow rate as a function of time.





**Test case 403**

Figures B.43 and B.44 shows the results were in agreement with the other calculation methods.

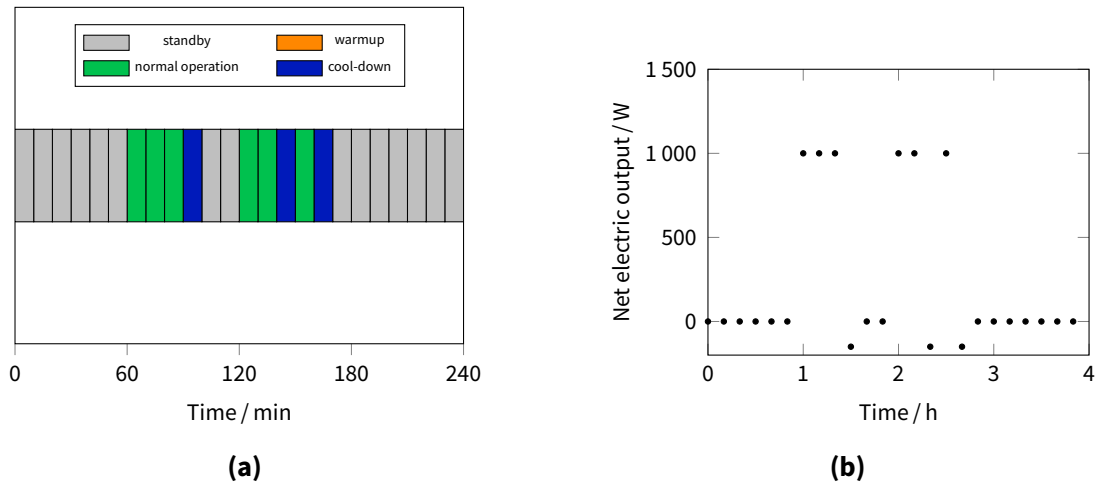


**Figure B.43 | Test case 403 results: (a) time spent in each mode of operation, and (b) net power as a function of time.**

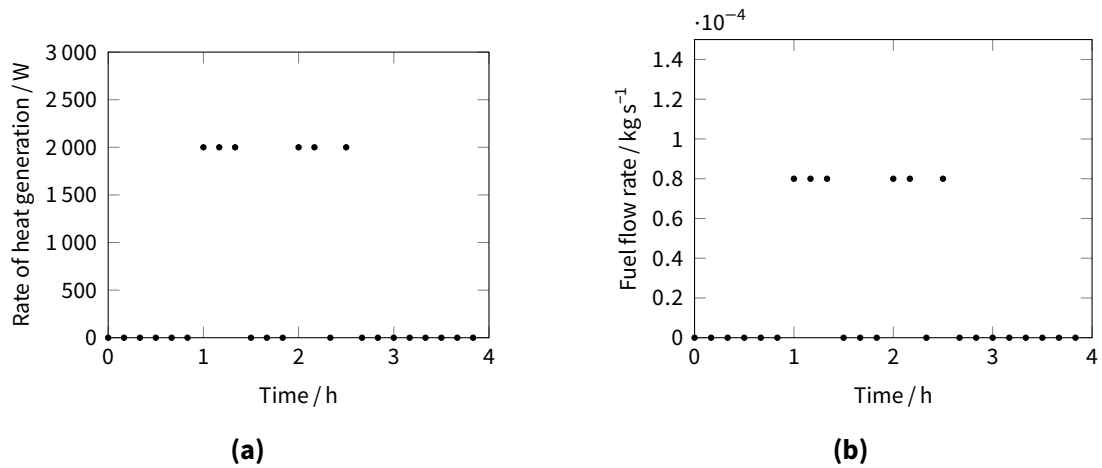


**Figure B.44 | Test case 403 results: (a) rate of heat generation, and (b) fuel flow rate as a function of time.**

**Test case 404**

This test specifies a cool-down period shorter than the simulation time-step, where similar discussion as in test case 402 applies. Figures B.45 and B.46 shows the results were in agreement with the other calculation methods with respect to the aforementioned issue.



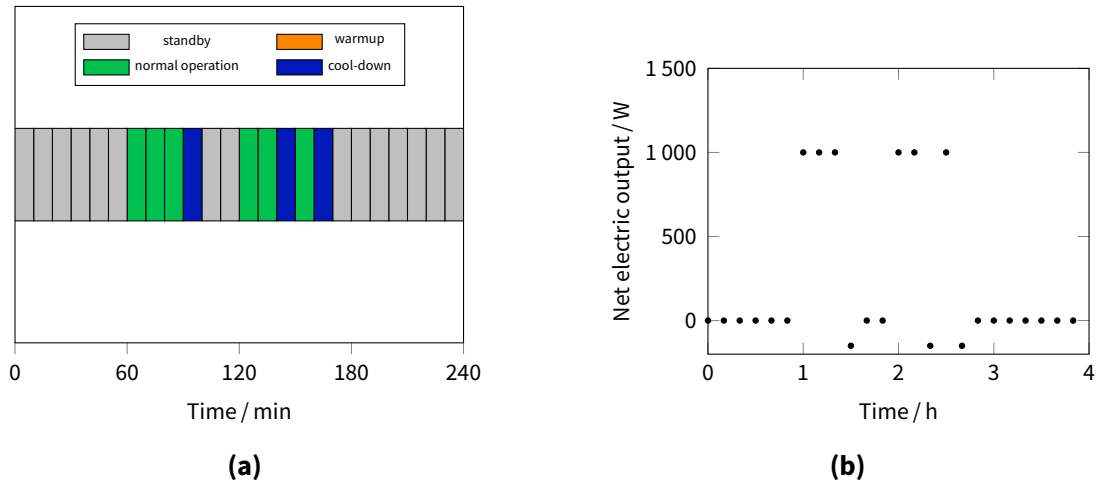


**Figure B.45 | Test case 404 results: (a) time spent in each mode of operation, and (b) net power as a function of time.**

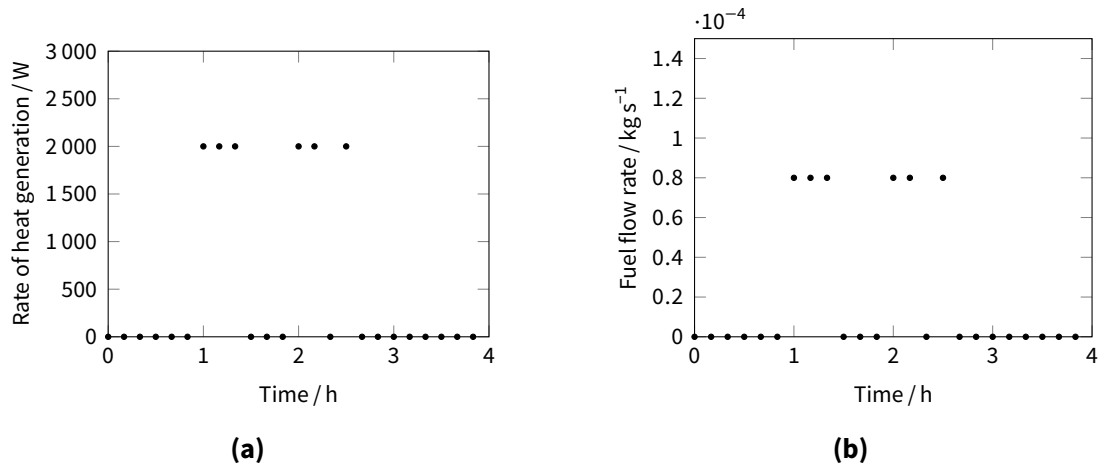


**Figure B.46 | Test case 404 results: (a) rate of heat generation, and (b) fuel flow rate as a function of time.**

**Test case 405**

Figures B.47 and B.48 shows the results were in agreement with the other calculation methods.



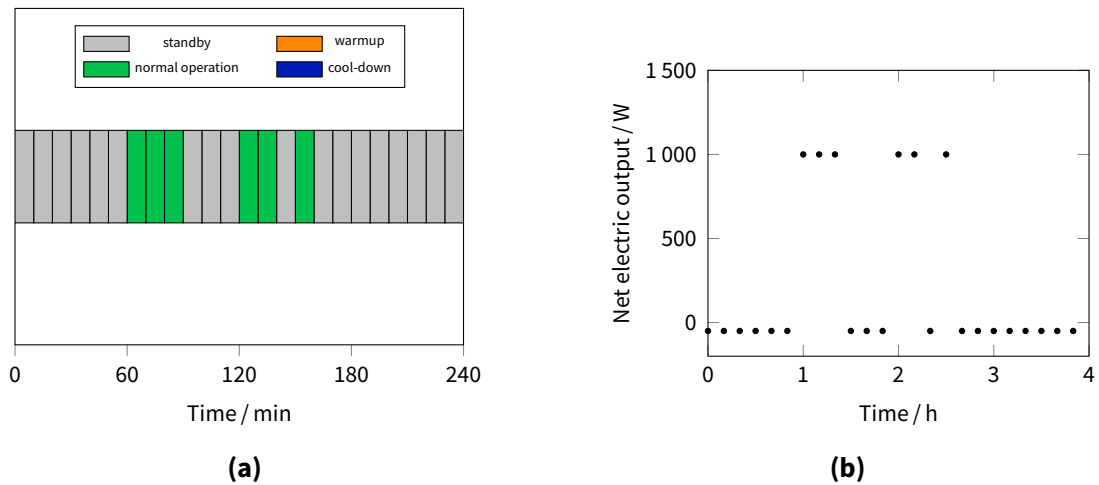


**Figure B.47 | Test case 405 results: (a) time spent in each mode of operation, and (b) net power as a function of time.**

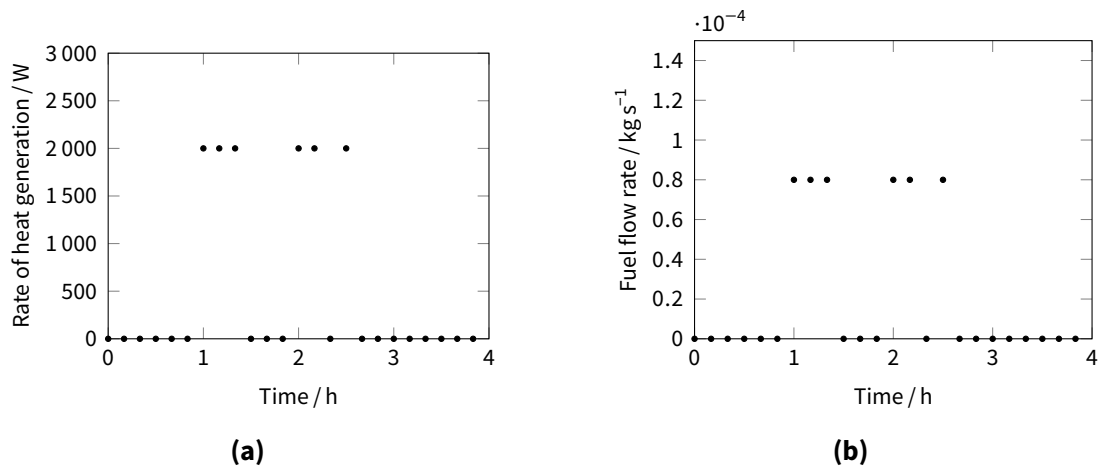


**Figure B.48 | Test case 405 results: (a) rate of heat generation, and (b) fuel flow rate as a function of time.**

### Test case 406

There is a discrepancy in the specifications for this test. Table III-13 of (2) states that the warm-up and cool-down periods be set to 1200 s while the text in on page III-90 of (2) states that it should be set to 600 s. The model shows exact agreement with the 1200 s value as shown in Figures B.49 and B.50. It is assumed that this is the intended value for this test case.



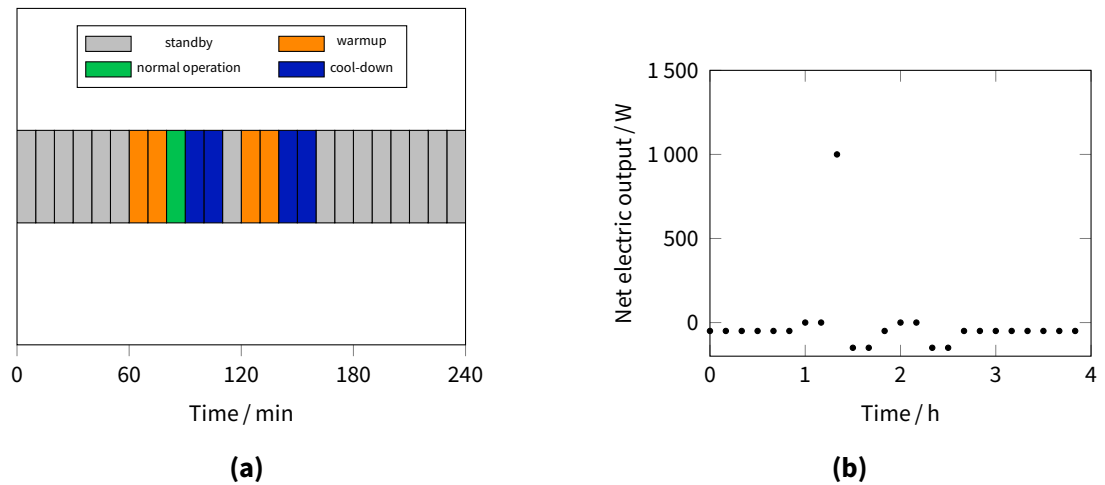


**Figure B.49** | Test case 406 results: (a) time spent in each mode of operation, and (b) net power as a function of time.

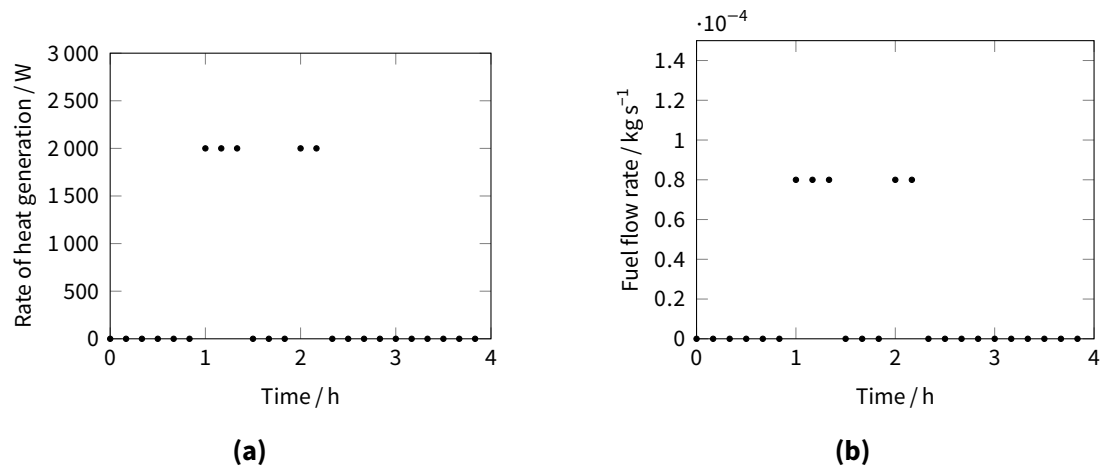


**Figure B.50** | Test case 406 results: (a) rate of heat generation, and (b) fuel flow rate as a function of time.

### Test case 407

As with test cases 402 and 404, this test specifies mode transitions that occur between time steps. Again, this implementation assumes behaviour (2) where no change of mode occurs between time steps. Figures B.51 and B.52 shows the results were in agreement with the other calculation methods with respect to the aforementioned issue.





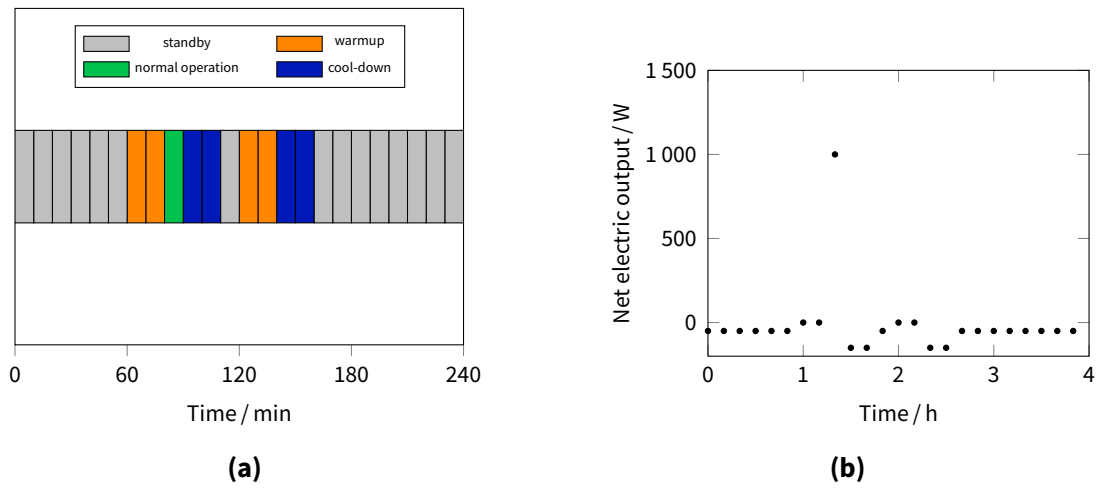


**Figure B.51 | Test case 407 results: (a) time spent in each mode of operation, and (b) net power as a function of time.**

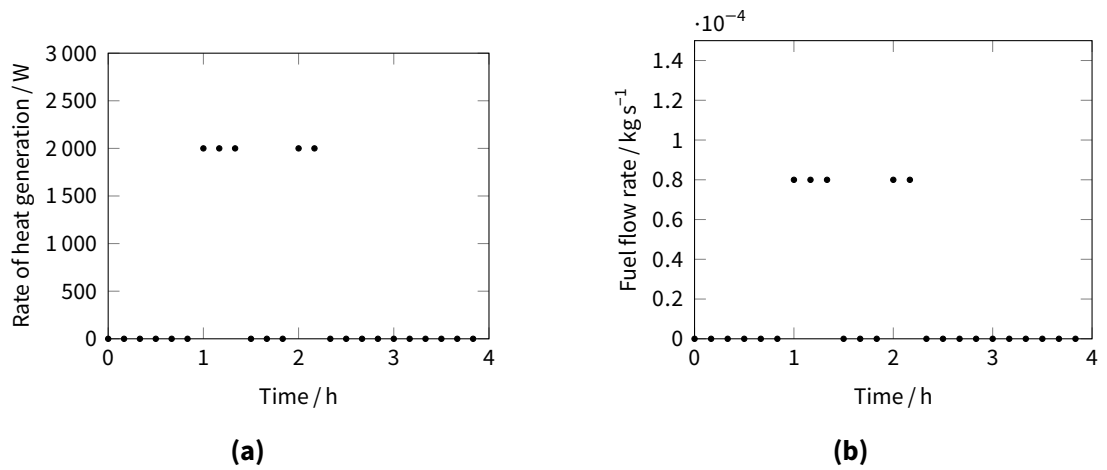


**Figure B.52 | Test case 407 results: (a) rate of heat generation, and (b) fuel flow rate as a function of time.**

### Test case 408

Figures B.53 and B.54 shows the results were in agreement with the other calculation methods.



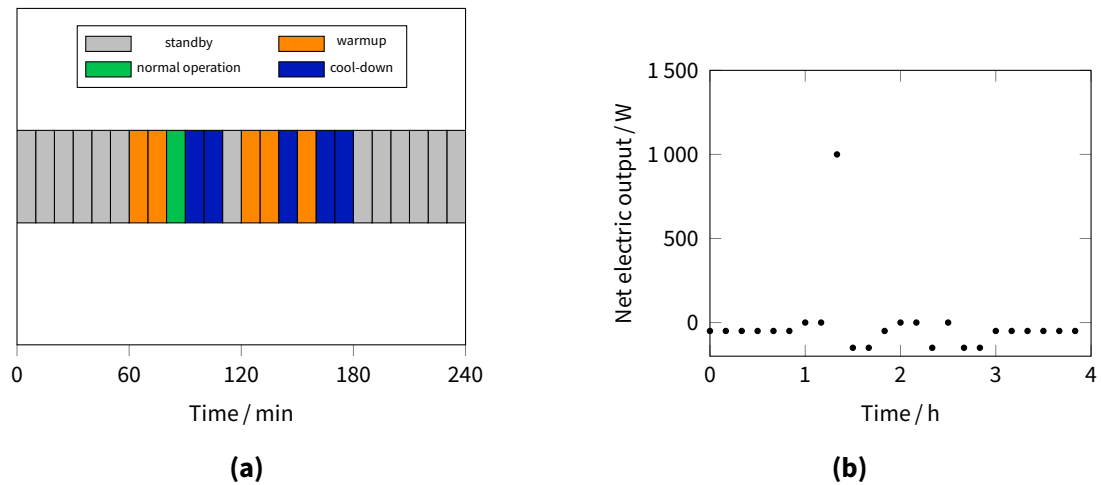


**Figure B.53** | Test case 408 results: (a) time spent in each mode of operation, and (b) net power as a function of time.

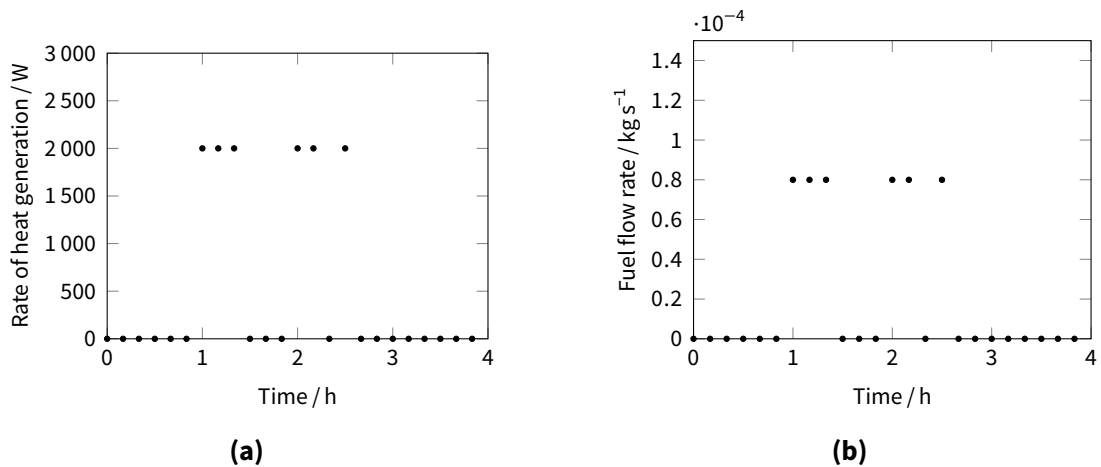


**Figure B.54** | Test case 408 results: (a) rate of heat generation, and (b) fuel flow rate as a function of time.

### B.1.5 500 series tests

The 500 series tests are designed to check the model’s treatment of the Stirling engine warm-up procedure. Specifically, the fuel flow rate and heat & power generation during the warm-up procedure are correlated to the engine block temperature.

#### Test case 501

Figures B.55 to B.57 shows the results were in agreement with the other calculation methods.



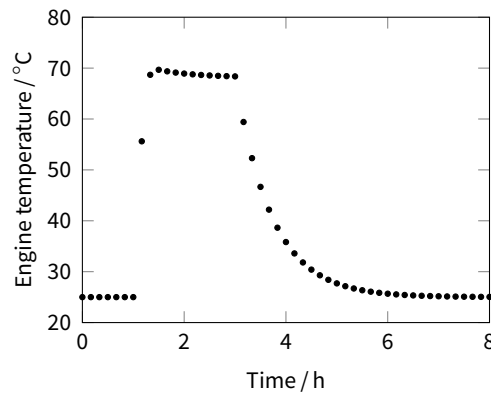


**Figure B.55** | Test case 501: engine control volume temperature as a function of time.

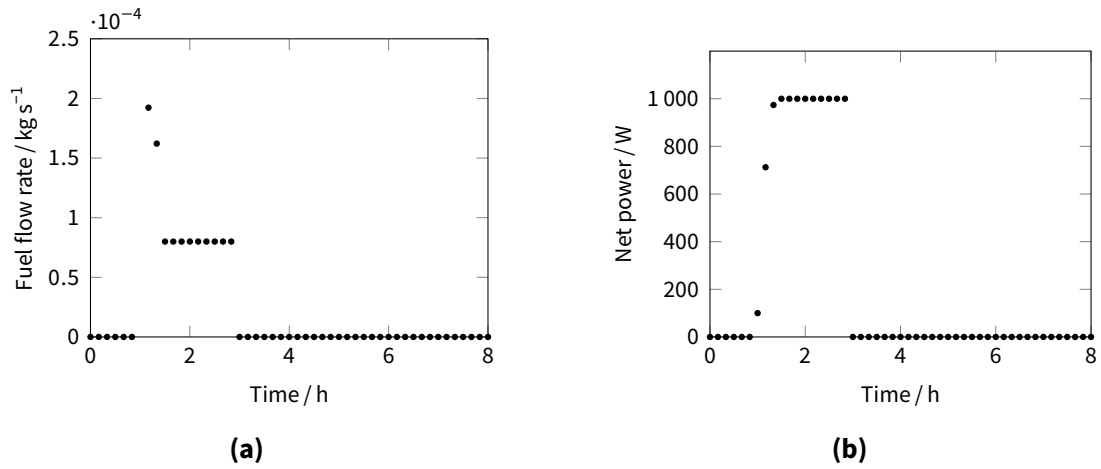


**Figure B.56** | Test case 501 results: (a) fuel flow rate, and (b) net electric output as a function of time.

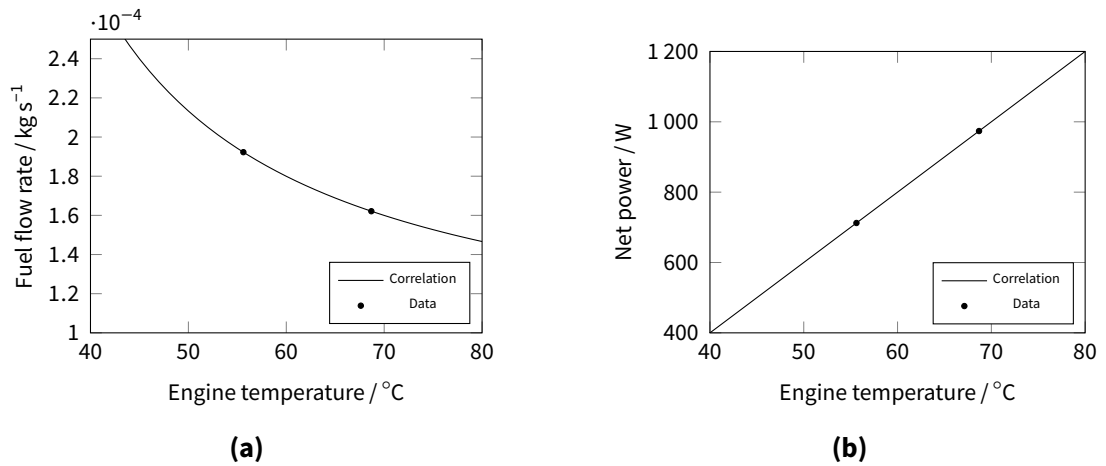


**Figure B.57** | Test case 501 results: (a) fuel flow rate, and (b) net electric output as a functions of engine temperature during warm-up.



Test case 502

Figures B.58 to B.61 shows the results were in agreement with the other calculation methods.

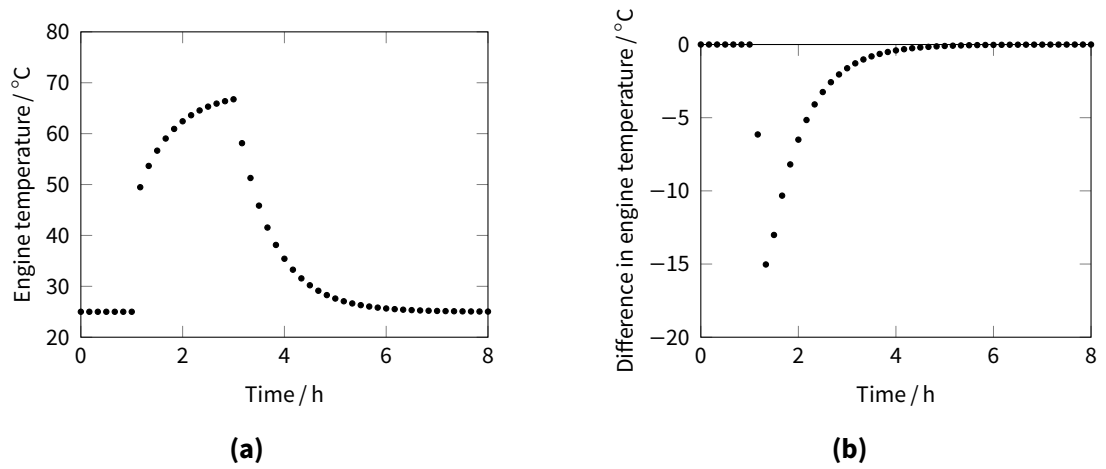


**Figure B.58 |** Test case 502 results: engine temperature as a function of time for (a) case 502, and (b) differential between cases 502 and 501.

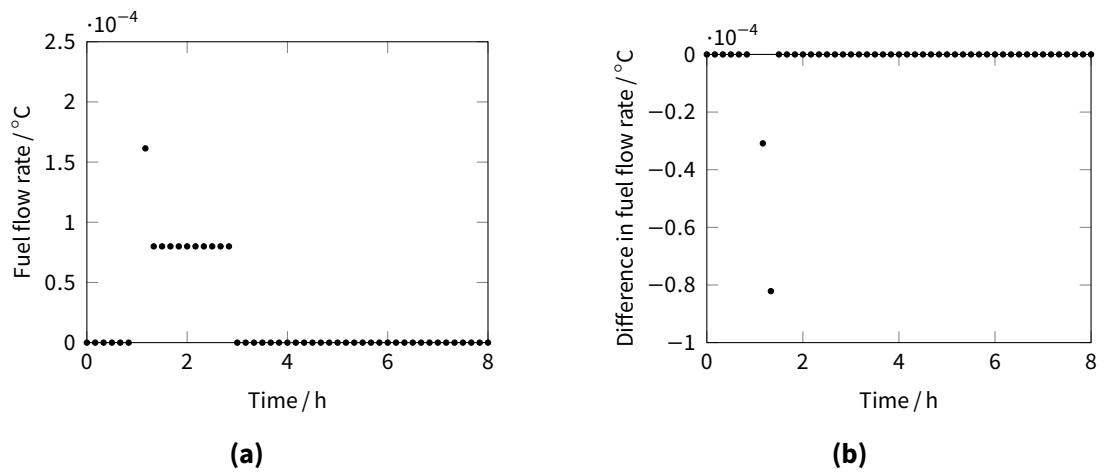


**Figure B.59 |** Test case 502 results: fuel flow rate as a function of time for (a) case 502, and (b) differential between cases 502 and 501.





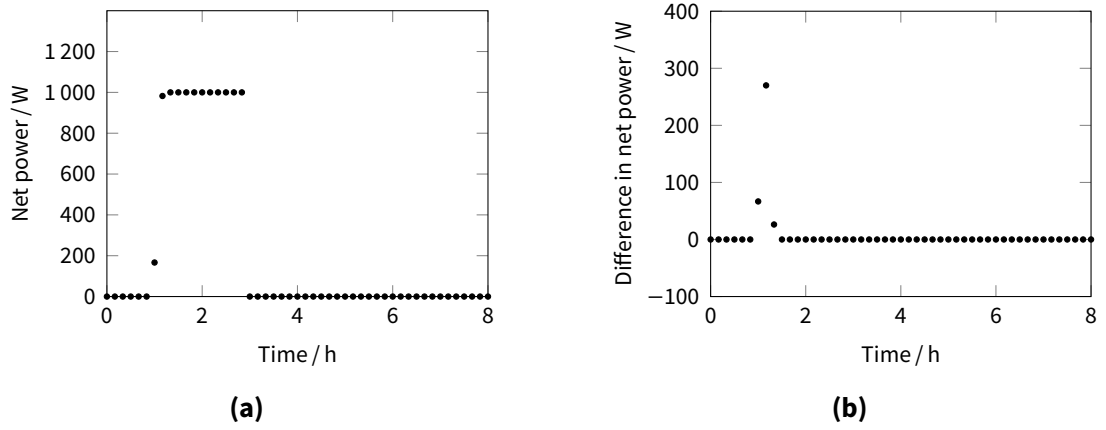


**Figure B.60** | Test case 502 results: net electric output as a function of time for (a) case 502, and (b) differential between cases 502 and 501.

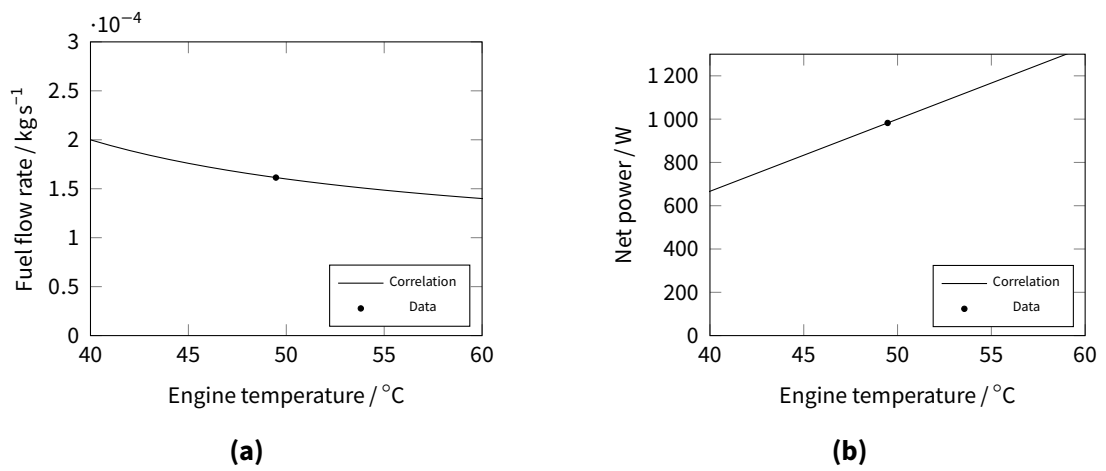


**Figure B.61** | Test case 502 results: (a) fuel flow rate, and (b) net electric output as a functions of engine temperature during warm-up.

### Test case 503

Figures B.62 to B.65 shows the results were in agreement with the other calculation methods.



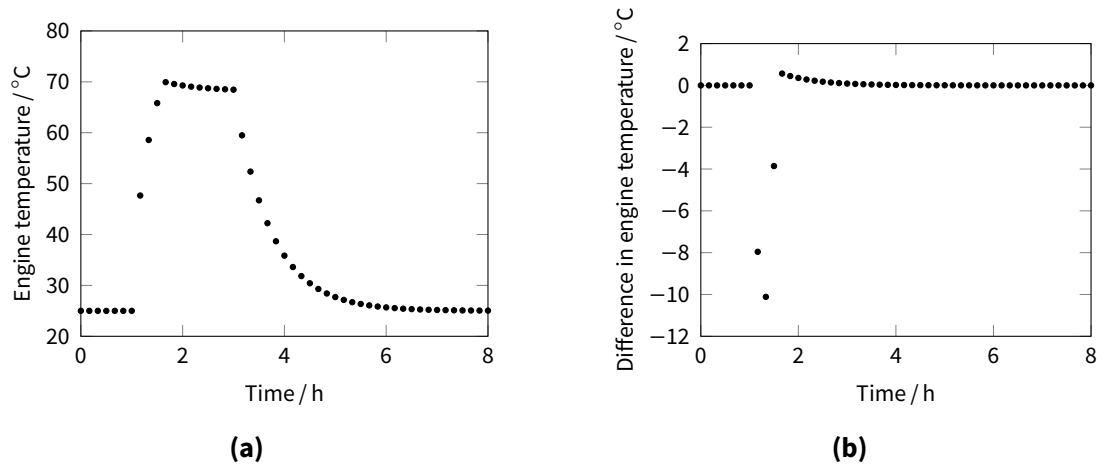


**Figure B.62** | Test case 503 results: engine temperature as a function of time for (a) case 503, and (b) differential between cases 503 and 501.

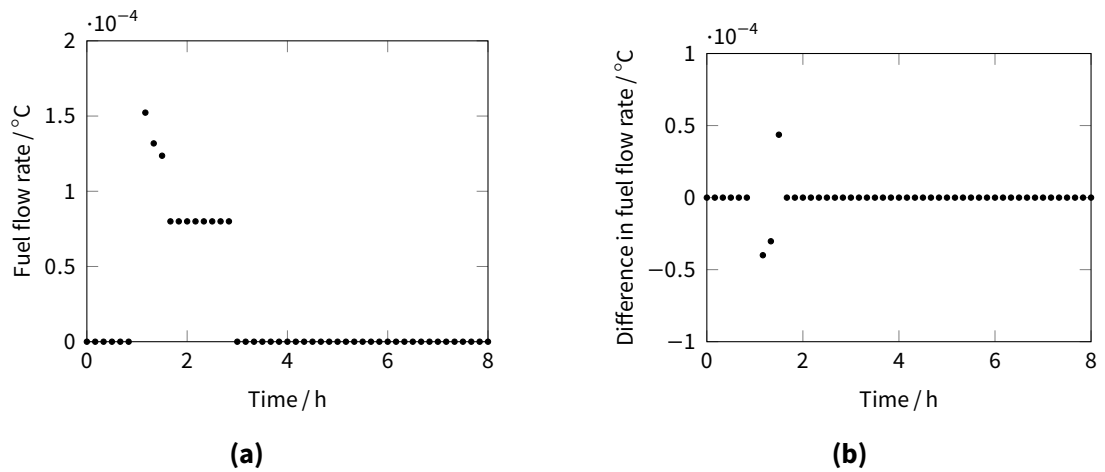


**Figure B.63** | Test case 503 results: fuel flow rate as a function of time for (a) case 503, and (b) differential between cases 503 and 501.

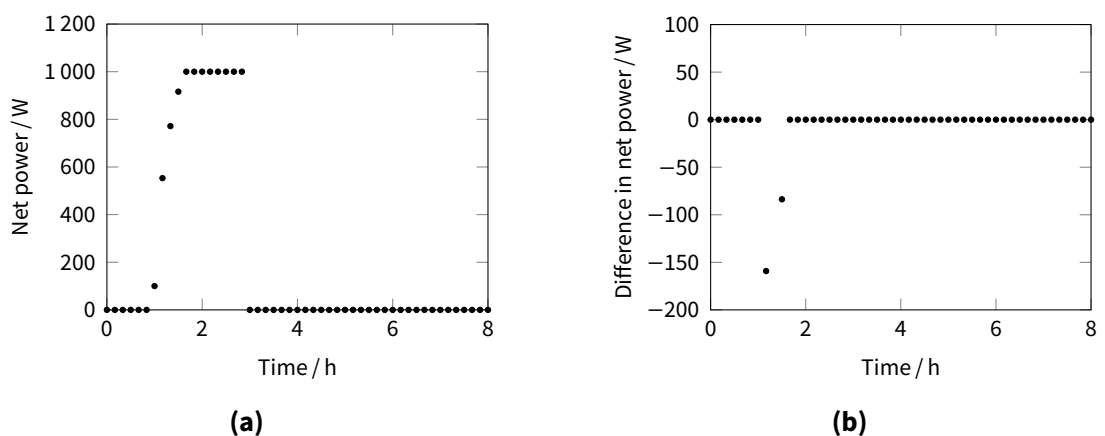
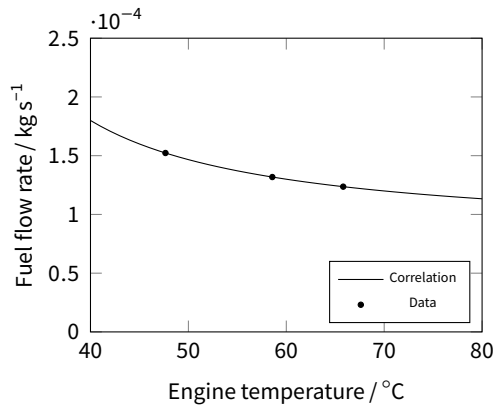
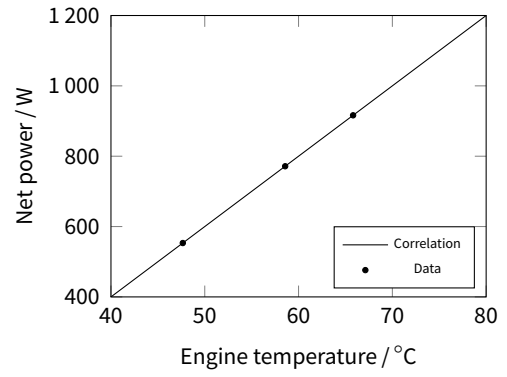


**Figure B.64** | Test case 503 results: net electric output as a function of time for (a) case 503, and (b) differential between cases 503 and 501.





(a)

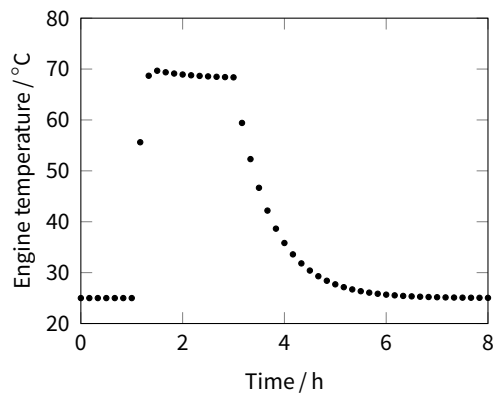


(b)

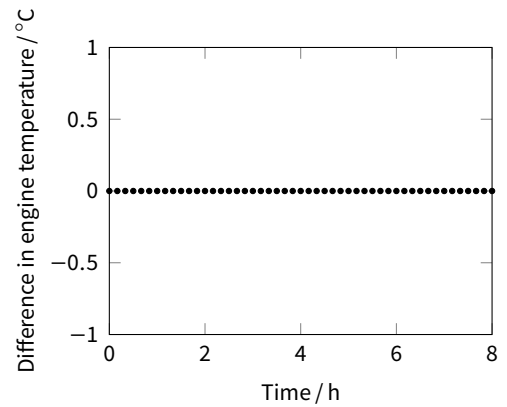
**Figure B.65** | Test case 503 results: (a) fuel flow rate, and (b) net electric output as a functions of engine temperature during warm-up.

**Test case 504**

Figures B.66 to B.69 shows the results were in agreement with the other calculation methods.



(a)



(b)

**Figure B.66** | Test case 504 results: engine temperature as a function of time for (a) case 504, and (b) differential between cases 504 and 501.



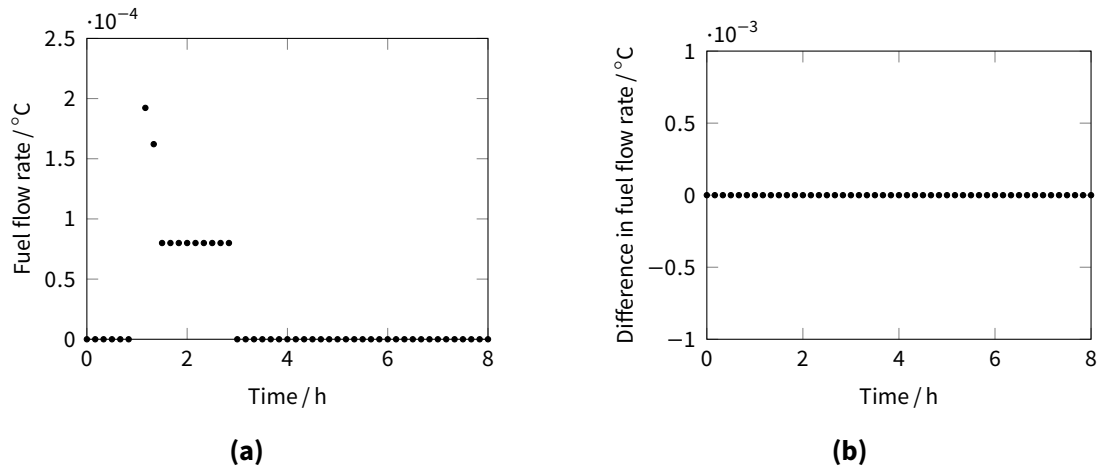


**Figure B.67** | Test case 504 results: fuel flow rate as a function of time for (a) case 504, and (b) differential between cases 504 and 501.

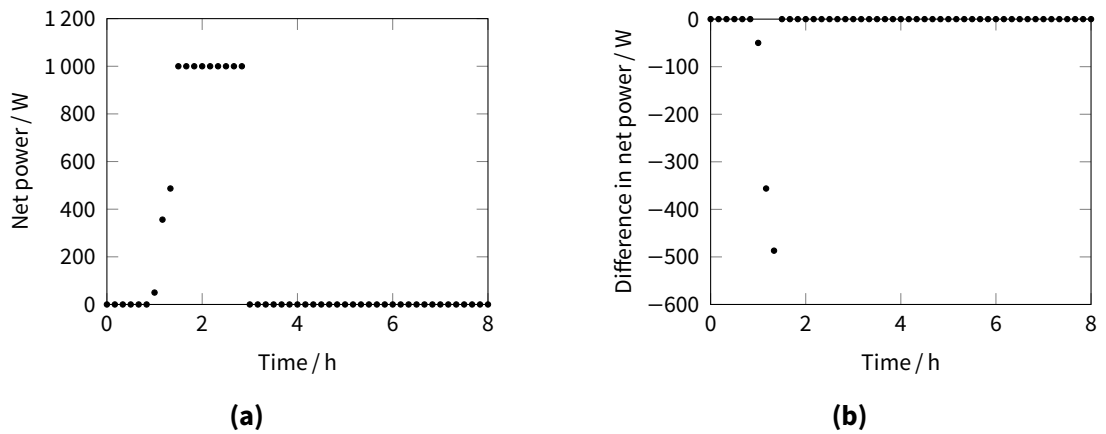


**Figure B.68** | Test case 504 results: net electric output as a function of time for (a) case 504, and (b) differential between cases 504 and 501.

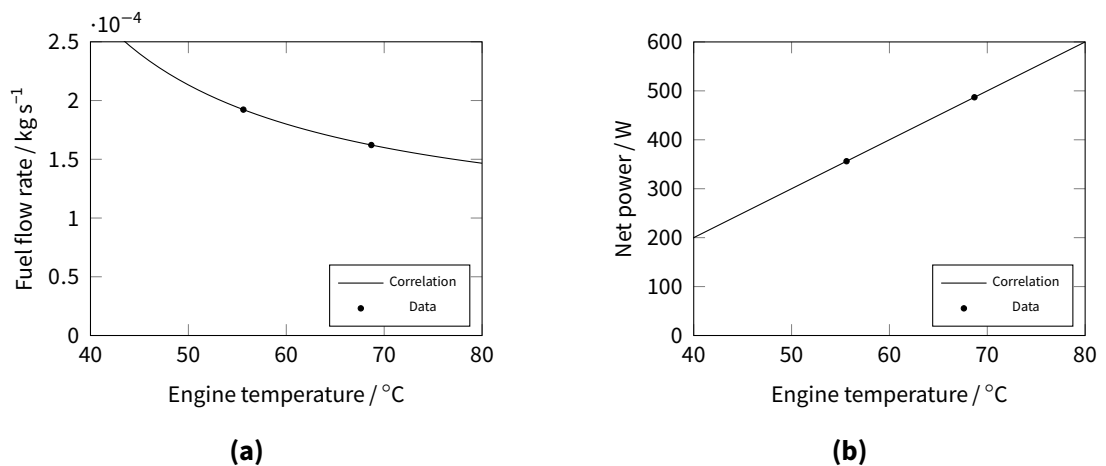


**Figure B.69** | Test case 504 results: (a) fuel flow rate, and (b) net electric output as a functions of engine temperature during warm-up.





### Test case 505

Figures B.70 to B.73 shows the results were in agreement with the other calculation methods.

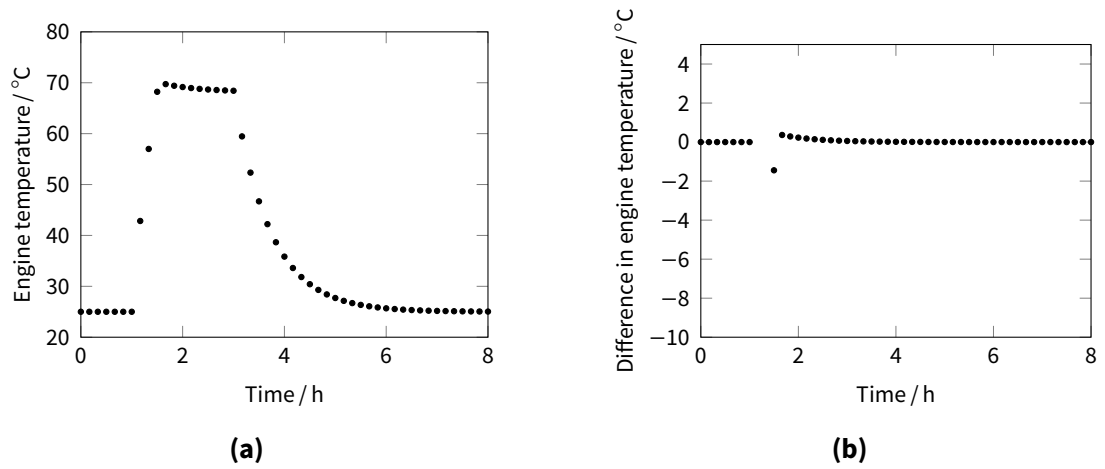


**Figure B.70** | Test case 505 results: engine temperature as a function of time for (a) case 505, and (b) differential between cases 505 and 501.

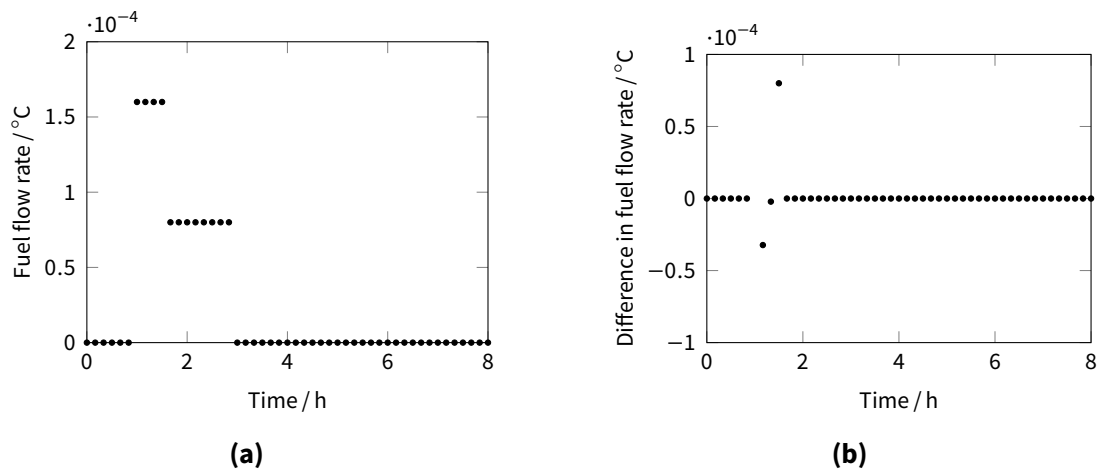


**Figure B.71** | Test case 505 results: fuel flow rate as a function of time for (a) case 505, and (b) differential between cases 505 and 501.



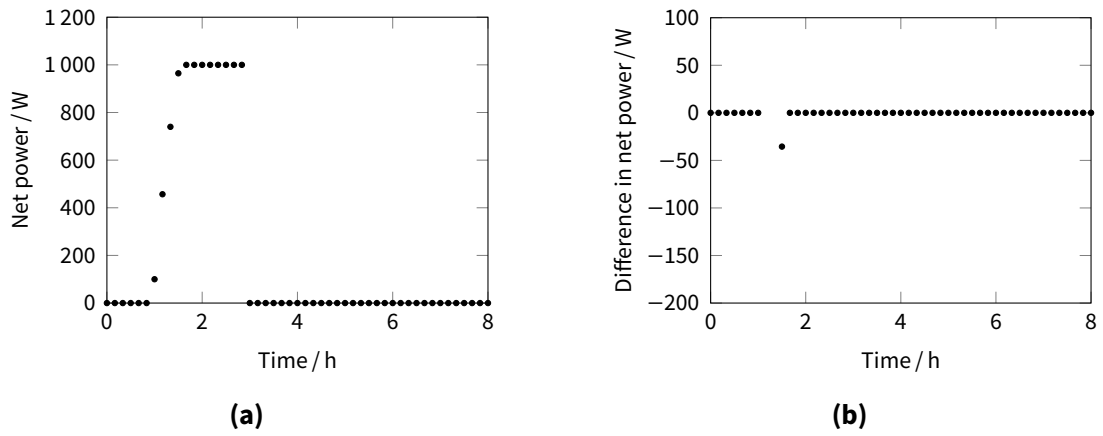


**Figure B.72** | Test case 505 results: net electric output as a function of time for (a) case 505, and (b) differential between cases 505 and 501.

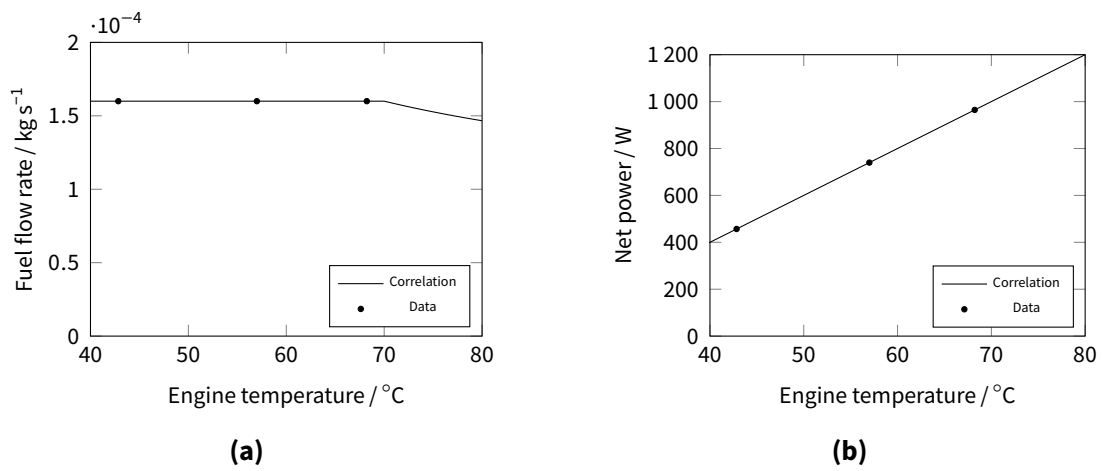


**Figure B.73** | Test case 505 results: (a) fuel flow rate, and (b) net electric output as a functions of engine temperature during warm-up.

### Test case 506

Figures B.74 to B.77 shows the results were in agreement with the other calculation methods.



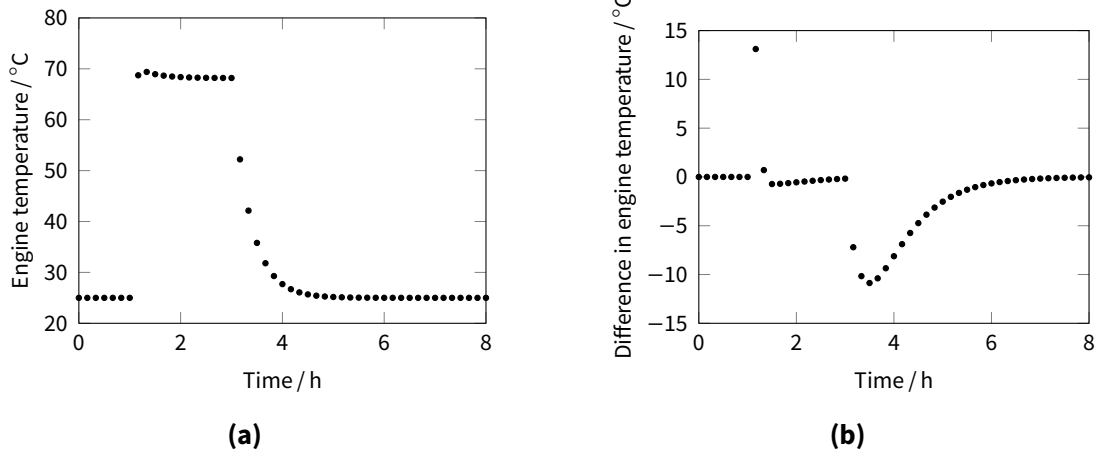


**Figure B.74** | Test case 506 results: engine temperature as a function of time for (a) case 506, and (b) differential between cases 506 and 501.

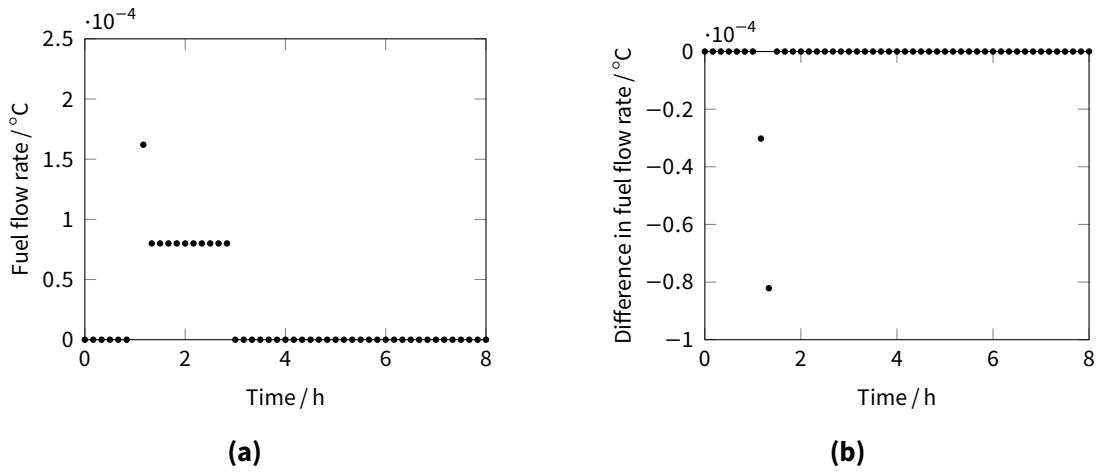


**Figure B.75** | Test case 506 results: fuel flow rate as a function of time for (a) case 506, and (b) differential between cases 506 and 501.

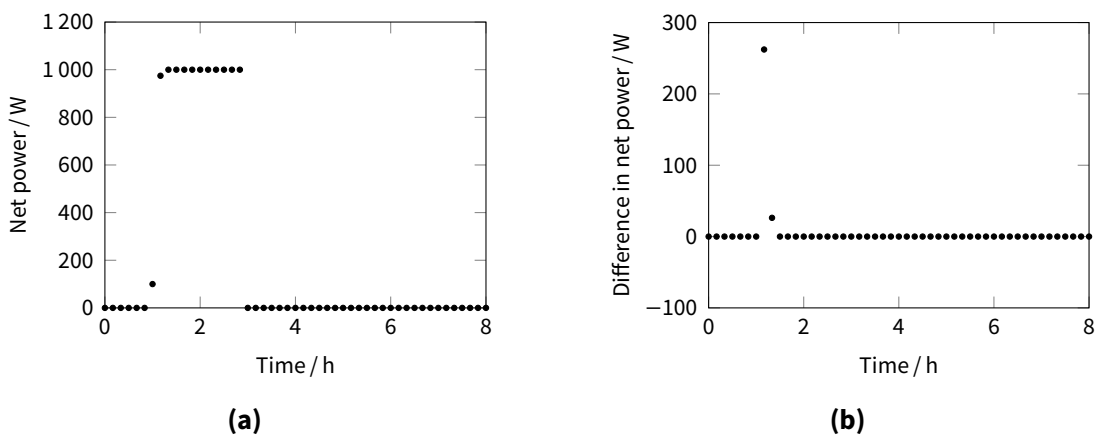


**Figure B.76** | Test case 506 results: net electric output as a function of time for (a) case 506, and (b) differential between cases 506 and 501.



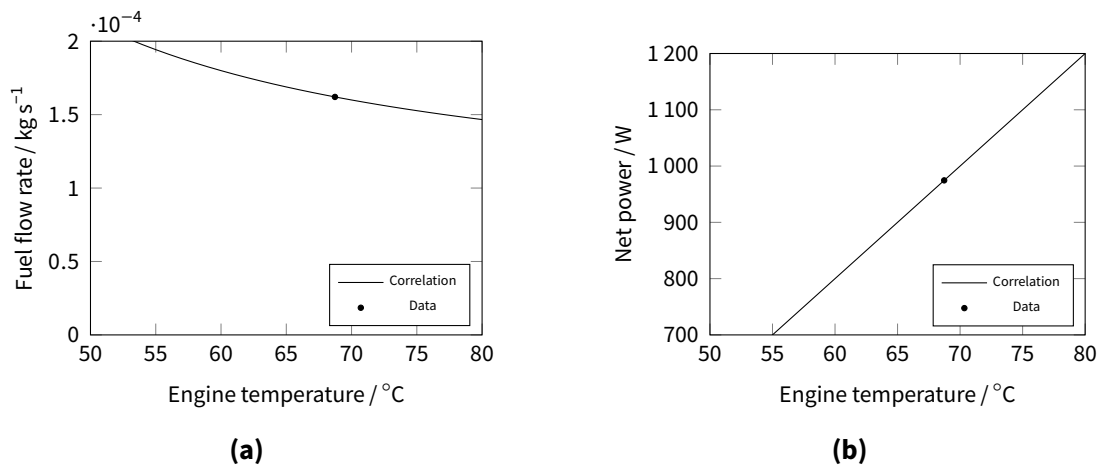


**Figure B.77** | Test case 506 results: (a) fuel flow rate, and (b) net electric output as a functions of engine temperature during warm-up.

**B.1.6 600 series tests**

The 600 series tests are designed to check the model’s ability to limit the rate-of-change of the fuel flow rate and electrical power output. The electrical power output is limited by restricting the change in the control signal sent to the model. The fuel flow rate limitations are imposed by the cogeneration model’s final control elements.

**Test case 601**

Figure B.78 shows the results were in agreement with the other calculation methods.

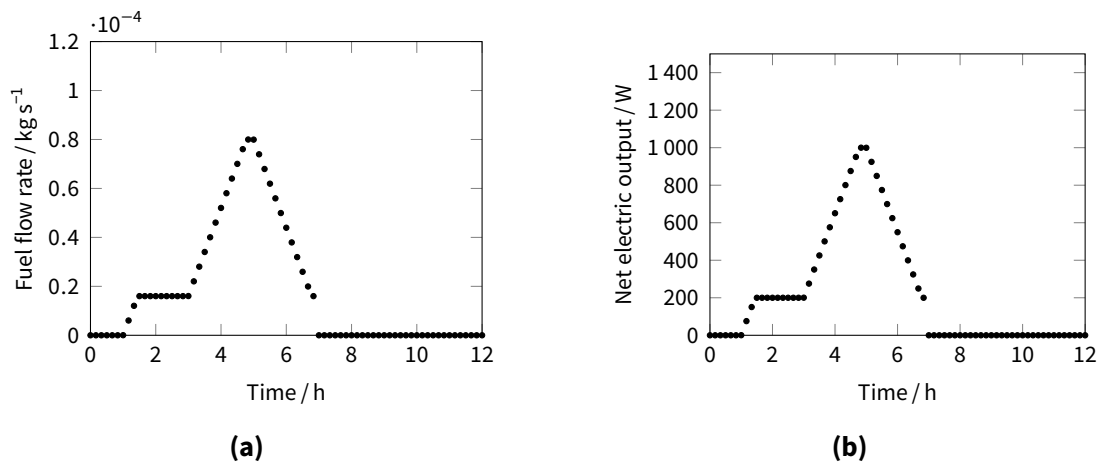


**Figure B.78** | Test case 601 results (a) fuel flow rate, and (b) net electric output as a function of time.





### Test case 602

Figure B.79 shows the results were in agreement with the other calculation methods.

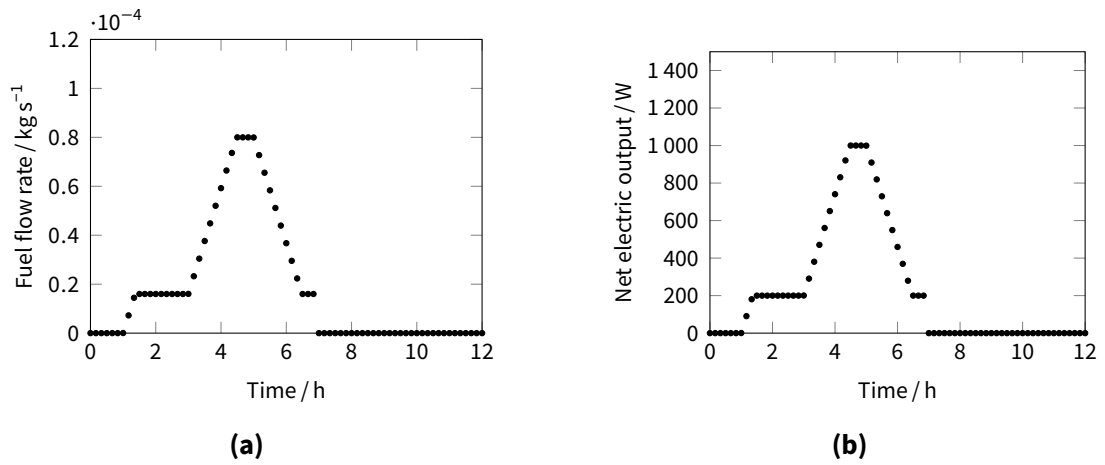


**Figure B.79** | Test case 602 results (a) fuel flow rate, and (b) net electric output as a function of time.

### Test case 603

Figure B.80 shows the results were in agreement with the other calculation methods.

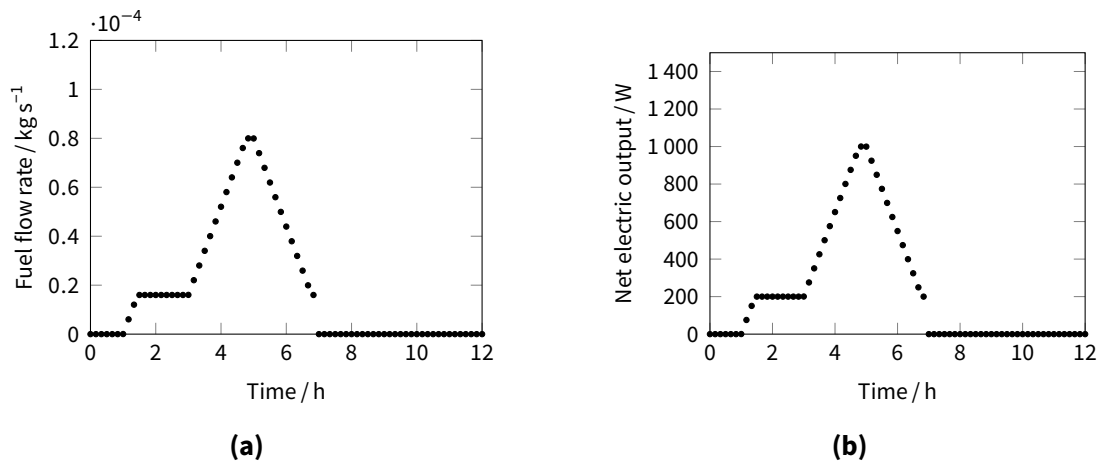


**Figure B.80** | Test case 603 results (a) fuel flow rate, and (b) net electric output as a function of time.

### Test case 604

Figure B.81 shows the results were in agreement with the other calculation methods.



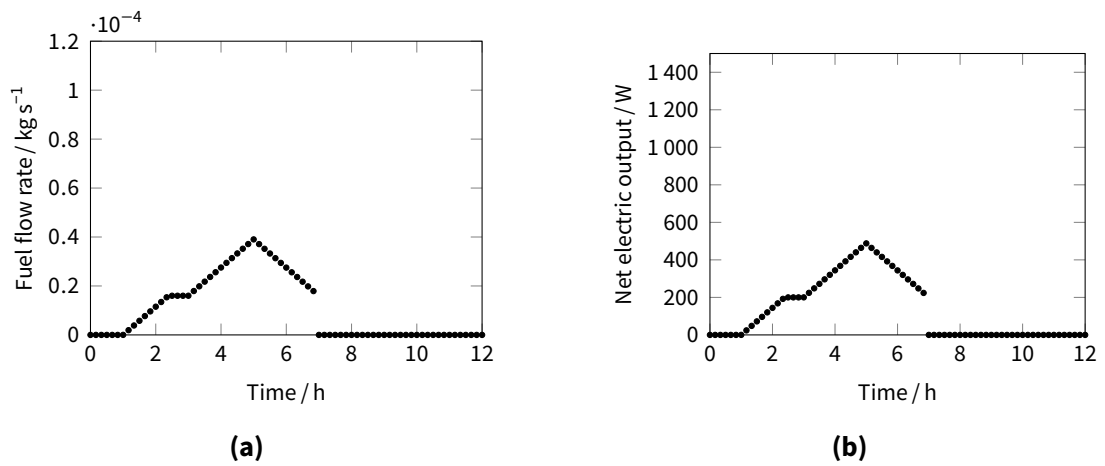


**Figure B.81** | Test case 604 results (a) fuel flow rate, and (b) net electric output as a function of time.

### B.1.7 700 series tests

The 700 series tests are designed to check the model's implementation of the low-level controls, which protect the unit from overheating when the cooling water temperature is too high, or the flow of the cooling water is interrupted.

#### Test case 701

Figures B.82 and B.83 shows the results were in agreement with the other calculation methods.

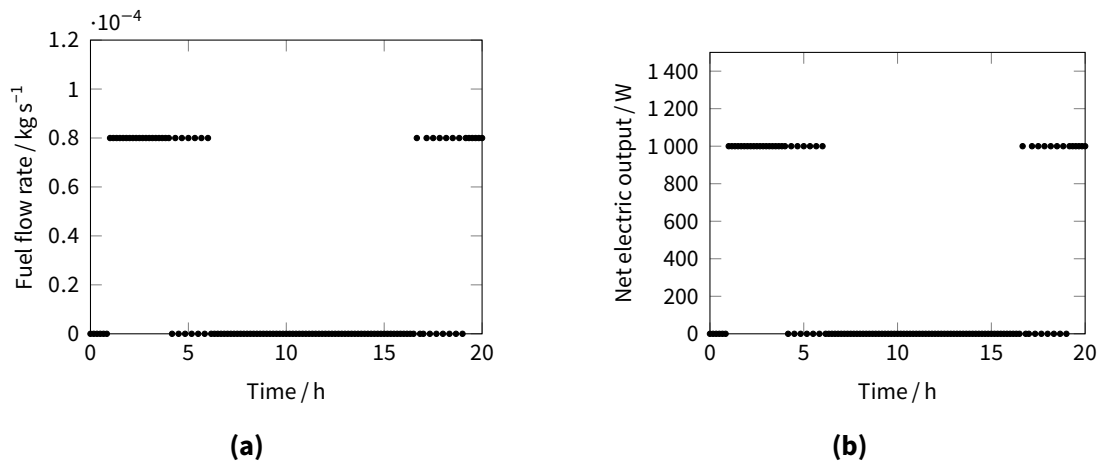


**Figure B.82** | Test case 701 results: (a) fuel flow rate, and (b) net electric output as a function of time.



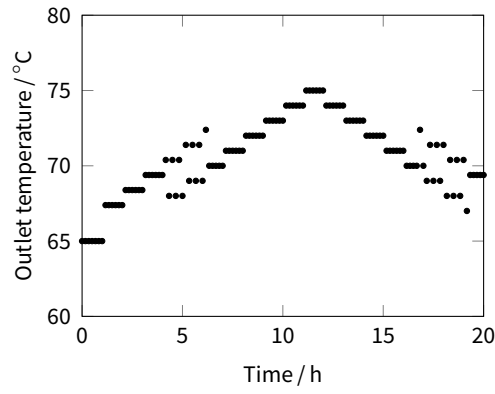


Figure B.83 | Test case 701 results: cooling water outlet temperature as a function of time.

Test case 702

Figures B.84 and B.85 shows the results were in agreement with the other calculation methods.

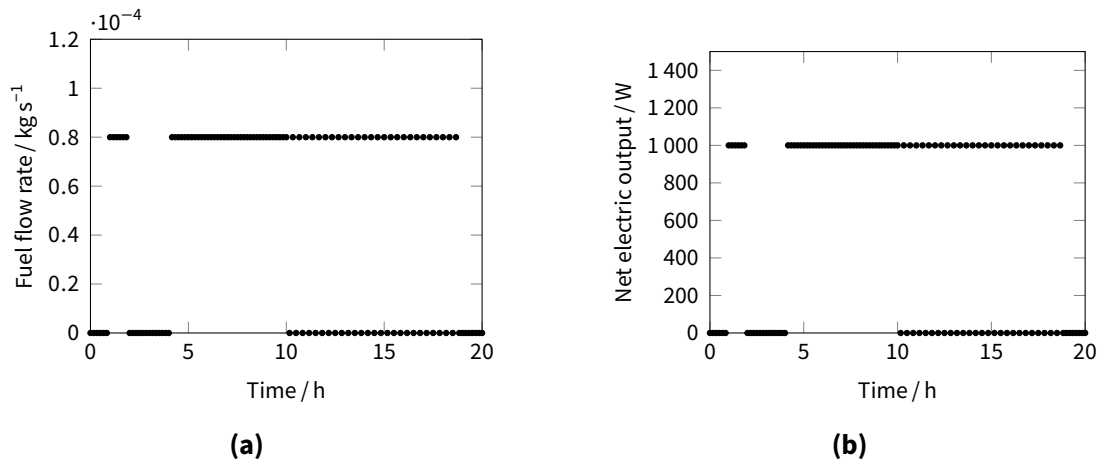


Figure B.84 | Test case 702 results (a) fuel flow rate, and (b) net electric output as a function of time.

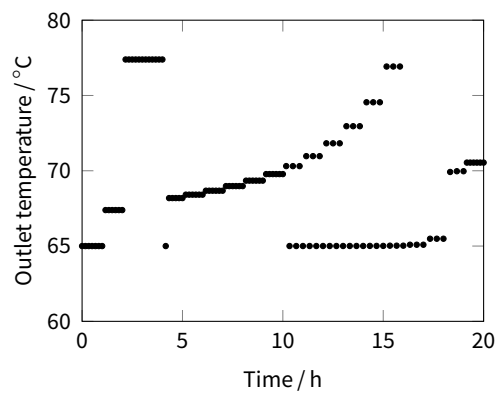


Figure B.85 | Test case 702 results: cooling water outlet temperature as a function of time.



### B.1.8 800 series tests

The 800 series tests are designed to check the model's implementation of the dimensionless control signal interface. While this work does not utilise the Annex 42's control interface, this has been implemented in the MATLAB/Simulink model for completion.

#### Test case 801

Figure B.86 shows the results were in agreement with the other calculation methods.

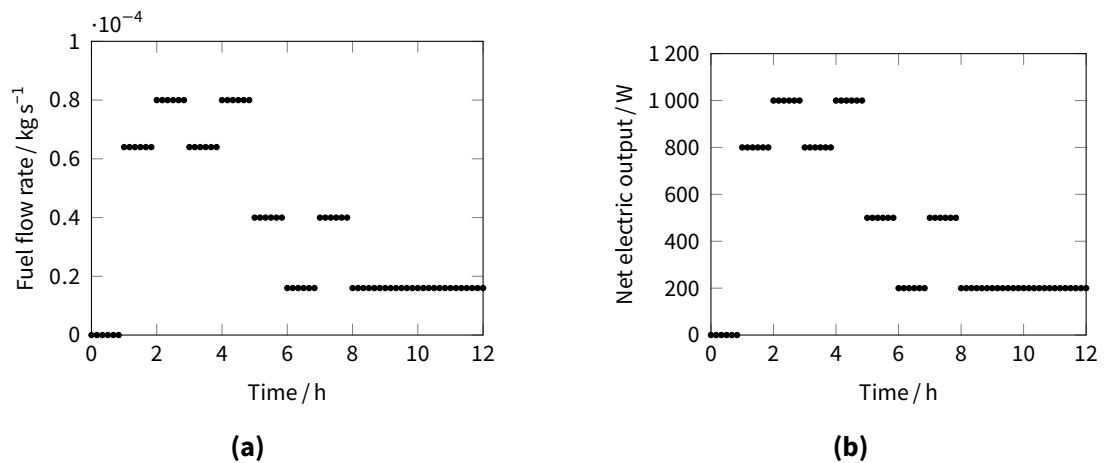


**Figure B.86** | Test case 801 results (a) fuel flow rate, and (b) net electric output as a function of time.

#### Test case 802

Figure B.87 shows the results were in agreement with the other calculation methods.

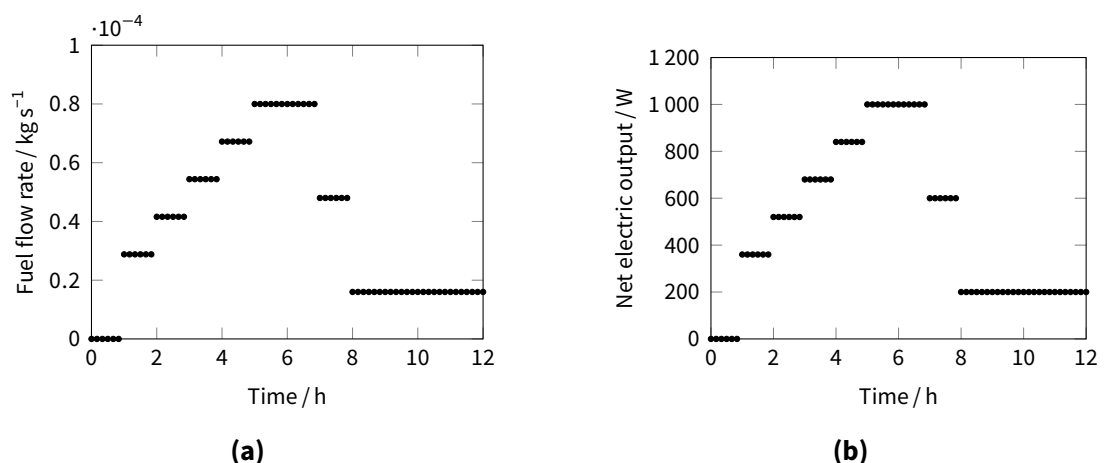


**Figure B.87** | Test case 802 results (a) fuel flow rate, and (b) net electric output as a function of time.





**B.1.9 900 series tests**

The 900 series tests are designed to check the model’s emissions calculations.

**Test case 901**

Figure B.88 shows the results were in agreement with the other calculation methods.

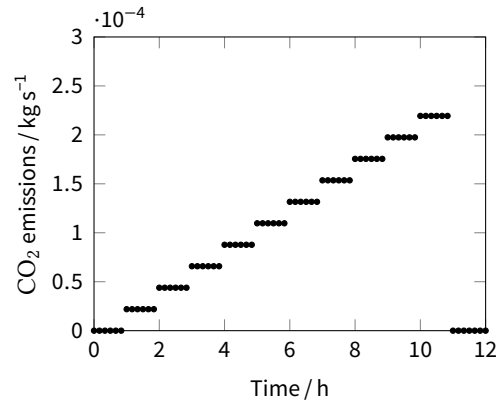


**Figure B.88** | Test case 901 results: carbon dioxide emissions as a function of time.

**Test case 902**

Figure B.89 shows the results were in agreement with the other calculation methods.

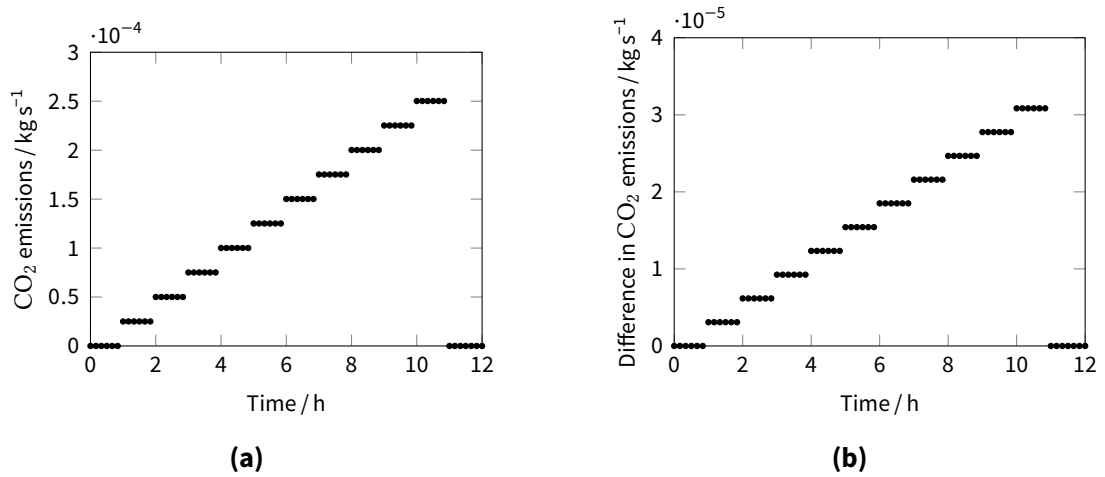


**Figure B.89** | Test case 902 results: carbon dioxide emissions as a function of time for (a) case 902 and (b) differential between cases 902 and 901.

**Test case 903**

Figure B.90 shows the results were in agreement with the other calculation methods.



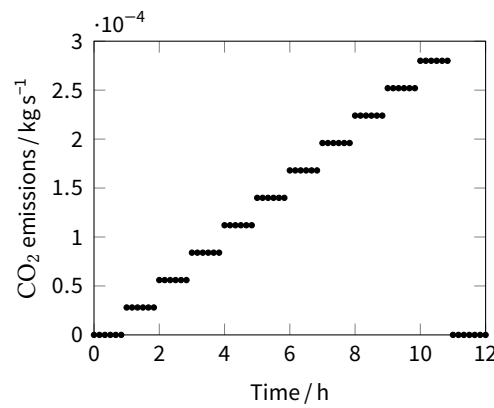


**Figure B.90** | Test case 903 results: carbon dioxide emissions as a function of time.

## B.2 Heat emitters

The model of the heat emitters utilised in this work is the hydronic radiator model that was developed by Hensen (3) that was extended in this work to a generalised continuous  $n$ th-order dynamic radiator model suitable for state-space controller design. Crommelin and Ham (1982) published experimental data for the dynamic behaviour of radiators and convectors subject to varying inlet flow conditions. This section presents the results from the validation of the dynamic model with the empirical results. This appendix provided enough information to ensure the validation test can be repeated. The model (4.52) was implemented in MATLAB/Simulink in order to simulate the time response of the model and compare with the experimental data.

### B.2.1 Test case 101

**Table B.1** | Radiator parameters for validation test 101

$m$	mass of the radiator and encapsulated water	20.6 kg
$c_p$	mass weighted average specific heat	1 275 J kg <sup>-1</sup> K <sup>-1</sup>
$\kappa_{\text{rad}}$	radiator exponent	1.3
$\phi_0$	nominal heat emission of radiator	925 W
$\Theta_{s,0}$	nominal supply temperature	91.0 °C
$\Theta_{x,0}$	nominal exit temperature	70.4 °C
$\Theta_{e,0}$	nominal environmental temperature	28.2 °C

Substituting the values from table B.1 into the model equations eqs. (4.49) and (4.50) gives the derived model parameters as  $H_{\text{rad},i}^* = 5.4614 \text{ WK}^{-\kappa_{\text{rad}}}$  ( $n = 2$ ),  $H_{\text{rad},i}^* = 1.8205 \text{ WK}^{-\kappa_{\text{rad}}}$  ( $n = 4$ ),  $H_{\text{rad},i}^* = 0.7802 \text{ WK}^{-\kappa_{\text{rad}}}$  ( $n = 8$ ) and  $\Delta\Theta_{\text{nom}} = 51.8194 \text{ K}$ .

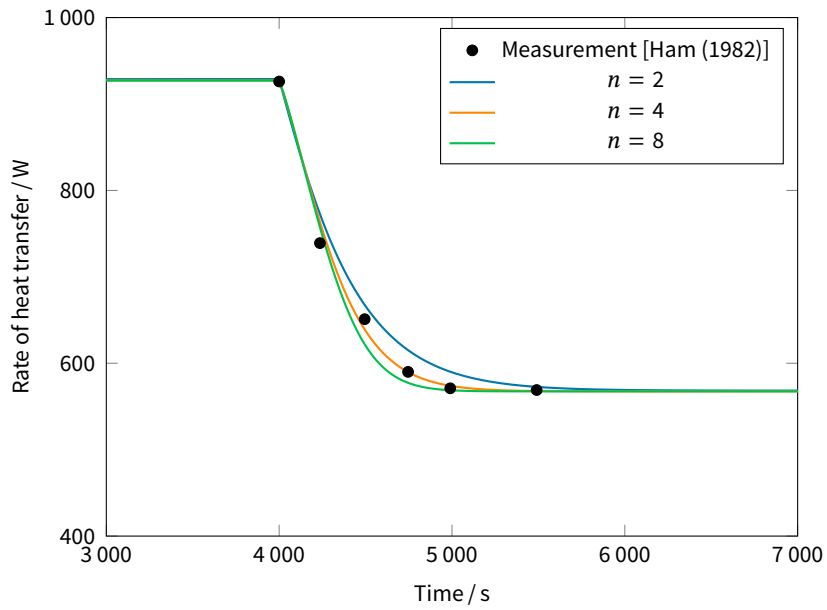


**Figure B.92** | Radiator empirical validation T101 results: heat emission,  $\Phi_{\text{rad}}$ , as a function of time.

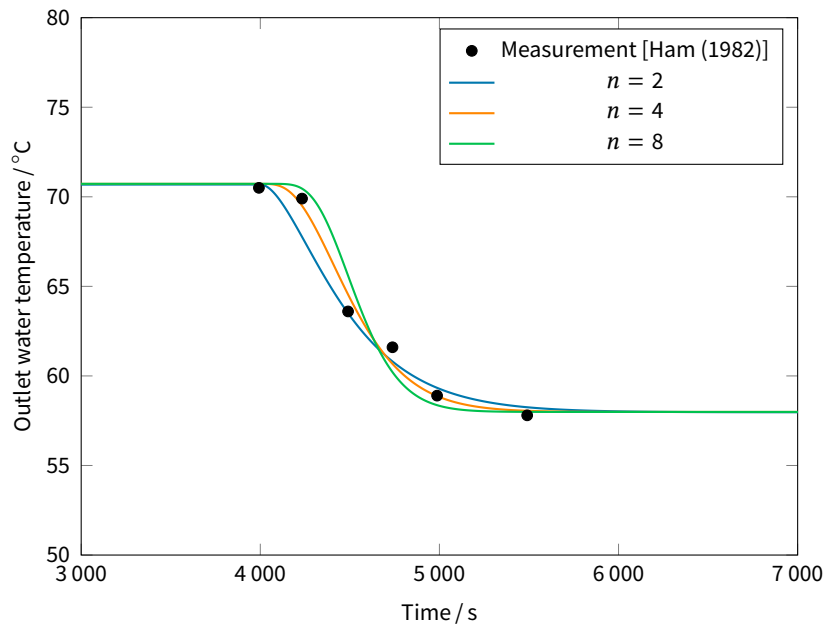


**Figure B.93** | Radiator empirical validation T101 results: outlet water temperature,  $\Theta_e$ , as a function of time.

The test consists of a step change in the radiator inlet water temperature from 91.0 °C to 70.4 °C at a constant mass flow rate of  $\dot{m} = 1.092 \times 10^{-2} \text{ kg s}^{-1}$ . The environmental temperature is set to the nominal environmental temperature in table B.1.

Figures B.92 and B.93 shows that for even the two node model sufficient accuracy will be attained for the purposes of controller design.

### B.2.2 Test case 102

**Table B.2 | Radiator parameters for validation test 102**

$m$	mass of the radiator and encapsulated water	20.9 kg
$c_p$	mass weighted average specific heat	1350 J kg <sup>-1</sup> K <sup>-1</sup>
$\kappa_{\text{rad}}$	radiator exponent	1.3
$\phi_0$	nominal heat emission of radiator	1030 W
$\Theta_{s,0}$	nominal supply temperature	89.7 °C
$\Theta_{x,0}$	nominal exit temperature	68.5 °C
$\Theta_{e,0}$	nominal environmental temperature	22.2 °C

As before, substituting the values from table B.2 into the model equations eqs. (4.49) and (4.50) gives the derived model parameters as  $H_{\text{rad},i}^* = 5.4679 \text{ WK}^{-\kappa_{\text{rad}}}(n = 2)$ ,  $H_{\text{rad},i}^* = 1.8226 \text{ WK}^{-\kappa_{\text{rad}}}(n = 4)$ ,  $H_{\text{rad},i}^* = 0.7811 \text{ WK}^{-\kappa_{\text{rad}}}(n = 8)$  and  $\Delta\Theta_{\text{nom}} = 56.2356 \text{ K}$ .

The test consists of a step change in the mass flow rate from  $1.193 \times 10^{-2} \text{ kg s}^{-1}$  to  $5.524 \times 10^{-3} \text{ kg s}^{-1}$  at a near constant temperature which varies from 89.7 °C to 88.6 °C during the change in mass flow rate. The environmental temperature is set to the nominal environmental temperature in table B.2.

Figures B.91 and B.94 shows that greater accuracy is achieved as the number of nodes increases. Contrary to the previous test, changing the mass flow rate suddenly causes nonlinear dynamic behaviour which is why additional nodes are required to accurately capture the time response.



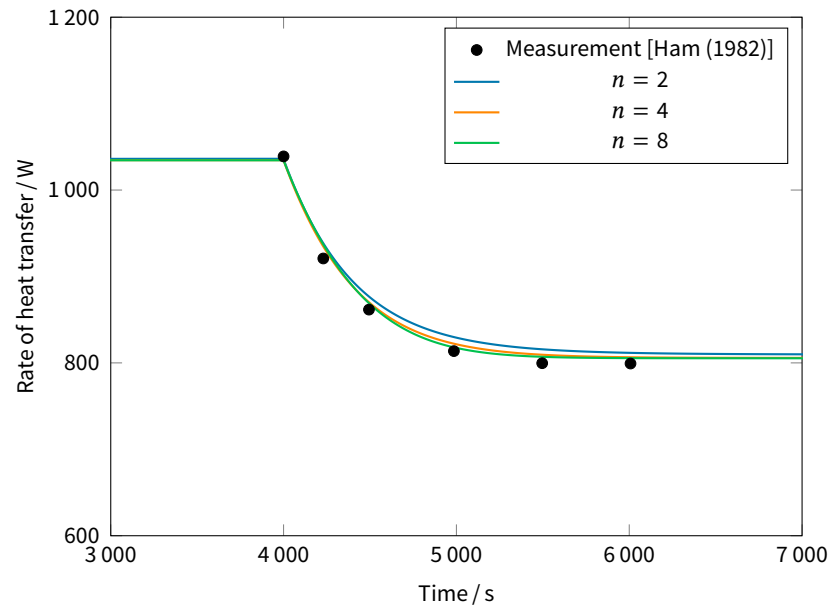


**Figure B.91** | Radiator empirical validation T102 results: heat emission,  $\Phi_{\text{rad}}$ , as a function of time.

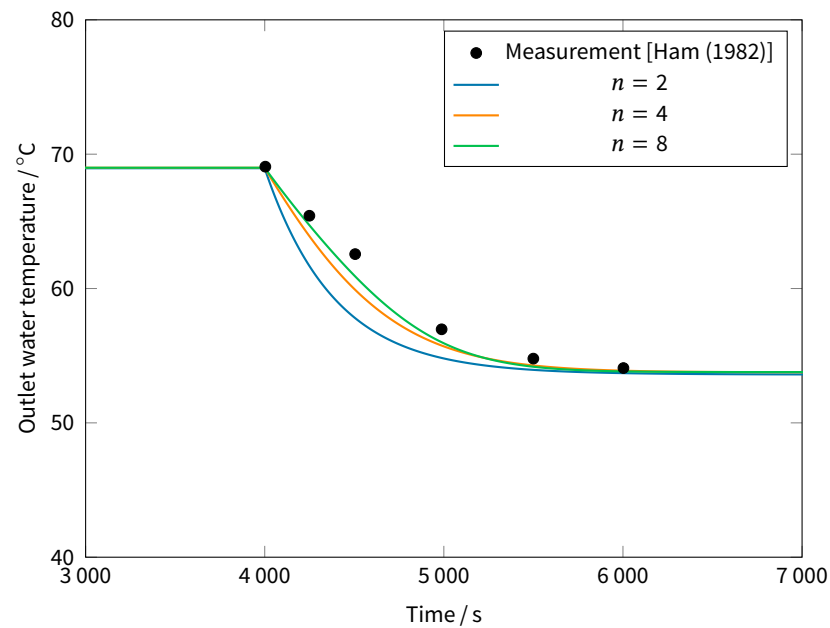


**Figure B.94** | Radiator empirical validation T102 results: outlet water temperature,  $\Theta_e$ , as a function of time.

### **B.3** Building model

The state-space building zone model that is used for controller design and analysis is validated with CEN standard BS EN 15265:2007 (4) for the energy performance of buildings – calculation of energy needs for space heating and cooling using dynamic

**Table B.3 | Thermophysical properties of constructions.** Material layers are ordered from external to internal.

<b>Type 1</b>					
Material	$d$ /m	$\lambda$ /W m <sup>-1</sup> K <sup>-1</sup>	$\rho$ /kg m <sup>-3</sup>	$c_p$ /kJ kg <sup>-1</sup> K <sup>-1</sup>	$\check{R}$ /m <sup>2</sup> KW <sup>-1</sup>
outer layer	0.115	0.99	1 800	0.85	0.166
insulating layer	0.06	0.04	30	0.85	1.500
masonry	0.175	0.79	1 600	0.85	0.222
internal plastering	0.015	0.70	1 400	0.85	0.021
<b>Type 2</b>					
gypsum plaster	0.012	0.21	900	0.85	0.057
mineral wool	0.10	0.04	30	0.85	2.500
gypsum plaster	0.012	0.21	900	0.85	0.057
<b>Type 3c</b>					
plastic covering	0.004	0.23	1 500	1.5	0.017
cement floor	0.06	1.40	2 000	0.85	0.043
mineral wool	0.04	0.04	50	0.85	1.000
concrete	0.18	2.1	2 400	0.85	0.086
<b>Type 3f</b>					
concrete	0.18	2.1	2 400	0.85	0.086
mineral wool	0.04	0.04	50	0.85	1.000
cement floor	0.06	1.40	2 000	0.85	0.043
plastic covering	0.004	0.23	1 500	1.5	0.017
<b>Type 4c</b>					
plastic covering	0.004	0.23	1 500	1.5	0.017
cement floor	0.06	1.40	2 000	0.85	0.043
mineral wool	0.04	0.04	50	0.85	1.000
concrete	0.18	2.1	2 400	0.85	0.086
mineral wool	0.10	0.04	50	0.85	2.500
acoustic board	0.02	0.06	400	0.84	0.333
<b>Type 4f</b>					
acoustic board	0.02	0.06	400	0.84	0.333
mineral wool	0.10	0.04	50	0.85	2.500
concrete	0.18	2.1	2 400	0.85	0.086
mineral wool	0.04	0.04	50	0.85	1.000
cement floor	0.06	1.40	2 000	0.85	0.043
plastic covering	0.004	0.23	1 500	1.5	0.017
<b>Type 5</b>					
rain protection	0.004	0.23	1 500	1.3	0.017
insulating	0.08	0.04	50	0.85	2.500
concrete	0.20	2.1	2 400	0.85	0.095
<b>Shaded DP</b>					
2 mm shade	0.002	80	1 800	1.0	0.080*
4 mm glass	0.004	0.7	2 800	0.75	0.167*
4 mm glass	0.004	0.7	2 800	0.75	0.006
<b>DP</b>					
4 mm glass	0.004	0.7	2 800	0.75	0.167*
4 mm glass	0.004	0.7	2 800	0.75	0.006

\* The R-value of these layers have been adjusted to account for the gaps between the layers and doesn't directly correspond to the value that would be obtained from  $d/\lambda$  for the material layer.



methods. This appendix include all necessary information to allow the calculations to be repeated.

### B.3.1 Input data

The climatic data used is provided in Annex A of BS EN 15265:2007 (4) and is not reproduced here, otherwise all requisite input data is included in the following section.

### Building description

The building is located in Trappes, France. It is rectangular in shape with dimensions of 3.6 m × 5.5 m × 2.8 m. A schematic of the building zone is shown in fig. B.95.

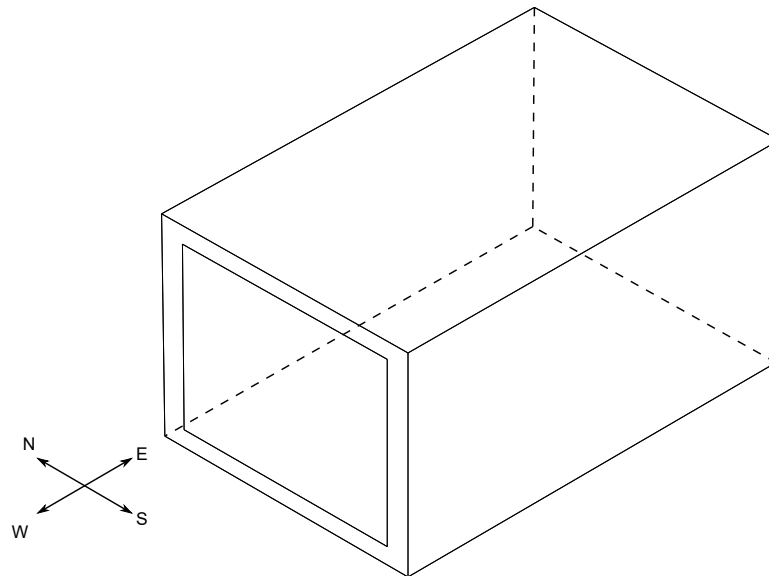


**Figure B.95** | Wire-frame of building zone with orientation.

In all test cases it is specified that there is no infiltration or thermal bridges in the building envelope i.e.  $h_{nm} = 0$ .

### Constructions

Table B.3 provides the thermophysical properties for all constructions used in the validation tests. The windows have a solar transmission factor of 0.2 with shading installed (Shaded DP), and 0.77 without (DP).

### Systems

The heating and cooling device is assumed to be a convective device that acts immediately on the internal air of the zone. The heating or cooling load is calculated at each time step to maintain the prescribed internal conditions defined by the system control:

**Table B.6 | Geometrical data & boundary conditions for Test 4 & 8.**

Envelope	Surface area m <sup>2</sup>	Boundary condition	Construction	Windows	Surface area m <sup>2</sup>
South	15.4	Adiabatic	Type 2	DP	7
East	10.08	Adiabatic	Type 2		
North	15.4	Adiabatic	Type 2		
West	3.08	Exterior	Type 1		
Ceiling	19.8	Adiabatic	Type 4c		
Floor	19.8	Adiabatic	Type 4f		

**Table B.7 | Geometrical data & boundary conditions for Test 9 & 11.**

Envelope	Surface area m <sup>2</sup>	Boundary condition	Construction	Windows	Surface area m <sup>2</sup>
South	15.4	Adiabatic	Type 2	Shaded DP	7
East	10.08	Adiabatic	Type 2		
North	15.4	Adiabatic	Type 2		
West	3.08	Exterior	Type 1		
Ceiling	19.8	Exterior	Type 5		
Floor	19.8	Adiabatic	Type 4f		

**Table B.8 | Geometrical data & boundary conditions for Test 10.**

Envelope	Surface area m <sup>2</sup>	Boundary condition	Construction	Windows	Surface area m <sup>2</sup>
South	15.4	Adiabatic	Type 2	Shaded DP	7
East	10.08	Adiabatic	Type 2		
North	15.4	Adiabatic	Type 2		
West	3.08	Exterior	Type 1		
Ceiling	19.8	Exterior	Type 4c		
Floor	19.8	Adiabatic	Type 3f		

**Table B.9 | Geometrical data & boundary conditions for Test 12.**

Envelope	Surface area m <sup>2</sup>	Boundary condition	Construction	Windows	Surface area m <sup>2</sup>
South	15.4	Adiabatic	Type 2	DP	7
East	10.08	Adiabatic	Type 2		
North	15.4	Adiabatic	Type 2		
West	3.08	Exterior	Type 1		
Ceiling	19.8	Exterior	Type 5		
Floor	19.8	Adiabatic	Type 4f		

Test	Controlled variable	Time active	$\Theta_{H,set}$	$\Theta_{C,set}$
1–4	Air temperature, $\Theta_a$	continuous all days of the week	20 °C	26 °C
5–12	Air temperature, $\Theta_a$	intermittent: 08:00/18:00 Mon–Fri	20 °C	26 °C

For test cases 1, 2, 4, 5, 6, 8, 9, 10, and 12 internal gains are  $20 \text{ W m}^{-2}$  (396 W) and act directly on the internal air. They are scheduled to be active 08:00/18:00 during weekdays. There are no internal gains for test cases 3, 7 and 11.

For all tests ventilation is specified as 1 air change per hour 08:00/18:00 during weekdays.

The time schedules for all Systems (air temperature control, internal gains and ventilation) are given in legal time, which is 2 h ahead of solar time in summer (hour 1996 to hour 7032) and 1 h ahead of solar time in winter.

### Geometrical data & boundary conditions

Tables B.4 to B.9 provide the geometrical data and boundary conditions for all of the test cases.

**Table B.4 | Geometrical data & boundary conditions for Test 1, 3, 5, & 7.**

Envelope	Surface area $\text{m}^2$	Boundary condition	Construction	Windows	Surface area $\text{m}^2$
South	15.4	Adiabatic	Type 2	Shaded DP	7
East	10.08	Adiabatic	Type 2		
North	15.4	Adiabatic	Type 2		
West	3.08	Exterior	Type 1		
Ceiling	19.8	Adiabatic	Type 4c		
Floor	19.8	Adiabatic	Type 4f		

**Table B.5 | Geometrical data & boundary conditions for Test 2 & 6.**

Envelope	Surface area $\text{m}^2$	Boundary condition	Construction	Windows	Surface area $\text{m}^2$
South	15.4	Adiabatic	Type 2	Shaded DP	7
East	10.08	Adiabatic	Type 2		
North	15.4	Adiabatic	Type 2		
West	3.08	Exterior	Type 1		
Ceiling	19.8	Adiabatic	Type 3c		
Floor	19.8	Adiabatic	Type 3f		

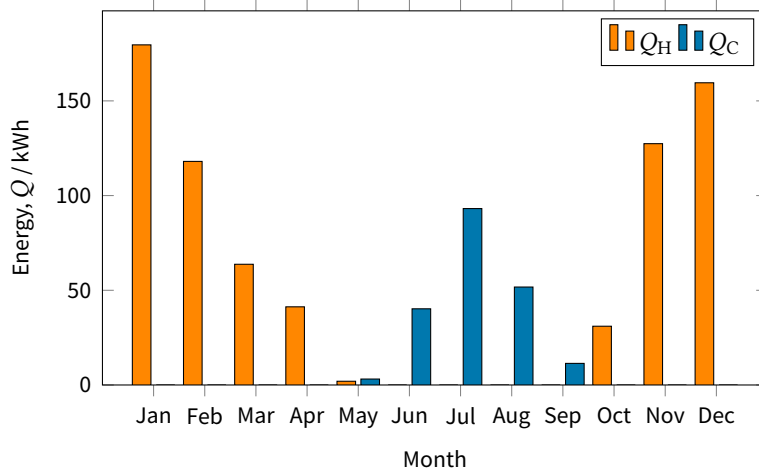


**Figure B.98 | Test 2: Monthly energy needs for heating and cooling.**

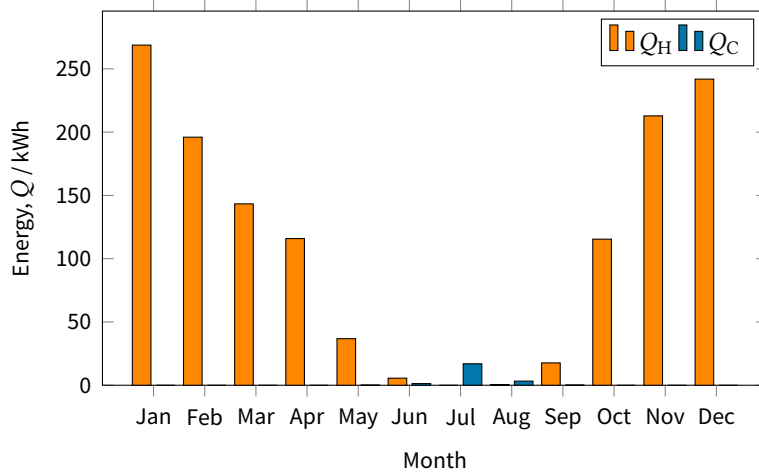


**Figure B.99 | Test 3: Monthly energy needs for heating and cooling.**

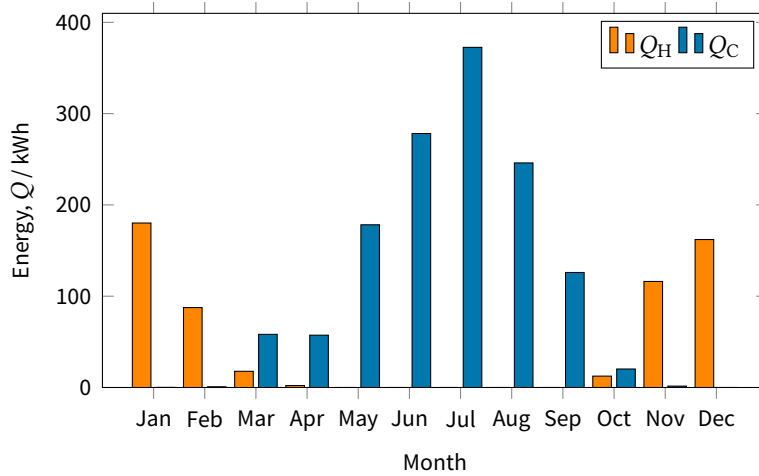


**Figure B.100 | Test 4: Monthly energy needs for heating and cooling.**

### Internal solar distribution

The solar radiation is time independent and is given for each internal surface in table B.10.

**Table B.10** | Internal solar distribution for all test cases.

Envelope	Solar distribution factor
South	0.184 3
East	0.120 6
North	0.184 3
West	0.036 9
Ceiling	0.237 0
Floor	0.237 0
Window	0

#### B.3.2 Output results

The calculated energy needs for heating and cooling are given on monthly basis for each Test in figs. B.96 to B.107 and for the whole year in fig. B.108.

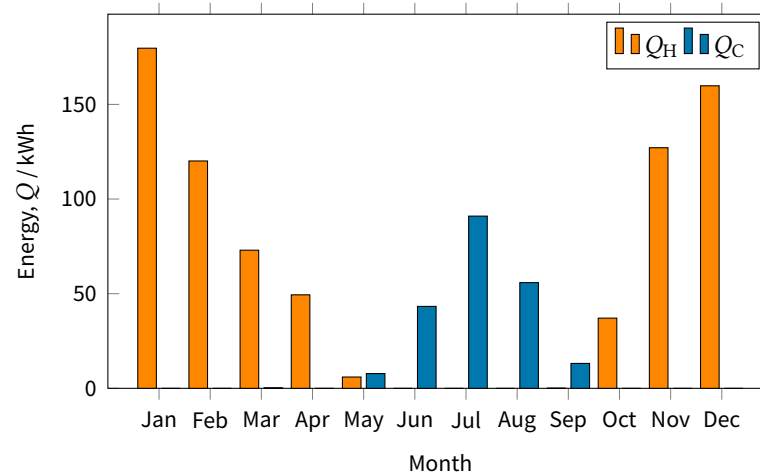


**Figure B.96** | Test 1: Monthly energy needs for heating and cooling.

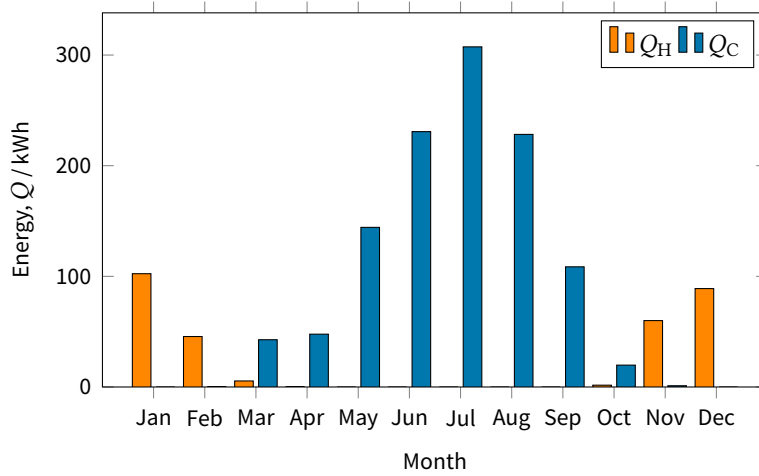


**Figure B.104 | Test 8: Monthly energy needs for heating and cooling.**

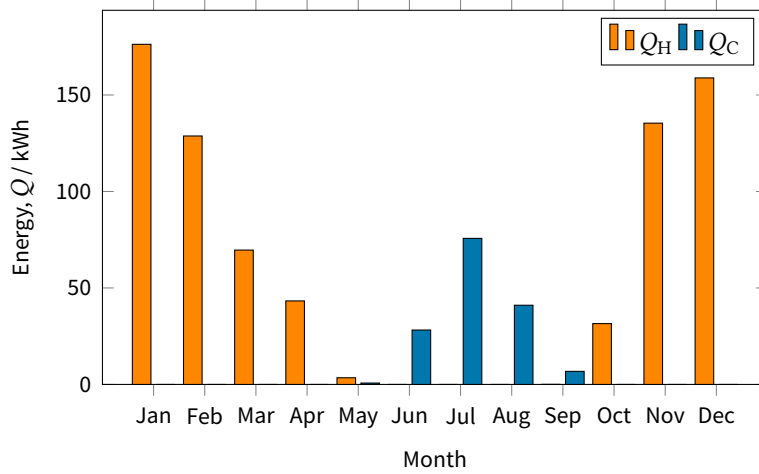


**Figure B.105 | Test 9: Monthly energy needs for heating and cooling.**

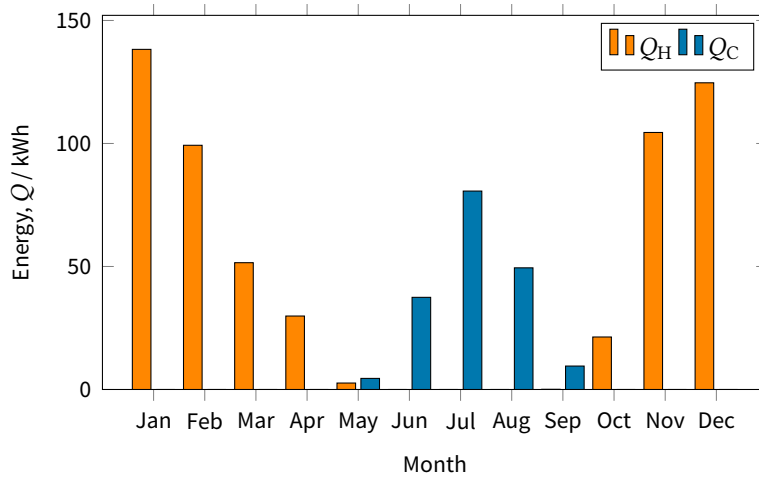


**Figure B.106 | Test 10: Monthly energy needs for heating and cooling.**

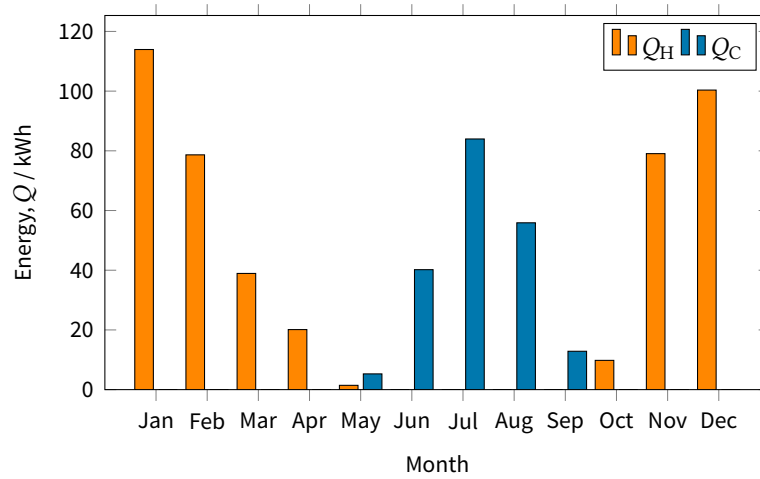


Figure B.97 | Test 5: Monthly energy needs for heating and cooling.

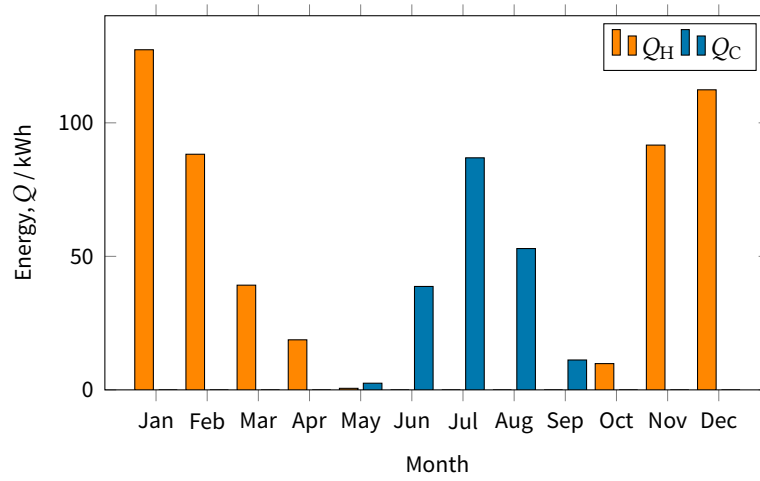


Figure B.101 | Test 6: Monthly energy needs for heating and cooling.

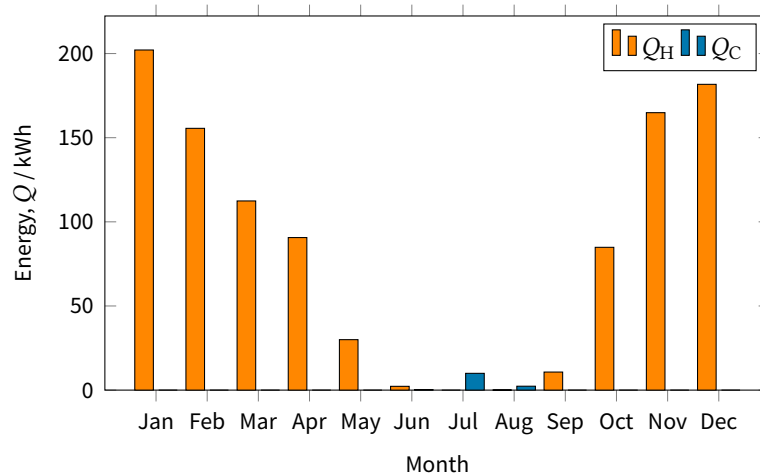
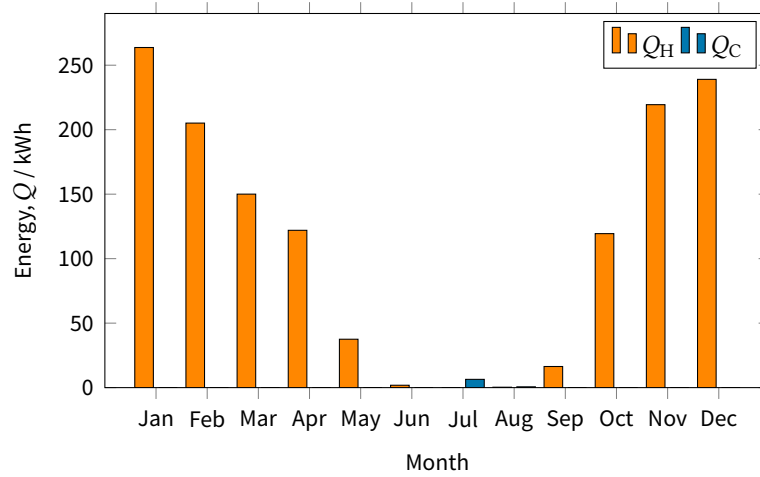


Figure B.102 | Test 7: Monthly energy needs for heating and cooling.







**Figure B.103 | Test 11: Monthly energy needs for heating and cooling.**

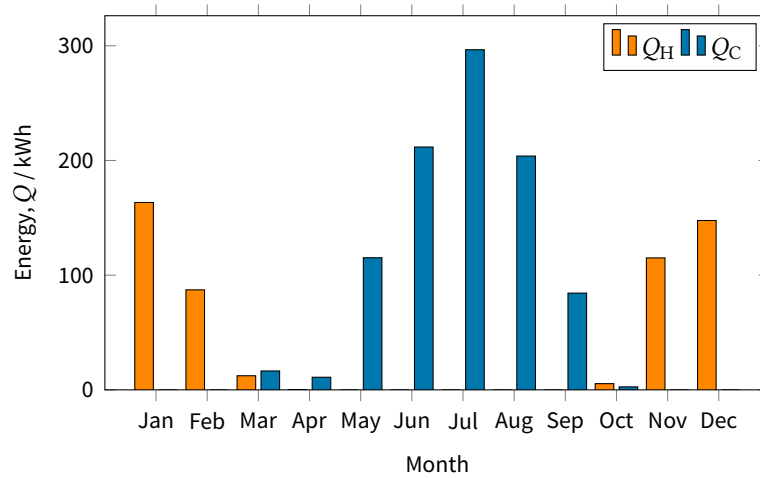


**Figure B.107 | Test 12: Monthly energy needs for heating and cooling.**

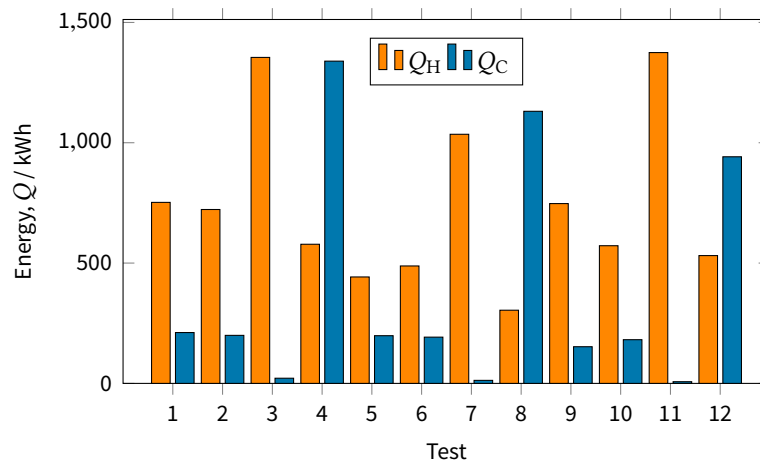


**Figure B.108 | Yearly energy needs for heating and cooling for each test case.**

The yearly values for heating and cooling energy needs and the total sum of both

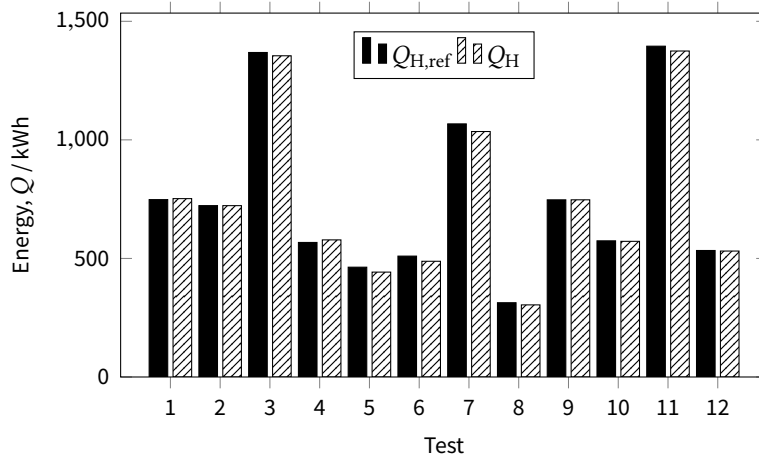


Figure B.109 | Yearly heating energy needs compared with the reference results.

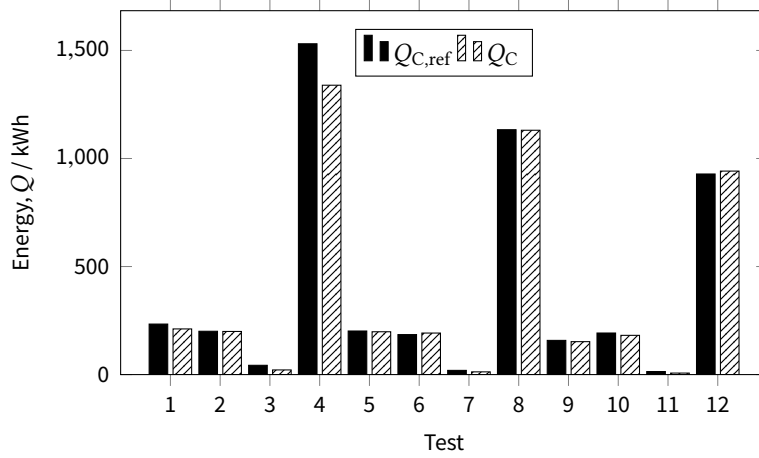


Figure B.110 | Yearly cooling energy needs compared with the reference results.

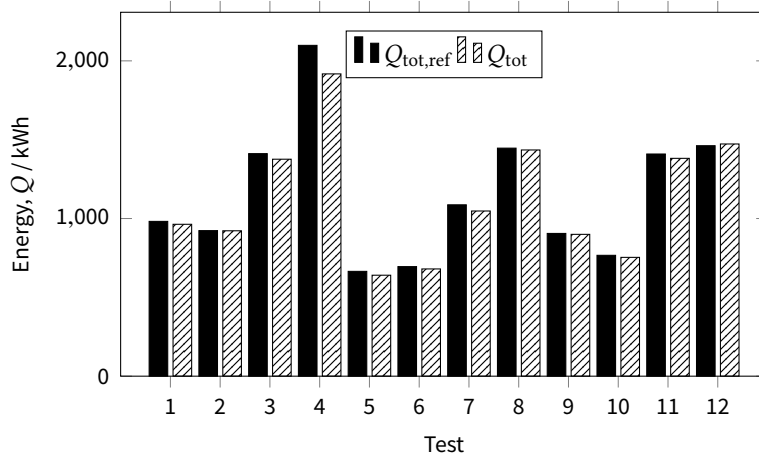


Figure B.111 | Yearly total energy needs compared with the reference results.

are compared with the reference results in figs. B.109 to B.111.

The dynamic building model is considered to be compliant with the CEN standard if for each of the test cases 5 to 12:

$$\text{compliance level} = \begin{cases} \text{Level A} & \text{if } rQ_H \leq 0.05 \wedge rQ_C \leq 0.05 \\ \text{Level B} & \text{if } rQ_H \leq 0.10 \wedge rQ_C \leq 0.10 \\ \text{Level C} & \text{if } rQ_H \leq 0.15 \wedge rQ_C \leq 0.15 \end{cases} \quad (\text{B.1})$$

where

$$rQ_H = |Q_H - Q_{H,\text{ref}}|/Q_{\text{ref,tot}} \quad (\text{B.2a})$$

$$rQ_C = |Q_C - Q_{C,\text{ref}}|/Q_{\text{ref,tot}} \quad (\text{B.2b})$$

From the criteria given in eq. (B.1) the classification level A, B or C was determined for each test case and is provided in table B.11.

**Table B.11** | Yearly energy needs and classification level for each test.

Test	$Q_{H,\text{ref}}$ kWh	$Q_{C,\text{ref}}$ kWh	$Q_{\text{tot,ref}}$ kWh	$Q_H$ kWh	$Q_C$ kWh	$Q_{\text{tot}}$ kWh	$rQ_H$	$rQ_C$	Result
1	748.0	233.8	981.8	752.2	211.3	963.4	0.00	0.02	Level A
2	722.7	200.5	923.2	722.6	199.6	922.2	0.00	0.00	Level A
3	1368.5	43.0	1411.5	1354.6	21.5	1376.2	0.01	0.02	Level A
4	567.4	1530.9	2098.3	578.2	1339.1	1917.3	0.01	0.09	Level B
5	463.1	201.7	664.8	442.3	198.2	640.4	0.03	0.01	Level A
6	509.8	185.1	694.9	488.0	192.2	680.2	0.03	0.01	Level A
7	1067.4	19.5	1086.9	1035.2	12.6	1047.7	0.03	0.01	Level A
8	313.2	1133.2	1446.4	304.1	1130.7	1434.8	0.01	0.00	Level A
9	747.1	158.3	905.4	747.2	152.4	899.6	0.00	0.01	Level A
10	574.2	192.4	766.6	572.1	181.6	753.6	0.00	0.01	Level A
11	1395.1	14.1	1409.2	1374.7	7.0	1381.7	0.01	0.01	Level A
12	533.5	928.3	1461.8	531.1	941.7	1472.8	0.00	0.01	Level A

As the classification level for test case 5–12 are all Level A, then the overall validated level of accuracy of the state-space building zone model developed in chapter 5 is Level A. The cause of the high cooling value demonstrated in informative test case 4 is unknown, however, tests 1–4 are not mandatory and are provided by the standard to check the basic operation of the model.



## References

1. Beausoleil-Morrison, I. *An experimental and simulation-based investigation of the performance of small-scale fuel cell and combustion-based cogeneration devices serving residential buildings*. Tech. rep. 2008: 70. URL: [http://www.ecbcs.org/docs/Annex%7B%5C\\_%7D42%7B%5C\\_%7DFinal%7B%5C\\_%7DReport.pdf](http://www.ecbcs.org/docs/Annex%7B%5C_%7D42%7B%5C_%7DFinal%7B%5C_%7DReport.pdf) (cited p. 269)
2. Beausoleil-Morrison, I., Ferguson, A. *Inter-model Comparative Testing and Empirical Validation of Annex 42 Models for Residential Cogeneration Devices*. Tech. rep. Annex 42 of the International Energy Agency Energy Conservation in Buildings and Community Systems Programme, 2007 (cited pp. 269, 281, 290)
3. Hensen, J. L. M. *On the thermal interaction of building structure and heating and ventilating system*. 1991: 197. ISBN: 903860081X (cited p. 309)
4. BS EN 15265:2007. *Energy performance of buildings. Calculation of energy needs for space heating and cooling using dynamic methods. General criteria and validation procedures*. 1st ed. London, UK: British Standards Institution, 2007. ISBN: 978-0-580-55627-2. DOI: [10.3403/30136887](https://doi.org/10.3403/30136887) (cited pp. 311, 312)



“They say no plan survives first  
contact with implementation...”

—ANDY WEIR, *The Martian*

C

## Control theory addendum

### C.1 LEDR of cogeneration device

For the LTI state-space system,  $\Xi$ , from eq. (6.24):

$$\begin{aligned}\dot{x}_1(t) &= \left(-\frac{H_{\text{HX}} + H_{\text{loss}}}{C_{\text{eng}}}\right)x_1(t) + \frac{\overline{\text{LHV}}\eta_{\text{Q}}}{C_{\text{eng}}}\mu_1(t) + \frac{H_{\text{HX}}}{C_{\text{eng}}}x_2(t) + \frac{H_{\text{loss}}}{C_{\text{eng}}}\mu_3(t) \\ \dot{x}_2(t) &= \frac{H_{\text{HX}}}{C_{\text{cw}}}x_1(t) + \left(-\frac{H_{\text{HX}} + (c_p\dot{m})_{\text{cw}}}{C_{\text{cw}}}\right)x_2(t) + \frac{(c_p\dot{m})_{\text{cw}}}{C_{\text{cw}}}\mu_2(t) \\ y_1(t) &= x_2(t) \\ y_2(t) &= -(\overline{\text{LHV}}\eta_{\text{E}})\mu_1(t) + \mu_4(t),\end{aligned}$$

the state-space matrices are given by

$$\begin{aligned}\mathbf{A} &= \begin{bmatrix} -\frac{H_{\text{HX}} + H_{\text{loss}}}{C_{\text{eng}}} & \frac{H_{\text{HX}}}{C_{\text{eng}}} \\ \frac{H_{\text{HX}}}{C_{\text{cw}}} & -\frac{H_{\text{HX}} + (c_p\dot{m})_{\text{cw}}}{C_{\text{cw}}} \end{bmatrix}, & \mathbf{B} &= \begin{bmatrix} \frac{\overline{\text{LHV}}\eta_{\text{Q}}}{C_{\text{eng}}} & 0 & \frac{H_{\text{loss}}}{C_{\text{eng}}} & 0 \\ 0 & \frac{(c_p\dot{m})_{\text{cw}}}{C_{\text{cw}}} & 0 & 0 \end{bmatrix}, \\ \mathbf{C} &= \begin{bmatrix} 0 & 1 \\ 0 & 0 \end{bmatrix}, & \mathbf{D} &= \begin{bmatrix} 0 & 0 & 0 & 0 \\ -\overline{\text{LHV}}\eta_{\text{E}} & 0 & 0 & 1 \end{bmatrix}.\end{aligned}$$

The characteristic equation is given as  $\delta(s) = \det(s\mathbf{I}_2 - \mathbf{A}) = s^2 + \alpha_2s + \alpha_3$ , where

$$\begin{aligned}\alpha_2 &= \frac{C_{\text{cw}}(H_{\text{HX}} + H_{\text{loss}}) + C_{\text{eng}}(H_{\text{HX}} + (c_p\dot{m})_{\text{cw}})}{C_{\text{cw}}C_{\text{eng}}}, \\ \alpha_3 &= \frac{H_{\text{HX}}H_{\text{loss}} + (H_{\text{HX}} + H_{\text{loss}})(c_p\dot{m})_{\text{cw}}}{C_{\text{cw}}C_{\text{eng}}}.\end{aligned}$$





The input and initial-state polynomial matrices of  $\Xi$  are

$${}^{\mu}\mathbf{N}(s) = \begin{bmatrix} \frac{H_{\text{HX}}\overline{LHV}\eta_{\text{Q}}}{C_{\text{cw}}C_{\text{eng}}} & \frac{(c_p\dot{m})_{\text{cw}}\left(s + \frac{H_{\text{HX}}+H_{\text{loss}}}{C_{\text{eng}}}\right)}{C_{\text{cw}}} & \frac{H_{\text{HX}}H_{\text{loss}}}{C_{\text{cw}}C_{\text{eng}}} & 0 \\ -\overline{LHV}\eta_{\text{E}}\delta(s) & 0 & 0 & \delta(s) \end{bmatrix},$$

$${}^0\mathbf{N}(s) = \begin{bmatrix} \frac{H_{\text{HX}}}{C_{\text{cw}}} & s + \frac{H_{\text{HX}}+H_{\text{loss}}}{C_{\text{eng}}} \\ 0 & 0 \end{bmatrix}.$$

Now the LEDR of  $\Xi$  in the frequency-domain is given by eq. (6.11):

$$s^n y_i(s) = - \sum_{j=1}^n \alpha_{j+1} s^{n-j} y_i(s) + \sum_{j=1}^m {}^{\mu}N_{ij}(s)\mu_j(s) + \sum_{j=1}^n {}^0N_{ij}(s)x_j(0)$$

$$\implies s^2 y_i(s) = - \alpha_2 s y_i(s) - \alpha_3 y_i(s)$$

$$+ {}^{\mu}N_{i1}(s)\mu_1(s) + {}^{\mu}N_{i2}(s)\mu_2(s) + {}^{\mu}N_{i3}(s)\mu_3(s) + {}^{\mu}N_{i4}(s)\mu_4(s)$$

$$+ {}^0N_{i1}(s)x_1(0) + {}^0N_{i2}(s)x_2(0)$$

Substituting the values

$$s^2 y_1(s) = - \frac{C_{\text{cw}}(H_{\text{HX}} + H_{\text{loss}}) + C_{\text{eng}}(H_{\text{HX}} + (c_p\dot{m})_{\text{cw}})}{C_{\text{cw}}C_{\text{eng}}} s y_1(s)$$

$$- \frac{H_{\text{HX}}H_{\text{loss}} + (H_{\text{HX}} + H_{\text{loss}})(c_p\dot{m})_{\text{cw}}}{C_{\text{cw}}C_{\text{eng}}} y_1(s) + \frac{H_{\text{HX}}\overline{LHV}\eta_{\text{Q}}}{C_{\text{cw}}C_{\text{eng}}} \mu_1(s)$$

$$+ \frac{(c_p\dot{m})_{\text{cw}}\left(s + \frac{H_{\text{HX}}+H_{\text{loss}}}{C_{\text{eng}}}\right)}{C_{\text{cw}}} \mu_2(s) + \frac{H_{\text{HX}}H_{\text{loss}}}{C_{\text{cw}}C_{\text{eng}}} \mu_3(s)$$

$$+ \frac{H_{\text{HX}}}{C_{\text{cw}}} x_1(0) + \left(s + \frac{H_{\text{HX}} + H_{\text{loss}}}{C_{\text{eng}}}\right) x_2(0)$$

$$s^2 y_2(s) = - \frac{C_{\text{cw}}(H_{\text{HX}} + H_{\text{loss}}) + C_{\text{eng}}(H_{\text{HX}} + (c_p\dot{m})_{\text{cw}})}{C_{\text{cw}}C_{\text{eng}}} s y_2(s)$$

$$- \frac{H_{\text{HX}}H_{\text{loss}} + (H_{\text{HX}} + H_{\text{loss}})(c_p\dot{m})_{\text{cw}}}{C_{\text{cw}}C_{\text{eng}}} y_2(s)$$

$$+ (-\overline{LHV}\eta_{\text{E}}(s^2 + \alpha_2 s + \alpha_3)) \mu_1(s) + (s^2 + \alpha_2 s + \alpha_3) \mu_4(s)$$



Taking the inverse Laplace transform

$$\begin{aligned}
\ddot{y}_1(t) + \delta(t)y_1(0) + \dot{y}_1(0) &= -\frac{C_{cw}(H_{HX} + H_{loss}) + C_{eng}(H_{HX} + (c_p\dot{m})_{cw})}{C_{cw}C_{eng}}(\dot{y}_1(t) + y_1(0)) \\
&\quad -\frac{H_{HX}H_{loss} + (H_{HX} + H_{loss})(c_p\dot{m})_{cw}}{C_{cw}C_{eng}}y_1(t) + \frac{H_{HX}\overline{LHV}\eta_Q}{C_{cw}C_{eng}}\mu_1(t) \\
&\quad + \frac{(c_p\dot{m})_{cw}}{C_{cw}}(\dot{\mu}_2(t) + \mu_2(0)) + \frac{(c_p\dot{m})_{cw}(H_{HX} + H_{loss})}{C_{cw}C_{eng}}\mu_2(t) \\
&\quad + \frac{H_{HX}H_{loss}}{C_{cw}C_{eng}}\mu_3(t) + \frac{H_{HX}}{C_{cw}}x_1(0) + \delta(t)x_2(0) + \frac{H_{HX}+H_{loss}}{C_{eng}}x_2(0) \\
\ddot{y}_2(t) + \delta(t)y_2(0) + \dot{y}_2(0) &= -\frac{C_{cw}(H_{HX} + H_{loss}) + C_{eng}(H_{HX} + (c_p\dot{m})_{cw})}{C_{cw}C_{eng}}(\dot{y}_2(t) + y_2(0)) \\
&\quad -\frac{H_{HX}H_{loss} + (H_{HX} + H_{loss})(c_p\dot{m})_{cw}}{C_{cw}C_{eng}}y_2(t) \\
&\quad -\overline{LHV}\eta_E(\ddot{\mu}_1(t) + \alpha_2\dot{\mu}_1(t) + \alpha_3\mu_3(t) \\
&\quad + \dot{\mu}_1(0) + \delta(t)\mu_1(0) + \alpha_2\mu_1(0)) \\
&\quad + \ddot{\mu}_4(t) + \alpha_2\dot{\mu}_4(t) + \alpha_3\mu_4(t) + \dot{\mu}_4(0) + \delta(t)\mu_4(0) + \alpha_2\mu_4(0).
\end{aligned}$$

The initial conditions are found from the recursive derivation of the output equation:

$$y^{(k)}(0) = CA^k x(0) + D\mu^{(k)}(0) + \sum_{\substack{j=1 \\ j \leq k}}^k CA^{k-j} B\mu^{(j-1)}(0)$$

From which results:

$$\begin{aligned}
y_1(0) &= x_2(0) \\
\dot{y}_1(0) &= \frac{H_{HX}}{C_{cw}}x_1(0) - \frac{H_{HX} + (c_p\dot{m})_{cw}}{C_{cw}}x_2(0) + \frac{(c_p\dot{m})_{cw}}{C_{cw}}\mu_2(0) \\
y_2(0) &= \mu_4(0) - \overline{LHV}\eta_E\mu_1(0) \\
\dot{y}_2(0) &= \dot{\mu}_4(0) - \overline{LHV}\eta_E\dot{\mu}_1(0)
\end{aligned}$$

Substituting the initial conditions and cancelling terms results in the time-domain LEDR of the system  $\Xi$  as given in eq. (6.27).

## **C.2** Performance metrics for underdamped PDF system

The output of the general second-order system is in the Laplace domain as

$$y(s) = G(s)y_d(s) = \frac{K_I}{s^2 + K_Ds + K_I} \frac{y_d(s)}{s}.$$



The exact solution to the response is given by

$$y(t) = y_d \left( 1 - \frac{\sqrt{K_I}}{\sigma} e^{-\frac{K_D t}{2}} \sin(\sigma t + \phi) \right), \quad (\text{C.1})$$

where  $\sigma = \sqrt{K_I - K_D^2/4}$  and  $\phi = \tan^{-1}(2\sigma/K_D)$ .

### C.2.1 Calculation of peak time

The peak time will be the first time at which the derivative of the output is zero. The derivative in the Laplace domain is

$$\mathcal{L}\{\dot{y}(t)\} = sy(s) = y_d \frac{K_I}{s^2 + K_D s + K_I}.$$

Taking the inverse Laplace transform gives

$$\dot{y}(t) = y_d \frac{2K_I e^{-\frac{K_D}{2}t} \sinh\left(\frac{t\sqrt{K_D^2 - 4K_I}}{2}\right)}{\sqrt{K_D^2 - 4K_I}}.$$

For underdamped systems there are imaginary roots, which makes  $4K_I > K_D^2$  therefore  $\sqrt{K_D^2 - 4K_I} = j\sqrt{4K_I - K_D^2}$ . Then using the identity  $\sinh(\cdot) = -j \sin(\cdot)$  yields

$$\dot{y}(t) = y_d \frac{2K_I e^{-\frac{K_D}{2}t} \sin\left(\frac{t\sqrt{4K_I - K_D^2}}{2}\right)}{\sqrt{4K_I - K_D^2}}.$$

Then  $\dot{y}(t) = 0$  when the sinusoid is first zero. Therefore,

$$\frac{t\sqrt{4K_I - K_D^2}}{2} = \pi.$$

Solving for the time gives the time of the first peak of the underdamped response:

$$T_p = \frac{2\pi}{\sqrt{4K_I - K_D^2}}.$$

### C.2.2 Calculation of overshoot

The overshoot is the fraction by which the peak response is greater than the final value:

$$\overline{OS} = (y_{\max} - y_{ss})/y_{ss}.$$



Substituting the peak time equation into eq. (C.1) the maximum response is given by

$$y_{\max} = y_d \left( 1 + e^{-\pi K_D / \sqrt{4K_I - K_D^2}} \right),$$

which gives the overshoot fraction as

$$\overline{OS} = e^{-\pi K_D / \sqrt{4K_I - K_D^2}}.$$

### C.2.3 Calculation of settling time

The settling time corresponds to the time at which the decaying exponential in (C.1) is

$$\frac{\sqrt{K_I}}{\sigma} e^{-\frac{K_D t}{2}} = c_s,$$

where  $c_s$  is the settling time criterion i.e. the settling time will be the time for the response to reach and stay within  $\pm c_s(\%)$  of the steady-state value. Solving for the time gives the settling time of the underdamped response:

$$T_s = -\frac{1}{K_D} \ln \left( \frac{c_s^2 (4K_I - K_D^2)}{4K_I} \right)$$

## C.3 H-infinity loop shaping controller

The  $H_\infty$  optimal controller design methods are applied to LTI systems. Therefore, using the method described in appendix D.2 the Jacobian linearisation of the original affine in input continuous-time nonlinear dynamical system eqs. (8.1) to (8.3) is

$$G : \begin{cases} \dot{\mathbf{x}} = \mathbf{A}\mathbf{x} + \mathbf{B}\boldsymbol{\mu}, \\ \mathbf{y} = \mathbf{C}\mathbf{x} + \mathbf{D}\boldsymbol{\mu}, \end{cases}$$

where

$$\mathbf{A} = \begin{bmatrix} -0.0019697 & 0.0017189 & 0 & 0 \\ 0.0011317 & -0.14918\bar{m}_{cw} - 0.0011317 & 0 & 0 \\ 0 & 0 & 0 & -0.33333 \end{bmatrix},$$

$$\mathbf{B} = \begin{bmatrix} 0 & 0.030725 & 0 & 0.00025081 & 0 \\ 0.14918(\bar{\Theta}_{cw,i} - \bar{\Theta}_{cw,o}) & 0 & 0.14918\bar{m}_{cw} & 0 & 0 \\ 0 & -18.146 & 0 & 0 & 0.33333 \end{bmatrix},$$

$$\mathbf{C} = \begin{bmatrix} 0 & 1 & 0 \\ 0 & 0 & 1 \end{bmatrix}, \quad \mathbf{D} = \begin{bmatrix} 0 & 0 & 0 & 0 & 0 \\ 0 & 0 & 0 & 0 & 0 \end{bmatrix}.$$

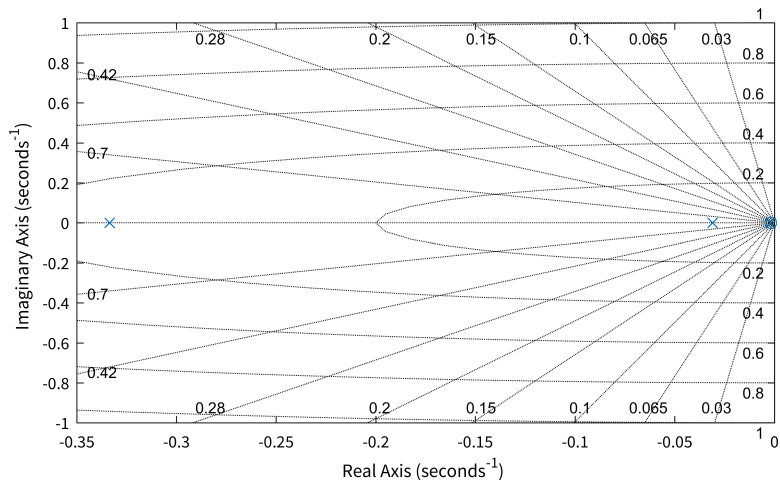


**Figure C.1 | Pole-zero plot of linearised dynamic system.**

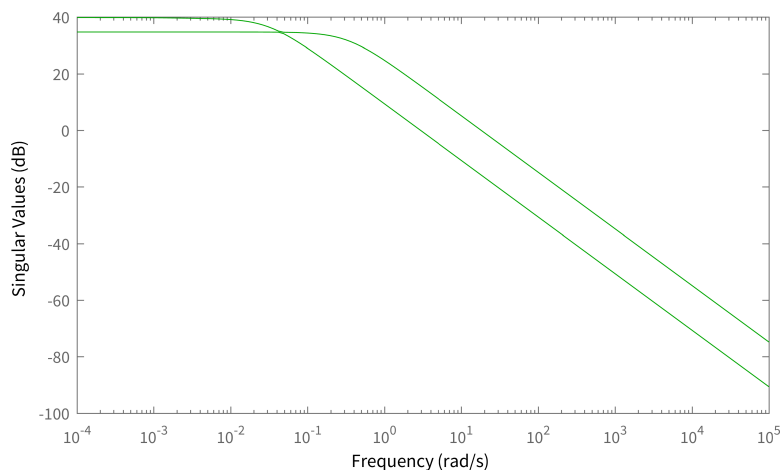


**Figure C.2 | Singular value plot for linearised dynamic system.**



The linearised system,  $G$ , relies on nominal values  $(\bar{\Theta}_{\text{cw,i}}, \bar{\Theta}_{\text{cw,o}}, \bar{m}_{\text{cw}})$ . For this controller design the inlet and outlet temperatures are selected as the manufacturers design temperatures of 40 °C and 60 °C respectively. The design flow rate is selected as 0.13 kg s<sup>-1</sup>.

Taking the same input partitioning as §§ 8.2.2:  $\mathbf{w} = (\mu_3, \mu_5) = (\Theta_{\text{cw,i}}, P_{\text{load}})$ ,  $\mathbf{u} = (u_1, u_2) = (\mu_1, \mu_2) = (\dot{m}_{\text{cw}}, \dot{m}_{\text{fuel}})$  and  $d = \mu_4 = \Theta_{\text{env}}$ . Substituting the design values and partitioning the system matrices according to input type gives the linear system to be controlled  $G_c$ :

$$G_c : \begin{cases} \dot{\mathbf{x}} = \mathbf{A}_c \mathbf{x} + \mathbf{B}_c \mathbf{u}, \\ \mathbf{y} = \mathbf{C}_c \mathbf{x} + \mathbf{D}_c \mathbf{u}, \end{cases}$$

$$\mathbf{A}_c = \begin{bmatrix} -0.0019697 & 0.0017189 & 0 \\ 0.0011317 & -0.030968 & 0 \\ 0 & 0 & -0.33333 \end{bmatrix}, \quad \mathbf{B}_c = \begin{bmatrix} 0 & 0.030725 \\ -2.9389 & 0 \\ 0 & -18.146 \end{bmatrix},$$

$$\mathbf{C}_c = \begin{bmatrix} 0 & 1 & 0 \\ 0 & 0 & 1 \end{bmatrix}, \quad \mathbf{D}_c = \begin{bmatrix} 0 & 0 \\ 0 & 0 \end{bmatrix}.$$

### C.3.1 Analysing the system dynamics

In this example, the linearised system model has three stable left-half plane poles. It has one zero, which is in the left-half plane. Therefore, the system is stable and minimum phase around the selected operating point. Figure C.1 shows the pole-zero plot for the linearised system model.

$H_\infty$  methods often utilise **sigma plots**, which plot the min and max I/O gain as a function of frequency i.e. the singular values of the frequency response of a dynamic system. The singular values of the frequency response extend the traditional Bode magnitude response for MIMO systems and are useful in robustness analysis. The singular value response of a SISO system is identical to its Bode magnitude response.

The system is transformed from the time domain into the frequency domain as

$$\mathbf{G}_c(s) = \mathbf{D}_c + \mathbf{C}_c(s\mathbf{I}_n - \mathbf{A}_c)^{-1}\mathbf{B}_c,$$

where  $s$  is the Laplace variable that is the complex number frequency parameter  $s = \sigma + j\omega$ .

In continuous time, the **frequency response** at a frequency  $\omega$  is the transfer function value at  $s = j\omega$  i.e. set the real part of the Laplace variable equal to zero. For state-space models, this value is given by  $\mathbf{G}_c(j\omega) = \mathbf{D}_c + \mathbf{C}_c(j\omega\mathbf{I}_n - \mathbf{A}_c)^{-1}\mathbf{B}_c$ . Figure C.2 shows the singular value plot for the linearised system model.



### C.3.2 Specifying the desired loop shape

Loop shaping is a frequency-domain technique for enforcing requirements on response speed, control bandwidth, roll-off, and steady state error (1). The idea is to specify a target gain profile or “loop shape” for the open-loop response  $L(s) = K(s)G_c(s)$ . Using the controller performance specifications from §§ 8.2.1, a reasonable loop shape for this application should have an ideal first-order response from both controlled outputs, the target loop shape from input  $i$  to output  $i$  will be

$$G_{d,ii}(s) = \frac{1}{\tau_i s},$$

where  $\tau_i$  is the time constant of the response. For perfect decoupling between the outputs,  $G_{d,ij} = G_{d,ji} = 0$ .

A first-order system without zeros can be described by the following transfer function

$$G(s) = \frac{1}{(1/\tau)s + 1}.$$

The response to a unit step of  $1/s$  is given by

$$c(t) = 1 - e^{-(1/\tau)t}. \quad (\text{C.2})$$

The requirement on the performance of the grid response is a 0 % to 95 % rise time of 9 s. The rise time, however, is typically defined as the time for the response to go from 10 % to 90 % of its final value (2, p. 159). Therefore, this application requires solving eq. (C.2) for the difference in time at  $c(t) = 0.95$  and  $c(t) = 0.0$ . This gives the following expression for determining rise time as a function the time constant:

$$T_r = \tau (\ln(1) - \ln(0.05)),$$

which results in the design time constant for the grid output as  $\tau_2 = 3.0043$ .

The requirement on the performance of the supply temperature response is to reach and maintain the supply temperature set-point – within a 2 % error band – in a period less than or equal to 20 min from start-up. This is known as the 2 % settling time, and can be calculated from eq. (C.2) as

$$T_s = -\tau \ln(0.02),$$

which results in the design time constant for the supply temperature output as  $\tau_1 = 306.75$ .

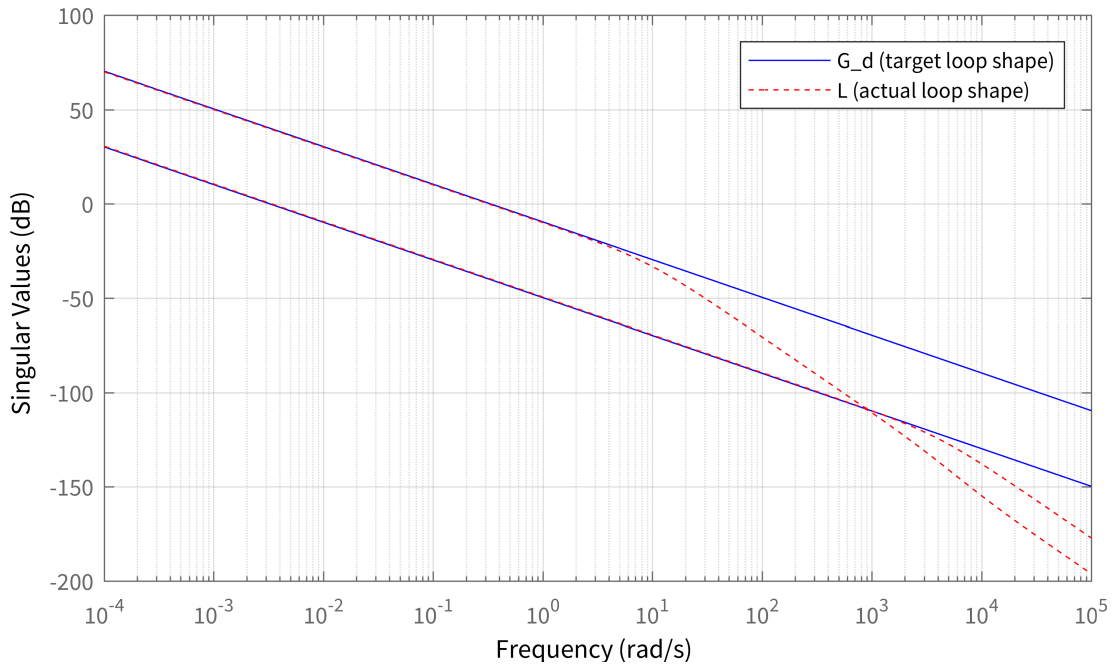


**Figure C.3 | Singular value plot for target- and actual-loop shape.**

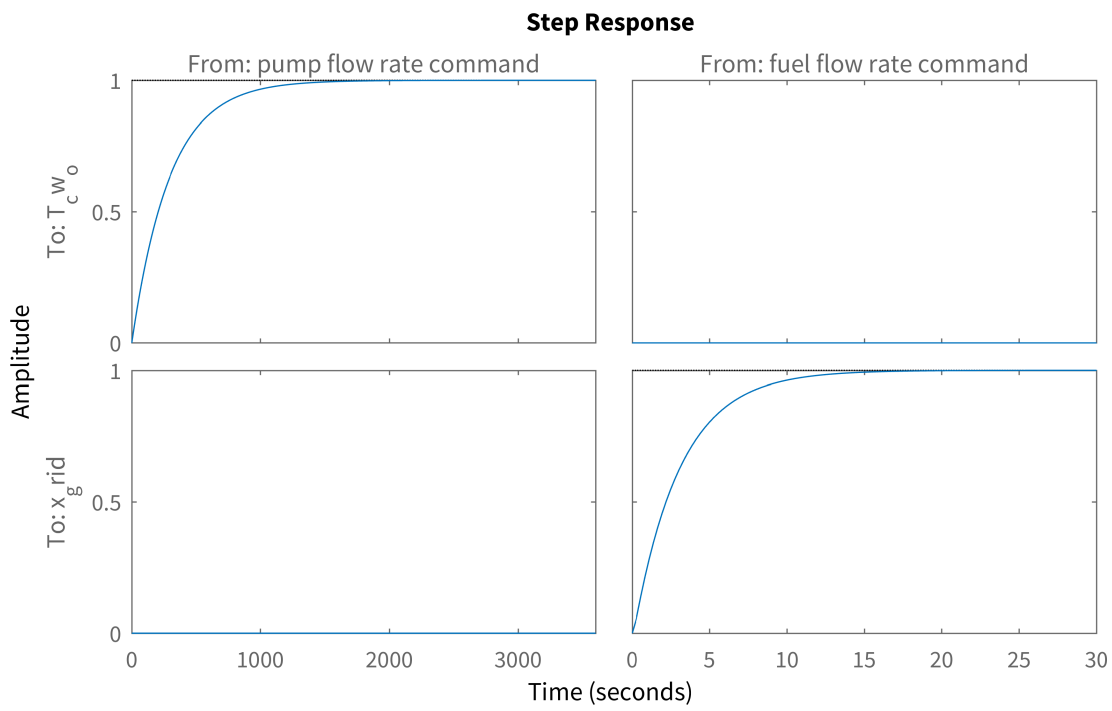


**Figure C.4 | Responses to step commands.**

For this design the target loop shape for each output can be represented by the following transfer function matrix

$$\mathbf{G}_d(s) = \begin{bmatrix} \frac{1}{306.75s} & 0 \\ 0 & \frac{1}{3.0043s} \end{bmatrix}.$$

### C.3.3 Compute the optimal loop-shaping controller

It is now possible to design an H-infinity controller  $\mathbf{K}(s)$ , such that the gains of the open-loop response  $\mathbf{G}(s)\mathbf{K}(s)$  match the target-loop shape  $\mathbf{G}_d(s)$  as well as possible (while ensuring the system dynamics remain stable). This work utilises the work of (3–5) to design the optimal loop-shaping controller. This has been implemented into MATLAB®'s Robust Control Toolbox™ and is invoked by using the function  $[K, \overline{CL}, \gamma] = \text{loopsyn}(G_c, G_d(s))$ , where  $\gamma$  denotes the loop-shaping accuracy<sup>1</sup>, and  $\overline{CL}$  is the resulting closed-loop system.

The resulting controller,  $\mathbf{K}(s)$ , is the following MIMO transfer function matrix:

$$\mathbf{K}(s) = \frac{1}{\delta(s)} \begin{bmatrix} N_{11}(s) & N_{12}(s) \\ N_{21}(s) & N_{22}(s) \end{bmatrix}$$

where

$$\delta(s) = s^8 + 1.639 \times 10^4 s^7 + 1.008 \times 10^8 s^6 + 2.756 \times 10^{11} s^5 + 2.834 \times 10^{14} s^4 + 1.978 \times 10^{15} s^3 + 3.896 \times 10^{12} s^2$$

$$N_{11}(s) = -4.819s^7 - 5.925 \times 10^4 s^6 - 2.43 \times 10^8 s^5 - 3.329 \times 10^{11} s^4 \\ - 2.338 \times 10^{12} s^3 - 7.667 \times 10^{10} s^2 - 1.374 \times 10^8 s + 2.858 \times 10^{-5}$$

$$N_{12}(s) = 9.276 \times 10^{-7} s^7 + 0.0114 s^6 + 46.69s^5 + 6.377 \times 10^4 s^4 \\ + 3.247 \times 10^4 s^3 + 3764s^2 + 7.288s + 3.806 \times 10^{-12}$$

$$N_{21}(s) = 7.95 \times 10^{-8} s^7 + 0.0009759 s^6 + 3.985s^5 + 5358s^4 \\ - 2.915 \times 10^5 s^3 - 3.045 \times 10^8 s^2 - 1.015 \times 10^8 s - 3.797 \times 10^{-5}$$

$$N_{22}(s) = -0.04735s^7 - 956.2s^6 - 6.984 \times 10^6 s^5 - 2.21 \times 10^{10} s^4 \\ - 2.573 \times 10^{13} s^3 - 8.626 \times 10^{12} s^2 - 1.689 \times 10^{10} s - 3.814 \times 10^{-6}$$

The loop-shaping accuracy is  $\gamma = 1.441$ . This indicates the target-loop shape was met within  $\pm 3.2$  dB.

For implementation into a dynamic simulation the transfer function matrix is

<sup>1</sup> $\gamma \geq 1$  and  $\gamma = 1$  indicates a perfect fit.

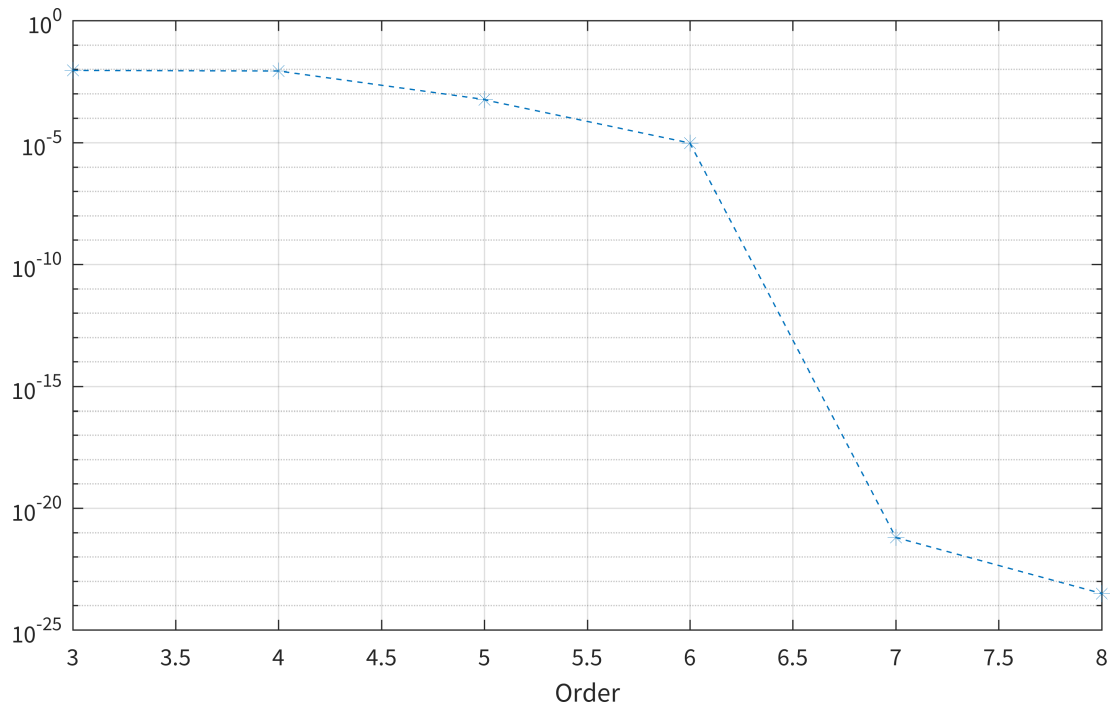


Figure C.5 | Hankel singular values of  $K$ .

transformed into the following state-space representation:

$$K : \begin{cases} \dot{\mathbf{z}}(t) = \mathbf{A}\mathbf{z}(t) + \mathbf{B}\mathbf{e}(t), \\ \mathbf{u}(t) = \mathbf{C}\mathbf{z}(t) + \mathbf{D}\mathbf{e}(t), \end{cases}$$

$$\mathbf{A} = \begin{bmatrix} -0.0019697 & 0.0017189 & 6.9347 & -7.4456 \times 10^{-11} & 3.3906 & -1.08 \times 10^{-19} & -1.9505 \times 10^{-23} & 6.4623 \times 10^{-27} \\ 1.0842 \times 10^{-19} & -4.096 & -2.2586 \times 10^{-22} & -218.45 & -4.0309 \times 10^{-7} & 6.2863 \times 10^{-27} & 7.14 \times 10^{-27} & 0 \\ -3.1787 \times 10^{-45} & -1.2009 \times 10^{-22} & -4.096 & 4.3974 \times 10^{-8} & -2.002.5 & 6.819 \times 10^{-17} & 1.6867 \times 10^{-20} & 5.1699 \times 10^{-26} \\ 0 & 0 & 0 & 0 & 0 & 2.3162 \times 10^{-9} & -7.2601 \times 10^{-10} & -0.0051991 \\ 0 & 0 & 0 & 0 & 0 & 1.0946 & 0.00031512 & 6.7398 \times 10^{-10} \\ 0 & 0 & 0 & 0 & 0 & -7.026 & 2.2032 & -4.1717 \times 10^{-9} \\ 0 & 0 & 0 & 0 & 0 & -1.5574 & -4.096 & -9.2565 \times 10^{-10} \\ 0 & 0 & 0 & 0 & 0 & 2.9885 \times 10^{-9} & -9.1608 \times 10^{-10} & -4.096 \end{bmatrix}$$

$$\mathbf{C} = \begin{bmatrix} -0.00038507 & -1393.7 & -5.294 \times 10^{-23} & -74.332 & -1.3716 \times 10^{-7} & -2.9532 \times 10^{-27} & 6.8347 \times 10^{-28} & 0 \\ -1.7517 \times 10^{-46} & -6.6177 \times 10^{-24} & -225.7 & 2.4233 \times 10^{-9} & -110.35 & 4.4606 \times 10^{-18} & 1.1606 \times 10^{-21} & 0 \end{bmatrix}$$

$$\mathbf{B} = \begin{bmatrix} 1.034 \times 10^{-25} & 9.4816 \times 10^{-25} \\ 1.9704 \times 10^{-19} & 3.1476 \times 10^{-28} \\ -1.9927 \times 10^{-25} & 6.0287 \times 10^{-22} \\ 0.064831 & -1.0703 \times 10^{-9} \\ -8.4041 \times 10^{-9} & 0.00042905 \\ 5.2618 \times 10^{-8} & 3.0968 \\ 1.1542 \times 10^{-8} & -0.00063024 \\ 0.083186 & -1.3733 \times 10^{-9} \end{bmatrix}$$

$$\mathbf{D} = \begin{bmatrix} -2.1684 \times 10^{-19} & 3.2312 \times 10^{-27} \\ -2.5849 \times 10^{-26} & 1.6941 \times 10^{-21} \end{bmatrix}$$

Figure C.3 compares the singular values of the open-loop  $L = GK$  with the target-loop shape  $G_d(s)$ :

### C.3.4 Verifying time-domain response

Figure C.4 shows the step responses of the closed-loop system. It shows that the controls are perfectly decoupled, the settling time of the supply temperature is 1156 s (19 min 16 s) and the 0% to 95% rise time of the grid output is 9.1 s. This indicates that the design performance is met by controller  $K$  for the linearised system  $G_c$ .

### C.3.5 Controller simplification

Although the MIMO  $H_\infty$  controller  $K$  has demonstrated satisfactory performance, it is of high-order, as it is of order 8. It is possible to use model reduction algorithms to simplify this controller while retaining performance characteristics. Figure C.5 shows the Hankel singular values (HSV) of  $K$ . The HSV measure the relative energy of each state in a balanced realisation of  $K$ , which can be used to assess how many controller states effectively contribute to the control law. Notice that the HSV for the 7th state is 17 orders of magnitude smaller than the 6th state. Therefore, a 6th-order

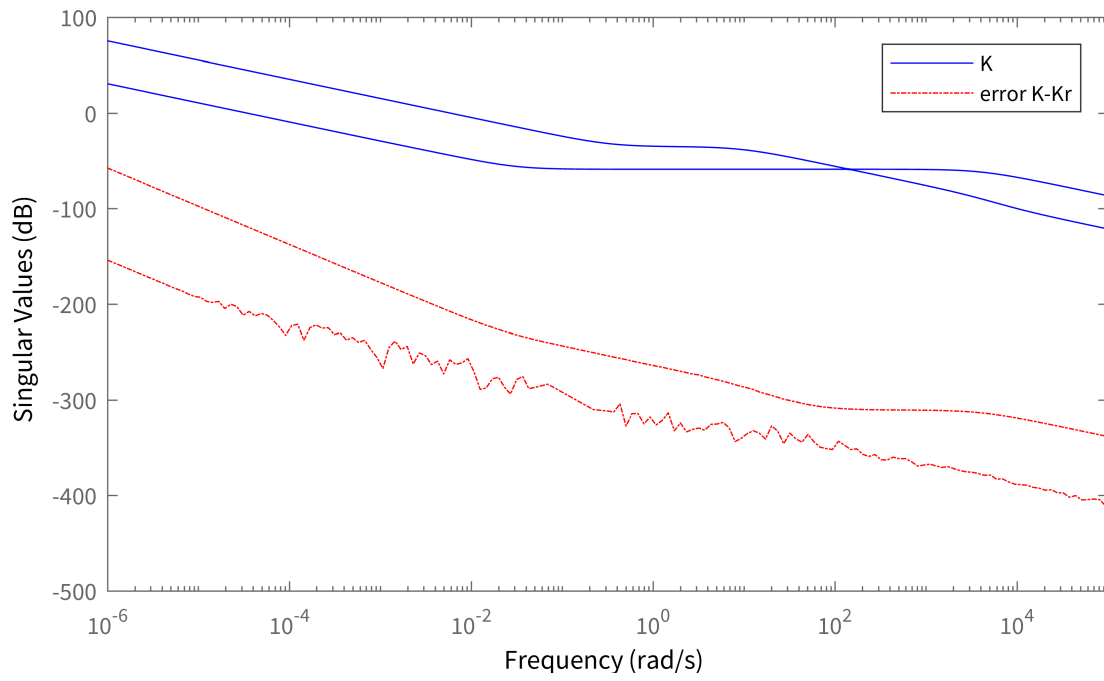


**Figure C.6** | Singular values of  $K$  and approximation error  $K - K_r$ .

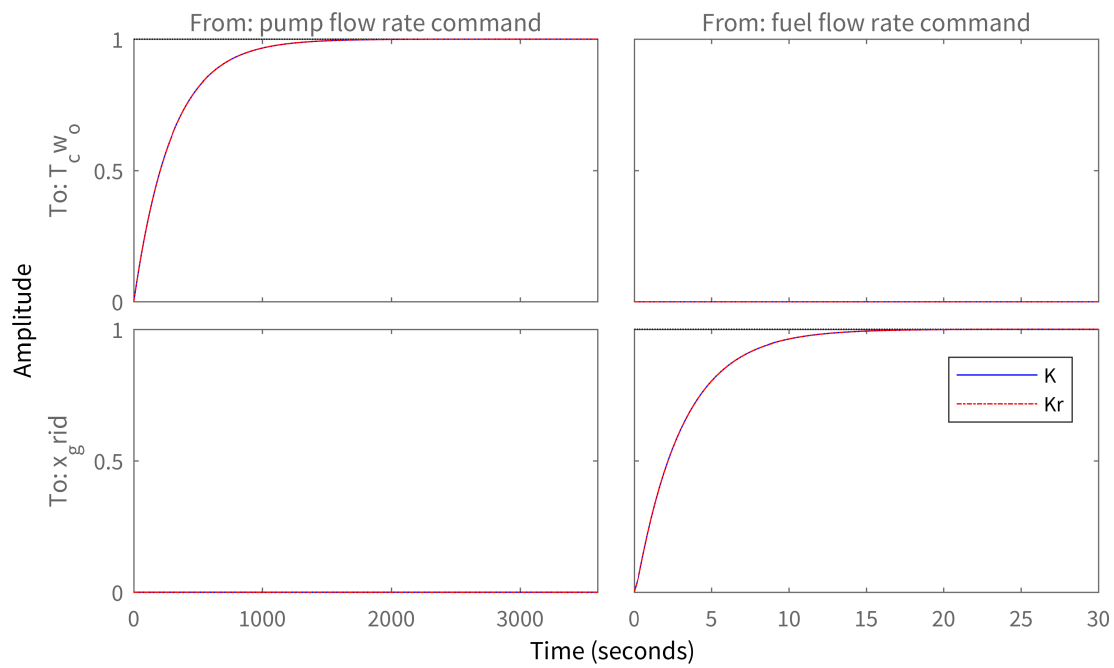


**Figure C.7** | Responses to step commands for original and reduced-order controllers.



approximation of  $K$ , denoted  $K_r$  can be used.

Figure C.6 shows the approximation error  $K - K_r$  across frequency with the gains of  $K$ . The figure suggests that the approximation error is small. Finally, compare the closed-loop time-domain responses between controllers. Figure C.7 shows the step responses of the closed-loop system with original and reduced-order controllers  $K$  and  $K_r$ . It indicates that the reduced-order controller  $K_r$  retains the same performance as the original controller  $K$ . The  $H_\infty$  optimal controller used in the example of § 8.2 is now given by

$$A = \begin{bmatrix} -0.70828 & 2.3955 & 1.3913 & -3.5287 & 0 & 0 \\ 2.531 & -8.5864 & 0.41013 & 12.645 & 0 & 0 \\ 0.13363 & 0.041602 & -4.096 & 1.3334 \times 10^{-5} & 0 & 0 \\ 3.5332 & -12.645 & -6.6004 \times 10^{-5} & -4.096 & 0 & 0 \\ 0 & 0 & 0 & 0 & 0 & 1.571 \times 10^{-14} \\ 0 & 0 & 0 & 0 & -8.4655 \times 10^{-15} & -2.2737 \times 10^{-13} \end{bmatrix}$$

$$C = \begin{bmatrix} 0.0057888 & 0.0016171 & -2.1718 & -3.1521 \times 10^{-7} & -0.00053083 & -6.4168 \times 10^{-5} \\ -0.11265 & 0.38212 & 2.4608 \times 10^{-6} & -0.28105 & 1.9326 \times 10^{-13} & -0.010054 \end{bmatrix}$$

$$B = \begin{bmatrix} -0.00092146 & 0.11279 \\ -0.00027166 & -0.38212 \\ 2.1718 & -3.1122 \times 10^{-7} \\ -2.2834 \times 10^{-8} & -0.28105 \\ 0.065039 & -0.0041777 \\ -1.4581 \times 10^{-9} & 0.58665 \end{bmatrix} \quad D = \begin{bmatrix} 0 & -1.2925 \times 10^{-26} \\ -2.068 \times 10^{-25} & -4.8704 \times 10^{-21} \end{bmatrix}$$

## References

1. McFarlane, D., Glover, K. A loop-shaping design procedure using H-infinity synthesis. *IEEE Transactions on Automatic Control* **37**(6): 759–69 (1992).  
DOI: [10.1109/9.256330](https://doi.org/10.1109/9.256330) (cited p. 325)
2. Nise, N. S. *Control Systems Engineering*. 5th ed. Hoboken, NJ, USA: John Wiley & Sons, 2008: 861.  
ISBN: 978-0471-79475-2 (cited p. 325)
3. Le, V. X., Safonov, M. G. Rational matrix GCDs and the design of squaring-down compensators—a state-space theory. *IEEE Transactions on Automatic Control* **37**(3): 384–92 (1992-03).  
DOI: [10.1109/9.119644](https://doi.org/10.1109/9.119644) (cited p. 326)
4. Glover, K., McFarlane, D. Robust stabilization of normalized coprime factor plant descriptions with H-infinity-bounded uncertainty. *IEEE Transactions on Automatic Control* **34**(8): 821–30 (1989-08).  
DOI: [10.1109/9.29424](https://doi.org/10.1109/9.29424) (cited p. 326)
5. Chiang, R. Y., Safonov, M. G. H-infinity synthesis using a bilinear pole shifting transform. *Journal of Guidance, Control, and Dynamics* **15**(5): 1111–7 (1992) (cited p. 326)



“Karma police.  
Arrest this man...  
He talks in maths”

---

—RADIOHEAD, *OK Computer*

# D

## Mathematical review

### D.1 Blockwise matrix inversion

The following is a proof for the blockwise inversion of a  $2 \times 2$  block (partitioned) matrix.

Let  $M$  be an  $m \times n$  matrix partitioned into block form such that:

$$M = \begin{bmatrix} A & B \\ C & D \end{bmatrix} \quad (\text{D.1})$$

Then, the block inverse matrix of eq. (D.1) is given by the following

$$\begin{bmatrix} A & B \\ C & D \end{bmatrix} \begin{bmatrix} W & X \\ Y & Z \end{bmatrix} = \begin{bmatrix} I_m & 0 \\ 0 & I_n \end{bmatrix} \quad (\text{D.2a})$$

$$\begin{bmatrix} W & X \\ Y & Z \end{bmatrix} \begin{bmatrix} A & B \\ C & D \end{bmatrix} = \begin{bmatrix} I_m & 0 \\ 0 & I_n \end{bmatrix} \quad (\text{D.2b})$$

From eq. (D.2a)

$$\begin{aligned} AX + BZ &= 0 \\ X &= -A^{-1}BZ \end{aligned} \quad (\text{D.3})$$

and

$$CX + DZ = I_n \quad (\text{D.4})$$

Substituting eq. (D.3) into eq. (D.4)

$$-CA^{-1}BZ + DZ = I_n$$



$$(D - CA^{-1}B)Z = I_n$$

Note that  $D - CA^{-1}B$  is known as the Schur compliment of  $D$ , denoted  $S_D$ . Now,

$$\boxed{Z = S_D^{-1}}. \quad (\text{D.5})$$

Substituting eq. (D.5) into eq. (D.3) gives

$$\boxed{X = -A^{-1}BS_D^{-1}}. \quad (\text{D.6})$$

From eq. (D.2b)

$$YA + ZC = 0 \quad (\text{D.7})$$

$$WA + XC = I_m \quad (\text{D.8})$$

Substituting eq. (D.5) into eq. (D.7) and rearranging

$$\boxed{Y = -S_D^{-1}CA^{-1}}. \quad (\text{D.9})$$

Substituting eq. (D.6) into eq. (D.8) and rearranging

$$\boxed{W = A^{-1} + A^{-1}BS_D^{-1}CA^{-1}}. \quad (\text{D.10})$$

Therefore, the block inverse matrix of  $M$  is given from eqs. (D.5), (D.6), (D.9) and (D.10) as

$$M^{-1} = \begin{bmatrix} A^{-1} + A^{-1}BS_D^{-1}CA^{-1} & -A^{-1}BS_D^{-1} \\ -S_D^{-1}CA^{-1} & S_D^{-1} \end{bmatrix} \quad (\text{D.11})$$

Note that, it can be inferred from eq. (D.11) that in order to utilise this analytic inversion technique,  $A$  and  $S_D$  must be non-singular i.e. invertible.

## **D.2** Jacobian linearisation of nonlinear systems

A function  $f_i(x)$  can be approximated by using a finite number of terms of its Taylor series expansion about some point  $x = x_0$  (1, p. 820). The expansion for a single variable function is given as

$$f_i(x) = f_i(x_0) + (x - x_0) \left. \frac{df_i}{dx} \right|_{x=x_0} + \frac{(x - x_0)^2}{2!} \left. \frac{d^2f_i}{dx^2} \right|_{x=x_0} + \frac{(x - x_0)^3}{3!} \left. \frac{d^3f_i}{dx^3} \right|_{x=x_0} + \dots$$



or in compact notation

$$f_i(x) = \sum_{k=0}^{\infty} \frac{f_i^{(k)}(x_0)}{k!} (x - x_0)^k.$$

If the series is truncated at  $k = 1$  it results in the linear approximation of  $f_i(x)$ :

$$f_i(x) \approx f_i(x_0) + (x - x_0) \left. \frac{df_i}{dx} \right|_{x=x_0}.$$

Now for a multi-variable function  $f_i(x_1, \dots, x_n, \mu_1, \dots, \mu_m)$  the approximation around a point  $(x_{1_0}, \dots, x_{n_0}, \mu_{1_0}, \dots, \mu_{m_0})$  can be written as

$$\begin{aligned} f_i(x_1, \dots, x_n, \mu_1, \dots, \mu_m) &\approx f_i(x_{1_0}, \dots, x_{n_0}, \mu_{1_0}, \dots, \mu_{m_0}) \\ &+ (x_1 - x_{1_0}) \left. \frac{\partial f_i}{\partial x_1} \right|_{\substack{x=x_0 \\ \mu=\mu_0}} + \dots + (x_n - x_{n_0}) \left. \frac{\partial f_i}{\partial x_n} \right|_{\substack{x=x_0 \\ \mu=\mu_0}} \\ &+ (\mu_1 - \mu_{1_0}) \left. \frac{\partial f_i}{\partial \mu_1} \right|_{\substack{x=x_0 \\ \mu=\mu_0}} + \dots + (\mu_m - \mu_{m_0}) \left. \frac{\partial f_i}{\partial \mu_m} \right|_{\substack{x=x_0 \\ \mu=\mu_0}}. \end{aligned}$$

For all  $(f_1, \dots, f_n)$  functions in eq. (6.1) the linear approximation can be written as

$$f(\mathbf{x}(t), \boldsymbol{\mu}(t)) \approx f(\mathbf{x}_0, \boldsymbol{\mu}_0) + \left. \frac{\partial f}{\partial \mathbf{x}} \right|_{\substack{x=x_0 \\ \mu=\mu_0}} (\mathbf{x}(t) - \mathbf{x}_0) + \left. \frac{\partial f}{\partial \boldsymbol{\mu}} \right|_{\substack{x=x_0 \\ \mu=\mu_0}} (\boldsymbol{\mu}(t) - \boldsymbol{\mu}_0), \quad (\text{D.12})$$

and similarly for the output functions  $(h_1, \dots, h_p)$

$$\mathbf{h}(\mathbf{x}(t), \boldsymbol{\mu}(t)) \approx \mathbf{h}(\mathbf{x}_0, \boldsymbol{\mu}_0) + \left. \frac{\partial \mathbf{h}}{\partial \mathbf{x}} \right|_{\substack{x=x_0 \\ \mu=\mu_0}} (\mathbf{x}(t) - \mathbf{x}_0) + \left. \frac{\partial \mathbf{h}}{\partial \boldsymbol{\mu}} \right|_{\substack{x=x_0 \\ \mu=\mu_0}} (\boldsymbol{\mu}(t) - \boldsymbol{\mu}_0), \quad (\text{D.13})$$

where  $\frac{\partial f}{\partial \mathbf{x}}$  denotes the so-called Jacobian matrix of  $f$  with respect to  $\mathbf{x}$ , where each  $ij$ -th element of the matrix is  $\frac{\partial f_i}{\partial x_j}$  (and similarly for  $\frac{\partial f}{\partial \boldsymbol{\mu}}$ ,  $\frac{\partial \mathbf{h}}{\partial \mathbf{x}}$ , and  $\frac{\partial \mathbf{h}}{\partial \boldsymbol{\mu}}$ ). Equations (D.12) and (D.13) can be expressed as

$$\dot{\mathbf{x}}(t) = \mathbf{A}\mathbf{x}(t) + \mathbf{B}\boldsymbol{\mu}(t) + \mathbf{E}, \quad (\text{D.14a})$$

$$\mathbf{y}(t) = \mathbf{C}\mathbf{x}(t) + \mathbf{D}\boldsymbol{\mu}(t) + \mathbf{F}, \quad (\text{D.14b})$$

where

$$\mathbf{A} = \left. \frac{\partial f}{\partial \mathbf{x}} \right|_{\substack{x=x_0 \\ \mu=\mu_0}}, \quad \mathbf{B} = \left. \frac{\partial f}{\partial \boldsymbol{\mu}} \right|_{\substack{x=x_0 \\ \mu=\mu_0}}, \quad \mathbf{C} = \left. \frac{\partial \mathbf{h}}{\partial \mathbf{x}} \right|_{\substack{x=x_0 \\ \mu=\mu_0}}, \quad \mathbf{D} = \left. \frac{\partial \mathbf{h}}{\partial \boldsymbol{\mu}} \right|_{\substack{x=x_0 \\ \mu=\mu_0}}$$





$$\begin{aligned}
E &= f(\mathbf{x}_o, \boldsymbol{\mu}_o) - \left. \frac{\partial f}{\partial \mathbf{x}} \right|_{\substack{\mathbf{x}=\mathbf{x}_o \\ \boldsymbol{\mu}=\boldsymbol{\mu}_o}} \mathbf{x}_o - \left. \frac{\partial f}{\partial \boldsymbol{\mu}} \right|_{\substack{\mathbf{x}=\mathbf{x}_o \\ \boldsymbol{\mu}=\boldsymbol{\mu}_o}} \boldsymbol{\mu}_o \\
E &= f(\mathbf{x}_o, \boldsymbol{\mu}_o) - \mathbf{A}\mathbf{x}_o - \mathbf{B}\boldsymbol{\mu}_o \\
F &= \mathbf{h}(\mathbf{x}_o, \boldsymbol{\mu}_o) - \left. \frac{\partial \mathbf{h}}{\partial \mathbf{x}} \right|_{\substack{\mathbf{x}=\mathbf{x}_o \\ \boldsymbol{\mu}=\boldsymbol{\mu}_o}} \mathbf{x}_o - \left. \frac{\partial \mathbf{h}}{\partial \boldsymbol{\mu}} \right|_{\substack{\mathbf{x}=\mathbf{x}_o \\ \boldsymbol{\mu}=\boldsymbol{\mu}_o}} \boldsymbol{\mu}_o \\
F &= \mathbf{h}(\mathbf{x}_o, \boldsymbol{\mu}_o) - \mathbf{C}\mathbf{x}_o - \mathbf{D}\boldsymbol{\mu}_o
\end{aligned}$$

If the chosen evaluation point  $(\mathbf{x}_o, \boldsymbol{\mu}_o)$  is an equilibrium point of the system then  $\dot{\mathbf{x}}_o = 0 = f(\mathbf{x}_o, \boldsymbol{\mu}_o)$ , and the small-signal changes from the equilibrium point are defined as  $\Delta \mathbf{x}(t) = \mathbf{x}(t) - \mathbf{x}_o$ ,  $\Delta \boldsymbol{\mu}(t) = \boldsymbol{\mu}(t) - \boldsymbol{\mu}_o$ , and  $\Delta \mathbf{y}(t) = \mathbf{y}(t) - \mathbf{h}(\mathbf{x}_o, \boldsymbol{\mu}_o)$ , then eq. (D.14) becomes

$$\begin{aligned}
\Delta \dot{\mathbf{x}}(t) &= \mathbf{A}\Delta \mathbf{x}(t) + \mathbf{B}\Delta \boldsymbol{\mu}(t), \\
\Delta \mathbf{y}(t) &= \mathbf{C}\Delta \mathbf{x}(t) + \mathbf{D}\Delta \boldsymbol{\mu}(t).
\end{aligned}$$

For the rest of the work in this thesis the  $\Delta(\cdot)$  notation is dropped and it is understood that  $\mathbf{x}(t)$  and  $\boldsymbol{\mu}(t)$  refer to the deviation from the equilibrium. Then the set of LTI differential equations in state-space that approximate the dynamics of the nonlinear system  $\Xi$  in eq. (6.1) are given as

$$\dot{\mathbf{x}}(t) = \mathbf{A}\mathbf{x}(t) + \mathbf{B}\boldsymbol{\mu}(t), \quad (\text{D.15a})$$

$$\mathbf{y}(t) = \mathbf{C}\mathbf{x}(t) + \mathbf{D}\boldsymbol{\mu}(t), \quad (\text{D.15b})$$

where  $\mathbf{x}(t) \in \mathbb{R}^n$  is the state vector,  $\boldsymbol{\mu}(t) \in \mathbb{R}^m$  is the input vector,  $\mathbf{y}(t) \in \mathbb{R}^p$  is the output vector,  $\mathbf{A} = (a_{ij}) \in \mathbb{R}^{n \times n}$  is the plant matrix,  $\mathbf{B} = (b_{ij}) \in \mathbb{R}^{n \times m}$  is the input matrix,  $\mathbf{C} = (c_{ij}) \in \mathbb{R}^{p \times n}$  is the output matrix and  $\mathbf{D} = (d_{ij}) \in \mathbb{R}^{p \times m}$  is the feedforward matrix.

### **D.3** Derivatives of control-affine nonlinear systems

Consider a general nonlinear system given by

$$\begin{aligned}
\dot{\mathbf{x}}(t) &= \mathbf{f}(\mathbf{x}(t)) \\
\mathbf{y}(t) &= \mathbf{h}(\mathbf{x}(t))
\end{aligned}$$

where  $\mathbf{x}(t) \in \mathbb{R}^n$ ,  $\mathbf{y} \in \mathbb{R}$ ,  $\mathbf{f} : \mathbb{R}^n \rightarrow \mathbb{R}^n$  is a smooth vector field on  $\mathbb{R}^n$  and  $\mathbf{h} : \mathbb{R}^n \rightarrow \mathbb{R}$  is a smooth scalar function. The gradient of  $\mathbf{h}$  is denoted by  $\nabla \mathbf{h}$  and is given as a



row-vector:

$$\nabla h = \frac{\partial h}{\partial \mathbf{x}} = \left( \frac{\partial h}{\partial x_1}, \dots, \frac{\partial h}{\partial x_n} \right).$$

Similarly, the Jacobian of  $f$  is denoted by  $\nabla f$ , which is the matrix of the partial derivatives of  $f$  with respect to  $\mathbf{x}$ :

$$\nabla f = \begin{bmatrix} \frac{\partial f_1}{\partial x_1} & \cdots & \frac{\partial f_1}{\partial x_n} \\ \vdots & \ddots & \vdots \\ \frac{\partial f_n}{\partial x_1} & \cdots & \frac{\partial f_n}{\partial x_n} \end{bmatrix}.$$

Now consider the first time-derivative of  $y(t)$ :

$$\dot{y}(t) = y^{(1)}(t) = \frac{dh}{dt} = \frac{\partial h}{\partial \mathbf{x}} \frac{d\mathbf{x}}{dt} = \nabla h \dot{\mathbf{x}} = \nabla h f(\mathbf{x})$$

The following notation is now defined, with  $\mathcal{L}_f h = \nabla h f(\mathbf{x})$  denoting the **Lie derivative** of  $h$  with respect to  $f$ . It follows that the zeroth Lie derivative  $\mathcal{L}_f^0 h = h$ . This makes successive differentiation of  $y(t)$  simpler as the Lie derivative can be defined recursively so that

$$\mathcal{L}_f^k h := \mathcal{L}_f \left( \mathcal{L}_f^{k-1} h \right) = \nabla \left( \mathcal{L}_f^{k-1} h \right) f,$$

so that the  $k$ -th time-derivative of the output is given as

$$y^{(k)}(t) = \mathcal{L}_f^k h.$$

With this new notation, consider a input-affine<sup>1</sup> nonlinear system given by

$$\begin{aligned} \dot{\mathbf{x}}(t) &= f(\mathbf{x}(t)) + g(\mathbf{x}(t))\boldsymbol{\mu}(t) = f(\mathbf{x}(t)) + \sum_{j=1}^m g_j(\mathbf{x}(t))\mu_j(t) \\ y(t) &= h(\mathbf{x}(t)) \end{aligned}$$

where  $g_j : \mathbb{R}^n \rightarrow \mathbb{R}^n$  are smooth vector fields.

The first time-derivative of  $y(t)$  in this case is:

$$\begin{aligned} \dot{y}(t) = y^{(1)}(t) &= \frac{dh}{dt} = \frac{\partial h}{\partial \mathbf{x}} \frac{d\mathbf{x}}{dt} = \nabla h \dot{\mathbf{x}} = \nabla h \left( f(\mathbf{x}) + \sum_{j=1}^m g_j(\mathbf{x}(t))\mu_j(t) \right) \\ y^{(1)}(t) &= \mathcal{L}_f^1 h + \nabla h \left( \sum_{j=1}^m g_j(\mathbf{x}(t))\mu_j(t) \right) \end{aligned}$$

---

<sup>1</sup>input-affine simply means that the inputs appear linearly.



$$y^{(1)}(t) = \mathcal{L}_f^1 h + \sum_{j=1}^m \mathcal{L}_{g_j} h \mu_j(t)$$

if  $\mathcal{L}_{g_j} h = 0, i = 1, \dots, m$ , then the second-derivative of  $y(t)$  is

$$y^{(2)}(t) = + \mathcal{L}_f^2 h + \sum_{j=1}^m \mathcal{L}_{g_j} \mathcal{L}_f h \mu_j(t)$$

Continuing in this fashion for each successive derivative where it is assumed that each time  $\mathcal{L}_{g_j} \mathcal{L}_f^k h = 0$  for  $k < \rho - 1$  until the  $\rho$ -th derivative where

$$y^{(\rho)}(t) = + \mathcal{L}_f^\rho h + \sum_{j=1}^m \mathcal{L}_{g_j} \mathcal{L}_f^{\rho-1} h \mu_j(t)$$

where the integer  $\rho$  is the relative degree of output  $y$ , and at least one  $\mathcal{L}_{g_j} \mathcal{L}_f^{\rho-1} h \neq 0$ .